INDIRA GANDHI CENTRE FOR ATOMIC RESEARCH

2014

ANNUAL REPORT

सत्यमेव जयते

Government of India
Department of Atomic Energy
Indira Gandhi Centre for
Atomic Research
Kalpakkam 603 102

IGCAR

2014

INDIRA GANDHI CENTRE FOR ATOMIC RESEARCH

ANNUAL REPORT

Government of India
Department of Atomic Energy
Indira Gandhi Centre for
Atomic Research
Kalpakkam 603 102

“Actions today mould our tomorrows”

- Indira Gandhi

".... The relative role of indigenous science & technology and foreign collaboration
can be highlighted through an analogy.
Indigenous science and technology plays the part of an engine in an aircraft,
while foreign collaboration can play the part of a booster.
A booster in the form of foreign collaboration can give a plane an assisted take-off,
but it will be incapable of independent flight unless it is powered by engines of its own.
If Indian industry is to take-off and be capable of independent flight,
it must be powered by science & technology based in the country ..."

- Homi Jehangir Bhabha

".....There is a totality about modernisation, and in order to gain confidence, we must experiment with our resources even at the risk of failure. There is a need for a constant interplay between basic sciences, technology, industrial practice and management, if economic progress is to result from the activity undertaken"

- Vikram Sarabhai

Address for Correspondence
Dr. P. R. Vasudeva Rao
Chairman, Apex Editorial Committee
Director
Indira Gandhi Centre for Atomic Research
Kalpakkam - 603 102
Phone : +91-44-2748 0240/234
Fax : +91-44-2748 0060/301
Email : dir@igcar.gov.in
vasu@igcar.gov.in
Website : www.igcar.gov.in

CONTENTS

Back Cover

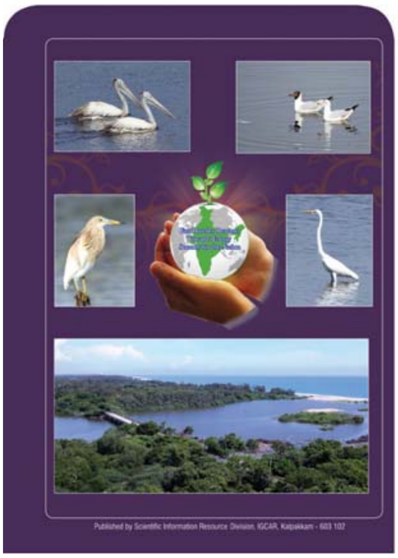

Front Cover

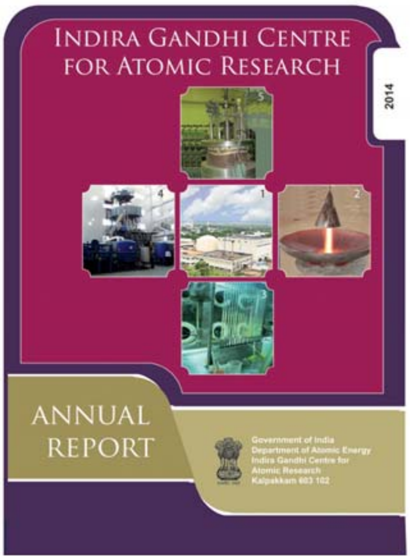

Front Cover

1. Fast Breeder Test Reactor
2. Experimental simulation of gravitational fall of B_4C granules
3. Mixer-settler experimental setup in a glove box
4. Inclined fuel transfer machine with auxiliary systems in position
5. Thermal striping test vessel

Back Cover

Flora and Fauna at Kalpakkam

Published by
Scientific Information Resource Division, Resources Management Group
Indira Gandhi Centre for Atomic Research, Kalpakkam - 603 102

Foreword

It is always a pleasure to write the foreword for the Annual Report of IGCAR. As the second largest R&D organization of the Department of Atomic Energy, IGCAR has established a reputation for outstanding research in a number of frontline areas, with a focus on the development of technologies for the fast reactor programme and at the same time addressing a variety of basic research issues.

During 2014, the operation of the Fast Breeder Test Rector has continued to provide us valuable experience and inputs for the fast reactor programme. We are particularly proud of utilization of FBTR as an irradiation facility. Today the reactor has carbide, oxide and metal fuels under irradiation which is now a unique feature of FBTR. The refurbishment of FBTR and strengthening of safety features have continued and we have now the confidence that the reactor is guarded against severe challenges including heavy flooding and earthquakes.

PFBR is now in its final stage of commissioning and we are looking forward to the first criticality of PFBR in the year 2015. IGCAR has worked closely with BHAVINI to address minor issues that crop up during the commissioning stages and also to obtain safety clearances for the operations. Simultaneously, we are studying several design aspects of FBR-1 and 2 towards enhancing the safety and economy so that we could provide the conceptual design to BHAVINI to enable it to launch the FBR projects at an appropriate stage.

CORAL has continued to operate very well and during the year, we had the unique experience of processing short cooled high burn-up, carbide fuel from FBTR, which demonstrated the robustness of the process flow sheet to provide adequate decontamination from the radioactive fission products and yield product of Uranium and Plutonium of high purity. The work on the Fast Reactor Fuel Cycle Facility has also started in right earnest and IGCAR is putting its best efforts with a small project team to drive the construction as per schedule. Towards developing metal fuelled FBRs, the irradiation of sodium bonded metallic fuels in FBTR has been continued and the work of establishing a Pilot Plant Scale Facility with a high temperature electrorefiner is in progress to demonstrate the pyrochemical processing of uranium and its alloys at 10 kg scale. Meanwhile, we have started planning for a facility to undertake pyrochemical processing of the irradiated metallic fuels that will be discharged from FBTR.

R&D on several domains related to fast reactor technology, spanning a wide range of disciplines including physics, chemistry, metallurgy, instrumentation etc. has continued and the report brought out highlights several unique results that have been obtained in these programmes. We are particularly happy that our expertise and knowledge base in high temperature materials has helped us to develop materials for fusion programme as well as for advanced ultra supercritical thermal power projects.

KAMINI has continued to provide neutron radiography support to Space programme. The work on MEG/MCG as well as infrared thermography among others are finding several applications for society at large.

As in the previous years, this year also IGCAR has had honour of receiving a number eminent scientists and technologists whose visits have provided great inspiration for our colleagues. The celebration of the Technology Day involving all technical staff, Peer Review programmes and mentoring of young colleagues were some of the unique programmes related to Human Resources Development and planning for future activities of the Centre.

IGCAR has also conducted a number of programmes during the year, celebrating the International Year of Crystallography and the Diamond Jubilee of the Department of Atomic Energy. Such programmes with participation from eminent personalities have further strengthened the scientific ambience in the centre.

The Annual Report provides more details of all the aspects that have been dealt with above, and it is to the credit of the editorial team, that we have put together the Annual Report with optimized content and enhanced quality.

I would like to convey my sincere thanks particularly to Dr. M.Sai Baba and his team for their earnest efforts in the challenging task of putting together a large variety of articles in a concise manner and at the same time comprehensive. I would like to acknowledge the contributions of Shri G.Pentaiah and Shri K.Varathan of SIRD for their efforts in the publication of the annual report. I look forward to the inputs from the readers about the report and its contents, and particularly, suggestions for improvement.

(P. R. Vasudeva Rao)
Director, IGCAR

Mission of IGCAR

« *To conduct a broad based multidisciplinary programme of scientific research and advanced engineering development, directed towards the establishment of the technology of Sodium cooled Fast Breeder Reactors (FBR) and associated fuel cycle facilities in the Country*

« *The development and applications of new and improved materials, techniques, equipment and systems for FBRs and*

« *To pursue basic research to achieve breakthroughs in fast reactor technology*

Vision

To be a Global Leader in Sodium cooled Fast Breeder Reactor and associated Fuel Cycle Technologies by 2020

Homage to Shri N. Srinivasan

Shri N. Srinivasan, the First Director of the Centre passed away on May 18, 2014. Shri N. Srinivasan was born on May 11, 1930. He joined the department in 1953 after graduating as Chemical Engineer and spent a few months at the Reactor School in Argonne National Laboratory, United States. He was responsible for the design of the plutonium plant at Trombay and also established indigenous technologies to reprocess spent fuels from thermal reactors. Shri Srinivasan established comprehensive facilities and initiated programmes towards development of fast reactors and associated fuel cycle, as the first Project Director of this Centre (erstwhile Reactor Research Centre). After his stint at IGCAR, he took over as the Chief Executive of the Heavy Water Board in 1982 and enabled the country to attain self sufficiency in heavy water production. He also served as the Chief Executive of the Nuclear Fuels Complex and Member, Atomic Energy Commission.

Shri N. Srinivasan was a recipient of Padma Bhushan in 2000 and Life Time Achievement Award of DAE in 2009, as well as several other awards/honours.

In the passing away of Shri N.Srinivasan, this Centre has lost a pioneering leader, well wisher and guide. The nation has lost a patriotic scientist whose every breath was for the growth and well being of India in general and Indian nuclear programme in particular.

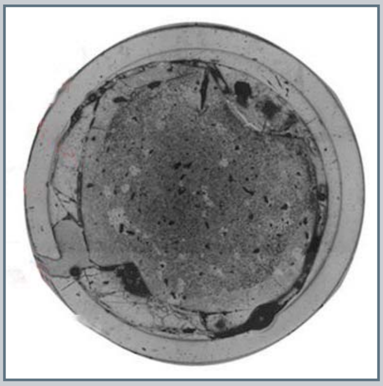

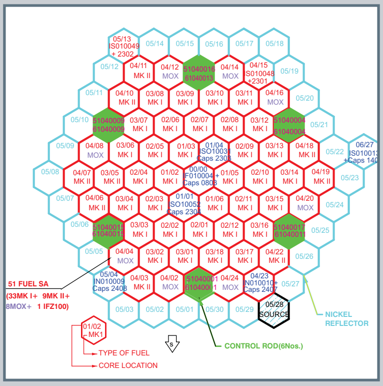

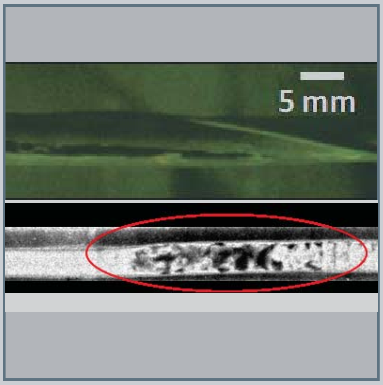

CHAPTER
I

Fast Breeder Test Reactor

I.1 Highlights of 22nd and 23rd Irradiation Campaigns of FBTR

Two irradiation campaigns, 22A and 22B were completed during the year. Campaign 22A was carried out for irradiation of the sphere-pac fuel pins in two steps at different linear heat rating (LHR) and durations as per the users' requirements. At the beginning of 2014, irradiation campaign 22A that had started in November 2013 was in progress. Reactor was in shutdown state till 11th January for rectification of high vibration in the primary west loop Ward-Leonard drive system. On 11th, the reactor was started and operated at 13.9 MWt for 200 hours for irradiation of the sphere-pac fuel test pins at 205 W/cm. Power was raised to 18 MWt on 29th January, corresponding to the linear heat rating of 260 W/cm for 100 hours of irradiation of the sphere-pac fuel test pins. After completing the irradiation, campaign 22A was concluded on 31st January and reactor was shut down. Subsequently, the irradiated sphere-pac fuel pins were discharged for post-irradiation examination.

Campaign 22B was started on 28th February. During this campaign, reactor was operated at 20.3 MWt with turbo-generator synchronized to the grid developing a power of 3.7 MWe for continuing the irradiation of the experimental subassemblies with metallic test fuel pins, low dose irradiation samples, etc. Reactor was shut down on 1st April when the Mark I fuel subassembly at 03/16 and Mark II fuel subassembly at 04/07 reached their target burn-up.

Based on the recommendation of SARCOP, four control rods (CRs) along with their outer sheaths which had seen close to their limiting fluence were replaced. Control rod's replacement requires transferring of six surrounding fuel subassemblies to outer locations after discharging the steel reflector subassemblies to facilitate discharging of the control rods with outer sheath. The fuel subassemblies were transferred back to their original locations after charging the new control rod and its outer sheath. The vacant locations after shifting the fuel subassemblies back to their original locations were filled with fresh thoria blanket subassemblies. Control rod replacement had to be done sequentially, each time starting the reactor to verify the availability of required worth of the loaded control rod. This involved a large number of fuel handling operations for charging, discharging and transfer of subassemblies. There were start ups for control rod calibration and worth measurement. After replacing of the four control rods and obtaining clearance from safety authorities, the 23rd campaign was started in November 2014 (Figure 1).

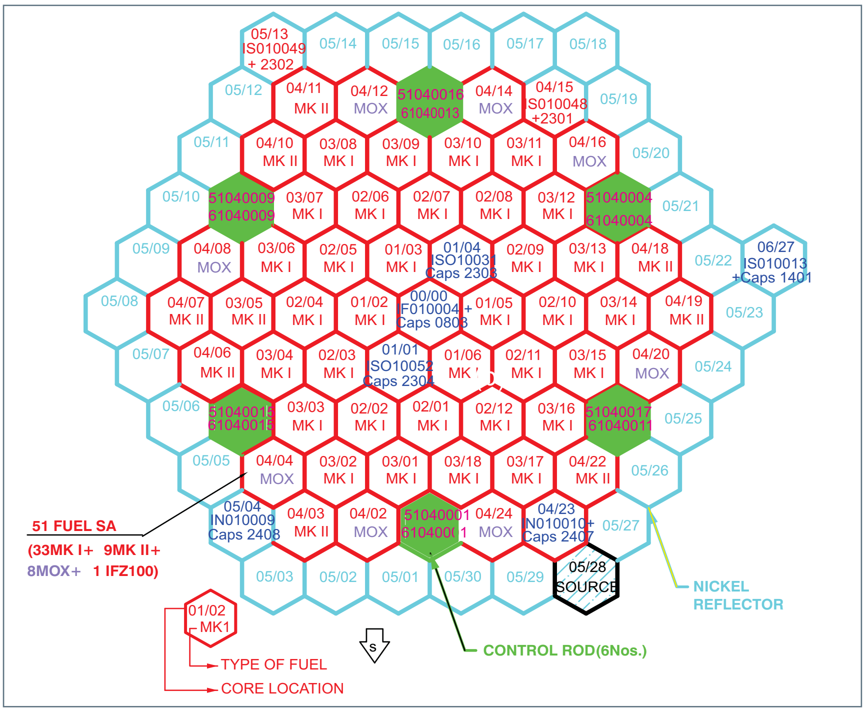

***Fig. 1** Core configuration for 23rd irradiation campaign*

Some of the major works and important surveillance carried out before the starting of 23rd campaign were visual inspection of reactor vessel and its internals, particulate and iodine test of reactor containment building filter banks, volumetric examination of the critical weld joints in secondary sodium system and inspection of steam generator hot roller supports.

During the operation at 24 MWt with feed water flow at 42 m^3/h, the highest so far, the silica level at the outlet of the steam generator was found to increase above the limit for operation with turbine, possibly due to removal of the silica deposited in steam generator during its operation. Turbine was shutdown and reactor power was reduced to 7 MWt. Cleaning of steam generator tubes was carried out by circulating hot water to remove the deposits to bring down silica level. Reactor was started after this and operated at 24.5 MWt with turbo-generator at 5 MWt.

I.2 Replacement of Four Control Rods in FBTR

In FBTR, six boron carbide control rods are used for reactor shutdown (SCRAM and LOR), regulation of reactor power and for burn-up compensation. These six control rods are placed symmetrically in the core in the 4th ring. During any campaign, the reactor power is regulated by the movement of these control rods. Also, these six control rods are required to shutdown the reactor safely in case of any abnormal state. The hindrance-free movement of the control rods is, therefore, essential for the safe operation of the reactor.

Control rod assembly

The control rod assembly consists of

- The support sleeve on the grid plate
- The outer sheath in which control rod moves and
- The control rod containing boron carbide

The sleeve of the control rod assembly is a long hexagonal piece extending 242 mm above the guide plate of the grid plate assembly. It rests on the support plate and is held in position by a screwed sleeve. It is held vertical by close fit in the guide plate region. The support sleeve has got a “L” shaped slot (Bayonet type) at the top for receiving and locking the control rod outer sheath.

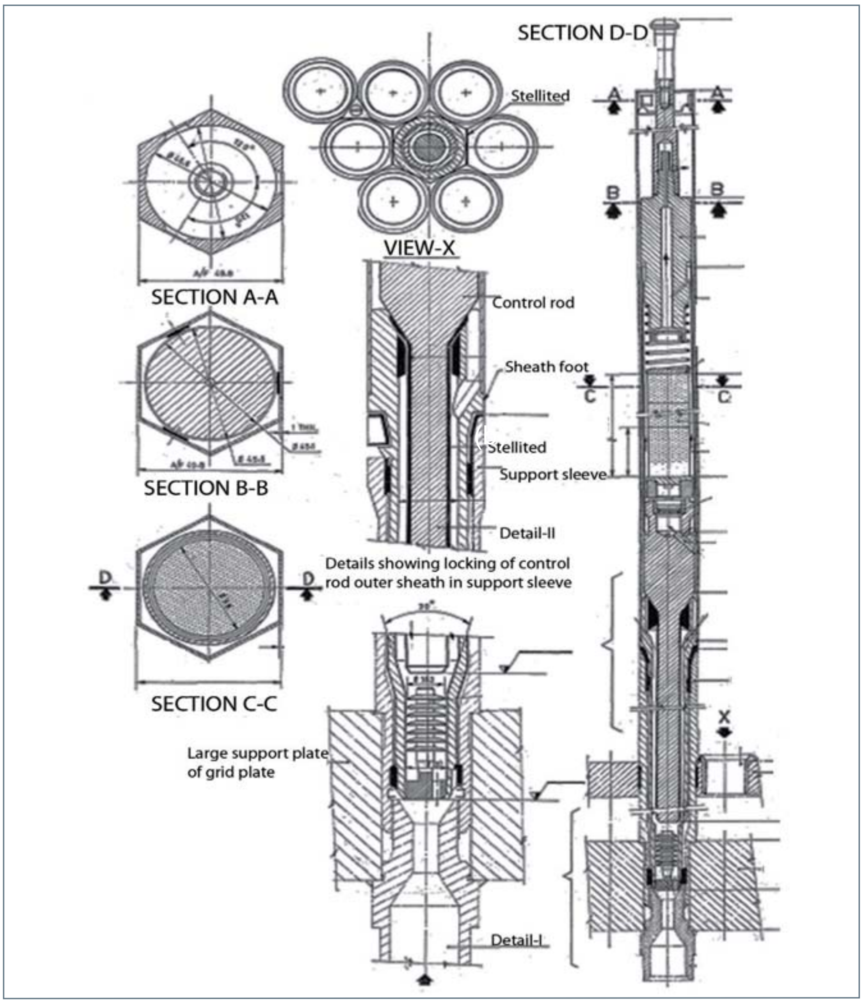

Fig. 1 Control rod assembly - vertical sectional view

The outer sheath of control rod is made of three parts namely foot, hexagonal sheath and handling sleeve welded together. In addition to guiding the control rod, it also houses the labyrinth orifice at the entry to limit the flow to the required value. To prevent the lifting of the outer sheath due to sodium pressure and movement of the control rod, the foot of the outer sheath is locked in the sleeve by a Bayonet type of locking arrangement. Outer sheath is made of stainless steel AISI 316L. The foot has a stellited conical shoulder to provide seating surface for the control rod when it is disengaged from the drive mechanism. Guiding the control rod is achieved by close fit between the cylindrical hole just below the conical cylinder and the long stem of the control rod (Figure 1).

The control rod contains neutron absorbing material boron in the form of sintered B_4C pellets. Natural boron has 90% ^{11}B and 10% ^{10}B. The latter isotope has higher neutron absorption cross section than the former. To enhance the effectiveness of the control material, it is enriched with 90% of ^{10}B.

The control rod is conceived to have a small sodium flow between the boron carbide pellets and the clad. This helps in better cooling of the boron carbide pellets and releasing the helium formed due to absorption of neutrons in boron (n, α reaction). Thus, the accumulation of helium gas and consequent pressure build-up is minimized. Hence, the life of the control rod is increased.

The residence time of control rod and its outer sheath in the core is limited by the neutron fluence seen by them. The technical specification limit on the fluence for

- Control rod is $<1.14 \times 10^{23}$ nvt
- Outer sheath is $<2.43 \times 10^{23}$ nvt

At the end of 22nd campaign (Figure 2), it was estimated that fluence limit on control rod would be crossed before the end of the 23rd irradiation campaign. Hence, as recommended by SARCOP, replacement of control rods A, B, D and F along with their outer sheath was completed. Control rods C and E have seen a fluence of only 1 x 10^{22} nvt as they were replaced in 2003 and 2005 respectively. Even though, fluence had not reached the limit for control rod outer sheath, it was necessary to replace it along with the control rod since the life of the control rod not only depends on the fluence limit, but also on the diametrical clearance between the control rod and outer sheath and the stem diameter of the control rod. This clearance is required to ensure smooth movement of the control rods.

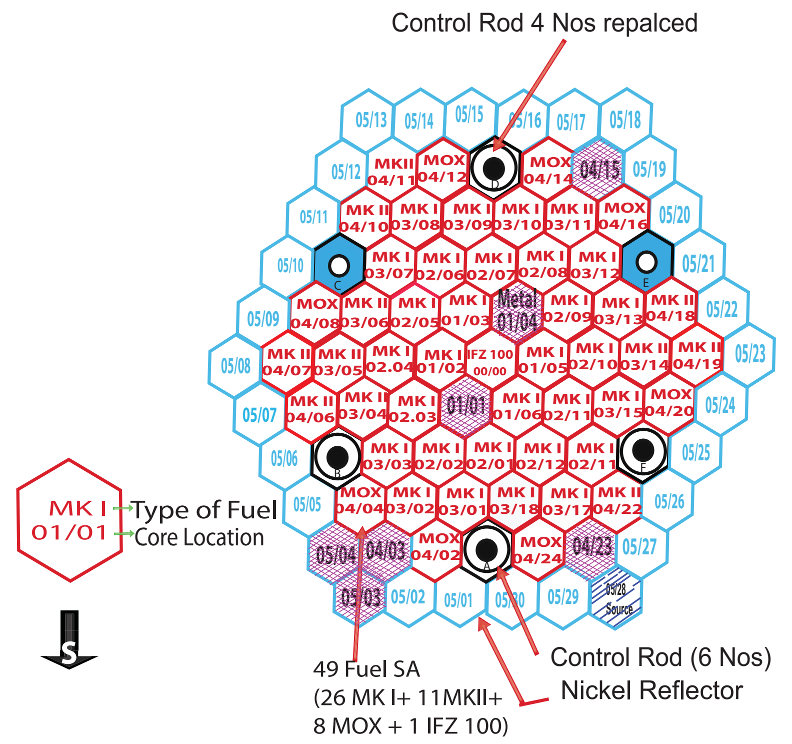

Fig. 2 Core configuration for 22nd campaign

Procedure for replacement of control rod

First, control rod was discharged from the reactor and charged in the discharge pot kept in the Transfer Block area of reactor containment building using the discharging flask. Before lifting the outer sheath of control rod from its location, it has to be rotated by 60° in anti-clockwise direction to unlock it from its supporting sleeve. Similarly during charging of the outer sheath of control rod it has to be rotated by 60° in clockwise direction to lock it to its support sleeve provided in the grid plate. To enable unlocking of the outer-sheath, six surrounding stainless steel subassemblies have to be transferred to vacant peripheral locations. To create vacancies, five subassemblies were discharged from the reactor during each campaign. Thus six vacancies were created including the permanent vacant position (16/33) for transferring the subassemblies surrounding the outer-sheath of control rod. After replacing the outer sheath of control rod and control rod, six subassemblies around the outer sheath of control rod were brought back to their original position from the peripheral locations where they were kept temporarily for storage. Five thoria blanket subassemblies were loaded in the vacant locations and one position remained as vacant storage location at the end of each campaign. The worth of control rod was measured after replacing the control rod with a new one. No other fuel handling operations were carried out during replacement of control rod. This sequence of operations was followed during replacement of every control rod and outer sheath of control rod. Table 1 gives the worth of the control rods before and after the replacement. The variation in the worth of all the control rods before and after replacement was found to be ±3% which is due to measurement error and difference in isotopic composition of absorber material (B_4C) of the control rod.

The results were reported to SARCOP and clearance was obtained for commencement of the 23rd irradiation campaign, which is currently in progress.

Table 1: Worth of the control rods before and after the replacement

Control Rod	Worth measured (pcm)	
	Before replacement	After replacement
A	1499.4	1526.4
B	1502.0	1627.9
C	1510.0	Not replaced
D	1408.0	1529.4
E	1442.7	Not replaced
F	1498.1	1505.4

I.3 Above-core Fast Flux Facility in FBTR

One of the main aims of FBTR is to gain experience in the operation of sodium cooled fast reactors and serve as an irradiation facility for the development of fuels and structural materials for future fast reactors. Normally irradiation is done in subassemblies loaded in the core. A new facility was added for fast flux irradiation above the core without contact with sodium. The temperature of the sodium, that emerges from each subassembly is monitored using thermocouples. Four thermocouples are provided as an integral part of the central canal plug (a part of the control plug) to monitor the temperature of the sodium at the outlet of the central subassembly. There is a cavity in the central canal plug which extends from the top to the bottom; the bottom is just above the central fuel subassembly head. This cavity was envisaged as a potential irradiation location above the core. The cavity is closed using a small auxiliary shield plug which ensures that the dose at the top of the plug due to neutron and gamma streaming is within the regulatory limits, while the reactor is operating.

In order to enable experiments to be carried out, the auxiliary shield plug of the central canal plug has been modified by attaching a long rod with a sample holder at its end. The position of the sample holder is below sodium level and about 15 cm on top of the central fuel subassembly (Figure 1). Insertion and removal of samples would be from the top of the reactor. The samples would not be in contact with sodium, but it is necessary that they are stable at the temperatures of sodium seen during reactor operation.

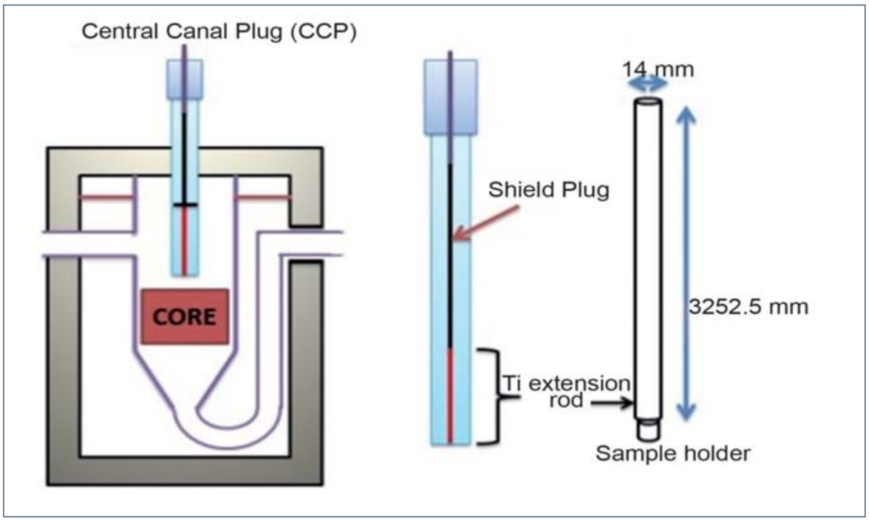

Fig. 1 Position of the sample holder

Various materials like pure nickel, stainless steel and titanium were examined for use as the extension rod. The major factors influencing the choice of material were the mechanical integrity under the irradiation conditions and the gamma dose seen due to the activation of the material and the impurities in the material. Both pure nickel and stainless steel showed very high gamma dose due to activation and hence, were discarded. Titanium was found suitable as the major reactions led to stable isotopes and the impurities produced were also not long-lived. The impurities in titanium were obtained by neutron activation analysis of a sample piece at DHRUVA, BARC. Based on these data, dose computations were carried out and it was seen that after operation for 10 days at 400 kW, the dose due to the titanium rod was about 125 mR/h at a distance of 2 cm and reduced to <1 mR/h at 1 metre distance.

Based on the above, a titanium extension rod of 3252.5 mm length and 14.0 ± 0.1 mm diameter was attached to the bottom end of the shielding plug. A titanium sample holder of 50 mm length and 12 mm diameter was attached to the bottom of this rod by screw joint. The bottom of the sample holder was in the form of a solid hexagon with a diameter of 12.12 mm across the flats (Figure 2).

Two test irradiations were carried out using the modified central canal plug with the sampler attached. In both cases about 10/15 mg of gold, wrapped in high purity aluminium foil was used. The irradiation time was about four hours at a power of 25 kW. The foils were assayed by high resolution gamma spectrometry and the gold equivalent flux was computed to be 2.5×10^9 $ncm^{-2}s^{-1}$.

Necessary regulatory permission for use of this facility is expected soon and the facility is expected to be operational for experiments.

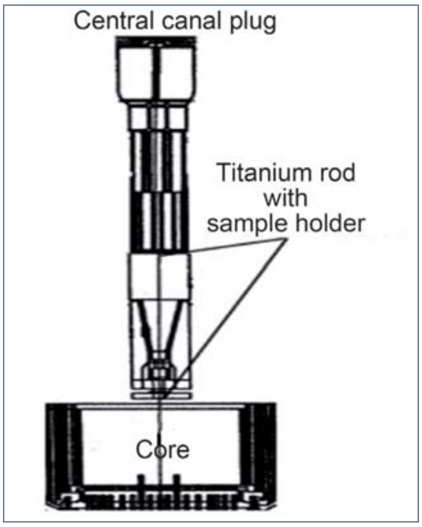

Fig. 2 Bottom of the sample holder

I.4 Civil Retrofits for FBTR due to Higher Design Basis Flood Level for Kalpakkam Site

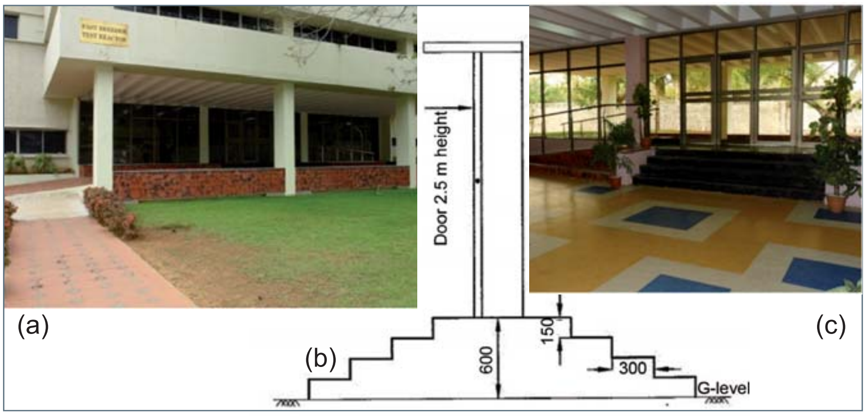

Fig. 1 *(a) Modified FBTR main entrance with steps and ramps, (b) schematic and (c) a view from inside*

In keeping with the aim of maintaining good safety culture, AERB initiated post Fukushima safety review of Nuclear Power Plants, Research Reactors, Fuel Cycle Facilities and other nuclear facilities.

In the above context and also in view of the increased flood level of Kalpakkam site and as per the studies carried out in the aftermath of Tsunami in 2004, safety review of FBTR complex was carried out by a in-house taskforce. The task force identified the vulnerabilities by plant walkdown method.

The finished floor level (FFL) of FBTR is 11.5 metres (RL-reduced level) with a margin of 3.5 metres above the design basis flood level of the FBTR site due to cyclonic conditions combined with high tide and heavy rain fall.

The revised flood level of FBTR site is 12.1 metres (RL) for the case of cyclonic storm with precipitation and 1000 years return period and in the event of a major tsunami triggered from Andaman, the water level could reach 13.1 metres (RL) as against the original design basis flood level of 8 metres (RL) for FBTR.

Reactor containment building of FBTR extends up to -15.6 metres below the reactor containment building floor level. Below the FFL, FBTR buildings except reactor containment building are interconnected through the peripheral gallery, technical galleries, cable and pipe trenches.

The secondary sodium storage tanks are located in the steam generator building in pits with large sodium lines below and above the floor level in this building. This building also houses the once through steam generators. A large number of control & instrumentation, electrical system panels, junction boxes and equipment and the relay room are also located at ground floor. The fresh and irradiated fuel storage areas are located outside reactor containment building in the Active Building.

Hence, flooding of any building up to the revised flood level will result in flooding of all areas and up to +600 mm from -15.6 metres around reactor containment building. This has other implications also since there are many cable penetration assemblies, Personnel Airlock and Material Airlock (PAL and MAL) for material and personnel access isolating reactor containment building from other buildings and providing leak tightness. These will see a large force due to water column.

In the case of beyond design basis flood, water can enter through any of the entry points around FBTR and RML, through the cable and pipe trenches below the flood level, drain lines of shower and toilets in the ground floor, openings and hatches provided through roof of peripheral gallery around reactor containment building.

Modifications required to individually address the various equipment and locations are not only complicated and needs extensive engineering but also impractical as they are time and cost intensive. Hence, retrofits were provided to prevent water entry to the plant buildings.

The revised design basis flood level of 12.1 metres for cyclonic conditions with precipitation and tsunami level of 13.1 metres were taken as the basis for civil retrofits.

The civil retrofits are to raise all the entry points by 600 mm above the earlier level.

FBTR main entrance has been modified keeping the aesthetics intact. The portico level was elevated and provided with a ramp from the approach road (Figure 1a). A flight of ascending and descending steps lead one to the zero level. (Figures 1b and 1c).

Fig. 2 *Truck entry areas provided with ramps*

The truck entry areas have been provided with ramps with suitable landings and steps (Figure 2).

Though the offsite power supply will be switched off in case of severe flooding, from electrical safety point of view after normalisation, flooding is to be avoided. Hence, the outdoor transformer cubicles are provided with short brick walls up to the revised flood level (Figure 3).

Leak tight flood barriers are attached to the rolling shutters up to 13.1 metres (RL) to prevent water entry into FBTR (Figure 4). These are designed to withstand the pressure of flood water.

The cable and pipe penetrations will be sealed with flood barrier materials.

The reactor containment building basement raft has been designed with suitable features to collect the ground water seepage and dispose it off. The annular portion between reactor containment building and peripheral galleries is covered with a reinforced cement concrete slab at ground level. This slab will be subjected to a pressure of 600 mm water in case of flood due to cyclonic condition and precipitation.

Fig. 3 *Outdoor transformer cubicles provided with short brick walls*

Fig. 4 *Rolling shutters with leak tight flood barriers*

The capability of the slab above the peripheral gallery to withstand the water column up to tsunami level has been verified by analysis and found to be adequate.

It is also planned to modify the windows in the ground floor to prevent water entry in case of tsunami.

Flooding due to precipitation is a slow phenomenon and the campus may remain flooded for days. The current retrofits protect against this. Tsunami forewarning system will give adequate time for the operator to manually shutdown the reactor before the tsunami strikes.

The current retrofits address floods due to cyclonic precipitation. For the postulated tsunami level of 13.1 metres, additional mobile flood gates have been designed and are being installed. The mobile shutters can be moved to the respective locations and fixed.

Thus, FBTR is safeguarded as per the revised flood level of designs.

I.5 Post Irradiation Analysis of a Mark-I Mixed Carbide Fuel Pin in FBTR

A Mark-I carbide failed fuel subassembly (FFSA) was received in the hot cells of Radiometallurgy Laboratory for post irradiation examinations (PIE) to investigate the cause of the failure. The FFSA located in the III ring of FBTR core had attained a burn-up of 148.3 GWd/t at the time of failure. Initial studies showed that a single fuel pin in the FFSA had failed with a longitudinal rupture of ~60 mm length and a maximum opening width of ~1 mm. Figures 1a and 1b show the photograph of the failed pin and neutron radiograph respectively.

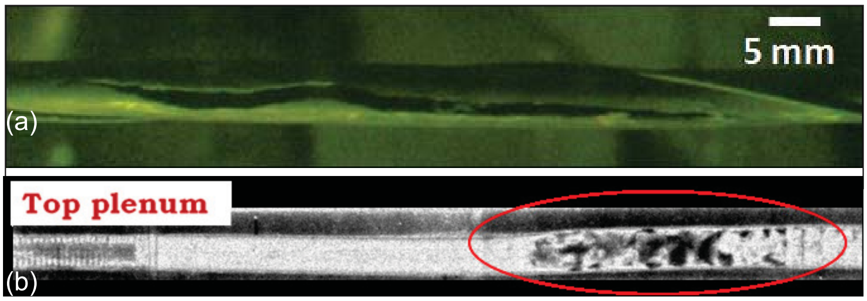

Fig. 1 *(a) Photograph of the failed pin and (b) neutron radiograph showing adherent fuel at the location of rupture*

Integrity of the remaining pins of the FFSA was confirmed through Eddy current testing and leak testing. The failed pin and twelve selected pins from the FFSA were subjected to comprehensive examinations to identify the cause of failure. The twelve pins were chosen based on their proximity to the failed pin and the extent of displacement damage seen by them. Investigations on these twelve pins were planned to assess the condition of the fuel and clad for signatures of impending failure, if any. Comparisons were also made with the results obtained from PIE of a subassembly from I ring which had safely reached a burn-up of 155 GWd/t (FSA$_{\text{I ring-155 GWd/t}}$) to arrive at the root cause and mechanism of failure. Fuel pins from another III ring FSA (FSA$_{\text{III ring-155GWd/t}}$) were also examined to ascertain whether conditions contributing to the failure are of generic nature.

Complementary non-destructive examination techniques including X-ray and neutron radiography, axial gamma scanning, eddy current testing and profilometry were performed to characterise the twelve pins that were intact. Based on the results, a few fuel pins of FFSA were selected for further examination through fission gas analysis, metallography, high-temperature tensile testing and swelling measurements of clad.

Neutron radiography of the failed fuel pin revealed adherence of the remnant fuel to the inner surface of the cladding indicating strong bonding of the fuel with clad (Figure 1b). Local bending of the fuel pins was observed in the X-ray and neutron radiographs in the failed pin and other fuel pins in the vicinity of failure location. Stack length increase measured by X-ray, neutron radiography and gamma scanning indicated higher increase (12-16 mm as compared to 8.5-11.7 mm observed in the pins of FSA$_{\text{I ring-155GWd/t}}$), indicating higher fuel swelling in the pins of the FFSA. Higher fuel swelling is due to lower linear heat rating experienced by the fuel in III ring.

Metrology of fuel pins of FFSA indicated higher diameter and length increase (max ΔD: 0.32 mm, max ΔL: 5.92 mm), as compared to 0.27 mm and 4.28 mm respectively in pins of FSA$_{\text{I ring-155GWd/t}}$. Fuel pins from another III ring FSA (FSA$_{\text{III ring-155GWd/t}}$) also exhibited similar trends in diameter, length increase as well as localised bending, as that of the FFSA.

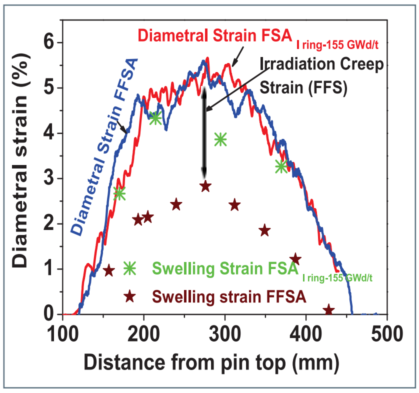

Fig. 2 *Swelling and irradiation creep components of diametral strain*

Pin diametral strain comprised swelling and creep components and their decoupling revealed that the swelling component is low with significant creep strain caused by Fuel Clad Mechanical Interaction (FCMI) stresses as compared to the pins of FSA$_{\text{I ring-155GWd/t}}$ (Figure 2)

The fuel pins with higher stack length increase were also seen to exhibit higher pin length increase suggesting significant contribution of FCMI to axial clad strains in addition to that of swelling. Higher radial and axial strains on the clad due to FCMI had also caused local bending in a few pins probably due to constraints from adjacent pins or spacer wire.

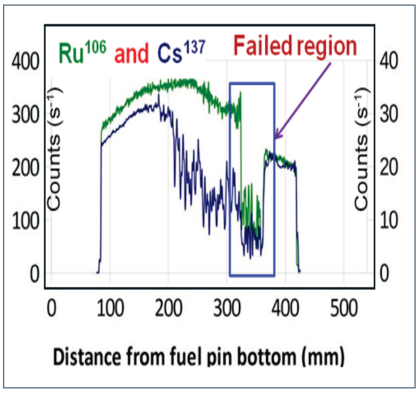

Fig. 3 *Axial gamma ray profile of failed fuel pin showing extensive migration of volatile fission product*

Axial gamma scanning of the fuel pins adjacent to the failed pin exhibited extensive migration of volatile Cesium isotopes at axial locations starting near the peak power location and ending near the failure location, while no such migration was noticed in the far away pins within the FFSA. This is indicative of higher fuel temperatures in the fuel pins adjacent to the failed pin. Figure 3 shows the axial gamma ray profile of the failed fuel pin. Fission gas release and pressure in the fuel pins adjacent to the failed pins were also found to be significantly higher as compared to far away pins. Similar trends of Cs migration and fission gas release were also noticed in the fuel pins of the FSA$_{\text{III ring-155GWd/t}}$.

Metallographic examinations of the failed pin (Figure 4) and an adjacent fuel pin showed asymmetric circumferential cracking pattern in some of the axial locations suggestive of non uniform temperature distribution around the pins. While the axial locations at the bottom of the fuel column indicated symmetric cracks similar to those observed in the fuel pins of FSA$_{\text{I ring-155 GWd/t}}$, those above the peak power location towards the top of the fuel pin showed asymmetric circumferential cracks. This asymmetry is attributed to the constriction of coolant flow in localised spots around the pins, where the pins are in near-contact with the adjacent pins due to

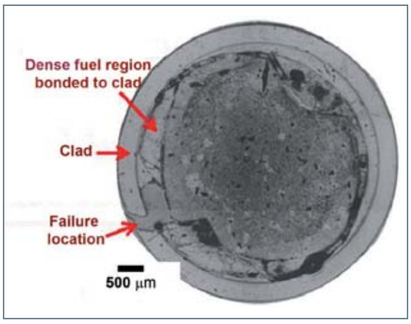

Fig. 4 *Microstructure of transverse section of failed fuel pin taken at the failed location*

diameter increase and localised bending. Clad microstructure did not indicate any carburization on the clad inner diameter and this was also confirmed by micro-hardness measurements.

Tensile tests on 60 mm long clad tube sections along the fuel column from an adjacent pin showed no evidence of severe loss of tensile strength and ductility of cladding at axial locations close to failure. The micro hardness of the clad at locations of failure was marginally higher than that of unirradiated clad suggesting plastic deformation of the cladding associated with failure. Fracture surface analysis of the replicas taken from the middle of the fractured location indicated mixed mode of fracture showing both brittle and ductile features in the failure region (Figure 5).

It may be noted that the fuel pins in the III ring FSAs have undergone lower linear heat rating as compared to I ring FSA due to the lower neutron flux resulting in higher fuel swelling. After the plugging of a few steam generator tubes in FBTR to achieve higher sodium inlet and outlet temperature for materials irradiation, clad mid-wall temperatures have increased by around 63° (after 14th campaign of FBTR), at the axial location corresponding to the failure. The higher fuel swelling and lower clad swelling has led to severe FCMI stresses on the cladding of the FFSA. The increased diametral strain combined with local bending could have led to coolant flow constriction between the adjacent pins, resulting in localized fuel and clad temperature increase.

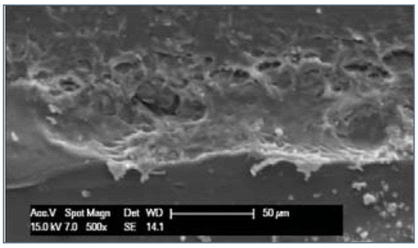

Fig. 5 *Replica of the failed fuel pin fracture surface showing mixed mode of failure, as seen in SEM*

The higher stresses combined with higher clad temperature have resulted in failure of the clad by creep rupture.

The single pin failure could be attributed to an adverse combination of operating conditions and local stress/temperature environment. Thermochemical modelling would provide insights into the deformations of fuel pin in the IIIrd ring fuel subassemblies.

I.6

Testing of High Temperature Fission Chambers of PFBR in KAMINI

In the Prototype Fast Breeder Reactor, three high temperature fission chamber detectors with the sensitivity of 0.1 cps/nv are provided one over the other in the instrumented central subassembly for monitoring the flux during fuel loading and startup of reactor. Six high temperature fission chambers with sensitivity of 0.2 cps/nv provided in the control plug are used for intermediate power level. Six fission chambers with sensitivity of 0.75 cps/nv are installed in tubes below the safety vessel and are used for safety actions in power level.

To qualify the high temperature fission chamber detector, the environment in PFBR such as neutron flux (10^9 nv), gamma field (100 kR/h) and temperature (570 ºC) had to be simulated simultaneously.

In FBTR, it was tested in 1.0×10^9 nv neutron flux, 100 kR/h gamma field and temperature up to 450°C.

As the first two conditions can be simulated in KAMINI reactor, a special high temperature fission chamber detector housing (high temperature test set-up) was designed, fabricated and installed in KAMINI reactor to simulate the 3rd condition of high temperature (570°C) for qualifying the high temperature fission chamber.

Set-up for high temperature fission chamber's testing at KAMINI

A special high temperature test set-up (size 200 mm dia x 3700 mm long) was designed and fabricated from Inconel-600 (Figure 1).

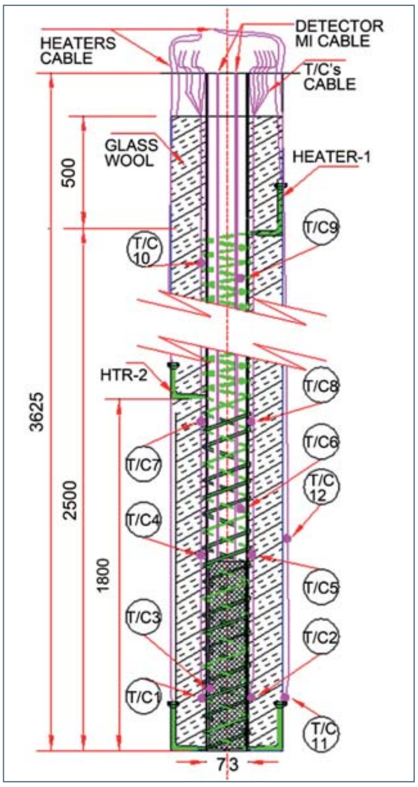

Fig. 1 *Schematic of the test setup*

Three mineral insulated cable type heaters and seven K-type (2 mm) thermocouples have been provided in the inner tube of the detector housing.

The assembly has been provided with two mineral insulated (comprises magnesium oxide layer) cable type heaters having 1.625 and 1.425 kW heating capacity wrapped around the inner tube (outer dia 73 mm) with a uniform pitch length of 30 mm. For temperature monitoring of water pool three thermocouples are provided, two on the outer surface of the assembly and one dipped into water pool. An embedded system having 'auto' (PID and 'ON/OFF') and 'manual' modes of temperature control is used for heater control and temperature monitoring. To prevent heat loss from the test assembly and reduce reactor water temperature rise, rock wool blanket as thermal insulation is provided between inner and outer tubes.

A location, just above the in-tank fuel storage assembly area in KAMINI water pool (-2.7 metre elevation from top of the reactor tank) was selected for installation of the high temperature test setup to achieve a neutron flux level of 10^9 n/cm^2/s at the detector location. In order to arrest the buoyancy effect in water pool, the setup (weight ~250 kg) was supported with a fabricated stainless steel split clamp support bracket and bolted to the existing structural member at top of the reactor tank. Before testing high temperature fission chambers in KAMINI, a mock-up test was conducted outside for checking the pool temperature rise (Figure 2).

Table 1: Detector specifications

Description	Detector type	
	0.2 cps/nv detector	0.1 cps/nv detector
Dimensions (long)	63 mm OD x 668 mm	63 mm OD x 417 mm
Electrode gap	0.8 mm	0.8 mm
Charge collection time	40 ns	40 ns
Gas fill	Ar+N_2 (3%) at 6 bar	Ar+N_2 (3%) at 6 bar
Coated area	714 sq.cm	172 sq.cm
Material	Inconel-600	Inconel-600
Cable	Two tri-axial MI cables	Single tri-axial MI
Inter-electrode capacitance	450 pF	100 pF
Gamma tolerance	270 kR/h	270 kR/h

As the set-up removes axial shielding provided by the water pool, an annular ring shield filled with ferro boron (about 400 mm is provided between inner tube and outer tube, which also facilitates routing of mineral insulated cable, thermocouples and detector cables. A stainless steel cylindrical trough & tray type complementary shielding (350 mm dia x 400 mm height) is attached to minimize the radiation streaming. After supporting this setup adequately, the reactor tank was closed with temporary top covers (two 4 mm stainless steel sheets) (Figure 3).

A test tank was fabricated (1.076 m^3 volume as against 14 m^3 reactor tank of KAMINI). The mock-up test for eight hours with detector at 570°C showed that the temperature rise was 8°C, equivalent to ~0.6°C rise of KAMINI pool water.

High temperature fission chambers testing was carried out with detector temperature at 570°C with reactor power increased in steps up to 30 kW for three hours. Measured flux at the detector location was about 5×10^6 n/cm^2/s and temperature rise of the reactor tank water was about 2°C.

Detector specifications are given in Table 1.

Installation of the High Temperature Test setup in KAMINI has provided a permanent facility for testing and calibration of high temperature fission chambers of PFBR as and when required.

Fig. 2 *High temperature fission chamber test setup*

Fig. 3 *Complementary shielding*

CHAPTER
II

Prototype Fast Breeder Reactor

II.1 Construction Status of Prototype Fast Breeder Reactor

Supply and erection of all major critical reactor components and Nuclear Steam Supply System (NSSS) have been completed. Transfer arm which is used for in-vessel transfer of subassemblies has been received and erected. Pre-commissioning of the same is under progress. Inclined fuel transfer machine which is used for ex-vessel transfer of subassemblies has been erected and the trial run of transfer pot movement in primary and secondary systems have been completed (Figures 1 and 2).

Motors of primary sodium pumps were erected and integrated with the pump. High temperature boron coated neutron detectors required for initial fuel loading operation has been received and erected in control plug. Control safety rod subassemblies and diverse safety rod subassemblies were erected in control plug.

The construction of fuel building has been completed and erection of major fuel handling components has been completed. Most of the equipments have been commissioned locally from local control panels. Fuel handling equipments commissioning from control room console is under progress. Commissioning of switchgear interface programmable logic controllers has been completed.

Fig. 1 *Erection of inclined fuel transfer machine*

Pre-commissioning of all main control room, handling control room and local control panels have been completed.

The civil construction work of turbine building has been completed and erection of turbine equipments and all auxiliary equipments have been completed. Turbine box-up and main steam piping has been completed and major milestone of turbine rolling on barring gear has been completed. Auxiliary boiler burn-up and steam blowing activities have been completed. Condenser water fill test on shell side has been completed. In Turbine Plant, no load test for Motor Driven Boiler Feed Pump (MDBFP) has been completed. No load test of jacking oil pump for Turbine Driven Boiler Feed Pump (TDBFP) has been completed (Figure 3).

Sample pre-heating of the main vessel by air has been completed. Preliminary reactor containment building leak test has been carried out in various pressures up to 250 mbar, the leaks were identified and arrested. This leak test has indicated directions to improve the AERB indicators.

Commissioning of integrated secondary sodium system first loop in steam generator building-1 has commenced and pressure hold test of argon lines has been completed. Commissioning of the conventional and auxiliary supporting systems such as raw water, emergency service water, demineralized water, compressed air have been completed.Service building air washer system has been

Fig. 2 *Transfer arm erection*

Fig. 3 *Overall view of turbine floor*

Fig. 4 Intake structure

Fig. 5 Overall view of PFBR

commissioned.

The civil construction works of sea water pump house has been completed and erection of condenser cooling water pumps, auxiliary sea water pumps have been completed. The lining concrete of sea water intake structure sub marine tunnel has been completed up to 567 metres (Figure 4). The horizontal sea water intake tunnel and vertical shaft of the tunnel has been connected and made through. Concrete of column and wall of intake super structure has been completed up to RL (reduced level) 13.95 metres .

Initial core cofiguration document has been made ready. One hundred and nine fuel subassemblies and one hundred and twenty blanket subassemblies are ready for initial core loading of PFBR.

The project has achieved an overall physical progress of 97.635% at the end of December 2014 (Figure 5). Two major milestones, i.e. first criticality in July and power operation in September have been planned in the forthcoming year.

II.2 Confirmation of PFBR Preheating Scheme by Mock-up Studies on Reactor Assembly and Fuel Subassembly Models

As the melting point of sodium is ~98°C, all the components of sodium system and piping have to be preheated to ~150°C, before sodium filling. Nitrogen is circulated in a closed loop by blowers through a bank of heaters, at a flow rate of 10 kg/s for preheating reactor assembly internals in PFBR. Uniform heating of all the components to 150°C is a challenging task due to the presence of multiple complicated parallel flow paths of the heating medium (nitrogen).

The proposed strategy for PFBR is to raise nitrogen temperature by a maximum of 10 °C per day.

Mock-up facility is established to confirm the preheating strategy of PFBR on 1/13 scale down model of PFBR reactor assembly with all internals and one full scale model of fuel subassembly. In the scaled down model of reactor assembly, core thermal inertia and flow fractions are simulated without the exact geometrical features of subassembly. Air flowing in an open loop is used as preheating medium to simulate PFBR preheating scheme in both the models.

Description of mock-up facility models

Scaled reactor assembly model

Major reactor assembly components of scale down model are: i) safety vessel, ii) main vessel, iii) inner vessel, iv) grid plate, v) core support structure, vi) core, vii) top shield viii) control plug, ix) primary sodium pump, x) intermediate heat exchanger and xi) decay heat exchanger.

Fuel subassembly model

There are 217 pins with the internals similar to the actual fuel subassembly and the flow path is exactly same as the prototype. Fuel pins are simulated with equivalent solid steel pins. The subassembly is vertically erected on a single sleeve support. The simulation of temperature is focused in the tube bundle region as this is the most complex portion of the subassembly heating.

Preheating mock-up facility

The preheating mock-up facility (Figure 1) consists of a blower which sucks air from atmosphere and drives it through an inlet manifold. A bypass valve is connected to the inlet manifold to regulate the flow rate through the system. Air flows through the heaters and gets heated up to the desired temperature by controlling heater power.

The metered air flow from the blower can be sent through either of the mock-up facilities (reactor assembly/fuel subassembly) by control of valves.

In reactor assembly preheating, hot air enters the model through two inlets connected to hot pool locations of main vessel and three inlets to main vessel-safety vessel (MV-SV) inter space. Air comes out of the model through the outlet from cold pool location and three outlets from the MV-SV inter space after transferring heat to the internals and is vented out to atmosphere. Temperatures of air inlet, outlet, at outlet of each heater and temperatures of the critical locations (56) in the model are monitored continuously by K-type thermocouples (61 numbers) with error band of 1.1°C or 0.4%. In the fuel subassembly mock-up, flow enters at the top of the subassembly through a diffuser and passes through the subassembly and leaves through the foot to exhaust line. Twenty two thermocouples are mounted at various locations of the subassembly to monitor the temperature distribution.

Electrical heater

Cartridge type electrical heaters are used as heat source to give the required heat input to air. Three heater modules with 7 kW each (Figure 1) are connected in series. 230 V, single phase AC power supply is given to each heater module. Temperature of air entering the mock-up facility is maintained by heater control unit.

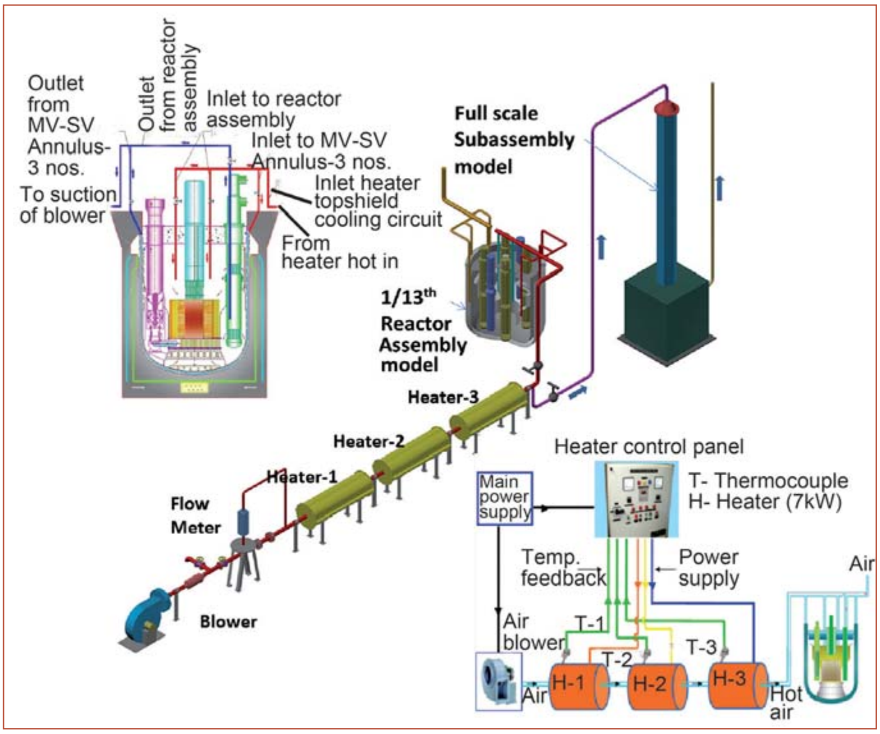

Fig. 1 *Schematics of pre-heating mock-up facility for 1/13th reactor assembly model and a full scale subassembly model*

Instrumentation

All thermocouples are connected to two numbers of data acquisition systems. Data acquisition systems are connected to a personal computer using ethernet cable for continuous monitoring and recording of the temperature data. Recording of data is done at two levels for diversity with one level at data acquisition system and the other in a computer. Mimics for the data acquired are made to visualise the preheating process online.

Preheating methodology

Before heating, the facility (Figure 2) is at normal atmospheric conditions. Mock-up on reactor assembly model is conducted by keeping the inlet valve to subassembly pipe in a

Fig. 2 *Reactor assembly and fuel subassembly mock-up facilities*

fully closed condition. Blower is then started keeping bypass valve fully open and inline valve fully closed. Inline valve is subsequently opened in an incremental manner to adjust the flow through the system to the required flow rate and is further stabilised. At this condition, heaters are switched on to raise the temperature of the air flowing through the model. The system is allowed to stabilize and temperatures are monitored to notice the stabilization time.

Once stabilized temperatures are reached, air inlet temperature is raised by 10°C and allowed for thermal stabilization in the model for the new inlet air temperature. The process is continued till all structures reach 180°C. Temperature evolution thus obtained from the experiment gives the data on temperatures of all the structural members.

Similarly, mock-up test is carried out on the fuel subassembly model by keeping the flow control valve in reactor assembly inlet fully closed.

Reactor assembly model

The observed temperature evolution during the preheating mock-up of model of reactor assembly is shown in Figure 3a. The mean temperature of structures has attained a stable temperature after considerable time from the change in inlet air temperature.

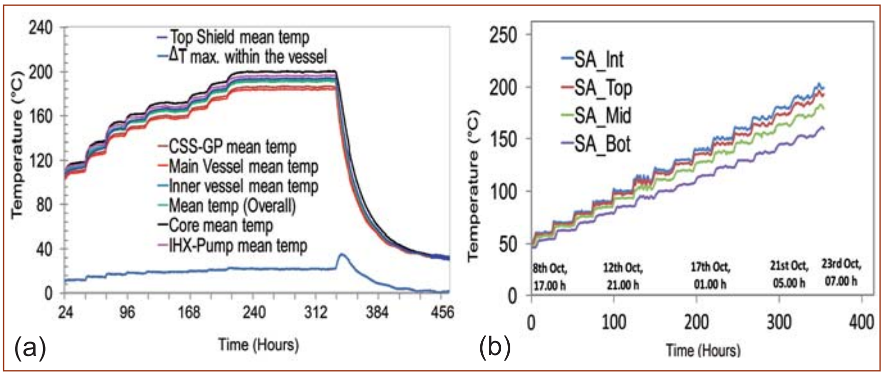

Fig. 3 *Evolution of temperatures in the components during preheating of (a) 1/13th reactor assembly model and (b) full scale fuel subassembly*

It is observed from the results that all the components are getting heated up simultaneously and uniformly. The trend of temperature evolution has followed theoretical prediction for PFBR (Figures 4a and 4b). In reactor assembly, the maximum temperature difference observed is between the top portion of core and bottom portion of main vessel. At the end of the campaign ΔT between these two locations is 22°C (which is within the tolerance limit).

Subassembly model

The temperature evolution in the fuel subassembly with time is shown in Figure 3b. The maximum temperature difference between the central and peripheral pins at any axial location is less than 20°C at any point of time. Variation of temperature along the length of the subassembly is shown in Figure 5. Fall of temperature is due to the loss of heat through the subassembly surface. In the actual case the loss is expected to be very less since neighboring subassemblies are also at almost same temperature. The estimated temperature distribution matches with the measurements and is shown in Figure 5. This trend along with Figure 4, confirms that the preheating scheme envisaged for PFBR is fairly qualified.

Thus, mock-up facility to simulate 1/13th model of PFBR reactor assembly and full scale fuel subassembly preheating has been commissioned at our Centre. It is confirmed that all the structures are heated up at a uniform rate and the ΔTs are within allowable limits and there is sufficient margin for any differences for model to full scale results.

The need for experimental validation of the preheating procedure was felt as a prerequisite to PFBR commissioning and, as the related activities at the site are in an advanced stage, the entire task including design, construction, commissioning and mock-up studies were completed within a short span of time.

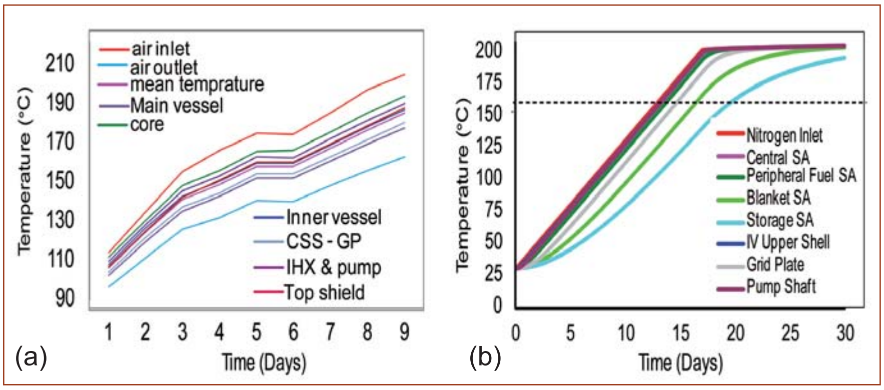

Fig. 4 *(a) Evolution of temperatures in model during mock-up and (b) estimated thermal evolution in PFBR during preheating*

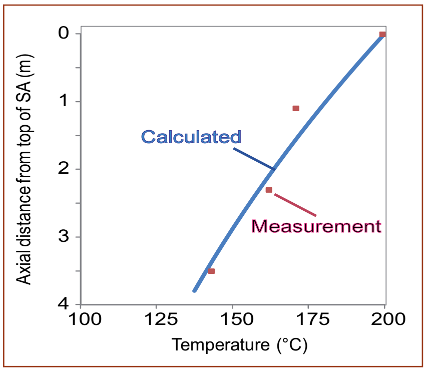

Fig. 5 *Calculated versus measured temperature distribution within the fuel subassembly*

II.3 Flow Induced Vibration Studies on Seven Subassembly Cluster

Flow induced vibration studies were carried out on seven subassembly cluster, at Engineering Hall-II. The experiments are conducted using water as test fluid. The simulation criterion from water to sodium is established from the Burgreen correlation for the fuel subassembly vibration and the required test flow is 1316 m^3/h. Figure 1 shows the water test loop. A perspex window was embedded to the top of the test section to visualize the movement of subassemblies during the testing (Figure 2).

Subassembly vibration was measured using under-water accelerometers installed on the subassemblies and flow through the subassembly was measured using annular flow meter. Pump B of capacity 1200 m^3/h at 100 metres head in the SAMRAT model was used for the studies. The maximum flow rate achieved during the experiment was 1150 m^3/h, which corresponds to 87% of the test flow. Experiments were conducted for various flow rates ranging from 350 to 1150 m^3/h.


Fig. 1 *Flow induced vibration test loop*

Fig. 2 *Test section perspex window*

Vibration time signal (acceleration) and its spectra were recorded during the testing for each flow conditions. Figure 3a shows the typical time signal and its spectra corresponding to a flow rate of 550 m^3/h and Figure 3b shows the typical time signal and its spectra corresponding to a flow rate of 1150 m^3/h.

From the measured acceleration signal, the displacement signal was derived. Root-mean-square (RMS) displacement in 1-100 Hz frequency range was calculated for all the flow conditions at the sensor locations of 0° and 120° and plotted in Figure 4.

The maximum amplitude of displacement at the subassembly top was found to be 0.38 mm for the flow rate of 1150 m^3/h and is found to be within the limit. Testing at higher flow rates is planned to be carried out in seven subassembly test loop at Engineering Hall-IV.

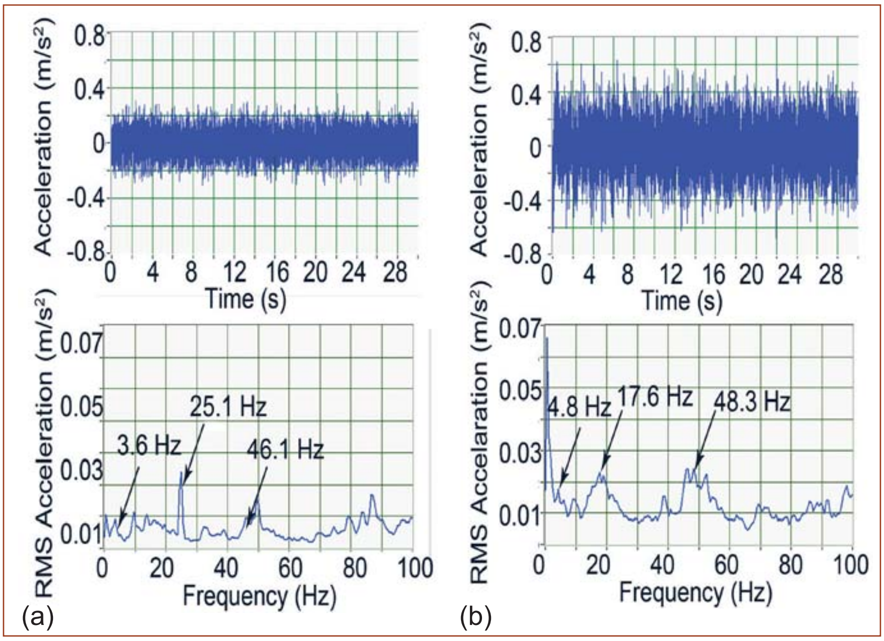

Fig. 3 *Vibration measured on top of subassembly at (a) 550 m^3/h and (b)1150 m^3/h. (The top portion of the figures gives the time signal while the bottom portion gives the fast fourier transform acceleration)*

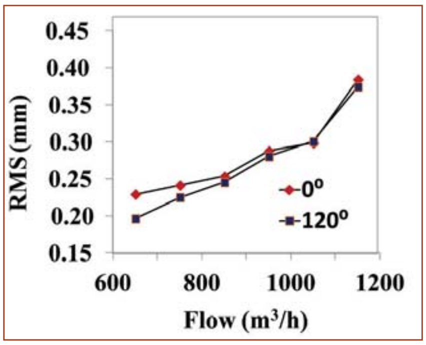

Fig. 4 *Displacement root-mean-square versus flow of sensor locations (0° and 120°)*

II.4 Calibration of PFBR Permanent Magnet Flowmeters

Permanent magnet type flowmeters (PMFM) are used to measure the sodium flow in pipelines of PFBR circuits. Permanent magnet type flowmeters of pipe size varying from 15 to 200 NB were designed and manufactured for PFBR. There are totally 62 permanent magnet flowmeters of 12 different categories which are to be used in PFBR. It is planned to calibrate one flowmeter in each category in-sodium. Flowmeters of size 80 NB and above are calibrated in large component test rig (LCTR) and flowmeters of size below 80 NB are calibrated in thermal shock test facility (TSTF). These flowmeters are calibrated by absolute volumetric method. Flowmeters are installed in test vessal-2/test vessal--3 dump line of LCTR and TP-2 dump line of TSTF to calibrate them in sodium.

During the first campaign, 80 NB double wall, 100 and 150 NB single wall permanent magnet flowmeters were installed in the test vessel-3 dump line of LCTR and 50 NB single wall permanent magnet flowmeter was installed in the TP-2 dump line of TSTF. In LCTR and TSTF, when the respective dump valve is opened, sodium in test vessel flows to dump tank by gravity. An instrumentation system was made ready for acquiring millivolt output from each pair of electrodes by using a data logger. Scan interval was set at one second so that for every one second millivolt output from all pairs of electrodes of the flow meter was scanned and stored. While draining sodium from test vessel, millivolt output of flowmeters was acquired at every second and stored in the personal computer. From this data, the sensitivity of the flowmeter was calculated. Calibration runs were repeated at different sodium temperatures and different flow rates. Figure 1 gives the photograph of flowmeter installed in dump line for sodium calibration. Figure 2 shows the schematic of the calibration setup with data logger. Flow trace during calibration of 150 NB single wall permanent magnet flowmeter is given in Figure 3.

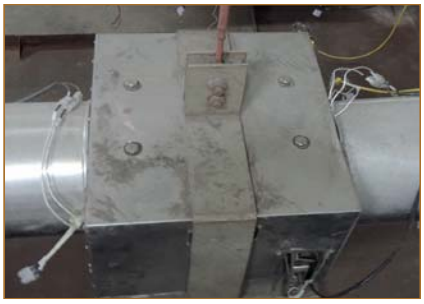

Fig. 1 *Flowmeter in dump line*

Based on millivolt readings and time obtained from the trial runs, total millivolt seconds was estimated for known sodium volume draining. The total millivolt seconds (mV.s) and the quantity of sodium drained were equated to obtain millivolt output per one cubic meter per hour flow. So far, calibrations of 80 NB double wall, 100, 150 and 50 NB single wall permanent magnet flowmeters were completed. Sensitivity was found to be 0.2189 $mV/m^3/h$ for 80 NB double wall flowmeter, 0.1858 $mV/m^3/h$ for 100 NB single wall flowmeter, 0.1172 $mV/m^3/h$ for 150 NB single wall flowmeter and 0.4048 $mV/m^3/h$ for 50 NB single wall flowmeter respectively. Accuracy of the calibration is well within 0 ± 1.5%.

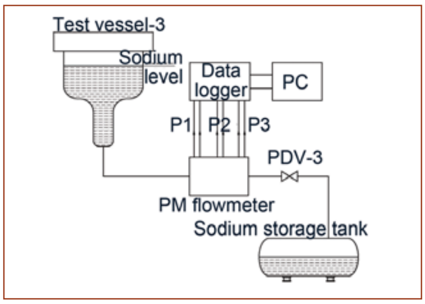

Fig. 2 *Calibration setup with data logger*

Calibration results of 150 NB single wall permanent magnet flowmeter are given in Figures 4 and 5. It was seen from the calibration results, that there was no significant change in the flowmeter output due to variation in sodium temperature and sodium flow. Calibration of remaining flowmeters is under progress.

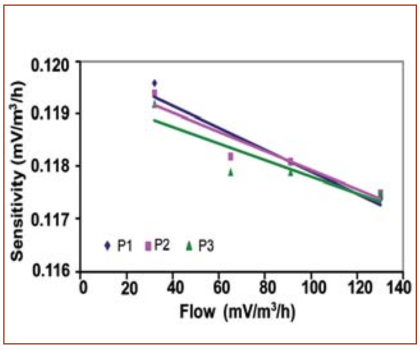

Fig. 3 *Flow trace during calibration (flow versus sensitivity curve at 350°C)*

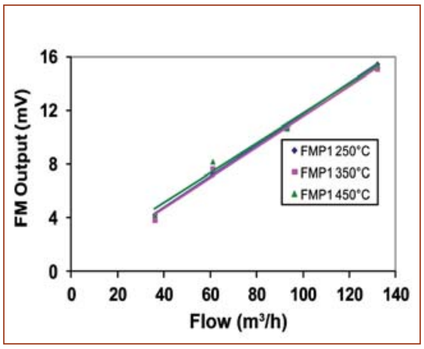

Fig. 4 *Flow versus output of 150 NB flowmeter at differential temperatures*

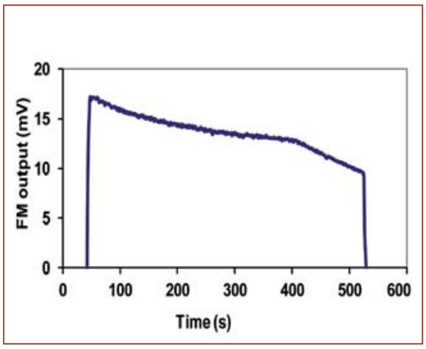

Fig. 5 *Calibration curve of 150 NB permanent magnet type flowmeter*

II.5 Design, Fabrication & Commissioning of the Test Facility for In-Sodium Testing and Qualification of the Bearings used in IFTM Transfer Pot

Inclined fuel transfer machine (IFTM) is used for ex-vessel transfer of core subassemblies in PFBR. Transfer pot (TP) carrying subassembly moves in the guide and tilting rails provided in various parts of the IFTM. Guide/tilting rollers are provided on TP for its movement in the guide/tilting rails provided on parts of IFTM. Bearings made of SS-440C material is used in both guide and tilting rollers. During the ex-vessel transfer, one cycle comprises of movement of transfer pot from in-vessel transfer position (IVTP) location to ex-vessel transfer position (EVTP) location and vice versa, which is approximately 60 metres of travel distance. In each cycle, the bearings provided on transfer pot moves inside the sodium at 200°C for initial and final 7 metres travel (i.e 14 metres) and subsequent 29 metres travel is in cover gas at 150°C. Remaining 17 metres travel is at 50°C argon ambience in secondary side. The envisaged number of cycles of IFTM operation during 40 years of reactor life is 6000. It is important to assess the performance of the bearing in sodium, the performance of the sodium wetted bearing in hot and cold argon ambience. It is also important to demonstrate the cycle life of the bearings under the simulated loading and operating conditions as in reactor. Testing and qualification of the bearings was carried out in sodium at conditions simulating reactor fuel handling. Testing of the guide roller bearings validates both guide and tilting roller bearings as guide roller bearings are smaller and see more load. The axial load on guide roller bearings is 302 N and the radial load is 1005 N. The equivalent static load of the bearings is 1005 N and equivalent dynamic load is 3600 N. It was planned to carry out the performance testing in TP-2 of SILVERINA loop in Hall-1 by simulating equivalent dynamic load.

Initially the bearings were tested in air. The setup mainly consists of support structure, support plate, top flange, inner shaft, outer pipe, top flange for test setup, disc spring stack, drive system and bearings. The top flange supports the drive motor with gear box and other components in the test setup. The bearing to be tested was mounted on inner shaft. The outer race of the bearing was rigidly held in a bearing housing which was welded with the outer pipe. The outer pipe was welded with the top flange of the test setup. The load was applied on the test bearing using disc spring stack. By compressing the disc spring stack, load was applied on the inner race of the bearing with respect to the outer race through the inner shaft. The drive system consisting of electric motor with reduction gear box, chain and sprockets rotates the test bearing at 15 revolutions per minute. The inner race of the test bearing was rotated along with the inner shaft.

Testing of the bearings in air was completed. The torque measured for the rotation of the bearing was 3 Nm before applying load. The disc spring stack was compressed by 1.8 mm to apply a load of 3774 N. After loading, the torque measured was 4 Nm. However, this value was increasing with continuous dry running of the bearing in air beyond 150 rotations. By immersing the bearing in acetone bath, the torque measured was constant and it was around 4 Nm. This was taken as the base line data. The constant torque in acetone environment is possibly due to flushing of particles produced during running and uniform temperature across the bearing. After operating for around 50000 cycles in air, the top flange along with the test setup was lifted and assembled on TP-2 of SILVERINA sodium loop. Figure 1 shows the test setup for in-sodium testing. Short time rotation in argon at 50 and at 150°C shows that torque values are around 4 and 5 Nm respectively. After charging sodium, bearing was rotated under load for 1.1×10^5 rotations. It was seen that the torque value was around 4 Nm and there was no increase in the trend with increase in the number of rotations in sodium. Subsequently, sequential testing in sodium at 200°C for 7 minutes, argon at 150°C for 15 minutes and in argon at 50°C was done for 8 minutes and the torque values measured were 4, 5-6 and 17 Nm respectively. Repeatability of the measured values was observed during 20 cycles of operation. Bearings were rotated in argon at 150°C for 4×10^5 rotations and the torque value was constant. Bearings were rotated in cover gas at 50°C for 50000 cycles and the torque value measured was 16 Nm. The increase in torque is due to presence of solidified sodium between races and balls.

Fig. 1 *Bearing test setup in sodium*

The experiment shows that bearings perform smoothly in sodium and in argon cover gas at 150°C cover gas (up to secondary gate valve in IFTM). In EVTP cell, at 50°C, the effective clearances of the bearing may reduce due to solidification of sticking sodium resulting in increase in running torque.

II.6 Testing of Inclined Fuel Transfer Machine in Hot Air at Manufacturer's Shop

Inclined fuel transfer machine is used for handling and transfer of subassemblies into and out of the main vessel. Using this machine, the subassembly loaded at in-vessel transfer position (IVTP) located in the periphery of the core is transferred to the ex-vessel transfer position (EVTP) located in fuel building and vice versa. Manufacture of the machine and cyclic testing in air was completed. It was planned to test 10% of envisaged life in reactor (600 cycles) to qualify the performance of the machine. Primary tilting mechanism (PTM) and primary ramp (PR) of IFTM were tested in sodium under simulated conditions in the reactor for 600 cycles and installed in PFBR. Testing and qualification of the shield plug and primary gate valve under simulated conditions as in reactor i.e. in cover gas with sodium aerosol ambience was carried out. Rest of IFTM components are exposed to argon. Components up to secondary gate valve are at 150°C and remaining of the components of IFTM in EVTP cell are at 50°C. Hence, integral testing of IFTM with non reactor grade PR & PTM was planned for 600 cycles, out of which, 65 cycles were tested in air at room temperature and remaining 535 cycles were tested in hot air with simulated temperature distribution. Figure 1 shows IFTM during integral testing in hot air.

During hot air testing of the IFTM, non reactor grade PR & PTM were heated by tape heaters such that PTM is maintained at 200°C and PR temperature varies from 200°C to 140°C from the bottom to top. An solid state relay based control panel with the necessary control thermocouples is provided for heating PR & PTM. Hot air was used for heating rotatable shield leg (RSL) liner, sprocket in argon chamber to 150°C (simulating hot argon heating in reactor). The temperature on RSL liner was monitored and based on thermal hydraulic analysis of the IFTM components the temperatures to be maintained on transfer pot (TP) surface were arrived at. The temperature of RSL liner for 180°C on TP surface is 80°C and this is achieved by a heating and cooling system. Air heating system consists of a 3 m^3 air buffer tank maintained at 800 mbar pressure with feed/bleed arrangement. Air was circulated (406 m^3/h @ 200°C /280 m^3/h @ 45°C) by means of a blower and this flow was measured by a flow transmitter. Cooled air flow of 10 m^3/h measured by metal tube rotameter, was tapped from the discharge of the hot air blower, supplied to the space between support table and Leak Tight Cell, below the bottom inflatable seal. Balance air was supplied to a tubular electric heater of approximately 14.5 kW capacity (4 heater banks, each 3.625 kW capacity), where it was heated to 200°C. A flow of 6 m^3/h tap off from hot air supply was used to heat sprocket region of hoisting system. Return flow from RSL was passed through a cooler with cooling capacity of 8 kW and cooled to 50°C. Two-stage cooling was adopted for cooling the return hot air to 50°C. After installation and preliminary checks, the heating system was interfaced to IFTM through piping systems. The piping system was complicated and installation was completed without interferences after preliminary trials. Heaters of 12 kW capacity were used in the inlet line of the hot air system to maintain the temperature till RSL. Cooling of the region of the inflatable seals & sprocket seals was achieved by an air cooling system. Air cooling system was installed and commissioned and the required flow rates of 55 m^3/h flow to inflatable seals and 5 m^3/h flow to sprocket seals was achieved. The required temperatures of IFTM components were also achieved. Inflatable seals were actuated using Argon gas at pressure of 700/400 mbar. Leak testing of the IFTM and piping system connecting IFTM to auxiliary systems was carried out by pressure hold testing. The leak rate achieved by pressure hold test of the machine for the region between the gate valves was 0.7 scc/s. The existing sealing between the sprocket shaft and seal housing was changed from O rings to V seals based on feedback during PR & PTM testing in sodium. Tension sensing mechanism was modified to a new design. Visual, dimensional and pressure hold test of all inflatable seals was carried out. Dimensional inspection of the seals was carried out before testing and the seals were found acceptable. The leakage of the seals is around 6.3×10^{-2} to 6.45×10^{-2} scc/s at 300 mm bar and 1.8×10^{-1} scc/s, when tested at 700 mbar.

Fig. 1 *Inclined fuel transfer machine with auxiliary systems in position*

Hot air testing of IFTM for 535 cycles was completed. During testing, the movement of transfer pot was smooth. The motor current and torque recorded were found to be within the specified limits for both hoisting and RSL rotation. Smooth locking and unlocking of RSL was also achieved. After completion of testing, all components were inspected visually and cleared for delivery.

II.7 Qualification of Coupling of Primary Sodium Pump and Trailing Cable System for PFBR

Coupling of pump

In PFBR, the primary sodium pump (PSP) is designed to run at an inclination of 0.146° for long period during various reactor operating conditions. Hence, the motor-pump coupling shall be uniquely capable of absorbing the relatively large inclination and operate for prolonged periods. This requirement is in variance to requirement of the coupling between the driver 'motor' and driven 'pump' shafts that are aligned as close as possible in general applications. A gear type spacer coupling was originally conceived and the same was tested for performance at the manufacturer's site. This type of couplings are heavy and due to the restriction posed by the construction, dynamically balancing to finer grade is difficult. Further, continuous lubrication is also a very important requirement for the smooth functioning of the gear coupling, hence, requiring close monitoring and frequent maintenance. Alternately, to overcome above difficulties, disc type laminae coupling is considered (Figure 1), which are capable of withstanding large misalignment and can be balanced to finer grades. Also, they do not require any lubrication and frequent maintenance. Therefore, a judicious decision was taken to replace the gear type spacer coupling with a disc type coupling for the primary sodium pumps.

A detailed testing and qualification program was undertaken to prove the functionality and suitability of the disc type coupling. The testing program was conceived in a novel way to simultaneously qualify both the coupling and the ball transfer unit.

Fig. 1 *Disc type laminae coupling*

Fig. 2 *Ball transfer unit of coupling*

During the first phase trial testing of 48 hours under inclined condition in a test set up, the pivot supporting the spacer load in the coupling exhibited minor rubbing marks. To overcome this aspect, further improvement in the design was incorporated after detailed discussions with coupling manufacturer. The new design adopting standard ball transfer unit (Figures 2 and 3) for the bottom part and the mating top part (AISI SS 410 material) was tested for 48 hours. Prior to testing, the top part was indented to a depth of 30 microns to match the spherical profile of the ball transfer unit. During this trial, the top part showed an impression/wear of about 120 microns depth and 7 mm diameter. The wear was observed to be 90 microns (i.e. 120-30 μm) depth. It was decided to proceed with the same pivot assembly (ball transfer unit and top plate) to test the second coupling assembly (i.e. further 48 hours of testing) to confirm that the wear is not increasing and stable. The final indentation/wear in the ball transfer unit was observed to be close to 120 microns. Thus the above sets of trails simultaneously qualified entire coupling assembly including the ball transfer unit. Also, in-parallel theoretical calculation carried out proved that the induced contact stresses with the intended profile in the top plate was within acceptable limits. Hence, the

Fig. 3 *Coupling during balancing*

disc coupling was systematically qualified for use in primary sodium pump.

Trailing cable system

Two rotatable plugs i.e., small and large rotatable plugs (SRP & LRP) are provided to facilitate in-vessel handling of core subassemblies using transfer arm. These plugs are rotated during refuelling. The control and instrumentation signals and power to various systems/components located on the rotatable plugs are carried by cables and connecting them to their respective control panels located outside. Among large number of signals/power supply, some are needed during rotation of the plugs also. Hence, their cables are routed through trailing cable system which ensures continuous connectivity during plug rotation as well.

The trailing cable system consists of three posts mounted one each on SRP/LRP & roof slab and set of overhanging arms (cantilevers) through which, cables are routed in a predetermined way. The overhanging arms are supported from the posts at a higher elevation in order to avoid interference with transer arm during rotation of the plugs.

The cables from LRP are first taken up to the LRP post top and routed between LRP-SRP posts through two overhanging arms A & B as shown in Figure 4. The loop of cable between the overhanging arms gets twisted whenever SRP is rotated relative to LRP and this span of cable provides the required flexibility during rotation. The maximum rotation of SRP with respect to LRP is ½ turns and a free cable length of ~1 metre is provided in the loop to accommodate this twist. The overhanging arms are positioned radially towards SRP centre to avoid need for any extra length of the cables during rotation of SRP relative to LRP.

Over SRP, the cables from SRP (16 numbers) join those from LRP and are combined by taking up further along SRP post. The cables are then routed through another set of overhanging arms 'C'&'D' and cable spacing/guiding mechanism to the outside of roof slab. The overhanging arm 'C' brings the cables to the centre of SRP where as the overhanging arm 'D' which is ~3 metres above the arm 'C' takes the cables out from the centre of LRP. These two arms are interconnected through the cable spacing/guiding mechanism.

The cable spacing/guiding mechanism consists of clamping discs at the ends and several guiding/spacing discs between them. The thin circular cable guiding/spacing discs having slots along the periphery for the passage

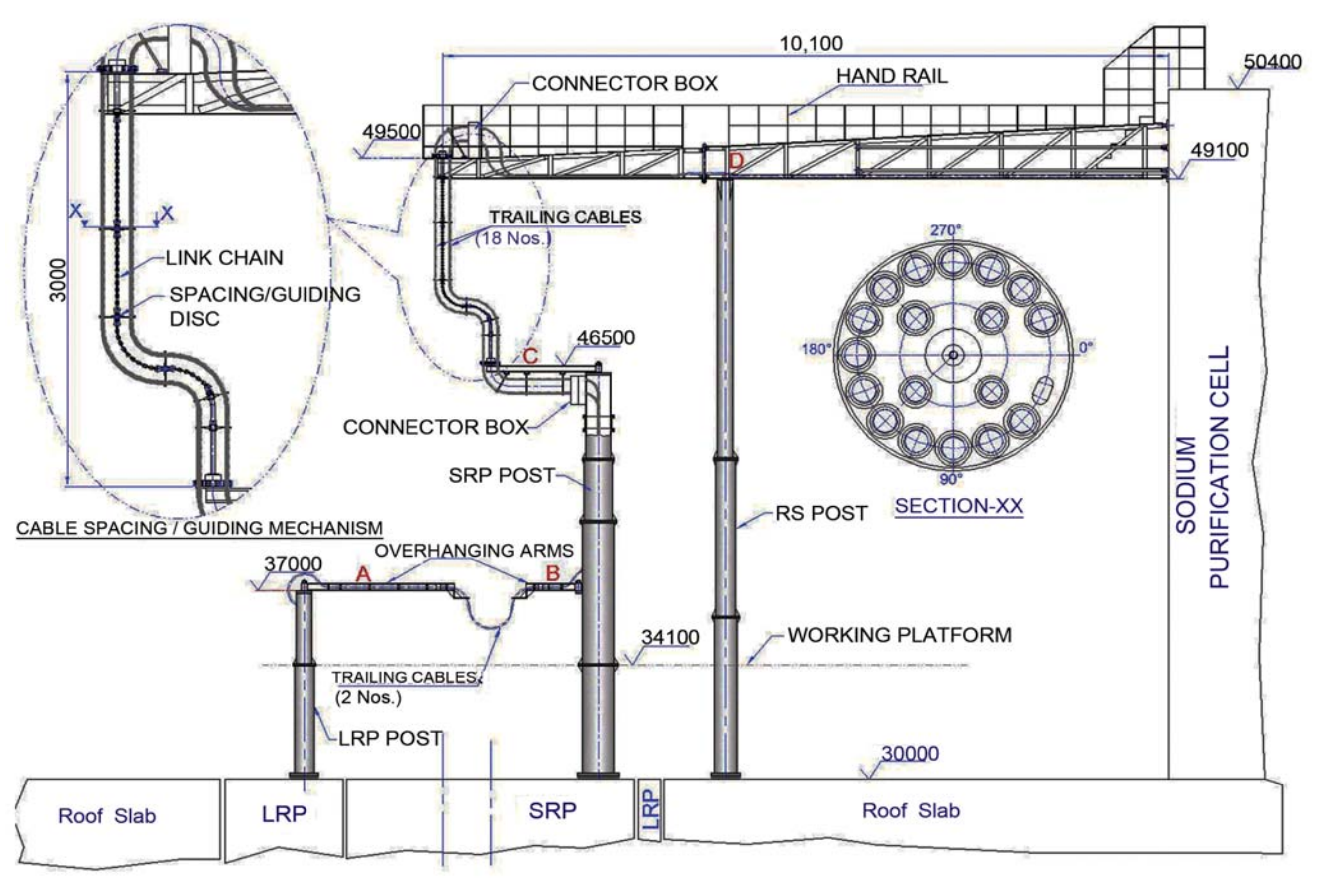

***Fig. 4** Schematic of trailing cable system*

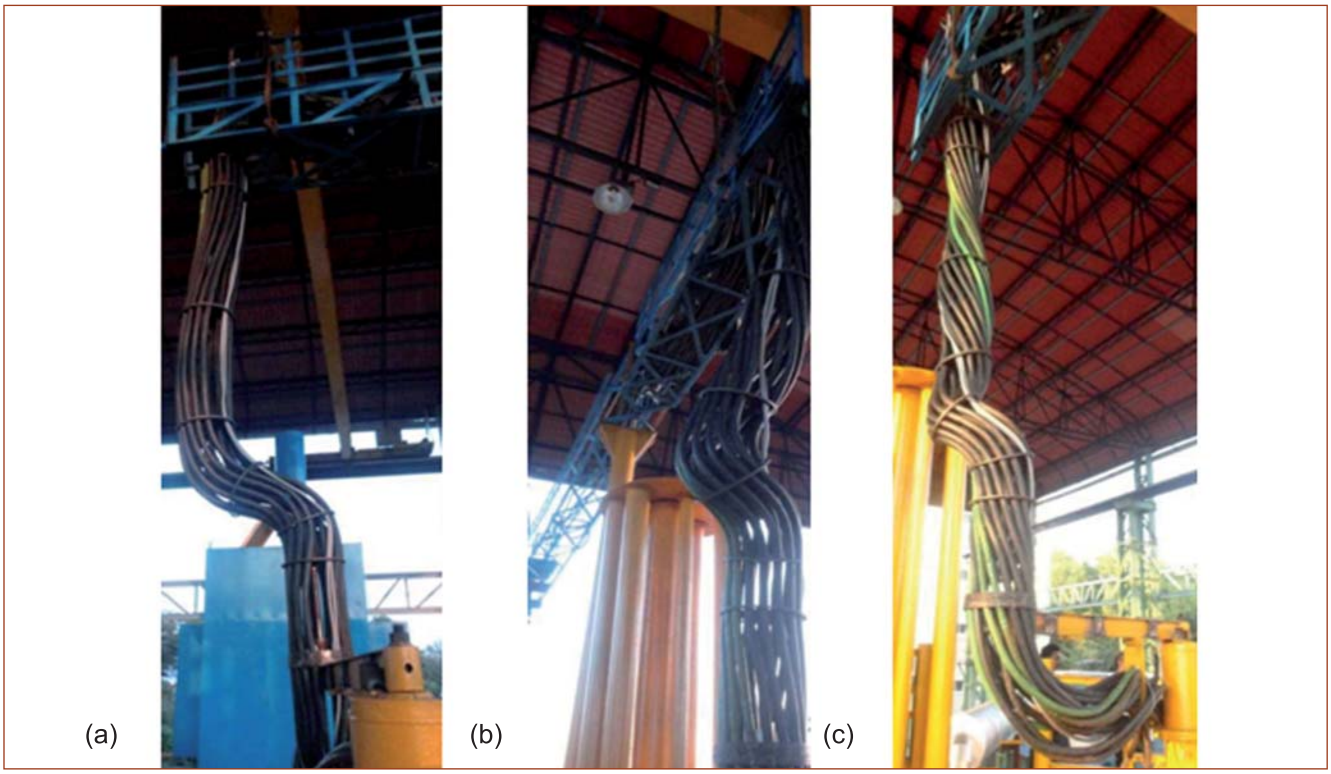

Fig. 5 Profile of trailing cables under different plug positions (a) SRP-0° & LRP-0°, (b) SRP-0° & LRP-360° and (c) SRP-180° & LRP-360°

of individual cables, separates and guides the cables when plugs are rotated and thus prevent any entanglement. The discs are supported from the arm 'D' through flexible chain links connected at the centre of the discs. Since the maximum angle of rotation of SRP is 180° and that of LRP is 360°, the cables between the two overhanging arms 'C' and 'D' get twisted to a maximum of 540° (1.5 turns). The level difference of 3 metres between the two arms 'C' and 'D' ensures the availability of ~3.2 metres of cables to accommodate this twist and this translates to a twist of 180° per meter length of cable.

As part of overall qualification trials of the trailing cable system as per design intent, the parts of the system were fabricated and erected with 18 numbers of trailing cables at top shield layout model (TSLM).

Following objectives were identified for qualification.

- Finalising assembly/erection methodology
- Establishing the profile of cables and demonstrating slackness/extra length of the cables provided is sufficient to absorb the total twist of 540° resulting from plug rotations
- Finalising the positions of the spacing discs
- Verifying the smooth sliding of the cables through the discs and bringing out the required measures to ensure the same
- Demonstrating smooth twisting & untwisting of the cables
- Demonstrating overall functionality of the mechanism

Subsequent to erection of system over TSLM, the plugs were rotated into & pro motion to observe and verify the functionality of trailing cable mechanism. The shape of the bunch of cables at different stages, viz., home position, after rotation of LRP by 360° and after additional rotation of SRP by 180° are shown in Figure 5.

From the above qualification exercise, the important observations are:

- The mechanism conceived is capable of accommodating the twisting of the cables during rotation of the plug
- An additional cable length of only 300 mm is required between the two clamping discs to have uniform twisting of the cables without entanglement
- Teflon bushes are to be provided at the interface of the cables and the passage holes provided in the discs to avoid cable damage and smooth sliding
- Finalisation of the location of spacing discs
- Since the cable guiding/spacing mechanism is located at higher elevation at PFBR site, it is preferred to complete the assembly of all the discs with the cables to obtain the required shape for the bunch of cables in horizontal condition itself on the floor level and then using a fixture, to install the same at elevated location.

With the above, the trailing cable system is successfully qualified.

II.8 Experimental Study on Sodium Freezing in Electrochemical Hydrogen Meter

An electrochemical hydrogen meter (ECHM) is used to monitor the dissolved hydrogen concentration in sodium. Steam generator tube leak detection system (SGLDS) in PFBR has electro chemical hydrogen meter (ECHM) at the outlet of every steam generator module and at the common outlet of four steam generator modules of secondary loop (Schematic shown in Figure 1). Experiments are conducted with a model ECHM housing to characterize the formation of sodium frozen seal in the housing. Numerical studies are also performed for this geometry with the same process conditions and the experimental data is used to validate the predictions.

ECHM assembly consists of a cylindrical housing through which sodium flows at 450°C. A sleeve of 22 mm inside diameter and 2 mm thickness is welded on the top of the housing through which ECHM probe is inserted from the top. Sodium will rise in the annular gap between the outer sleeve and the probe due to pressure of sodium inside the ECHM housing. Leak tight flanged joint with metal gasket is provided to avoid leaking of sodium to exterior. As the sodium reacts with the atmosphere, proper and reliable leak tightness to atmosphere is required. To achieve this, a sealing is provided by means of frozen sodium seal. This is achieved by maintaining the temperature of sodium in the annular space below its freezing temperature of 97.7°C. To improve the heat transfer rate from the sodium to the atmosphere for maintaining the sodium temperature below its freezing point in the annular space, twenty numbers of horizontal circular fins are welded to the outer surface of the sleeve.

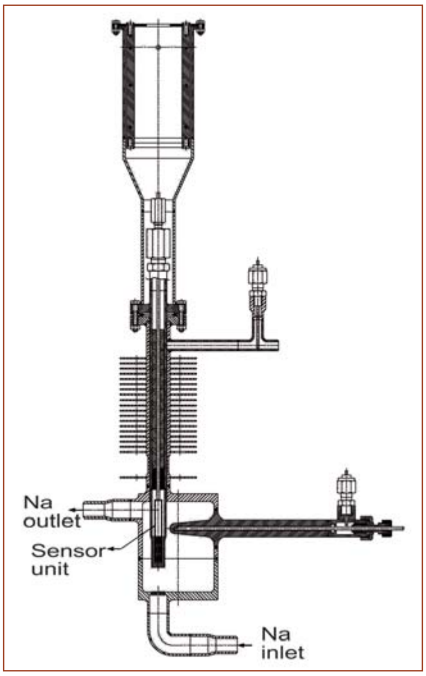

Fig. 1 *Schematic of electrochemical hydrogen meter housing of PFBR*

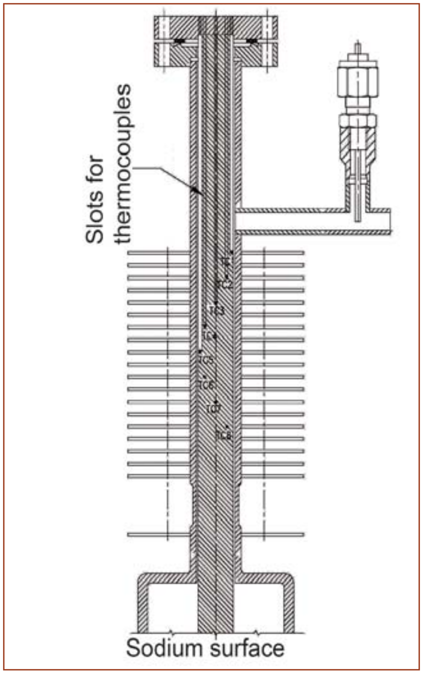

Fig. 2 *Schematic of experimental set up with thermocouple arrangement*

An experimental study was conducted to evaluate the formation of sodium frozen seal in the ECHM housing. The experimental model was of full scale of the ECHM housing. Dummy sensor geometry was used for simulating the sensor parts. Sodium was allowed to fill in the annular gap of dummy probe and housing. Eight numbers of thermocouples with 1 mm outer diameter were inserted through eight longitudinal slots of different lengths at the dummy ECHM probe. Thermocouples inserted in each slot will be in direct contact with the sodium in the annular gap and measure the sodium temperature in the annular gap at that particular elevation. The experimental set up with thermocouple arrangement used for the experiment is shown in Figure 2.

The outer pipe is welded with twenty numbers of radial fins as in the case of ECHM housing. The overall arrangement simulates annular gap geometry, heat conduction to the frozen seal area and the heat removal from the frozen seal area. There is a lateral connection at the top of the housing to admit/vent argon during sodium filling and at the time of removal of sensor from housing.

Experiments were conducted in SILVERINA facility with flowing sodium through ECHM housing. SILVERINA is a multipurpose sodium facility to conduct experiments with sodium components at actual operating conditions. The flowing sodium temperature in the sodium flow path is maintained at 450°C. Temperature of sodium inside the annular gap is measured using the bare thermocouples routed through dummy probe. Experiments are conducted in a large engineering hall and during the experiments, an air movement with a velocity of 0.25 m/s was measured in horizontal direction near to the experimental set up.

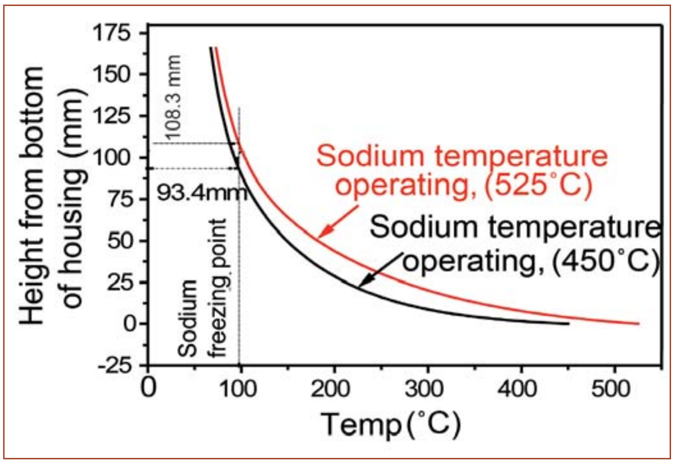

Fig. 3 *Temperature profile of sodium inside the annular space (experimental data)*

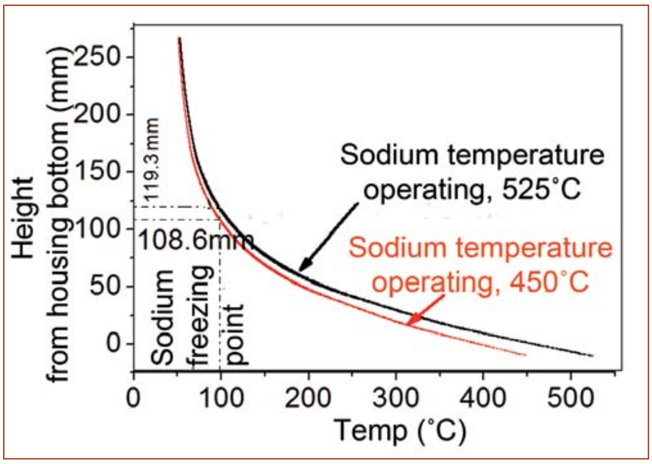

Fig. 4 *Numerically evaluated temperature profile of sodium inside annular space*

A frozen seal of sodium is formed near to the 7th fin from the bottom of ECHM. This is 97 mm above the ECHM housing top surface. Figure 3 shows the temperature profile of the sodium inside the annular space.

Even though the flowing sodium temperature through the ECHM housing is maintained at 450°C, during transients the maximum expected sodium temperature in ECHM will raise to 525°C which is the nominal inlet sodium temperature to the steam generator.

The same experiments are repeated with a flowing sodium temperature of 525°C through ECHM housing. The formation of frozen seal is observed 108 mm above the ECHM housing top surface which is near to 9th fin from bottom. The nature of the temperature profile is same as in the previous study.

A numerical computational fluid dynamics study is performed to evaluate the formation of frozen seal of sodium. Same process parameters as in the case of the experimental study including the horizontal air velocity are used as boundary conditions. Governing equations for continuity, momentum and energy are solved with standard k-ϵ turbulence model. Bossineque's approximation is used to account for the variation of density in gravity terms of the energy equation.

From the numerical mixed convection heat transfer study results, sodium is found to be freezing at around 109 mm from the bottom of the housing which is near to 9th from the bottom with 450°C sodium operating temperature. The variation of temperature of sodium in the annular gap along the length is shown in Figure 4. The temperature contours of sodium in the annular gap and the outer surface of the sheath and fins are shown in Figures 5a and 5b respectively.

Numerical mixed convection heat transfer study is also carried out with sodium operating temperature of 525°C. From the results of the study, sodium is found to be freezing at around 119 mm from the bottom of the housing which is near to 11th from bottom with 525°C sodium operating temperature. The variation of temperature of sodium in the annular gap along the length is shown in Figure 4. The results obtained from experiments and numerical studies are in close agreement. This validated the numerical procedure used for calculation. The experimental results ensured the formation of a stable sodium frozen seal during normal operating conditions and at design basis transient condition.

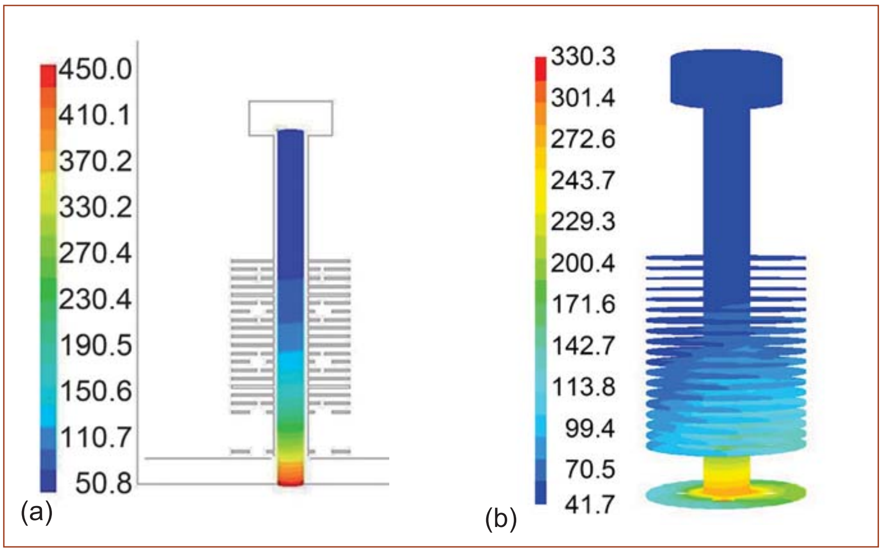

Fig. 5 *(a) Numerically evaluated temperature contours of sodium inside annular space and (b) temperature contours of outer surface of sheath and fins with 450°C sodium temperature*

II.9 Out-of-Pile Testing of Absorber Rod Drive Mechanisms of PFBR

Prototype Fast Breeder Reactor (PFBR) consists of two independent, fast acting, diverse shutdown systems, each comprising of sensors, logic circuits, drive mechanisms and neutron absorber rods having B_4C pellets. The absorber rod of the first system is called as control and safety rod (CSR) and that of the second system as diverse safety rod (DSR). The respective drive mechanisms, control and safety rod drive mechanism (CSRDM) and diverse safety rod drive mechanism (DSRDM), are housed in control plug, which is a part of top shield of the reactor. There are totally nine numbers of CSR & CSRDM and three numbers of DSR & DSRDM in PFBR.

During development of these mechanisms, important subsystems were identified and subjected to extensive standalone testing in simulated conditions. Further, full scale prototypes of these mechanisms were subjected to integrated performance testing and endurance testing in sodium. During endurance testing, mechanism was subjected to higher number of cycles than expected during the entire design life and the number of test cycles was based on ASME guidelines. Subsequently, certain minor design improvements were made and totally twelve numbers of CSRDM and four numbers of DSRDM, with 1/3rd as spare, were manufactured for PFBR. Thus manufactured mechanisms are referred as project CSRDM and DSRDM.

A comprehensive test programme of project CSRDM and DSRDM is envisaged before commencement of reactor operation to ensure the intended functioning of the mechanisms and to maintain the required reliability of functioning. The test programme consists of testing of each and every mechanism at various stages starting from subassembly of the mechanism to integrated assembly of the mechanisms at manufacturer’s shop, at site and also on pile before and after filling sodium in reactor vessel and before fuel loading.

Testing was done in a dedicated test station, under controlled environment. A relay based control panel was used for testing. Testing was carried out in aligned condition in air. Dummy weights were used to simulate CSR & DSR. The following tests were carried out: Verification of straightness of component, synchronization of electrical and mechanical zero, verification of translation operation and micro switch function, translation torque measurements, verification of translation speed and stability, checking of pre-compressive force of disc spring and angular position of micro switches of gripper assembly (only for CSRDM), verification of gripper operation (only for CSRDM), verification of straightness of travel, verification of inter seal leak tightness, verification of mobile assembly weight and frictional force during translation, verification of stiffness of component (lateral force versus misalignment of gripper), verification of electromagnet minimum holding current, verification of plug rotation sequence & verification of SCRAM operation and deceleration (only for CSRDM). The performance of all the mechanisms is satisfactory.

Out-of-pile testing, done earlier has provided rich experience with respect to the design and operation of both CSRDM and DSRDM. Some of them are highlighted below:

During subassembly testing at manufacturers shop, the electromagnet response time was found to be very high. Detailed analysis revealed that the change of the material of electromagnet to soft iron from low carbon steel is the root cause of the high response time. Electrical conductivity of soft iron is higher which gives rise to higher eddy current during detachment resulting in high response time.

Dashpot body was found rusted heavily before taking up for testing. The rusting is attributed to the cleaning procedure adopted before packing. Rust was removed using slightly acidic chemical solution. A chemical loop was erected to clean inaccessible regions of dashpot bodies.

During initial testing of CSRDM, high torque was observed without any abnormal friction value. Examination into the problem revealed a manufacturing defect of a spline shaft, which was rectified is all CSRDM.

A design change was made in lower part of CSRDM to facilitate handling of lower part with CSR in case of gripper jamming. However, a redundant locating pin was mistakenly added to the lower part in the design change. This resulted in deviation in straightness of mechanism. The redundant pin was removed and the problem was rectified.

High response time was observed for some control and safety rod drive mechanism, the main cause being the eccentricity between electromagnet and armature. The

Table 1: Salient results of out-of-pile testing for control and safety rod drive mechanism

Parameter	C - 1	C - 2	C - 3	C - 4	C - 5	C - 6	C - 7	C - 8	C - 9	C - 10	C - 11	C - 12
Average frictional force (N)	170	125	115	85	85	50	105	85	125	90	65	50
Translational torque (N-m)	6.0 - 8.2	6.3 - 7.0	6.4 - 7.6	6.4 - 8.0	7.0 - 9.0	6.0-6.8	6.0-7.0	6.4 - 8.0	10	8	5.0 - 6.5	4.4 - 6.2
Electromagnet minimum holding current (A)	0.5	0.5	0.5	0.45	0.5	0.45	0.5	0.4	0.45	0.5	0.5	0.55
Electromagnet response time (ms)	63	85	68	73	61	60	95	61	80	64	68	73
Free fall time (ms) (excluding electromagnet response time)	432	452	450	433	446	444	453	436	430	437	454	446
Braking time (ms)	251	203	178	173	324	295	210	228	247	194	286	220
Note: 'C' in each column represents 'CSRDM'												

problem is rectified by making electromagnet concentric with armature by increasing the guide pad thickness between electromagnet and guide columns.

In one occasion, electromagnet could not lift the mobile assembly due to dust collection (thickness ~0.2 mm) at parting plane

In case of diverse safety rod drive mechanism, one set of O-ring seals failed requiring disassembly and replacement. The cause of failure is attributed to a sharp edge in the mating item.

The tool used for coupling/decoupling of upper and lower parts of control and safety rod drive mechanism has caused many difficulties. In one occasion, it got stuck-up in the upper part, requiring complete disassembly of mechanism. In another occasion, its operation resulted in unscrewing of a screwed joint in lower part. Root cause analysis of all the problems was done and necessary design changes were made in the tool.

With respect to electrical and instrumentation system, on one occasion, potentiometer cable got crushed in the mechanism resulting in insulation failure. Failure of pins in a connector occurred in another occasion. Other than these issues, these systems performed well.

A comprehensive out-of-pile testing of absorber rod drive mechanisms of PFBR was carried out and all the tests which characterise the performance were done. Performance of all the mechanisms is satisfactory and the mechanisms are erected on pile in PFBR. The variations of all the parameters among different mechanisms were well studied. The testing provided rich experience and important lessons were learnt for developing and maintaining highly reliable absorber rod drive mechanisms.

The salient test results are given in Tables 1 and 2.

Table 2: Salient results of out-of-pile testing for diverse safety rod drive mechanism

Parameter	DSRDM 1	DSRDM 2	DSRDM 3	DSRDM 4
Average frictional force (N)	85	30	50	65
Translational torque (N-m)	4	3	4	3.2
Electromagnet minimum holding current (A)	0.55	0.45	0.45	0.4
Electromagnet response time (ms)	84	96	96	94

II.10 Seismic Qualification of Special Components and Equipments of PFBR

Seismic excitation is an important load considered for the design of nuclear power plant components. All critical components and equipment are designed to withstand two types of earthquakes: operation based earthquake (OBE) and safe shutdown earthquake (SSE). The OBE level is defined as the largest earthquake which can sensibly be anticipated to take place at the site. A power reactor could continue to operate safely during an OBE. SSE is evaluated based on the largest conceivable earthquake in the region. The plant's safety systems would be effective during an SSE to ensure safe shutdown without any leaks in the system. The ground vibrations or motion at the base of the plant building gets transmitted through the intermediate structures of the building to the respective locations in which those special components and equipment are mounted on the floors or walls of the building.

This report presents the shake table testing carried out for the seismic qualification of some of the special components and equipment for PFBR. They are mainly the annular linear induction pump (ALIP), high resolution differential pressure monitoring system and the control panel used to ensure the automatic operation of the material airlock in reactor containment building. The seismic qualification test has been carried out using the 10 tonne capacity tri-axial shake table of size 3 x 3 m available in the Structural Mechanics Laboratory (SML). The table is capable of operating upto the frequency range of 50 Hz. The maximum possible translational displacement of the shake table is ±150 mm (horizontal) and ±100 mm in the vertical direction. The maximum magnitude of the acceleration of the table is 1.5 g along horizontal and 1.0 g along vertical direction.

ALIP is an electromagnetic pump used for pumping sodium in the PFBR piping system. It essentially contains a sodium duct for the sodium to flow and it is surrounded by a stator winding. The sodium flows in the annulus formed between the outer and inner pipes of the duct. One of the typical ALIP has been tested to confirm the healthiness of the electromagnetic pump under seismic condition. The test arrangement for the ALIP is shown in Figure 1.

Differential pressure monitoring system (DPMS) is a high resolution pressure monitoring instrument developed by our Centre for online monitoring and control of low pressure in the ranges of 0-25 and 0-60 mbar deployed in the various locations of safety vessel (SV) nitrogen circuit of PFBR. The performance of this system under OBE is important to ensure integrity of main vessel (MV) for the design life. The test arrangement for the DPMS is shown in Figure 2a.

Material Air Lock with double door concept is provided in reactor containment building for the material access from steam generator building. The performance of the control panel has to be ensured satisfactorily to confirm the automatic operation of the material airlock under seismic condition. Towards this, the control panel along with the pushbutton stations, variable voltage variable frequency drives and motors are tested for five operating based earthquakes and one safe shutdown earthquake conditions. The shake table test arrangement is shown in Figure 2b.

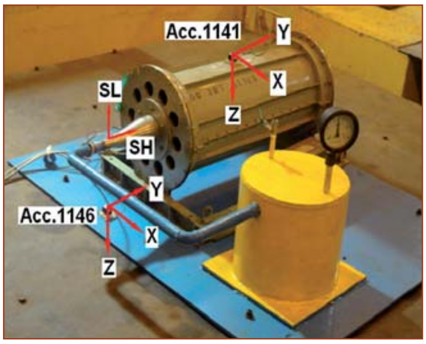

Fig. 1 *Test arrangement for annular linear induction pump*

The seismic qualification tests are conducted as per the recommended test procedure of IEEE standards. It includes mainly the resonance search test followed by five OBE and one SSE for the components designed for seismic category-1. Components designed as per seismic category-2 are not required to be qualified for SSE. A respective spectrum compatible

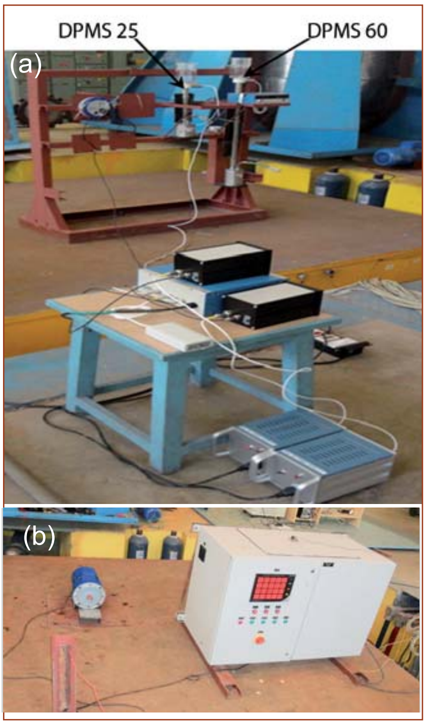

Fig. 2 *Test arrangement for the (a) differential pressure monitoring system and (b) material airlock control panel*

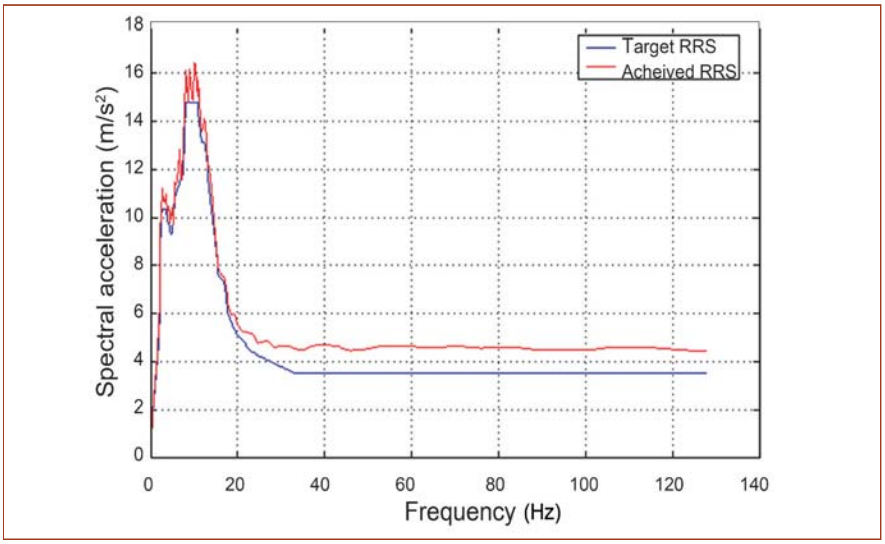

Fig. 3 *Typical spectrum compatible time history (SSE-horizontal) used for the testing of annular linear induction pump*

time history will be generated for both OBE & SSE in all the three orthogonal directions. One of such representative spectrum compatible time history used for the testing of the ALIP under SSE is shown in Figure 3. The enveloped and broadened floor response spectra (FRS) available on the support location of each component with appropriate specified damping is used. The base excitation time history required for the experiment is generated such that the test response spectra (TRS) is enveloped 10% more than the required response spectra (RRS) in all the frequency range given in the envelope floor response spectra as shown in Figure 3.

Triaxial accelerometer is mounted at the support location to confirm, the correctness of the input excitation. Another triaxial accelerometer is mounted very close to test specimen to capture the dynamic amplification and also to get the frequencies associated with the mounted specimen. All these instruments are connected to the 64 channels Dewetron data acquisition towards capturing the dynamic response during testing. One of such typical dynamic response of the acceleration captured for the DPMS assembly during the OBE testing is shown in Figure 4. Before the start of the experiment, all the pre-testing requirements have been checked. This includes the mounting arrangements, rigidity of the support arrangements, orientation of the test specimen, the similarity of the support arrangement and interactions with the neighboring system as per the site conditions. The functional test for each component is tested before, during and after the experiment. The healthiness and smooth working of each component are ensured before the start of the experiment. It has been confirmed that there is no degradation in the functional performance of the components such as ALIP, DPMS and for the material airlock control panel even after the applicable type tests.

The structural integrity of these components are ensured from the information obtained from the strain gauges pasted at critical locations. One of such typical strain gauge information observed during the OBE testing of the ALIP is shown in Figure 5. The maximum strain amplitude observed during the OBE testing is much lower than the elastic limit. Hence, there is no concern in the structural integrity.

Both functional and structural integrity was demonstrated during and after the seismic qualification. Based on the above tests, all the components satisfy the applicable seismic design requirements with a comfortable margin. Hence, it can be concluded that all the special components met the specified seismic qualification criteria.

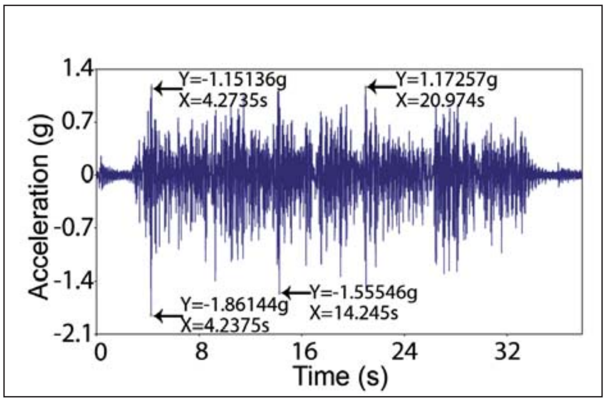

Fig. 4 *Typical acceleration time history at the DPMS assembly observed during OBE testing*

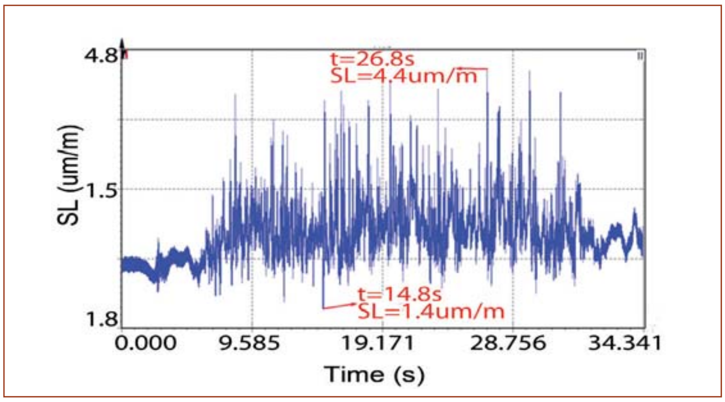

Fig. 5 *Typical strain guage results observed during OBE testing of ALIP*

II.11 Development of Plant Dynamic Models for Operator Training Simulator

Training simulator forms an important tool for training of operating personnel towards safe and economic operation of a nuclear power plant. A simulator is developed in such a way that it is able to illustrate general concepts and is capable of demonstrating fundamental physical processes of a plant. Thus, a full-scope simulator incorporates detailed modeling of important plant systems with which the operator interfaces in the actual control room environment. An exact replica of power plant control room along with operating consoles are a part of the full-scope simulator. Various physical processes of the plant are represented by suitable numerical models. Full-scope simulator has been developed for training of operators of PFBR.

Important physical processes that are represented in the simulator include,

(i) neutronic modeling of core,

(ii) thermal modeling of core,

(iii) thermal hydraulics of primary sodium circuit,

(iv) thermal hydraulics of secondary sodium circuit,

(v) thermal hydraulic modeling of steam water system and

(vi) dynamics of electrical systems.

Here details of thermal hydraulic modeling of various systems are presented. Real time representation of whole plant is the essential objective of a simulator. Therefore, the numerical models incorporated are based on one-dimensional system dynamics approach. This is due to the fact that the computer simulation time for a real time phenomenon is desired to be lower such that the real time evolution of various plant parameters can be mimicked in the simulator control room.

Numerical models representing the heat transfer in the core, thermal hydraulics of primary and secondary sodium systems have been incorporated from the safety analysis code developed for PFBR (DYANA-P). Reactor core comprises of several subassemblies of varying power and coolant flow through them. For the convenience in numerical modeling, the reactor core is divided into 10 radial zones with 16 subdivisions in the axial direction. Based on the power estimated through the kinetic modeling of the reactor core, thermal calculations are carried out. Governing equations for the thermal modeling are formulated based on the principle of conservation of energy for a single average pin in each core zone. This will result in system of ordinary differential equations for thermal balances of fuel, cladding and coolant. These equations can be solved in a sequential manner using finite difference method. Schematic of numerical modeling of each core zone is shown in Figure 1.

Hydraulic modeling of primary and secondary sodium flows in the circuit are carried out through conservation equations for

(i) momentum balance,

(ii) mass balance and

(iii) torque balance of the pump shaft.

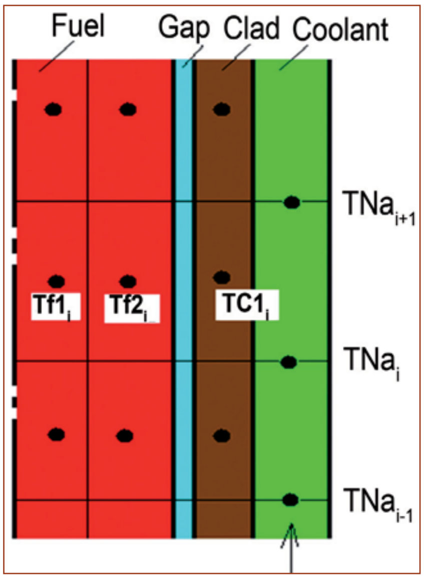

Fig. 1 *Nodal representation of core*

Momentum balance equations are formulated through integral momentum balance between important segments of the circuit and mass balance equations are formulated by flow balancing for various tanks in the circuit. The system of ordinary differential equations thus formulated for primary and secondary sodium circuits are solved by predictor corrector methods. The momentum balance equations for the circuit would have terms representing head developed by pumps. These terms are obtained from pump characteristic curves. Generalized homologous characteristics available in the literature for centrifugal pumps have been employed for this purpose. These characteristic curves for pumps follow close relationship with respect to specific speed of pumps. The nodalzation scheme adopted for primary and secondary sodium circuits of PFBR is shown in Figure 2. Estimation of buoyancy induced head is given special consideration in the formulation such that the system of equations are applicable for situations under pump tripped condition also.

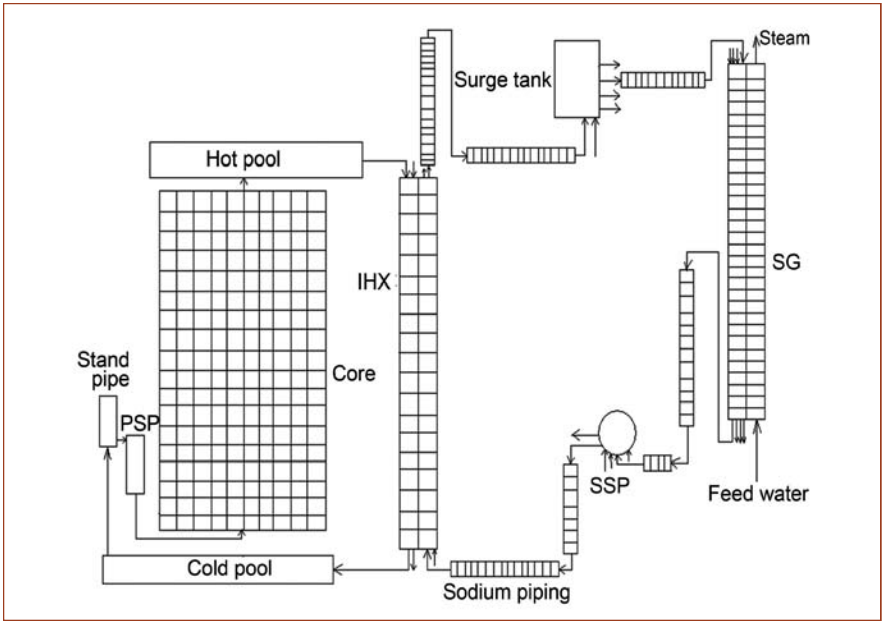

Fig. 2 *Nodalization scheme of primary and secondary sodium circuits*

Other important models of physical significance are heat exchange model for intermediate heat exchangers, steam generators and heat loss along piping. These equations are formulated based on the principle of conservation of energy. Simple temperature based heat transfer formulation in counter current mode is sufficient for intermediate heat exchangers since there is no phase change of coolant in it. In the case of steam generators, enthalpy based heat exchange formulation is adopted to model the phase transition of water to steam in it. Stable numerical solution with these models has been made possible with the use of weighted nodalization approach. Nodalization approach of steam generator is shown in Figure 3. Heat loss along the piping is simulated through heat balance between convective heat loss of coolant flowing inside the pipe and heat loss to ambient through conductive mode of heat transport through pipe wall and insulation.

Another important system of PFBR is the safety grade decay heat removal circuit. This is a natural convection based system having intermediate sodium and air circuits. Flows of sodium and air in this system are driven by natural convection. Thermal hydraulic phenomena in this system is modeled through a quasi steady state approach. In this approach, a look up table is generated based on steady state heat transfer and hydraulic balance equations. Heat removal by this system and flow rates of sodium and air in this system are estimated based on this model for any combination of hot pool sodium temperature and opening condition of dampers. This approach can very well satisfy the requirements of a training simulator. However, for the purpose of safety analysis detailed dynamics models based on integral momentum balance of sodium and air circuits and energy balance in

(i) sodium to sodium heat exchangers,

(ii) sodium to air heat exchangers and

(iii) piping are required to be considered.

Thermal stratification effects in sodium pools is another important consideration of safety analysis codes which is not considered for the simulator model.

Similar models are developed for systems and equipment in steam water system also. This is carried out using the tools available with the simulator software. Some of the special equipment of the steam water system such as moisture separator tank and flash tanks are modeled using in-house developed models. These equipments are modeled based on mass balance and energy balance between the different phases of fluid involved. Inter-linking between the in house developed models and the simulator code system is another important activity. The geometrical location considered for the inter link is the steam header which is the outlet of all the steam generators. The interlinking has been carried out based on mass balance and equation of state. The integrated code system has successfully under gone validation and verification exercise and is being used for operator training at BHAVINI.

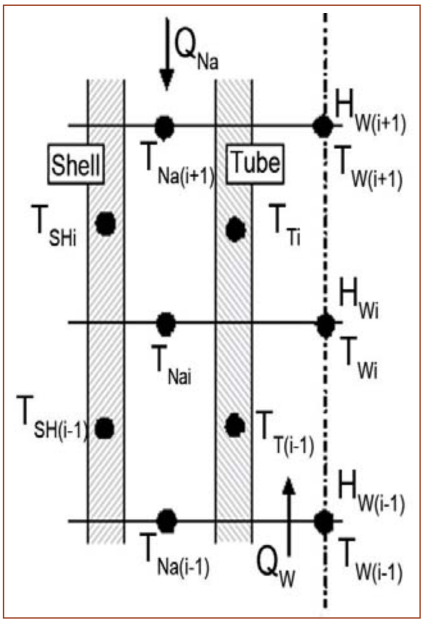

Fig. 3 *Nodalization approach for steam generators*

II.12 Indigenous Development of Glass-to-Metal Seal based Leak Tight Penetrations for Nuclear Instrumentation Cables

Glass-to-metal seal based high frequency and ultra low current application leak tight penetrations, to be used with neutron detector signal cable across the reactor containment building penetration boundary, were designed and fabricated in an effort to indigenously develop a low cost substitute to the present reactor containment building penetrations. In a nuclear reactor system, it is important that reactor containment building boundary allows flow of the electrical signal with minimum losses and provide a leak proof path so as to physically isolate the two different environments across it. Glass-to-metal seals are widely regarded as one of the high end technology seals used for leak tight application viz., sensor packaging, battery sealing and packaging of integrated circuits etc. In neutronic instrumentation, neutron detectors produce picoampere (pA) to nanoampere (nA) range of currents that need to be carried to signal processing and monitoring electronics situated far off the sensor outside the reactor containment building.

The signals, often when measured at low process level operation, encounter errors due to the varying amount of non-linearity in the form of leakage current, inductive and capacitive loading coupled with effect of external electro-magnetic field interferences. If the design of the cable in the penetration system is not incorporated with features to minimize the above effects, it may significantly impact the monitoring and control of the reactor. One of the main requirements on minimizing the leakage current is to have a high insulation resistance material with good dielectric properties: chemical, physical and electrical between the conductor and its return path, besides the surface properties viz., surface conductivity (σ_S), self inductance (L) and permeability (μ) of the conductors. The surface conductivity plays an important role in the design due to *skin effect* phenomenon dominant at high frequency. The skin depth is defined as the thickness of the outer surface which accounts for 63% of the current flow in a conductor and is given by:

skin-depth (δ) = $\mathrm{sqrt}(2/\omega\sigma\mu)$

where,

ω is the frequency,

σ is conductivity and

μ is the permeability of the conductor.

Above equation shows that skin-depth decreases with the square root of the frequency.

If W is the conductor's cross-sectional width

(for a circular wire, W = 2πr).

Rewriting:

$R_L = (1/W)\mathrm{sqrt}(\omega\mu/2\sigma)$

Hence, the conductor for high frequency signal operation shall be chosen accordingly. Here the high frequency operation is considered to be 10 MHz. In addition to this, the dielectric loss caused by insulating material (tan δ) is considered for the cable design so as to minimize this loss too.

After a comparative analysis of various ceramics available commercially and being practiced in such applications, glass was chosen mainly due to its very low water absorption coefficient, compatible linear thermal expansion with metals and non-aggressive behavior with almost all acids. The matching thermal expansion allows it to be used for vacuum sealing and packaging. The glass is basically a composite material having oxides of silicon, boron and aluminium. A few metals and iron based alloys such as KOVAR, ALLOY-52 etc. are used for sealing with the glass. There are two types of sealing-matched and compressed which are widely performed in the industry. Based on deign specification requirements, matched seal type was selected.

The leak rate was targeted to be less than 1×10^{-6} std.cc/s for dry helium(He) as stipulated in the standard IEEE 317 for penetrations of nuclear containment building at operating pressure of 4 bar(g). The prescribed insulation resistance is 10 GΩ or higher at 373 K.

Based on above requirements, two types of penetrations were conceptualized and designed for prototyping and testing-triaxial and twinaxial. Both can cater to signals which are generated with pulse width of 100 ns & rise time of 1-10 ns or ultra low current in DC modes or both. Pulse mode application requires differential transmission for better signal reception at the processing end. This necessitates twinaxial differential mode transmission of the signal from the detector to signal processing electronics. Similarly, DC mode of operation compels to use noise immune triaxial type signal transmission media. Following are main features incorporated in the conceptual design of penetration cables:

- ✓ Double sided sealing
- ✓ Easily replaceable connectors
- ✓ 50 and 75 Ω characteristic impedance
- ✓ Built-in leak gauge
- ✓ SS 304 as structural material for

modular penetration pipes

- ✓ Alloy-52 with less than 0.5% cobalt (^{60}Co) as center conductor and shield
- ✓ Radiated noise screening
- ✓ Standard IEEE317 compliance fabrication, testing of prototypes.

The triaxial cable was designed to have 50 Ω cable characteristics with an additional layer of conducting metal shield for enhanced EMI screening, as shown in Figure 1a. Most of the detectors are terminated with $(Z_0=50\Omega)$ characteristic impedance, hence, 50 ohms cable was considered. The dimensions were computed based on formula to determine the impedance of a cable as:

$$Z_0 = 138 * V_P * 10 \log (D/d)$$

where,

Zo = Characteristic impedance

V_P = Velocity of propagation

D = Diameter of the dielectric

d = Diameter of the conductor

Characteristic impedance (Z_o) is the total opposition to the flow of electrical energy within the cable. It is a complex value defined by the cable's capacitance, inductance and conductance, and is the equivalent value of these items combined. It is not length dependent as evident from the above equation and is expressed in Ω.

Similarly, capacitance of the cable is calculated as follows:

$$C = 7.36 * \varepsilon_r / \log_{10} (D/d) \text{ pf/ft}$$

where,

ε_r = Dielectric constant of insulating material (glass = 4.5 @ 10 MHz)

The length of the conductors was selected based on its self inductance (L) which is given by:

$$L=0.002l\ [2.3 \log (4l/d)-0.75]\ \mu H$$

where,

l is length of the conductor and

d is diameter.

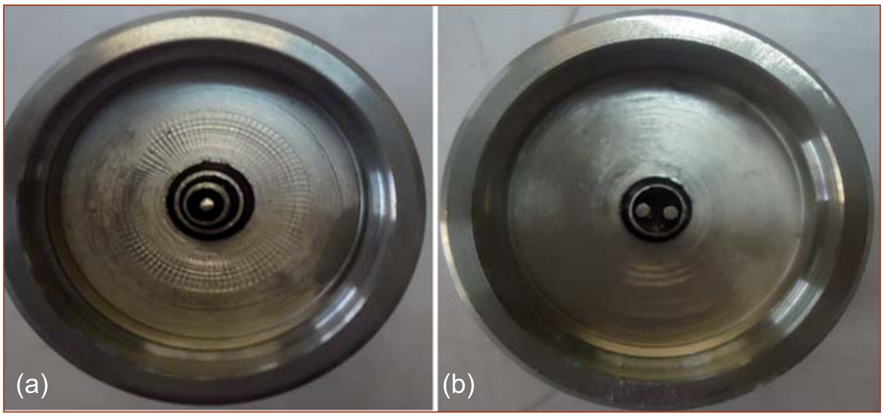

Fig. 1 *Cross section view of (a) triaxial type penetration and (b) twinaxial type penetration*

The above equations show the variation of inductance with diameters and lengths of the conductor. This suggests that the length shall be minimized for having reduced self inductance effect and accordingly 6 mm length of the center conductor having 0.95 mm diameter was considered in the design.

Twinaxial type penetration was also designed with glass as dielectric as shown in Figure 1b. Computer communication standards recommend that the characteristic impedance $(Z_0=75\ \Omega)$ for this type of differential communication shall be used.

Glass-to-metal sealing is a special process carried out under control environment in high temperature furnaces. The fabrication of glass-to-metal seals is carried out with glass pre-forms made by compaction of glass powder and subsequently baked with Alloy-52 at a very high temperature (typically 600-800ºC). The temperature is allowed to fall in a controlled manner and sealing is obtained through expansion and compression mechanism of the glass-metal and vice-versa.

The prototype has been tested for leak tightness up to 4 bars (g) and dielectric breakdown test has been conducted up to 1.4 kV/mm successfully. The leak rate (dry helium) was measured to be 1.09 E-9 std. cc/s and Insulation Resistance (IR) values were found more than 10 GΩ at 1000V DC at room temperature. The hydraulic test was carried out with dry nitrogen up to 10 bar pressure and no increase in leak rate was observed. The indigenization is expected to bring the cost down by ~30-40% when compared with leak tight penetrations of PFBR (Figure 2).

Fig. 2 *Assembled leak tight penetrations*

II.13 Ultrasonic Imaging Experiments in Water using Indirect Imaging Technique for PFBR

Liquid sodium, the coolant in PFBR, is opaque to light and hence viewing of internal components immersed in sodium is not possible by visible means. Hence, an under sodium ultra-sonic scanner (USUSS) has been developed for PFBR to detect protrusion, growth and bowing of the fuel-subassemblies before every fuel handling operation. Two methods, namely-direct imaging and indirect imaging methods have been envisaged for this purpose. In indirect imaging method, protrusion is detected by shadowing effect of protruded object on cylindrical peripheral blocking subassemblies. The peripheral blocking subassemblies has 100 mm extra projection above any other subassembly and located in the last row of the core. The possible protruded objects are hexagonal fuel subassembly head and absorber rod drive mechanisms which are not geometrically favorable to ultrasonic beam in some orientation. In indirect imaging technique, there is a change in the echo pattern and reduction in amplitude received from the blocking subassembly due to the protruding object. The challenge is to analyse the data using specific methodology for protrusion detection.

The PFBR core consists of different sectors. Each sector consists of group of subassemblies arranged in specific patterns. These patterns are simulated in water tank of five metres diameter and experiments are carried out using 0.6 MHz frequency to simulate the beam divergence effect equivalent to that in sodium for one MHz frequency. A water proof transducer with PZT crystal of 500 kHz resonant frequency was fabricated and is excited using 0.6 MHz frequency sine wave.

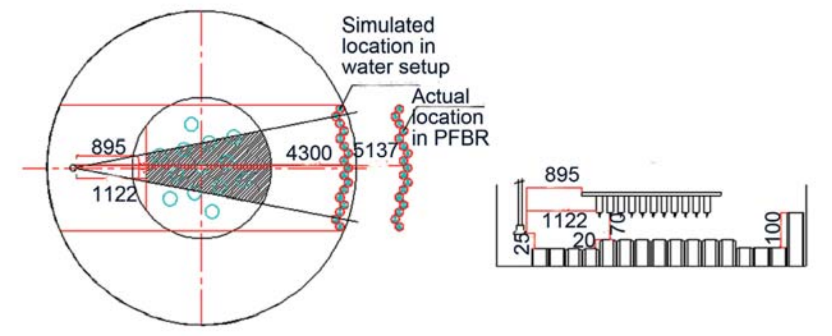

Fig. 1 *Sector-1 setup in water*

The reactor conditions such as average fuel subassembly growth of 20 mm and the above core plenum of 90 mm from normal subassembly top were simulated in water. Considering average fuel subassembly growth of 20 mm, the gap of 70 mm from grown subassembly top is simulated. The differential protrusion of 45 mm of fuel subassembly was also simulated. The complete core was simulated in 5m water tank in five different sectors (sector 1-sector 5) with 40 degree scan angle. The scanning experiment was carried out with 1° step angle and 1 mm vertical distance. The six numbers of retro reflectors were used in prescribed pattern according to the sector being simulated. The retro reflectors are used to measure the vertical orientation of the side viewing transducers. The experiments for all the five sectors were completed, but results of sector-1 are represented in detail here.

The signal strength from each cylindrical blocking subassemby varies due to its orientation. Due to beam divergence effect, there will be a bunch of echoes received from the blocking subassemblies. The reflections from the adjacent blocking subassemblies due to divergence effect arrived at different time of flight compared with the reflections from blocking subassembly at direct line of sight. Only the time range of highest peak was considered in this algorithm using angle specific gate settings. The method used is that if two peaks are considerably close then both the peaks are considered for gate setting. The difficulty in detecting the smaller components and CSRDM's using common gate algorithm is overcome by using different gate settings at different angles.

Sector-1 was simulated at a distance of 4.3 m in water as in Figure 1. The subassemblies beneath the in-vessel transfer port are not grown as they are in the storage location. The transducer is positioned 25 mm above the normal subassembly top. The effective ultrasonic scan region is 65 mm from transducer position. The distance in the reactor is 5137 mm whereas in the simulation it is 4300 mm in sector-1 due to dimensional limitation of water tank.

The ultrasonic data was collected using a personal computer based automatic scanning system for various conditions, such as without any protrusion and with 65 mm protrusion (leaving clear space of 25 mm from the top of the thermowell sleeve) from normal subassembly top at 1, 2 and 3 metres distance from transducer. It was found that there was a clear dip in

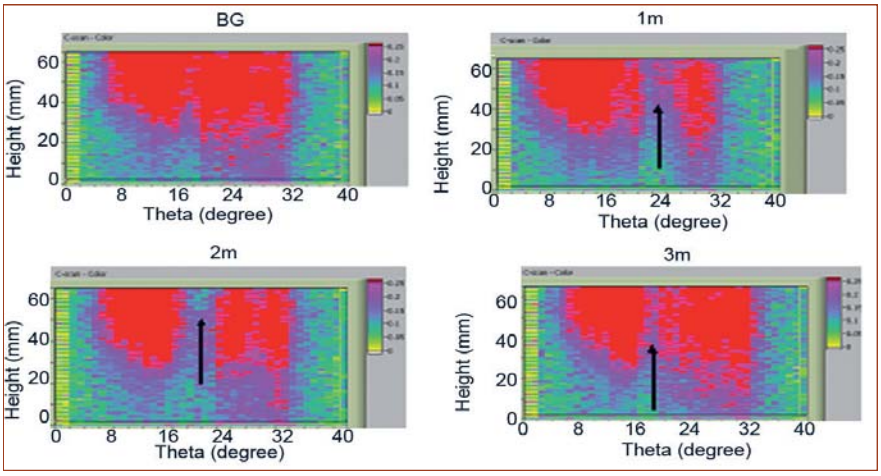

Fig. 2 Sector -1 C-scan image by protruding the subassembly at same angle at different distances 1, 2 and 3 metres and background

echo signal strength when hexagonal subassembly is protruded at different distances. As the protrusion is nearer, the blocking effect was seen in wider angles compared with protrusion at longer distance. The same effect was seen in the C-scan images as in Figure 2. The dip in amplitude gives the angle at which the object is protruded. The protruded object is marked with an arrow. The C-scan image obtained shows that there is no useful data from 0 to 25 mm of ultrasonic scan region.

As the CSRDM conical portion is not detectable by direct imaging technique, experiments were carried out in sector-1 by protruding the conical portion of CSRDM from the top of the core cover plate. The farthest CSRDM slot was selected to simulate longer distance of around 2.8 m as in Figure 3.

In the case of CSRDM, the C-scan image was taken first without protrusion as a background reference data. From the bottom of thermowell sleeves, various protrusion of conical portion from 60, 40 and 20 mm was simulated and the C- scan image was constructed. From the image in Figure 4, it was found that, 60 mm conical portion was detected easily and for protrusion of 40 mm and 20 mm also, there was a clear decrease in the signal strength.

Similarly from the sector-2 to sector-5 experiments, it is concluded that protrusion is detectable in all the cases and could be ascertained from the corresponding C-scan images. Also other experiments like, effect on inclination of objects from vertical axis with respect to ultrasonic beam and effect of random protrusion of 20 mm were studied.

In the case of indirect imaging technique, protrusion of objects which is geometrically unfavorable to ultrasonic beam can be detectable using angle specific gating with summation algorithm. Initially without any protrusion the core was scanned and the C-scan image was constructed which served as background data. The objects such as hexagonal subassembly having differential growth of 45 mm can be detectable and is demonstrated in water experiments.

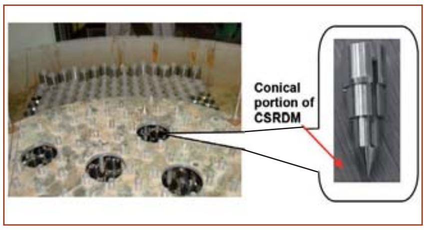

Fig. 3 Position of protrusion of CSRDM conical portion

The objects such as conical shape or any irregular shape hanging from the top of the thermowell sleeves by 20 mm is also detectable. The inclination effect of peripheral blocking subassembly was also studied and found that beyond 0.44 degree from vertical axis with respect to ultrasonic beam, the signal strength becomes less and not detectable which shows that inclination upto 0.44 degree is tolerable to ultrasonic beam.

In the reactor, once in every ~8 months, fuel handling operation is carried out and one third of the core will be handled. The freshly loaded fuel subassemblies grow to a smaller extent than the old fuel subassemblies. The probable maximum growth of the fuel subassembly is ~20 mm which is due to neutron irradiation and differential expansion. Therefore, the experiments are carried out by providing equal protrusion of 20 mm growth and the random protrusion of partially 5, 10, 15 and 20 mm growth. This experiment is carried out in sector-I and C-scan images are obtained. The result shows that equal fuel subassembly growth is conservative.

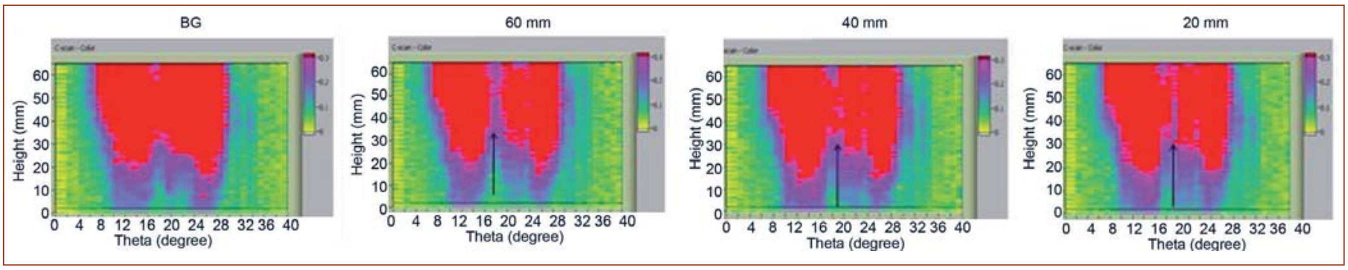

Fig. 4 C-Scan image of protruded CSRDM conical portion at different lengths from top (2.8 metres distance) and background

II.14 Innovative Liquid Level Sensing Device for Continuous Monitoring of Oil Level in Dashpots of CSRDM in PFBR

The safety of the Prototype Fast Breeder Reactor (PFBR) as a whole depends upon the reliable performance of control safety rod (CSR) and control safety rod drive mechanism (CSRDM). The mobile assembly of CSRDM is held by an electromagnet (EM). During SCRAM action of control rod the EM is de-energized and the mobile part falls under gravity. At the end of free fall travel, the mobile assembly is decelerated by an oil dashpot and this causes a sudden change in oil level in dashpot. During reactor operation the level of oil in dashpot is maintained at a constant height. From reactor safety point of view, it is essential to monitor any small shift in oil level in dashpot continuously.

The active region of dashpot is of 60 mm height where continuous surveillance of oil level within 2 mm uncertainty in level measurement is essential. Towards this a high resolution, fast response with excellent precision online level monitoring device, meeting all the stringent requirements for reactor application, is indigenously developed. This innovative device will be deployed in CSRDM for continuous monitoring of oil level in all the nine dashpots used in CSRDM.

The sensing methodology involves monitoring digitally, the minor shift in capacitance of a specially designed capacitor assembly in the oil vessel with small change in oil level. An assembly of uniformly spaced multiple number of rectangular stainless steel plates is the capacitor whose capacitance changes with the change of oil level on account of change in fractions of two dielectric media - oil and air, within the electrode gaps. The capacitor is placed in the timing circuit of a compact logic gate oscillator (LGO) and, hence, shift in digital pulse frequency at the output of the oscillator is directly related to change in oil level. The relation between pulse frequency and oil level is generated by multipoint calibration of the sensor.

The dashpot oil level sensor (DOLS) consists of five polished rectangular stainless steel electrodes fastened with nylon nuts and bolts at two places of top half with the gap maintained by Teflon spacers. The electrodes are partially embedded in a resin within a Teflon cap for better mechanical stability. A miniature signal generation circuitry is mounted and embedded in the same resin, right on top of the electrodes within a cylindrical Teflon enclosure. A capacitance based in-house made temperature sensor is embedded on the top of the electrodes assembly along with level sensor electronics. The thermal sensor is fixed onto the system to measure temperature which will be used for temperature compensation in level measurement. The LGO is powered by 5 V DC. One shielded four core Teflon cable is connected to the probe as the only cable for power supply and signal outputs from level and temperature sensors within the probe. A cylindrical stainless steel sleeve is provided over probe head for protection and mounting. The photograph of the probe is shown in Figure 1.

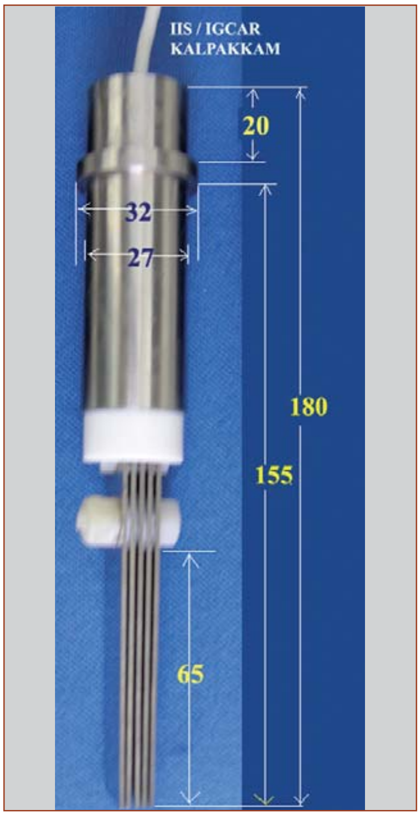

Fig. 1 *Photograph of dashpot oil level sensor (all dimensions in mm)*

The trains of rectangular transistor-transistor logic (TTL) pulses at the outputs of the level and thermal sensors from a given probe are processed by a standalone embedded signal processing and data presentation systems. For long distance signal transmission, the output pulses from the probe are transmitted in the form of differential signals using a differential line driver and a differential line receiver. Then signal from the line receiver is routed to the embedded system through polytetrafluoroethylene signal cables terminating with industrial grade connectors. TTL pulse signals from the level and temperature probes are optically isolated using high speed opto-isolators. The optically isolated signals are simultaneously counted using two programmable 16-bit counters and are stored with the time stamp using a real-time clock. An eight-bit micro-controller is used to calculate the frequency and conversion of frequency to oil height after neutralization of thermal effect. The liquid crystal display (LCD) module displays the liquid

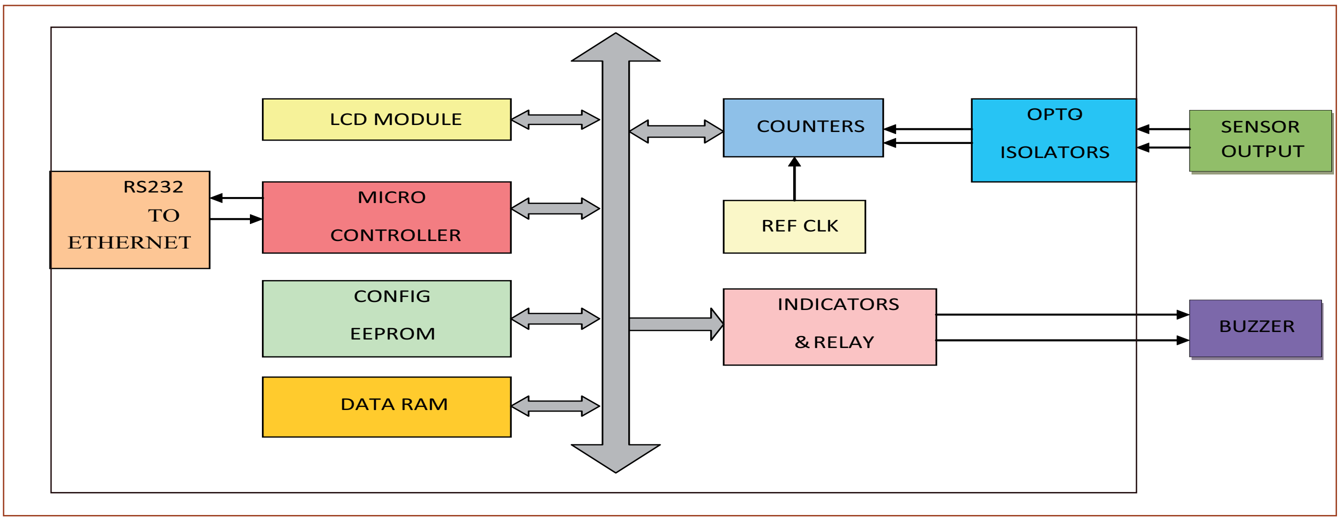

Fig. 2 *Block diagram of embedded system*

height in mm or the frequency in kHz as per the level/frequency select panel switch. Besides level measurement, the level controller is provided, to control the alarm status of the LEDs and potential free contacts as per the threshold values in comparison with the actual oil height. Lower level threshold (LLT) indicates that liquid level has come down below the expected low level, whereas upper level threshold (ULT) indicates liquid level in dashpot has crossed the expected upper level. The controller sends the data through serial and ethernet port for remote data logging. The schematic of the block diagram of the stand-alone system is shown in Figure 2. The stand-alone embedded processor performs the following functions: (i) pulse counting for determination of pulse frequencies at the outputs of level and thermal sensors from the probe, (ii) conversion of pulse frequencies to heights of oil level from the tips of the level sensing electrodes after neutralization of thermal effect, (iii) displays and stores liquid level data at two seconds interval, (iv) provides alarm signal through potential free contact points, and (v) instructs to configure via serial and ethernet Interface.

In CSRDM of PFBR total nine numbers of level sensing devices will be used. Three such stand-alone embedded processors have been arranged in a compact instrument cabinet in order to provide connectivity to all nine DOLS probes (Figure 3). The instrument is powered from dual 5 V power supply which is EMI/EMC compatible. The chassis of the system is properly earthed to reduce radiated noise and to increase the immunity to radiated susceptibility and all the PCBs are subjected to conformal coating in order to protect them during environmental tests. The DOLS and the instrument successfully passed environmental, EMI/EMC and seismic qualification tests. The success behind all these stringent qualification tests is due to robust design of probe as well as the associated instrumentation.

Before the deployment of DOLS in reactor the performance of the level sensor has been investigated thoroughly. The precision, response time, sensitivity and detection limit as evaluated are 0.04% RSD, ~1 second, ~100 Hz/min and 0.5 mm respectively. Besides these, stable background for a long period, negligible effect on oil level even up to 200 Gy irradiation without re-calibration of sensor, easy way of calibration, withstand to humid atmosphere, minor thermal effect and compensation for error free reading, rapid response to sudden change in oil level are some of the key factors for recommending such in-house level sensor in crucial reactor application. The introduction of such dash pot level sensor in PFBR is first of its kind in the world.

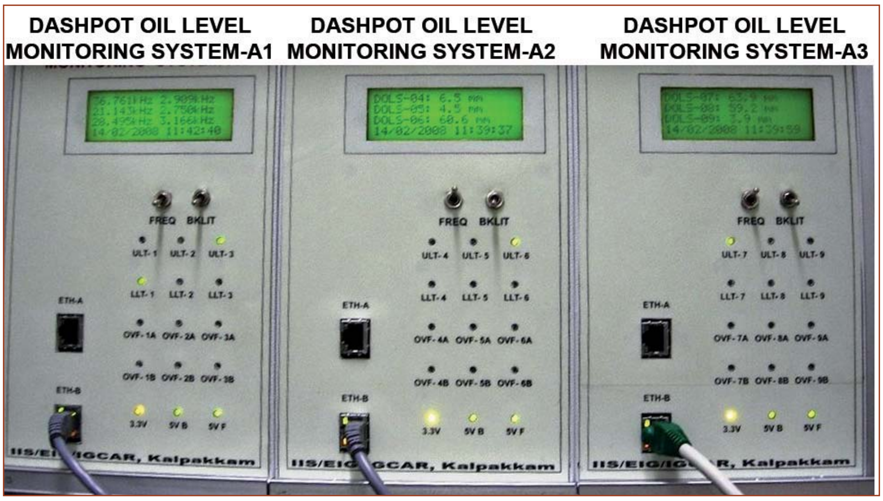

Fig. 3 *Photograph of dashpot oil level monitoring system*

II.15 Demonstration on In-situ Regneration of Model Secondary Cold Trap of PFBR

In PFBR, secondary cold trap is designed to trap the hydrogen for 4.5 years and oxygen load likely to be generated for 40 years. It is proposed to regenerate the cold trap once in 4.5 years by vacuum decomposition technique in the presence of hot sodium at 400˚C temperature and the process was experimentally demonstrated with a scaled down model of the cold trap.

During the regeneration of the cold trap in the absence of oxide impurities the expected chemical reaction is as follows:

$$NaH \Leftrightarrow Na + \frac{1}{2}H_2$$

In the operating reactor, sodium oxide present may react with sodium hydride above sodium temperature of 410˚C and form sodium hydroxide. To avoid NaOH formation, temperature during cold trap regeneration is limited to 400°C.

Secondary cold trap of PFBR is of 2.8 metres diameter and 5.3 metres height. During regeneration, the height of sodium column inside the cold trap will be maintained at 4.3 metres. The static head of sodium is maintained similar to the model cold trap. The dimensions of model cold trap for regeneration is selected as 0.6 metres diameter and 5 metres height. To reduce the time required to load the sodium hydride in model secondary cold trap, the volume of wire mesh provided is 0.209 m^3 against 9.2 37 m^3 in PFBR. Figure 1 compares the secondary cold trap for PFBR and model secondary cold trap. A comparison of key parameters for secondary cold trap of PFBR and model secondary cold trap for regeneration is given in Table 1.

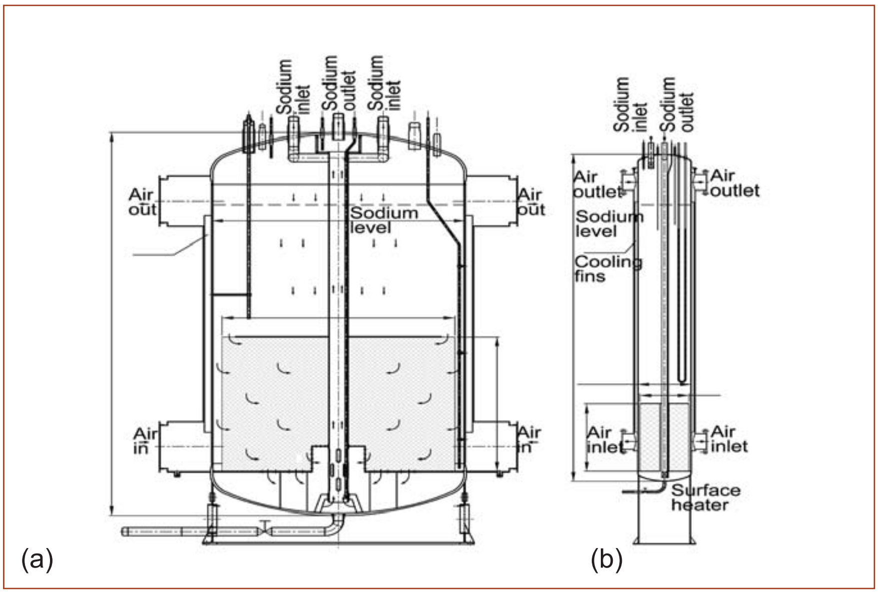

Fig. 1 *Comparison of (a) secondary cold trap of PFBR and (b) model secondary cold trap*

In-situ regeneration of model secondary cold trap was demonstrated in steam generator test facility (SGTF) sodium loop. For loading the cold trap with hydrogen, measured volume of hydrogen was injected to the flowing sodium in a dynamic loop. The injected sodium was trapped in the cold trap to generate the sodium hydride for regeneration. During cold trap regeneration, diaphragm type oil free vacuum pump was used for continuously evacuating the evolved hydrogen from cold trap. An absolute pressure of 10 mbar was maintained in the cover gas space of the cold trap.

The volume of hydrogen evolved from cold trap during regeneration was converted into water using a fuel cell and the quantity of hydrogen recovered by fuel cell was estimated. The unreacted hydrogen exiting from fuel cell was quantified by using an electrochemical based hydrogen sensor and a polymer based hydrogen sensor.

During the loading of hydrogen to sodium, the sodium flow was maintained at 1.2 kg/s with a sodium temperature of 400°C and cold point of 140°C.

Table 1: Comparison of key parameters for secondary cold trap of PFBR and model secondary cold trap for regeneration

Parameters	Unit	PFBR	Model
Wire mesh volume	m^3	9.2	0.2
Volume of cold trap	m^3	30.8	1.4
Height of cold trap	m	5.3	5
Radial width of mesh	m	1.2	0.2
Height of wire mesh	m	1.9	0.9
Sodium surface area	m^2	6.2	0.3
Sodium level	m	4.3	4.3
Sodium hold up	ton	22.5	0.9
Cover gas space	m^3	3.9	0.2
H_2 load (30%)	kg	93.2	2.1

Hydrogen injection rate into the system was maintained around 60 ml/min (5.3 mg/min) for 25 days. During the injection of hydrogen in sodium, the hydrogen concentration in sodium was continuously monitored by using calibrated electro chemical hydrogen meters (ECHM). The total quantity of hydrogen injected to the sodium in the dynamic sodium loop was 0.19 kg (2.142 m^3 at STP), which was completely trapped in the cold trap. Weight of sodium hydride thus precipitated in the cold trap was 4.5 kg of NaH (0.005 m^3). This corresponds to 2.4% of the total wire mesh volume of 0.2 m^3 provided in model secondary cold trap. After loading of sodium hydride in the cold trap, the sodium level in the cold trap was lowered to 4.3 metres and temperature of sodium in the cold trap was raised upto 200°C. The cold trap was isolated from sodium loop by establishing sodium freeze seals.

The sodium inside the cold trap was heated gradually by using surface heaters provided at the bottom part of the cold trap. The evacuation of cover gas was started when sodium temperature reached 300°C. It was observed that small pulses of hydrogen were release with a time period of 5 to 10 seconds when the sodium temperature reached 320°C. With increase of sodium temperature the time period of pulses reduced. At a sodium temperature of 346°C, hydrogen release a sustained was observed. Figure 2 shows the hydrogen release rate and sodium temperature of cold trap during the regeneration operation with respect to time. The maximum rate of hydrogen release was observed as 6.77 l/min. Two peaks of hydrogen release was observed during the process, resulting in a progressive decrease in cover gas pressure due to evacuation by vacuum pump. The cold trap temperature was raised gradually upto 400°C. The total volume of hydrogen released was estimated as 1.472 m^3 at STP.

The evolution of hydrogen with respect to time during regeneration is shown in Figure 3. Hydrogen is expected to be evolved from the cold trap by two mechanisms. They are: (1) hydrogen transport through bubble convection from NaH surface where it disengages and raises to the sodium-gas interface, (2) diffusion of hydrogen from NaH through the liquid sodium to the sodium-gas interface. The diffusion mechanism is few orders slower than the bubble convection mechanism.

During regeneration, nearly 1.3 m^3 of hydrogen (this is 90% of the total hydrogen released from the cold trap) evolved from the cold trap in 2500 minutes. Around 0.67 m^3 of hydrogen was not recovered during the regeneration process. This quantity of hydrogen is expected to be present in sodium as dissolved sodium hydride.

The dissolved hydrogen in sodium holdup is expected to be released only by diffusion mechanism. The average hydrogen release rate during hydrogen bubble convection and diffusion was estimated as 0.5 lit/min. whereas, the average hydrogen release rate during only diffusion was estimated as 0.009 lit/min.

Although this cold trap regeneration study is preliminary in nature, several significant conclusions that may be drawn from the results are:

(i) Sustained hydrogen evolution started at 346°C

(ii) The maximum rate of hydrogen release was observed around 6.77 lit/min and the total volume of hydrogen evolved was 1.472 m^3 out of 2.142 m^3

(iii) During hydrogen evolution, two peaks of hydrogen release were observed. The maximum pressure and temperature during first and second hydrogen releases were around 0.278 bar at 349°C and 0.577 bar at 378°C respectively

(iv) The average hydrogen release rate during hydrogen bubble convection and diffusion was estimated as 0.5 lit/min. whereas, the average hydrogen release rate during only diffusion was estimated as 0.009 lit/min.

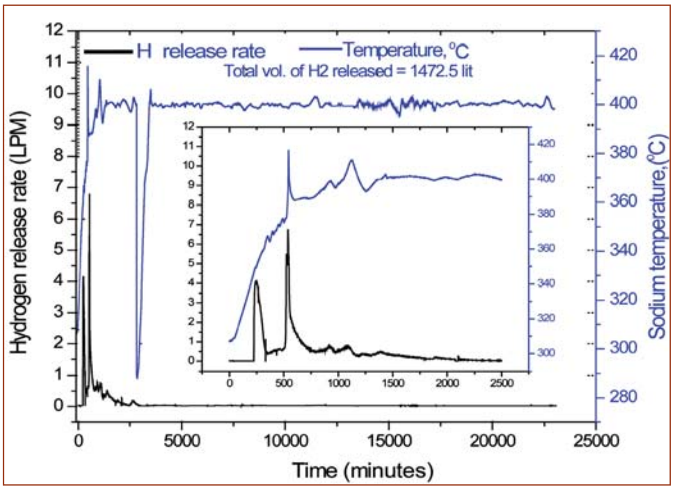

Fig. 2 *Hydrogen release rate and sodium temperature of cold trap*

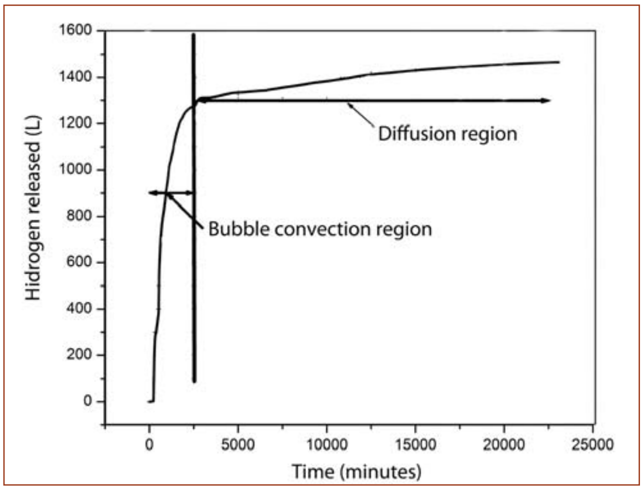

Fig. 3 *Evolution of hydrogen with respect to time*

II.16 Sodium Bubbler for Primary Argon Cover Gas System of the Prototype Fast Breeder Reactor

The primary argon cover gas system of PFBR located inside the reactor containment building, consists of a bubbler which connects argon gas streams with the reactor cover gas space. Generally NaK is used as bubbler medium in sodium cooled fast reactors and behaves as a passive unidirectional flow device, which allows gas flow from argon buffer tanks (ABTs) to the reactor cover gas space but prevents flow in the reverse direction and hence is helpful in avoiding pressure loss in the reactor cover gas space under transients like safety control rod accelerated movement (SCRAM). In addition, NaK bubbler acts as a final barrier to ensure purity of argon gas flowing to the reactor by removing oxygen and moisture from the gas in case of any incidental air ingress into the system. The bubbler also acts as a physical separation between the inactive fresh argon supply systems and the radioactive primary argon system. The NaK alloy was specifically selected as liquid medium for the bubbler as it is a liquid at room temperature and has high affinity towards oxygen and moisture. However, NaK handling involves a high level risk and any inadvertent handling is posed with the risk of an explosion. Any possibility of fire in the reactor containment building has to be avoided, as the layout of reactor containment building in PFBR is very compact and the components, piping, instrumentation and electrical systems are at commissioning stage. From the feedback of difficulties associated with the handling of NaK in the bubbler due to the explosive nature of potassium super oxide reaction product, it is proposed to opt for Na bubbler instead of NaK bubbler for primary argon cover gas purification.

Table 1: The removal efficiencies calculated for a liquid height of 90 mm as in the case of PFBR bubbler geometry

Medium (liquid height=90 mm)	Removal efficiencies (%) for			
	O_2 in Na at 200°C	O_2 in NaK at 37°C	Moisture in Na at 200°C	Moisture in NaK at 37°C
Without wire mesh	98.4	89.85	99	90.51
With wire mesh	99.99			

An in-house methodology has been developed to understand the effectiveness of using Na/NaK alloy as a bubbling medium with and without wire mesh for removing oxygen and moisture impurities from argon cover gas. The efficiency of the bubbler for cover gas purification is predicted by solving Fick's law of diffusion for spherical geometry. The methodology considers the diffusion of impurity from the bubble center to the bubble wall as the bubble rises in the Na/NaK liquid medium with and without wire mesh. This method assumes that the film mass transfer resistance for the impurity transport through the liquid boundary layer surrounding the bubble wall surface is negligible. Furthermore, it is also assumed that the impurity is immediately consumed by reaction or swept away once it reaches the bulk liquid solution (infinite sink). The resistance offered by the sodium oxide scales for the mass transport in the wire mesh is not considered in this analysis. The efficiencies for oxygen and moisture removal as predicted from the methodology are shown in Figures 1a and 1b. The removal efficiencies calculated for a liquid height of 90 mm as in the case of PFBR bubbler geometry are given in Table 1.

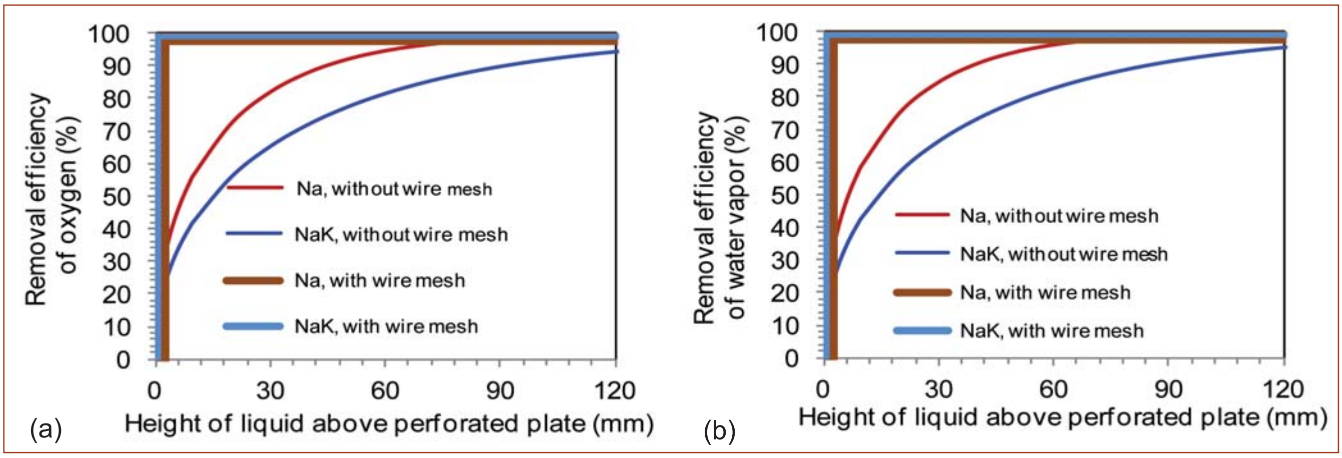

Fig. 1 *Removal efficiencies for (a) oxygen and (b) moisture as predicted from the methodology*

In order to validate the functional performance of sodium bubbler, a mock-up study was conceived. The schematic of the mock-up facility is shown in Figure 2 and the photograph of the facility is shown in Figure 3. The facility consists of a 1.5 metres long cylindrical stainless steel sodium container with 1" central argon inlet pipe with four stainless steel perforated plates welded to it with a gap width of 400 mm as shown in Figure 2. The gap between the parallel perforated plates is packed with stainless steel wire mesh of 100 numbers. Each perforated plate consists of 27 numbers of 10 mm holes. The central argon inlet pipe opening is 33 mm below the bottom perforated plate. Liquid sodium maintained at 200°C by means of heaters, is filled to a height of 90 mm above the bottom perforated plate. Oxygen analyzer, Nucon model number 4316 P, was used for the concentration measurements. The bubbler is double walled and the annular gap is inerted with argon gas to ensure that there is no sodium fire even in case of sodium leak.

After solidification of sodium by switching off the heaters, the argon cover gas purity inside the bubbler was brought down to the value of argon gas purity in the source cylinder by means of evacuation and purging method. Then sodium was reheated to 200°C and the argon gas inlet pipe was heated to 350°C. Hot argon gas (200°C) at a gauge pressure of 10 kPa was fed into sodium through the central inlet pipe. Online measurement of oxygen concentration in the argon cover gas inside the sodium bubbler was carried out for evaluating the performance of the bubbler. Preliminary tests carried out have provided some important guidelines for modifying the bubbler setup towards achieving improved performance. Many challenges were overcome during the experiment: splitting the inlet argon gas into bubbles by the combination of perforated plates and wire mesh, repeated evacuation and purging of argon gas inside the chamber to achieve oxygen concentration in the cover gas region equivalent to inlet argon and measuring trace levels of oxygen (5 ppm) in the argon cover gas.

Purification of argon gas at 200°C in sodium bubbler was demonstrated in the mock-up facility. Parametric studies are being carried to optimize the system for maximum efficiency.

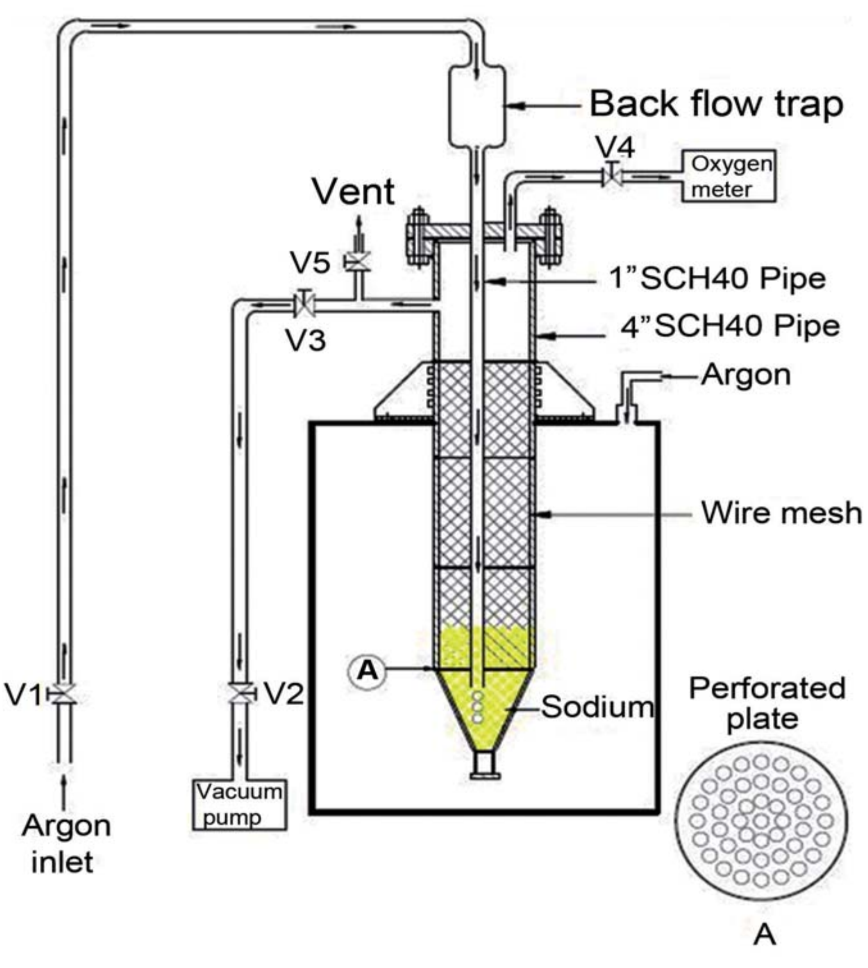

Fig. 2 Schematic of sodium bubbler facility

Fig. 3 Wire mesh arrangement and sodium bubbler facility

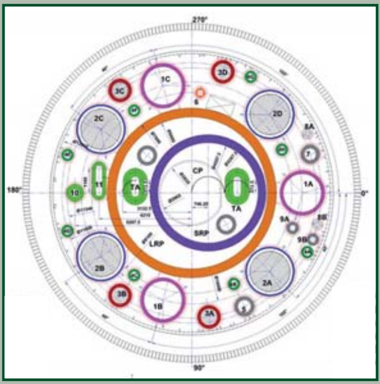

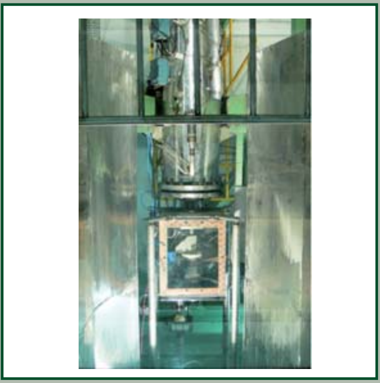

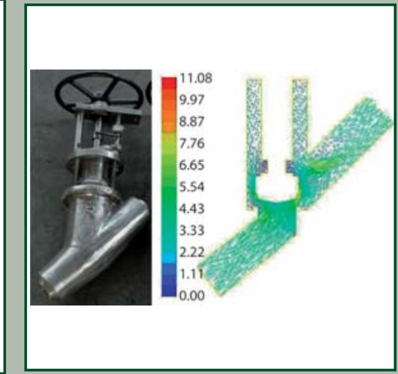

CHAPTER III

Research & Development for FBRs

III.1 Development and Testing of Integrated Cold Trap

The primary sodium in PFBR is purified by a cold trap placed outside the reactor vessel which leads to additional safety features including double wall piping and radioactive shielding around the sodium purification system. To avoid the transport of radioactive sodium outside the reactor vessel, in-vessel sodium purification philosophy in which entire sodium purification system will be immersed in the hot sodium pool is planned for future FBRs and thus enhance the safety. The challenging part of the design is the achievement of sodium cold point temperature in the order of 110˚C inside a hot pool of sodium at around 547˚C within a short radial gap of around 300 mm.

Integrated cold trap is conceptualized to remove the impurities from primary sodium at 547˚C temperature inside the reactor vessel. The maximum impurity level expected in the primary sodium corresponds to a plugging temperature of 153˚C after refueling operation. From this impurity level, the impurity level of primary sodium has to be brought down to a level corresponds to the plugging temperature of 110˚C by the operation of two numbers of integrated cold trap, in minimum possible time duration. Considering these factors the sodium flow through the integrated cold trap is fixed as 2 m^3/h. However, the reactor can be started only after the oxygen concentration in sodium goes below 3 ppm which is corresponding to a plugging temperature of 150˚C. Considering an effective utilization factor of 0.2 and wire mesh replacement time as two years the estimated volume of wire mesh required inside the single integrated cold trap with 20% additional margin is 0.31 m^3. The cold trap wire mesh has to be replaced after every two years of service and other parts of integrated cold trap can be utilized throughout the life of reactor.

A direct current conduction pump circulates sodium through the integrated cold trap and a permanant magnet flow meter monitors the sodium flow through the trap. Drainage cum bypass path is also provided for draining of the trapped sodium inside the cold trap vessel during removal of cold trap vessel for any maintenance activity. The full assembly of integrated cold trap will be supported at the roof slab of the reactor with proper support arrangement. The material of construction of the integrated cold trap is chosen as SS 316LN grade austenitic stainless steel which is same as that of reactor hot pool components.

From the geometrical constraint and maximum length below the normal sodium level and outer diameter of the integrated cold trap are fixed as 4.5 and 0.62 m respectively. The schematic of integrated cold trap is shown in Figure 1.

Figure 2 gives the schematic flow path of sodium, nitrogen and air in the integrated cold trap system.

The reduction of sodium temperature from the hot pool temperature to the cold point temperature is achieved by sodium to sodium economizer and a finned sodium cooler by compressed nitrogen. In the process of cooling the sodium oxide, sodium hydride impurities get precipitated in the wire mesh surface and thus the sodium gets purified. The pure sodium leaving the wiremesh flows through the

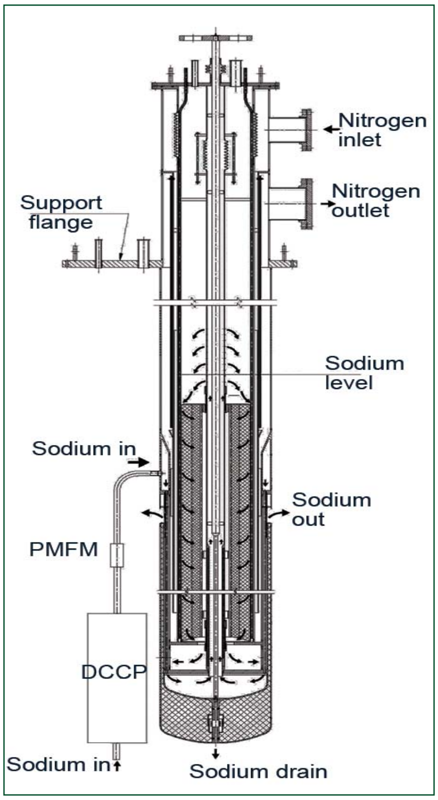

Fig. 1 *Schematic of integrated cold trap*

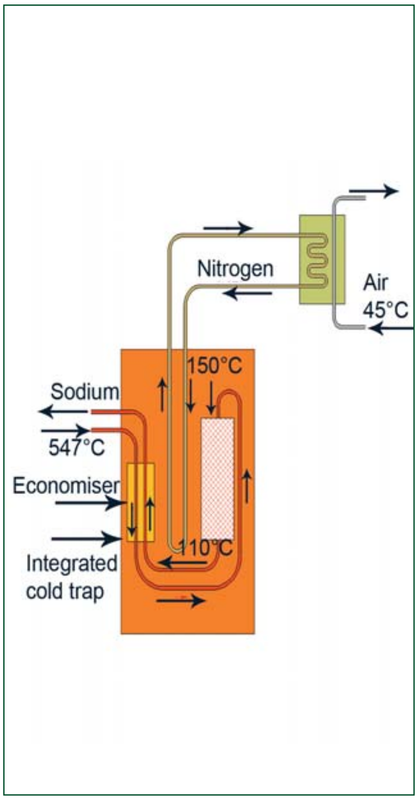

Fig. 2 *Schematic of flow path of sodium, nitrogen and air in the integrated cold trap system*

shell side of the economizer and gets heated up by the incoming sodium from the hot pool. The pure sodium discharges to the hot pool.

A full scale model of ICT was fabricated, the main components being economizer, heat exchanger, bellows and eight concentric shells used for making boundaries of sodium purification circuit and nitrogen cooling circuit. To reduce heat flow from hot sodium pool to cold sodium inside the ICT, thermal insulation is provided in between two hermetically sealed stainless steel shells. To accommodate the high differential thermal expansion between the inner shell and outer shell, stainless steel bellows are provided.

Dimensional tolerance was achieved for the different parts of the ICT for maintaining the gap between shells so as to ensure uniform fluid flow through the annular gaps. Fin welding was carried out in shell with restrainer arrangement and aqua purging to minimize distortion. The wire mesh AISI 304 continuous knitted type of 6 mesh per linear inch of grade 36SWG and 30SWG has been cleaned in tri-chloro ethylene bath and required weight has been wound within the specified dimensions to achieve the necessary packing density. Mating parts in two seating locations of ICT have been hard faced by stellite. All necessary non-destructive testing at various stages of fabrication have been carried out. The nitrogen side of integrated cold trap was subjected to pneumatic test and helium leak test. The integrated cold trap was packed and held rigidly inside a steel structure and transported from manufacturer's site to Engineering Hall-III.

The DC conduction pump was fabricated at M/s Krison Engineering, Baroda. DC conduction pump is a sodium submersible electromagnetic pump. DC conduction pump was also safely transported from manufacturer's site to Engineering Hall - III.

Assembly of ICT with direct current conduction pump and permanent magnet flow meter was carried out in a separate assembly structure in Engineering Hall - III. The hangers are used to support the DC conduction pump in ICT flange. The permanent magnet flow meter along with mineral insulated cables was positioned in the assembly.

The actuator system of ICT has been fabricated and assembled on the top of flange. Immersion heaters were provided in test vessel to maintain the constant sodium temperature of 547˚C in test vessel - 3 (TV - 3). The full scale model of integrated cold trap (ICT) has been erected in TV - 3. Figure 3 shows the photograph on erection of ICT in TV - 3.

The nitrogen cooling circuit for ICT has been manufactured and erected. The dry commissioning of nitrogen cooling circuit has been carried out separately.

After filling the sodium at 200°C in theTV-3 of large component test rig, the sodium temperature gradually raised to 550°C with a rate of 30°C/h. The cold point of the cold trap was maintained 120°C during the operation. 0.28 kg/s nitrogen flow rate at 1.3 bar(a) pressure was required to cool the sodium inside the cold trap. The nitrogen temperature increased from 54 to 233°C during the process.

The heat removed from sodium in ICT was 52 kW. The temperature difference within the wire mesh region was around 22°C. Thus, the establishment of cold point in the order of 110°C and above in the sodium pool temperature of 550°C was demonstrated.

Fig. 3 *Erection of integrated cold trap in test vessel-3 of large component test rig sodium loop*

The behavior of the system during transient conditions due to specific incidents during station blackout conditions were studied. To study the DC conduction pump trip with nitrogen cooling, the pump was tripped from normal operating conditions when the cold point temperature was 120°C. Nitrogen flow rate was controlled to maintain the required cold point temperature of integrated cold trap. During this study, the stability of cold point without the DC conduction pump operation was confirmed. Further to study the response of integrated cold trap on loss of sodium flow as well as nitrogen flow, DC conduction pump and nitrogen blower were tripped from the normal operating conditions when the cold point temperature was 120°C. The rise in cold point temperature was continuously monitored. The time taken for raise in cold point from 120 to 160°C was around 50 minutes and 120 to 400°C was 4 hours.

The performance of integrated cold trap is in line with the design expectation. Further transient experiments and impurity loading experiments on integrated cold trap are being carried out.

III.2 Decay Heat Removal Systems for FBRs

Decay heat continues to be generated even after the reactor shutdown. For the safety of the reactor after shutdown, the decay heat removal (DHR) operation has to be carried out at an adequate rate with very high reliability. In FBR-600, DHR will be ensured under 5 situations:

(1) fuel handling,

(2) in-service inspection,

(3) design basis events,

(4) station blackout and design extension conditions and

(5) post accident conditions.

Figure 1 shows the DHR setup of FBR-600. For meeting the DHR requirements for the first three situations, dedicated DHR systems (4 x 10 MW) will be introduced in the secondary sodium circuits (SSDHRS) instead of operation grade decay heat removal system in steam water system in PFBR. This decision is taken after detailed assessment of design, operational simplicity and availability. The necessity of steam water system, water and power for DHR is eliminated in FBR-600. In addition, during Class-IV power failure, controlled cooling can be achieved using SSDHRS which is not possible with DHR system riding on steam water system.

Each circuit of SSDHRS consists of sodium-air heat exchanger (AHX) connected to secondary sodium system with sodium piping. An EM pump in the sodium circuit and blower in the air circuit ensures forced circulation in the AHX. This system will be designed to work in passive mode at reduced capacity by suitably locating AHX at higher elevation and providing a small stack on the AHX.

Based on the design requirements, three possible configurations of SSDHRS connecting to secondary sodium circuit are identified viz. connecting to the hot leg, connecting to the cold leg, connecting between hot and cold legs. Out of the three configurations, the third configuration where hot sodium is drawn from the surge tank, exchanged heat with air and returned to pump tank is considered to be a better configuration from natural circulation considerations. This requires an additional heat exchanger to avoid thermal striping problem at the junction of SSDHRS cold leg and secondary sodium cold leg.

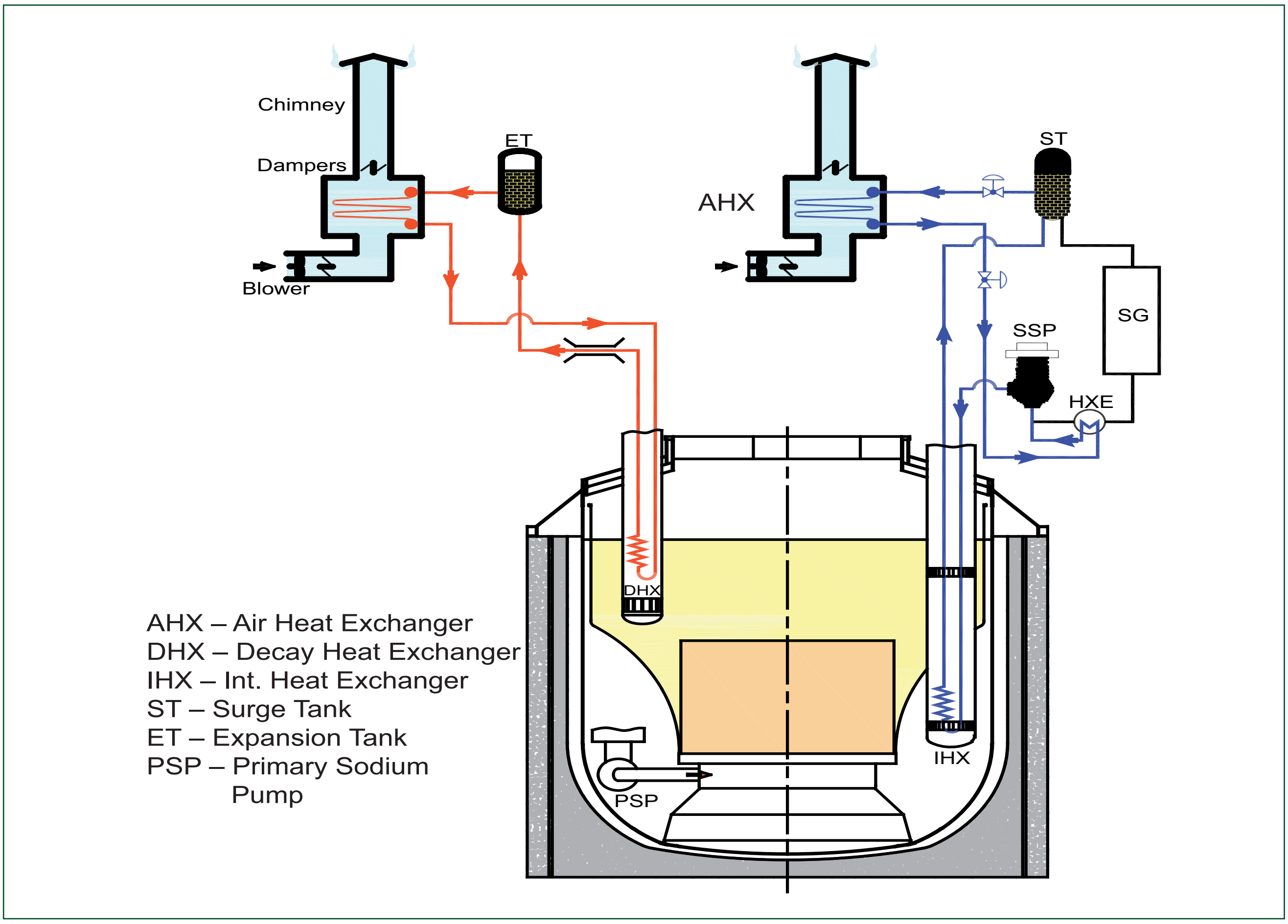

Fig. 1 Decay heat removal systems in FBR-600

For taking care of DHR during station blackout and design extension conditions (situation 4), safety grade decay heat removal system (SGDHRS) will be available as in PFBR. SGDHRS consists of 2 x 8 MW active and passive circuits. The active circuits are provided with an EM pump in the intermediate circuit and blower in the air circuit. The active circuits can also work at reduced capacity (6 MW/circuit) in passive mode. In FBR-600, in order to avoid complete loss of SGDHRs due to common mode failure, it is planned to keep the AHX of passive type SGDHR circuits on SG building and the AHX of active type SGDHR circuits on Fuel handling building. The SGDHR operation is similar to that in PFBR.

In PFBR main vessel (MV) and safety vessel (SV) are periodically inspected and thus simultaneous leak in the main vessel and safety vessel is a beyond design basis event. In the case of FBR-600, this event is considered for the design. The fall in hot pool sodium level is minimized by having a reduced main vessel-safety vessel gap and reduced safety vessel-reactor vault gap. The fall in hot pool level in FBR-600 following simultaneous main vessel and safety vessel leaks is shown in Figure 2. Proper design of DHX will ensure adequate DHR by SGDHRs even after the leak. Further, R&D will be carried out on high temperature sodium resistant concrete for the reactor vault.

Detailed 3-D computational fluid dynamics studies carried out for PFBR showed that even under complete loss of power supply, the natural circulation flow around the subassembly (inter-wrapper flow) can limit the temperatures below design safety limits. The same will be true for FBR-600 also.

The DHR requirement during post accident situations (after core disruptive accident) is met by the SGDHRS as in PFBR. Further improvements required are for ensuring the heat removal capacity features in case of core debris resulted from whole core meltdown. Though it has been shown by computational fluid dynamics analysis that large perforation created by the molten fuel while melting through the grid plate and CSS facilitate adequate natural circulation of sodium to remove the heat from debris settled on the core catcher and to transport to SGDHRs inlet windows through natural convection mode, considerations are being given to incorporate a few pipes penetrating through inner vessel as shown in Figure 3 for providing alternate/additional passages for the sodium flow once the mean temperature exceeds a certain value. R&D on validation of this concept is in progress in the PATH facility commissioned at our Centre for this purpose.

With incorporation of above mentioned systems, the unavailability of DHR system in FBR-600 can be reduced to 1×10^{-7}/ry.

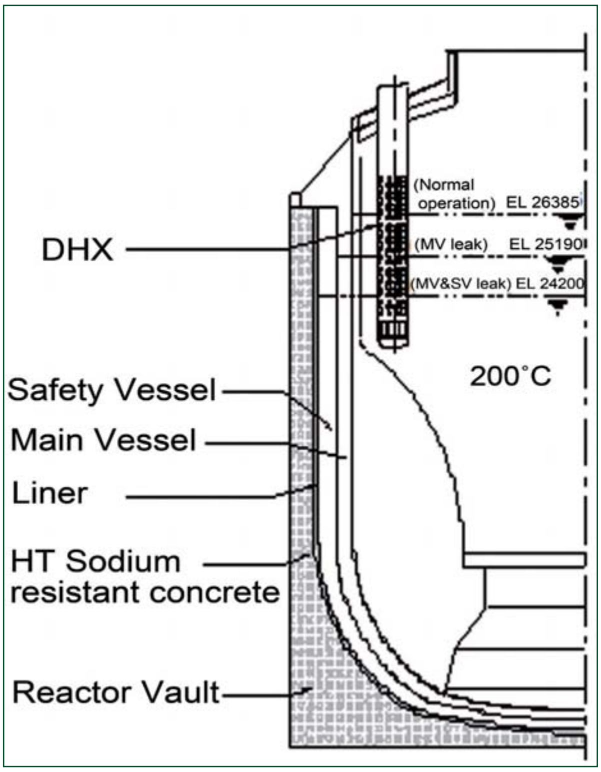

Fig. 2 *Schematic of hot pool level following main vessel and safety vessel leak at 200°C*

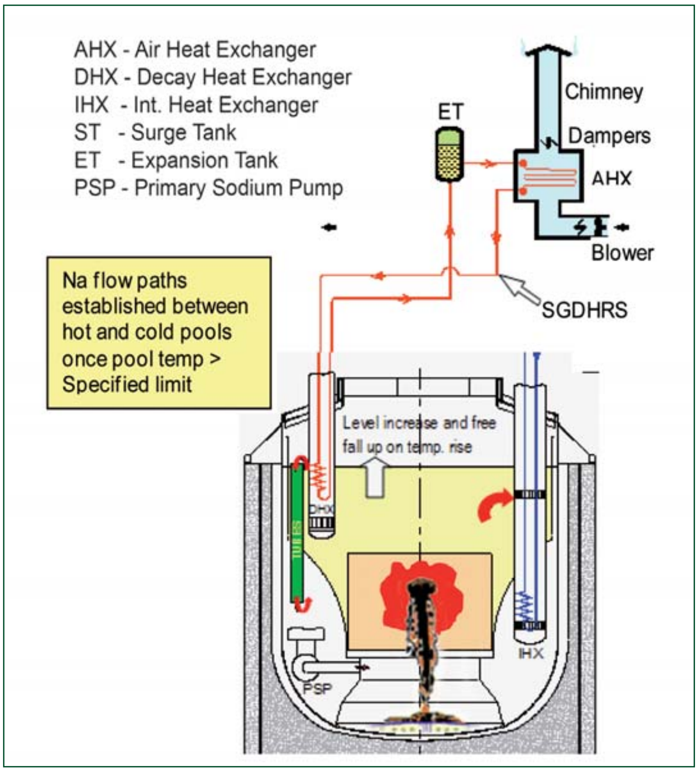

Fig. 3 *Post accident decay heat removal in FBR-600*

III.3 Development of Passive Shutdown System: Gravity Fall of B_4C Granules Stimulated by Sodium Temperature Rise

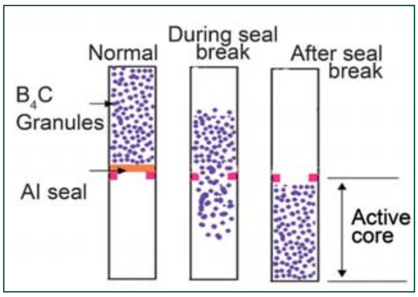

Fig. 1 *Granules concept with fusible seal*

Fig. 2 *Experimental simulation of fall of granules*

PFBR has two independent, reliable, fast-acting, automatic, diverse shutdown systems with enriched boron-carbide (B_4C) pellets managed by nine control and safety rod drive mechanisms (CSRDM) and three diverse safety rod drive mechanisms (DSRDM). The functions of control and safety rod are to control the reactor power and facilitate start-up and control shutdown of the reactor and also to SCRAM the reactor in abnormal conditions. The function of diverse safety rod is to facilitate shutdown of the reactor during SCRAM. For the future reactors, in addition to these systems, it is contemplated to have a passive system which is independent of other systems and act based on the feedback from the core, referred as ultimate shutdown system (USS). The proposed ultimate shutdown system uses a thermal fusible seal which holds the B_4C granules above the active core during normal operation. During untoward events, when the sodium temperature goes beyond the melting temperature of the seal, the granules get released into the active core and thereby shutting down the reactor. This is schematically shown in Figure 1. The experimental simulation of a single pin with an aluminium seal was carried out for concept validation and to choose optimum fusible seal. The fall of granules after break of seal is shown in Figure 2. The experiment has been done with two types of fusible seals viz. 1) circular disc and 2) conical plug and are shown in Figure 3. The experiment revealed that in a ‘circular disc’ seal concept, the granules were unable to drop due to the surface tension of the molten seal since the load offered by the granules in small diameter tubes was very small despite seal reaching its melting temperature. Whereas, in a conical type of seal, after melting of seal at periphery, the plug has been pulled down by its self-weight. The shapes of the seals before and after melting are shown in Figure 3.

For subassembly development based on the above concept, two choices are available viz., (a) multiple numbers of absorber pins with seals and (b) single tube with B_4C granules with a single central seal. The second design seems to be better than the first concept from the reliability point of view, absorber pin failure detectability, simplicity in construction and the negative reactivity worth inserted during an untoward incident.

Fuel pins are provided around absorber pins for increasing the sodium temperature according to power to flow conditions of the reactor. Thus the fuel pins, coolant flows around, gets heated up, further flows past the seal of the B_4C chamber and leaves the subassembly at the top. Hence, the seal always sees coolant outlet temperature from the fuel pins. Once the seal fails, B_4C granules rush to the bottom chamber which is in line with active core leading to reactor shut down.

The results of these experiments are encouraging and provided a good insight into the chosen concept and response of seals towards detailed engineering of the system.

The proposed subassembly schematic is shown in Figure 4.

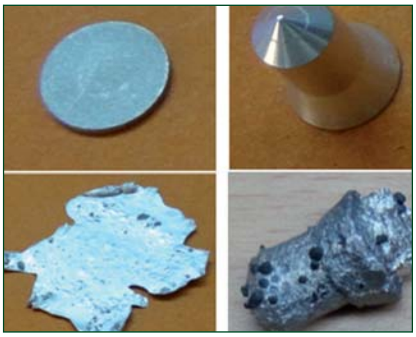

Fig. 3 *Aluminium seals before and after melting*

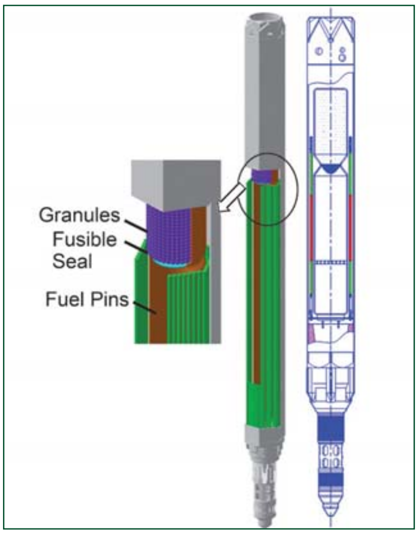

Fig. 4 *Ultimate shutdown system subassembly*

III.4 Characterization of Sodium Aerosol in Cover Gas Region of SILVERINA Loop

In the normal operation of Sodium Cooled Fast Reactor (SFR), the thermal gradient between the sodium pool surface (550˚C) and roof top plug (120˚C) results in the evaporation of sodium from the hot pool surface. This leads to evaporation of sodium aerosols within the cover gas space and aerosol deposition on cooler surfaces such as rotating plug and fuel handling machine. The deposited aerosol may hinder the movement of rotating plug and operation of fuel handling machine and that of cover gas purification system. It is essential to know the aerosol concentration and droplet size distribution in order to predict effectively the heat and mass transfer phenomena, which may be altered due to interaction of thermal radiation with aerosols and mass transfer due to deposition of aerosols on cooler surface. A detailed review of literature revealed that sodium aerosol properties get modified due to (i) temperature difference between the sodium pool surface and the bottom of the roof top plug and (ii) presence of intense gamma rays resulting in possible enhanced coagulation of sodium aerosols upon interaction with gamma radiation and consequent increase in sizes. In order to predict the heat and mass transfer phenomenon effectively, it is essential to have data pertaining to aerosol concentration and droplet size distribution. In view of this, a series of experiments were conducted in the SILVERINA loop to characterize the size distribution and mass concentration of sodium aerosols in the cover gas region by adopting suitable procedures.

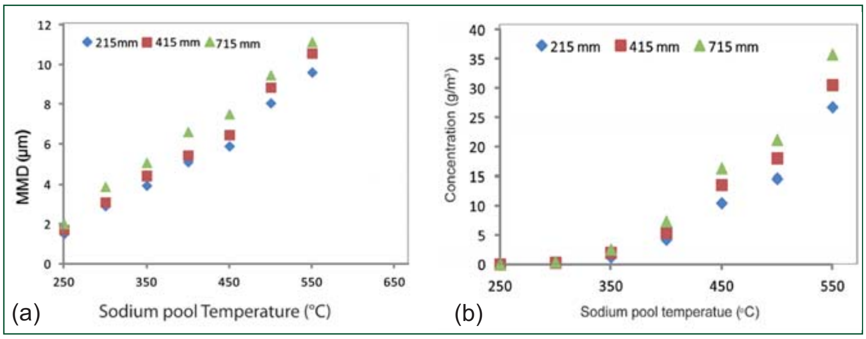

Fig. 1 Variation of sodium aerosol (a) mass median diameter and (b) mass concentration with pool temperatures for three different levels

The aerosol sampling system consists of (a) aerosol sampling tube, (b) aerosol sampling bottle, (c) line heaters, controller and (d) aerosol flow controlling device. The sampling bottle is filled with paraffin oil (~ 600 ml) and maintained at ambient temperature. The aerosol sample laden cover gas is made to pass through the bottle. Thus, solidification of aerosol particle would occur as the cover gas enters into the paraffin oil. The residence time of the cover gas is increased due to baffle arrangement, which ensures that all sodium aerosols get trapped from the cover gas before it goes out of the bottle. The paraffin oil filled in the sampling bottles are taken for analysis. The sodium aerosol size distribution is determined by using Mastersizer and the mass concentration is carried out by conductivity method.

The experiments are conducted by inserting a sampling tube of required length (215, 415, and 715 mm from the top) in TP-1. The height of the cover gas region is 820 mm from the top of the TP-1. The pressure of cover gas region is kept 0.35 bar above the atmosphere and sampling line temperature is kept at 110°C. The sodium pool temperature is varied from 250-550°C in steps of 50°C. The sampling flow rate was 2 lpm and sampling time was set at 20 minutes for the sodium pool temperature of 250°C and progressively reduced to 2 minutes at the sodium pool temperature of 550°C.

After sampling, the paraffin oil is analyzed and sodium aerosol mass median diameter (MMD) is found to vary from 1-2 μm and increases with than increase of sodium pool temperature (Figure 1a). For all the pool temperatures, the MMD is found to be higher near the pool compared to near the roof and middle level of cover gas region. Particles formed in the cover gas space tend to coagulate while they are transported by the convection current. Since the bigger particles experience higher gravitational force, they remain near the pool. The mass concentration of sodium aerosols is found to vary from 0.026 to 35.6 g/m^3 and increases with the increase of sodium pool temperature. The variation of sodium aerosol mass concentration is shown in Figure 1b. It is observed that, for all pool temperatures, the sodium aerosol mass concentration is higher near the pool surface than near the roof and middle level of cover gas region. The theoretically predicted and experimentally measured mass concentration (Figure 2) are in good agreement (±20%) for all the pool temperatures.

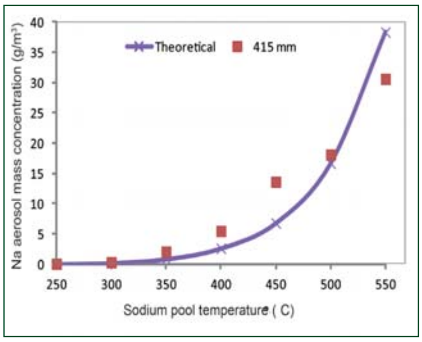

Fig. 2 Theoretical and experimental comparison of sodium aerosol mass concentration

III.5 Testing and Evaluation of Innovative Fusible Plug for Sodium Leak Collection Trays

Despite sound design provisions, sodium leaks are considered in sodium piping and systems in the secondary circuit as safety issues at various operating conditions of Sodium cooled Fast Reactors (SFR). The leaked sodium can undergo combustion in spray, pool or combined form, generating dense white smoke and flame leading to rise in ambient gas temperature as well as causing a potential hazard for the plant and operating personnel. Sodium pool fires are usually extinguished by applying dry chemical powder whereas sodium spray fires in isolated chambers are extinguished by nitrogen flooding. However, for handling large scale fires a passive leak collection system is used.

The leak collection system includes a series of leak collection trays (LCT) provided below the sodium pipelines and tanks. A large number of leak collection trays are strategically arranged under the secondary sodium piping to collect leaking sodium into a sodium dump tank connected through a low melting fusible plug system as depicted in Figure 1. The sodium fire will be extinguished due to oxygen starvation.

Transient thermal analyses have been carried out to arrive at the suitable thickness of the woods metal fusible plug required in the header-transfer tank junction, for effective melting of the fusible plug and complete draining of the leaked sodium. Vent port with fins attached to outer surface to promote freezing of sodium, to arrest sodium leakage and allowing only entrapped gases to escape for smooth flow of sodium in the sodium storage tank is investigated numerically. It is found that 15 NB Sch 40 steel pipe of 500 mm long with 20 fins, as vent port is sufficient to plug the possible leak of sodium without any secondary leakage to ambient through port.

Experiments on functionality and performance evaluation of such sodium leak collection system including the melting of fusible plug system and subsequent draining of sodium into dump tank have been conducted.

Experimental facility

The experimental facility consists of a sodium supply tank, connecting pipelines, fusible plug and dump tank as shown in Figure 2. The bottom of the sodium supply tank is connected to a nozzle, which is provided with a rupture disc release system. The rupture disc will open-up under rated pressure, which is applied to the sodium supply tank for sodium release. Downstream the rupture disc, the inner diameter of nozzle is maintained as 11 mm to form 1 cm^2 leak area simulating a possible sodium pipe leak as per leak before break theory. An arrangement is made to heat the sodium of 10 kg in the top vessel at desired temperatures. The melted sodium is retained in the vessel using rupture disk as described above. The vessel is then pressurised by dedicated argon supply system to rupture the disc and drain the hot sodium through 100 NB pipe line. The hot sodium comes in contact with woods metal disc and it absorbs the heat and finally melts the fusible plug. The sodium is then drained to the bottom hold up vessel. Temperatures are monitored at various locations for ensuring draining of sodium. Two dedicated video cameras are employed for monitoring the bellow expansion of dump tank. The experimental setup is installed

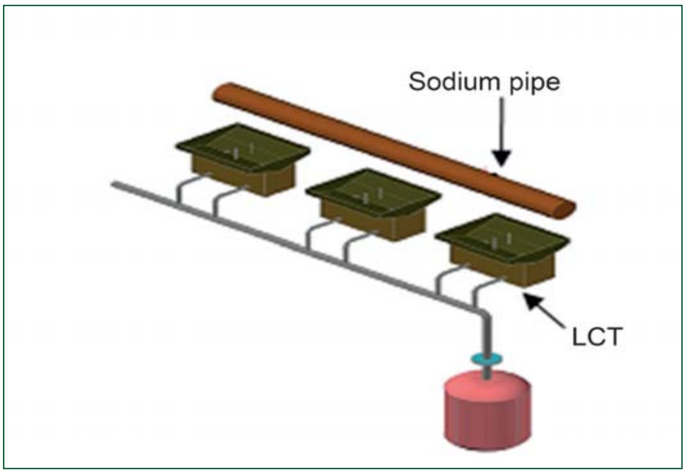

Fig. 1 *Leak collection system*

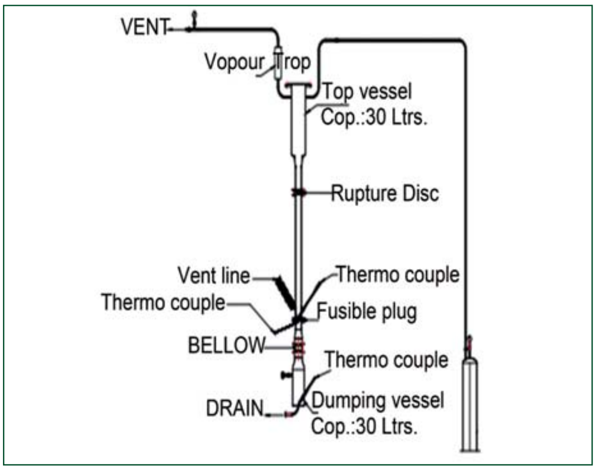

Fig. 2 *Experimental facility*

Fig. 3 *Photograph of the experimental facility*

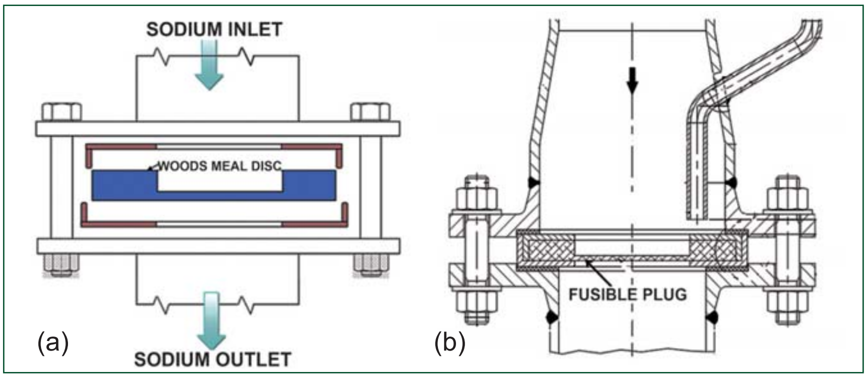

Fig. 4 *Enlarged view of system (a) fusible plug assembly and (b) plug with vent port*

inside the test chamber of sodium fire experimental facility as shown in the photograph in Figure 3. The fusible plug system was designed, fabricated and mounted in the sodium drain pipe in between rupture disc and dump tank. The enlarged view of the fusible plug and vent port system is depicted in Figure 4. The melting of fusible plug is expected to occur in less than 11 seconds for the sodium temperature of about 115ºC.

Qualification of fusible plug

The dump tank connected with a series of leak collection trays is isolated by a woods metal fusible plug and kept under nitrogen atmosphere to prevent sodium fire in the dump tank as discussed above. The fusible plug has to be qualified for its melting within a short period of time to avoid overflow of sodium in the leak collection tray. In the unlikely event of a sodium leak, the leaked sodium by virtue of its high temperature has to heat up the fusible plug to melt the same and drain into the transfer tank, thus mitigating the consequent sodium fire potential.

However, it has to be established whether the heat capacity of the leaking sodium is adequate to heat up the entire header and melt the fusible plug. The main concern is that the sodium should not freeze due to heat loss to the header and the plug. In case of sodium freezing in the header, the sodium instead of draining to dump tank will spill over the leak collection tray, which is to be avoided. Temperature evolution in sodium depends on the thickness of the header, its diameter, thickness of the fusible plug and its heat capacity. Woods metal is the preliminary choice for the fusible plug. It is an alloy of Bi-50%, Pb-25%, Sn-12.5% and Cd-12.5% with 72ºC melting point. Computational heat transfer analysis has been carried out to predict the temperature evolution in the header system of 100 NB schedule -40 and schedule-10 pipe lines with woods metal fusible plugs. The temperature of the leaking sodium has been varied systematically from 300 - 400°C to investigate the risk of sodium solidification and to understand the stages of melting propagation of the fusible plug. Evolution of temperature on the top and bottom surfaces of the fusible plug at 10 seconds is depicted in Figure 5. It is evident from these figures that within 5 seconds, the fusible plug melts and at the same time only a 3 mm thick sodium layer solidifies, momentarily. However, within about 10 seconds, the sodium re-melts enabling draining of the sodium into the tank. It is established that the complete melting of the fusible plug of 3 mm is expected to occur in less than 11 seconds for the sodium temperature of about 115ºC.

Series of experiments were conducted to confirm the thermal design of the entire system by leaking 10 kg of sodium at different temperatures through rupture disc into the fusible plug. Observation showed melting of fusible plug within 10 seconds and collection of leaked sodium into dump tank. The collection of hot sodium in dump tank is also confirmed by LVDT measurement and video image of stainless steel bellow on which dump tank is hanged. The experiment qualified the fusible plug for leak collection tray system of PFBR. The melted fusible plug after the experiment is shown in Figure 6.

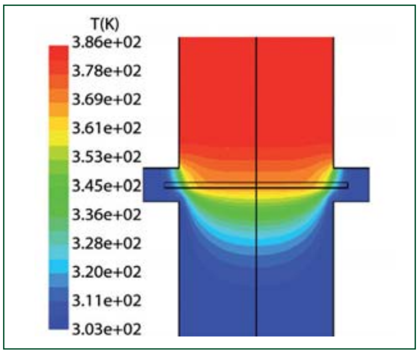

Fig. 5 *Isotherms obtained at plug*

Fig. 6 *Fusible plug after melting*

III.6 Performance Evaluation of Sodium Submersible Annular Linear Induction Pump

A sodium submersible annular linear induction pump (SALIP) was designed and developed with the help of industry for draining of primary sodium from PFBR, if situation warrants. Presently, there is no system for draining of primary sodium in PFBR. Hence to overcome this constraint, a developmental work was initiated to design and develop sodium submersible annular linear induction pump. The developed, submersible pump is of capacity 2 m^3/h at 4 kg/cm^2 and is first of its kind which uses mineral insulated stainless steel sheathed cable for its winding. SALIP is capable of operating in radiation environment under sodium submerged condition at 200°C with winding thermal withstand capacity up to 550°C. Schematic of SALIP is shown in Figure 1 and manufactured SALIP is shown in Figure 2a. Sodium testing of SALIP for its performance evaluation has been carried out.

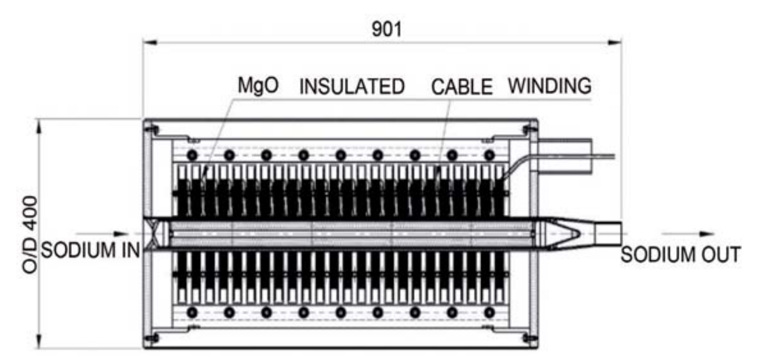

Fig. 1 *Schematic of submersible annular linear induction pump*

The sodium testing of SALIP was planned in two phases. In the first phase, pump was tested as per any conventional methodology for determining its characteristics without submerging in sodium pool because measurement of pressure (head) developed is not feasible in submerged condition. In second phase, it is planned to test its operational functionality in sodium submerged condition.

First phase of sodium testing was carried out in BIM loop of FRTG. Pressure measuring system based on constant sodium level differential pressure balance technique was installed in BIM loop along with flow measuring device and other instrumentation and control systems required for SALIP testing. Sodium testing of SALIP was carried out in a conventional methodology. During testing in sodium submerged condition, a temperature of 200°C was simulated by heating pump surface by trace heaters fixed on the outer surface of the SALIP. SALIP installed in BIM Loop is shown in Figure 2b. In the first phase of testing, pressure versus flow, input power versus flow and efficiency versus flow characteristics were obtained to evaluate pump performance. Hydraulic characteristics of SALIP obtained from sodium testing at 200°C is shown in Figure3. Pump has also completed 1000 hours endurance test operation. Successful evaluation of pump characteristics through sodium testing has validated new design concept of sodium submersible annular linear induction pump using mineral insulated stainless steel sheathed cable winding and successful endurance testing has proved the robustness of the design. Functional testing in sodium submerged condition is planned shortly.

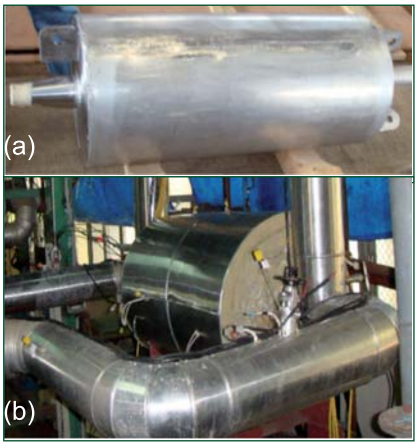

Fig. 2 *(a) Manufactured SALIP and*
(b) SALIP installed in BIM Loop

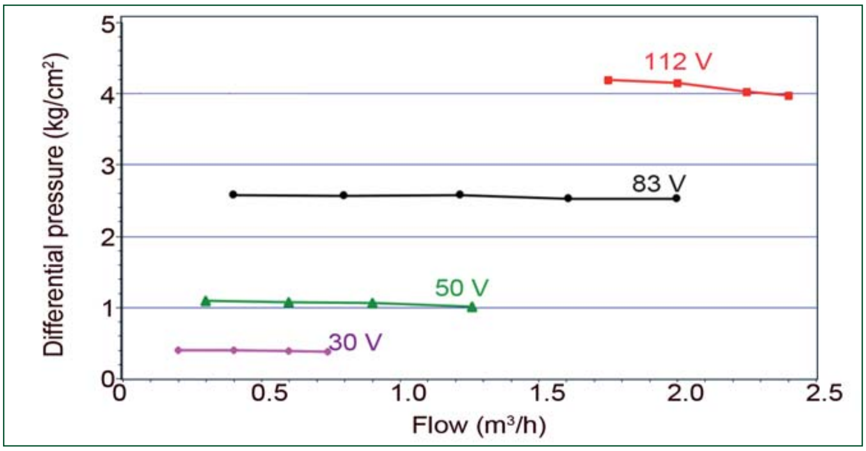

Fig. 3 *Head versus flow at 200°C (hydraulic characteristics)*

III.7 Development of Ferritic Steel Bellow Sealed Sodium Valves

The usage of 2¼ Cr-1Mo and Modified 9Cr-1Mo grade steels instead of SS 304LN and SS 316LN as material of construction of secondary sodium system and safety grade decay heat removal system in future FBRs have economical advantage. In addition to the low material cost, the usage of ferritic steel pipes in high temperature system reduces flexibility requirement at elevated temperature and hence reduces the overall pipe length in the system. This makes the plant layout simple and economical. The reduction of the piping length in SGDHR system will increase the capability of that system for the transport of decay heat through the buoyancy induced sodium flow. As part of this program, bellows sealed sodium valves made of 2 ¼ Cr-1Mo and modified 9Cr-1Mo grade steels are developed in collaboration with the valve industry. Five numbers of DN50 valves were designed, manufactured and tested in each material as per ANSI B 16.34 special class requirements.

Material of construction of the valve body and bonnet is ferritic steel where as the bellows were made with SS 316 Ti grade austenitic stainless steel. The valve plug and stem were made of SS 316LN grade steel. Photograph of a finished bellow sealed sodium valve is shown in Figure 1a. One end of the bellows is welded to the stem of the valve made of SS 316LN whereas the other end is welded to the bonnet of the valve made of ferritic steel. The dissimilar welding between top bellow collar and bonnet were done with inconel buttering. The valve body and bonnet are connected with bolted joints and the leak tightedness of this joint is achieved by lip seal welding. The valve body and bonnet were manufactured by close die forging and other parts were machined from bar stock.

The bellows sealed valves were designed to withstand an internal pressure of 0.6 MPa at 600°C temperature. The design was verified by structural analysis using finite element analysis for normal operation and thermal transient condition. The thermal shock considered for the transient analysis was 60°/minute. The hydraulic characteristic of the valve was also studied by numerical methods and ensured that the flow resistances are within specified limits. The numerically derived sodium flow field inside the valve is shown in Figure 1b.

All the stage qualification for body, bonnet, bellows and trim material were performed in the appropriate stage of manufacturing. All the forged parts were throughly inspected by means of visual inspection methods. Ultrasonic inspections were carried out on all the raw materials and forgings to ensure that the parts are free from unacceptable defects. The valve body was subjected to hydrostatic test after machining. Tests on finished valves such as pneumatic proof test, seat leakage test and helium leak test were performed as per the specification. In addition to these tests the valves were subjected to helium leak test across the seat of the valves at room temperature with an acceptable leak rate of 10^{-7} pa-m^3/s. One valve was heated to 560°C by means of electrical heaters and the operation of the valve was checked manually. This valve was subjected to a thermal cycle from 100° to 560°C and back to 100°C three times. No requirement of additional torque was observed during the high temperature operation at 560°C. The valve was tested for leak tightness after the thermal cycling at room temperature and no deviation in the leak tightedness was observed.

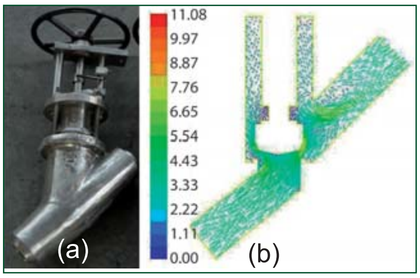

Fig. 1 *(a) Finished bellow sealed sodium valve (b) sodium velocity (m/s) profile inside the valve when it is fully opened*

One valve from the manufacturing lot was tested for its hydraulic characteristics at Fluid Control Research Institute. The testing gave a valve coefficient (C_v) of 65.0 at fully opened condition. This excellent C_v gives minimum flow resistance to sodium during its service. The experimentally obtained flow characteristics of the valve are shown in Figure 2.

Design, manufacturing and testing of bellows sealed sodium service valves ferritic steel body materials has been completed. All the specified tests were completed sucessfully and have been accepted. Qualification of these valves by sodium testing will be performed in sodium loops shortly.

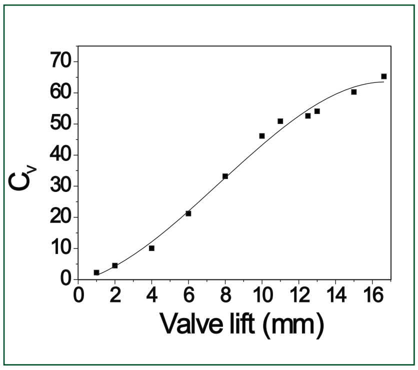

Fig. 2 *Flow characteristics of the valve*

III.8 Development of Side Wall Type Permanent Magnet Flowmeter for Sodium Flow Measurement in Large Pipes

Conventional permanent magnet flow meters (PMFM) based on motional voltage require magnetic field with planar symmetry with respect to horizontal and vertical axes passing through the center of stainless steel pipe. The weight and size of PMFM increases with increase in diameters of stainless steel pipes to produce magnetic field of desired symmetry. To reduce the weight and size of PMFMs for flow measurement in large pipes, a new flow meter design based on magnetic field with planar symmetry with respect to only vertical axes passing through center of stainless steel pipe is conceptualized. In the new design, a single block of permanent magnet (ALNICO-V) is mounted on one side of stainless steel pipe in which sodium flow is to be monitored. This new flow meter is named as side wall flow meter (SWFM). Similar to conventional PMFM, SWFM works on the principle of measurement of motional voltage generated in liquid sodium flowing in steady magnetic field. As the magnetic filed in SWFM is not symmetric along the horizontal axes, the flowmeter voltage signal depends on position of electrodes. The cross sectional and side view of SWFM for flow measurement in 100 NB stainless steel pipe is shown in Figure 1.

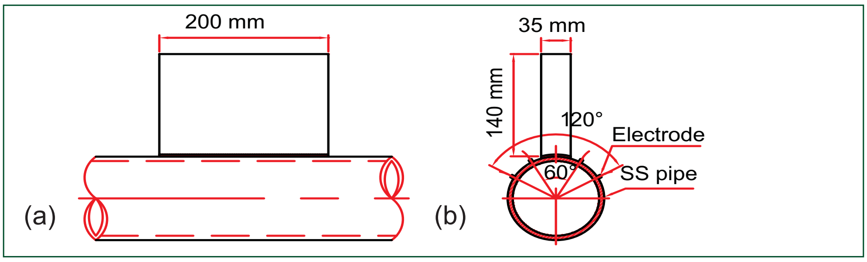

Fig. 1 *(a) Cross sectional and (b) side view of side wall flow meter*

Sensitivity of side wall flowmeter

Sensitivity of a SWFM is defined as the flowmeter output voltage signal in mV across flowmeter electrodes for a unit flow rate (1 m^3/h) in flowmeter pipe. The unit of sensitivity is mV/m^3/h. Sensitivity of SWFM depends on electrical conductivity of fluid flowing through the pipe, size and wall thickness of the pipe, electrical conductivity of the pipe, magnetic flux density distribution across the pipe, velocity profile of sodium in the pipe and electrode position.

Analysis of side wall flowmeter

In SWFM magnetic flux density is not uniform in stainless steel pipe, hence sensitivity of flowmeter depends on position of the electrodes. Motional voltage plot across the pipe cross section was simulated using finite element modelling (FEM) code COMSOL 3.5 to determine the electrode position with maximum sensitivity. Modelling involves magnetostatics, incompressible Navier Strokes and DC conduction application modes of the software. Tetrahedral mesh elements are used in simulation due to presence of stainless steel pipe in model. Model becomes highly non linear due incorporation of BH curves and flow simulation, hence problem is divided into three parts and sequential approach is adopted to solve the model.

In first step, liquid sodium is kept stationary and magnetic field generated by magnetic circuit is simulated using BH curves. In second step, liquid sodium flow is simulated using physical properties like density and dynamic viscosity of sodium corresponding to sodium temperature and flow rate in stainless steel pipe. Finally voltage signal developed due to interaction of moving sodium in steady magnetic field is calculated. To account for loss of voltage signal in modelling, electrical conductivities of stainless steel and liquid sodium at different temperatures is calculated and used in modelling. Magnetic flux density in pipe cross section due to side wall permanent magnet is shown in Figure 2. It can be seen that magnetic flux density is not uniform across horizontal axes.

Motional voltage plot and motional current density across the pipe cross section at a flowrate of

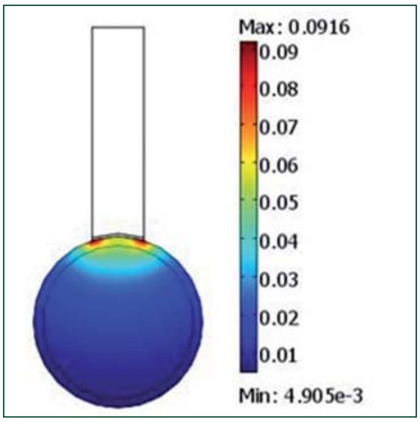

Fig. 2 *Magnetic flux density (T) in cross section of stainless steel pipe*

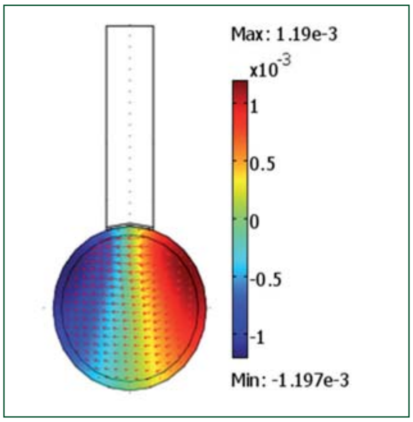

Fig. 3 *Electric potential plot in stainless steel pipe*

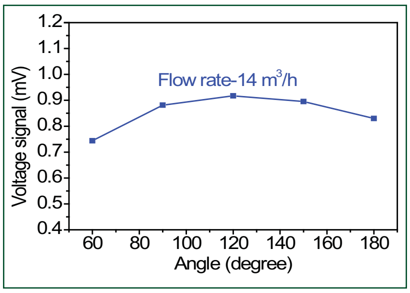

Fig. 4 *Variation of side wall flow meter voltage signal with electrode position*

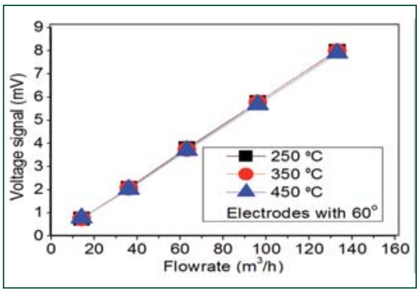

Fig. 5 *Side wall flow meter voltage signal verses flow with electrodes 60° apart*

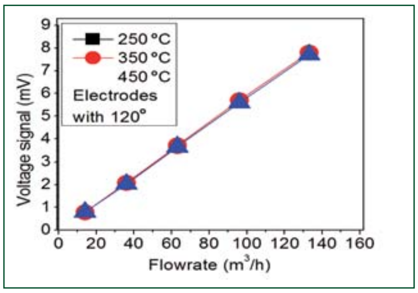

Fig. 6 *Side wall flow meter voltage signal verses flow with electrodes 120° apart*

36 m^3/h is shown in Figure 3. It can be seen that motional voltage is not uniform across pipe cross section. Voltage signal developed in SWFM for a particular flow depends on magnetic flux density values and distance between the electrodes. As we go away from magnet, magnetic flux density values reduce and the distance between electrodes increases. Voltage signal first increases due to increase in the distance between electrodes, attains a maximum value and then starts decreasing as the reduction in magnetic flux density plays a dominant role. It can be seen in Figure 4 that a maximum potential difference for the rated sodium flow is developed across electrodes welded at 120° apart.

Testing and calibration of PM based SWFM for sodium

Based on analytical design and FEM analysis, SWFM for 100 NB pipe was fabricated and tested in an existing sodium rig (LCTR). Calibration of SWFM was done by absolute constant volume method. During calibration flow rates were varied from 14 to 143 m^3/h. Sodium flow was in turbulent region as Reynolds number varied from 1.12×10^5 to 1.56×10^6 for above mentioned flow rates. The calibration runs were repeated at 250, 350 and 450°C, for assessing the variation in sensitivity with temperature. Plots of SWFM voltage signal measured in experiments across stainless steel electrodes welded at 60° and 120° angle verses flowrates at different temperatures are shown in Figures 5 and 6 respectively. Both the pairs are giving measurable output voltage which confirms the functionality of this type of flowmeter. The output is found to be fairly linear over the range of flow up to 140 m^3/h.

Figure 7 shows the variation of SWFM sensitivity with respect to temperature at a flowrate of 136 m^3/h for both the pairs of electrodes. SWFM voltage signal decreases by 2.5% when electrodes are 60° apart, while it decreases by 2.6% when electrodes are 120° apart, when temperature of sodium increases from 250 to 450°C. The output and hence sensitivity of the flowmeter decreases with respect to temperature marginally. The above mentioned decrease in sensitivity is due to increase in ratio of stainless steel conductivity to sodium conductivity with temperature and negative temperature coefficient of magnetic flux density. Increase in ratio of conductivity with temperature leads to increase in loss of voltage signal by short circuiting in the pipe wall and negative temperature coefficient of magnet leads to reduction in magnetic flux density in pipe cross section.

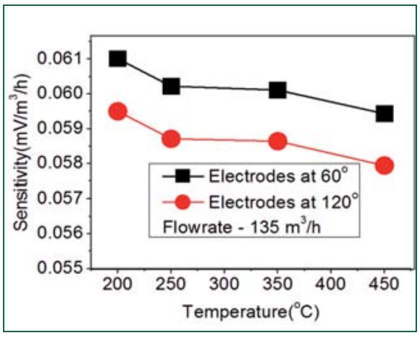

Fig. 7 *Side wall flow meter voltage signal verses sodium temperature*

Experimental and simulation results for potential difference developed across electrodes welded at 60° and 120° angle from the center of pipe are compared and shown in Figure 8. At maximum flow rate of 140 m^3/h variation in experimental and simulation results of potential difference developed across electrodes welded at 60° and 120° is -11.6 and +13.2 % respectively. At a flow rate of 14 m^3/h, the variation in experimental and simulation results is only +1.66%.

The feasibility of using the SWFM for sodium flow measurements in 100 NB stainless steel pipe was established with experiments. It was established that FEM analysis can be used for design optimization and sensitivity prediction of SWFMs. In future same concept of flowmeter with design optimized with FEM analysis will be tried for flow measurement in 200 and 800 NB stainless steel pipes.

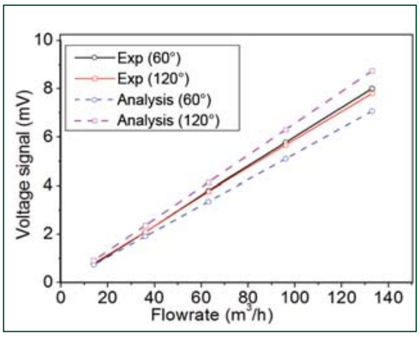

Fig. 8 *Flowmeter output versus flowrate*

III.9 Optimization Study on Bypass Flow Meter for Enhancing the Sensitivity

Bypass type flow meter with a permanent magnet flow meter (PMFM) sensor has been selected to measure the sodium flow in large pipes of secondary sodium loop of PFBR. The bypass line of the flowmeter is of 25 NB size and a permanent magnet flow meter sensor of size 25 NB is provided to measure the sodium flow rate in bypass line.

The volumetric sodium flow rate in main line is established from the bypass flow meter reading by a multiplication factor. An optimization study is conducted to assess the method of enhancing the sensitivity of bypass flow meter. The velocity of sodium in bypass line depends upon the kinetic head of flowing sodium in main line and flow resistance of the parallel flow paths. By modifying the hydraulic characteristics of the bypass line flow resistance through bypass line can be reduced and sodium velocity through the permanent magnet flow meter sensor can be increased. It will increase the strength of generated emf and lead to a higher sensitivity for the estimation of sodium flow in the main line. The higher emf generated will reduce the measurement errors including the percentage random errors, which lead to higher accuracy of sodium flow measurement in main line.

Various bypass configurations were studied and finally an optimized configuration has been arrived at. Combined numerical and experimental approach was adopted for design and validation of the optimised bypass flow meter configuration. The numerical results of the optimised bypass circuit are validated by experiments in water with scaled down models.

The testing of scaled down optimized bypass configuration was conducted and found that the analysis results obtained for scaled down models are in fair agreement with the experimental results. The optimised configuration increases the bypass flow by 72% of the original value as shown in Figure 1a. The validated numerical methodology has been used to analyze the actual PFBR bypass circuit configuration and optimized bypass circuit in reactor scale for future LMFBRs. Bypass flow rates have been estimated for different temperature conditions at 200 and 400°C.

The variation of flow multiplication factor (F_m) with respect to the Reynold Number (Re) of the sodium flow in main line was determined. F_m is the ratio of volumetric sodium flow in main line and through bypass line. The volumetric flow ratio is plotted against Re number in the main line for PFBR and optimized bypass circuit is shown in Figure 1b.

The correlation between F_m and Re number in main line for PFBR bypass configuration is given by the following equation.

$$F_m = 331.12e^{\left(\frac{-Re}{5.2\times10^6}\right)} + 1198.6$$

The same correlation for optimized bypass configuration is

$$F_m = 150.4e^{\left(\frac{-Re}{5.54\times10^6}\right)} + 700.4$$

However, these correlations are valid only in Re range of 10^5 to 10^8.

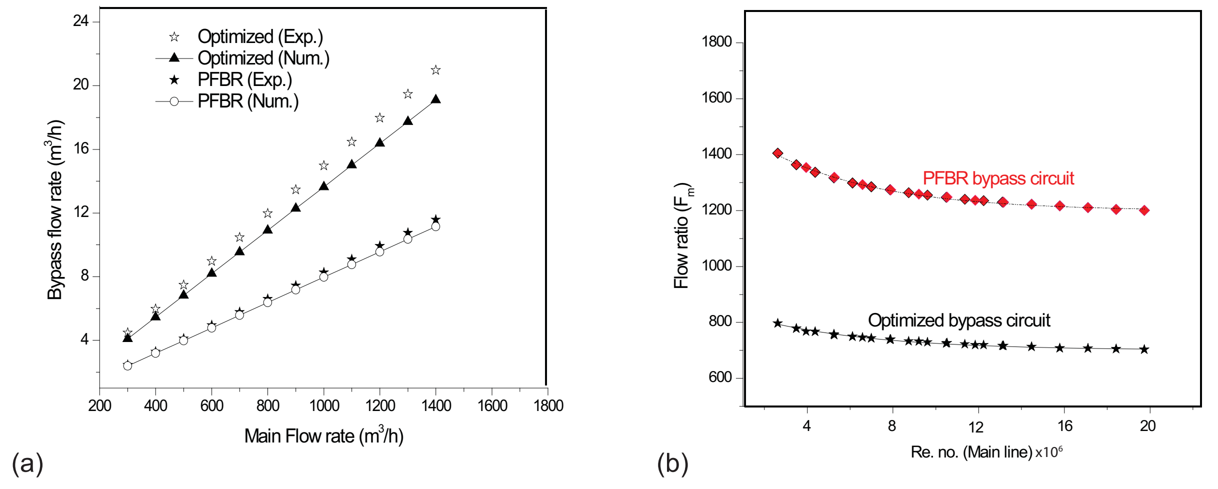

Fig. 1 *(a) Main flow versus bypass flow for scale down optimized and PFBR bypass flowmeter configurations and (b) temperature independent plot for PFBR and optimized bypass configurations*

III.10 Advanced Thermal Hydraulics Analyses

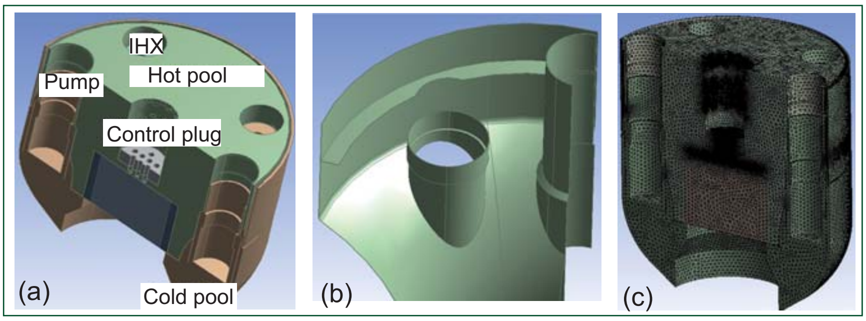

Fig. 1 *Computational model for integrated thermal hydraulic study (a) computational fluid dynamics domain, (b) inner vessel with anti-gas entrainment baffle and (c) computational fluid dynamics mesh*

The primary sodium is divided into hot pool and cold pool by 'inner vessel'. A specific design of inner vessel with single toroidal shell (redan) that directly connects the grid plate with the upper cylindrical shell has been proposed for future FBR, to have high buckling strength. This new configuration was validated for structural stability and has to be tested for the temperature distribution so as to verify and validate its design for thermal loading. Continuous transfer of heat from hot pool to cold pool through the inner vessel takes place. Because of this heat transfer, the temperature of hot pool sodium that enters the intermediate heat exchangers (IHX) reduces by ~3ºC. The hot sodium leaves the hot pool through 4 IHX where transfer of heat occurs between sodium of primary and secondary sides. Subsequently, primary sodium enters the cold pool at ~394°C. Due to the difference in sodium temperatures on both sides of inner vessel, the vessel is subjected to temperature gradients across its thickness. The velocity and temperature distributions of sodium on both the sides of inner vessel are highly non-uniform. This non-uniformity leads to axial temperature variation in inner vessel. Further, the sodium levels in the cold pool, hot pool and primary sodium pump (PSP) standpipe are different. Hence, inner vessel is exposed to argon cover gas at different elevations. The sodium-argon interface is a region of large temperature variation in inner vessel. Further, during plant transients, the inner vessel is subjected to hot and cold shocks in local regions. For detailed investigations of inner vessel structural integrity, knowledge of steady and transient temperature distributions in the vessel is essential. Towards these, an integrated conjugate thermal hydraulic study of hot and cold pools for steady and transient conditions has been carried out.

The computational fluid dynamics model consists of hot and cold pools including main vessel, inner vessel, IHX, PSP standpipe and control plug (Figure 1a). The entire core including fuel, blanket, reflector and storage subassemblies are explicitly represented. The shielding subassemblies and the hexcan wrappers below core top (i.e., the inter-wrapper flow region) are simulated using a porous body model. Main vessel cooling flow is modeled along with the inner and outer thermal baffles. The IHX tube bundle is simulated by porous body model with appropriate heat sink distribution. In addition to steady state, the transient arising out of one secondary sodium pump trip is also investigated. The anti-gas entrainment baffle is also simulated to provide realistic flow conditions (Figure 1b). Due to the geometric complexity involved in the 3-dimensional model, unstructured tetrahedral mesh is adopted. To better capture the heat transfer between two adjacent cell zones, conformal interfacing is done at the surfaces separating two cell zones. The entire geometry consisted of 2.27 million elements (Figure 1c). Turbulence in the flow is modeled using the standard k-ε model. Buoyancy effect in the mixed convection flow is considered using the Boussinesq approximation.

Figure 2a depicts sodium velocity distribution in the pools in a vertical plane between two IHX.

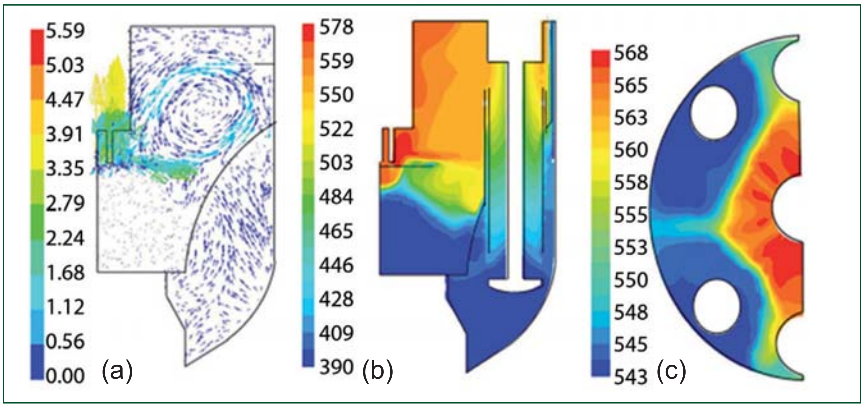

Fig. 2 *Steady state flow and temperature fields in pools (a) sodium velocity (m/s) in a vertical plane, (b) sodium temperature (°C) in a vertical plane thro' intermediate heat exchanger and (c) sodium temperature at free surface*

It may be highlighted that the anti-stratification skirt provided below the control plug increases the radial velocity of sodium entering the hot pool. This was found essential to avoid thermal stratification in hot pool that could develop due to the vastly different temperatures of sodium streams from fuel, blanket and storage subassemblies. Also, due to large hydraulic resistance offered by the skirt plate (only 10% porous), the flow passing through the skirt is minimum and hence the flow is diverted downwards inside the anti-stratification skirt. This downward flow bends the sodium streams from the blanket and storage subassemblies. The radial jet emanating below the anti-stratification skirt travels towards the inner vessel and turns upwards. This upward flow is obstructed by the horizontal anti-gas entrainment baffle attached to the upper shell of inner vessel and is finally diverted towards control plug, thus minimizing the free surface velocity. The free surface velocity has a bearing on gas entrainment phenomenon. The maximum sodium velocity at the free surface was found to be 0.45 m/s which is acceptable from gas entrainment considerations.

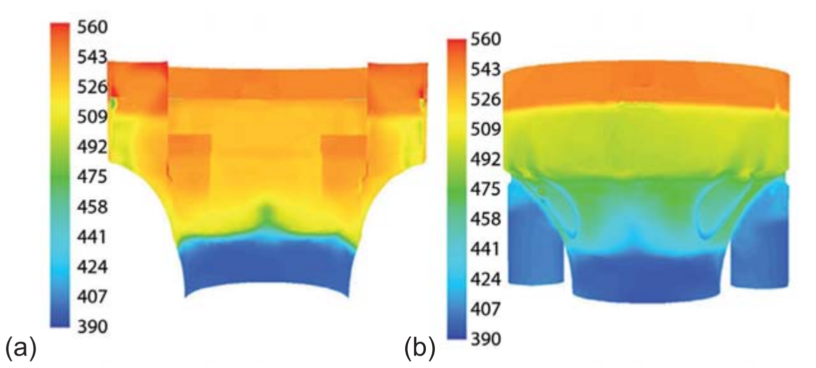

Fig. 3 *Steady state inner vessel temperature (°C) (a) hot pool side and (b) cold pool side*

The primary sodium flow within the IHX is primarily axial in most of the IHX length, except near inlet and outlet windows. The cold pool below IHX is well mixed. The temperature distribution through IHX is depicted in Figure 2b. It is clear that the inter-wrapper flow maintains the bottom zone of hot pool favorably cold. The downward penetration of hot sodium into the inter-wrapper region is limited. It establishes an interface with the upward flowing inter-wrapper sodium leaking from grid plate. The primary sodium temperature difference in the IHX outlet is 45 K. This data is useful for determining the temperature distribution in inner and main vessels. The cross flow velocity of sodium at IHX outlet is 3.1 m/s, which would be used for flow induced vibration analysis of the tube bundle. The free surface is non-isothermal with peak temperature of 568ºC (Figure 2b).

The steady state temperature field on inner vessel on the cold pool side and hot pool side are depicted in Figures 3a and 3b respectively. During steady state, the vessel temperature is nearly axi-symmetric, exhibiting variation only in the vertical direction. The bottom of the vessel is nearly at cold pool temperature while the vessel above the cold pool free level is nearly at hot pool temperature. The temperature drop along the thickness of inner vessel is found to be 72ºC. This occurs in a zone just below the core top. Heat transfer from hot pool to cold pool through inner vessel is found to be 15 MW.

During trip of one secondary sodium pump, heat removal from the IHX attached to the affected pump reduces sharply. As a consequence of this, the primary sodium passing through this IHX exits into the cold pool at a high temperature. On the other hand, heat removal from the other IHX that is connected to the working secondary sodium pump is unaffected. Hence, primary sodium from unaffected IHX exits into the cold pool at a low temperature. These are evident in Figure 4, where primary sodium temperatures in two vertical planes through affected and unaffected IHX are depicted. This event poses large axial and circumferential temperature variations in inner vessel. These simulations provide thermal load on inner and main vessels for structural analysis of these components.

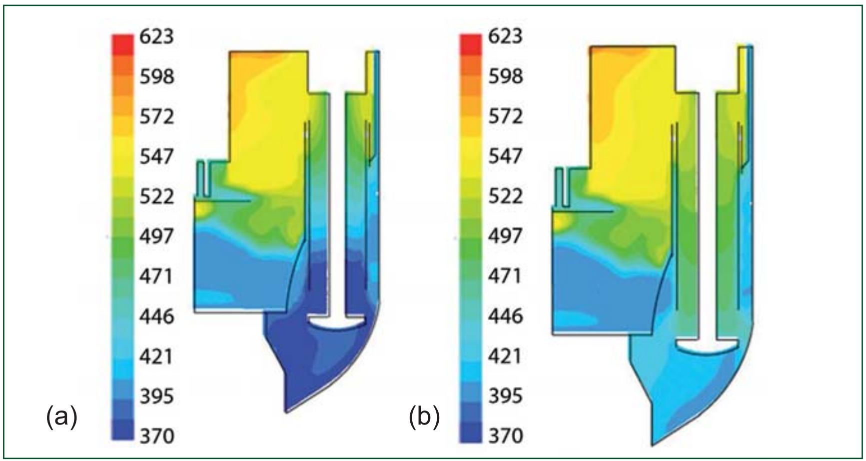

Fig. 4 *Transient temperature in pools during one secondary sodium pump trip (°C) (a) unaffected IHX and (b) affected IHX at 180 seconds*

III.11 Molten Fuel Coolant Interaction Studies for Fast and Thermal Reactors on SOFI Platform

Under severe accident condition, melting of fuel and its interaction with coolant is postulated as a beyond design basis accident. Understanding fragmentation process of molten fuel and morphological characteristics of generated debris bed is vital for assessment of post accident heat removal.

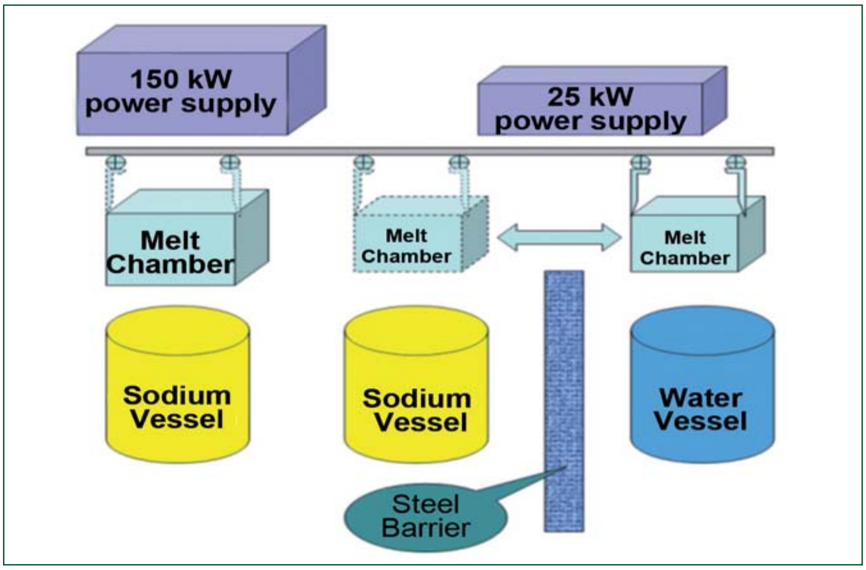

***Fig. 1** SOFI platform*

To address the above, a test facility, SOFI-platform is setup with a prime objective to generate data set for molten fuel-coolant interaction (MFCI) studies independently for LWR and SFR applications. The facility houses two induction furnaces, one with low frequency (up to 2 kHz) and low power (up to 25 kW) induction generator and other with 200 kW capacity and 200 kHz frequency. Both the power supplies cater to study molten fuel-coolant interaction for sodium as well as water cooled reactors. Low power supply will cater to the experiments with small inventories of melt charge and lower temperatures up to 2500˚C whereas, other system is used for melting of higher masses to temperatures >2500˚C.

The SOFI-platform is designed such that, the melt chamber assembly will be shared between sodium as well as water systems, which are separated by a physical barrier as shown in Figure1. The melt chamber houses cold crucible, induction coil, melt release and slider valve mechanisms. It is mounted on a rail for ease of mobility between water and sodium systems. The induction generators are also sharable, depending upon the charge mass and configuration. Test setups for sodium and water applications are shown in Figures 2 and 3 respectively.

***Fig. 2** Test setup for sodium experiments*

***Fig. 3** Test setup for water experiments*

Fig. 4 *Coil crucible assembly of high capacity generator*

Both induction furnaces are installed at the site and integrated to the respective systems. To cater to the increased cooling demand arising from a higher melt inventory and high temperatures, a high capacity cooling circuit is also commissioned. The new system employs one combined loop to cool both crucible and induction coil. 'Therminol-55' oil is chosen as heat transfer fluid in lieu of its excellent characteristics and non-reactivity with sodium. A water chiller is employed for cooling the induction generators separately.

As a part of commissioning, preliminary runs were conducted with high capacity induction generator, using magnesium oxide powder (melting point of about 2800°C) as charge and tungsten as susceptor. Typical crucible and induction coil assembly is shown in Figure 4.

During the testing, charge temperature of 2300°C were successfully achieved. Subsequently, runs on UO_2 melting at about 3000°C are planned.

In addition to this, melting of uranium and alumina to form eutectoid at about 2300°C was carried out with low power induction generator. During the run, pyrometer and "C" type thermocouple were calibrated for temperature. The charge configuration and molten UO_2-alumina are shown in Figures 5.

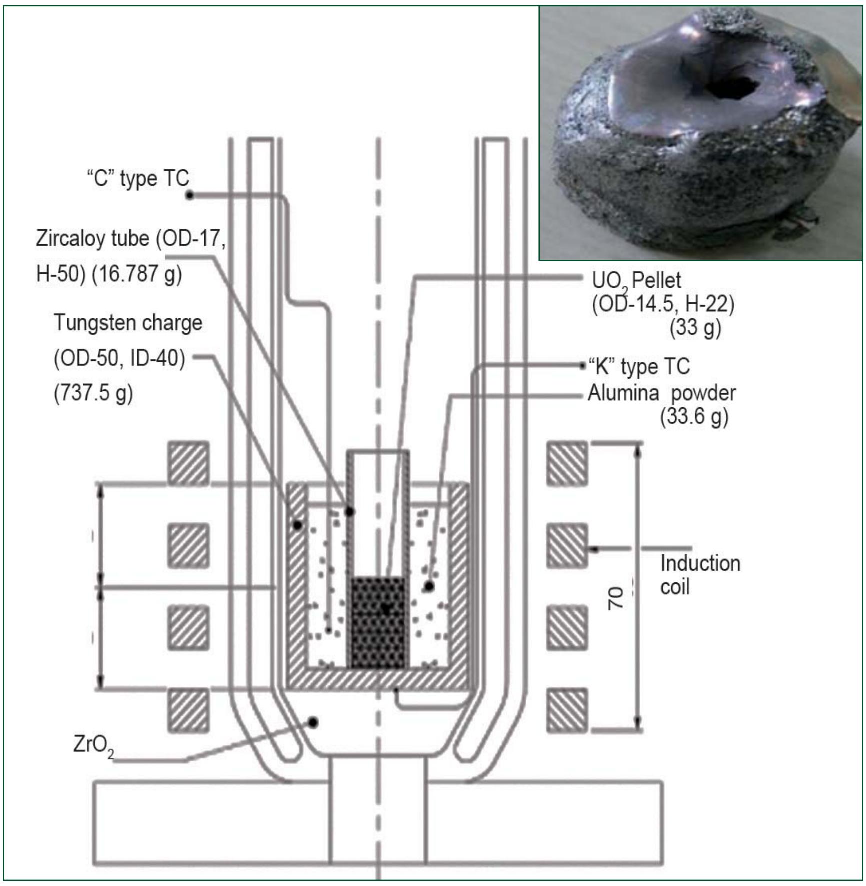

Fig. 5 *UO_2 & Al_2O_3 charge in crucible (inset UO_2 and Al_2O_3 molten charge)*

The input power and corresponding charge temperature are depicted in Figure 6.

Further experiments are planned to be conducted with simulant materials in the water system to obtain the debris characteristics and dynamic pressure pulse (if any). For this, an interaction vessel is fabricated and integrated with the water system. A piezolelectric dynamic pressure transducer is integrated for peak pressure measurement. Experiments are planned in due course.

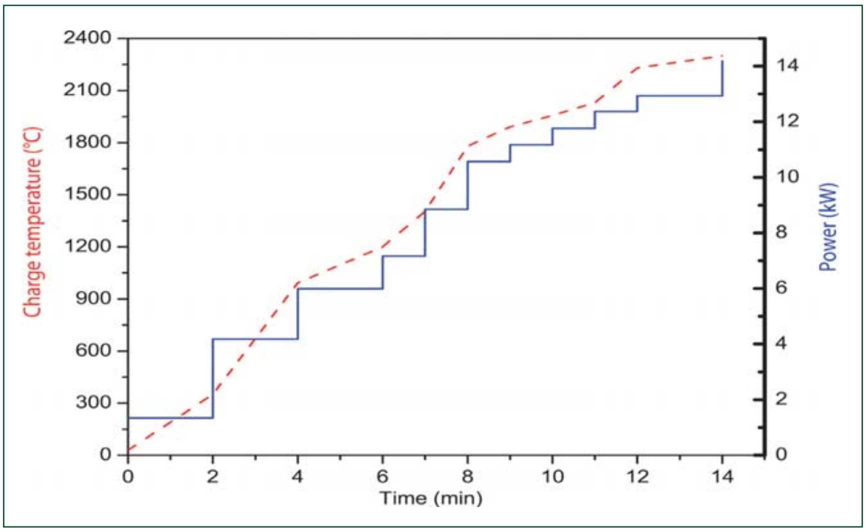

Fig. 6 *Power and charge temperature*

III.12 Simplification of Component Handling System for Future FBRs

Component handling system deals with handling and storage of fresh and spent subassemblies (core subassembly handling), handling and decontamination of sodium wetted primary system components like primary sodium pump, intermediate heat exchanger, decay heat exchanger etc. (special handling).

The core subassembly handling scheme is shown in Figure 1. In-vessel handling is carried out using two rotatable plugs and two transfer arms identical to PFBR. One transfer arm is located in small rotatable plug (SRP) and the other in large rotatable plug (LRP). The in-vessel transfer pot (IVTP) is located in the periphery of the core. An additional offset handling machine is provided in roof slab. This machine performs simplified function of receiving the fuel in sodium filled pot at IVTP and delivering it at a higher elevation below fuel transfer port in roof slab for ex-vessel handling by flask.

The spent fuel subassemblies are stored in the internal storage locations for two fuel handling campaigns, while the internal blanket subassemblies are stored for one campaign. The external blanket subassemblies are discharged 13 days after shutdown.

PFBR construction experience has shown that the inclined fuel transfer machine (IFTM) is costly, needs additional supporting systems like heating and cooling systems with additional cost and is time consuming to manufacture and erect. Hence, it is replaced by a simple shielded flask similar to FBTR. The flask transfers the subassembly to the transfer carriage, which moves and positions the pot below fuel transfer port located inside the fuel transfer cell (fuel building). Further, the cell transfer machine (CTM) transfers it to the sodium washing facility and further to the spent fuel pool as in PFBR. The other ex-vessel handing provisions in fuel building are similar to PFBR.

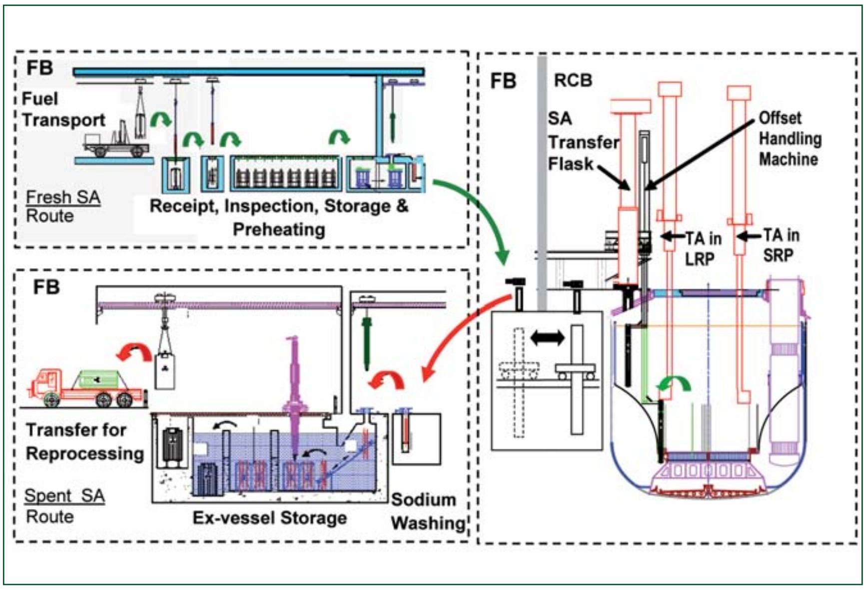

Fig. 1 *Core subassembly handling scheme*

The spent fuel storage is shared between the twin units and is sized to meet the requirements of one fuel handing campaign of each unit plus emergency core unloading requirements of one unit.

Fuel building (FB) houses all fresh and spent subassembly handing equipment. Being a twin unit, a separate decontamination building (DCB) is provided and all special handling equipment are shifted to decontamination building. This minimises use of water inside reactor containment building (RCB) and minimizes length of effluent piping from the decontamination system leading to enhanced safety. Transfer of flasks from reactor containment building to the decontamination building is done through a traverser. Most of the component handling equipment is shared between the twin units and a unique twin unit layout has been arrived at as shown in Figure 2.

Though additional machines are employed for in-vessel handling, the average time for replacement of a spent subassembly with a fresh one is estimated as ~230 minutes and is comparable to PFBR (~200 minutes). The overall reduction in material consumption is ~42.5% indicating potential for realization of significant economy.

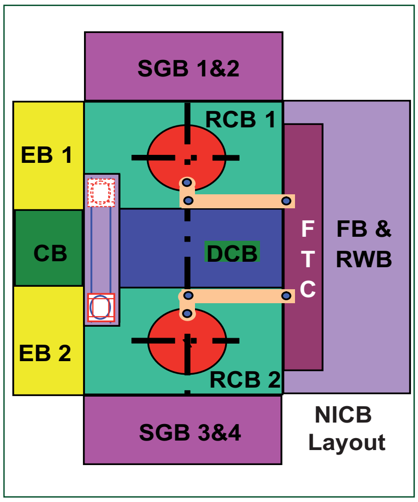

Fig. 2 *Layout facilitating sharing between twin units*

III.13 Structural Optimization of Dome Shaped Roof Slab

The present work is carried out as a design improvement exercise to its predecessor, PFBR roof slab. PFBR roof slab is a 1.8 meter height box type structure made up of 30 mm thick plates welded together and is supported from the top. The plates are further strengthened by the radial stiffeners between the top and bottom plates. Roof slab for FBR-600 is conceived to be of box type dome structure supported from the bottom side through conical skirt (Figure 1). The material for the construction is SS304L to avoid lamellar tearing.

The main functions of the roof slab are to provide an enclosure to reactor vessel as well as to support various components mounted over it. Apart from providing closure and support for the top mounted component, the roof slab also provides the top thermal and radiation shielding. Roof slab also contains the radioactive cover gas in the main vessel. The major component supported by the present roof slab includes three primary sodium pumps (PSP) and four intermediate heat exchangers (IHX) leading to 180° symmetry of the roof slab (ignoring other smaller penetrations).

The major functional limits of roof slab include the limit of 3 mm on the vertical deflection based on reactivity addition during seismic event, the large rotatable plug (LRP) flange seals are designed with a maximum undulation limit of 0.3 mm to ensure leak tightness of the LRP seal and slope at PSP and IHX penetration limited to a value of 1.8×10^{-3} to avoid interaction between components.

Mechanical stress analysis

Three dimensional shell model has been used to optimize various parameters for the design.

The 3D-shell model mesh (Figure 2) consists of more than 2×10^5 linear, triangular and quadrilateral elements. In view of the complexity of the geometry, the structure has been meshed using free meshing algorithm with local seed control in order to generate good quality mesh.

The optimization study has been performed in order to optimize geometrical parameters like shape of tri-junction, location and number of stiffeners, thickness of plates and functional parameters like undulation, slopes, global downward deflection etc. The study was performed by analyzing the effect of variation of one parameter while keeping all other parameters constant. Design limits are respected by performing detailed analysis of the component with the help of FEA code.

As the reactor vault and LRP flange positions (elevation) are fixed, change in the dome angle would lead to change in elevation of roof slab-MV weld joint (tri-junction). The box cone angle has been optimized by varying the angle in steps of 5° from 5° to 25°. With greater cone angle, the stiffness of the roof slab is more and hence the vertical deflection would be less. But at the same time the gap between the tri-junction and sodium free level is reduced which will result in higher thermal stress. Due to these aspects an optimum angle of 20° has been fixed.

In the case of PFBR, height of the stiffeners is ~3 times more than the present roof slab stiffeners. The height to thickness ratio is ~12 in the present case whereas for PFBR it is ~60 to 90. It is reported in the literature that when the value of h/t is sufficiently low (<85) critical shear stress for buckling failure mode increases above the value of yield stress. Hence, stiffener will yield under shear before shear buckling mode of failure. With a stiffener thickness of 25 mm it is found that nowhere the shear stresses are more than 33 MPa. Furthermore, a number of stiffeners have been considered to maximize the stiffness of the geometry as well as to reduce the stresses.

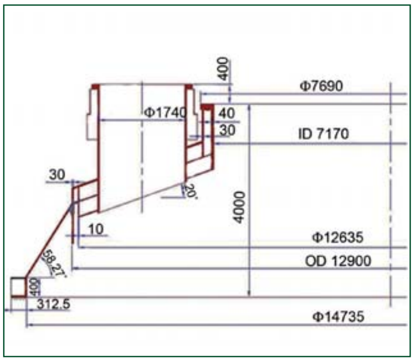

Fig. 1 *Dome shape roof slab*

Height of stiffeners at reactor vault support location is increased from 300 to 400 mm for increasing stiffness of the conical support shell. Also, to reduce local peak stress at top corner of these stiffeners, a ring is welded at stiffener's top face.

Initial configuration of the

Fig. 2 *Meshed model of roof slab*

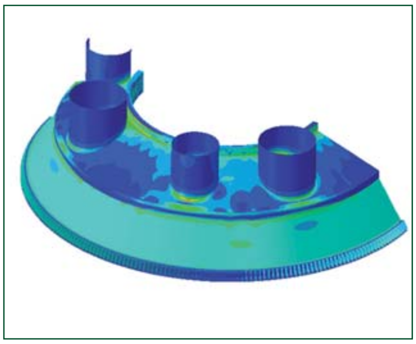

Fig. 3 *Stress distribution in roof slab*

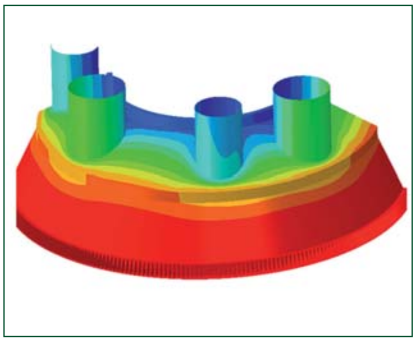

Fig. 4 *Vertical displacement in roof slab*

tri-junction forged piece had an 80 mm nominal thickness with the curved mean line. During the investigation it is found that the curve present in the tri-junction is producing bending stresses in the forged piece. In the present configuration, support shell curvature is removed thereby leading to a conical support shell.

Now more load is transferred through membrane action as compared to the earlier configuration where major part of the load is transferred through bending action of support.

After changing the curvature to straight conical shape, it was found that a shell of 60 mm near tri-junction and 30 mm for support is sufficient instead of 80 mm thickness (earlier configuration). This reduction in thickness of the tri-junction would produce less thermal stress in the main vessel support location. Figure 3 shows the mechanical stress distribution in the roof slab.

The performance of the large rotatable plug seals is strongly related to undulation of the large rotatable plug flange. In order to ensure effective sealing, the undulations should be kept as low as possible. The reason for the undulations is asymmetry in the load as well as asymmetry in the stiffness of the structure. Asymmetry in the load is because of the different load for PSP and IHX whereas the asymmetry in the stiffness is because of penetration shells. The loading cannot be changed, but the stiffness can be changed by arranging the radial stiffeners in proper manner. It can be achieved by increasing the number of stiffeners in the region where more load is acting and by reducing the number of stiffeners in region where less load is acting. Figure 4 shows the vertical displacement in roof slab.

Thermal stress analysis

For thermo-mechanical analysis, an axisymmetric model has been used. The axisymmetric model is meshed using 3D continuum elements. This model is similar to the previous mechanical analysis model except for the fact that the main vessel height has been sufficiently included in order to account for end effect and discontinuity stresses. This thermal stress analysis is carried out for optimizing the shape near tri-junction under thermal loads. After removing the material as shown in the Figure 5 to provide flexibility to the structure, the final stresses are reduced as shown in Figure 6.

The dome shaped roof slab has better stiffness compared to horizontal roof slab.

A 20° cone angle is an optimum value as it offers higher stiffness as well as greater elevation of ~270 mm for the tri-junction from the sodium free level compared to a cone angle of 25 degrees.

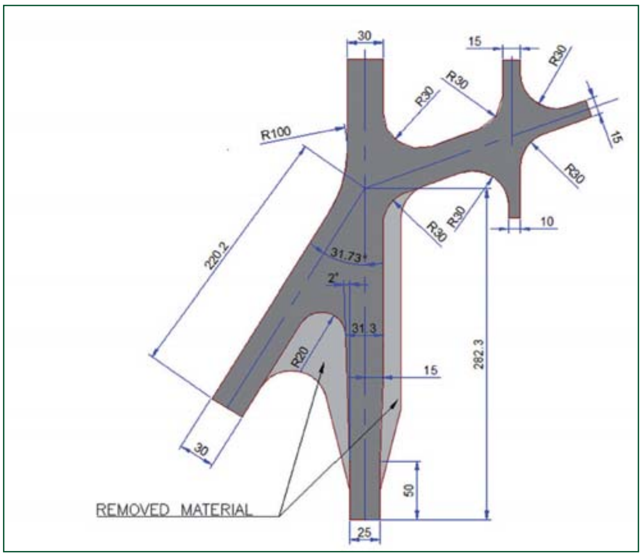

Fig. 5 *Modified shape of tri-junction after thermal analysis*

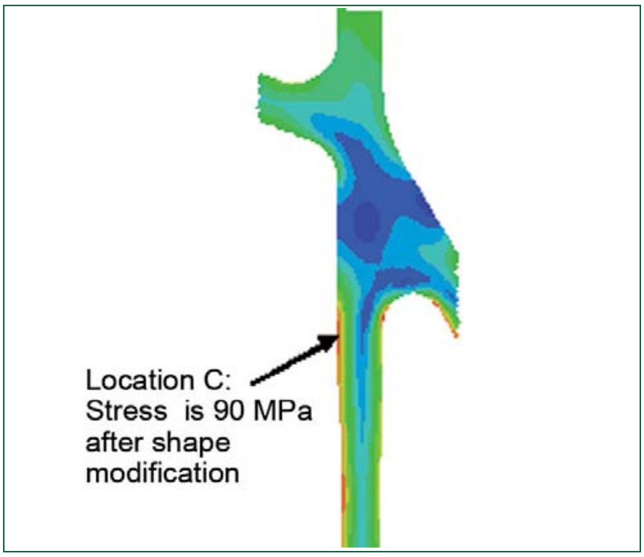

Location C:
Stress is 90 MPa
after shape
modification

Fig. 6 *Reduced thermal stresses after modification*

Due to low h/t ratio of stiffeners, shear buckling is not a concern for the present design.

To reduce the undulations, large rotatable plug stiffeners should be applied only at selected locations depending upon the final load and geometrical configuration.

A straight conical support shell of the roof slab is better as compared to curved support shell for the present configuration.

Based on thermal stress analysis, thickness near tri-junction is further reduced.

Table 1 shows the details of various parameters of the new design.

Table 1: Details of various parameters of the new design

Parameter	New design	
	Value	Allowable limit
Maximum deflection	2.61 mm (LRP)	3 mm
Undulation at LRP flange	0.194 mm	0.3 mm
PSP Slope	4.66E-4 (radian)	1.8E-3 (radian)
Shear stress in radial stiffeners	32.1 MPa	0.6 S_m (63.6 MPa)
Shear stress in circumferential stiffeners	25.6 MPa	0.6 S_m (63.6 MPa)
Maximum shear stress in roof slab (conical support stiffeners)	24.4 MPa	0.6 S_m (63.6 MPa)
Maximum primary membrane stress	67 MPa	S_m (106 MPa)
Maximum primary membrane + Bending stress (Local)	98 MPa	1.5 S_m (159 MPa)
Weight of roof slab	119 tons (Without weight of small penetration)	
S_m - Allowed stress intensity as per design code		

III.14 Compact Layout of Primary Sodium Circuit Components for Future FBRs

The background for the design of future sodium cooled FBRs with advanced mixed oxide fuelled core is to achieve

(i) possible higher breeding ratio

(ii) near zero or smaller positive sodium void coefficient of reactivity affordable in design and acceptable to public

(iii) higher reactor power to achieve improved economy

(iv) adoption of fuel subassembly construction similar to that in PFBR.

This option would give the advantage of using the existing MOX fuel based front and back end fuel cycle technology and at the same time deriving the benefit of higher breeding similar to metallic fuel. From the economic considerations, it is proposed to enhance the power of future FBRs to 600 MWe. To meet the enhanced sodium flow requirement, it is proposed to increase the number of sodium pumps from two to three while retaining the number of secondary loops at two, as in PFBR. Retaining the number of secondary loops as in PFBR gives economic advantage whereas increasing the number of pumps to three with slightly reduced capacity pre-empts the need for re-design/re-development associated with higher capacity pumps. The steam water system will be similar to that in PFBR with increased capacity. As in PFBR, all the reactor internals are contained in a single vessel called Main Vessel and it is closed with top shield.

Optimisation studies with pump

To reduce the overall capital cost and to reduce the number of components, a combination of three primary sodium pumps (PSP) with 4 IHX and 2 secondary loops is chosen as the option for 600 MWe FBR after detailed studies, as the combination does not require any change of main vessel size, which is a desirable advantage in reducing any further developmental activity/cost involved with larger sized vessels/components etc. The size of the PSP influences the opening in the roof slab and the same is finalized considering the number of PSP as 3. The major design requirements for PSP of FBR-600 are listed below:

- Size and weight shall be lesser than that of PFBR PSP
- Shaft natural frequency over the operating speed shall be ≥1.3
- Impeller shall be of single stage, single suction with design life of at least 20 years
- Provision of spherical seat to permit tilting of the entire pump assembly below reactor roof slab
- Provision of sleeve valve (flow blocking device) at the suction inlet to have operational flexibility
- The cavitation criteria shall be same as in the case of PFBR PSP

All the above said parameters influence the size of the pump and hence the opening in the roof slab.

The major change compared to PFBR is with respect to the increase in the length of the shaft and the pump as a consequence of change in the height of reactor assembly of 600MWe FBR. Preliminary estimates of natural frequency is carried out with as minimum shaft length as possible after rearrangement of sthe location of the spherical seat bearing. Another requirement was provision of sleeve valve in the pump suction to facilitate single pump starting and flexibility in pump operation during commissioning. Efforts were made not to revise the opening for the PSP (Φ1850 mm) in roof slab even with sleeve valve. Also, it is taken care to accommodate any minor variations in pump size that may result during development stage.

Optimisation of reactor assembly

Based on the experience gained during design, manufacture and erection of PFBR components, detailed and exhaustive design/optimisation exercises were done towards improving the economic competitiveness of future FBRs as well as improving their safety. As an outcome of this exercise, several design features and improvements are suggested for incorporation in the design of future FBRs. Further, it is observed that vessel dimensions contribute immensely to the overall capital cost as well as decreasing fabrication difficulties. In this context, an exercise was undertaken to optimise the overall dimensions of the reactor assembly components as well as locations of components for the future FBR (600 MWe) so that a compact layout could be achieved. Some of the optimisation exercises are described below:

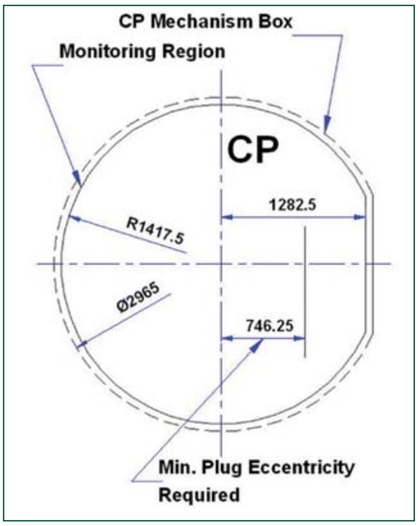

Fig. 1 *Core monitoring dimensions*

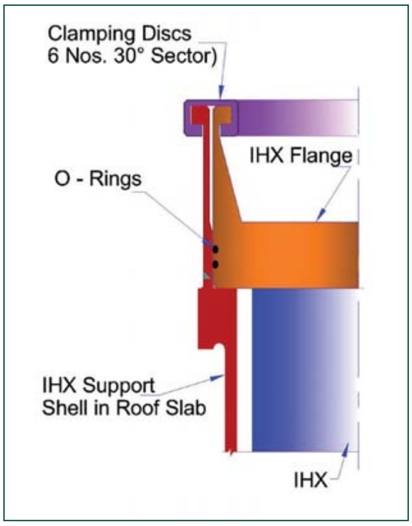

Fig. 2 *Clamping arrangement for IHX*

Dimensions of rotatable plugs contribute a large extent to overall dimensions of reactor and also, dictate the layout of major components. Since it is proposed to retain the same in-vessel fuel handling concept as in PFBR, eccentric plug option is also retained. Control plug dimensions and the eccentricity between the two plugs are the two important deciding factors for plug dimensions. The control plug dimensions are governed by the core monitoring dimensions, which also decides the eccentricity required so that control plug can be shifted to out of core location to enable handling machine to access the core subassemblies.

In order to reduce eccentricity, it is proposed to exchange a few fuel subassemblies in core periphery along 0° axis and also truncate the lower shell a control plug accordingly (Figure 1) so that transfer arm can be brought closer to centre of core. The reduction in eccentricity due to this exercise is 67.5 mm.

Intermediate heat exchangers are the other major components, which decide the equipment layout over top shield. Since the diameter of IHX is higher than that of any other component over roof slab, it influences the overall diameter of reactor assembly. The total space required for IHX is divided into those required for passage of tube bundles and that required for supporting the IHX. Since, IHX is the largest component outside the rotatable plugs, any increase in its dimension results in corresponding increase in reactor assembly size.

IHX passage diameter in roof slab is governed by the number of tube bundles in IHX which in-turn is decided by the heat removal capacity. However, the flange width which is decided by the sealing and clamping functions can be optimised. In the conventional arrangement used in PFBR, two 'O' rings in series (in horizontal direction) are provided followed by clamping holes. The total flange width needed to take care of these is ~150 mm. In order to reduce this width, an alternate arrangement is conceived (Figure 2) where in O-rings are provided in vertical direction and instead of fasteners for clamping, sectors of clamping disc is used to lock the spline like projections provided at the top edge of the support shell and IHX support flange.

The above arrangement contributes to overall diameter reduction of reactor assembly by ~170 mm.

Optimisation exercises are carried out to achieve compact layout of equipment within the main vessel. The exercise is repeated for in-vessel components as well. For a two loop arrangement, the radial position of pump and IHX are governed by the dimensions of rotatable plugs and IHX, whereas beyond the location of these components, the vessel diameter is governed by other in-vessel components and gap between them. The important parameters are width of IHX-IV seal and gaps between various concentric shells like inner vessel, thermal baffle and main vessel. The width of IHX-IV seal is 150 mm and a uniform gap of 95 mm is considered between IV, Thermal Baffles and Main Vessel in PFBR. With the use of stainless steel for roof slab, at higher operating temperature, the differential thermal expansion between penetrations in roof slab and corresponding standpipes in inner vessel is smaller, compared to PFBR. Hence, IHX-IV seal design is relooked and it is observed that a width of 100 mm is sufficient to meet the requirements.

Further, by specifying tolerance on gaps between various concentric shells in combination with tolerances on their diameters, it is observed that requirements can be met. Taking advantage of this aspect, the gaps between IV-Thermal Baffles-MV are optimised to be 65-70 mm against 95 mm in PFBR. This resulted in reducing the MV diameter by ~210 mm.

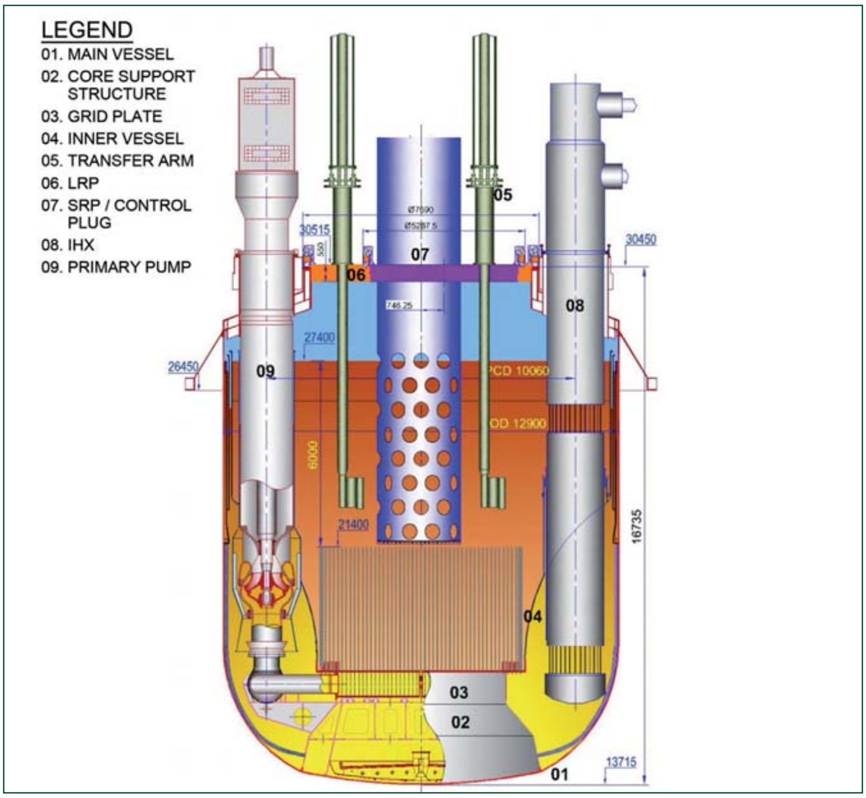

Fig. 3 *Cross sectional view of reactor assembly*

With the above exercises, the overall diameter of reactor assembly is optimised to be 12.9 m. The cross sectional view of reactor assembly is shown in Figure 3.

Layout of equipment over top shield

The overall diameter obtained from the exercise as above needs to be verified from the consideration of layout of equipment over top shield. The rotatable plugs are positioned at centre with large rotatable plug centric to core so that control plug can be positioned in-line with core subassemblies. Since, IHXs are the largest components outside the plugs, the same

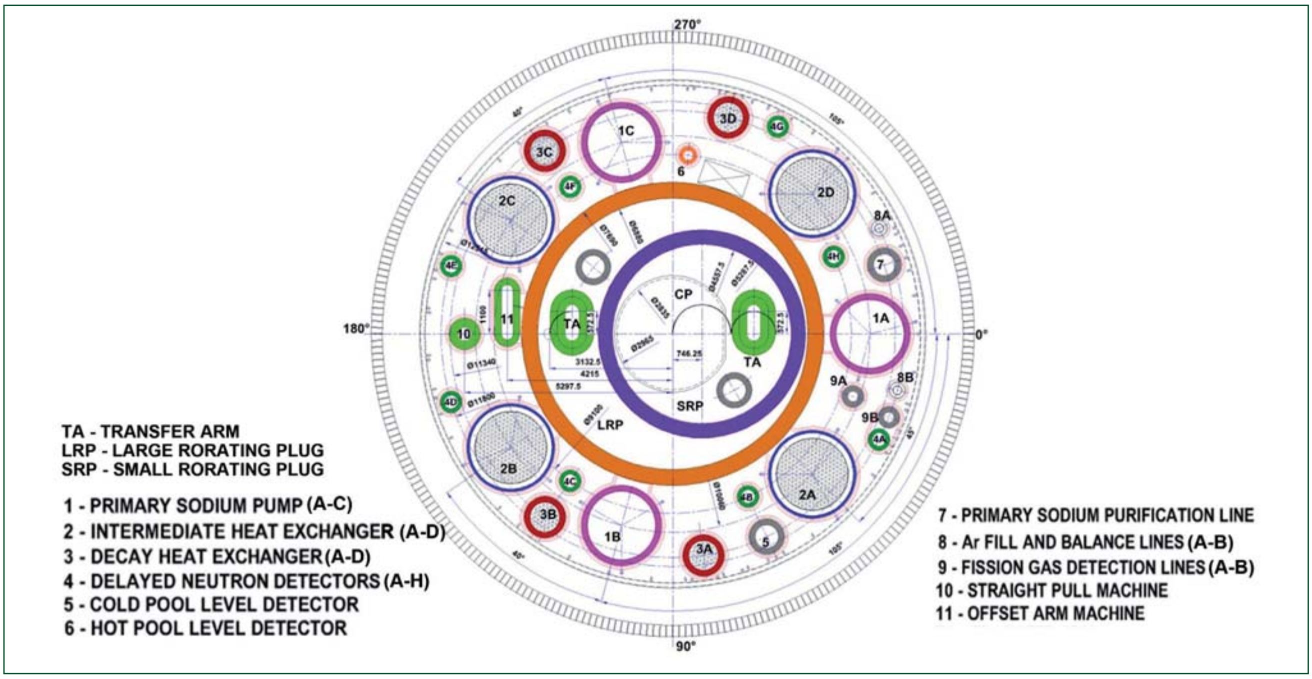

Fig. 4 *Equipment layout over top shield*

are positioned just adjacent to rotatable plugs with minimum gap to facilitate handling. The pitch circle of the location radius of IHX is obtained to be 10060 mm. Since, pumps are also of equally large dimensioned components, they are also positioned in this PCD. Ideally, pumps (3 numbers) are to be positioned symmetrically. However, large space (~3 m in circumferential direction) is to be allocated at one location to facilitate movement of fuel handling flask over the corresponding port provided in roof slab. Hence, the pumps are angularly positioned with slight offset, whereas IHXs are more or less symmetrically positioned. The spaces between IHXs and pumps are effectively utilised to locate four numbers of decay heat exchangers, eight numbers of delayed neutron detector housings and other auxiliaries. The overall layout of equipment over top shield is shown in Figure 4. With this arrangement, a layout could be achieved leading to overall compactness of reactor assembly.

III.15 In-Sodium High Temperature Experiments in Creep and Fatigue Loops of INSOT Facility

The facility for materials testing in-sodium (INSOT) was constructed to study the mechanical properties of structural materials used in Fast Breeder Reactors (FBR) under the influence of dynamic sodium at high temperature. INSOT facility comprises of two independent sodium loops one for creep and another for fatigue studies at high temperatures up to 600°C. The experiments have been conducted simulating the various reactor conditions to generate indigenous data on mechanical properties in sodium like creep, low cycle fatigue (LCF), creep-fatigue interaction (CFI), thermal striping studies and Friction and Wear studies by pin on disc tribolometer (PODT) on different materials for the PFBR.

The creep and fatigue loops have logged around 41810 and 21358 hours of operation respectively. Ninth test campaign of four numbers of creep experiments in creep loop (Figure 1) was started during April 2014 in four test sections (TS-2A, 2B, 3A & 3B) simultaneously at 600°C, while maintaining sodium flow in the creep test chambers at 0.5 m^3h^{-1}. Out of four creep experiments, two experiments were completed and remaining two are in progress at 600°C on SS 316L(N) with 0.14% N base material at two stress levels of 200 and 210 MPa in test sections TS-2B and TS-3A; elongations of specimens are 0.488 and 0.789 mm respectively with a cumulative test duration of around 6524 hours till December 2014. Friction and wear testing of different combinations of materials used in FBRs are being carried out in sodium, using the indigenously developed PODT (Figure 2) in fatigue loop of INSOT.

After fixing the new disc and pins specimens on spindle assembly, the PODT was inserted into the sodium test vessel. The loop operation was carried out sequentially and after stabilizing at test temperature and subsequent sodium purification, the PODT experiment was started and test data was acquired by data acquisition system (DAS). PODT test was completed after attaining the desired sliding distance. During the test, the experimental parameters like normal force, friction force, wear and co-efficient of friction are recorded in the data acquisition system. All the activities like removal of tribometer from test vessel, sodium cleaning of tribometer spindle, removal of tested pin/disc specimens, fixing of new pin/disc specimens, and erection of PODT (Figure 2) in the test vessel were carried out systematically as

Fig. 1 *Creep loop*

Fig. 2 *Indigenously developed pin on disc tribometer*

per procedure and adequate care has been taken to ensure that there is no air ingress into the system.

It was observed that there was no vibration in the tribometer during the conduct of the PODT experiments. Detailed analysis of the test data for estimating the wear, co-efficient of friction, performance of hardfaced coating, metallurgical studies of the pins, disc specimens etc. are being carried out.

Fatigue damage due to thermal striping phenomenon occurs due to mixing of hot and cold sodium jets on the surface of structural components. Ninety four thermal striping experiments have been completed in three successive test campaigns during 2014 in the thermal striping test setup in fatigue loop. These fundamental studies of the temperature fluctuations aim to characterize the distribution of the thermal behaviour in the mixing zone of two non-isothermal sodium jets. The thermal striping test setup consists of a test vessel having two inlet circular jet nozzles connected to the loop piping for maintaining hot and cold sodium at different temperatures. The two sodium jets impinge on a stainless steel instrumented plate supported from the top flange by a screw-nut mechanism which can vertically traverse the instrumented plate towards or away from the twin nozzles. The instrumented plate was completely immersed in a pool of sodium maintained in the test vessel (Figure 3) and the sodium level was monitored by discrete and continuous type MI level probes. The temperature distribution across the mixing zone was measured by a series of 0.65 mm diameter, K-type thermocouples embedded on the instrumented plate inside the test vessel.

The minimum vertical gap of instrumented plate from nozzles was 85 mm for the first four test campaigns which were completed by end of December 2013. Then the instrumented plate was brought down closer to the cold and hot nozzles by modifying the central spindle of the top flange assembly and the gap was reduced from 85 to 5 mm. Flow rates of sodium in the hot and cold nozzles were established and after stabilizing at the test temperature, the temperatures from the instrumented plate thermocouples were acquired using high speed data acquisition system.

The readings were taken at eleven vertical positions for every 10 mm by varying the height of the instrumented plate with reference to the hot and cold nozzles at a frequency of 100 Hz (top to bottom & bottom to top).

Twenty one sets of temperature data were acquired by the data acquisition system for each set of sodium flows in hot and cold nozzles. Thermal striping experiments were conducted with axis of cold and hot nozzles parallel and perpendicular positions to the axis of the instrumented plate. Thermal striping experiments were conducted at high temperatures of 550, 500 and 450°C in hot and 400 and 300°C in the cold nozzle respectively while maintaining the temperature difference between the hot and cold nozzles at 100 and 150°C. The thermal hydraulic parametric studies have been conducted at various combinations of flow rates of sodium in the hot and cold nozzles ranging from 0.193 up to 0.805 m^3/h to maintain equal velocity, Reynolds (Re), Peclet (Pe) dimensionless numbers, different Re and Pe ratio between the two jets and temperature distribution acquired across specific elevations from the two nozzle levels covering two mutually perpendicular planes. Analysis of these data focuses mainly on two parameters; mean temperature distribution and the peak-to-peak temperature fluctuation for the thermal characterization of the mixing phenomena. The analysis of the test data is being carried out. The performance of the mechanisms, maintaining the loop operation and process parameters were smooth.


Fig. 3 *Thermal striping test vessel*

During the test campaign and sodium sampling operation in both loops, the purity of sodium has been periodically checked by taking plugging runs and oxygen level was maintained within acceptable limits by continuous online purification. Sodium sampling operation using an overflow type sampler has been carried out for both loops and the chemical analysis results of oxygen, carbon and trace elements were found to be within acceptable limits. The test temperature was maintained within ±1°C by PID controller with immersion heater vessels. The functioning of the PODT, thermal striping test setup, loop components i.e, sodium to sodium shell and tube heat exchangers, ALIP type EM pump were smooth during the operation of the loop for carrying out the long term in-sodium creep, tribology and thermal striping experiments.

III.16 Time-dependent Low Cycle Fatigue Behavior of Nitrogen Enhanced 316LN Stainless Steel

Currently 316LN stainless steel with 0.06-0.08 wt.% nitrogen has been the structural material for many primary side components (inner vessel, intermediate heat exchanger, main vessel, etc.) of PFBR. One of the means of achieving economic competitiveness of FBRs is to extend the reactor design life from the current 40 years life to at least 60 years. Significant efforts are underway to realize this goal, and development of structural materials with enhanced high temperature fatigue and creep strength form a vital part of this endeavor. As a part of these efforts, development of nitrogen enhanced 316LN SS has been taken up and an extensive study is being carried out to evaluate the high temperature low cycle fatigue (LCF) behavior of SS 316LN with nitrogen contents of 0.07, 0.11, 0.14 and 0.22 wt.%.

Low cycle fatigue tests were conducted at strain rates in the range 3×10^{-3} to 3×10^{-5} s^{-1} and at temperatures of 773, 823 and 873 K. Nitrogen content in 316LN SS is observed to play a dual-role (beneficial or detrimental) in influencing the fatigue life and is found to be primarily controlled by time-dependent processes such as dynamic strain aging, precipitation, thermal recovery, oxidation and creep. In particular, nitrogen is beneficial in improving the fatigue life upto 0.11-0.14 wt.%, under the test conditions (case-1) that promoted transgranular fatigue failure (for e.g. tests at 773 K and at the above strain rates, see Figures 1a and 1b). In contrast, nitrogen addition induces significant reduction in fatigue life for the test conditions causing intergranular damage (case-2), such as in low cycle fatigue tests at temperatures above 773 K and at strain rates $\leq 3\times10^{-4}$ s^{-1} (for e.g. see Figures 1a and 1c). Intergranular damage in the latter case is evident in the form of networks of grain boundary decohesion and triple point cracks, driven by grain boundary sliding, as shown in Figure 1c.

In case-1, increase in planar slip tendency with increasing nitrogen content caused maximum beneficial effect of planar slip upto 0.11-0.14 wt.% nitrogen. Above 0.14 wt.% N, increase in material strength due to high nitrogen content and dynamic strain aging lead to strong slip localization that lowered the fatigue life. On the other hand, in case-2, due to the combination of test temperatures above 773 K with low strain rates ($\leq 3\times10^{-4}$ s^{-1}), grain boundary is amenable to intergranular damage by dynamic strain aging, creep, oxidation and carbide precipitation. Although dynamic strain aging causes planar slip, it introduces stress gradients near the grain boundaries by slip band impingements. This in turn enhances the creep damage by grain boundary sliding and nucleation of triple point cracks. In addition, high nitrogen contents and dynamic strain aging develop significant cyclic tensile stresses that further accentuate the evolution of the above intergranular damage and associated increase in crack propagation rates in case-2.

The high temperature low cycle fatigue results suggest a beneficial effect of nitrogen content on low cycle fatigue life only when the time-dependent effects are minimal and the fracture is predominantly by transgranular mode.

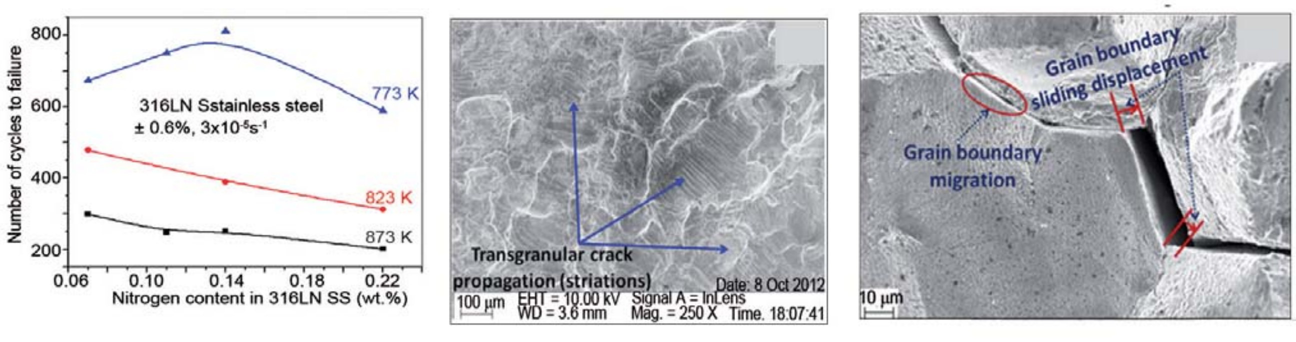

(a) (b) (c)

Fig. 1 *(a) Effect of nitrogen content on low cycle fatigue life at 3×10^{-5} s^{-1} strain rate, (b) typical features of transgranular fracture at 773 K and (c) intergranular fracture (illustrating grain boundary sliding displacements and grain boundary decohesion) at temperatures above 773 K*

III.17 Methods for Detection of Creep Rupture in Pre-pressurized Capsules

In-pile creep rupture behaviour of cladding tubes due to fission gas pressure generated in the fuel pins is an important design criterion in determining the allowable burn-up of the fuel pins. In-pile creep rupture experiments are generally carried out in reactors by using thermocouples or tag gases. Developmental activities towards joining thermocouple to the high pressure region of pressurized capsule (Figure 1) and out-of-pile testing in electrical furnace have been successfully carried out. Also, as an alternate method of detecting creep rupture, development of miniaturized Sodium Leak Detector (SLD) and joining of it to the pressurized capsule have also been accomplished successfully.

Fig. 1 *Sketch of pressurized capsule and the ruptured pressurized capsule*

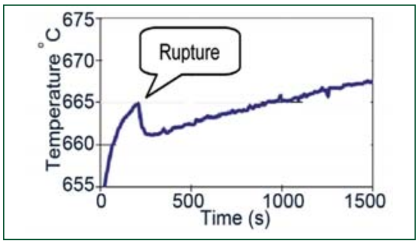

Fig. 2 *Temperature profile indicated by thermocouple attached to the pressurized capsule*

Development of pressurized capsule with thermocouple and out-of-pile testing in furnace

Pressurized capsules are small size capsules made of fuel cladding tubes filled with argon at high pressure. Laser welding was employed in joining SS316 sheathed thermocouple of 1 mm diameter with a sheath thickness of 0.18 mm to the gas region of the pressurized capsule with sufficient weld penetration but without puncturing the thin sheath of the thermocouple. These critical joints should withstand the high temperature and the associated high pressure of argon at the temperature of testing in the electrical furnace. Pressurized capsule joined with the thermocouple and filled with argon at 60 bar pressure at room temperature was successfully developed and encapsulated in a leak tight safety tube. The experimental set up was subjected to a temperature of about 650°C in an electrical furnace. The pressure of argon inside capsule would increase to about 185 bar at 650°C. The thermocouple was connected to a data acquisition system for temperature measurement. The typical data obtained with thermocouple during testing in a furnace is shown in Figure 2. It can be noticed that there is a definite shift in the temperature profile at the time of rupture and this occurrence of shift can be used to identify the rupture event. This behavior is observed due to sudden expansion of the pressurized argon into the surrounding safety tube at the time of rupture. The ruptured pressurized capsule is also shown in Figure 1.

Development of miniaturized sodium leak detector and joining with pressurized capsule

Miniaturized sodium leak detector has been developed successfully in the laboratory with stainless steel sheathed mineral insulated cable of overall diameter 1.5 mm having twin stainless steel core wires. Figure 3 shows the photograph of the miniaturized SLD developed. The MI cable was cut open to expose the twin core wires and the opening of the cable was closed with a thin ceramic disc. The functioning of the miniaturized SLD was verified by making its exposed wires to come in contact with liquid sodium. On contact with sodium, the DC voltage applied across its circuit reduced from 10 to 0 V indicating the proper functioning of the miniaturized SLD. Miniaturized SLD was joined to the gas region of the pressurized capsule by laser welding using a similar procedure adopted for joining of thermocouple. Figure 4 shows pressurized capsule with SLD inside the glove box after filling of sodium in the surrounding safety tube. Experiments with pressurized capsules joined with miniaturized SLD and surrounded by static sodium are being carried out in electrical furnace to validate their performance in detection of creep rupture.

Fig. 3 *Photograph of miniature sodium leak detector*

Fig. 4 *Pressurized capsule with sodium filled in the safety tube inside the glove box*

III.18 Studies on the Interaction of Lubricating Oil with Sodium

In the event of a core disruptive accident (CDA) occurring in a fast reactor, a hot bubble of short life is formed inside the core. This leads to ejection of cover gas and some sodium out of the reactor vessel through the openings of the roof plug. Elastomeric sealants are normally employed for sealing of the roof plug and other components penetrating through it. These sealants are lubricated with high molecular weight hydrocarbons. Thus, during CDA, momentary contact between high temperature sodium and the lubricating oil takes place, resulting in the formation of various products. The nature of the products, viz. physical status, density, susceptibility for interaction with air etc., formed during the interaction helps in the management of the post-accidental scenario. From literature, the interaction of lubricating oil gives hydrogen and methane as the main products along with black tar:

$$C_nH_{2n+2} \xrightarrow[T \geq 300^oC]{Na} H_2 + CH_4 + C_2H_4 + C_mH_{2m+2} + C \quad \text{where } (m < n)$$

Other hydrocarbons formed are reported to be 1 or 2 orders less than methane. It was also reported that reaction kinetics below 573 K is sluggish, whereas the reaction is faster above 673 K. The present studies are aimed at understanding the evolution of the gaseous products as a function of temperature. Experiments were carried out by maintaining lubricating oil (Cabol 32; flashpoint: 483 K) to sodium (molar) ratio as 1:10 at different temperatures of sodium, ranging from 623 to 823 K.

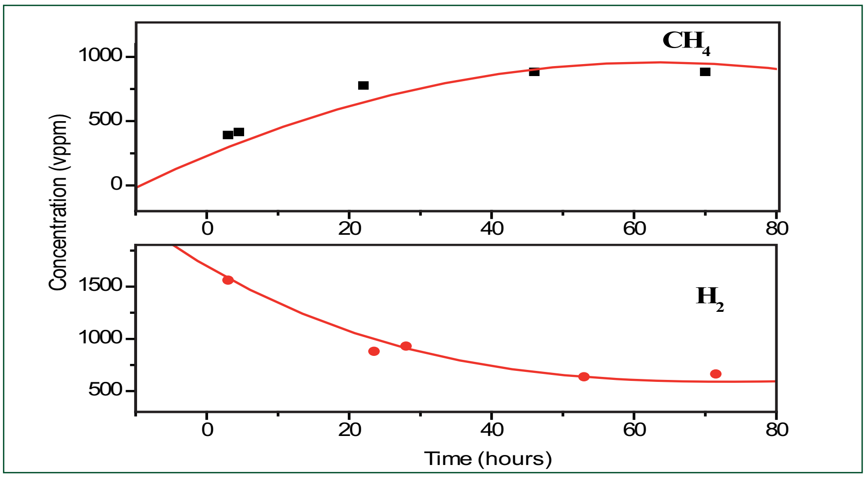

Fig. 1 *Typical plot of the concentration of hydrogen and methane for the reaction between high temperature sodium to lubricating oil at 673 K (volume of the reaction vessel ~150 ml)*

The kinetics of the reaction was followed by analyzing the hydrogen and methane evolved as a function of time. Typical trace showing the ratio of the concentrations of these two species with time at 673 K is shown in Figure 1. As evident from the trace, the relative concentration of hydrogen to methane decreases during the course of the reaction. The trend was found similar for all the temperatures studied. Hydrogen concentration is found to be higher during the initial phase of the analysis, which decreases gradually and remains nearly constant with time. Concentration of methane is low during the initial stages and increases with time and attains an equilibrium value. This behaviour in change of concentration of both hydrogen and methane can be explained as follows: when oil falls on hot sodium surface, it gets cracked leading to evolution of large concentration of hydrogen and low levels of methane instantaneously (as shown in equation). As time progresses, hydrogen is probably getting consumed by the interaction on the hot black tarry product layer formed over sodium with the higher alkanes, resulting in the formation of methane and lower alkanes. The plateau region indicates the equilibrium between the rate of consumption of hydrogen and formation of methane. The time taken for the steady state equilibrium will depend on the temperature of sodium. The ratios of concentration of hydrogen to methane after 15 minutes of introduction of oil to sodium at 623 and 723 K were found to be 0.54 and 0.80 respectively. The increase in the hydrogen to methane ratio showed that the instantaneous production of hydrogen was more than methane at higher temperatures.

It is to be noted that on dropping the oil on hot sodium, splashing will occur. The low boiling fraction is expected to vapourize instantaneously and deposit on the cooler regions of the reaction, while high boiling fraction of the oil will interact with sodium leading to the reaction mentioned. The splashed oil on the hot internal surface of the stainless steel container may also undergo the reaction resulting in a significant contribution of hydrogen and methane.

III.19 Novel Thermomechanical Processing, Characterisation of Microstructures and Evaluation of Mechanical Behavior of 9Cr Ferritic Martensitic Steels

Creep deformation and rupture behavior of modified 9Cr-1Mo steel in thermo mechanically processed steel

ASME P91 heat resistant steels employed for steam generator applications possess adequate high temperature creep strength, resistance to oxidation, stress corrosion cracking, good weldability, high dislocation density, intra-lath MX type carbides and nitrides. However, the rapid rate of coarsening of $M_{23}C_6$ than the MX precipitates results in decrease in creep rupture life of the steel. Hence, methods to reduce coarsening rate of $M_{23}C_6$ and enhanced precipitation of stable MX precipitates in the steel are important.

Investigations on thermo mechanically process modified 9Cr-1Mo steel exhibited extensive and homogeneous distribution of precipitates as compared to the normalized and tempered steel, which also resulted commensurately with higher tensile strengths beyond 673 K. The microstructures of modified 9Cr-1Mo and thermo-mechanical treatment (TMT) processed steel are shown in Figures 1a and 1b. The increase in tensile strength and lower tensile ductility at higher test temperatures are attributed to the presence of fine precipitates, which delay the dynamic recovery of the dislocation structure.

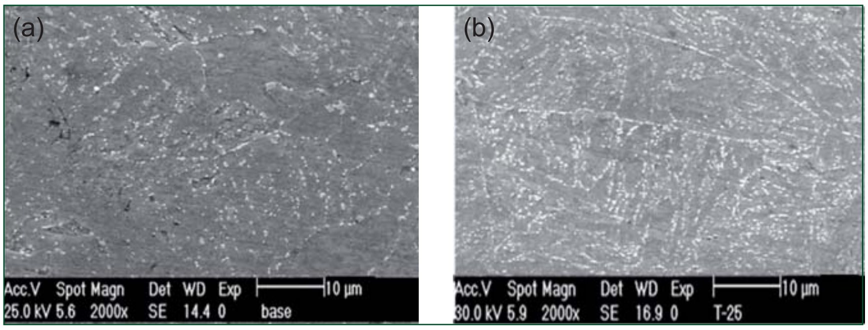

Fig. 1 *Microstructure of (a) modified 9Cr-1Mo and (b) TMT processed steel*

The creep curves of modified 9Cr-1Mo and steels processed thermo mechanical treatment (TMT) at 100 MPa stress is shown in Figure 2. The decrease in creep rate and increase in creep rupture life of TMT processed steel is clearly observed (Figures 2 and 3). At lower stress levels, the difference in rupture life between the two steels is significant. The increased creep strength of TMT processed steel is attributed to the sub-boundary hardening and delay in recovery of dislocation sub-structure due to the presence of fine precipitates in the steel.

Creep crack growth behavior of a P91 steel weld

Modified 9Cr-1Mo steel weld joints operating at elevated temperatures are known to fail prematurely due to cracking in the heat affected zone (HAZ), popularly known as Type IV cracking. Creep crack growth (CCG) being a principal failure mechanism at elevated temperatures, CCG data, especially for the welds, is an important input for integrity assessment. Therefore, creep crack initiation and growth properties of different regions of P91 welds were studied in the temperature range 798 to 898 K.

CCG tests at 898 and 798 K in fatigue pre-cracked (~5mm) compact tension (CT) specimens with notch within the weld metal (A) and in HAZ (B), using DCPD for

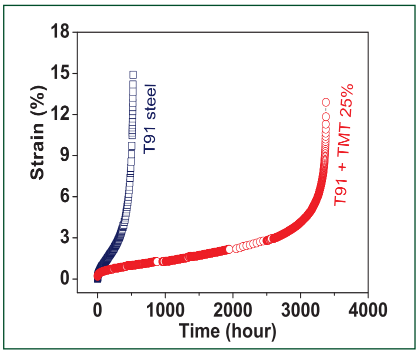

Fig. 2 *Creep curves of modified 9Cr-1Mo and TMT processed steel at 100 MPa and 923 K*

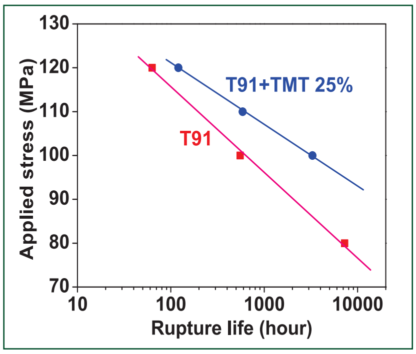

Fig. 3 *Variation of creep rupture life with applied stress at 923 K*

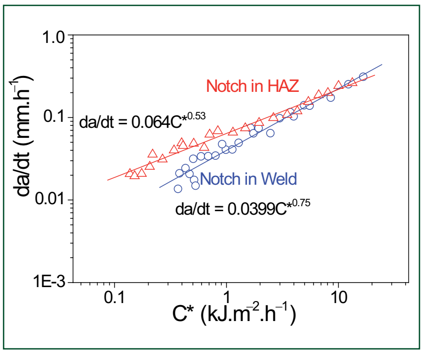

Fig. 4 *CCG data for types A (O) and B (Δ) specimens at similar initial K (P91 weld joint 898 K)*

crack length measurement showed a change in its course to follow HAZ region, as the crack grew in type A specimen (Figure 4). A higher intercept *A* (0.064) and lower slope *m* (0.533) for B specimens, in comparison to A specimens (0.0399 and 0.75 respectively) was observed indicating the higher creep crack growth in HAZ, confirming type IV cracking. The difference decreases at higher *C** levels corresponding to long term behavior. Heavy creep damage was observed in HAZ (Figure 5), compared to weld metal, which showed relatively less damage. CCG data for type A and B specimen fall in the same scatter band (Figure 6), indicating the lower CCG resistance of HAZ.

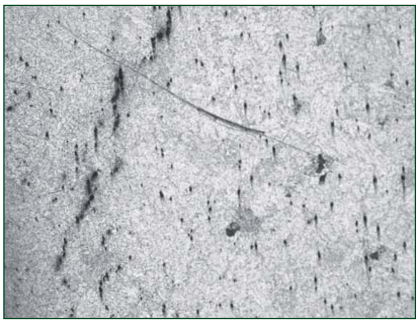

Fig. 5 *Extensive creep damage in the HAZ*

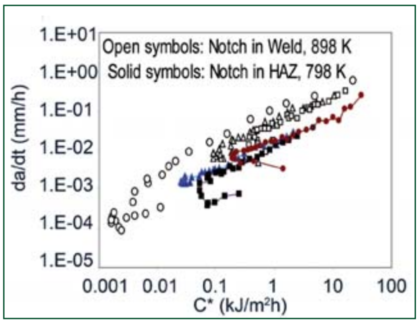

Fig. 6 *Comparison of da/dt as a function of CCG parameter C**

Creep crack growth in fine-grained HAZ is characterized by extensive creep void formation, which is highly susceptible to creep damage accumulation due to the fine (average grain size of <5 μm) equiaxed grain structure with no martensitic laths. Extensive creep damage in HAZ of type A specimens despite being away from the highest stress concentration notch regions is in contrast to type B specimens, where more damage due to closer proximity to the notch tip and a higher crack growth rate is expected. The complex metallurgical and mechanical heterogeneities introduced by solid state phase transformations, residual stresses and heat treatments during the welding process brings in significant differences in properties in the weld and HAZ, as compared to base metal. In the intercritical zone due to partial austenitization, of the microstructure consists of fresh transformation products and re-tempered martensite along with coarse $M_{23}C_6$ carbides. Creep deformation and damage evolution are significantly influenced by the presence of fine precipitates and second phase particles, in addition to the solid solution hardening. Various types of carbides and carbonitrides such as $M_{23}C_6$, M_6C, M_3C, M_7C_3, M_5C_2, M_2X, MX etc and secondary phases (Laves) are reported to be present in this class of steels and influence grain boundary sliding and grain boundary migration which accompany creep deformation. Formation of Z phase, Cr(V,Nb)N, at the expense of VN-precipitates is another factor that leads to the long term degradation effect in this steel.

Estimation of martensite feature size by microtexture analysis

It is well known that the 9Cr-1Mo steels are used in normalized and tempered (N&T) condition with a tempered martensite microstructure possessing optimum mechanical properties for power plant structural applications. During normalizing, the γ-phase of high temperature austenite (face centred cubic crystal) undergoes a displacive mode of transformation to martensite α' (body centred tetragonal). Each prior-γ grain is transformed to product α' crystals with a complex substructure (in hierarchical arrangement as packets, blocks, sub-blocks and laths) with high density of grain boundary and dislocation defects. In tempering, the excess carbon in α' diffuses out to form carbides and remnant α (body centred cubic) ferrite with a reduction in dislocation density although the martensite substructure is largely unaltered. Optical microscopy is generally used to characterize and evaluate prior austenite grain size (PAGS), but the other morphological features of martensite are not consistently resolved. A new

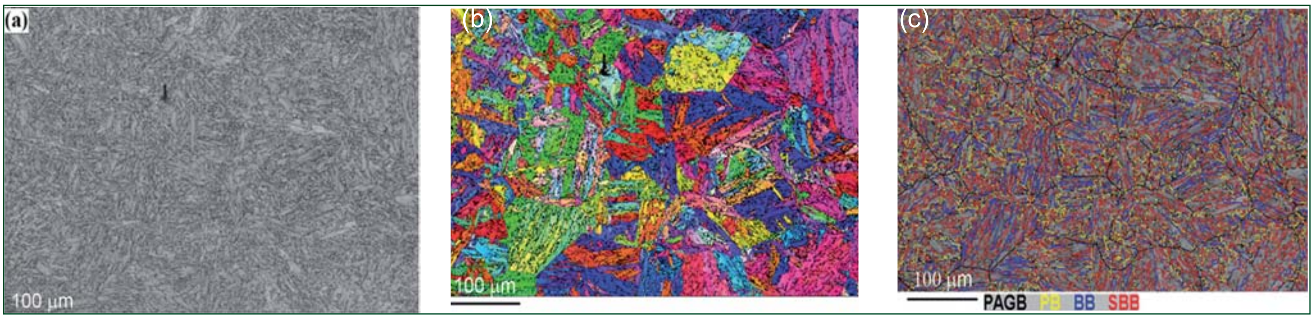

Fig 7 *EBSD results of 9Cr-1Mo steel (a) band contrast map showing a tempered martensite microstructure, (b) crystal orientation map of α crystallites and (c) grain boundary map of the different types of interfaces superposed on band contrast map*

procedure has been developed for evaluating the PAGS as well as martensite packet and block sizes by analysis of microtexture data. The scanning electron microscopy-electron backscatter diffraction (SEM-EBSD) technique was used to characterize and measure the orientation of room temperature α crystallites in normalized and tempered 9Cr-Mo steel. The electron backscatter diffraction band patterns deteriorate at crystal interface regions and the band contrast image (Figure 7a) shows the characteristic martensite structure. The crystal orientation map in Figure 7b depicts the type of crystallographic plane aligned with the sample plane. In martensitic transformations, the parent γ and product α'/α are known to be related by specific orientation relationships. A given γ crystal can transform upto 24 distinct α orientations, and the α variants are then inter-related by specific misorientations. The interface separating a pair of α variants could be packet boundary (PB-12 types), block boundary (BB-3 types) or a sub-block boundary (SBB). The misorientation between neighboring pixels was calculated and compared with the theoretical misorientation set, to classify the interface as PB, BB, SBB or PAGB (Figure 7c). The electron backscatter diffraction scan data was analyzed in detail to determine the underlying orientation relation, and to make optimum tolerance angles for boundary classification. The average intercept length of PAGS, packet, block and sub-block was evaluated as 31, 14, 9 and 4 µm respectively.

Study of austenite to martensite transformation by automated crystal orientation imaging microscopy

The tungsten and tantalum added 9Cr reduced activation ferritic martensitic (RAFM) steels are employed in the normalized and tempered condition. The 1.4W RAFM steel in normalized condition consists of a martensitic structure with a few undissolved carbides, which are W and Cr rich $M_{23}C_6$ and Ta and V rich MX, while the tempered steel possessed higher amounts of the same type of carbides. XRD analysis using synchrotron radiation indicated the presence of retained austenite in the normalized steel, which was not observed after tempering.

Figure 8 shows the Mossbauer spectra of the steel in both conditions. Presence of a singlet along with a six line pattern in the normalized steel suggests the presence of a low amount of non magnetic cubic phase, which could either correspond to the undissolved fcc carbides or retained austenite, if any. However, in the normalized and tempered steel (Figure 8b), only a six line pattern corresponding to the ferromagnetic martensite is observed, despite the presence of higher amount of carbides. Hence, the singlet observed in the Mossbauer spectra of normalized steel supports the presence of retained austenite.

Identification of retained austenite by conventional TEM imaging techniques was difficult. An emerging technique namely automated orientation imaging in TEM has been employed for an unambiguous confirmation of the presence of retained austenite. Figure 9a shows the crystal orientation map of normalized steel, which has

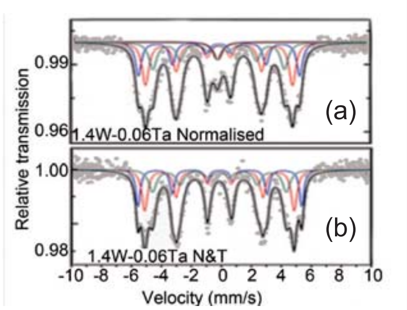

Fig. 8 *Mossbauer spectra of 1.4W-0.06Ta steel showing presence of (a) singlet in normalized steel along with the sextet and (b) only a sextet in N&T steel*

been indexed with inputs of both ferrite and austenite phases. The different orientations of martensite laths within the austenite grains are clearly revealed in Figure 9a. However, presence of fine retained austenite was observed along prior austenite grains and lath boundaries, which can be seen in the phase map in Figure 9b, while the tempered steel showed no evidence for the presence of austenite. The retention of austenite in normalized steel is rather unexpected, since the martensite start and finish (M_s and M_f) temperatures of the 9Cr RAFM steel are far above room temperature. The presence of austenite is attributed to the inhomogeneous microstructure resulting from the sluggish dissolution of W and Ta containing $M_{23}C_6$ and MX precipitates during solution treatment at 1253 K, which influences the kinetics of martensitic transformation. The role of W and Ta on the α↔γ transformation kinetics has been established by systematic calorimetry investigations.

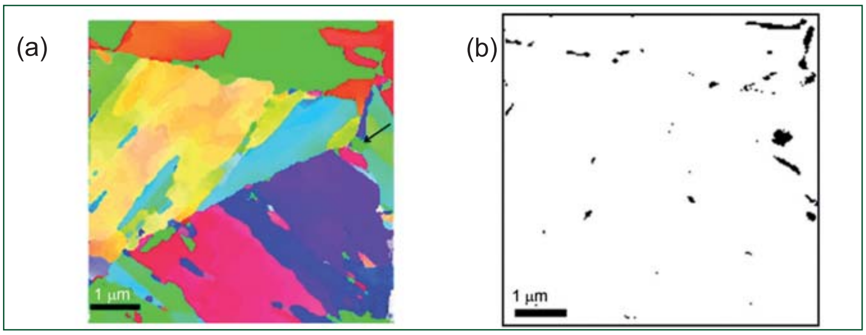

Fig. 9 *(a) Crystal orientation map of 1.4W-0.06Ta steel showing different orientations of martensite laths and (b) phase map showing retained austenite*

III.20 Thixocasting of 304L SS: Demonstrating the New Manufacturing Method for Austenitic Stainless Steels

Thixo-casting is an alternative to conventional manufacturing techniques such as casting and forging. This technology combines the benefits of both conventional casting and forging processes. Near-net shape products are manufactured using thixo-casting with minimum intermediate process steps, compared to forging process. The products manufactured using this technology show better mechanical properties compared to its conventional cast counterparts. As alloys exhibit thixotropy (a property by virtue of which alloy flows like fluid when shear stress is applied and behaves like a solid when it is allowed to stand still) in the semi-solid stage, thixo-casting requires the alloy in its semi-solid state, rather than in solid state as used in forging process or in molten state as used in conventional die casting technology. Though, there are many requirements imposed on the potential feedstock for semi-solid processing, the key feature which determines its suitability for the above processing is the formation of unique microstructure that contains solid spheroids in a liquid matrix. The microstructure responsible for better property in the material is obtained by breaking of the growing dendrites in the solidifying alloy. The growing dendrites during solidification are broken by employing methods such as mechanical stirring, electro-magnetic stirring, ultrasonic vibration and cooling slope etc.

Thixo-casting was restricted to non-ferrous alloys with lower melting points. Thixo-casting of steel has not been tried extensively considering the complexity involved with the processing of the steel. In view of the imminent importance of thixo-casting and its potential application, thixo-casting of austenitic stainless steel was taken up for the first time in India. 304L SS was used for this investigation as a representative of the 300 series austenitic stainless steels. To obtain the liquidus and solidus temperatures, liquid fraction evolution during melting of the steel and information about solidification behavior of 304L SS, differential scanning calorimetry experiments were carried out. The solidus and liquidus temperatures (1653 and 1752 K, respectively) were measured from differential scanning calorimetry endotherms. Then the thixo-casting temperature was decided from the liquid fraction evolution. Using the experimental data obtained from the differential scanning calorimetry experiments and computational fluid dynamics analysis of the metal pouring process, a cooling slope was designed and manufactured by IISc, Bengaluru. Using this indigenously developed cooling slope, the thixo-casting of 304L SS was carried out at DMRL, Hyderabad and a thixo-cast ingot of 10 kg weight was produced. The thixo-casting process is shown in Figure 1. To compare the microstructure of the steel and subsequent analysis, an ingot of 10 kg weight was subsequently produced by conventional casting route using the same furnace. From the microstructural analysis, it was observed that thixo-cast microstructure consists of small clusters of skeletal δ-ferrites in the austenitic matrix, whereas the microstructure of the conventional cast material contains long chains of dendrites. Comparison of these microstructures demonstrates the effectiveness of cooling slope to produce non-dendritic structures in the stainless steel. The dendritic microstructure in stainless steel castings is often considered as detrimental for long term usage of critical components. Thixo-casting can be used as an alternate manufacturing route to conventional casting process, for producing critical components of stainless steel.

Fig. 1 *Photograph showing thixo-casting process*

III.21 Weldability Study on AISI 304B4 Borated SS

Borated stainless steel 304 B4 Grade A as per ASTM A 887-89 containing 1.3 wt.% boron is specified for neutron shielding of intermediate heat exchanger (IHX) in PFBR. The neutron shielding is provided by a half-cylindrical shell of dimensions 1915 mm OD x 20 mm thick × 4580 mm length covering the intermediate heat exchanger on the core side. Additionally, shielding is provided at the bottom portion by a double-shell envelope of 5 mm thick plate of 304B4, which is specified only for shielding. Considering the importance of weldability of the borated stainless steel, a systematic study has been taken up.

The evaluation of the weldability of an alloy usually involves application of strain or some form of restraint during welding and assessing the weld metal for cracking. During this test, strain is applied pneumatically by bending the specimen rapidly over a die block of fixed radius when the weld puddle is at the middle of the specimen. The straining is completed within 15 milli seconds so that the weld puddle is essentially frozen. The augmented strain experienced by the specimen is related to the radius of the die block using the relation $\varepsilon = t/(2R+t)$, where ε is the strain on the outer fibre, t is the specimen thickness and R is the radius of the die block. Tests were conducted with five different die blocks with augmented strains of 0.25, 0.5, 1, 2 and 4%, respectively.

The hot cracking assessment parameters that were evaluated were: (i) total crack length, (ii) maximum crack length and (iii) brittleness temperature range. The crack lengths were measured using a stereo-microscope at 60x.

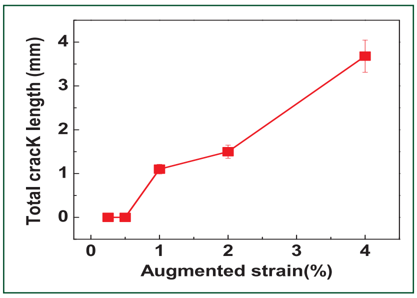

Fig. 1 *Total crack length versus augmented strain*

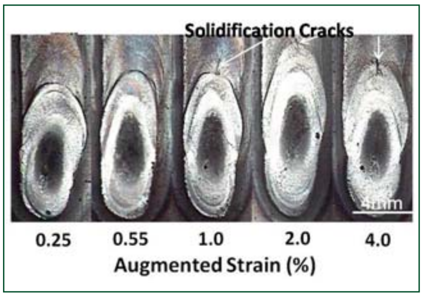

Fig. 2 *Photographs of hot crack tested specimen for different augmented strain*

The brittleness temperature range is derived by superimposing maximum crack length on cooling curve obtained experimentally under the same welding conditions.

The results of the hot crack test indicate that the material is not severely susceptible to hot cracking as the total crack length is below ~4 mm, Figure 1. The tested specimens revealed a few hot cracks running along the weld centre line perpendicular to the fusion boundary on the weld surface as shown in Figure 2.

The microstructural analysis of the hot cracked specimens revealed extensive back filling of the hot cracks by austenite/boride eutectic constituents (Figure 3). Microchemical analysis of back filled cracks using scanning electron spectroscopy/energy dispersive spectroscopy confirms that eutectic consists of $(Fe,Cr)_2B$ type of borides as shown in Figure 4.

The volume of the eutectic liquid in the weld metal is 55% as estimated using Scheil's simulation.

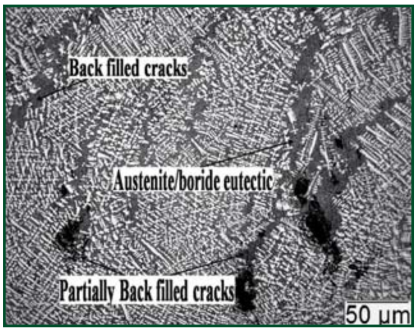

Fig. 3 *Photomicrograph of hot cracks*

In general, the solidification temperature range of an alloy is proportional to its "brittleness" temperature range and hot cracking susceptibility is greater when the solidification temperature range is wider. It may be noted that solidification temperature range is higher for an alloy containing 0.5 mass% boron compared to that with 1.3 mass%.

The brittleness temperature range or the solidification cracking temperature range of the tested alloy is 192°C wide, which is high compared to other stainless steels. But, 304B4 Grade B stainless steel has been found to possess reasonably good weldability compared to other stainless steels and this is attributed to backfilling effect by the low melting eutectic to the cracks. Further, weld joint design was modified such that high restraint does not arise during fabrication.

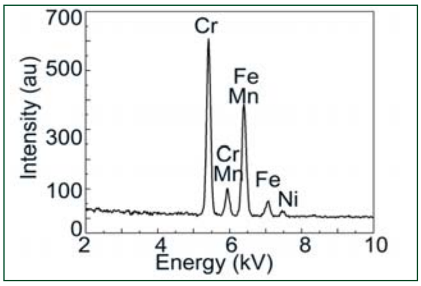

Fig. 4 *Energy dispersive spectroscopy spectra showing enrichment of chromium*

III.22 A-TIG Welding of Alloy D9 Hexcan with 316LN Stainless Steel Foot Assembly of a Fuel Subassembly

A variant of TIG welding process called the activated tungsten inert gas (A-TIG) welding process has been found to overcome the limitations of the conventional TIG welding process. A-TIG welding process involves application of thin coating (15-20 μm thick) of activated flux on the joint area prior to welding and the process is found to produce dramatic increase in penetration of 300% in single pass welding. A-TIG welding process has been developed for austenitic stainless steels and it is patented. The use of activated flux was found not to cause any significant change in the chemical composition of the weld metals compared to that of the base metal. There was no degradation in the microstructure and mechanical properties of the A-TIG welds compared to that of the welds produced by TIG welding. The creep rupture life of 316LN A-TIG weld joints is enhanced by 75% compared to that of the TIG weld joints. Residual stresses and distortion are reduced significantly in A-TIG weld joints. The A-TIG welding does not involve edge preparation and filler metal addition.

Figure 1 shows the typical fuel subassembly. Hexcan welds of fuel subassemblies are currently made by multi-pass TIG welding procedure. Both manual and automated A-TIG welding procedures have been developed to weld alloy D9 hexcan with SS 316LN foot assembly. Figure 2a shows the photograph of the weld joint. A-TIG welding has been successfully employed for the first time for welding D9 hexcan with 316LN stainless welding procedure. The welding process parameters have been optimized.

Full penetration was achieved in single pass welding with 130 A current in A-TIG welding. Figure 2b shows the cross section of the weld exhibiting full penetration. Figure 2c shows the inside of the component exhibiting no decoloration and excessive heating. Figure 2d shows the weld metal microstructure. The weld joint successfully passed the ultrasonic testing for lack of penetration defect. The weld joint cleared all the test requirements as per the PFBR specifications including the bend test, inter granular corrosion test and tensile test for qualifying the procedure for welding of D9 hexcan with SS 316LN foot assembly of the PFBR fuel subassembly. A-TIG welding process can also be adapted for the topside welding of hexcan with head component of the fuel subassembly. A-TIG welding procedure, if adopted for fuel subassembly fabrication can considerably bring down both the cost and time of fabrication of the fuel subassemblies and also improves the mechanical properties.

Fig. 1 *Fuel subassembly fabrication*

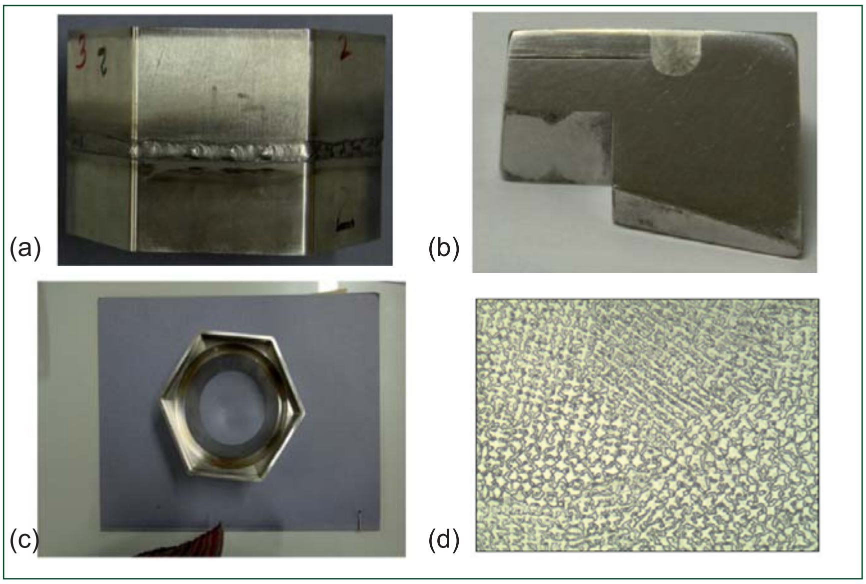

Fig. 2 *(a) A-TIG weld joint of alloy D9 hexcan with SS 316LN foot assembly, (b) cross section of the weld showing complete penetration in single pass, (c) the inside of the hexcan weld joint showing no excessive heating and decoloration and (d) weld metal microstructure*

III.23 Qualification of Filler Wire Samples by a Novel Technique

Process vessels and associated piping of nuclear spent fuel reprocessing plants, handling highly radioactive and acidic solution have to be designed and constructed for ensuring maintenance-free service during the life of the plant. AISI 304L grade austenitic stainless steel has been chosen as the material of construction due to its ability to withstand this kind of demanding service conditions. Gas tungsten arc welding process (GTAW) using ER 308L filler wire is used for welding due to good root-weld quality and its superior resistance to intergranular corrosion (IGC).

The filler wire used for welding should be qualified for chemical analysis by making the weld deposit as described in ASME Section-II Part C, which is laborious, time consuming and complicated. A novel method called "single layer meshing (SLM)" has been developed as an alternative to the above method; SLM method is advantageous over the conventional method of sample preparation which calls for huge volume of weld deposit in order to get undiluted weld metal specimen. The scatter (inconsistency) in the results of chemical composition observed in the conventional methods is also eliminated in this novel method. The results obtained have been compared with that of conventional technique by means of mock-ups.

In normal practice, preparation of weld pad (fused sample) is done by depositing filler wire over a compatible base material. For instance, during the preparation of weld pad for ER308L filler wire, SA240 GR 304L stainless steel plate is chosen as the base over which the weld metal would be deposited. In conventional weld-pad preparation, the chance for dilution of base metal by filler wire deposit is very high, which may give erroneous information while testing. The factors responsible for dilution are voltage, current, welding speed, polarity etc., However, to minimize the dilution problem, weld metal is deposited in multiple layers, one over the other and the specimen would be machined out from top side of the pad after leaving sufficient thickness of filler wire deposit from the base metal, where the possibility for dilution is maximum. ASME standard was followed in obtaining an undiluted sample from the chosen size of pad at the selected distance above the base metal by analyzing chips removed from successively lower layers of the pad. Layers which are undiluted will have the same chemical composition. Therefore, determination of identical compositions for two successive layers of deposited filler metal will provide evidence that the last layer is undiluted. Thus, for avoiding dilution problem and minimising the deposition thickness, SLM technique has been developed.

Two types of specimen were prepared and were designated as type-1 and type-2. Type-1 (Figure 1) refers to the specimen prepared by conventional method and type-2 (Figure 2) refers to the specimen prepared by single layer meshing method. Size of specimen shall be minimum as required for spectrometric analysis. Type-1 was prepared by depositing ER308L filler wire directly on SA240 type 304L stainless steel base material. Preparation of type-2 specimen involved the following stages. The filler wire was cut into lengths as required to be spread over a rectangular field as shown in Figure 2. Subsequently, the array of filler wires was made integral by fusing their ends. Finally type-2 specimen could be prepared by depositing filler metal in multiple layers one over the other above the bed of filler wires. After depositing filler metal for a thickness equivalent to that of the conventional specimen, the weld metal deposited was detached from the bed of filler wires easily, either by chipping or chiseling. Table 1 compares the details on various factors involved in the preparation of type-1 and 2 samples. Composition of all the elements in each layer of deposit had been analysed to know the

Fig. 1 *Type-1 specimen*

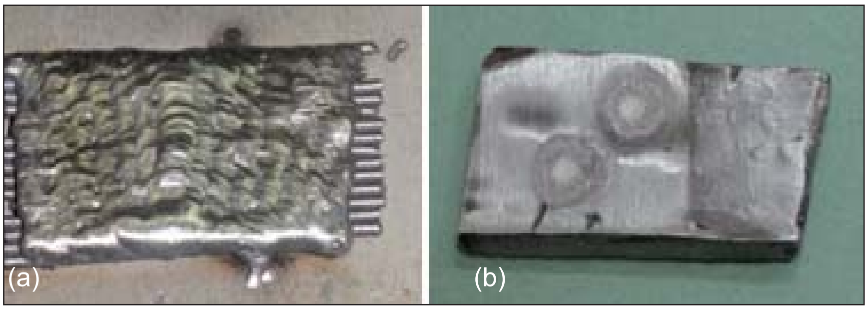

Fig. 2 *Type-2 specimen (a) before and (b) after machining*

variation in weight percentage of elements in different layers and to compare the values with that provided in the manufacturer's test certificate. Comparison of the spectroscopic test results of type-1, type-2 and manufacturer's test certificate revealed that there was no significant difference or dilution in the composition of all the elements, except for carbon and silicon. In the case of silicon, the test results showed a marginal variation in weight percentage from the manufacturer's test certificate, which might be due to the loss of elements during welding process. The variation in carbon percentage was higher than that of manufacturer's test certificate results. Variation in carbon becomes more significant because a marginal increase in carbon beyond 0.03% would increase the risk of sensitization and IGC attack. It is evident from Figure 3 that the first layer of type-II specimen had 0.019% carbon, which matches with the filler wire composition as compared to other layers of type-2 specimen and all the layers of type-1 specimen. This is due to the fact that the bare filler wire, which acts as the percentage of base metal, would not influence the quality of layers of weld metal deposited above. The SLM method of pad preparation will provide reliability compared to conventional method.

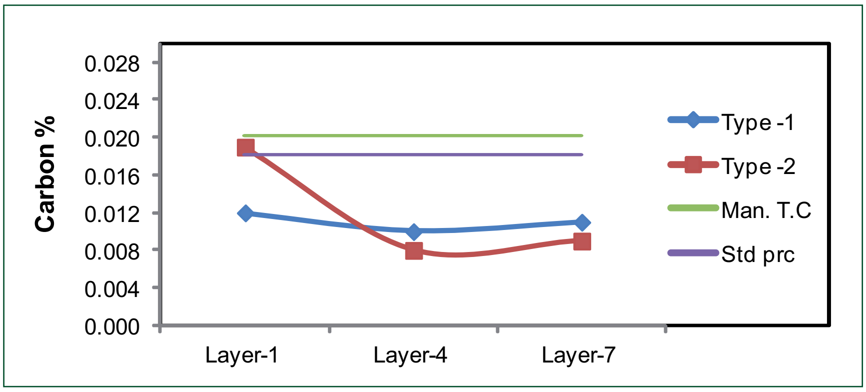

Fig. 3 *Comparison of the weight % carbon in different layers of type-1 and type-2 specimens with that from manufacturer's test certificate*

Table 1: Material and time requirement for specimen preparation

Sl. No.	Description	Type-1 (conventional technique)	Type-2 (SLM technique)	Time saved
1	ER308L filler wire; 2 mm diameter	78 g	31 g	60%
2	Argon gas consumption	203 L	29 L	85%
3	Time taken for preparation	286 minutes	41 minutes	85%

For standardization and validation of the process, three more specimens were prepared and chemical analysis was performed to ensure reliability and confidence levels regarding the quality of the filler wire. The chemical compositions of elements in different layers of type-2 specimen were found to be uniform. The results also revealed that variation of carbon in the first layer of type-2 specimen was insignificant when compared to the manufacturer's test certificate. The % variation in the concentration of other elements between manufacturer's test certificate and our standardized procedure was observed to be minimum. For standardizing the process, it is recommended that a minimum of two weld pads should be prepared and tested as per the recommended standard practice.

III.24 Kinetics of Uniaxial Tensile Work Hardening Behaviour of Type 316LN SS in the Framework of Two-internal-variable Approach

Uniaxial tensile flow and work hardening behavior of type 316LN austenitic stainless steel have been examined in the framework of physically based two-internal-variable approach. In this approach, the evolution of forest dislocation density (ρ_f), mobile dislocation density (ρ_m) and mean free path (L) with plastic strain (ε_p) are coupled with the evolution of flow stress (σ) with plastic strain in order to predict the macroscopic deformation and work hardening behaviour of the steel for wide range of temperatures and strain rates. The steel exhibited three-stage work hardening behavior in the variations of $\theta\sigma_d$ with σ_d, where $\theta\sigma_d$ is the product of instantaneous work hardening rate, θ ($\theta = d\sigma_d/d\varepsilon_p$) and flow stress contribution from dislocations (σ_d) and ε_p is the true plastic strain. The three-stage work hardening was characterized by a gradual increase in $\theta\sigma_d$ at low stresses (transient

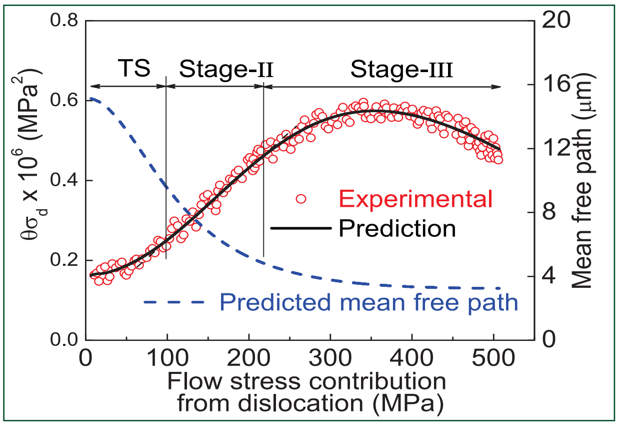

Fig. 1 *The variations of instantaneous work hardening rate as a function of flow stress contribution from dislocation (σ_d) at 673 K ($\dot{\varepsilon}=3.16\text{x}10^{-4}s^{-1}$)*

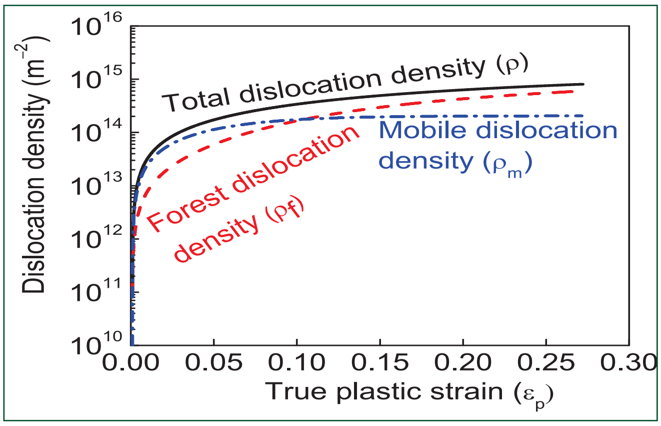

Fig. 2 *The evolution of predicted forest, mobile and total dislocation densities as a function of true plastic strain (ε_p) at 673 K ($\dot{\varepsilon}=3.16\text{x}10^{-4}s^{-1}$)*

stage) followed by a linear increase in $\theta\sigma_d$ in stage-II and inverted parabolic hardening at high σ_d in stage-III (Figure 1). At all the strain rate and temperature conditions, the flow and work hardening behavior were appropriately described by the two-internal-variable model as shown in Figure 1. The observed variations in predicted mean free path with σ_d exhibited a rapid decrease from initial high value in the transient stage and stage-II to a saturation in stage-III clearly demonstrate the applicability of the approach for the steel (Figure 1). It has been also shown that the mobile dislocation density saturates faster than the forest dislocation density (Figure 2). The comparatively rapid evolution of mobile dislocation density over forest dislocation density obtained in the early stages of deformation clearly suggests the mobile dislocation density as a fast response variable. The variations in flow stress and work hardening parameters associated with two-internal-variable model with respect to temperature and strain state exhibited three distinct temperature regimes manifested by the anomalous behaviour due to dynamic strain ageing at intermediate temperatures and the dominance of dynamic recovery at high temperatures. The anomalous variations due to dynamic strain ageing have been obtained as the peaks/plateaus in the flow stress, higher $\theta\sigma_d$ values and the predicted dislocation densities at uniform plastic strain and minima/minimum in the dynamic recovery parameter (k_2) and final mean free path (L_S) at intermediate temperatures. The dominance of dynamic recovery at high temperatures was observed in terms of the rapid decrease in flow stress and dislocation densities, and rapid increase in the work hardening parameters with increasing temperature and decreasing strain rate. The variations in the predicted forest dislocation density at uniform plastic strain and final mean free path with temperature exhibiting three distinct temperature regimes are shown as examples in Figures 3 and 4. Good agreement between the predicted and experimentally observed evolution of dislocation substructure in terms of hard zone size and cell/subgrain size with respect to plastic strain and temperature has been demonstrated for type 316 stainless steel .

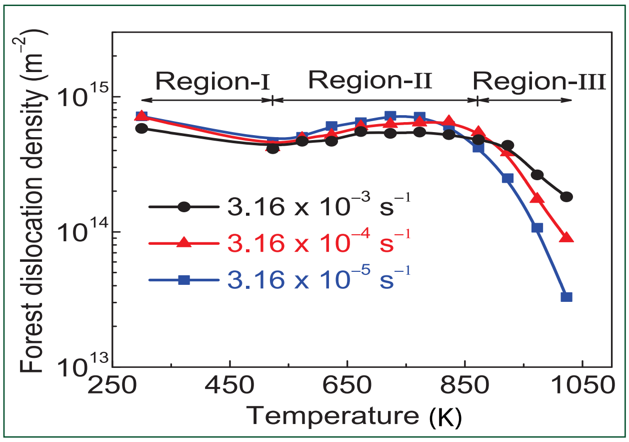

Fig. 3 *Variations of predicted forest dislocation densities at uniform plastic strain with temperature for different strain rates*

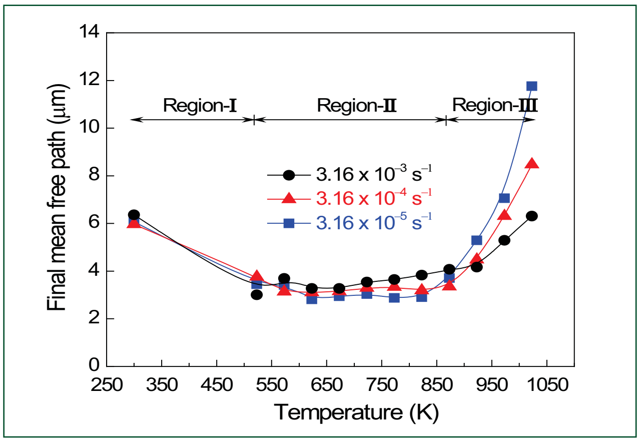

Fig. 4 *Variations of final mean free path with temperature for different strain rates*

III.25 Development of Instrumentation and Control Systems for Fast Breeder Reactors

Relay based diverse safety logic system for third shutdown system of future FBRs

Safety logic is the part of reactor shutdown system (SDS) chain responsible for making a decision (based upon the status of the SCRAM parameters) for shutting down the reactor. PFBR is provided with two independent shutdown systems; namely SDS-1 and SDS-2. Each shutdown system is equipped with independent safety logic system. To further enhance the safety of future FBRs, a 3rd shutdown system is being proposed. As part of the R&D for FBR, it was decided to explore the feasibility of developing a diverse implementation of safety logic system for 3rd shutdown system of future FBRs.

A prototype model of the relay based safety logic system was designed and fabricated for detection of three SCRAM parameters. Triplicated auto inhibition was considered as 1st SCRAM parameter and manual inhibition was considered as the remaining two numbers of SCRAM parameters. Being a prototype model only the core functionality i.e. 2/3 voting logic, auto/manual inhibition logic, and EM-coil drive logic have been considered in the design.

SCRAM parameters and auto/manual inhibition input signals have been processed using relays. The relay contacts for the respective SCRAM parameter channels have been configured to perform 2/3 voting logic and auto/manual inhibition logic.

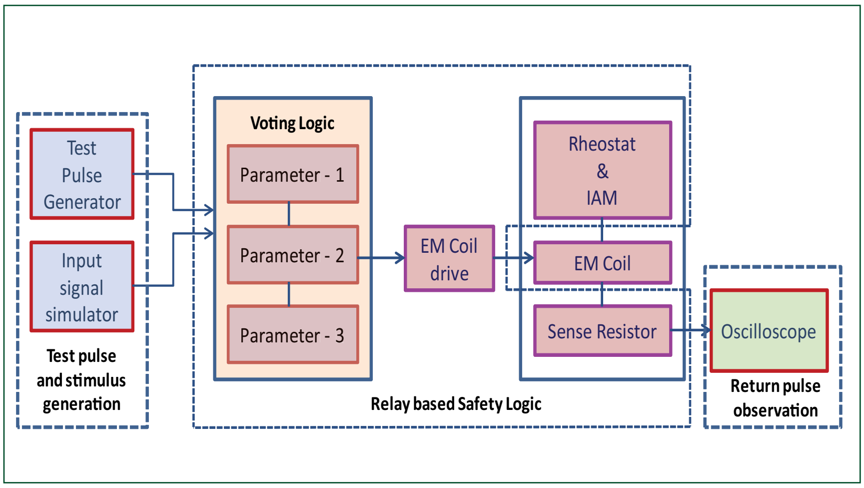

Fig. 1 *Test setup block diagram of relay based safety logic system*

The 2/3 voting logic blocks of SCRAM parameters are connected in series and finally the electromagnetic (EM) coil drive relays are energized. Each electromagnetic coil drive relay has two set of contacts and hence two electromagnetic coils are connected. The current in individual electromagnetic coils is adjusted using the rheostat and the same is indicated through the indicating alarm meter (IAM). As long as all the SCRAM parameters are healthy, the electromagnetic coils will remain energized and if any two channels of a SCRAM parameter go to the SCRAM state, it will lead to de-energization of electromagnetic coils.

For online testing of entire safety logic chain, test pulses are injected at the input of all the SCRAM parameter channels in a pre-determined sequence. At a time one SCRAM parameter is selected for testing. Whenever two channels are simultaneously selected for testing and test pulses are injected simultaneously to both the channels; the test pulse propagates through the safety logic chain and appears at the sense resistor. Figures 1 and 2 show the test setup block diagram and laboratory test setup respectively. The return test pulse captured is shown in Figure 3.

Test pulses with pulse width >6 ms duration are able to de-energise the corresponding relays in safety logic chain and can be captured across the sense resistors. Response time of the system was found to be about 11 milli seconds.

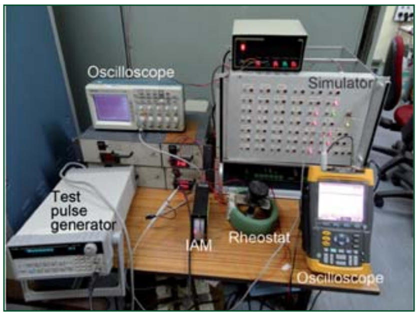

Fig. 2 *Laboratory test setup of relay based safety logic system*

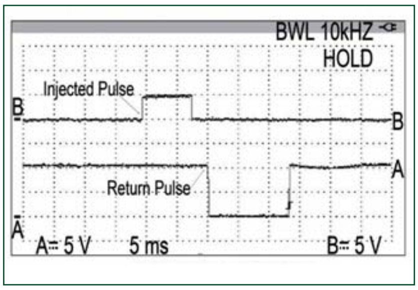

Fig. 3 *Eight milli second test pulse with 1 amp current in electromagnetic coil*

Assertion based verification of hardware description language designs of primary sodium pump speed and eddy current flow measurement systems

Primary sodium pump speed measurement system (PSMS) & eddy current flow measurement (ECFM) systems are safety critical systems in PFBR intended to protect against primary pump seizure and primary pipe rupture events respectively. The systems are designed using hardware description languages (HDL) and built using programmable logic devices which perform safety functions. PSMS uses a field programmable gate array (FPGA)-device, which is designed using VHDL. ECFM uses complex programmable logic devices (CPLD) designed using Verilog HDL. When HDL code and PLDs are used in safety critical applications, verification becomes a necessity, since undetected bugs can be catastrophic. Assertion based verification methodology was adopted using System Verilog as the verification language.

The verification environment used for verification of digital designs is shown in Figure 4. Test creation involves test benches for generation of stimuli based on the constraints provided. Drivers include the simulator interface and the necessary mechanism to drive the generated test vectors into the design under test (DUT). Receivers include the simulator interface and the necessary mechanism to receive data from the DUT after the stimulus is applied to the DUT. Data checkers perform data value checks to compare the output data values against the expected data. Protocol checkers consist of temporal assertions that monitor the functional protocol at important interfaces. Coverage monitors report how much of the design has been tested and help to decide if the test plan goals have been met.

System Verilog language has built-in features to specify powerful and flexible assertions. Assertions were written based on the properties of the DUT to monitor the signals in the DUT and verify the correctness of the design.

Comprehensive verification plans were prepared to cover all the functional aspects of the designs under test. The test cases and properties required to validate each of the functional requirements were identified as part of the verification plan. As part of the test bench, bus functional models (BFMs) were written for each of the components such as analog to digital converters, memories, etc. in the operating environment of the DUT. The interaction between the DUT and the verification environment is shown in Figure 5.

For all the properties, System Verilog assertions were specified external to the DUT and explicitly associated to the DUT. The SystemVerilog bind construct was used for observing internal nodes in the DUT. A mix of black-box and white-box approaches to verification was used. Mixed language simulation was carried out and the assertions were continuously monitored during functional simulation. Functional coverage analysis was performed to check if all typical scenarios have been covered and if all the corner cases have been exercised.

Design of tele-alarm and fire protection system using remote terminal unit

Tele-alarm systems are largely used in PFBR to ensure that the operator in every shift performs area surveillance of all the equipment to check their healthiness and identify

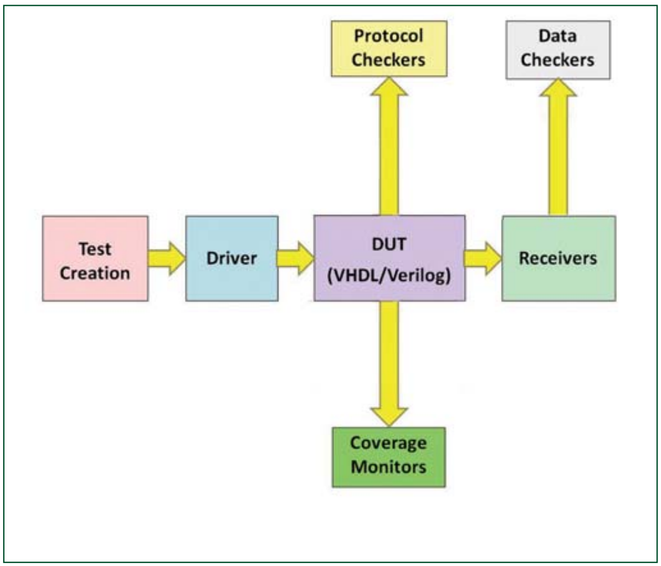

Fig. 4 *Components of a verification environment*

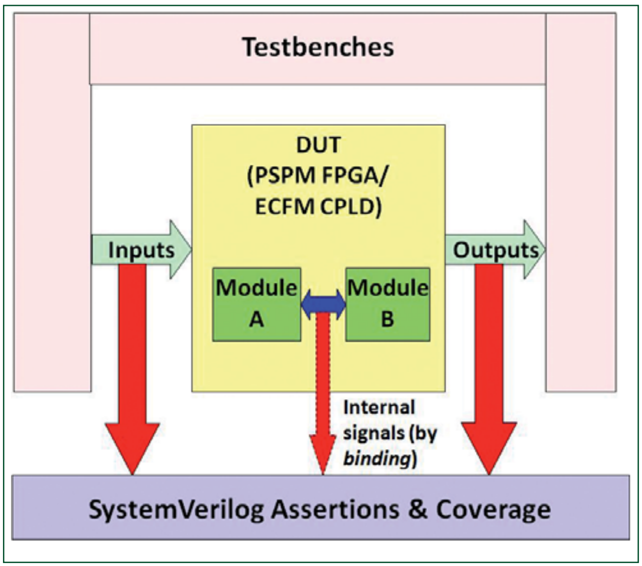

Fig. 5 *Interaction between DUT and verification environment*

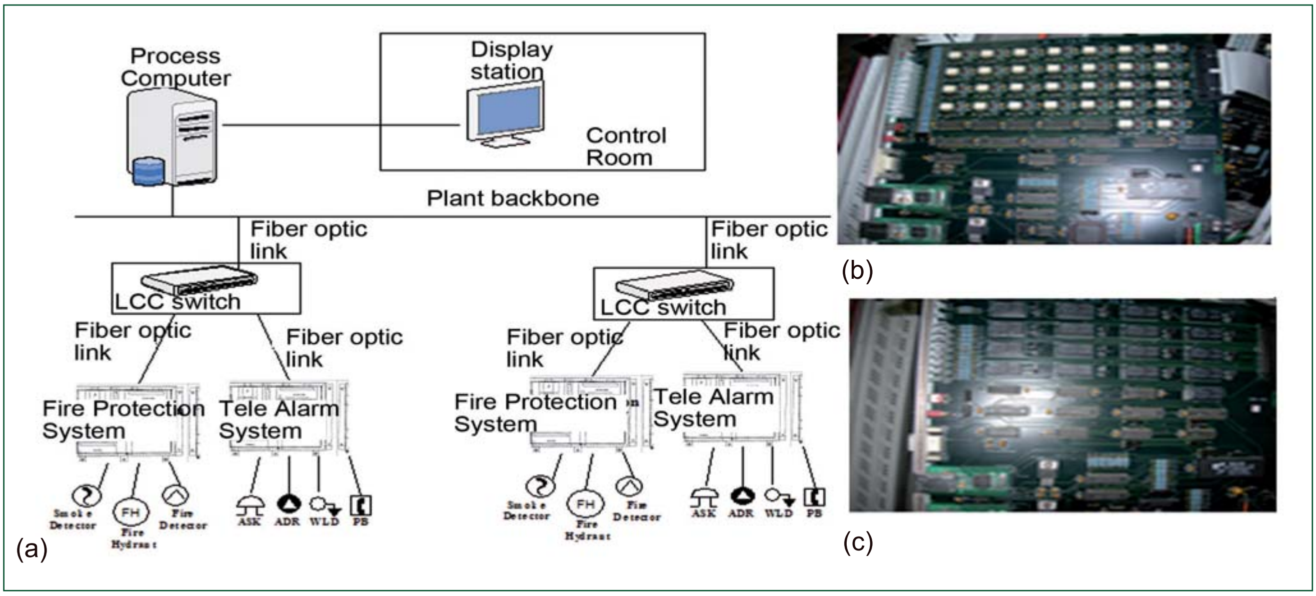

Fig. 6 *(a) Implementation of tele-alarm & fire protection system using remote terminal unit board, (b) digital Input and (c) relay output*

maintenance requirements. During the surveillance, maintenance personnel operate a key called area surveillance key that is provided at strategic locations such that no area in the plant is left unattended in every shift, as some of the equipment/buildings are unmanned normally. Water logging detectors are mounted near sumps, in pits, trenches/tunnels and other areas in the plant where water is likely to be accumulated and affect other systems. Call buttons are provided at different locations in the plant to enable the personnel to draw immediate attention of the control room in case they need assistance in the event of some emergencies. Argon being used as cover gas for sodium storage tank, there is a potential danger of depleting oxygen from the atmosphere in the event of leak/hazard. Hence, oxygen deficiency detector plays a major role for the safety of plant personnel. Similarly, Fire Protection systems which are connected to detection devices detect fire and activate or alert for implementation of emergency action and are sometimes used to actuate fire-extinguishing systems in the incipient stage so as to minimize the fire damage to structures, systems and components in nuclear power plant. These two systems are important echelons of the defence-in-depth approach to achieve a degree of safety necessary in nuclear facilities. The purpose of these systems are to monitor the presence of smoke/fire phenomena, key operated switches for area surveillance personnel, sensors deployed for water logging & detectors used to detect oxygen deficiency in the atmosphere and transmit the same to main control room for operator's attention by way of alarm display and facilitating the operator to actuate fire-extinguishing system remotely.

System implementation

Field deplorable signal processing cabinets are built using 8051 micro-controller based remote terminal unit (RTU) designed to handle digital input(DI) and relay output (RO) card along with power supply, interface module, ethernet switches with RJ45 connectors and two fiber ports all housed in a wall mounting panel.

Signals from fire detectors (such as smoke, thermal and flame detectors), area surveillance key (ASK), call button (PBN), water logging detector (WLD) & oxygen detector (ADR) are terminated at the nearest signal processing cabinets to generate soft alarms in the form of data packets and sent to process computer through plant backbone for display on display station (DS). Similarly all digital output channels connected to relay output card receive command from display station and generate potential free contact output for solenoid valve/actuator situated in the field to release either gas or water depending on type of fire. The overall architecture of networked tele-alarm fire protection system is shown in Figure 6 . The human machine interface (HMI) running on display station at control room indicates the alarm condition of each channel and facilitates control action to be generated based on the operator's decision.

III.26 Design & Development of Compact PCI (cPCI) Bus based Diversified Real Time Computer System for Safety Related I&C of FBRs

The current safety related computer system of Prototype Fast Breeder Reactor consists of two redundant *versa module europa* (VME) bus based real time computer system with a switch over logic circuit (SOLC). Since both the VME systems are exactly identical, the dual redundant system is prone to the common cause failure (CCF).The probability of CCF can reduced by adopting diversity. This article discusses the design and development of a diversified real time computer which will replace one of the computer systems in the dual redundant architecture. Towards the initial development the following activities were carried out:

- CPU card (Figure 1) based on an ARM-9 processor
- 16 channel relay output (RO) card (Figure 2)
- 30 channel analog input (AI) card (Figure 3).
- A 32 bit cPCI target controller IP with hotswap and geographic addressing support was developed and verified using a SystemVerilog based universal verification methodology compliant test bench.

CPU card specifications

- KSZ9692PBI SoC from Micrel with ARM922T core processor
- 64MB DDR memory and 8 MB NOR flash for boot program loader
- Gigabit ethernet interface
- Two serial and two USB ports
- PCI/PCI bridge
- Real time clock with battery back-up

Operating system & device driver

- U-boot as boot loader and ARM Linux 2.6 as initial OS
- Board specific low level (DDR controller and clock module) initialization code written in ARM assembly language
- Other peripheral initialization code and drivers written in C language.

RO card specifications

- 16 channel,5V DPDT Relays with 2A contact rating
- cPCI target controller IP and local bus glue-logic integrated in to a single Spartan-6 FPGA
- Relay contact with the readback facility
- Watchdog timer provided
- Full hot-swap capable
- Clock fail detection provided

AI card specifications

- Number of channels: 30 (differential)
- Fault protected dual level multiplexing
- 750V bank isolation between Analog front end and Backplane
- Full hot-swap capable
- High accuracy Programmable Gain Amplifier with gain selection of 1/2/4/10 per channel
- Input range: +/-10 V,+/-5 V,0-5 V, -5-0 V,0-10V user selectable
- Accuracy: 0.05% of FSR
- Scan time :100 μsec per channel.


Fig. 1 *Fabricated CPU card*

Testing of AI & RO cards

Device drivers were written as Linux kernel module along with user mode API library and test applications. Boards were tested successfully in cPCI reference platform.

A diversified system based on cPCI bus consisting of a CPU, RO and AI card were developed and tested successfully for future FBRs (Figure 4). Development of other input/output cards like analog output, digital input, digital output, synchro to digital cards are in progress.

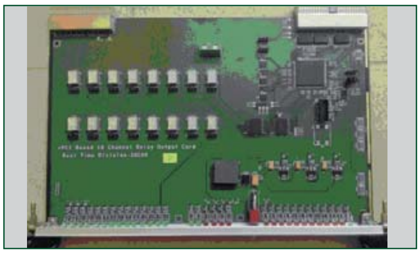
Fig. 2 *Fabricated relay output card*


Fig. 3 *Fabricated analog input card*

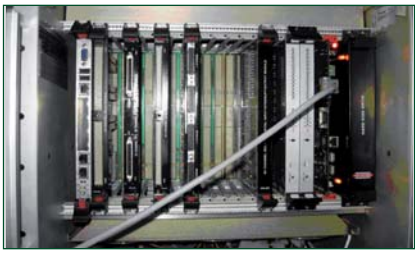
Fig. 4 *Test setup*

III.27 Development of Fieldbus based Instrumentation for Fast Breeder Reactors

Fieldbus is the technological evolution that allows multiple devices like sensors and actuators to reside on the single 'digital' communication bus as opposed to the concept of 'one device, one wire' of the past. It allows significant savings in wiring cost, real-time diagnostics, remote calibration, enhanced process data and easier predictive maintenance of field devices over traditional devices. Fieldbus based network carries both data & power for effective data transmission in the digital domain. Digital data is sent on the Fieldbus at a rate of 31.25 Kbits/second. Foundation Fieldbus is a subset of IEC/ISA standard (IEC 61158 and ISA s50.02).

Fieldbus overview

In a traditional 4-20 mA control system, each device is connected to the controller with two dedicated wires as shown below in Figure 1.

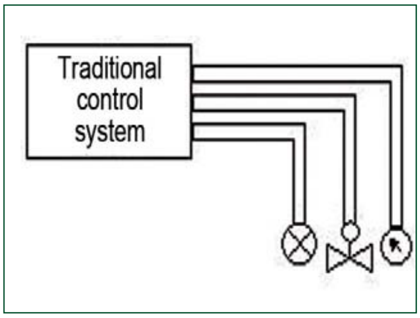

Fig. 1 *Traditional wiring of field devices*

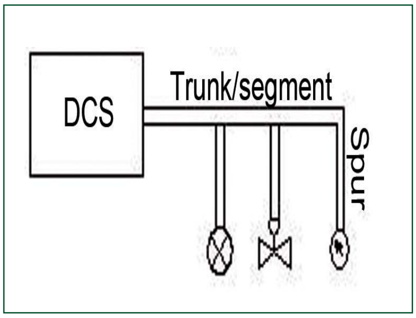

Fig. 2 *Fieldbus devices wired on single cable*

In this process, thousands of cables sneak their way through cable trays, termination racks, cabinets, enclosures and conduit. Instead of running individual cables, Fieldbus allows multiple instruments to use a single cable called a "trunk" or "segment". It is a single twisted pair wire carrying both a digital signal and direct current power that connects field devices like temperature, flow, level and pressure transmitters, smart valves, actuators, etc. to a linking digital control system (DCS), as shown in Figure 2.

This allows removing bulk of these cables and at the same time enhances data available from the plant. Because devices share the wires, the field devices can send data to each other without a digital control system controller (host) enabling peer-to-peer communication for effective "control-in-the-field". From the data shared between the devices, the devices can be configured to control the process. The host then only supervises the operation.

Laboratory setup of foundation Fieldbus

A laboratory set up has been established to study foundation Fieldbus (FF) technology using softing FG110 gateway and linking device, 8-channel temperature multiplexer, field display unit, redundant power supply as shown in Figure 3. A gateway between FF H1 and modbus/TCP (modbus over ethernet) serves as a gateway between foundation Fieldbus components and a widely distributed automation solution. A single gateway and linking device allows four FF H1 segments with as many as 64 field devices into control systems. This provides access to process data, while making use of foundation fieldbus advantages like reduced cabling, central field device parameterization, diagnosis functionality and Fieldbus-powered field devices. In addition, the gateway and linking device provides an integrated web server, which allows defining the mapping of foundation fieldbus functions to modbus registers or monitor the process values. The 8-channel temperature multiplexer transfers signals from thermocouples via Foundation Fieldbus. The cold junction temperature measured by a built-in temperature sensor is used for compensation. Normally 24 Vdc is supplied to the devices through redundant power supplies on the segment. Linking device is connected to personal computer via Modbus TCP for segment configuration and data supervision. Temperature reading from thermocouples are acquired via Fieldbus and the results are displayed through remote web browser.

Fig. 3 *Laboratory setup of foundation fieldbus for distributed temperature measurement*

III.28 Thermal Interaction of Flowing Sodium with Concrete

In the event of a sodium leak incident in the secondary sodium circuit of Fast Breeder Reactor, sodium will be ejected out under pressure and may interact with the underlying structural concrete. The reaction is exothermic and causes degradation of concrete. Hence, a limestone sacrificial layer is provided on the structural concrete. The interaction of limestone concrete with liquid sodium depends on whether sodium is impinging over the concrete surface [jet effect] or stagnant or it has flown over the surface.

To understand this phenomenon, assess the depth of sodium penetration and investigate thermal and chemical impact of sodium on the limestone concrete, experimental studies were carried out at MINA facility.

In order to assess the static and flowing sodium effect over concrete floors, blocks with an axi-symmetric trapezoidal cross section with three zones i.e., impact, sloping and stagnant were used as test specimens as shown in Figure 1a.

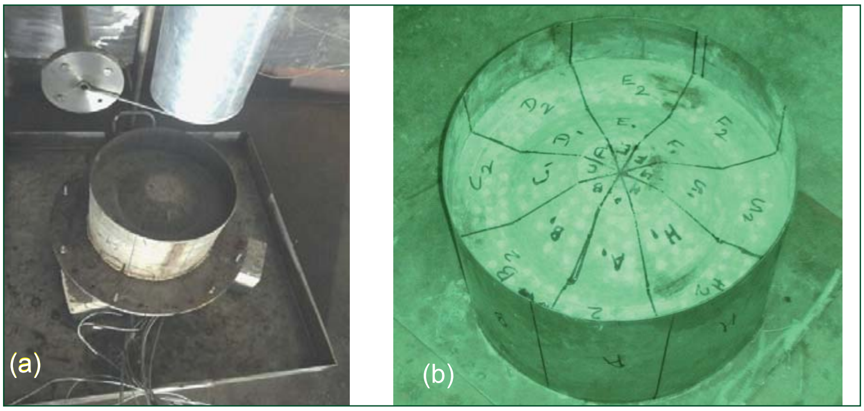

Fig. 1 *(a) Experimental setup and (b) concrete specimen*

Composition similar to that used in PFBR has been selected in this study. The specimens were cast in a stainless steel vessel of 500 mm diameter for avoiding tensile cracks at extreme layers of the concrete due to the thermal gradient. About 25 thermo-wells were embedded from bottom for positioning thermocouples at 5, 25 and 45 mm depths from the surface at all the three zones. After casting, the specimens were maintained at controlled humidity and temperature for 28 days and then ultrasonic pulse velocity (UPV) tests were conducted over surface with sector wise identifications as shown in Figure 1b.

Three experiments were conducted, each with sodium of 2 kg at 550°C temperature. The sodium was released onto the specimen at about 25 g/s. Temperatures were monitored inside the concrete specimen and MINA facility. Other important parameters like gas composition, pressure buildup and aerosol distribution resulting from burning sodium were also monitored in the test chamber. High speed imaging was employed during the run for capturing the event.

During the experiment, it was observed that sodium was impinged on the central zone of the concrete then flown to the stagnant zone. Scenarios of sodium fire in the concrete are shown in Figure 2.

Fig. 2 *Scenarios of sodium fire on concrete specimen*

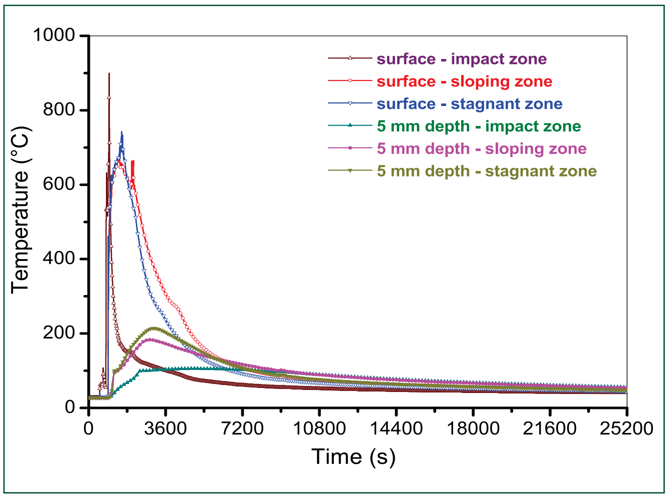

***Fig. 3** Sodium flow temperature profile*

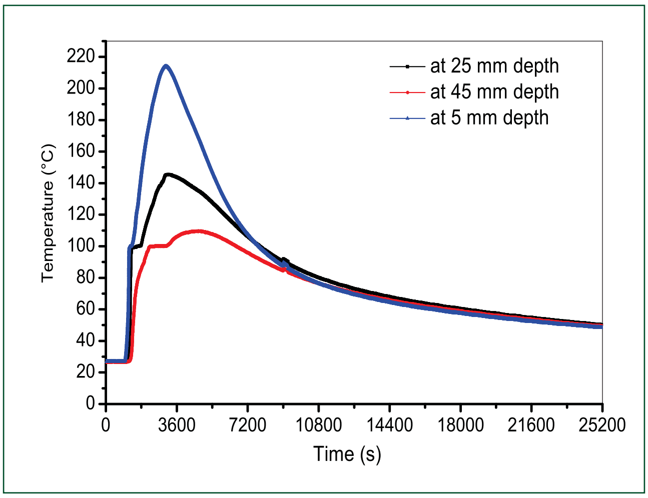

***Fig. 4** Temperature profile at various depths of stagnant zone*

Sodium flame temperatures reached up to 900°C. However, the peak temperature at 5 mm depth was observed to be about 200°C at stagnant zone as shown in Figure 3.

The corresponding temperatures at central and sloping zones were 110 and 180°C indicating the accumulation and burning of sodium at stagnant zone.

Investigation of temperatures at stagnant zone at 5, 25 and 45 mm depths indicated a considerable drop of temperature with depth. Figure 4 shows that the temperatures below the sacrificial layer (50 mm) are within tolerable limits.

Ultrasonic pulse velocity measured in the identified locations of concrete blocks before and after sodium exposure shown significant loss in velocity at impact zone, indicating substantial degradation compared to stagnant zone.

Post experimental analysis of concrete for determining sodium penetration depth was carried out after removing sodium fire residue on the surface of the concrete. The sodium exposed concrete specimen is as shown in Figure 5.

The surface was cleaned with methanol and drilled using concrete drilling machine for collecting samples at various depths (up to a depth of 70 mm) in the impingement zone, sloping and stagnant zones. About 500 mg of each concrete sample was digested with 20 ml of 1.0 N HF and the solution was made up to 100 ml. The sodium content in each solution was analyzed using flame photometer. By comparing the measured sodium concentrations in concrete before and sodium interaction, the sodium penetration depth values were obtained. It was observed that in stagnant zone, the measured value varies between 30 to 40 mm. In both sloping and impingement zones, sodium penetration depth was less than 10 mm. From the results, it is concluded that there is no need for laying stainless steel liner on the vertical wall at PFBR.

The pressure rise in the chamber was in the range of 5-10 mbar during the runs and the aerosol concentration in the test chamber (140 m^3 volume) was observed to be reduced to 1 mg/m^3 from 1600 mg/m^3 within 3.5 hours.

***Fig. 5** Post test concrete sample*

III.29 Biofouling Control of Titanium in Coolant Water using Ultrasonic Methods

Titanium is selected as the condenser material of the PFBR due to its technical superiority. Owing to its biocompatibility, titanium is prone to intense biofouling. Present fouling control strategies in condensers include a combination of mechanical and chemical treatments; although these cleaning methods are efficient in the case of macrofoulants, they do not guarantee complete removal of microfoulants, such as bacteria and unicellular algae. It is reported that sponge ball cleaning enhances subsequent biofilm formation. Chemical treatments release toxic byproducts causing environmental concern. Ultrasound is currently employed for killing microbes in many industries; food technology, environmental decontamination applications etc. In cooling water systems, high frequency ultrasound was used in side-stream systems to enhance the biocidal activity.

Ultrasonication is capable of inactivating waterborne bacteria. When ultrasonic waves pass through a liquid, an acoustic pressure is produced with sufficient amplitude and this can induce cavitation bubbles. When these bubbles collapse, high pressure (up to 100 MPa) and high temperature (up to 5000 K) is momentarily produced which can disrupt bacterial cell membranes and kill them. Ultrasound of 24 kHz, 400 W high power through a 14 mm horn type stainless steel sonicator with medium intensity sonication (amplitude at 60%) for 30 minutes were applied to kill bacteria in cooling water and bacterial cultures. Typically three orders of magnitude decrease in total bacterial density in different cooling waters like reservoir water and seawater, five orders and three orders decrease for *Pseudomonas* sp. and *Flavobacterium* sp. respectively and two orders and less than one order decrease for *Bacillus* sp. and *Micrococcus* sp., respectively were obtained. Detailed growth curve analysis showed that ultrasonication delayed the lag phase and reduced the logarithmic population and specific growth rate of gram-negative bacteria. On the other hand, for gram-positive bacteria which have thicker cell walls, the specific growth rate increased after ultrasonication. Thus the differential response of gram-negative and gram-positive bacteria to high power ultrasound in this study clearly supported that the mechanical effects, thinning of cell wall, membrane rupture and cell lysis are the major effects of ultrasonication.

Due to ultrasonication onset of lag phase in the growth curve of these bacteria increased from 10 minutes to 9 hours (Figure 1) indicating probability of good biofilm control by applying ultrasonication for 30 minutes every 8 hours. Studies on the biofilm formation tendency of these ultrasonicated mediums on titanium surface showed two orders reduction in seawater (Figure 2).

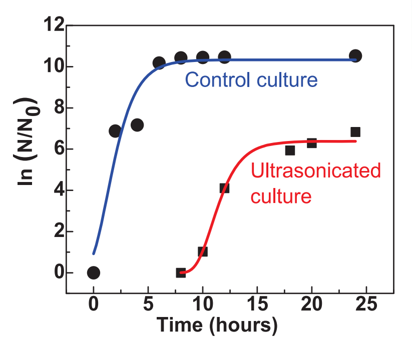

Fig. 1 *The bacterial growth curve of ultrasonicated and control gram negative Pseudomonas sp. culture showing 9 hour lag in initiation of growth due to ultrasonication*

Detailed biofilm imaging by advanced microscopic techniques like atomic force microscopy, scanning electron microscopy and epifluorescence microscopy clearly visualized the lysed/damaged cells and membrane perforations due to ultrasonication. Combination of ultrasonication of cooling waters and anodization of titanium surface brought maximum decrease in bacterial density and biofilm formation with greater than two orders decrease in seawater, two orders decrease in *Bacillus* sp. culture and more than four orders decrease in *Flavobacterium* sp. culture establishing the synergistic effect of anodization and ultrasonication in controlling biofouling of titanium.

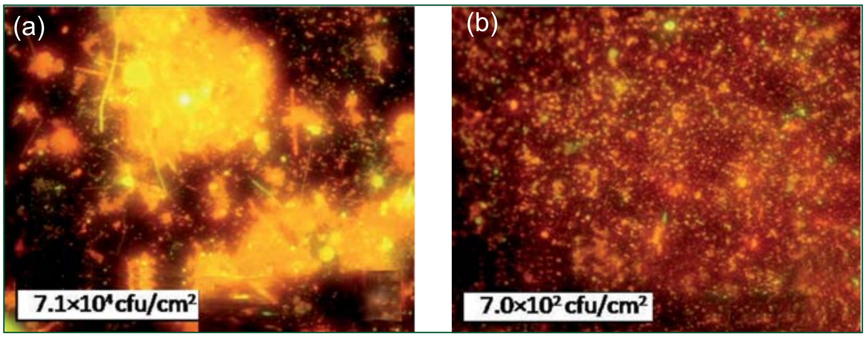

Fig. 2 *Epifluorescence micrographs of 24 hours biofilms formed on titanium specimens (a) without and (b) with ultrasonication*

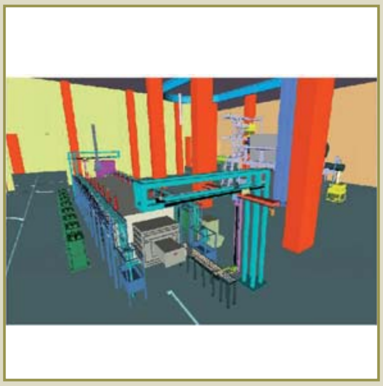

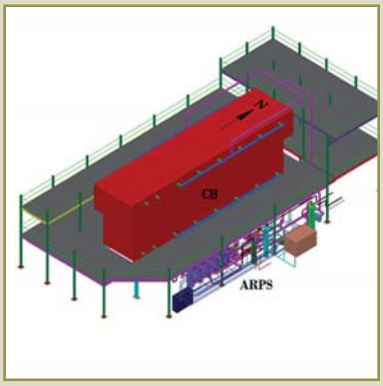

CHAPTER
IV

Fuel Cycle

IV.1 Construction Status of Fast Reactor Fuel Cycle Facility

Construction activity of Fast Reactor Fuel Cycle Facility (FRFCF) project that is being piloted by Indira Gandhi Centre for Atomic Research with technical support from Bhabha Atomic Research Centre and Nuclear Fuel Complex has commenced. The aim of FRFCF is to close the fuel cycle of Prototype Fast Breeder Reactor. All the necessary statutory clearances for commencing construction work have been obtained and excavation for foundation of plant buildings, with necessary de-watering systems, is being carried out. Excavation in the trial pit in the plant building area has reached a depth of over 11 metres (Figure 1). All the soil excavated is stored securely to enable refilling at appropriate time. The construction work on training centre, administration building, canteen building, extension of stores and workshop buildings is also under progress (Figure 2). Periodic analyses of soil and water samples, during excavation, have domonstrated absence of any man-made radioactivity. The pumped out water was found to be potable and is being channelled to the reservoir.

Fig. 1 *Excavation activity on trial pit in plant area of FRFCF in progress*

About 4250 tons of pig lead required for radiation shielding purposes has been procured. Conversion of the lead into shielding bricks will be done progressively to match the project schedule. Manufacturing of stainless steel sheets and plates required to be issued as free issue material for fabrication of tanks and vessels has started and a few consignments of finished plates have been received at site. Procurement action for seamless stainless steel pipes, master slave manipulators, standard glove boxes, fume hoods, radiation shielding window glass slabs and a few process equipment has been initiated and is in progress.

Jacketing investigations are in progress in the area earmarked for construction of the first phase of housing sanctioned for FRFCF project. After augmentation of manpower and creation of a Board, action for which is in progress, the work progress at site is expected to accelerate to meet the milestones set for the project.

Successful commissioning of FRFCF is an essential step for embarking on construction of second stage nuclear power plants based on plutonium fuel that would pave the way for achieving energy security for the nation.

Fig. 2 *Backfilling in progress for extension of stores building of FRFCF*

IV.2 3D Modeling and Animation of Reprocessed Uranium-Oxide Plant of Fast Reactor Fuel Cycle Facility

Reprocessed Uranium-oxide Plant (RUP) is part of FRFCF at Kalpakkam. The aim is to create a virtual FRFCF 3D model to aid in design validation and help in reducing the construction period. It consists of modeling in 3D in 1:1 scale, creation of walkthroughs and animations of operating sequences of all the plants.

The Reprocessed Uranium-oxide Plant building has three sections namely powder section, pin section and pellet section. The powder section comprises of powder bunker storage facility, furnaces that convert the tri-uranium octoxide powder to uranium oxide powder and compaction presses for forming the pellets. The pellet section consists of sintering furnace, centre-less grinding machine, washing and drying unit, pellet visual inspection facility and pellet storage area. The pin section consists of bottom plug and top plug welding machines, X-ray radiography unit, helium leak testing facility, pellet stacking and loading stations, helical wire wrapping machine, laser inscription machine and pin magazine loading machine. All the material handling in this building will be performed using EOT cranes, automated Jib cranes, groove guided vehicles and overhead pin tray transfer system. Figure 1 shows the 3D model of sintering furnace of reprocessed uranium-oxide plant.

The 3D models of civil structure of reprocessed uranium-oxide plant and other subsystems mentioned above were created part by part in 1:1 scale dimensions. The models of the systems were arranged at their respective positions in the civil structure to create the complete model of the plant. Animations representing the processes involved in the production of blanket pellets, fuel sub-assembly axial pellets and blanket pins were created. The automation involved in the process flow of the plant is also animated. To capture the animation, rendering elements such as cameras, lights, 3D and 2D text frames were introduced. Subsequently, for timing and assigning specific behavior to the rendering elements, scripts were created. Verification of design for space constraints, clash detection study, inter sub-system automation and process flow continuity were studied and feedback was given.

The various challenges met and overcome during animation are: animation of rotary compaction press involving synchronization of rotation and translation motions of compacting rods of the press, animation of helical wrapping of spacer wire on the fuel pin, animation of a robot at visual inspection facility simulating six degree of freedom for handling the pellet, animation of a Jib crane at powder handling facility involved calculating the angle of the crane hands for handling powder bunker.

An audio narration explaining the work flow animation of RUP was created and it runs in synchronization with the animation. This enhances the depth of the visualization by providing a better understanding of the system. Finally, the 3D models and animations were exported to Advanced Visualization Centre for 3D visualization.

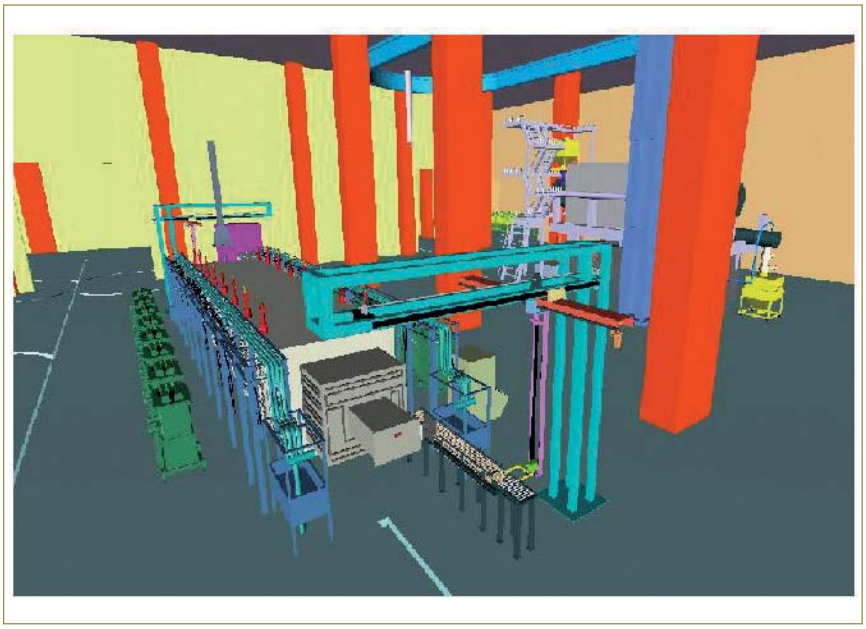

Fig. 1 *3D model of sintering furnace of Reprocessed Uranium-oxide Plant*

IV.3 Dissolution Kinetics of Sintered UO_2 Pellets - Effect of Initial Acidity and Temperature on the Dissolution Rate

During dissolution, the fuel is converted into a suitable chemical and physical form for the separation of fissile materials from the bulk of the fission products in the spent fuel. The dissolution kinetics of MOX spent fuel gets sluggish if plutonium content is high, as in the case of a FBR MOX fuel. The design of a suitable dissolution process requires the determination of the intrinsic kinetics of dissolution of the spent fuel. Thus, experiments were carried out using sintered natural UO_2 pellet, to establish its dissolution kinetics and mechanism. Similar approach, with necessary changes, would be then extended to study the dissolution of plutonium rich MOX fuel. A glass bubble reactor with off-gas scrubbers, shown in Figure 1 was fabricated and employed for this purpose.

Various factors influence the dissolution, viz, burn-up of the fuel, nitric acid concentration, mixing, temperature, presence of other species etc. In this study, the quantitative effect of initial nitric acid concentration and the reaction temperature on the dissolution of UO_2 pellet have been established as given in Figures 2 and 3.

In all the experiments, nitric acid of required concentration was first heated to a preset temperature. Then, an UO_2 pellet was carefully immersed and the timer was set. Samples were removed periodically for the analysis of uranium and nitric acid concentrations to follow the kinetics. All pellets were stainless steel cladded to mimic the actual conditions. Heating was continued till the pellet dissolved completely. Similar experiments were carried out at different acid concentrations and temperatures to study their effect on dissolution and to compute the rate and activation energy. The results obtained were modelled using shrinking core approach. The results predicted by the model equation were found to reproduce the experimental observations satisfactorily.

The model equation used to predict the dissolution behaviour of cylindrical UO_2 pellets is given by

$$\left(1-\frac{[U]_t}{[U]_f}\right)^{1/3} = 1-\frac{2}{3}\,\frac{k.(x+1).C_{HNO_3}}{\rho_A.x.b.R}\,t$$

where, $[U]_t$ and $[U]_f$ are the molar concentrations of uranium at any time t and at the end of the reaction respectively, ρ_A is the molar density of the pellet, t is the time, b is the stoichiometric co-efficient of nitric acid taking part in the reaction, R is the initial radius of the pellet, x is the aspect ratio of the pellet and k is the first order rate constant. From the slope of the plot of $(1-([U]_t/[U]_f))^{1/3}$ against t, the rate constant can be determined (Figure 4) .

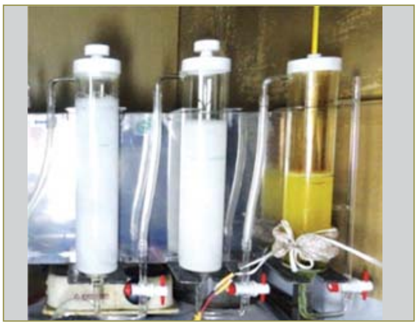

Fig. 1 *Dissolution setup*

Table 1: Rate constants at different temperatures

T (°C)	70	80	90
k x10^{-3} (m/s)	1.57	3.19	7.29

The k values estimated for the dissolution of UO_2 pellet in 8 M nitric acid at different temperatures are given in Table 1.

The apparent activation energies for the dissolution reaction at the starting acidities 8.05 and 10.28 M nitric acid were 85.2 and 97.5 kJ/mol respectively. These E_a values suggest a possible chemical reaction controlled regime for the given temperature range. Hence, contribution of diffusion process on the dissolution rate of UO_2 pellet could be assumed to be negligible under these conditions.

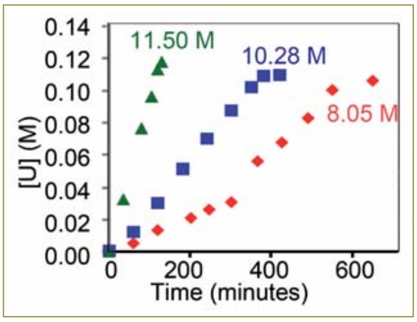

Fig. 2 *Effect of initial acidity on the dissolution rate at 80°C*

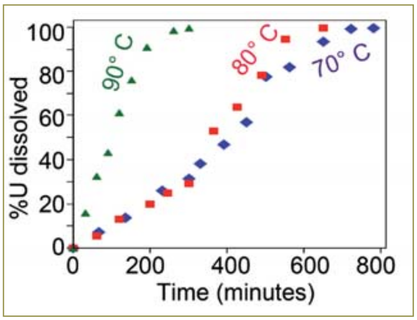

Fig. 3 *Effect of temperature on the dissolution rate in 8 M HNO_3*

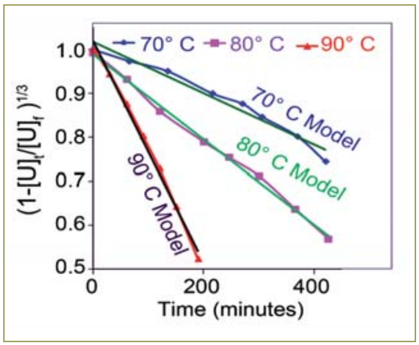

Fig. 4 *Evaluation of the model*

IV.4 Macro Level Extraction of U(VI), Pu(IV) and Zr(IV) from HNO_3 Medium by Tri-iso-amyl Phosphate (TiAP) and Tri-n-butyl Phosphate (TBP) as Extractants

Tri-iso-amyl phosphate (TiAP) has been identified as an alternate extractant for fast reactor fuel reprocessing in view of its lesser third phase formation tendency. Data on the third phase formation with Pu(IV)-HNO_3-TBP system are available in the literature. However, detailed data on Pu third phase formation with TiAP is scarce in literature and hence studies were carried out in our laboratory. In order to design a Purex-type flowsheet for the reprocessing of PFBR fuel, it is necessary to generate extraction data on U(VI)-Pu(IV)-HNO_3 system. The present study deals with the extraction of Pu(IV) as well as co-extraction of U(VI) and Pu(IV) as a function of equilibrium aqueous phase metal ion concentration and nitric acid concentration using 1.1 M TiAP/DD as the solvent.

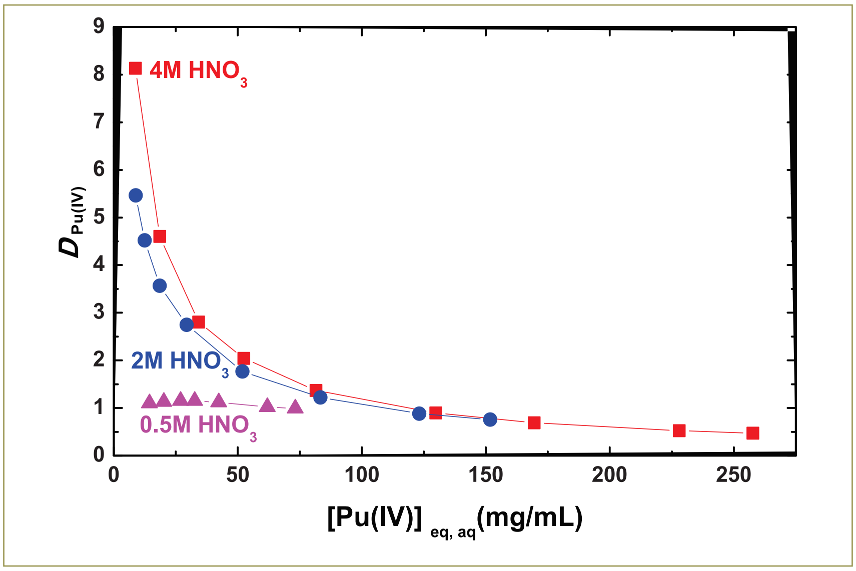

Fig. 1 *Variation of $D_{Pu(VI)}$ with $[Pu(IV)]_{eq,aq}$ for the extraction of Pu(IV) by 1.1M TiAP/DD from plutonium nitrate solutions in nitric acid media at 303 K*

Extraction of Pu(IV) with 1.1 M TiAP/DD at various HNO_3 concentrations under high solvent loading conditions has been investigated. It has been observed that 1.1 M TiAP/n-DD-Pu(IV)-HNO_3 extraction system does not form third phase with concentrated plutonium nitrate solutions. The variation of Pu(IV) distribution ratio ($D_{Pu(IV)}$) with respect to $[Pu(IV)]_{aq,eq}$ for various concentrations of HNO_3 are shown in Figure 1. It can be seen from Figure 1 that $D_{Pu(IV)}$ decreases with increase in $[Pu(IV)]_{aq,eq}$ which can be attributed to the reduction in free extractant concentration with increased metal loading. However, in the case of extraction from 0.5 M nitric acid solution, the initial increase in *D* with increase in equilibrium metal concentration can be attributed to the self-salting effect. Beyond a certain loading, the effect due to the decrease in free extractant concentration begins to dominate, resulting in the decrease in *D*.

The data on the variation of *D* as a function of equilibrium U(VI) and Pu(IV) concentration for the co-extraction of U(VI) and Pu(IV) from 4 M nitric acid solution at 303 K are shown in Figure 2. As seen in Figure 2, *D* values for the extraction of U(VI) and Pu(IV)

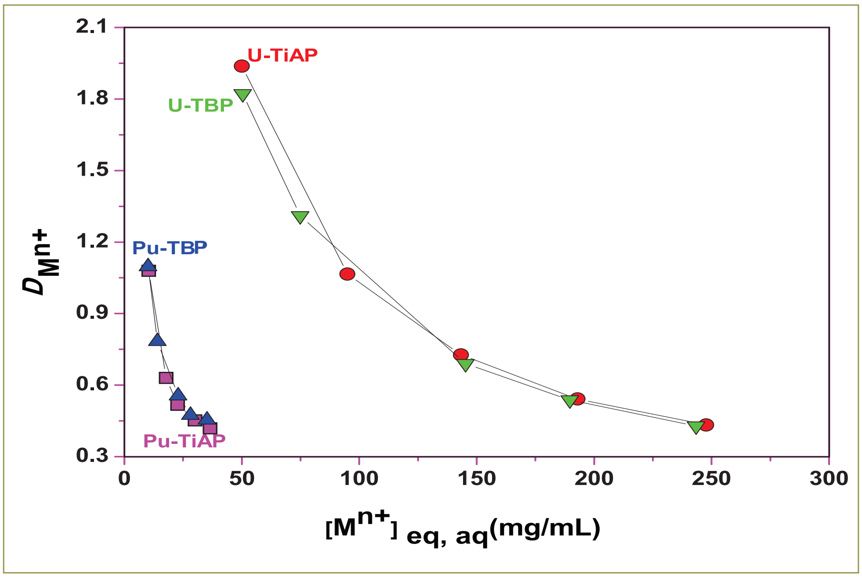

Fig. 2 *Variation of $D_{M^{n+}}$ with equilibrium aqueous phase metal ion concentration for the extraction of U(VI) and Pu(IV) by trialkyl phosphate (TalP) from a solution of U(VI) and Pu(IV) in 4M nitric acid at 303 K*

initially decrease steeply and then flatten as their concentrations in the aqueous phase increase for the extraction from 4M HNO_3. The maximum organic concentrations of U(VI), Pu(IV) and HNO_3 obtained under present experimental conditions are around 105 mg/mL, 16 mg/mL and 0.07 M, respectively with 1.1 M TiAP/DD system. It is also established that it is possible to achieve the loading up to saturation (120 mg/mL) without organic phase splitting under the experimental conditions. Results also indicated that the distribution data of 1.1 M TiAP/DD are comparable to 1.1 M TBP/DD system. The *D* values for uranium are higher than that of plutonium over a wide range of equilibrium aqueous phase metal ion concentrations for both the systems. The present study reveals that third phase formation does not take place with higher plutonium loading in TiAP based solvent. The studies on the co-extraction of uranium and plutonium with maximum organic loading indicated that TiAP can be employed for the processing of spent nuclear fuels.

Preliminary experiments were also carried out to develop a method for the processing of metallic fuels by aqueous route using PUREX process. A ternary alloy of U-19Pu-10Zr is considered as the reference fuel. Alloy fuel can be reprocessed either by pyrometallurgical process or by PUREX process. PUREX process is an alternative method for reprocessing of metallic fuels. The present study deals with the dissolution of metallic fuels (U-Zr and U-Pu-Zr), assay of metallic fuels by different analytical methods and solvent extraction studies with metallic fuels in nitric acid medium using 1.1 M TiAP/DD and 1.1 M TBP/DD at 303 K.

Initially, the metal fuels (U-Zr and U-Pu-Zr) were dissolved in HNO_3 and HNO_3-HF medium. The dissolver solution was assayed by different analytical methods. It was found that uranium can be dissolved quantitatively (~100%) and the Zr dissolution was not quantitative. However complete dissolution of uranium, plutonium and zirconium can be achieved with HNO_3-HF medium. In order to estimate zirconium in metallic alloys, a method has been developed to determine zirconium in a large excess of uranium and plutonium using xylenol orange as a chromogenic agent. Initially the interference of plutonium has been studied, and various masking agents were investigated to avoid the interference of plutonium. Effect of the concentration of nitric acid, ascorbic acid, uranium and plutonium etc has been studied. The above method has been employed for the estimation of Zr in various aqueous samples.

Subsequently, solvent extraction studies were carried out with a feed solution containing U, Zr and nitric acid concentrations of around 247 mg/mL, 29 mg/mL and 4.5 M, respectively. Results indicate that third phase formation takes place with 1.1 M TBP/DD under these feed conditions. Solvent extraction studies were also carried out with the similar feed solution and 1.1 M TiAP/DD under identical conditions. Third phase formation was not observed in case of TiAP based solvent system. The data on the variation of *D* values as a function of equilibrium U(VI) and Zr(IV) concentration for the extraction of U(VI) and Zr(IV) from 4.5M nitric acid solution at 303K shows that *D* values for the extraction of U(VI) and Zr(IV) initially decrease steeply and then flatten as their concentrations in the aqueous phase increases for the extraction from 4.5M HNO_3. Since 1.1M TBP/DD forms third phase with the above feed solution, in other experiments, the concentration of the feed solution was decreased to 90 mg/mL and 10 mg/mL of U(IV) and Zr(IV) respectively in nitric acid media (2-6M). Studies were also carried out with these feed solutions using 1.1M TBP/DD and 1.1 M TiAP/DD.

Results indicate that TBP does not form third phase under these conditions in various nitric acid media. The variation of distribution ratio with equilibrium aqueous phase nitric acid concentration for the simultaneous extraction of U(VI) and Zr(IV) with a feed concentration of around 90 mg/mL and 10 mg/mL, respectively, by 1.1 M TiAP and 1.1 M TBP in n-dodecane from nitric acid media at 303 K has been investigated. Results indicate that the $D_{U(VI)}$ value is almost constant as a function of the aqueous phase acidity, whereas the $D_{Zr(IV)}$ increase with an increase in the aqueous phase nitric acid concentration. Results clearly indicate that *D* values are slightly higher for the extraction of U(VI) by TiAP than that of TBP and in the case of Zr(IV), the *D* values are almost comparable for both the solvents. Thus, these studies reveal that TiAP can be employed for the processing of different types of spent nuclear fuels through aqueous route.

IV.5 Separation of U(VI) and Th(IV) from Nd(III) using Tri-iso-amyl Phosphate as the Extractant

Tri-*iso*-amyl phosphate (T*i*AP) which has less tendency to form third phase has been identified as an alternate extractant to tri-*n*-butyl phosphate (TBP) for the extraction of tetravalent metal ions such as Pu(IV), Th(IV) and Zr(IV). In the present study, separation of U(VI) and Th(IV) from Nd(III) in nitric acid medium has been carried out with T*i*AP by cross-current mode to investigate the feasibility of using T*i*AP as an alternate extractant to TBP for monazite processing. In general, 5% TBP (0.183 M) and 40% TBP (1.47 M) in an inert hydrocarbon diluent are being used for U(VI) and Th(IV) extraction, respectively, in monazite processing plants.

Initially, when a concentrated solution of Th(IV), Nd(III) and U(VI) near-saturation ([Th(IV)]=226.4 g/L; [Nd(III)]=262.1 g/L; [U(VI)]=7.17 g/L; [HNO_3]=4.02 M) was contacted with 0.183 M solutions of trialkyl phosphates (TBP and T*i*AP) in *n*-dodecane (*n*-DD) pre-equilibrated with 4 M HNO_3 it was observed that T*i*AP does not form third phase, whereas TBP forms third phase. As the volume of third phase formed was very small, third phase formation was further confirmed by analyzing the concentration of Th(IV) in the organic and aqueous phases after extraction, followed by checking the mass balance of Th(IV). The results of the Th(IV) mass balance experiment are shown in Table 1. It can be seen from Table 1 that in the case of T*i*AP, there is a good mass balance before and after the extraction indicating the absence of any deposits at the organic-aqueous interface. However, in the case of TBP, there is a mismatch in the mass balance before and after the extraction which in turn indicates the presence of a thin layer of third phase at the interface and it was found that the third phase can be eliminated only after 60% dilution of the above mentioned concentrated solution. The concentration of U(VI) in the sample solutions was determined by Davies-Gray Method and concentrations of Th(IV) and Nd(III) were determined by complexometric titration. Nitric acid in the sample solutions was estimated by acid-base titration after complexing the metal ions with pre-neutralized saturated potassium oxalate solution.

It was also observed that 1.47 M solutions of both the extractants in *n*-DD form third phase at 303 K during Th(IV) extraction after U(VI) separation. However, the limiting organic concentration and the critical aqueous concentration values of 1.47 M T*i*AP/*n*-DD are much higher as compared to TBP system. The concentrated aqueous solution mentioned above after slight dilution with 4 M HNO_3 was used as the aqueous feed for the separation of U(VI) and Th(IV) from Nd(III) by using 0.183 M and 1.47 M solutions of T*i*AP in *n*-DD (pre-equilibrated with 4 M HNO_3),

Table 1: Mass balance of Th(IV) before and after its extraction by 0.183 M trialkyl phosphate in n dodecane from a solution containing U(VI), Th(IV) and Nd(III) in 4 M HNO_3

Extractant	Before Th(IV) Extraction	After Th(IV) Extraction		
	Th(IV)-Feed (g/L)	Th(IV)-Aq (g/L)	Th(IV)-Org (g/L)	Th(IV)-Total (g/L)
TBP	226.4	213.8	2.3	216.1
	198.1*	189.7	2.5	192.2
	183.8*	171.9	2.8	174.7
	159.6*	151.9	3.0	154.9
	130.2*	124.9	4.1	129.0
	110.5*	104.8	4.9	109.7
	91.5*	87.3	4.3	91.6
T*i*AP	226.4	217.6	9.0	226.6

* Feed solutions used for TBP obtained after the dilution of concentrated solution with 4 M HNO_3

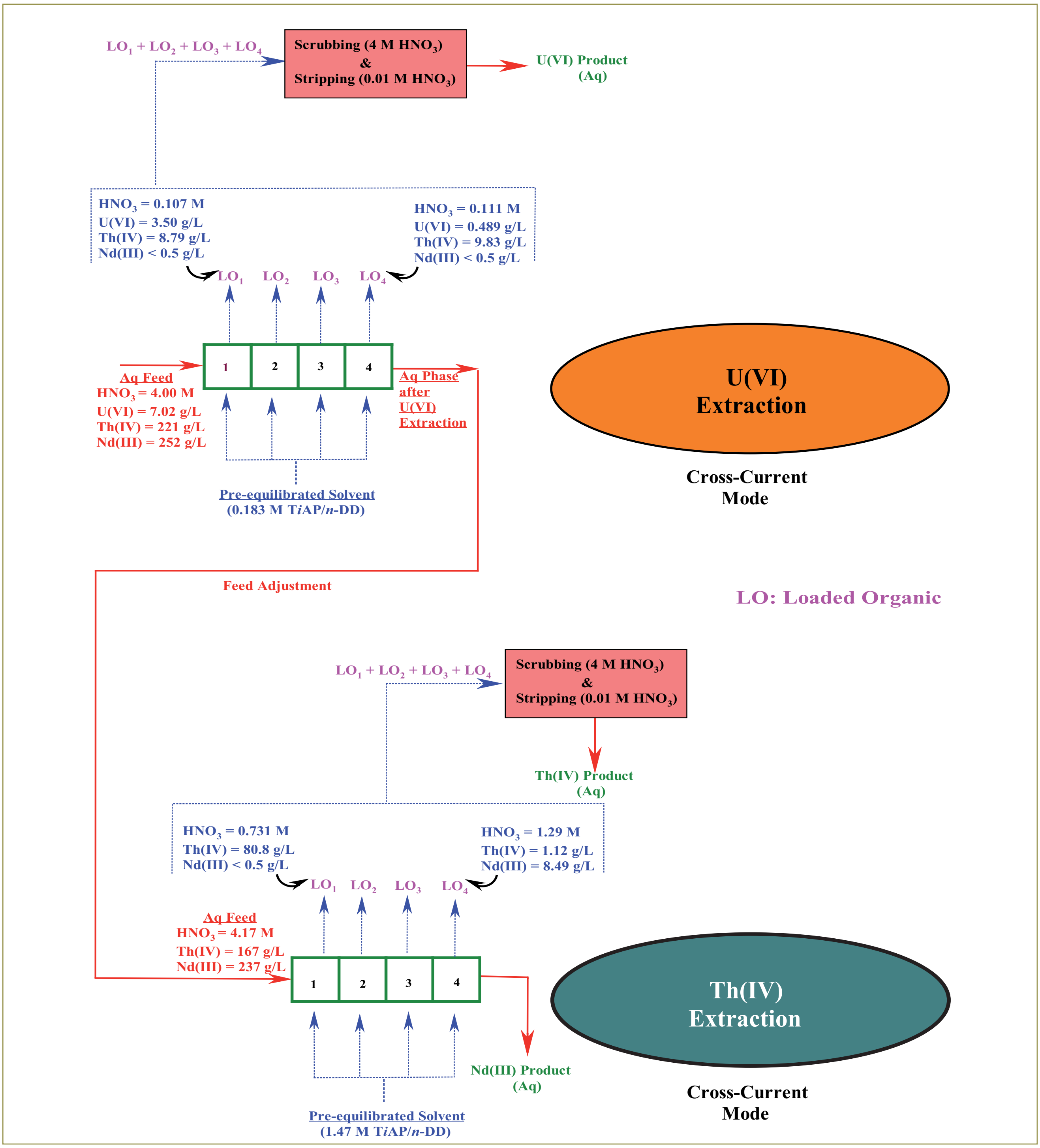

Fig. 1 *Flow sheet for the separation of U(VI) and Th(IV) from Nd(III) in 4 M HNO_3 solution with solutions of TiAP in n-DD at 303 K (organic/aqueous volume ratio = 1)*

respectively, and the results are shown in Figure 1. It can be seen from Figure 1 that four stages are sufficient for the complete extraction of U(VI) and Th(IV) from the aqueous feed solution. The mass balance of the metal ions before and after their extraction is also good.

Reports available in the literature reveal that the extraction of Th(IV) and its separation factor with lanthanides are maximum at 8 M HNO_3 for TBP. In order to achieve higher extraction of Th(IV) with good separation factor from lanthanides, the extraction of Th(IV) by 1.47 M T*i*AP/*n*-DD was also carried out with a feed solution in 8 M HNO_3 ([Th(IV)]=119.9 g/L; [Nd(III)]=116.5 g/L; [HNO_3] =7.93 M). As expected the extraction of Nd(III) by 1.47 M T*i*AP/*n*-DD from 8 M HNO_3 medium was lesser as compared to Nd(III) extraction from feed solution in 4 M HNO_3. The results of the present study indicate that the solvent extraction flowsheets can be developed for monazite processing with T*i*AP based solvents under high solvent loading conditions without organic phase splitting.

IV.6 Separation and Determination of Long Chain Organic Acids in the Degraded Solvent by Ion Pair Chromatographic Technique

Tri-n-butyl phosphate (TBP) dissolved in n-dodecane (DD) or normal paraffin hydrocarbon (NPH) is used to extract uranium and plutonium from an aqueous nitric acid solution. Problems in product contamination and recovery have been reported which could be due to solvent degradation. Solvent degradation studies with TBP in NPH showed that long chain organic acids and long chain alkyl/butyl phosphoric acids are formed by reactions with nitric acid. Undecanoic acid, lauric acid and tridecanoic acid were identified as some of the diluent degradation products in the recycled solvent that are problematic. These long chain organic acids affect phase separation and lead to low decontamination factors. A simple procedure has been optimized for the separation and determination of three long chain organic acids by ion-pair chromatographic (IC) method. Analyses were carried out using Metrohm modular IC system coupled with reverse phase column prontosil 5 C-18A Q and non-suppressed conductivity detector. Tetra butyl ammonium hydroxide dissolved in 75% methanol and pH adjusted to 7.6 using 4M phosphoric acid was used as the mobile phase.

For the calibration of long chain organic acids, a known weight of the mixture of acids was prepared in the mobile phase solution. Standard solutions of 2-25 ppm were prepared from the stock mobile phase solution by appropriate dilution and 20 μl was injected into the ion chromatography system. For the separation of long chain organic acids present in the degraded solvent, a simulated solution was prepared by adding known concentration of a mixture of long chain acids into 30% TBP-n-DD solution and mixed well. This solution was further equilibrated with the mobile phase (organic/aqueous ratio as 1:1 and 1:2) and subsequently both the phases were allowed to settle. The aqueous phase was collected and injected into IC system. Figure 1 shows the calibration graph obtained with different long chain organic acids. Correlation coefficient and relative standard deviation were 0.999 and 0.7 respectively.

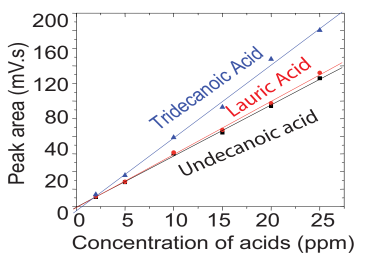

Fig. 1 *Calibration graph for the mixture of long chain organic acids (2-25 ppm)*

Figure 2 shows the typical ion chromatograms of undecanoic acid, lauric acid and tridecanoic acid.

Table 1 presents the percentage recovery of undecanoic acid and lauric acid after separation from 30% TBP-n-DD. These results reveal that the percentage recovery of undecanoic acid (C11) and lauric acid (C12) were 96 and 90% respectively. Using this method various long chain organic acids present in the degraded organic solvent can be separated and quantified simultaneously by ion-pair chromatographic technique.

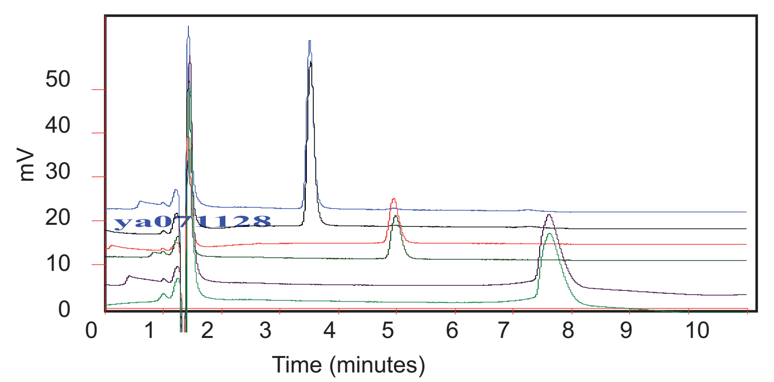

Fig. 2 *Typical ion chromatogram of undecanoic acid, lauric acid and tridecanoic acid*

Table 1: Percentage recovery of undecanoic acid and lauric acid from 30% TBP-n-DD solution

Organic : aqueous	Long chain organic acid (undecanoic acid)			Long chain organic acid (lauric acid)		
	Taken (ppm)	Obtained (ppm)	Recovery %	Taken (ppm)	Obtained (ppm)	Recovery (%)
1:1 (1 contacts)	25	24.0	96.0	-	-	-
1:1 (2 contacts)	25	24.0	95.9	25	22.6	90.3
1:2 (2 contacts)	40	38.7	96.8	40	35.7	89.3

IV.7 Oxidative Destruction of Dissolved TBP in Simulated Raffinate Stream of FBR Fuel Reprocessing Plant

Owing to the mutual solubility of aqueous and organic (tri-n-butyl phosphate, TBP) phases, the high level liquid waste contains some amount of entrained TBP and its degradation products, which is undesirable because it can lead to violent reaction during evaporation of these solutions. Ozone converts TBP and its degradation products to CO_2, H_2O and H_3PO_4. The major advantage of ozone oxidation is its simplicity and it does not generate additional waste. In recent years ozone has become the primary alternative oxidant to chloride, in both portable and waste treatment plants due to its extremely high oxidation potential. The reaction mechanisms involved in the oxidation of TBP and the intermediate products formed during oxidation by ozone in the aqueous phase are difficult to predict. Further, complications arise because oxidation of the organics can occur either through ozone molecules or by indirect reaction with the decomposition products of ozone. The structure of ozone is such that an oxygen atom can easily be detached, yielding a free oxygen radical to interact with the organic compounds. The reaction mechanism of ozone with organic substances can be via radical, electrophillic or nucleophillic attack. In aqueous medium ozone forms hydroxyl radicals. The hydroxyl radicals can subsequently react with organic substances in aqueous medium.

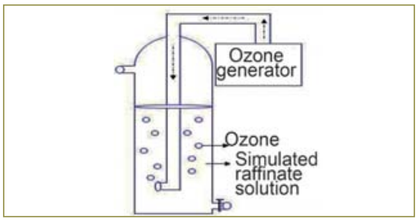

Fig. 1 *Ozone setup made of glass*

Fig. 2 *Simulated raffinate solution before and after passing ozone*

For obtaining a rate expression to describe the decomposition kinetics of TBP based compounds, it is assumed that oxidation by ozone is by direct reaction and the influence of the intermediate radicals on the main reaction is negligible. Although it is possible to develop models based on theoretical considerations, the inherent complexities and uncertainty in the reaction mechanisms make the use of these models undesirable in many instances. However, empirical models provide useful methods for correlating the important parameters of reaction systems.

Simulated raffinate stream was prepared by dissolving 250 ppm of TBP in 4 M nitric acid. Oxidative destruction of dissolved TBP was performed using ozone as the oxidative agent and the rate of oxidation was compared with that of electro-oxidation method. Ozone from the ozone generator was continuously sparged at a uniform flow rate of 2 ml/min, using a glass tube fitted with a frit at the tip to facilitate the formation of small bubbles in the organic-aqueous mixture. Figures 1 and 2 represent the ozone set-up made out of glass and the simulated raffinate solution before and after passing ozone, respectively.

A common mechanism of oxidation of TBP is the acid (nitric acid) hydrolysis of TBP, which occurs through the cleavage of carbon-oxygen bonds. The hydrolysis rate has been shown to increase with temperature and acidity. Butanol, DBP and MBP are the intermdiate products and eventually ortho phosphoric acid is formed as the end product of hydrolysis. This implies that the inorganic compounds CO_2, H_2O and H_3PO_4 could be the oxidative decomposition products of TBP. Thus, the overall chemical reaction for TBP oxidation is,

$$(C_4H_9)_3PO_4 + 12O_3 \rightarrow H_3PO_4 + 12CO_2 + 12H_2O$$

The rate expression for the oxidation of TBP can be written as,

$$-\frac{dC_{TBP}}{dt} = k_m C^n_{TBP}$$

where C_{TBP} refers to the concentration of dissolved TBP in aqueous solution at any time (t), k_m is the apparent reaction rate constant and m is the order of reaction. Experimental results, shown in Figure 3 indicated that the rate of destruction of TBP by ozone was higher than that of electrolytic method under similar experimental conditions.

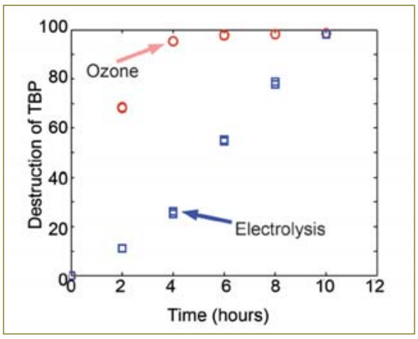

Fig. 3 *Comparison of the destruction rates of dissolved TBP using ozone and electro-oxidation methods*

IV.8 Magnetic Assisted Mutual Separation of Lanthanides and Actinides using Diglycolamic Acid Functionalized Iron Oxide

The radiotoxicity of high level liquid waste (HLLW) is essentially due to the alpha emitting radionuclides such as ^{241}Am and ^{243}Cm (minor actinides). Partitioning of these minor actinides from HLLW and transmutation into short-lived or innocuous products is an attractive and viable option for the safe management of HLLW. However, partitioning is a challenging task of separating trivalent actinides from chemically similar trivalent lanthanides, formed as fission products in significant quantities as compared to trivalent actinides. The current strategy of partitioning involves the separation of trivalent actinides from HLLW together with lanthanides in the first step, followed by separation of lanthanides from actinides or vice-versa in the second step. The mutual separation is necessary prior to transmutation, since lanthanides act as neutron poisons that reduce the efficacy of transmutation of actinides.

Though several methods based on solvent extraction have been widely used world-wide for the mutual separation of lanthanides (Ln) from actinides (An), separation methods based on solid phase such as ion exchange and chromatography are very limited. Magnetic solid phase separation is emerging as a promising technique for the separation of toxic and radiotoxic metal ions from various aqueous streams. In this method, illustrated in Figure 1, the magnetic particles are added to the waste solution to extract the target metal ion. The magnetic particles are then separated from the solution by means of an external magnetic force. The separated magnetic particles are then immersed in a stripping solution for recovery of metal ions from the adsorbed surface. This method offers several advantages especially for the treatment of nuclear wastes as compared to conventional solid phase extraction. There is no need for packing of magnetic particles in column as it is usually operated in batch mode and the phase separation is quickly achieved by external magnetic field. Figure 2 shows how an external magnetic field facilitates the fast separation of the sorbent from the aqueous phase.

In this report, we present the synthesis of iron oxide (Fe_3O_4) particle functionalized with

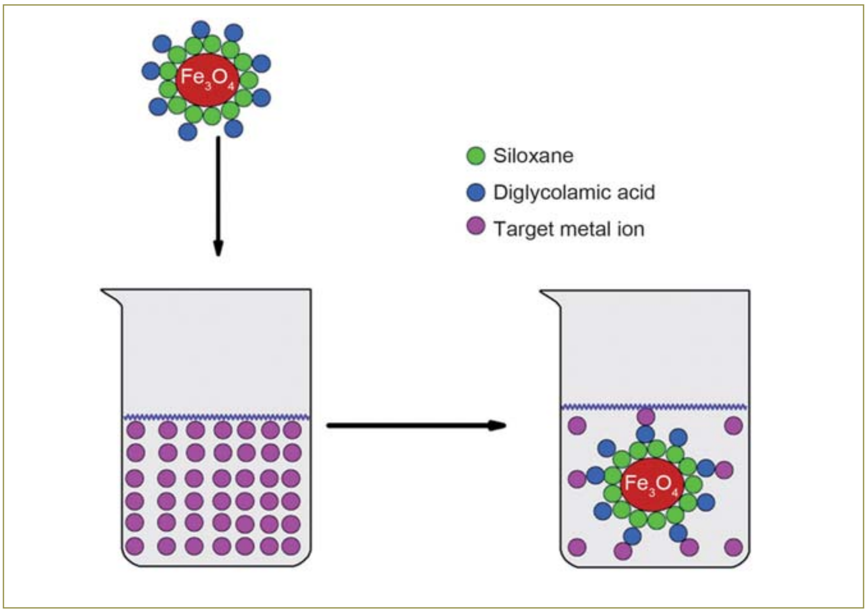

Fig. 1 An illustration of magnetic solid phase separation technique

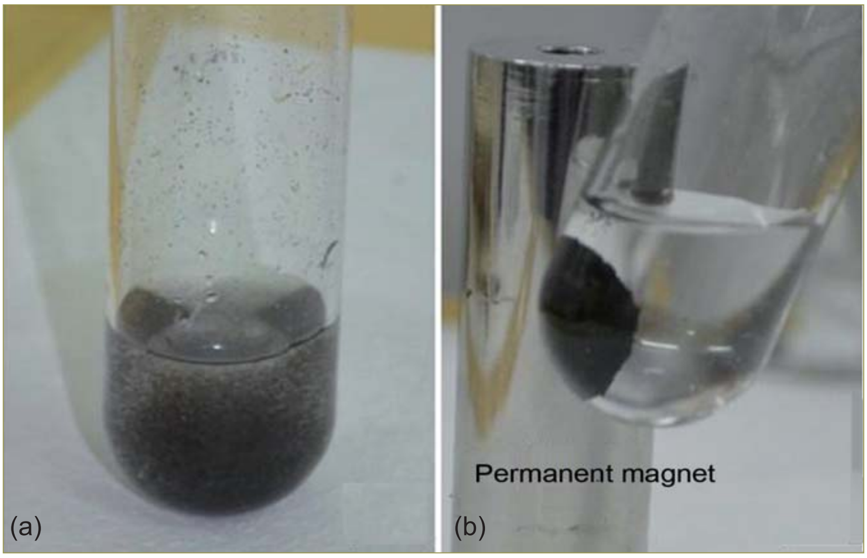

Fig. 2 (a) Metal ion solution and (b) separation in the presence of magnetic field diglycolamic acid (Fe-DGAH) for the mutual separation of Am(III) and Eu(III).

The magnetite nanoparticle was prepared by the co-precipitation of a mixture of anhydrous $FeCl_3$ and $FeSO_4$ in 2:1 ratio in the presence of ammonia. Silylation of iron oxide was carried out by reacting the iron-oxide particles with the tetraethoxysilane. Silane - diglycolamic acid (Si-DGAH) was synthesized by the condensation reaction between the diglycolic anhydride present in dichloro-methane and 3-aminopropyl-triethoxysilane. The final product Fe-DGAAH was prepared by refluxing the silylated iron oxide and Si-DGAH in toluene medium. The functionalized sorbent was collected by using a permanent magnet and was washed several times with toluene, isopropylalcohol, acetone, water and acetone. The product Fe-DGAH was dried in air, overnight and characterized by FT-IR, XRD and SEM techniques. The structure of Fe-DGAH is illustrated in Figure 3.

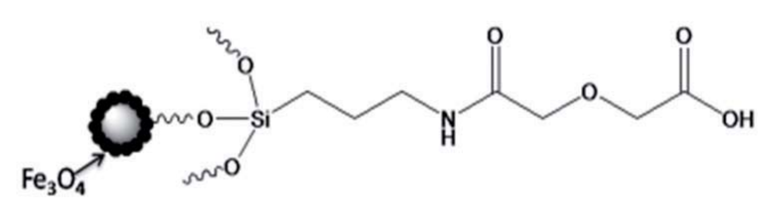

Fig. 3 *Structure of Fe-DGAH*

Characterisation of Fe-DGAH

The powder X-ray diffraction patterns obtained for pure Fe_3O_4, siloxane coated Fe_3O_4 and Fe-DGAH compared well with the pattern of standard Fe_3O_4. The scanning electron microscopy image of iron oxide particles showed that the particles are very fine and dense. In contrast to this, the silica coated iron oxide (Fe-Si) and diglycolamic acid functionalized iron oxide (Fe-DGAH) showed white coloured deposits on the surface indicating the bonding of siloxane and diglycolamic acid on the surface of iron oxide nano particles. The energy dispersive X-ray analysis of siloxane coated and Fe-DGAH surface also showed the presence of carbon, silicon and oxygen on the surface. All these observations indicated the functionalization of diglycolamic acid on the surface of iron oxide. Ion exchange capacity was found to be 1.5 m mol/g.

Extraction studies of Am(III) and Eu(III)

The sorbent, Fe-DGAH, contains acidic functional moieties on the surface of iron oxide particles. Therefore, Fe-DGAH is a cation exchanger. The variation in the distribution coefficients of Am(III) and Eu(III) as a function of nitric acid concentration is shown in Figure 4. It is observed that the distribution coefficient (K_d, mL/g) of both Eu(III) and Am(III) decreases with increase in the concentration of HNO_3, indicating the involvement of cation exchange mechanism.

Studies on the mutual separation of Eu(III) and Am(III)

Table 1 shows the distribution coefficients of Eu(III) and Am(III) in Fe-DGAH at pH 1.5 and 2. Diethylenetriaminepentaacetic acid (DTPA) was used as an aqueous complexing agent to improve the Eu(III)-Am(III) separation. In the absence of DTPA, the separation factor (quotient of K_d of Eu(III) and K_d of Am(III)) achieved for the extraction of these metal ions is very small. Since DTPA forms a complex with Am(III) in preference to Eu(III), the extraction carried out in the presence of DTPA facilitates the retention of Am(III) in the aqueous phase and thus enhances the separation factor of Eu(III) over Am(III). At pH 3, the separation factor increases from 1.3 in the absence of DTPA to the value of ~160 at 0.05 M DTPA concentration. Our results confirm the possibility of using DGAH functionalized iron oxide particles for the mutual separation of Am(III) and Eu(III).

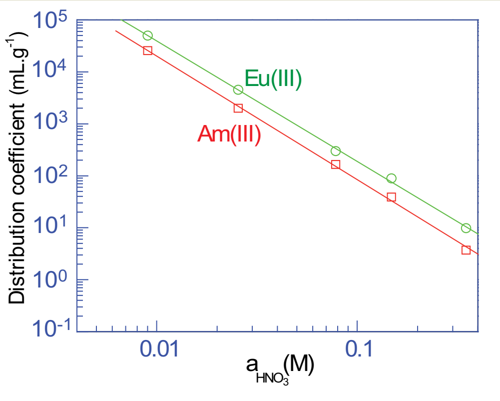

Fig. 4 *Extraction behavior of Eu(III) and Am(III)*

Table 1: Distribution coefficient of Eu(III) and Am(III) in Fe-DGAH as a function of DTPA concentration

[DTPA]/ M	Distribution coefficients, K_d (mL.g^{-1})		Separation factor
	Eu(III)	Am(III)	
0	20803	15841.0	1.3
0.001	4150	89.0	45.0
0.005	1190	26.0	46.0
0.050	190	1.2	158.0

IV.9 Demonstration of Modifier-free Minor Actinide Partitioning and Single-cycle Separation of Am(III) using Unsymmetrical Diglycolamide

Partitioning and transmutation of trivalent actinides is being considered as a viable strategy for the safe management of high-level liquid waste (HLLW). The HLLW generated from reprocessing of spent nuclear fuel is composed of a complex mixture of several elements such as the actinides, fission products and corrosion products present in 3-4 M nitric acid medium. Several reagents such as the organophosphorous compounds, malonamides, and diglycolamides have been proposed for partitioning of trivalent actinides from HLLW.

Significant efforts have been taken at our Centre to understand the problems associated with the existing diglycolamides (DGA) as well as with single-cycle approaches, and to provide technically viable solutions to the challenges posed during trivalent actinide partitioning. The drawbacks of the symmetrical octyl derivatives namely tetra octyl diglycolamides (TODGA) and tetra ethylhexyl diglycolamide (TEHDGA) are third phase formation and extraction of unwanted metal ions. However, it was realized that the extraction and stripping behaviour of trivalents were strongly dependent on the nature of alkyl group attached to the amidic nitrogen atom. Therefore, the separations achieved by using the DGAs can be influenced by the nature of alkyl substituents. In this context, we synthesised several unsymmetrical diglycolamides (UDGAs) and studied the extraction of actinides and fission products from nitric acid medium. The UDGAs synthesized in our laboratory are shown in Figure 1. Our findings have shown that the dodecyl group in conjunction with the octyl group present in the UDGA, N,N,-didodecyl-N’, N’-dioctyl-3-oxapentane-1, 5-diamide, (D^{3}DODGA), not only retained the excellent extraction properties of diglycolamides, but also surmounted the problem of third phase formation during the extraction of trivalent metal ions from 3-4 nitric acid medium. Our studies have shown that D^{3}DODGA does not require any phase modifier during the extraction of trivalent actinides from 3-4 M nitric acid medium, since the third phase formation limit for the trivalent metal ion in 0.1 M D^{3}DODGA in n-DD was more than 100 mM.

Studies with unsymmetrical diglycolamides

The extraction behavior of various metal ions present in the fast reactor simulated high level liquid waste (FR-SHLLW) that contained about 3.2 g/L of trivalent metal ions (Am(III) and Ln(III)) was studied in a solution of 0.1 M D^{3}DODGA/n-DD, by batch equilibration mode. During the extraction of Am(III), all lanthanides and many unwanted metal ions such as Zr(IV), Y(III), and Pd(II) were also co-extracted from FR-SHLLW. The co-extraction of unwanted metal ions was minimized by adding a suitable aqueous soluble complexing agent to FR-SHLLW. Trans-1,2-diamino-cyclohexane-N,N,N’N’-tetra-acetic acid (CyDTA) was identified as an appropriate reagent for preventing the extraction of zirconium and palladium, that posed problems during recovery of trivalent metal ions from the loaded organic phase.

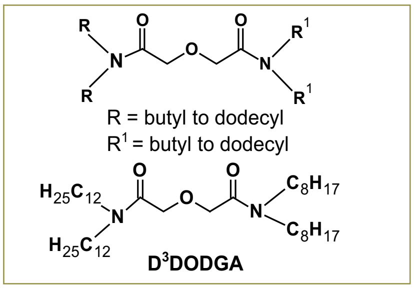

Fig. 1 *Structure of unsymmetrical diglycolamides*

Mixer-settler studies with simulated waste

Based on the batch results, a counter-current mixer-settler run was performed in a 20-stage mixer-settler. The extraction was carried out from FR-SHLLW containing 0.05 M CyDTA spiked with $^{(152+154)}$Eu(III) and ^{241}Am(III) tracer. It was observed that the extraction of Eu(III) in the organic phase was significant (> 90%) in the very first contact. The quantitative extraction of Eu(III) from FR-SHLLW was achieved in 4 contacts. Similarly, quantitative extraction of Am(III) was achieved in 7-8 stages. From the mixer-settler run, the preferential extraction of trivalents in 0.1 M D^{3}DODGA/n-DD follows the order Eu(III)>Sm(III)> Am(III)>Nd(III)>Pr(III)>Ce(III)> La(III).

A counter current stripping run was performed using the same mixer- settler in a separate run. The study revealed that a significant amount of trivalents were back extracted into the aqueous phase in the first contact itself, and all the trivalent metal ions were quantitatively back extracted into the aqueous phase in 5 stages. Based on this study, a flow-sheet shown in Figure 2 could be proposed for the separation of trivalent metal ions from FR-SHLLW using 0.1 M D^3DODGA/n-DD. It can be seen that the flow-sheet is simple as compared to other flow-sheets developed for trivalent actinide partitioning. It requires 20 stages for quantitative extraction of trivalents and 3-5 stages for stripping. It is important to note that this method does not demand any scrubbing stages before stripping. Perhaps scrubbing was needed in other flow-sheets where the solvent phase extracts significant concentration of unwanted metal ions such as Sr(II). In addition, the presence of phase modifier in organic phase in other systems also extracts substantial amount of nitric acid from aqueous phase leading to the requirement of scrubbing and large number of stages for back extraction of target metal ions. Such requirement does not arise in the present study.

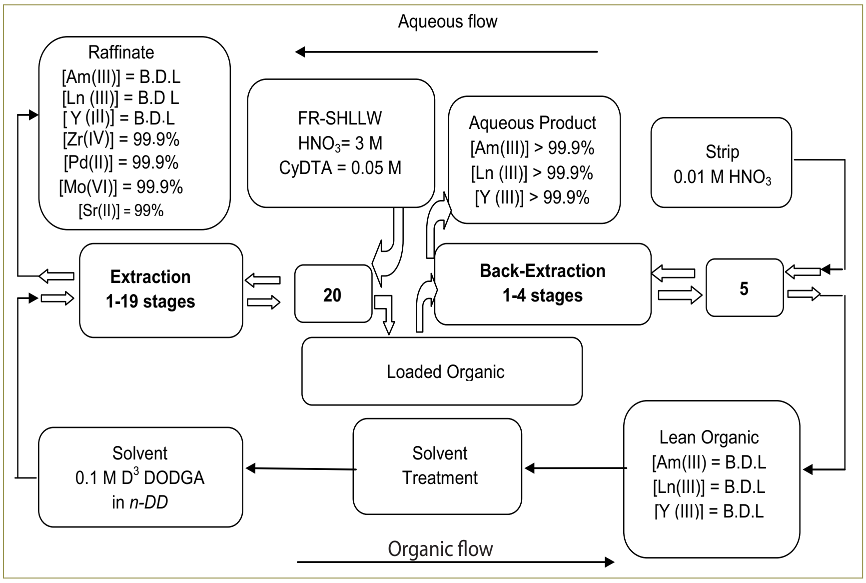

Fig. 2 Proposed flow-sheet for partitioning of trivalent actinides from FR-HLLW using modifier-free unsymmetrical diglycolamide, 0.1 M D^3DODGA/n-DD. The numbers 1 to 20 represents each mixer and settler

The study also indicated that the problems due to curd-formation or precipitation was not observed during the entire run, thus confirming the clean separation of trivalent metal ions from FR-SHLLW using 0.1 M D^3DODGA/n-DD. Therefore, D^3DODGA is a promising candidate for the separation of Am(III) from FR-SHLLW.

SMART approach

As discussed above, the extractant D^3DODGA has advantage over other diglycolamides and therefore a novel approach namely, Single cycle method for Minor Actinide partitioning using completely incinerable ReagenTs (SMART) was explored using D^3DODGA and Bis(2-ethylhexyl diglycolamic acid) (HDEHDGA). The diglycolamic acid is an acid derivative of alkyl-3-oxapentane, emerging as a promising candidate for lanthanide-actinide (Ln-An) separation. Unlike the other reagents in-use, the diglycolamic acid is made up of CHON-atoms and they are completely miscible with n-dodecane. The distribution ratio of various metal ions present in FR-SHLLW was measured in a solution of 0.1 M D^3DODGA+0.2 M HDEHDGA/n-DD. The extraction of Am(III) was accompanied by the co-extraction of lanthanides and unwanted metal ions such as Zr(IV), Y(III) and Pd(II). Since it was desirable to retain these troublesome metal ions in an aqueous phase, as discussed above, the complexing agent CyDTA, was added to FR-SHLLW and the extraction and stripping conditions were optimized. Based on the optimized conditions, the counter-current mixer-settler run was performed in a 20-stage mixer-settler. The mixer-settler profiles showed that Am(III) was quantitatively extracted in 4 stages. A similar extraction profile was also obtained for other lanthanides except lanthanum, which required 8-10 stages for complete extraction. Interestingly, Sr(II) exhibiting a distribution ratio of 0.51 was extracted to the extent of 90%. However, it was noted that the troublesome metal ions such as Zr(IV), Mo(VI), Fe(III), Cr(VI), Ni(II), Pd(II), Ru(III), Rh(III) were rejected to raffinate in addition to other elements. The recovery of Am(III) from the loaded organic phase was carried out using an aqueous formulation, 0.01 M DTPA +0.5 M CA at pH 1.5. It was observed that a significant amount of Am(III) was back extracted into the aqueous phase and stripping of Am(III) was observed in all 20 stages. About 55% of the Am(III) was recovered after 20 stages (product stream). It was also observed that significant amount of early-lanthanides (from lanthanum to samarium) are stripped to the aqueous phase along with Am(III), whereas the later-lanthanides (beyond samarium) behave similar to Eu(III). Depending upon the nature of lanthanides, the stripping of "early lanthanides" was determined to be 60-85% in 5-10 contacts. In contrast, the cumulative recovery of "later lanthanides" was lower than 5%.

The study clearly shows that recovery of Am(III) was accompanied by the stripping of "lighter lanthanides". Even though, the separation of Am(III) from lanthanides was not clean, as it was envisaged, the study is important from the point of view of a single cycle separation. Therefore, the studies foresee the possibility of intra-lanthanides as well as lanthanide-actinide separation in a single processing cycle.

IV.10 Studies on the Development of Pyrochemical Reprocessing of Metal Fuels

The development of pyrochemical reprocessing for metal fuels in the engineering scale facility was continued with molten salt electrorefining and cathode consolidation experiments on U-Gd-Zr alloy. U-Gd-Zr alloy was prepared by induction melting (Figure 1a). About 600 grams of the alloy was loaded in the anode basket for electrorefining. About 16 kg of LiCl-KCl electrolyte was used, which contained 6.1wt.% UCl_3 before electrorefining. About 7.0 x 10^5 C of charge was passed in constant potential mode. About 527 g of U with occluded salt was recovered at the cathode. A typical U deposit is shown in Figure 1b.

The concentration of UCl_3 after the end of electrorefining was estimated to be 4.9 wt.%. About 509 grams of U deposit was taken for salt distillation and consolidation. About 414 grams of U was obtained by salt distillation which was subsequently melted to form U ingot shown in Figure 2. The total weight of U ingot was found to be 368 grams after accounting for losses during distillation and consolidation. The current efficiency of the process was estimated to be 73%.

Basic electrochemical studies for the elucidation of redox behaviour of fission products were also carried out in LiCl-KCl eutectic. Electrode kinetics parameters like exchange current density were also measured for a large number of systems to be used as input for modelling of electrorefining process. The Tafel plots of various electrodes (anodic and cathodic) in LiCl-KCl eutectic at 773 K are shown in Figure 3.

Fig. 1 *(a) U-Gd-Zr alloy ingot and (b) a typical uranium electrodeposit*

Fig. 2 *Uranium ingot obtained after induction melting*

Cyclic voltammetry coupled with simulation was used to elucidate the electrode kinetics of $SmCl_3$ in LiCl-KCl eutectic. Various transient electrochemical techniques such as cyclic voltammetry, chronopotentiometry, square wave voltammetry and linear sweep voltammetry were also used to study Sm^{3+}/Sm^{2+} couple.

The diffusion coefficient of Sm^{3+} ion was calculated from convolution and chronopotentiometry. The validity of Arrhenius law was verified and the activation energy of the diffusion process was evaluated (37.5 $kJmol^{-1}$). The reversible half-wave potential, $E_{1/2}$, heterogeneous rate constant k_s, and charge transfer coefficient (α) have been calculated from logarithmic analysis of convoluted curves. According to Matsuda-Ayabe criterion, the Sm^{3+}/Sm^{2+} exchange was found to be quasi-reversible.

DIGISIM software was used for simulation of cyclic voltammograms. A good fit was observed between experimental and simulated curve for LiCl-KCl-$SmCl_3$ (1.3 x10^{-4} mol cm^{-3}) at 673 K at scan rate of 0.1 Vs^{-1}. The value of half wave potential $E_{1/2,}$ rate constant k_s and charge transfer coefficient α were found to be very close to the experimental values.

After a few batches of electrorefining, chlorides of fission products such as alkali, alkaline earth and rare earth metals accumulate in the electrolyte salt. The accumulation of fission products results in enhanced heat load, increase in the solidus temperature of the electrolyte salt and also reduction in the decontamination factors of cathode deposit. Hence, it is necessary to remove these fission products from the molten salt of lithium chloride-potassium chloride (LiCl-KCl) eutectic in order to reuse it. So, it is proposed that a portion of electrorefiner salt will be passed through zeolite ion exchange columns to remove these fission products and reuse the LiCl-KCl eutectic. Reuse of the electrolyte salt would greatly reduce the volume of ceramic waste produced during the pyroprocessing of spent nuclear fuel. This would also help in lowering the cost of the whole process.

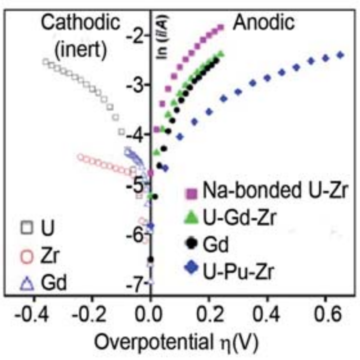

Fig. 3 *Tafel plot of U, Gd, Zr, Na-bonded U-Zr, U-Gd-Zr and U-Pu-Zr in molten LiCl-KCl eutectic. T=773 K*

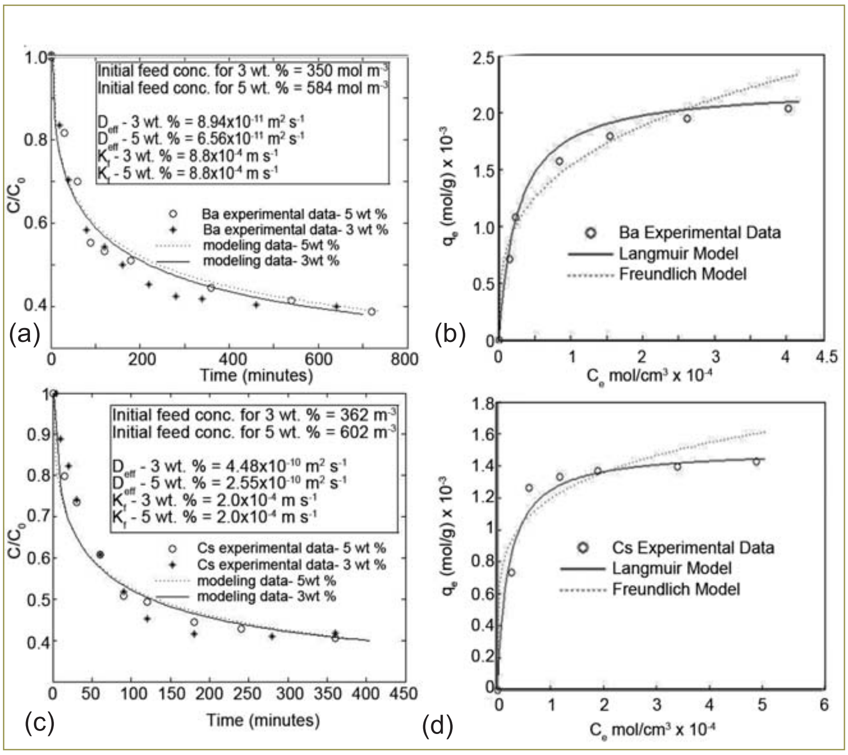

Fig. 4 *(a) Batch studies on Ba and model fits, (b) adsorption isotherm for Ba on zeolite 4A, (c) batch studies of Cs and model fits and (d) adsorption isotherms of Cs on zeolite 4A*

Studies on zeolite ion exchange columns pertaining to equilibrium and kinetics in batch mode for the adsorption of cesium, barium and neodymium from LiCl-KCl eutectic salt containing CsCl, $BaCl_2$ and $NdCl_3$ on zeolite 4A at 773 K were taken up. These elements are among the major fission product impurities in the spent electrolyte salt of molten salt electrorefining process. The results of batch studies along with model fits and adsorption isotherms for Ba and Cs are shown in Figures 4a to 4d respectively.

The recovery of actinides from used LiCl-KCl electrolyte has been developed using exhaustive electrolysis method. In this method, Li-Cd was taken as anode and U was recovered at solid cathode (SS-430). The alloy was prepared by taking Li and Cd in pure iron crucibles and melting it at 823 K. Both constant current and constant potential modes were used for the electrolysis experiments.

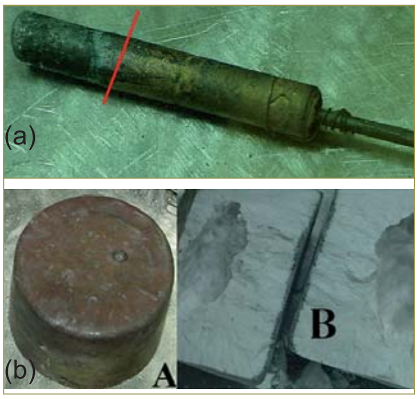

Fig. 5 *(a) Li-Cd (5.8 wt% Li) and (b) LiCl-KCl-UCl_3 electrolyte before (A) and after (B) exhaustive electrolysis*

It was observed that U deposit was poorly adhering to the cathode, and subsequently fell into the electrolyte bath. Li-Cd serves as a sacrificial anode which reacts with chlorine and forms dissolved LiCl. Figure 5a shows the Li-Cd anode (containing 5.8 wt.% Li) after exhaustive electrolysis. A part of Li-Cd anode rod dipped in molten salt changed its colour from golden copper to metallic silver. The uranium concentration was found to decrease from 3 wt% to ~0.1 wt% in LiCl-KCl which is shown in Figure 5b.

IV.11 Hybrid K-Edge/K-XRF Facility for Non Destructive Assay of Actinides

Assay of spent fuel solution from reprocessing plant based on the gamma rays and neutrons depend on the sample geometry, material properties etc., that limits the accuracy of the method if undefined accurately. However, spent fuel solution with high radiation background can be assayed using X-ray techniques of K-edge densitometry and fluorescence analysis of K series X-rays. A hybrid K-edge/K-XRF system is designed and fabricated adaptable for its operation inside a glove box with adequate radiation shielding and has been commissioned recently.

The system consists of an X-ray generator of 220 kV and 10 mA generating continuum with appropriate collimation system made from tungsten. An X-ray beam is collimated to 2 mm diameter for K-edge studies while another collimated beam of 10 mm at an angle of 157° is used for K-XRF studies. The leak tested glove box maintaining negative pressure and accommodating the system has a well-type extension welded at the bottom.

A sample holder is positioned

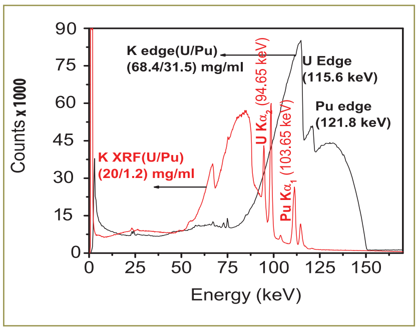

Fig. 1 *A typical K-edge/K-XRF spectrum of U & Pu*

Table 1: The results of the assay of U and Pu in the mixture by K-edge densitometry

Concentration (mg/ml)				$\Delta\rho/\rho$	
Actual		Experimental			
U	Pu	U	Pu	U	Pu
57.88	20.69	57.69	21.54	0.00	0.04
51.83	15.32	51.17	15.67	-0.01	0.02
36.70	10.85	36.37	11.70	-0.01	0.08
33.90	8.94	33.53	9.46	-0.01	0.06
24.29	2.72	24.29	0.002	0.00	-0.99
19.65	2.04	19.62	0.002	0.00	-0.99
17.1	0.75	17.22	-0.28	0.01	-1.37

Table 2: The results of the assay of Pu in the mixture by K-XRF

Concentration (mg/ml)		$\Delta\rho/\rho$
Actual	Experimental	
10.85	11.03	0.02
8.94	9.17	0.03
2.72	2.71	0.00
2.04	1.95	-0.04
0.75	0.71	-0.05

between shielded X-ray tube and HPGe planar detector for K-edge densitometry studies. The low energy photon detector is positioned at the largest possible backward angle with respect to the primary X-ray beam which removes the inelastically scattered radiation (90-120 KeV).

In the present system, X-ray from the generator interacts with the actinide in the sample making them to emit their characteristic K X-rays. Stock solutions of U of 74.6 mg/mL and Pu of 63.2 mg/mL, quantified earlier using Davies Gray and potentiometric methods respectively were used for the standardization of the hybrid system. These stock solutions were used to prepare a range of concentrations i.e. 17-68 mg/mL [U] and 0.75 to 31 mg/mL [Pu], for the calibration of the system. Pu assay in the lower range was carried out using XRF spectroscopic method. The ratio of the peak areas at 103.7 keV for Pu $K_{\alpha1}$ and at 94.6 keV for U $K_{\alpha2}$ was first obtained using Pu/U concentrations of (31.5/68.4) and (2.7/24.2) (mg.mL^{-1}/ms.mL^{-1}) respectively which was computed in both the cases and their average was used as calibration factor. The concentration of Pu in the mixture was obtained from the average calibration factor and the ratio of the peak areas of Pu and U in the mixture whereas the concentration of U was obtained using K-edge densitometry. A typical K-edge/K-XRF spectrum is shown in Figure 1.

The error in the assay of U and Pu in their mixture by K-edge densitometry is within the acceptable limits (Table 1). The error is higher for the actinide concentration of <15 mg/mL and hence K-XRF method is recommended for the same. However, the error for the assay of Pu by K-XRF method with its concentration in mixtures being <10mg/mL is within ± 5% (Table 2).

The FBTR-irradiated mixed carbide fuel of 155GWd/t burn-up is mechanically chopped into small pieces and dissolved in 11.3 M nitric acid. The acidity of the solution and the valence are adjusted to get the “conditioned” solution. A volume of 4 mL of the solution with the radiation dose of about 20R/h was taken in a poly-propylene vial which was placed concentrically into another poly-propylene vial. This solution was assayed by K-edge densitometry and the background correction was carried out using the spectrum obtained with the X-Ray tube in its OFF condition.

The diluted solution of the same with 4M HNO_3 was assayed using isotopic dilution mass spectrometry. The errors in the assay of U and Pu by K-edge method are within ±7 and ±0.6% respectively in comparison with the assay by mass spectrometry (Table 3).

This method was also used for the assay of actinides in powder samples. LiCl-KCl-UCl_3 electrolyte was prepared by equilibrating excess U metal with stoichiometric amounts of $CdCl_2$ in molten LiCl-KCl eutectic at 773 K for about 30 hours. However the LiCl-KCl eutectic was purified earlier by bubbling chlorine gas at 773 K for one hour. Similarly LiCl-KCl-$ThCl_4$ was also prepared. Uranium and thorium were estimated by Davies and Gray and HPLC method respectively.

Table 3: The results of the assay of U and Pu in conditioner solution by K-edge densitometry

Average concentration (mg/mL)				$\Delta\rho/\rho$	
Mass Spectrometrty		By K-edge Experiment			
U	Pu	U	Pu	U	Pu
15.10	28.93	14.09	28.75	-0.066	-0.0062

Table 4: The results of the assay of U and Th in the LiCl-KCl salt mixture

Element	Estimated amount (wt %)			Error (%)
	K-edge	Davies Gray	HPLC	
U	5.58	5.6	----	-0.4
U	8.56	8.4	----	2.00
Th	1.22	---	1.4	-13.0

Around 7 grams of uranium in LiCl- KCl salt mixture was taken separately in a poly propylene vial of 2.22 cm path length. The measurements were carried out with the X-ray tube maintained at 150 kV and 1 mA with the counting time fixed at 3000 s. Similarly LiCl-KCl-$ThCl_4$ was also analysed. The blank was obtained using 7 grams LiCl-KCl salt mixture.

The assay of U and Th by K-edge densitometry is compared with the other techniques (Table 4). The error in the assay of U LiCl – KCl salt mixture is within acceptable limits. This system can be used down to the concentrations of actinides of about 1.5 wt% with an error of about ±5 wt %. Lower concentrations lead to higher errors. In the case of Th (1.0 wt %), the error obtained in the estimation is higher.

The feasibility of non-destructive assay of actinides was established especially for U, Th and Pu in various matrices such as acid solution and chloride salt, a typical matrix encountered in the pyrochemical reprocessing.

IV.12 Waste Inspection Tomography for Non-Destructive Assay of Radioactivewaste

The radioactive wastes generated in the nuclear industries after treatment and classification are stored in standard 208 L drums till their disposal. Regulatory requirements necessitate the characterization of the waste contained in the drum. The technique of active (transmission) and passive (emission) γ-ray computed tomography (CT) provides the solution for assay of waste material. The waste inspection tomography (WIT) system combines active and passive computed tomography and nuclear spectroscopy to identify and quantify materials present in nuclear waste drums (Figure 1). A WIT system has been developed and commissioned in RSD, IGCAR for the non-destructive assay (NDA) of radioactive waste drum. The main objective is to assay special nuclear materials (SNM), transuranic (TRU) waste and fission products (FP). The system pinpoints where radioactive materials rest inside the drum and identifies and quantifies the isotopes. The WIT-NDA method improves on the segmented gamma scanning (SGS) method by performing low-resolution tomographic gamma emission and transmission scans (TGS) on each layer, yielding coarse images of the matrix density and radionuclide distributions.

WIT-NDA system consists of vertical source assembly, vertical detector assembly, horizontal detector assembly, drum translation/ rotation assembly, drum lifting mechanism, variable size tungsten collimator assembly, attenuator assembly, in-line automated conveyor system, ^{152}Eu (10 mCi) multi-gamma energy source, tungsten source shielding assembly, a 50% relative efficiency HPGe detector, multichannel analyzer (MCA) associated detector electronics, a collimated dosimeter, servomotors, servo controllers and human machine interface (HMI) based programmable logic controller (PLC).

Drum translation/rotation units, vertical source and detector assembly, horizontal detector assembly, variable size tungsten collimator assembly are servo motor driven mechanism. All the servo motors are controlled by delta tau turbo clipper controller. Drum lifting assembly is operated by induction motor and it is driven by TEK TDS-F8 VFD drive. In-line automated conveyor also operates through the same motor and drive. Source shutter assembly, attenuator assembly, drum marking system, isolation arm for the drum lifting assembly are operated pneumatically by the solenoid based system. Proximity optical sensors are used for drum sensing at the conveyor in feed and out feed location to operate and stop the conveyor respectively. Through-beam optical sensor are used to load the drum at the palate system. All the servo motor controllers, I/O modules, drivers and other mechanical movements are controlled by the control system PLC based controller. The PLC interfaces to the data acquisition software through ethernet. All coordinate positions are sensed by means of absolute shaft encoders. Closed loop operation with display of real time positional information in S/W screen. Positioning of the scanner is performed with a PLC acting as an interface between the electromechanical aggregates

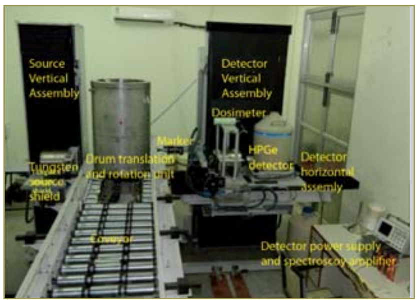

***Fig. 1** The waste inspection tomography system*

of the coordinate table and the supervising personal computer (PC). HMI in the electrical panel provides a convenient interface for control of the mechanism during testing or maintenance without going through the host computer. Mechanical movement and the input/output operation are controlled by a PLC and supervisory control and data acquisition (SCADA) software. SCADA also supervises the data acquisition from MCA and motion control of servo during TGS and SGS scan.

WIT-NDA is fully automated system controlled by SCADA program. SCADA will execute the programmed sequence of operations. The drum moves on a conveyor system and gets loaded on to the translation and rotational unit. The drum weight is measured and the positional indexing is done by placing an appropriate mark on the drum. The dose rate is then measured using a dosimeter which is located just above the detector. Depending on the dose rate, the scan type (TGS or SGS) is decided from the user written database. For SGS a wide collimation is required while for TGS a narrow collimation is essential. This is taken care by the SCADA based on the measured dose rate. The scan provides layer wise transmission and emission sinograms. These are then reconstructed using ART and MLEM algorithms. From the tomographic image the location of the radioisotope can be identified while the activity is estimated based on gamma spectrometry.

IV.13 Development of Stack Effluent Monitor using Novel Sensors and Customized Electronics

The gaseous waste effluents released into atmosphere by the plant through the stack have to be monitored continuously. In this regard, it is necessary to individually monitor for alpha particulates, beta particulates, ^{131}I and ^{85}Kr released through the stack. In CORAL, which reprocesses the spent carbide fuel from FBTR, a stack effluent monitor was designed and commissioned to meet the requirement using novel sensors and electronics as shown in Figure1.

Alpha and beta particulate activity monitor

For monitoring alpha and beta particulate activities simultaneously, glass fibre filter paper backed with a charcoal filter paper is provided in the continuous sampling system of stack effluent. The filter papers are continuously monitored using a dual phosphor based scintillation detector (3 mg/cm^2 thick ZnS(Ag) coated over 0.25 mm thick plastic scintillator). This single system is used instead of the conventional system which uses separate filter heads with ZnS(Ag) detector for alpha counting and end window type GM (Geiger Muller) detector for beta counting.

Online ^{131}I monitor

For monitoring ^{131}I, a charcoal filled in marinelli beaker geometry is used and the activity collected is monitored using a NaI(Tl) based scintillation detector. The iodine monitor has two channels. One channel monitors iodine energy range up to 400 keV where the predominant iodine energies are present. The other channel monitors above 400 keV region so as to identify and compensate for the interference of higher energy radionuclides like ^{137}Cs.

Online ^{85}Kr monitor

For monitoring ^{85}Kr, a flow through chamber is provided in which a plastic scintillator of dimensions 180 mm length and 25.4 mm dia, is fitted in the coaxial midpoint of the chamber. Krypton monitor also has two channels. First channel region is identified and set in such a way that 90% of counts fall in channel 1 using ^{85}Kr gas. The second channel is to identify any higher energy gaseous interference produced by radionuclides like ^{41}Ar in which case the ratio of two channels will be completely different. The conventional ^{85}Kr detector uses GM tube as detector which is of lower sensitivity than plastic scintillator.

Electronics

A single electronic unit capable of meeting the requirements of all the four channels is provided. To increase the reliability and reduce the down time of the system, the electronic unit is made with modular components. Three processing circuits are in place to generate logic pulse outputs based on the analog input signal from the detector. Extra high tension (EHT) modules with provision for remote adjustment as well as reading the value provide the high voltage to photomultiplier tubes. An eight channel analog input module is installed to read the EHT values and noise discriminator set values. Human machine interface (HMI) with I/O modules is used for acquiring and displaying counts and the output values of analog

Fig. 1 *Stack effluent monitor setup*

input module. The readings are communicated to the centralized radiation data acquisition server through the RS-485 port present in the HMI. The HMI also has an ethernet port as a parallel and redundant communication provision. Response of the stack monitor is shown in Figure 2.

Table 1: Efficiency of stack monitor

Channel	Source used	Efficiency (%)
Alpha	^{241}Am	23.0
Beta	^{90}Sr-Y	19.7
Iodine	^{131}I	3.1

Efficiency of each channel was calculated after calibration with standard radioactive sources and the results are shown in Table 1.

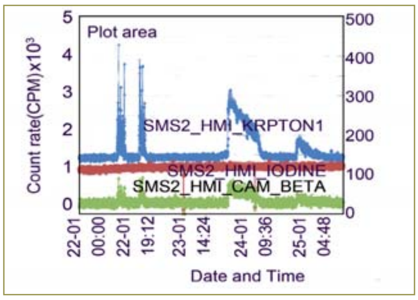

Fig. 2 *Stack monitor response during dissolution*

IV.14 Development of Systems for Pyrochemical Reprocessing R&D Facility

As part of the pyroprocessing technology development activities, a pyroprocessing research and development facility is under construction. Apart from electrorefining another important process step called cathode processing will also be demonstrated in this facility both at 10 kg of uranium metal/alloy per batch scale.

Electrorefining will be carried out in the high temperature electrorefiner (HTER) and the conceptual design has been completed. The system consists of four major subsystems viz. assembly station, electrorefining station scraping station and tilting station. Electro refiner is a rectangular vessel with 9Cr-1 Mo as the material of construction. The design and drawings for the electrorefiner and the tender specifications were finalized and procurement action is initiated.

The advanced cathode processor (ACP) is a distillation set-up heated using an induction heater. The advanced cathode processor will be used to separate the uranium from the cathode deposit covered with the salt obtained from solid rod cathode. The same advanced cathode processor will be used to distill cadmium from the solidified liquid cadmium cathode. Conceptual design of the advanced cathode processor has been completed.

High temperature electrorefiner and advanced cathode processor will be contained in an argon inert atmosphere. A large (~500 m^3) containment box has been designed to house the two systems. High purity argon atmosphere will be maintained inside the containment box with moisture and oxygen impurity levels maintained at below 50 vpm (each). It is made of SS 304L plates reinforced with MS sections. Broadly it can be divided into two sections, along the height: top section for crane and power manipulator with inner dimensions 18.9(L) × 4.3(B) × 2.2(H) m, Bottom section where high temperature electrorefiner, advanced cathode processor and associated systems will be erected with inner dimensions 17.3 × 3.5 × 3.8 m. The containment box is mounted at 4 metre elevation on steel columns and is surrounded by a steel structure as shown in Figure 1. Fabrication of containment box is under progress in Central Workshop (CWS), mock-up test were conducted for the window panels to ensure leak tightness and to finalize the manufacturing process.

A salt purification system has been designed to reduce the moisture content present in the commercially available LiCl and KCl used for preparing the eutectic mixture of the two salts. The system consists of a salt drying unit, chlorination unit, salt storing vessels and chlorine scrubbing unit. The chlorination vessel of the unit is housed inside a fume hood to prevent spread of any accidental leakage of chlorine inside the building. The salt storing vessels include the intermediate vessel in which the salt is transferred after chlorination; the transfer vessel which receives the salt from

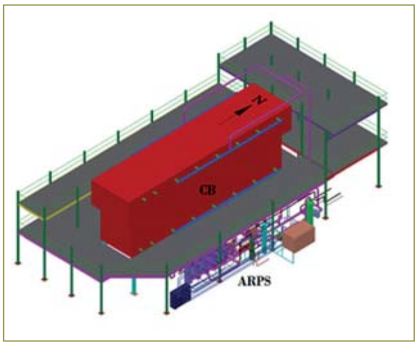

Fig. 1 *Containment box (shown as block), argon recirculation and purification system and steel structure*

intermediate vessel and from this vessel the salt is transferred to electrorefiner when required. There is also a storage vessel in which the used salt from the electrorefiner is stored. The chlorine scrubbing unit is provided to scrub any un-reacted chlorine gas, coming out of chlorination vessel, using sodium hydroxide. Purchase orders for salt drying unit and chlorination vessel are placed. Salt storage vessels and chlorine scrubbing unit including fume hood have been received at site.

To maintain oxygen and moisture concentration below 50 vpm (each) and the temperature of argon below 40°C inside the containment box argon recirculation and purification system (ARPS) has been designed. Removal of oxygen and moisture from argon will be done using palladium de-oxo catalyst and molecular sieves respectively. To remove any suspended particle present in the argon high efficiency particulate air (HEPA) filter will be used. The total heat load to the argon gas in the containment box was estimated to be 15 kW. Argon will be cooled to maintain the average temperature of argon inside the containment box to approximately 40°C. The argon recirculation and purification system will be used during regular operation for maintaining argon purity and temperature inside the containment box. Detailed design of the system is completed and indenting process is initiated.

Pressure control in the containment box at steady state conditions is achieved by two pressure control systems-argon pressure control systems, APCS-1 and APCS-2. APCS-1 will operate in the range of -20 to -40 mmWC. This system ensures minimal loss of argon from the system. APCS-2 will operate at -10 mmWC and -50 mmWC. This system will have direct feed and exhaust system only. This system will be put into operation at steady state conditions. APCS-2 system will be used if any issues arise with APCS-1 during steady state operation. This system will be actuated when the containment box pressure goes below -50 mmWC or the pressure rises above -10 mmWC. Fabrication of feed and bleed tanks is in progress in CWS, IGCAR and procurement of other components of the system is in progress.

Fig. 2 *Photograph of facility building under construction*

The containment box, argon recirculation and purification system and argon pressure control system will be housed inside a pre-engineered building which is in the final stage of completion (Figure 2). Only low level liquid wastes will be generated in this facility. For the same two 5 m^3 (each) tanks are provided outside the building. Fabrication of these tanks is also in progress in CWS, IGCAR Service utilities of the facility include chilled water system, compressed air system and gas cylinder banks.

IV.15 Development and Demonstration of Flowsheet for the Recovery of Uranium and Plutonium from Uranium-Plutonium-Zirconium Solution

Studies were carried out for the development of flowsheet for the aqueous reprocessing of spent metallic fuel with typical U-Pu-Zr composition, since ternary alloy is contemplated for Metallic Fuelled Breeder Reactor (MFBR). The objective of this study is to propose an extraction flowsheet for the quantitative recovery of uranium and plutonium with minimum

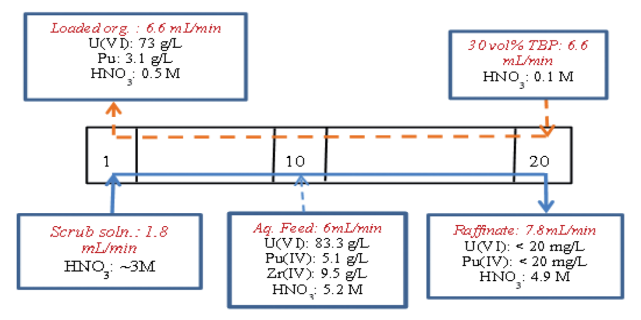

Fig. 1 *Proposed extraction flowsheet for the quantitative recovery of uranium and plutonium*

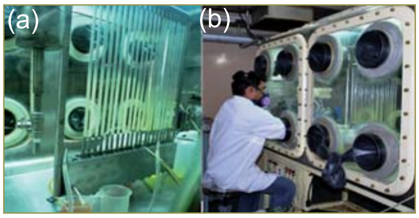

Fig. 2 *Experimental setup in a glove box*

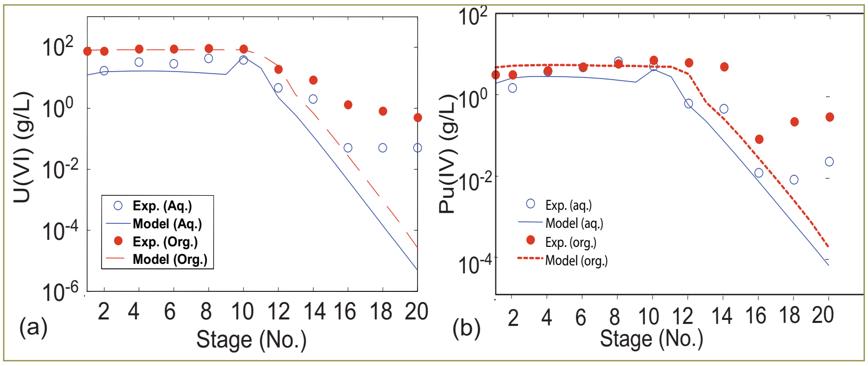

Fig. 3 *Experimental and calculated concentration profiles of (a) U(VI) and (b) Pu(IV) in mixer-settler stages*

contamination of zirconium by experimental validation. The flowsheet is formulated based on PUSEP (ver-2) computer code. For the experimental study, metallic fuel composition chosen was U(84%)+Pu(6%)+Zr(10%), which simulates the concentrations to address issues related to the extraction chemistry of Zr such that problems if any could be understood and resolved before taking up the irradiated fuel for reprocessing. Figure 1 shows the proposed flowsheet for the extraction of uranium/plutonium from U-Pu-Zr nitrate solution.

To validate the extraction flowsheet, a 20-stage mini-mixer settler bank in a glove box was used (Figures 2a and 2b). The stage hold-up of one stage is 35 ml with a mixer volume of 10 ml and settler volume of 25 ml. The hold-up of the mixer-settler unit is approximately 700 ml.

Comparison between experimental and calculated profiles of uranium and plutonium in the stages of mixer-settler bank are shown in Figures 3a and 3b respectively, and reasonably good agreement was achieved. During an experimental run, crud formation was noticed in some stage of mixer-settler bank when the scrub acidity was maintained at about 2 M, but it was absent at 3 M scrub acidity.

Experimental results indicated that the raffinate loss of plutonium was well below 5 mg/l (loss was <0.05%) and uranium loss was less than 0.05 mg/l (loss was <0.1%). Zirconium concentration in the product solution was found to be <1.8 mg/g of U+Pu.

IV.16 Development of Polymer Based Materials for Aqueous Reprocessing Applications

The polymer materials that are used in various applications in nuclear industry can be subjected to radiation dose rates over a range from low to high, at temperatures from ambient to high and environments which range from inert gases through air to aggressive vapours and liquids. Different combinations of these conditions result in different effects on the polymer that has to be taken into account in material selection and life time prediction.

In the reprocessing plant, radiation as well as vapour of acid and organic solvent are present. Hence, polymer materials resistant to both radiation and chemicals need to be developed for various components. For belt driven motor of centrifugal extractor (CE), ethylene propylene diene monomer based rubber (EPDM), polybutadiene rubber (PBR) and chloroprene rubber (CR) based compounds were developed. The properties of these rubber compounds were measured for evaluating their suitability for functioning in radiation environment. For this purpose, the rubber compounds along with reinforcements (aramid soft cord, glass cord, polyester cord, polyamide cord, nylon tyre cord, polycotton fabric and wide open fabric) were irradiated in the gamma chamber and were exposed to chemical vapour for assessing their radiation and chemical stabilities. The rubber compounds along with reinforcements were also exposed to gamma radiation and

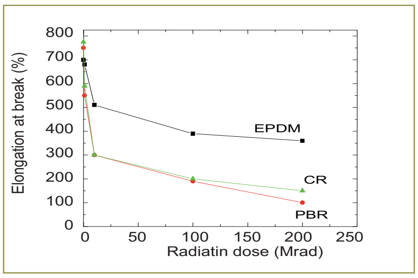

Fig. 1 *Elongation at break of the rubber compounds with radiation dose: (a) EPDM, (b) PBR and (c) CR*

***Fig. 2** Photograph of the EPDM belt*

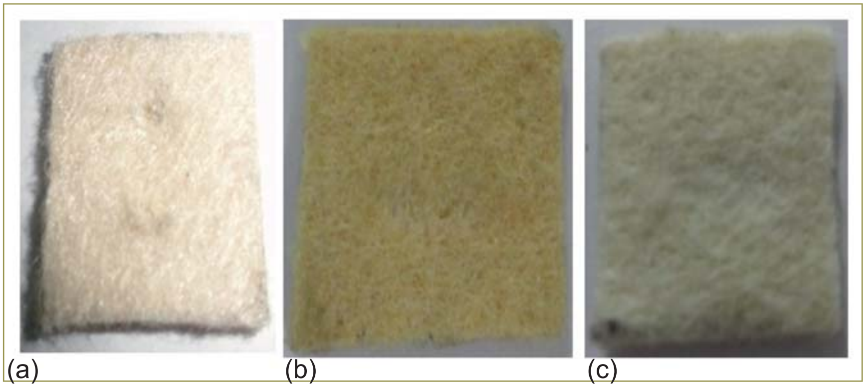

***Fig. 3** Photographs of (a) RYTON, (b) P-84 and (c) NOMEX samples*

chemical vapour simultaneously and the mechanical properties were measured. The elongation at break of the rubber compounds with radiation dose is shown in Figure 1.

It is evident from Figure 1 that 50% reduction in elongation at break occurred at 200, 10 and 10 Mrad for EPDM, PBR and CR compounds respectively. Since elongation at break value is considered as the index for the radiation tolerance of polymer materials, EPDM rubber compound was chosen. Based on the results of the irradiation and chemical exposure tests, EPDM compound, aramid and polyester fibre were found to be suitable for plant application.

For fabrication of the belt, multi-ribbed design was selected because the surface area of contact is high resuling in better load transfer. Belts based on EPDM compound with aramid and polyester fibre as reinforcement were fabricated. Testing of the belt (Figure 2) is in progress.

For the filtration of dissolver solution in the plant to remove suspended particles, three filter fabric samples Nomex (aromatic polyamide), Ryton (Polyphenylene sulphide) and P-84 (aromatic polyimide) were selected based on their properties reported in the literature. Photographs of the three samples are shown in Figure 3. Properties such as tensile strength, permeability, equivalent pore size, filtration efficiency, abrasive wear and coefficient of friction of the three samples were measured.

The tensile strength values measured for the three fabrics are given in Table 1. Permeability values estimated for the filter fabrics are presented in Table 2. The low permeability values could be due to small pore size and low pore interconnectivity. Abrasive wear and coefficient of friction were determined using ball-on-disc tribometer. The coefficient of friction of the three samples was found to be 0.5 to 1.0. Significant abrasive wear was not observed.

The filtration efficiency of the fresh samples of Nomex, Ryton and P-84, determined by mixing Al_2O_3 with water and allowing the mixture to pass through the filter media was approximately 99%.

To evaluate the suitability of the filter fabrics for application in reprocessing plant, the fabrics were exposed to gamma radiation in air at ambient temperature and immersed in 10 M nitric acid for 72 hours. The effect of radiation and nitric acid on the fabrics was evaluated from the tensile strength values of irradiated and chemically exposed samples of Nomex, P-84 and Ryton, which are given in Table 1. The degradation in tensile strength due to irradiation was found to be minimum in P-84 and Ryton. Nomex had very poor chemical resistance. The permeability values of irradiated and chemically exposed fabric samples changed by 25% for P-84 and Ryton. Thus, P-84 is preferred as the filter fabric for the plant.

Table 1: Tensile strength of the fabric samples

Sample type	Average tensile strength (MPa)		
	Nomex	P-84	Ryton
Fresh	5.9	3.9	7.1
Irradiated	4.6	3.7	6.2
Chemically exposed	0.2	2.8	4.1

Table 2:
Permeability values (darcy) of fabric samples

Nomex	P-84	Ryton
0.47	0.22	0.30

IV.17 Development of Ceramic Coatings on High Density Graphite for Uranium Melting Application

High density graphite (HDG) is chosen as the structural material for cathode processing and fuel casting crucibles for the pyrochemical reprocessing of spent metallic fuel from future metal fueled sodium cooled fast reactors. Ceramic coatings have been proposed on high density graphite for corrosion protection aginst aggressive molten LiCl-KCl salt and uranium. Since pyrochemical reprocessing is a batch process, the ceramic coated HDG crucibles should exhibit good thermal cycling life and should be inert to molten uranium, for applications at high temperatures. Thus, it is essential to subject the coated HDG crucibles to rigorous thermal cycling test to assess the durability and integrity of the coating, prior to using the crucibles for cathode processing and fuel casting.

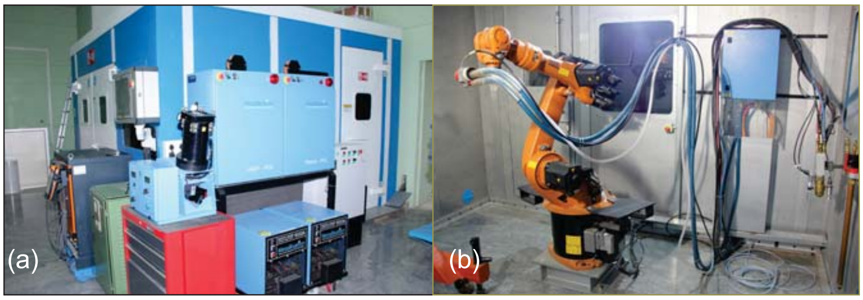

Fig. 1 *Atmospheric plasma spray and high velocity oxy-fuel spray systems*

The plasma coating parameters were optimized to get strongly adherent yttria coating on HDG. Yttria coatings of 250-300 µm thick on HDG disc samples and crucibles were prepared, with and without 50-60 µm thick NiCrAlY bond coat, by atmospheric plasma spray process using METCO 9 MB plasma torch. The HDG samples coated with NiCrAlY bond coat and yttria top coat were subjected to thermal cycling studies at 1000 and 1100°C for 1 hour duration, after vacuum sealing them in quartz ampoules at 10^{-3} bar pressure in order to avoid the oxidation of HDG. The microstructure and elemental composition of the as-received and thermal cycled yttria coated samples were analyzed by scanning electron microscopy coupled with energy dispersive spectroscopy. Phase identification of the coating, performed by X-ray diffraction and laser Raman spectroscopic techniques confirmed the presence of only cubic phase of yttria in the as-received as well as thermal cycled samples. Yttria coating with NiCrAlY bond coat failed after 35 thermal cycles at 1000°C and 19 cycles at 1100°C. Presence of cubic yttria phase alone in both as-received and thermal cycled samples indicated that the failure of coating could be due to thermal expansion mismatch between the coating and the substrate. To assess the integrity of yttria coating on HDG with NiCrAlY bond coat, initially copper melting experiments were carried out at 1150°C. The coating failed after 8th cycle at 1150°C. Uranium melting experiments were performed on yttria coated HDG samples with NiCrAlY bond coat in the induction heating setup, housed in argon atmosphere glove box at 1350°C for about 15-20 minutes. The coating was found to be adherent for three uranium melting cycles, without spallation. However, micro-cracks developed after three uranium melting experiments due to melting of the bond coat. Hence, yttria coating without any bond coat was developed on HDG crucibles for molten metal applications. The plasma sprayed yttria coating without bond coat performed well for more than 40 copper melting cycles at 1150°C and for about 5 copper melting cycles at 1400°C.

Based on the experience gained in the development of ceramic coatings on HDG discs and crucibles of smaller dimensions, we have succeeded in depositing 250-300 µm thick yttria coating without any bond coat on the inner side of engineering scale HDG crucible of dimensions 150 mm OD, 134 mm ID and 150 mm height for evaluating the performance of coating in Cu melting experiments at the metallic fuel fabrication facility. Figures 1a and 1b show the atmoshperic plasma spray (APS) and high velocity oxy-fuel spray system installed recently for developing various ceramic coatings on HDG and metallic substrates. Using this atmoshperic plasma spray system, yttria coating of 250-300 µm thick was deposited on engineering scale HDG crucibles without any bond coat (Figure 2).

Fig. 2 *As-received yttria coated HDG crucibles without bond coat for uranium melting experiments*

IV.18 Evaluation of Corrosion Behavior of Dissolver Materials in HNO_3 and Fluorinated HNO_3 as Media

Corrosion studies in nitric acid containing simulated fission products and corrosion products

Long term corrosion testing of a Zircaloy-4 (Zr-4) mock-up dissolver vessel proposed for the aqueous reprocessing of spent nuclear fuel of future FBRs, has been initiated. In this work, Zr-4 mock-up dissolver vessel was used as testing facility to evaluate the corrosion rate of several candidate materials based on zirconium and titanium in boiling and vapor phase of 11.5 M nitric acid containing simulated fission products and corrosion products (herein after called as the simulated dissolver solution). The composition is based on the calculation for the mixed carbide fuel (PuC: 70%, UC: 30%), at a burn-up of 150 GWd/t, after a cooling period of one year.

Several campaigns of corrosion testing for 100, 250, 500, 1000 and 2500 hours of operation were completed. Zirconium-702 (Zr-702), Zr-4, autoclaved Zr-4 and commercial pure titanium (CP-Ti) exhibited low corrosion rates of 0.08-0.23 μm/y (0.003-0.009 mpy) in the as-received and welded conditions, exposed to boiling liquid phase of simulated dissolver solution for 2500 hours. The commercial pure titanium and its welds exhibited marginally higher corrosion rates of 1.0 μm/y (0.04 mpy) and 1.9 μm/y (0.075 mpy), respectively in the vapor phase of simulated dissolver solution. The lowest corrosion rate of 0.08 μm/y (0.003 mpy) was obtained for the autoclaved Zr-4 sample exposed to boiling solution. SEM investigations did not reveal any corrosion attack on the titanium and zirconium samples. On the other hand, the CP-Ti/SS 304L and Zr-4/SS 304L dissimilar weld coupons severely corroded and failed at the interface when exposed to boiling liquid and vapor phase of simulated dissolver solution. Thus, to avoid such failures during service, dissolver solution should be transferred through the dissimilar weld joints, only at room temperature for the purpose of extending the service life. Also, the dissimilar welds should be placed far away from the dissolver vessel, so that the vapor phase attack can be minimized. Visual inspection of the outer surface of Zr-4 dissolver vessel and all the accessible welds revealed no corrosion attack on the Zr-4 dissolver vessel operated for 2500 hours. Long term corrosion data under plant simulated condition will be obtained through three years of operation and the results will be used to model and predict the life expectancy of Zr-4 dissolver vessel and the other candidate materials.

Corrosion studies in nitric acid containing free and complexed fluoride ions

Aqueous reprocessing of Pu-rich mixed oxide fuel requires fluoride as catalyst in boiling nitric acid for an effective dissolution of the spent fuel. The corrosion behavior of dissolver materials such as Zr-4 and commercial pure titanium in boiling 11.5 M nitric acid with the addition of 0.05 M NaF was evaluated. The immersion weight loss test was carried out for a period of 48 hours, and five such periods were done with fresh solution in boiling condition. Zr-4 exhibited high corrosion rates of 3085, 230 and 720 mpy in boiling liquid, vapor and condensate phases of fluorinated nitric acid and the sample exposed to liquid phase completely dissolved when exposed after 144 hours. The CP-Ti exhibited corrosion rates of 115, 155 and 2400 mpy in the liquid, vapor and condensate phases of fluorinated nitric acid. In general, complexing agents like $Al(NO_3)_3$ and $ZrO(NO_3)_2$ are used to fix the free fluoride ions so that the dissolver equipment can be saved from corrosion during dissolution of the fuel. The corrosion rates of Zr-4 in nitric acid when complexed with $Al(NO_3)_3$ were 2460, 60 and 65 mpy and when complexed with $ZrO(NO_3)_2$ the values were 18, 4 and 6 mpy respectively in liquid, vapor and condensate phases of nitric acid with complexed fluoride. Similarly, the corrosion rates of CP-Ti in nitric acid when complexed with $Al(NO_3)_3$ were 0, 4 and 101 mpy and that when complexed with $ZrO(NO_3)_2$ were 0, 1 and 5 mpy respectively in liquid, vapor and condensate phases of nitric acid with complexed fluoride ions. The corrosion rates were lowest for CP-Ti in all the conditions when complexed with $ZrO(NO_3)_2$. SEM images confirmed that Zr-4 undergoes uniform corrosion, whereas CP-Ti samples showed un-attacked corrosion surfaces in the liquid phase when complexed with $Al(NO_3)_3$ and $ZrO(NO_3)_2$.

IV.19 Development of Algorithm for Detection of Plutonium in Air from the Alpha-Spectrum of Continuous Air Monitors

Reprocessing of the spent fuels of fast breeder reactors involves handling of large amount of plutonium. Inhalation hazard from air-borne plutonium is a major risk in such facilities. Hence, it is desirable to have a dedicated monitor for plutonium in air, which provides spectrometric information, making the instrument capable of detecting much lower concentrations of plutonium than the conventional alpha gross counting based systems.

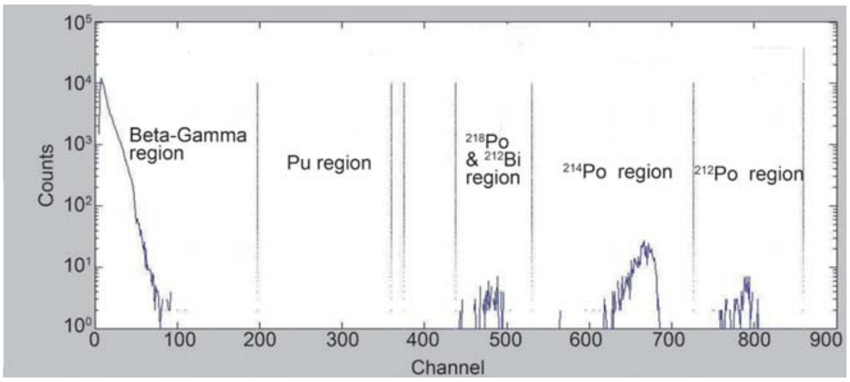

Fig. 1 *Alpha spectrum showing various regions of interest*

Method for detection of plutonium

The major issue regarding detection of plutonium is the background due to radon-thoron progenies (^{218}Po and ^{212}Bi), whose alpha energies are close to that of plutonium as shown in Figure 1. Experimental work and data collection were carried out to obtain alpha energy radiation-spectrum of the background by air sampling on the filter paper at different conditions. Modeling of plutonium spectrum on filter paper was carried out. Mathematical models were formulated for plutonium release and were validated on the background spectrum experimentally obtained. The information obtained was applied on the real time background spectrum to estimate the background in plutonium region of interest (ROI). Based on the estimate of background in plutonium region of interest, plutonium could be detected from the spectrum in the region of interest. The real time computation of minimum detectable activity (MDA), confidence level (%) and false alarm rate were carried out. Its implementation on specialized hardware is in progress along with optimization of alarm level and false alarm rate while generating the alarm for plutonium in air.

Strategy for plutonium detection

Within the plutonium region of interest, 15 channels near the peak were considered for calculation of line shape parameter (LSP). The line shape parameter is the ratio of peak area (15 channels) to the total area of the plutonium region of interest (242 channels).

Shift in distribution of the line shape parameter with background & plutonium and with background alone are shown in Figures 2a and 2b respectively. 3D graphs showing (background + plutonium) and background alone are represented in Figures 3a and 3b respectively. The 3D graph is for channel, counts and time. The plutonium peak could be seen building up with time.

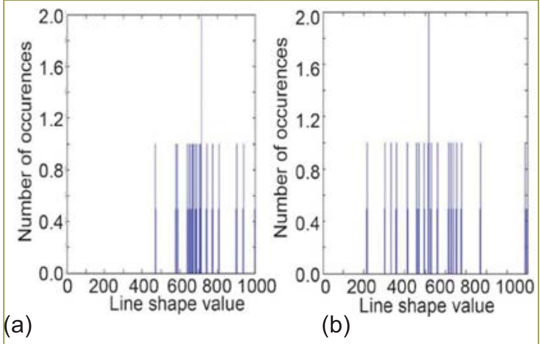

(a) (b)

Fig. 2 *Distribution of the line shape parameters (a) with background plus plutonium and (b) with background alone*

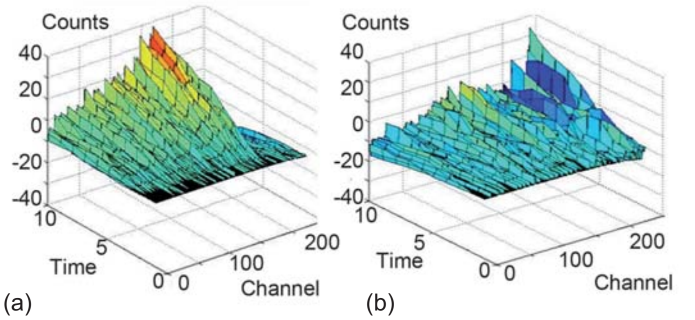

(a) (b)

Fig. 3 *Fit difference graph of (a) background plus plutonium and (b) background alone*

IV.20 Development of Dielectric Constant Meter for Solvents used in Actinide Separations

The dielectric constant correlates the solvent's ability to reduce the strength of the electric field surrounding a charged particle immersed in it. The dielectric constant of a solvent is an acceptable approximation of the solvent's ability to dissolve common ionic compounds and is a measure of its polarity. Higher ε means higher polarity, and greater ability to stabilize charges.

In solvent extraction, the polarity of the organic phase is very important as it decides the amount of metal that can be loaded in the phase.

As a result, knowledge of dielectric constant is an important parameter for such separations. This necessitated the development of a measurement unit which measures and displays the dielectric constant of the synthesized solvent.

The challenge of development of instrumentation for dielectric constant measurement is the development of dielectric probe and measurement of very low value of capacitance across the dielectric probe.

The dielectric constant of unknown solvent is measured by using dielectric probe and XR-2206 oscillator based hardware.

Basic principle

Dielectric Constant of solvent is calculated by measuring the capacitance of dielectric probe immersed in the solvent using the formula

$$C = \frac{\varepsilon_0 \varepsilon A}{d}$$

Where C = capacitance of the probe, 'ε_0' is the permittivity in vacuum, 'ε' is the dielectric constant of the solvent, 'A' is the area of the plates and 'd' is the distance between the plates. From above equation the capacitance of dielectric probe is directly proportional to dielectric constant of solvent because 'ε_0', 'A' and 'd' are constant.

Design and development of dielectric probe

The dielectric probe consists of two parallel metallic plates which act as electrodes. The probe acts as capacitor while the solvent acts as dielectric medium.

The design of dielectric probe is a challenge because it has to be small in size so that the quantity of solvent used for measurement is low. Also the capacitance value of the probe shall be in the measurable range which can respond to a small variation in dielectric constant of solvents used. The dielectric probe consists of two plates (25 x 25 mm) of brass metal separated by a distance of about 5 mm. The faces of the plates are well machined and later polished. The two conducting plates are encapsulated in suitable glass assembly. Two copper leads are taken out from the plates through a Teflon holder on top. The glass above the plates is sealed after taking the leads to top. This is to make sure that a fixed volume of solvent is present between the plates so that the capacitance is fixed. The length of leads is kept as small as possible. The design of dielectric probe for use with solvent is such that the structure of the probe is rigid, the variation of its capacitance due to strain is negligible and also it is less fragile.

We have optimized the size and shape of dielectric probe in such a way that the value of probe capacitance is maximum (measurable range in pF) and very less quantity solvent is required for measurement of dielectric constant (for complete dipping of probe in solvent). The photograph of the probe is shown in Figure 1

Fig. 1 *Dielectric probe*

Methodology

Several attempts have been made for measurement of dielectric constant of solvents which are based on wheatstone bridge, schering bridge, microwave bridge, resonance method, A.C. bridge techniques, impedance measurement method, XR-2206 function generator etc. The XR-2206 function generator method provided precision measurement. We have adapted the XR-2206 function generator based hardware method.

Basic hardware

The XR-2206 is a monolithic function generator integrated circuit capable of producing square waveform of high-stability and accuracy. The capacitance of the probe and an external fixed resistance form an RC oscillator. The frequency of operation can be selected over a range of 0.01 Hz to 1 MHz linearly using the external resistor/capacitance combinations. The output is suitable over a wide range of temperatures and power supply variations. The symmetry of all waveforms can be adjusted with external timing resistors.

The frequency of oscillation '*f*' is determined by the probe capacitance C and by the timing resistor R. The frequency is given as

$$f = \frac{1}{RC}$$

Hardware scheme

Basically the dielectric constant meter measures the capacitance value of the probe connected to XR-2206 function generator. The value of capacitance is processed into dielectric constant of solvent by suitable equation. The block diagram of instrumentation scheme is given in Figure 2.

Here R is fixed (8.2 kΩ) and the probe capacitance varies from 100 to 1000 pF. The frequency output from XR-2206 is fed to signal conditioning circuit adaptable with microcontroller. The microcontroller measures the frequency and converts the frequency into engineering units and displays on LCD display.

Calculation of dielectric constant

The frequency is measured by microcontroller using 16-bit counter by counting the pulses for a period of 1 second for more accurate values and the capacitance of the probe is calculated.

There are two modes of operations available in this unit, Calibration mode and Measurement mode.

In calibration mode, the capacitance of probe in air (C_0) and capacitance of probe in reference solvent (C_r) is measured by microcontroller. These values are stored in memory for calculation. Here toluene is taken as reference solvent.

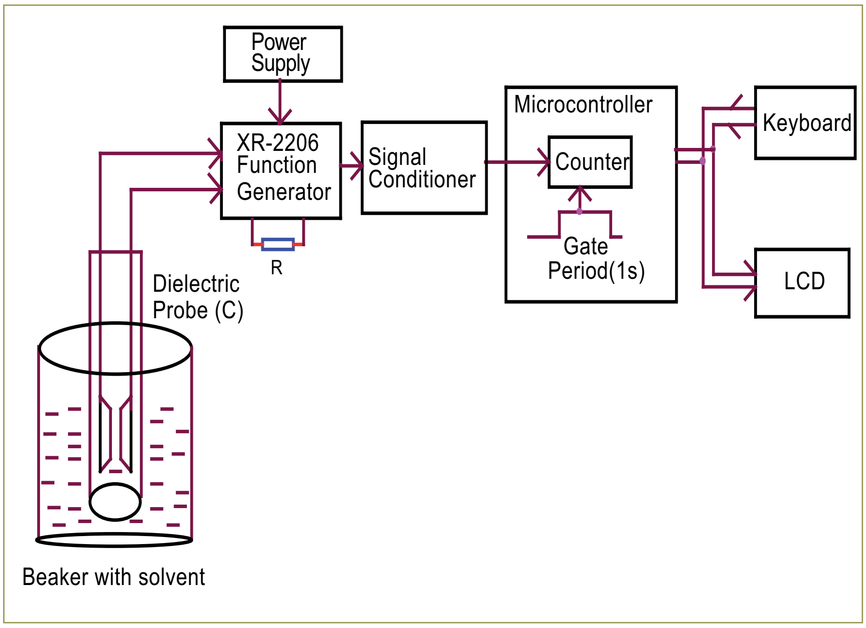

Fig. 2 *Block diagram of instrumentation scheme*

In measurement mode, the capacitance of probe in unknown solvent (C_x) is measured.

The calculation of dielectric constant of unknown solvent is done using the following relation:

$$\varepsilon_x = 1 + \frac{C_0 - C_x}{C_0 - C_r}(\varepsilon_r - 1)$$

ε_x = dielectric constant of unknown solvent

C_0 = capacitance of the probe in air

C_x = capacitance of the probe in solvent whose dielectric constant has to be measured

C_r = capacitance of the probe in reference solvent and

ε_r = dielectric constant of the reference solvent.

The value of dielectric constant of unknown solvent is displayed on LCD display.

The experiments were conducted with various standard solvents in the laboratory at room temperature and the measured values are in good agreement with the literature values. The results are shown in Table 1.

Table 1: Dielectric constants of solvents at room temperature
(* average of three readings)

S.No	Sample	Cap.(pF)	Dielectric constant	
			Present work*	Literature
1	Cyclohexane	150.00	2.13	2.02
2	Dioxane	150.40	2.31	2.12
3	Chloroform	155.60	4.80	4.81
4	TBP	164.13	8.92	8.10
5	Acetone	187.00	19.91	20.35
6	Ethanol	198.30	25.32	24.50

IV.21 Vacuum Distillation System for removing Sodium from Irradiated Sodium Bonded Metallic Fuel Pins

Metallic fuels will be used in future fast reactors due to their distinct advantages such as high breeding ratio and low doubling time. Sodium bonded metallic fuel pins are undergoing test irradiation in FBTR. Preparation of specimens for metallographic examination during post irradiation examination (PIE) of metal fuel pins requires removal of bond sodium from the fuel-clad gap and also from the porosities and cracks in the fuel matrix. Towards this, a sodium removal system based on vacuum distillation process has been developed for the removal of sodium from the fuel pins inside hot cell. The system facilitates evaporation of liquid sodium by reducing the pressure below the vapor pressure at the pre-selected operating temperature.

The vacuum distillation system (Figure 1) consists of a vacuum chamber in which the fuel pin with two punctured holes is subjected to high temperature and vacuum. The system comprises of heating coils surrounding the chamber, an insulation layer surrounding the heater, a cold trap to condense sodium vapour, a vacuum pump, a drainage tank to collect drained sodium, needle valves, and a supporting stand. The chamber has an opening at the top to facilitate vertical loading of the pin into it. Knife edge flanges and copper gasket ensure leak-proof closing of this opening. A worm gear arrangement helps to tilt the vessel for unloading the fuel pin.

Heat and mass transfer calculations were carried out using FEM to determine the heater power, thickness of insulation layer, time required for evaporation, required flow rate capacity of vacuum pump, etc. The vacuum chamber has been designed to withstand a vacuum of 0.1 Pa. In order to avoid metallurgical degradation of the fuel and clad during the process, permissible temperature for vacuum distillation is restricted to 400°C. Vapour pressure of sodium at this temperature is 47 Pa absolute.

Trials were carried out using three sodium filled experimental capsules (Figure 2a) to optimize the vacuum distillation process parameters for complete sodium removal from metallic pins. These capsules were made of 20% cold worked D9 alloy tubes of 6.6 mm outer diameter and 0.45 mm wall thickness. Filling of sodium (2 gm each) in the capsule was carried out in a glove box maintained with high purity argon environment with oxygen and moisture levels less than 5 ppm each. The hole through which sodium was filled was sealed using copper gaskets. The capsules have side opening of the order of 0.5 mm diameter to facilitate evaporative removal of sodium.

The pressure, temperature and pumping capacity used for vacuum distillation experiments were 10 Pa absolute, 400°C and 250 litres/min respectively. During the trials, the pressure inside the chamber was reduced to 10 Pa absolute, after placing the capsule inside it. Pure argon was then admitted inside the vessel and the pressure was maintained between +5 to +10 mm water column above atmospheric pressure. Heater module was then switched on until the chamber temperature got stabilized at 400°C. The molten sodium was collected in the drainage tank below. Subsequently, the tank was isolated and connection between vacuum pump and chamber was established, to start evaporative distillation.

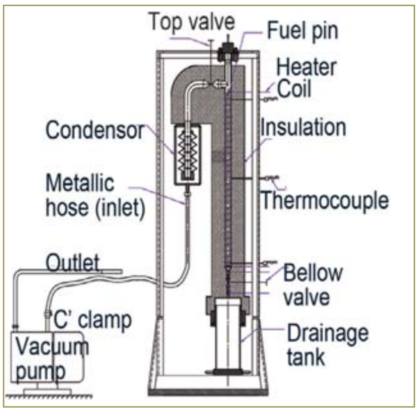

Fig. 1 *Vacuum distillation system*

The sodium vapour on its way to the vacuum pump is condensed in the cold trap and it supplements the build up of vacuum inside the vessel. Trials were conducted for durations of 72, 92 and 120 hours on the capsules.

Weight of each capsule was measured to analyze the extent of sodium removal after the experiments. It was observed that 95 to 97.3% w/w sodium was removed. Later, the capsules were cut longitudinally (Figure 2b) and examination revealed that most of the inner surfaces were clean and free of sodium or its compounds.

The experiments have validated the feasibility of vacuum distillation technique for removing sodium from sodium bonded fuel pins in the hot cells of RML. Further experiments are planned using sintered stainless steel pellets to refine the process especially to remove sodium from cracks and porosities in the fuel slug.

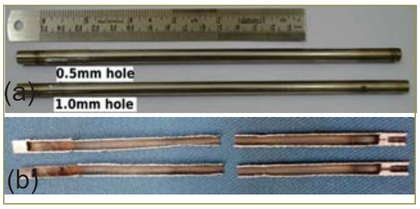

Fig. 2 (a) *Sodium filled capsules and (b) a view of longitudinally split experimental capsule*

IV.22 Iron Phosphate Glass Wasteform with Simulated HLW from Fast Reactor

Iron phosphate glass (IPG), is a suitable matrix for the immobilization of nuclear waste containing higher concentration of Cs, Mo, heavy elements, noble metals and rare-earths compared to borosilicate glass (BSG). IPG containing 20 wt% simulated fast reactor waste, henceforth referred as IP20FRW was synthesized without phase separation or crystallization. IP20FRW was characterized for its amorphous nature, density, glass transition temperature, thermal expansion behaviour, surface morphology and thermal stability.

Glass wasteform (IP20FRW) product performance parameters such as high temperature viscosity, specific heat, glass forming ability, glass stability were studied and compared with that of pristine IPG. These product performance parameters need to be known before immobilizing the actual HLW in IPG. In addition to the above characterizations, the present work also explores the glass network structure and Fe^{3+}/Fe ratio of IP20FRW using Raman and Mössbauer Spectroscopy respectively. In view of the fact that the devitrification of glass alters the fundamental physical properties and chemical durability of the glass wasteform, devitrification studies of IP20FRW were carried out using DTA and XRD techniques.

The measured viscosity of IPG and IP20FRW melt as a function of temperature are shown in Figure 1 along with that of IPG for comparison. The viscosity of IPG and IP20FRW are nearly same within experimental uncertainty beyond 1250 K. However, the viscosity of IP20FRW increases steeply below 1250 K. This steep increase in viscosity is due to the presence of simulated waste components preventing the atomic rearrangement below 1250 K. The pouring temperature is 1323 K. The variation of viscosity with temperature was analyzed using Arrhenius equation as given by

$$\eta = A \exp\left(\frac{E_\eta}{RT}\right)$$

where η is the viscosity of the melt, T is the absolute temperature in K and R is the gas constant. A and E_η are Arrhenius parameters namely, pre-exponential factor and activation energy of viscous flow respectively. The plot of ln(η) versus 1/T is shown as inset in Figure 1 and observed linearity clearly indicates that the ln(viscosity) obeyed the Arrhenius equation over the measured temperature range. A higher activation energy of viscous flow is observed for IP20FRW compared to IPG indicating the greater influence of temperature on the viscosity for IP20FRW compared to IPG.

The specific heat of IP20FRW measured using DSC is shown in Figure 2 along with that for IPG. The specific heat of IP20FRW is lower than that of IPG, signifying the lower degrees of freedom for IP20FRW. Thus addition of nuclear waste decreases the specific heat of IPG. Glass stability (GS) (resistance to crystallization of glass during re-heating) and glass forming ability (GFA) (resistance of

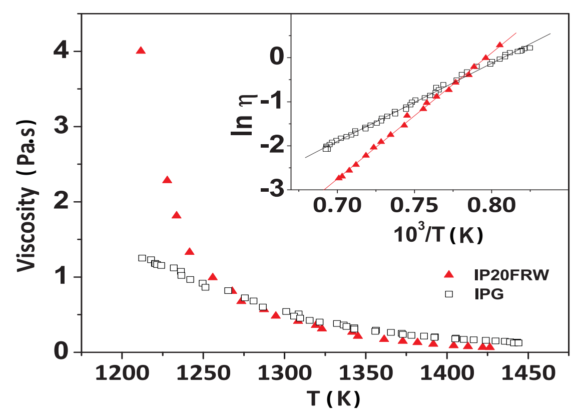

Fig. 1 *Viscosity curves of IPG and IP20FRW as function of temperature; ln(viscosity) versus 1/T is shown as inset*

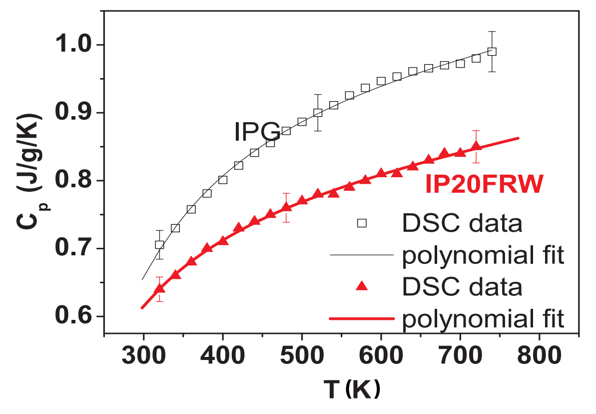

Fig. 2 *Specific heat of IP20FRW and IPG*

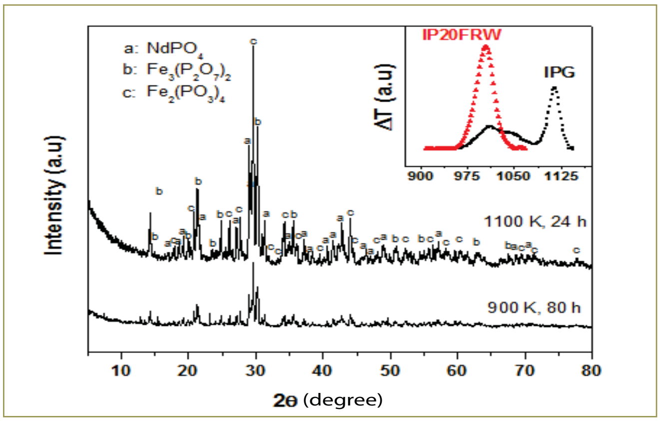

Fig. 3 *XRD pattern of the crystallized IP20FRW; Crystallization curves of IP20FRW and IPG is shown as inset*

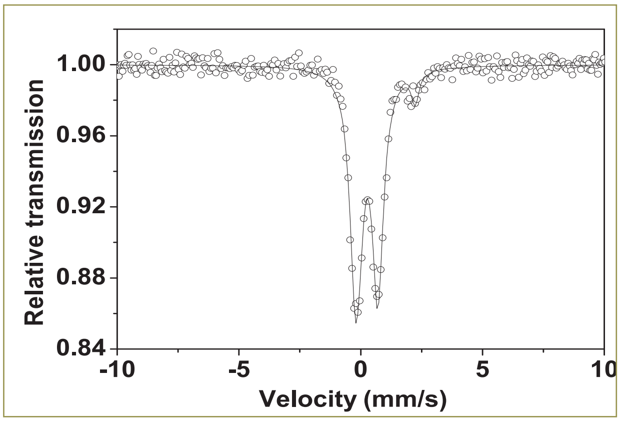

Fig. 4 *Mossbauer spectrum of IP20FRW*

melt to crystallization during cooling) of glass can be evaluated using characteristic temperatures such as glass transition temperature, onset of crystallization temperature and liquidus temperature. The GFA and GS parameters of IP20FRW are found to be comparable with IPG. The estimated critical cooling rate of IP20FRW is also similar to that of IPG. These studies clearly indicate that the glass forming characteristics are not much altered by the addition of 20 wt.% simulated fast reactor waste. It was well established that crystallization of IPG occurs in multi-stages whereas IP20FRW undergoes single stage crystallization (inset of Figure 3). IP20FRW was heated in flowing argon (50 ml/min.) at 1100 K for 24 h. The XRD pattern (Figure 3) of the heat treated IP20FRW clearly indicates the presence of $Fe_3(P_2O_7)_2$ along with $NdPO_4$ and $Fe_2(PO_3)_4$ phases.

Mӧssbauer spectrum of IP20FRW is shown in Figure 4. The spectrum consists of two kinds of quadrupole doublets owing to the variable valency of iron. The observed concentration of Fe^{2+} is slightly higher (8.6 %) for IP20FRW compared to that of IPG (4 %).

Raman spectra of IP20FRW are shown in Figure 5. Depending on the number of bridging oxygen atoms, the phosphate terahedra can be described as Q^3, Q^2, Q^1 and Q^0. Q^3 denotes a fully polymerized neutral unit of structure, while Q^2 is a structure based on chains and rings and it has a negative charge. Q^1 means two corner sharing tetrahedral units and Q^0 means isolated tetrahedra and their charges are -2 and -3 respectively. From the Raman spectra of IP20FRW, it is clear that Q^1 linkages are more predominant compared to Q^2 and Q^0. Though the Raman bands of IP20FRW is downshifted compared to that of IPG, overall structural phosphate network connecting units are similar to that of IPG. Based on the similar viscosity, glass forming ability, glass stability and thermal characterization, it can be concluded that IPG is a potential matrix for the immobilization of fast reactor waste.

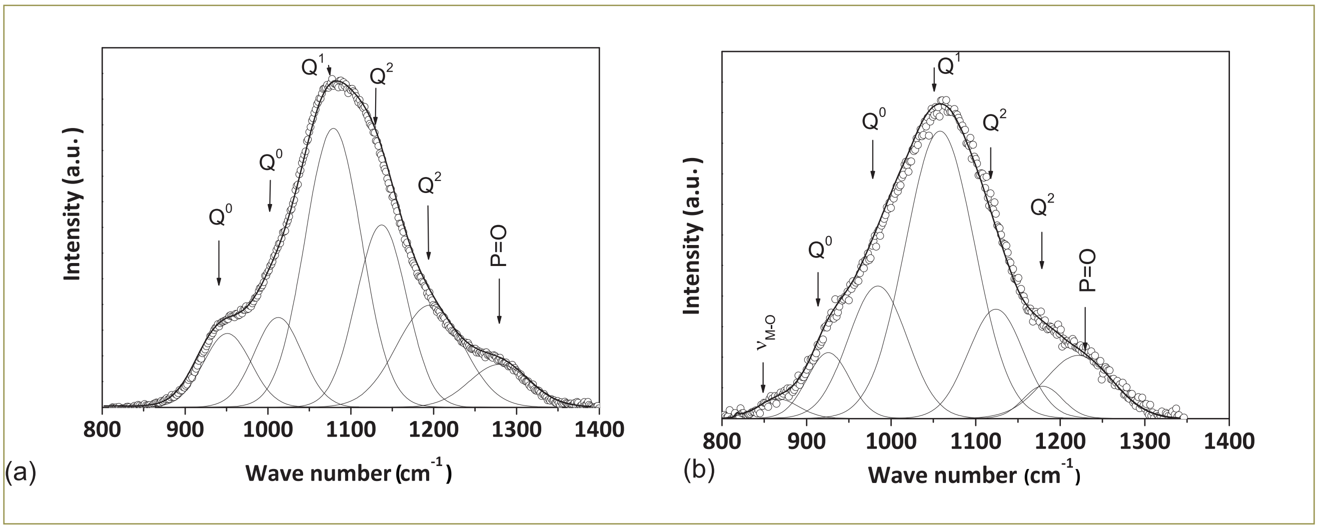

Fig. 5 *Raman spectra of (a) IPG and (b) IP20FRW*

IV.23 Qualification of Hydrogen Gas Sensor for Monitoring of High Level Liquid Waste Storage Tank

High active liquid wastes are stored in tanks in CORAL. The radioactivity associated with the waste results in the radiolysis of water, which leads to evolution of hydrogen. Air is continuously sparged into the tank to avoid H_2 buildup. Lower explosion limit (LEL) for H_2 is 4% v/v. Hydrogen concentration should never be allowed to reach LEL and this calls for purging air for dilution. To ensure that the levels are low, continuous monitoring of hydrogen concentration is required. For this purpose, the functioning of an electrochemical based hydrogen sensor was evaluated. The challenges are the reliability of sensing in the presence of moisture and NO_X gases.

The sensor's range is 40000 ppm (4%) and its resolution is 10 ppm. Figure 1a shows the picture of the hydrogen sensor. Before installation the sensor was tested at the H_2 sensor testing facility in Materials Chemistry Division, Chemistry Group. Parameters such as range, accuracy, flow requirements and cross interference with NO_X were evaluated to qualify the H_2 sensor.

Calibration of the sensor

Calibration of the sensor was carried out using standard high purity hydrogen and air cylinders. Both the gases were mixed in precise proportions using Mass flow controller (MFC). The gas mixture was then passed through the sensor. The current output from the sensor is proportional to the H_2 concentration. The schematic of the calibration setup is presented in Figure 1b.

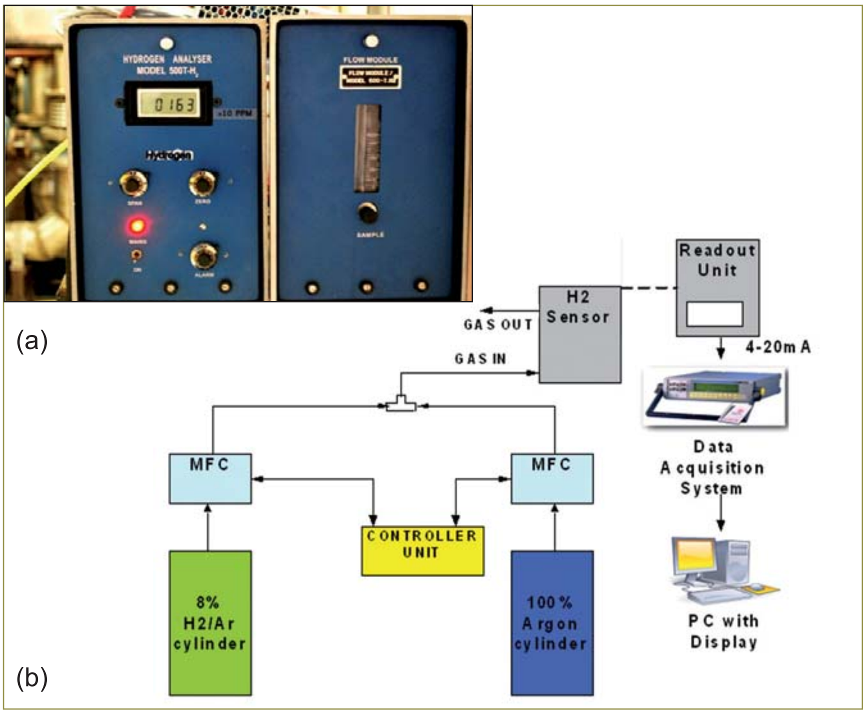

Fig. 1 (a) Hydrogen sensor & its indicator and (b) schematic of the calibration setup

The sensor was fed with known concentrations of H_2 gas. The sensor has a linear response with an accuracy of ± 2.5% of reading.

The sensor response was recorded as a function of flow rate from 50 to 500 sccm. At 50 sccm flow rate, the error was about ±20%. However, from 200 to 500 sccm, the error was found to be less than ±2.5% of reading. Hence, the minimum flow rate required for its operation is 200 sccm, as evidenced from Figure 2.

NOx interference

A synthetic solution simulating high level waste in 4 M HNO_3 was used for evaluating the response of the sensor in the presence of NO_X gases. Hydrogen in air mixture was bubbled through the simulated high level waste solution. The error was noted to be about +9.5% of the reading (Figure 3). Reproducibility in the performance of the sensor was ascertained by repeating the measurements using the same as well as different concentrations of H_2/Air mixture.

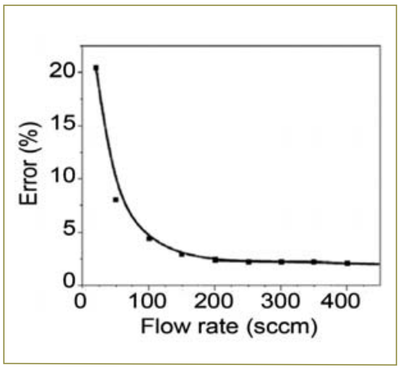

Fig. 2 Plot showing the error at lower flow rates (2.6% H_2/air)

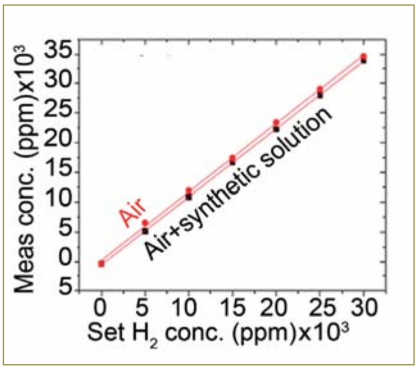

Fig. 3 NO_x interference in simulated high level waste solution

IV.24 Development of Floor Response Spectra for DFRP

The seismic re-evaluation of Demonstration Fuel Reprocessing Plant (DFRP) was undertaken due to revisions in seismic design standards in the recent past. This process was aimed at the assessment of the safety of the existing facility and to determine the seismic risk of the plant with respect to a review level earthquake (RLE). Among the DFRP buildings, extension to reconversion laboratory (ERL) is a two storey building located north of process plant facility (PPF) building, Zone-6. This article is on the generation of floor response spectrum for this building.

Seismic re-evaluation

The extension to reconversion laboratory is a two storied building, 42 metres long in east-west direction, 14.5 metres wide in north-south direction and 10.5 metres in height. The grade slab is at +0.0 metres level, the first floor slab has two levels at +3.5 & +4.75 metres and the corresponding roof levels are at +7.5 metres & +10.5 metres. The ground floor and first floor of the extension to reconversion laboratory houses glove boxes. Structural system of extension to reconversion laboratory is a reinforced concrete (RC) framed structure.

The first floor slab has thickness of 180 mm and roof slab has thickness of 150 mm. The floor response spectra are developed for seismic qualification of equipment that are not modeled with the primary structure.

Mathematical model

The 3D-mathematical model was developed using the finite element software NISA consisting of reinforced concrete slabs, beams, columns and equipment masses, including the effects of soil structure interaction (SSI) as shown in Figure 1. Reinforced concrete beams and columns were idealized using two noded elastic beam elements, which has three translational and three rotational degrees of freedom per node. Reinforced concrete floors were idealized using three dimensional four noded shell element, which has three translational and three rotational degrees of freedom per node. Soil was idealized using two noded spring element, which has three translational and three rotational degrees of freedom per node. Free vibration analysis/Eigen value analysis was carried out by Block Lanczos method to obtain the natural frequencies and mode shapes of the mathematical model of extension to reconversion laboratory building. Table 1 presents predominant modes from the analysis. The mode

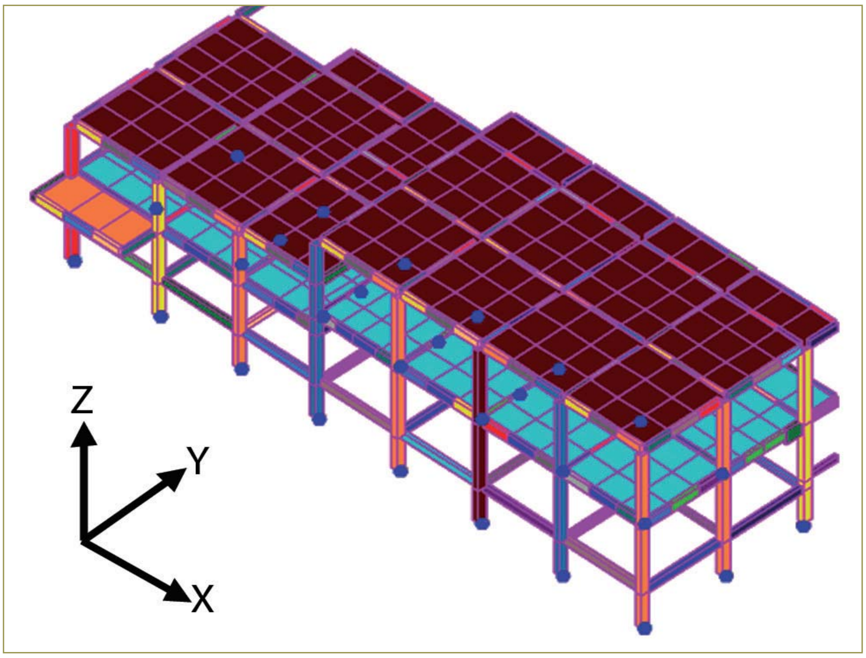

Fig. 1 *Finite element model developed in NISA*

Table 1: Summary of predominant modes in free vibration analysis

Mode No.	Frequency (Hz)	Mass participated (Ton)		
		X	Y	Z
1	1.46	1632.45	4.65	0.00
2	1.64	15.20	978.32	0.17
3	2.12	1.89	687.18	0.11
46	12.09	0.00	11.17	87.86
49	12.22	0.03	2.30	224.45
50	12.26	0.00	0.04	91.45
53	12.57	0.01	0.19	149.02

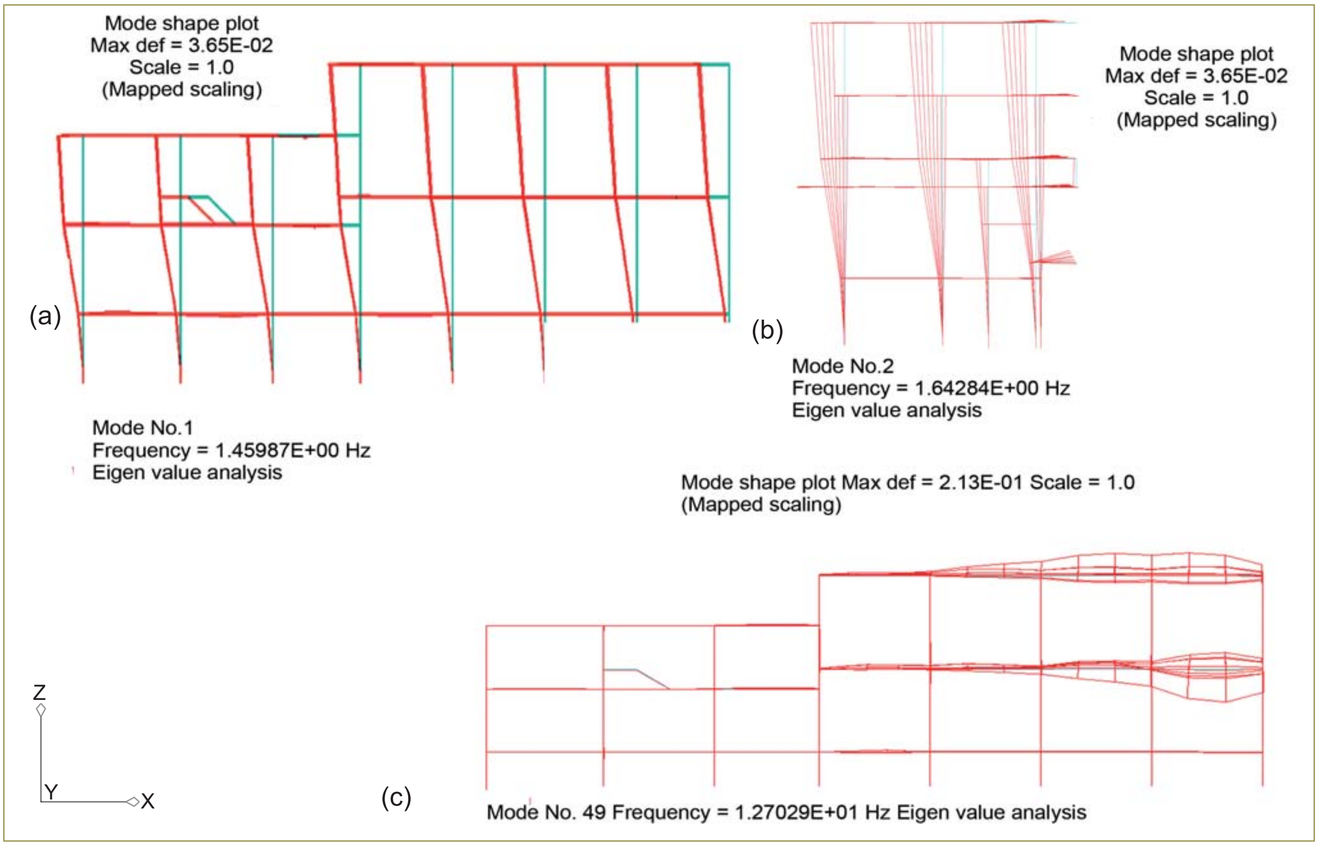

Fig. 2 *Mode (a) shape 1, frequency 1.46 Hz, (b) shape 2, frequency 1.64 Hz and (c) shape 49, frequency 12.22 Hz*

shapes of three predominant modes are shown in Figures 2a to 2c.

Floor response spectra

Time history analysis was carried out by modal superposition method with more than 90% mass accounted for in the modal analysis. For this, three independent spectrum compatible time histories corresponding to the review level earthquake are used as input. From the response histories at the respective nodal locations, the floor response spectra are obtained. The envelope of the floor response spectra at floor +3.50 metres and +4.75 metres floor levels are shown in Figures 3a and 3b respectively for various damping values. X and Y are the horizontal directions and Z is the vertical direction. Floor response spectra for the two floors was generated for different damping values ranging from 2% to 10% so that it may be used for different sub systems and components with different damping. The peak acceleration at both the floor level occurs at 13 Hz for the vertical direction (Z direction), at 2.5 Hz for the Y direction and at 1.5 Hz for the X direction.

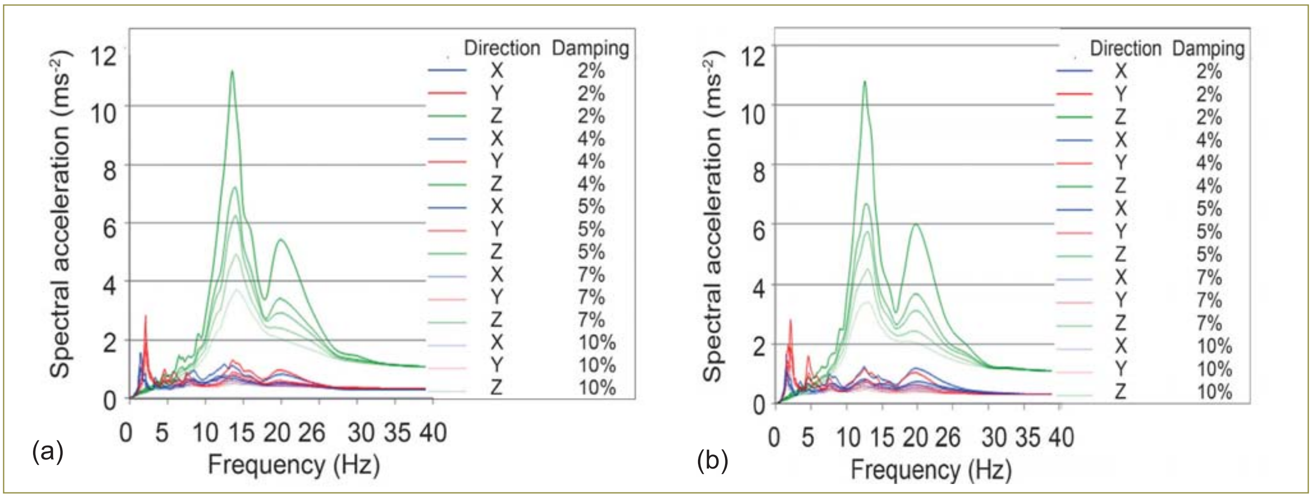

Fig. 3 *Floor response spectra for (a) +3.50 metres and (b) +4.75 metres floor level*

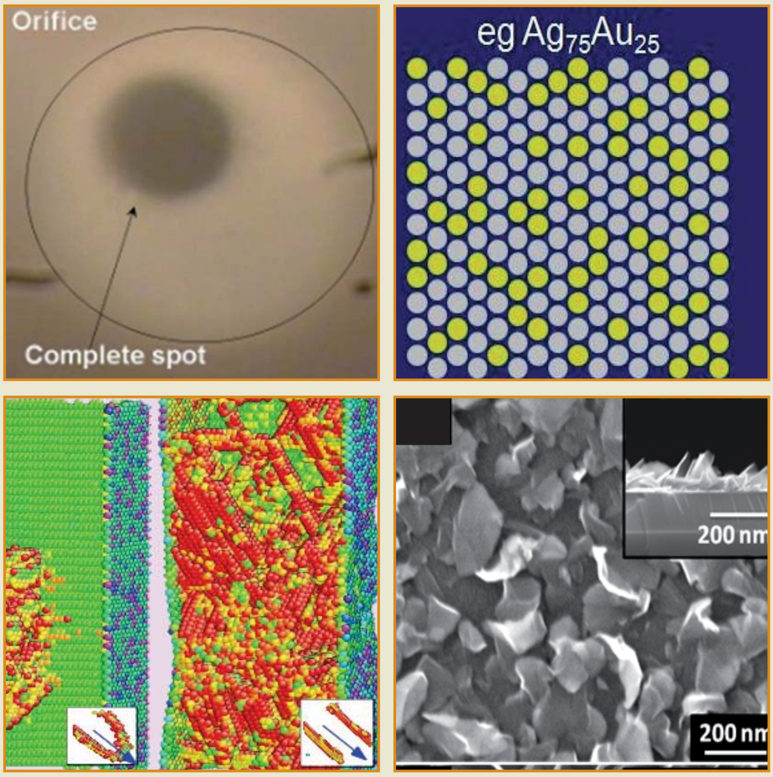

CHAPTER
V

Basic Research

V.1 Dislocation Density Based Constitutive Modelling of Work Hardening Behaviour of Tempered Martensitic Steels

The microstructure of P92 steel consists of initial high dislocation density inside lath, hierarchical boundaries in terms of prior austenitic grains and martensite packets, blocks, sub-blocks, laths and large amount of precipitates. An attempt has been made to investigate the role of geometrical obstacles such as hierarchical boundaries and precipitates present in the steel on the evolution of total dislocation density with plastic strain. In order to incorporate the immobilizing effects of both type of obstacles, i.e., the dislocation density inside lath and the impenetrable geometrical obstacles such as precipitates and the boundaries, the hybrid model for the evolution of total dislocation density with strain has been assumed to be more appropriate and the model has been chosen initially for the work hardening analysis. Parameter sensitivity analysis over optimization results clearly demonstrated the average mean free path arising from the dislocation dense lath/cell boundaries and precipitates act as effective barriers to glide of dislocations over total dislocation population inside the lath in P92 steel. The analysis indicated that the hybrid model reduced to Estrin-Mecking (E-M) one-internal-variable model and the flow behaviour of the steel was adequately described by the E-M approach for the range of temperatures and strain rates examined. The variations in work-hardening parameters associated with the E-M model with temperature and strain rate exhibited three distinct temperature regimes. Signatures of dynamic strain ageing (DSA) at intermediate temperatures and dominance of dynamic recovery at high temperatures have been observed. The variations in the dislocation accumulation parameter (k) and dynamic recovery parameter (k_2) with temperature and strain rate, displaying a marginal increase in values in the temperature range 300-723 K suggest that the dislocation sub-structural behaviour in its totality is not very different in the two temperature regimes of room and intermediate temperatures (Figures 1a and 1b). The rapid increase in the dynamic recovery parameter k_2 with increase in temperature and decrease in strain rate at high temperatures indicate the dominance of dynamic recovery (Figure 1b). This is also reflected in the variations of calculated dislocation density at saturation (ρ_{sat}) with respect to temperature and strain rate (Figure 2). The evolution of predicted dislocation density with plastic strain for different temperatures is shown in Figure 3. The rapid evolution of dislocation density towards steady state value at high temperatures can be seen at 823 and 873 K in Figure 3. This is in contrast to the observed variations in the evolution of dislocation density with plastic strain showing only marginal variations at room (300 K) and intermediate temperatures (573 and 648 K). The measurement of activation energy based on recovery model ($Q_{Cross\text{-}slip}$ = 4.47 kJ mol^{-1} for room and intermediate temperatures and Q_{Climb} = 754 kJ mol^{-1} for high temperatures) suggested that the dynamic recovery is controlled by the dominance of cross-slip of dislocations at room and intermediate temperatures (300-723 K) and climb of dislocations at high temperatures (773-873 K).

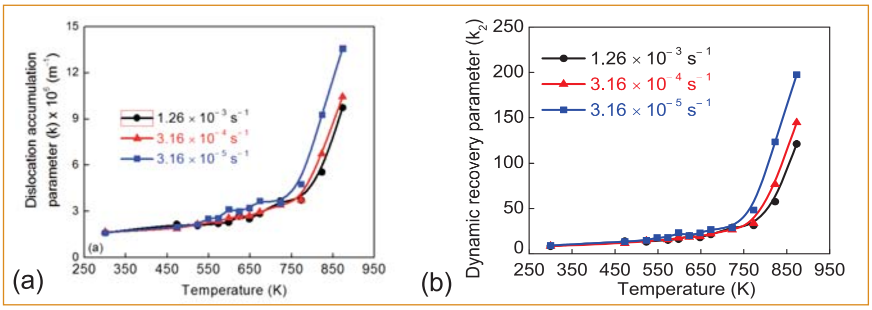

Fig. 1 *Variations of (a) dislocation accumulation parameter, k and (b) dynamic recovery parameter, k_2 with temperature and strain rate (P92 steel)*

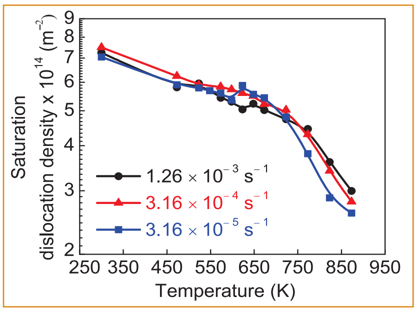

Fig. 2 *Variations of saturation dislocation density with temperature and strain rate (P92 steel)*

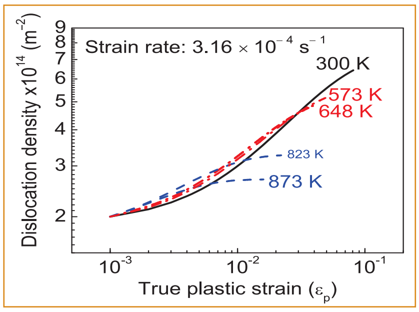

Fig. 3 *Evolution of predicted dislocation density with true plastic strain for different temperatures (P92 steel)*

V.2 HRTEM Study of Precipitate Interfaces in Long-term Aged IFAC-1 Stainless Steel

A phosphorus-enhanced type 316 austenitic stainless steel along with the minor additions of Ti and Si, designated as IFAC-1 is being considered as a candidate alloy for fuel cladding in future sodium-cooled fast reactors. Trapping and recombination of vacancies at the interfaces of austenite matrix with TiC and Fe_2P precipitates is expected to delay the onset of void swelling. Thus, enhancement in swelling resistance is dependent on the microstructural stability of TiC and Fe_2P. The alloy has been subjected to an accelerated thermal ageing test at a temperature of 700˚C for 2 years. The nominal operating temperature for the cladding is 550˚C.

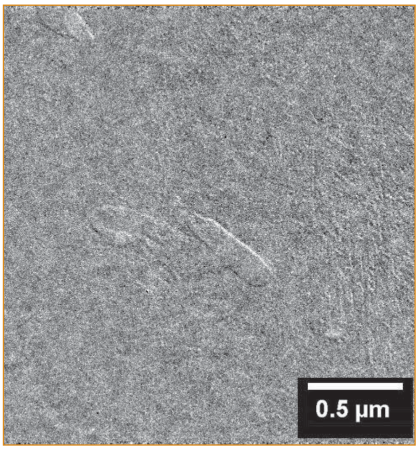

Fig. 1 *Phosphorous L edge EFTEM image showing region of P enhancement adjacent to a precipitate*

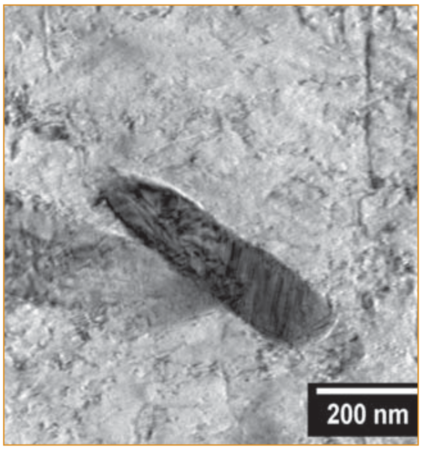

Fig. 2 *Low magnification bright-field micrograph showing the σ phase precipitate in austenite matrix*

Earlier studies have suggested that the Fe_2P occurs as needle shaped precipitates at a scale of 1-10 nm. At this scale, imaging the precipitates is quite difficult with conventional diffraction contrast imaging or X-ray energy-dispersive mapping. In the present work, we have used the electron energy-loss filtered imaging (EFTEM), with spectrometer slit set for 132eV (corresponding to phosphorous L edge) to systematically scan large areas and locate regions of enhanced phosphorous concentrations (Figure 1). In the present alloy, such regions have been found to be frequently associated with Laves, Chi, Sigma or carbide precipitates. Figure 2 shows bright-field image of the region corresponding to Figure 1, to be associated with a precipitate that has been identified as σ phase.Since conventional transmission electron microscopy techniques could not reveal the nature of the region with enhanced phosphorous, phase contrast microscopy has been carried out. Lattice resolution images of the region (Figure 3), were analyzed using Fourier techniques. Power spectra from the regions marked 1, 2 and 3 were carefully measured. Region 1 is found to correspond to the austenite matrix while region 3 is indexed to σ phase. Region 2, extending to about 5 nm from the interface corresponds to the region with higher phosphorous content, as indicated by energy-loss filtered imaging, shows a structure that is distinct from austenite and σ phases. This is indexed to the iron phosphide structure.

From the above studies it can be concluded that Fe_2P is microstructurally stable, without coarsening under long term (two years) thermal ageing at elevated temperature of 700ºC; this will ensure improved void swelling resistance under reactor operating conditions in sodium cooled fast reactors.

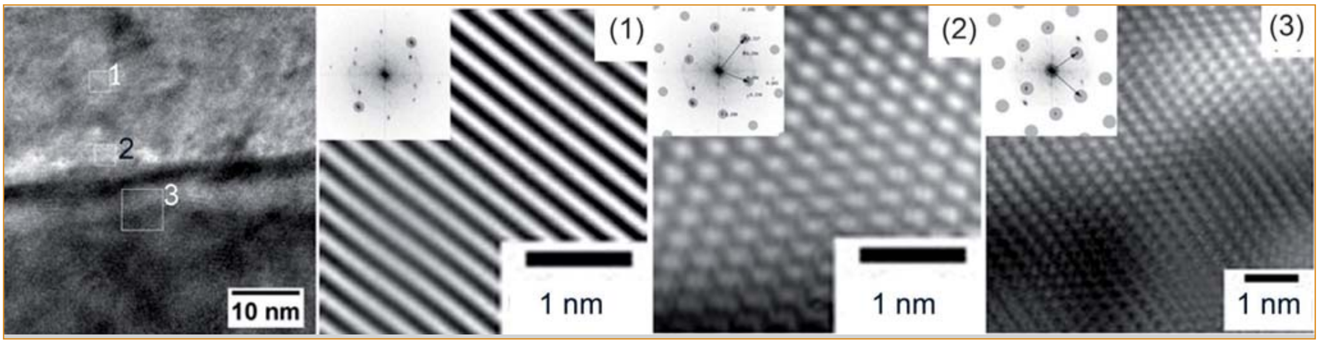

Fig. 3 *Phase contrast image from the interface region in Figure 1 showing (1) austenite, (2) Fe_2P and (3) σ phase lattice images*

V.3 Modeling, Analysis and Simulation of Static Balancing for Redundant Serial Manipulators

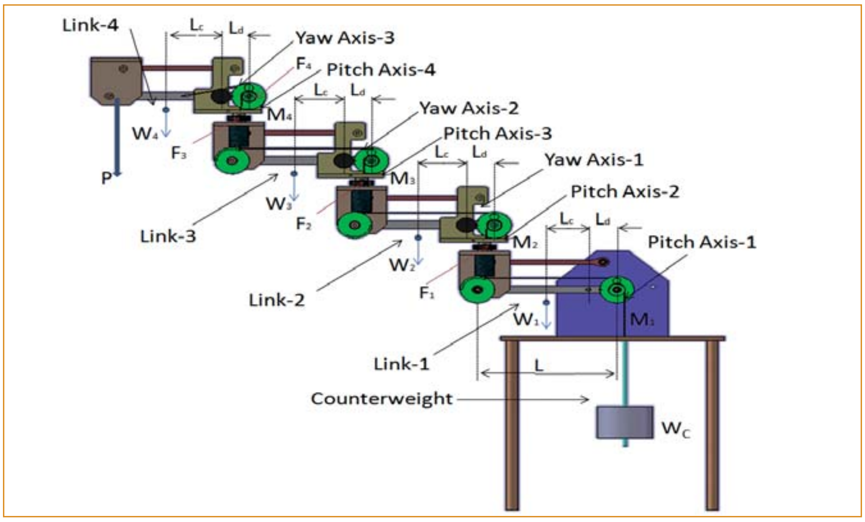

Fig. 1 *CAD model of the manipulator with static balancing mechanism*

All serial manipulator have unique characteristics of large work envelope, dexterity and manoeuvrability. Extending the concept of static balancing, a multilink manipulator with seven revolute joints using a single counterweight, has been conceptualised as shown in Figure 1. Each link has been made up of parallelogram linkages and successive linkages are connected by two orthogonal joints providing pitch and yaw motions. The base joint has only pitch motion along the gravity. This configuration provides the manipulator with a spatial work volume and seven degrees of freedom (DOF). The manipulator has four parallelogram linkages and has four joints. The parallelogram structure of the links makes the joint subject to a constant moment and makes it easier for balancing with a constant force independent of configuration of the manipulator. The single counterweight is located at the base at one end of the wire rope and the other end of the wire rope is routed up to the last link though pulleys located in each of the links. The base link-1 has an extended length (L_d), which carries an idler pulley through which the wire rope carrying the counterweight passes through and subsequently the wire rope passes through idler pulleys at the extended points on each link and respective joints up to the last link-4. Base joint has one degree-of-freedom (DOF) i.e. pitch-1 and subsequent joints have pitch and yaw motions respectively. Only the moment due to friction and inertia needs to be accounted for yaw motions.

Pulleys are of capstan type to prevent slip of wire rope while the links execute the pitching motion. Since the wire rope is connected to each link of the manipulator and each joint has 2-DOF, the manipulator moves with the wire rope during the pitch axis and yaw motions. In view of this, the wire rope is routed as close as possible to the center of the yaw axis. The kinematic parameters of the manipulator are given in Table 1. In this design, any one pitch axis can be actuated independently without disturbing other pitch axis, and the same was demonstrated by simulation. The weight and length of link j is denoted by W_j and L_j respectively, while the distance till the centre of mass of the link is denoted by L_{cj}. The moment from the distal joint to base joint through the adjacent joints can be de-coupled and for any arbitrary intermediate joint j, the gravity-induced moment is:

$$\tau_j = \left[W_j L_{cj} + L_j \sum_{k=j+1}^{n} W_k \right] \cos\theta_j$$

It can be inferred from the above equation that the gravity-induced moment at each joint varies only with its joint angle 'θ_j' and is independent of distal link configuration.

Due to parallelogram linkage structure of the manipulator, the joint takes up a moment due to the weight or load acting at which the joint angle θ_j is 0 and hence the above equation can be written as

$$\tau_j = \left[W_j L_{cj} + L_j \sum_{k=j+1}^{n} W_k \right]$$

The above equation clearly reveals the decomposing of gravity-induced moments into two components: the gravity-induced moment at the joint j due to the weight of the link j and moment due to the weight of all the distal links acting at the successive joint j+1, only over the length of link j (L_j). This results in use of this static balancing method for each

Table 1: Kinematic parameters of the manipulator

Link	Weight (kg)	Joint	Lower limit	Upper limit
1	0.4	Pitch axis-1	-5.5°	+38°
2	0.2	Pitch axis-2 Yaw-1	-40° -160°	+90° +160°
3	0.2	Pitch axis-3 Yaw-2	-40° -160°	+90° +160°
4	0.2	Pitch axis-4 Yaw-3	-40° -160°	+90° +160°

joint independently of other joint configurations. It is to be noted that the wire rope passes through idler pulleys located at the extended length of each link and will aid in independent control over the motion of each joint.

With the single counterweight at the base joint, counteracting force will be different in each joint and it is necessary to maintain counterbalancing force in each link. Hence, a stepped pulley with finite ratio of the radii R_1 and R_2 is used so that necessary tension in the wire will be generated in all the joints depending on the link location and its weight. This is illustrated for pitch axis-4 in the following section, along with Figure 2.

Since each pitch axis is statically balanced, the null moment at that joint will be zero. From Figure 2, the ratio R_1/R_2 can be determined from rope tensions F_3 and F_4, as follows:

$$F_4R_1 = F_3R_2$$

The necessary tension in the wire rope at link-4 and link-3 can be determined by the following analysis of pitch axis-4 and pitch axis-3 joints.

Analysis of joint pitch axis to determine forces

Moment balance at joint pitch axis -4 considering wire rope tension 'F_4':

$$F_4 = \frac{(PL)+(W_4L_c)}{L_d}$$

Similarly moment balance at joint Pitch axis -3:

$$F_3 = \frac{(P_3+P+W_4)L+(W_3L_c)}{L_d}$$

F_3 is the required wire rope tension at link 3. From the above equations, the ratio of R_1 to R_2 can be derived.

$$\frac{R_1}{R_2}=\frac{F_3}{F_4}=\frac{(P_3+P+W_4)L+(W_3L_c)}{PL+W_4L_c}$$

For a general case, the above equation for finding the ratio R_1 and R_2, the equation is formulated as follows:

$$\frac{R_1}{R_2}=\frac{F_i}{F_{i+1}}=\frac{(P_i+P+W_{i+1})L+(W_iL_c)}{PL+W_{i+1}L_c}$$

Simulation

Using the forward dynamics method, simulation was conducted on the model of the manipulator in multi-body dynamic tool to precisely determine the static balancing moment at each pitch joint. Forward dynamics was used for simulation purposes. In this method, a moment of finite value is applied to a pitch axis and the end-effector's motion is analysed. In the simulation of the proposed manipulator, the counterbalancing moment required at each pitch axis to achieve static balancing was studied with a payload of 3 N at the end-effector. The moment was applied at the pitch axis by applying force at a point on each link (where the counterweight is acting on the link) away from the pitch axis by 75 mm for pitch axis-1and 60 mm for pitch axes 2, 3 and 4.

Pitch axis-1

After several iterations, an input force of 112.22 N applied at 75 mm from the pitch axis-1 was just enough to generate the required counterbalancing moment at the pitch axis-1. The moment at the pitch axis-1 was further increased beyond 8.42 N·m by increasing the force to 115 N causing a moment of 8.625 N·m and the arm started moving upward.

Pitch axis-2

After several iterations, an input force of 98.06 N applied at 60 mm from the pitch axis-2 was just enough to generate the required counterbalancing moment at the pitch axis-2. The moment at the pitch axis-1 was increased further beyond 5.88 N·m by increasing the force to 100 N, causing a moment of 6 N·m and the arm started moving upward.

Pitch axis-3

As a result of several iterations, an input force of 57.07 N applied at 60 mm from the pitch axis-3 was just enough to generate the required counterbalancing moment at the pitch axis-3. The moment at the pitch axis-3 was increased further beyond 3.42 N·m by increasing the force to 59 N causing a moment of 3.54 N·m and the arm started moving upward.

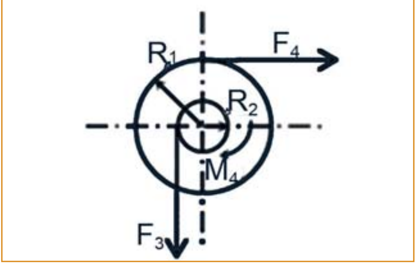

Fig. 2 *Stepped pulley at joint pitch axis-4*

Pitch axis-4

Similarly, an input force of 15.975 N applied at 60 mm from the pitch axis-4 was found to generate the required counterbalancing moment at the joint. The moment at the pitch axis-4 was increased further beyond 0.96 N·m by increasing the force to 16.5 N causing a moment of 0.99 N·m and the arm started moving upward.

The results from the theoretical and simulation studies of the moments without counterweight are given in Table 2. The simulation was conducted in multi-body dynamic tool with static and dynamic friction considered and hence the moments obtained in simulation are higher than the theoretical values. The net moments applied over the balancing moment indicate the torque required for the motors only for accelerating the particular link and this makes the effect of static balancing apparent.

The theoretical analysis and simulation studies clearly show that the proposed static balancing can be applied in n-link serial open kinematic chain to achieve a compact and low profile manipulator for industrial applications.

Table 2: Comparison between theoretical and simulation results

Pitch axis	Theoretical moment (N·m)	Simulation result (N·m)
1	8.24	8.42
2	5.10	5.88
3	3.14	3.42
4	1.17	0.96

V.4 Dynamic Light Scattering Studies of Th(IV) Hydrolysis and Polymerization

Hydrolysis reaction is the primary complexation reaction of actinide elements in aqueous solutions. Tetravalent actinide ions have a strong tendency towards hydrolysis in aqueous solutions and in particular, Pu$^{4+}_{(aq)}$ undergoes hydrolysis even under very acidic conditions. In the polymerisation process, the first step is the formation of mononuclear species which on further condensation leads to the formation of di-, tri- or polynuclear species of colloidal dimensions with more than one metal atom present in it. The Pu(IV) polymeric species formed during the processing of spent nuclear fuels has to be strictly avoided, because it can lead to emulsification in solvent extraction and criticality hazard due to accumulation of Pu metal. Owing to the complexity of Pu(IV) aqueous chemistry, hydrolysis and polymerization studies were perfomed on Th(IV), which was taken as surrogate for Pu(IV). Since aquatic colloids are delicately balanced systems, light scattering technique was employed to characterize the colloids without disturbing the whole system. The light source used was a 780 nm, 3 mW diode laser. The scattered light was measured at an angle of 180^o (Figure 1).

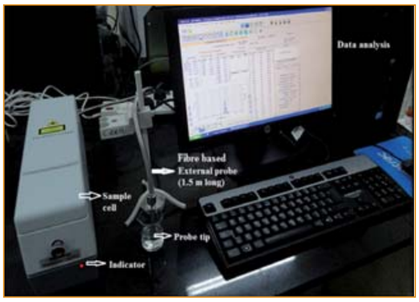

Fig. 1 Light scattering setup

Light scattering experiments were performed at ambient atmospheric conditions on 0.05-0.04 M Th(IV) solutions diluted to different pH. In 0.05 M Th(IV) solution, initial formation of colloids was observed at pH ~0.8. The average size of the colloids formed at this condition was ~15-20 nm. The initial colloids were mainly crystalline ThO$_2$ formed when the solubility of solid ThO$_2$ exceeded. When the concentration was increased to 0.4 M, colloids were observed; however, there was no significant change in size. This shows that well defined colloids were formed. The clear colloid containing solution stored for ageing started aggregating within a day and particles greater than 1000 nm were observed. Formation of small amounts of visible precipitate was noticed after 3 days in 0.2 and 0.3 M Th(IV) solutions (Figure 2).

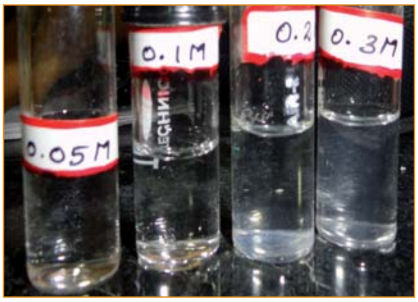

***Fig. 2** Precipitation in 0.2 and 0.3 M Th(IV) colloidal solutions after three days of ageing*

Though ThO$_2$ colloids were formed at very low pH (~0.8 in the present case), Th^{4+} is the predominant species under these conditions. Hence, experiments were repeated by increasing the pH of the solution. At pH ~2.0, colloids of 60-70 nm were formed. These colloids were stable for longer period and did not show variation in size even after ageing for a week. Refractive index (η) of different concentrations of colloidal Th(IV) solutions was measured at 298 K using Anton Paar RXA 156 refractometer equipped with integrated Peltier thermostat with the standard deviation of 2×10^{-5} n$_D$. As the concentration of solute increases refractive index of the solution also increases. The differential refractive index increment obtained from the slope of the plot was used for generating the Debye plot. Molecular weight of the polymer was obtained from the intercept of the Debye plot. The colloids formed at pH ~0.8 had a molecular weight of ~3,449 Da. It shows that these colloids had ~15 thorium atoms at the initial stage. The negative value of second virial coefficient implies that there was aggregation in the system leading to precipitation. The colloids formed at acidic pH tend to agglomerate causing precipitation in the system. But, the colloids formed at higher pH (~2.0) had the molecular weight of ~6,223 Da, with positive second virial coefficient. This polymeric colloid formed due to polynucleation contained about 20 atoms of thorium when initially formed. The solute-solvent interaction in this system is higher leading to greater stability of the system. Hence, it was aged further. The colloids upon ageing for 7 days showed only a marginal increase in the molecular weight (Table 1).

The results confirmed that thorium undergoes hydrolysis and forms polymers of high molecular weight which is similar in nature to Pu(IV) and hence, can be used as an analogue for studying the hydrolytic behavior of Pu(IV).

Table 1: Parameters calculated from the Debye plot

pH	Aging time (days)	Approximate molecular weight, Da
~0.8	0 (Fresh)	3,449
	3	Precipitation
~2.0	0 (Fresh)	6,223
	3	6,727
	7	9,600
	55	43,573

V.5 Ligand Sensitized Luminescence of Uranyl and Europium Ions in Acetonitrile Medium

Trace level estimation of lanthanides and uranyl ions using spectrofluorimetry in aqueous solution is challenging due to low absorptivity and poor fluorescent quantum yields. Fluorescence enhancement of metal ions can be achieved by a technique called ligand sensitized fluorescence. In this process, the metal ion is first complexed to an organic ligand. The organic ligand is then excited by absorption of light followed by energy transfer from the ligand to the excited levels of the metal ions, which then result in fluorescence from the metal ion. If the intra molecular energy transfer from the ligand to the metal is good, this method becomes more efficient in obtaining the fluorescence from the metal than a direct excitation of the metal. Aromatic carboxylic acids such as benzoic acid and diketones such as thenoyltrifluoroacetone, were found to serve as excellent ligands for sensitizing lanthanide ion fluorescence. These metal ligand complexes in presence of synergetic agents such as Trioctylphosphine oxide, enhance the metal fluorescence by another one to two orders by replacing the water co-ordinated to the metal ion. The problem of poor quantum yield can also be tackled if one can perform the experiment in non–aqueous medium. Since coordination of lanthanides to ligand in solution occurs in competition with solvent molecules, being a poor coordinating solvent, acetonitrile can be a good choice to study the luminescence and complexation of lanthanide and actinide ions.

Uranyl benzoate system in acetonitrile

Bare uranyl ion shows poor luminescence in aqueous medium. Improvement in luminescence intensities of uranyl ion have been achieved by ligand sensitized luminescence using ligands such as pyridine di-carboxylic acid and trimesic acid. However, when benzoate was used as a ligand, quenching in uranyl luminescence has been observed

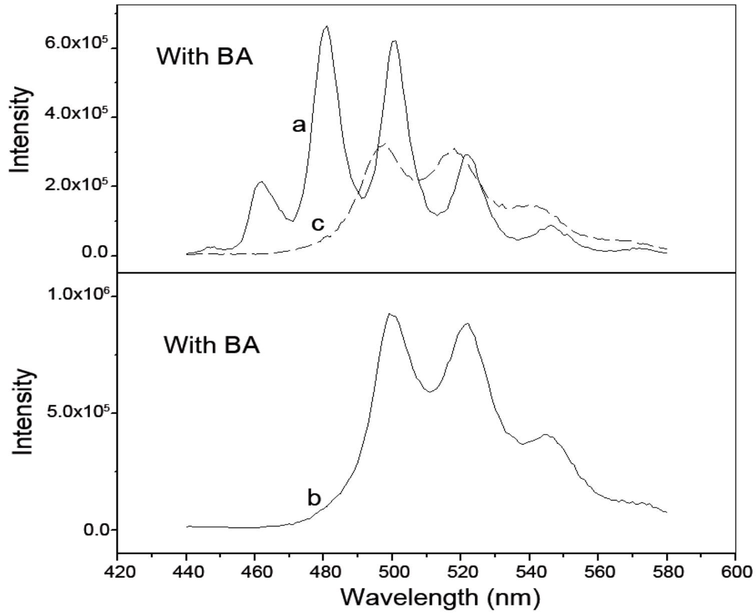

Fig. 1 *Emission spectra of uranyl in acetonitrile (a) with benzoic acid-[UO_2^{2+}]-8x10^{-7} M, (b) without benzoic acid- [UO_2^{2+}]-4x10^{-5} M and (c) with benzoic acid in water- [UO_2^{2+}]-4x10^{-4} M*

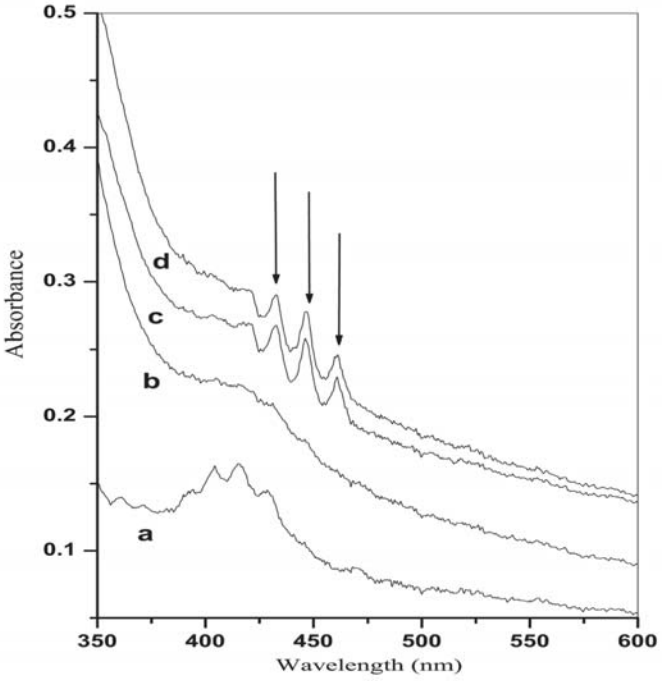

Fig. 2 *UV-Vis absorption spectra of uranyl with different uranyl to benzoate ratio (a) 1:0, (b) 1:2 , (c) 1:3 and (d) 1:4 in acetonitrile*

in aqueous medium. Improvement in luminescence intensity of uranyl benzoate complex (U-BA) was achieved using a non-aqueous media. Among the various non- aqueous media used, uranyl ions showed luminescence enhancement in acetonitrile. Figure 1 compares the emission spectra of uranyl ion in aqueous and acetonitrile medium. The concentration of uranium used in the experiment is given in bracket. The enhancement in luminescence is due to sensitization of the uranyl ion by benzoate. Life time studies on these solutions suggest that benzoate ions displace the water molecules from the primary co-ordination sphere, thereby reducing the non-radiative decay processes. UV-Vis spectroscopy (Figure 2) and luminescence spectroscopy (Figure 3) at different uranyl to benzoate ratio give evidence for tri benzoate species of uranyl i.e $[UO_2(C_6H_5COO)_3]^-$ in acetonitrile medium. The detection limit achieved using the above method is 4×10^{-9} M.

Europium benzoate system in acetonitrile

In the case of europium ion also, a large luminescence is observed from europium benzoate (Eu^{3+}-BA) complex in acetonitrile compared to aqueous medium. Figure 4 compares the luminescence spectra of different europium species in water and acetonitrile medium. There is an enhancement of about 300 times in the luminescence intensity in acetonitrile medium compared to water. The enhancement is a result of sensitization of europium luminescence by benzoate ion and reduction in non-radiative decay channels in acetonitrile medium. In this case also time resolved luminescence spectroscopy and UV-Vis spectroscopy in acetonitrile revealed the formation of ML_3 complex in acetonitrile medium.

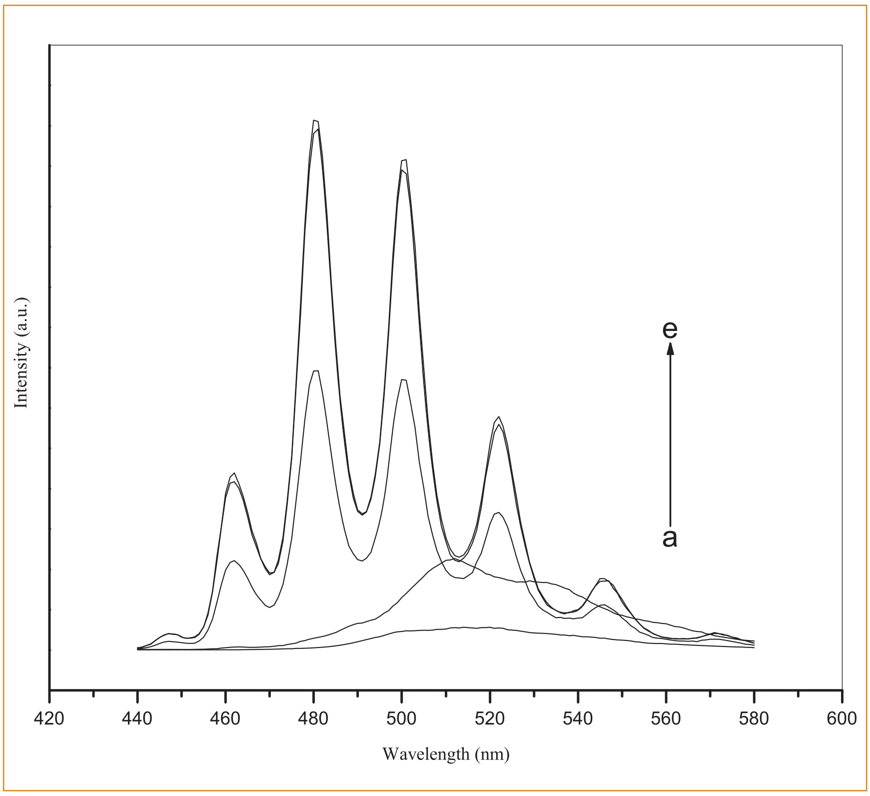

Fig. 3 *Luminescence spectra of uranyl with different uranyl to benzoate ratio a)1:1, (b) 1:2, (c) 1:3, (d) 1:4 and (e) 1:5 in acetonitrile;* λ_{ex} = *243 nm*

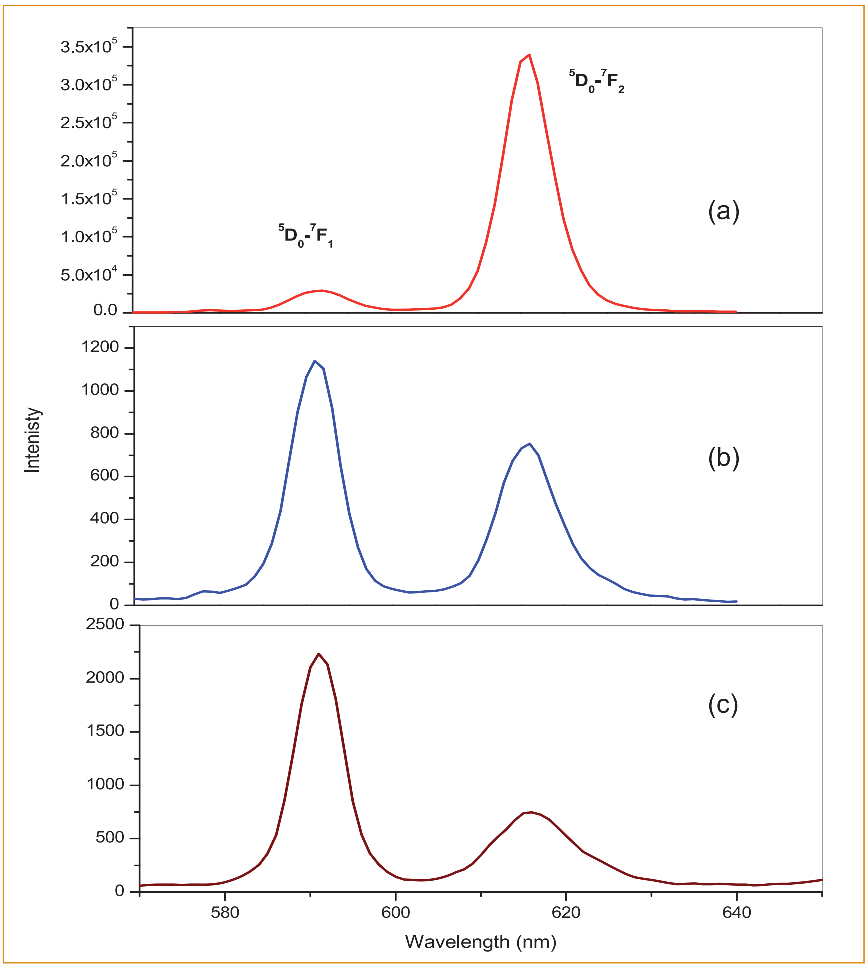

Fig. 4 *Luminescence spectra of (a) uncomplexed* Eu^{3+} *(*2.0×10^{-3}*M) in water, (b)* Eu^{3+} *(*1×10^{-5} *M)-BA (*5×10^{-4} *M) in water and (c)* Eu^{3+} *(*1×10^{-5} *M)-BA (*5×10^{-4} *M) in acetonitrile*

V.6 Structural Stability Studies of Yttria Doped Titania Synthesized by Wet Chemical Route

TiO_2 is a stable functional ceramic oxide used in a variety of technological applications. Doping titania with different metal ions has been extensively used to tailor its properties. These doped ions have been shown to have systematic effects on the thermally driven transformation in titania. The anatase-to-rutile transformation is found to depend on valence state of the dopants. The effect of doping on the structural stability of titania as well as the formation of the pyrochlore $Y_2Ti_2O_7$ is explored by doping titania with yttria. Yttria doped TiO_2 powders were prepared by a sol-gel reaction route from titanium isopropoxide (5 ml) and yttrium nitrate (0.05 Mol) and calcination at various temperatures upto 1673 K. X-ray diffraction data were analysed by Rietveld methodology using general structure analysis system and maximum entropy method. X-ray diffraction studies showed that the as-prepared sample contained anatase with small amount of brookite phase. The powder calcined in the range 423 to 873 K showed both anatase and brookite phases. Above 873 K, the brookite phase started to transform to rutile phase. The sample calcined at 973K showed three phase mixtures of anatase, brookite and rutile phases. At 1073 K, it was observed that the anatase and brookite phases completely transformed to rutile phase in addition to the formation of a small amount of $Y_2Ti_2O_7$ phase. The pyrochlore $Y_2Ti_2O_7$ phase was found to be structuraly stable up to 1673 K. The lattice parameter of Y-doped titania (rutile phase) was evaluated by Rietveld analysis (Figure 1) and was found to be a=4.59651(9) Å, c=2.9605(5) Å and cell volume = 62.549 $Å^3$ with the crystallite size of 384 nm. The lattice parameter and volume increase was in accordance with the size effect of yttria doping into the rutile phase. The lattice parameter of $Y_2Ti_2O_7$ pyrochlore phase at 1673 K was found to be 10.0925(5) Å with the crystallite size of 915 nm. The effect of Y doping was also analysed by maximum entropy method charge density studies that showed clearly the effect of yttria doping into the titania. It is found that the axial bonding between Ti/Y and oxygen becomes very strong (1.9366 Å) in the yttria doped titania as observed in the electron charge density studies (Figure 2).

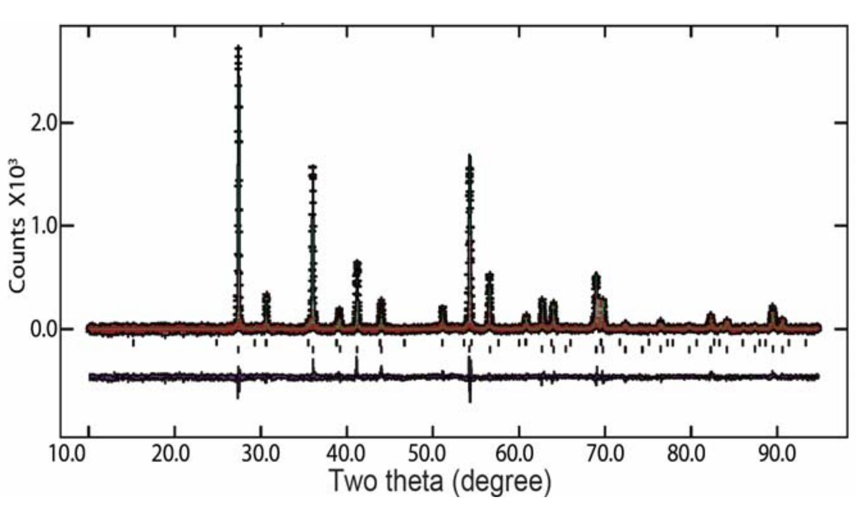

Fig. 1 *Typical Rietveld plot of yttria doped titania calcined at 1673 K shows two phase mixture of rutile and pyrochlore structure of* $Y_2Ti_2O_7$

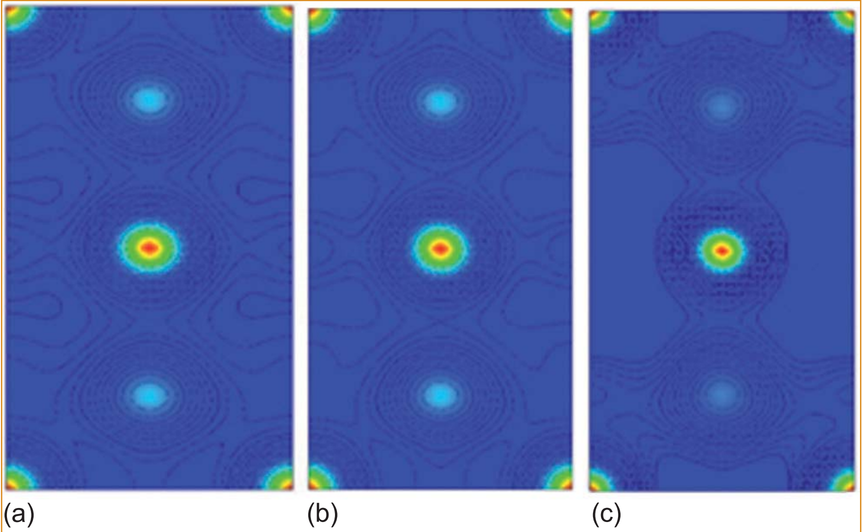

Fig. 2 *Two dimensional electron charge density in (110) plane of yttria doped rutile calcined at (a) 1273 K, (b) 1473 K and (c) 1673 K calculated by maximum entropy method*

V.7 Synthesis and Characterization of Magnetron Sputtered α-axis Oriented AlN Thin Films

Group III nitride semiconductors have attracted a considerable attention in the last two decades due to their unique properties such as wide band gap, electrical insulation, and high thermal conductivity. These properties have led to potential applications in short-wavelength light source/detector and high temperature/frequency devices.

AlN thin films of thickness around 350 nm were grown on Si (100) substrate by DC reactive magnetron sputtering equipment (MECA 2000, France). A 4N pure aluminum target with a diameter of 50 mm in an Ar/N_2 gas mixture (4:1) was used. The base pressure of the chamber was less than 6×10^{-6} mbar, while the sputtering pressure was maintained at 5×10^{-3} mbar. The substrates were heated up to 300°C, whereas the target to substrate distance(TSD) was varied between 100 and 180 mm. X-ray diffraction was used to evaluate the crystalline quality of AlN thin films. The optical constants and hardness were measured using rotating polarizer type ellipsometer (SOPRA ESVG) and a nano-indenter (CSM, Switzerland) with in-situ imaging capability.

Figures 1a to 1d display the XRD patterns of AlN thin films taken for target to substrate distance of 100 nm from room temperature (RT) to 300°C, while Figures 1d to 1f show the XRD patterns for target to substrate distance 100, 140, 180 nm at 300°C. Figures 1a to 1e were recorded in grazing incidence XRD mode. These patterns show polycrystalline hexagonal structure and agree with the JCPDS data card 25-1133 which corresponds to wurzite AlN. GIXRD mode was also utilized to study specimen grown at target to substrate distances of 180 nm and 300°C. However, no pattern could be recorded for this. This led us to speculate that texturing could have occurred and therefore, a B-B geometry was attempted to elucidate the structure.

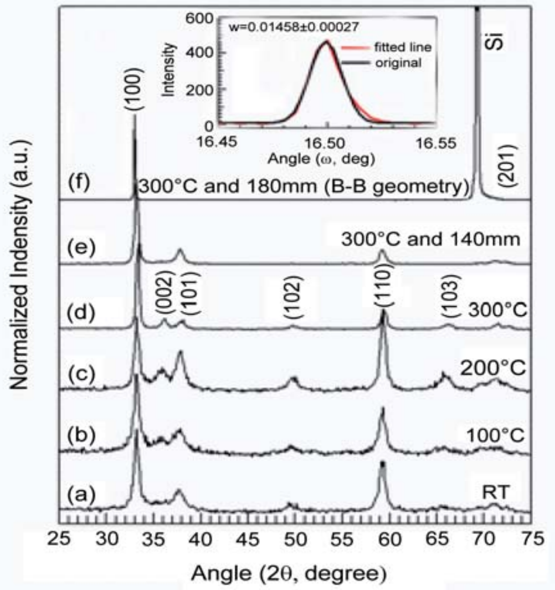

Fig. 1 *(a-d) display the XRD pattern of AlN thin films taken for TSD of 100 mm from RT to 300°C, while (d-f) show the XRD patterns for TSD 100, 140 and 180 mm at 300°C*

Figure 1f taken in B-B geometry clearly points to emergence of texturing, showing a strong peak at 33.170° (2θ) corresponding to (100) oriented a-axis AlN. Due to the presence of tensile residual stress concomitant with an increase in target to substrate distance, the peak (100) shifts to lower Bragg angle i.e. from 33.337 to 33.027°.

Figure 1 (inset) shows the X-ray rocking curve of the highly oriented AlN film with target to substrate distance 180 mm. $\omega^{-2\theta}$ *XRD* scans confirmed that these films are crystalline and show preferred orientation with wurtzite structure. Full width at half maximum (FWHM) from rocking curve of the AlN (100) reflection at 32.998° was measured as 52 arcsec. The increase in FWHM of rocking curve is an indication of relative disorientation of the crystals in the film. If the width of the angular range is small, then the diffracted intensity arises completely from the perfectly orientated crystals.

In wurtzite AlN, two types of Al-N bonds, namely, B1 and B2 co-exist. The energy of formation of B1 type bond is less than the B2 type. (002) and (101) planes are made up of B1 and B2 type bonds whereas (100) plane is constituted only by B1 bonds. Therefore, adatoms with lower energy content are suitable for the formation of (100) plane. According to the formation of a-axis oriented AlN is enhanced when the target to substrate distance is shorter than the mean free path of Al-N dimer. However, this is on the basis of the deposition of a-axis oriented AlN films using the cathodic arc evaporation with a shield, where the energy of the deposited ions is lower. The surface and cross sectional image of this highly oriented film is shown in Figure 2. The surface morphology of this film exhibits a columnar growth with few mound like features growing on the surface. The surface of this film with small protrusions that occur at quite uniform distances is an indication of the Volmer-Weber island type growth mode.

The optical response of the film that was synthesized at a substrate temperature of 300°C with a target to substrate distance of 180 mm which yielded a-axis oriented film (Figure 1) was examined. Figure 3 shows its refractive index (***n***) and extinction coefficient (***k***) in the wavelength range of 200 to 900 nm. While the value of **n** is 1.935 at a wavelength of 546 nm, ***k*** of the film is less than 10^{-2} in this wavelength span. This reveals transparent nature of the films due to the presence of wide band gap. Therefore, it is believed that this is the first report on a-axis oriented AlN thin films coated on Si (100) substrate. The optical property of AlN single crystals as well as thin films has value of ***n***=2.080 at a wavelength of 547 nm. Against this backdrop, a ***n*** value of 1.935 at 546 nm is a significant finding of these investigations.

Design of devices requires solving the problem of controlling residual stress/strain and the defect density contained in the thin solid film. The mechanical characterization is vital to get the above mentioned properties to understand the nature of the films. There are reports on evaluation of elastic stiffness coefficients of AlN and other III-V nitrides by ab initio calculations. The variation of hardness ***H*** with the indenter penetration depth, measured using nanoindentation, is shown in Figure 4. As seen, ***H*** values become steady after about 30 nm penetration depth. The initial ***H*** values (i.e., up to a depth of 30 nm) are not considered because it is known that at shallow penetration depths improper area function can erroneously enhance the hardness values. Therefore, we have reported the average ***H*** and ***E*** (elastic modulus) values of the films that have been recorded across 30-120 nm depth. The average hardness value in the plateau region is 17 GPa. Similarly, the elastic modulus of the films in this region is measured to be 190 GPa. The representative load-displacement curve at higher force (30 mN) is shown in the inset of Figure 4. It shows pop-out behaviour of silicon (film-substrate interface); known to occur due to phase transformation during unloading. However, below P_{max}=1000 μN, no such pop-out in the unloading curve is observed, which indicates that the indenter did not penetrate through the underneath Si substrate. Therefore, it is clear that there is no effect of substrate on the mechanical properties of AlN reported in this study. Moreover, the smooth loading nature indicates the absence of crack or heterogeneous deformation during application of load. In summary, it is observed that target to substrate distance and substrate temperature influence the orientation of the AlN films. The quality of grain orientation was analyzed using XRD rocking curve. The refractive index of a-axis oriented AlN film by ellipsometry is found to be 1.935 for a wavelength of 546 nm. These studies also established superior quality of AlN films synthesized by DC reactive magnetron sputtering. Value of optical response close to single crystal that illustrates absence of scattering centers in the form of defects and pores which is further corroborated from deformation response exhibiting superior mechanical properties as seen from the hardness and elastic modulus values.

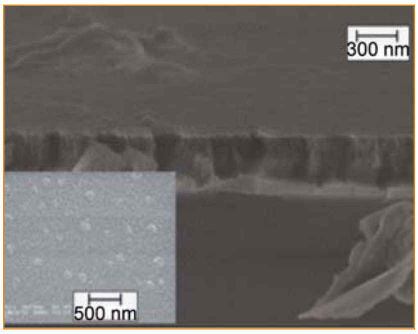

Fig. 2 *Cross sectional SEM image of a-axis oriented AlN*

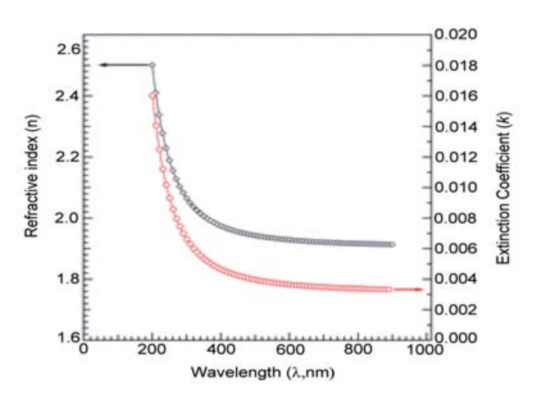

Fig. 3 *n and k values of a-axis oriented AlN film for the wavelength range of 200 to 900 nm*

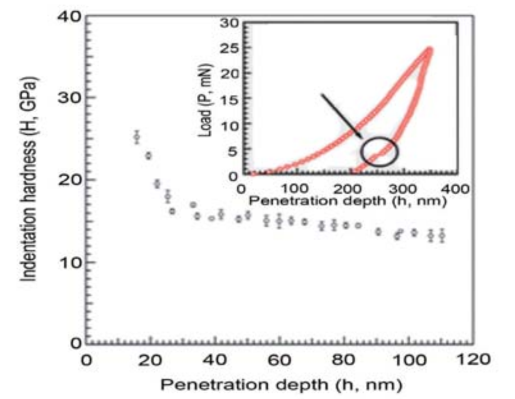

Fig. 4 *Indentation hardness of a-axis oriented AlN thin film*

V.8 Computational and Experimental Investigations on Systems of Relevance to U-Pu-Zr

The solidus and the liquidus temperature of the metallic fuel (U-19Pu-6Zr) was measured by using the spot technique. The experimentally measured solidus and liquidus temperature was 1305 and 1643 K, respectively with an uncertainty of ±5 K.

This spot technique is a method based on thermo-optometry wherein the sample is heated in a Kundsen cell and the optical reflection by its surface is monitored as a function of temperature. The liquid formed upon melting reflects the image of the orifice as a dark spot. When an alloy melts multiple irregular spots are observed at the solidus temperature. These coalesce to form a single spot at the liquidus temperature.

An experimental system housed in a glove box suitable for radioactive alloys was built in-house. Figure 1 shows the experimental system and Figures 2a and 2b show the pictures pertaining to the spots appearing at the solidus and liquidus of the ternary fuel alloy. Figures 3a and 3b show the pictures of the sample before and after melting, respectively that testify the melting of the sample.


Fig. 1 *The ''spot-technique'' equipment*

The phase stability of U-Pu-Zr alloys is important for the evaluation of various thermodynamic properties which subsequently can be utilized to predict properties at compositions and temperatures where experimentation is difficult. This extrapolation is done through the CALPHAD method which utilizes existing experimental data as input using which a Gibbs energy description of various phases is obtained. One of the requirements of modelling U-Pu-Zr system is to have accurate Gibbs energy description of the three binary sub-systems; U-Zr, U-Pu and Pu-Zr. The CALPHAD re-modelling of U-Zr has been recently taken up in our laboratory.

Solution calorimetry of two-phase U-Zr alloys was carried out for measuring their enthalpy of formation at 298.15 K. Aluminum as solvent at 1158 K was used for measuring the thermal effect of dissolution of U, Zr and U-Zr alloys. The enthalpy of formation at 298.15 K was obtained from the Hess's law of heat summation. The enthalpy of formation of x(Zr)=0.561 and 0.965 were estimated to be 0.19 ± 7.3 and -13.9 ± 4.1 kJ/mol-atom.. Apart from providing experimental data as input to CALPHAD modelling, first principle calculations can also be utilized for estimating various thermochemical properties of various phases. The enthalpy of formation of UZr_2 at 0 K was obtained through first principles calculations, using Wien2k and VASP packages within the framework of density functional theory. It was calculated to be -0.65 and 0.78 kJ/mol-atom, respectively which are in reasonable

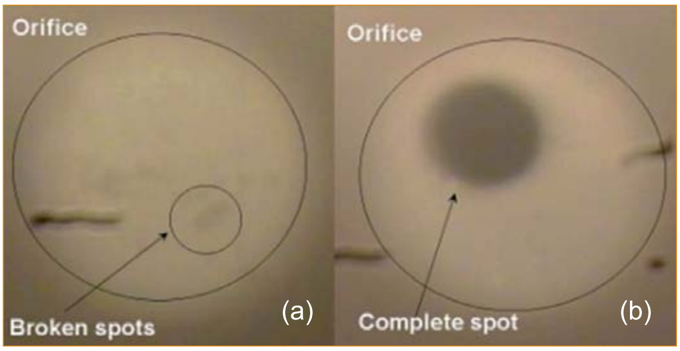

Fig. 2 *Spots observed at the solidus and liquidus of U-16Pu-9Zr (a) onset of melting and (b) completion of melting*

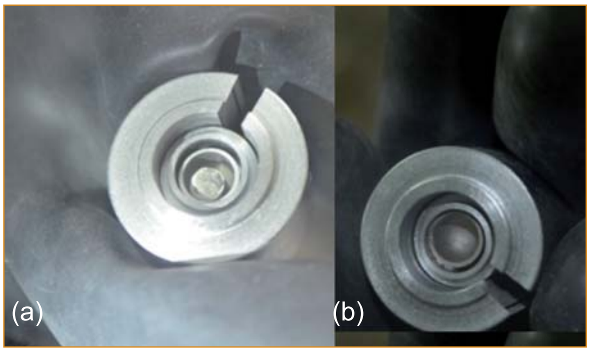

Fig. 3 *Metallic fuel sample (a) before and (b) after melting*

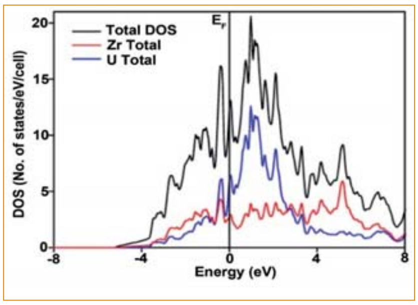

Fig. 4 *Density of states of UZr_2 showing the contribution of U-5f and Zr-4d states*

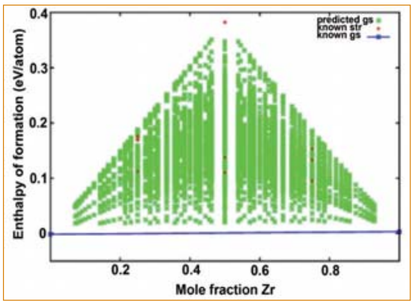

Fig. 5 *Cluster expansion of bcc U-Zr phase*

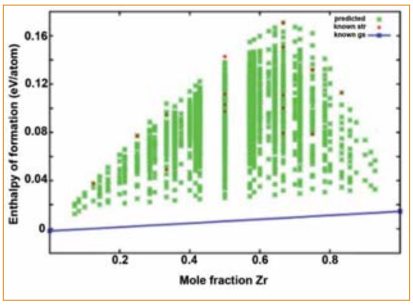

Fig. 6 *Cluster expansion of hcp U-Zr phase*

agreement with the experimental data of -1.3 ± 3.4 kJ/mol-atom. The density of states (DOS) of UZr_2 for a non-spin polarized case is shown in Figure 4 which shows there exists a strong hybridization of uranium-5f and zirconium-4d states around the Fermi level. The contribution to density of states by uranium-5f is maximum near the Fermi level.

The trend in the enthalpy of mixing as a function of composition for the bcc and hcp phases was also obtained through the cluster expansion formalism. This formalism essentially is a compact representation of configurational dependence on the energy of the alloy. This eventually would enable us to predict the energy of any configuration of a particular phase with the knowledge of the energies of a few configurations. The cluster expansion results of bcc and hcp phases of U-Zr system are represented in Figures 5 and 6, respectively suggesting a positive trend in the enthalpy of mixing in these phases.

V.9 Calorimetric Investigations on Rare Earth Titanates and Hafinates

Materials containing elements with large absorption cross-sections for neutrons such as cadmium, boron, hafnium, iridium and their compounds are generally used as control rod materials in nuclear reactors. The rare earth elements, samarium, europium, gadolinium and dysprosium also exhibit relatively large neutron absorption cross-sections, and hence the compounds of these lanthanides are considered as potential candidate materials for use in the control rods of future nuclear reactors. Titanates have been considered as the favorable host material for control rod applications due to their outstanding thermal properties, good mechanical resistance and high stability in corrosive environments. An accurate knowledge of the thermo physical properties of these materials and their behavior during the irradiation is necessary for design of control rod and for modeling their performance. Heat capacity is an important thermodynamic property that determines the temperature dependent variation of all other thermodynamic properties. Hence enthalpy increment measurements of rare earth titanate (Re_2TiO_5), hafinium titanate ($HfTiO_4$) and dysprosium hafinate ($Dy_2Hf_2O_7$) were carried out in the temperature range 750-1660 K (Figure 1) by inverse drop method by using a high

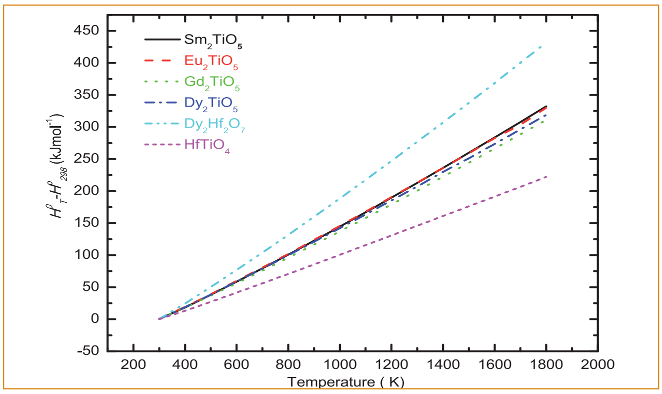

Fig. 1 *Enthalpy increments of Re_2TiO_5 ,$Dy_2Hf_2O_7$ and $HfTiO_4$*

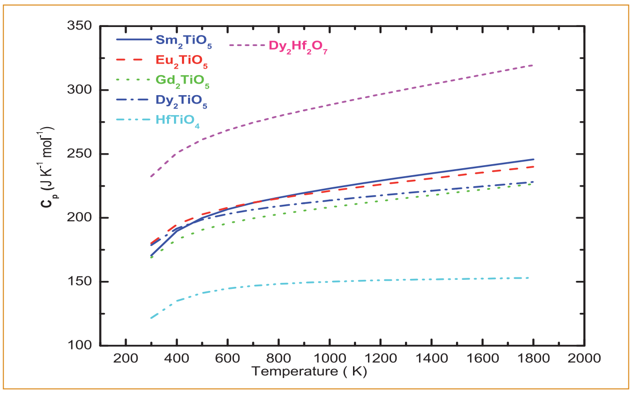

Fig. 2 *Heat capacity of Re_2TiO_5 ,$Dy_2Hf_2O_7$ and $HfTiO_4$*

temperature differential calorimeter. The compounds were prepared by standard solid-state synthesis (ceramic method) route as well as by wet chemical methods and characterized by XRD technique. The measured enthalpy increments were fitted to polynomials in temperature by using the least squares method and the resulting expressions were given in Table 1. From the fitted equation for the measured enthalpy increment data, other thermodynamic functions, namely, heat capacity (Figure 2) entropy and Gibbs energy functions were computed in the temperature range 298-1800 K.

Table 1: Enthalpy increments fitted polynomial equations in temperature using the least squares method

Compound	Enthalpy increment (H^0_T - H^0_{298} (Jmol^{-1})) = aT + 10^{-2}bT^2 + 10^6cT^{-1}- d			
	a	b	c	d
Sm_2TiO_5	200.808	1.2767	3.4154	72460
Eu_2TiO_5	200.490	1.1625	2.4603	69061
Gd_2TiO_5	190.022	1.0281	2.4656	65896
Dy_2TiO_5	199.988	0.8002	2.3560	68240
$Dy_2Hf_2O_7$	255.361	1.8066	3.0342	87918
$HfTiO_4$	151.393	6.8655	2.7114	54293

V.10 Vaporisation Studies over ($NiO+Ni_2Te_3O_8$) in the Ni-Te-O System by Transpiration Thermogravimetry and Knudsen Effusion Mass Spectrometry

Tellurium is one of the volatile and reactive fission products produced during nuclear fission, and it can attack the stainless steel (SS) clad of a fast breeder reactor forming binary metal tellurides, M-Te (M = Fe, Cr, Ni, Mo and Mn) or, if the oxygen potential is sufficient, ternary M-Te-O compounds. Vaporization thermodynamic studies on tellurium and its compounds with oxygen or clad components are of great importance in understanding the fuel-clad chemical interactions in nuclear technology. In continuation of our efforts to generate thermodynamic and phase diagram information on binary M-Te and ternary M-Te-O systems, vaporization studies over ($NiO+Ni_2Te_3O_8$) in the Ni-Te-O system were undertaken. The studies were carried out by transpiration thermogravimetry (TTG) and Knudsen effusion mass spectrometry (KEMS) in the temperature ranges of 960-1085 K and 850-960 K, respectively. From the vapor pressure data deduced over ($NiO+Ni_2Te_3O_8$), thermodynamic properties pertinent to the $Ni_2Te_3O_8$(s) phase were derived. In addition, an estimate of the threshold tellurium potential required for the formation of the $Ni_2Te_3O_8$ phase on the mixed U-Pu oxide fuelled fast breeder nuclear reactor has been made and compared with those available in the fuel-clad gap.

A commercial Mettler Toledo TG/SDTA 851 instrument has been adopted for transpiration thermogravimetric measurements. The TTG measurements involved the use of argon as the carrier gas for vapor transport and derivation of vapor pressures through many flow dependence runs. The KEMS measurements involved identification of the ions in the mass spectrum of the equilibrium vapor and measurement of ion intensities as a function of electron energy or temperature and derivation of vapor pressure through appropriate pressure calibration. The ions observed in the mass spectra of the equilibrium vapor were Te^+, Te_2^+, TeO^+, TeO_2^+ and O_2^+ and the corresponding neutral species were ascertained to be Te_2(g), TeO(g), TeO_2(g) and O_2(g). Because of the high background at the mass where the O_2^+ ion was detected, they were not used in any evaluation. The partial pressures of Te_2, TeO and TeO_2 were deduced from the temperature dependence of ion intensities. To compare the vapor pressures obtained by TTG (shown in Figure 1) and KEMS, it is necessary to calculate the p(O_2) in KEMS so that the total pressure P(tot) = (p(Te_2) + p(TeO) + p(TeO_2) + p(O_2)) could be computed and compared with that obtained by TTG. p(O_2) was computed by evaluating the gas

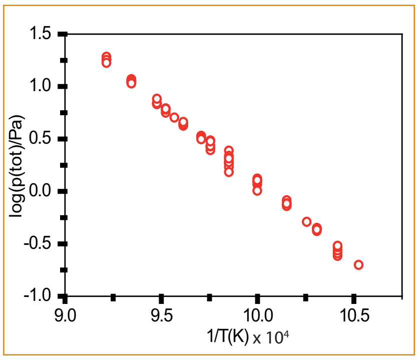

Fig. 1 *Log p(tot) versus 1/T(K) plot from transpiration thermogravimetry studies*

phase equilibria involving O_2(g). The total pressures obtained by TTG and KEMS showed a good agreement with each other. With huge discrepancies existing in the literature for the vapor pressures, the good agreement in the total pressures provides reliable partial and total pressures over this phase region. From the partial pressures, the enthalpies of various homogeneous and heterogeneous reaction were evaluated by the second and third law methods. Subsequently, enthalpy and Gibbs free energy of formation of $Ni_2Te_3O_8$ (s) at T = 298.15 K were deduced.

A thermochemical assessment was made to examine the conditions under which the ternary $Ni_2Te_3O_8$ phase could be formed on SS clad of mixed-oxide fuelled (MO_2; M = U+Pu) fast breeder reactors. Three Pu-fractions (0.20, 0.25, 0.30) and four O/M ratios (1.9998, 2.0000, 2.0002, 2.0004) were considered. The calculations indicate that this ternary phase, like the corresponding phase $Mn_2Te_3O_8$(s) in the Mn-Te-O system, might not be formed on stainless steel clad.

V.11 Thermochemistry of Rare Earth (RE) - Cd Systems (RE: Ce, Pr, Nd, Sm, Eu)

Pyrochemical reprocessing of spent metallic fuel is being developed by employing molten salts of alkali metals as electrolytes in which spent fuel is kept in anode basket and liquid Cd is used as one of the cathodes for depositing the metallic constituents. It has many technological advantages over the conventional PUREX process. Rare earth metals constitute a total of ~23% of fission products formed in fast fission of ^{239}Pu and the elements La, Ce, Pr, Nd, Sm, Eu and Gd are the constituents of this fission yield. It is necessary to avoid their co-deposition with fuel elements during electrorefining for further processing. Studies on RE-Cd systems are relevant to understand the process conditions and hence thermochemical studies employing emf technique to measure the activity of rare earth in RE-Cd (RE: Ce, Pr, Nd, Sm, Eu) systems were taken up. Cadmium rich RE-Cd alloys were prepared by the following procedure: required amounts of RE and cadmium metal were taken in tantalum crucible, sealed inside a quartz ampoule under vacuum and then heated at chosen temperatures for prolonged durations with one intermittent grinding. Using these samples, the following emf cell was constructed:

Ta, RE | LiCl-KCl eutectic + 0.5 wt% $RECl_3$ | RE-Cd alloy, Ta

The cell emf was measured for selected compositions in the same two phase field in the temperature range 400-500°C from which the activity of RE (RE: Ce, Pr, Nd, Sm, Eu) was determined. Figure 1 shows the typical plot of measured EMF for Ce-Cd alloys as a function of temperature. From the EMF value, activity of Ce was derived (Figure 2).

In the similar manner activities of Pr, Nd, Sm and Eu were determined from the respective Cd alloys. These data on activities of rare earth can be used as input for CALPHAD type calculations to optimise the process conditions of pyroprocessing.

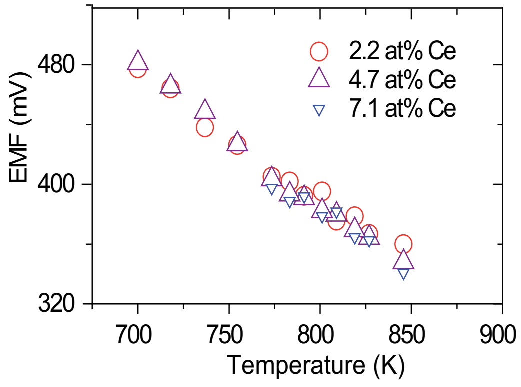

Fig. 1 EMF versus temperature plot for Ce-Cd system

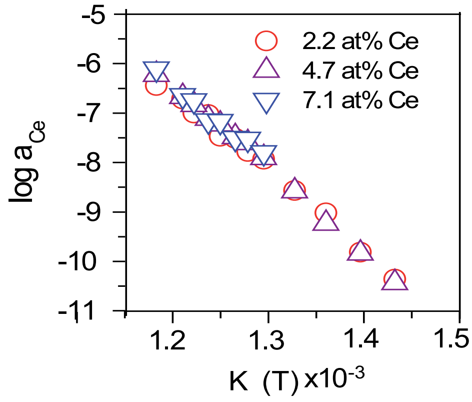

Fig. 2 Activity of Ce as a function of temperature in the Ce-Cd system

V.12 Phase Diagram Studies on Bi-M-O (M: Fe, Cr, Mo) and Pb-Mo-O Ternary Systems

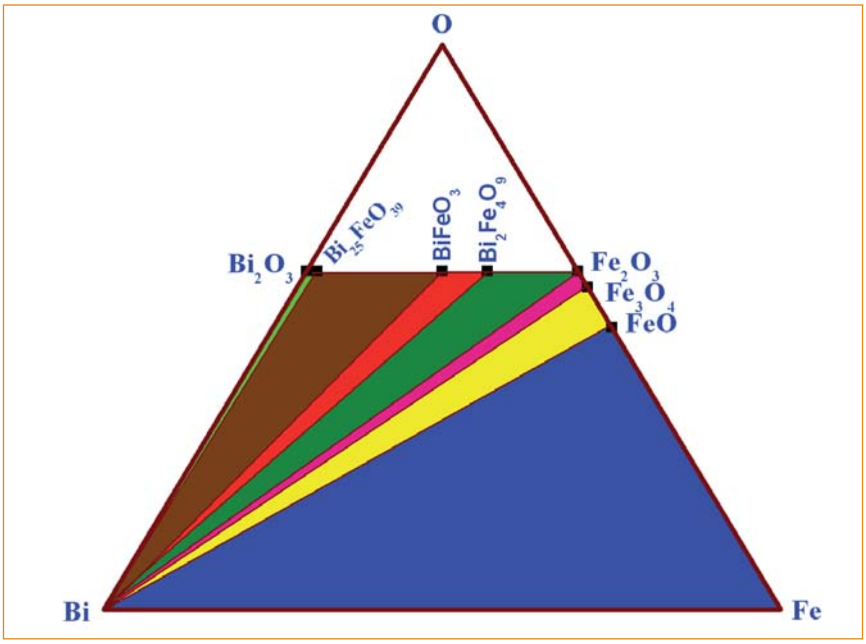

Fig. 1 *Ternary phase diagram of Bi-Fe-O system at 1023 K*

Lead and Lead-Bismuth Eutectic (LBE) alloy are proposed to be employed as spallation target and coolant in accelerator driven systems and as candidate coolant in advanced nuclear reactors. The high corrosivity arising from the dissolution of the components of the structural steel in these liquid metal coolants can be minimized by the in-situ formation of a passive oxide by controlled oxygen concentration. To understand the composition and stability of the passive oxide film, a detailed knowledge of phase diagrams of Pb-M-O and Bi-M-O (M = alloying elements in steel) systems and data on thermochemical properties of the ternary compounds of these systems are needed. Though ternary compounds and pseudo binary phase diagram of the oxides are reported in the literature, no ternary phase diagrams of these systems are reported.

In order to establish the isothermal sections of the ternary phase diagram, the following samples were subjected to long term equilibrations in low volume, evacuated and sealed capsules:

(i) samples with different molar ratios of binary oxides to identify ternary compounds other than those reported in the literature

(ii) samples with different molar ratios of binary oxides with overall compositions in the phase fields and

(iii) samples of ternary oxides after partial reduction under flowing hydrogen followed by thorough mixing of phases.

Further, the phases that coexist with liquid metal were identified by equilibrating appropriate samples with liquid metal. Products of these equilibrations were characterized by XRD analysis. Based on the results, isothermal cross sections of the ternary system valid in the temperature range of 773 to 1023 K were constructed.

Figures 1 and 2 shows the partial phase diagrams of Bi-Fe-O and Pb-Mo-O systems, respectively. In the similar manner, partial phase diagrams of Bi-Cr-O and Bi-Mo-O ternary systems were determined. These ternary phase diagrams were established for the first time.

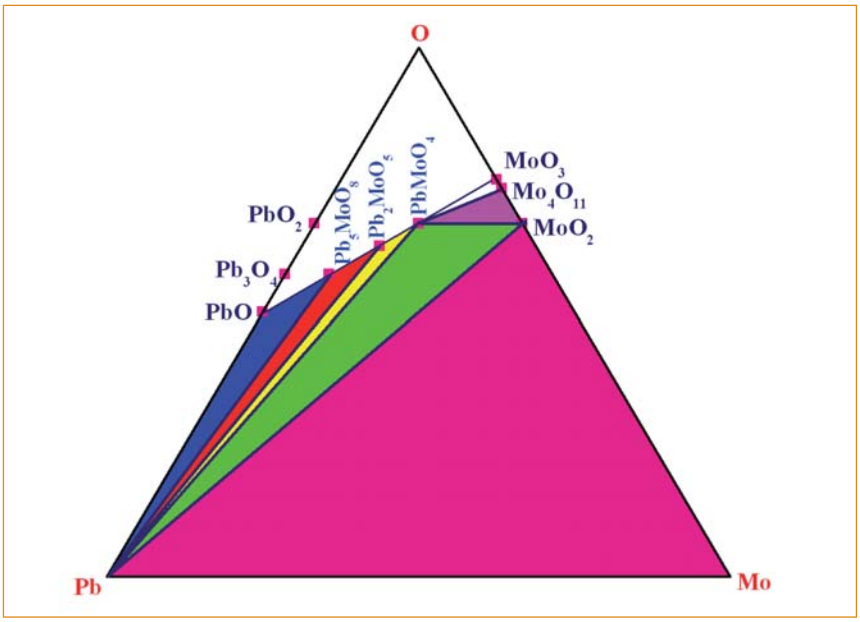

Fig. 2 *Ternary phase diagram of Pb-Mo-O system in the temperature range of 773-998 K*

V.13 A Calorimetric Investigation of High Temperature Phase Stability of U-Cr System

With the advent of U-Pu-Zr based metal fuel in combination with ferritic 9Cr based steel as clad for future FBRs, it becomes necessary to have a comprehensive understanding of the complex high temperature phase equilibria between metal fuel and steel cladding. In this regard, information is rather sparse on U-Cr binary alloys. It may be added that next to iron, chromium is the second most important constituent in ferritic alloys. There is at present little data on phase transformation enthalpies, and transformation kinetics in this important binary system. In view of this situation, an experimental study has been initiated to gather reliable data on high temperature phase stability of U-Cr alloys.

Using reactor grade U and highly pure Cr (99.99 wt.%), U-Cr alloys with x_{Cr}=0, 1, 2, 3, 4, 7, 9, 15 mass% were synthesized in a resistance furnace under flowing highly pure Ar-atmosphere. After a suitable homogenization treatment (1273 K/5h), the density of alloys were accurately measured by immersion technique. Each alloy was then subjected to a slow heating and cooling run (1 K min^{-1}) in a heat flux differential scanning calorimeter to monitor the sequence of on-heating and cooling phase changes including melting, together with associated enthalpy effects. The major results are described below.

Figure 1 illustrates the typical differential scanning calorimeter profile obtained with U-1 wt.% Cr alloy at 1 K min^{-1} heating and cooling rate. The transformation arrests associated with various solid state phase changes and melting are immediately apparent from this figure. The transformation temperatures and enthalpies are obtained from this slow heating DSC trace, after due calibration with pure uranium. A certain degree of undercooling is found for cooling induced phase changes, and this undercooling is also sensitive to Cr-content. In view of this, the measured on-heating phase transformation temperatures are used for phase diagram construction.

Figure 2, compares the measured data on transformation temperatures for various alloy compositions. It can be seen from the figure that measured liquidus and other transformation temperature data compare well with the assessed U-Cr equilibrium diagram. However, for higher Cr-content alloys, the measured liquidus temperatures deviate by +30 K from corresponding phase diagram estimates.

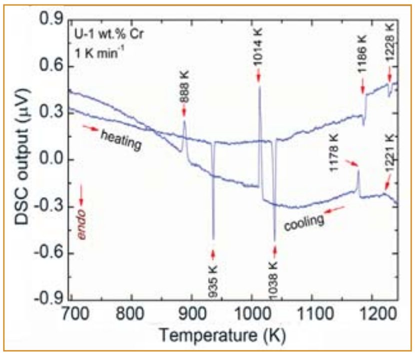

Fig. 1 *Typical slow on-heating and cooling differential scanning calorimeter trace obtained with U-1Cr alloy*

In Figure 3, the measured composition dependence of melting enthalpy, indicated as peak area is illustrated. Similar data have also been obtained for all solid state phase transformations, but are not presented here for the sake of brevity. The phase boundaries traced by present measurements exhibit good agreement with the assessed phase diagram. The measured phased transformation enthalpy data on U-Cr system constitute, probably the first report in literature so far. Further experimentation and modelling of the liquidus curve and kinetics of solid state phase transformations as a function of composition are currently under way.

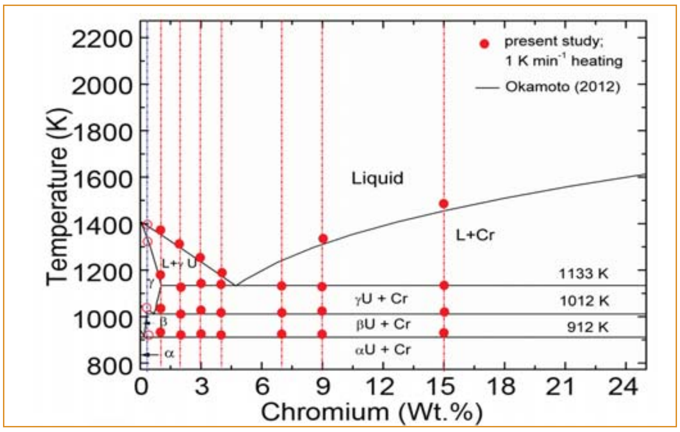

Fig. 2 *Assessed U-Cr phase diagram, on to which, the present measurements are superposed*

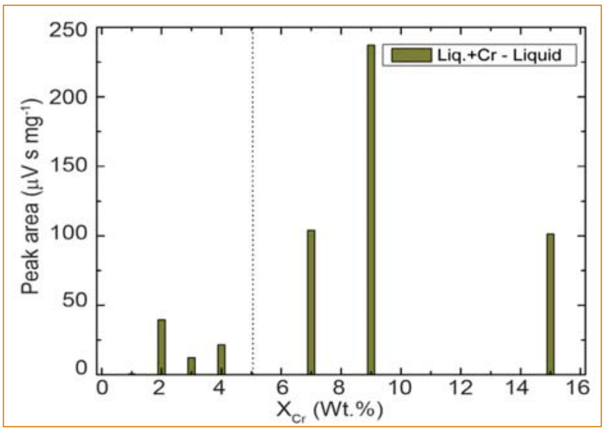

Fig. 3 *Variation of measured melting enthalpy as a function of Cr content*

V.14 Thermodynamic Stability of Oxide Phases of Fe-Cr based ODS Steels via Quantum Mechanical Calculations

The oxide dispersion strengthened (ODS) steels are known to have improved resistance to damages due to both irradiation and high-temperature creep. The ODS steels are manufactured by mechanical alloying (MA) of elemental metallic (Fe, Cr, Al, Ti) powder with Y_2O_3 powder in a ball mill followed by consolidation through hot extrusion. This produces a high density of uniform dispersion of oxide nano-precipitates in the ferrite matrix. These oxide precipitates are known to be ultra-stable, with no coarsening even after 14000 hours of creep tests at 800°C, or extended heat treatment at 1300°C and in intense neutron irradiation fields.

The structure and formation mechanism of the oxide precipitates in ODS steels have been studied widely using X-ray diffraction, high resolution transmission electron microscopy, small angle neutron and X-ray scattering and atom probe tomography. These studies show that ball milling mechanically dissolves Y_2O_3 in the ferrite matrix and produces highly supersaturated matrix. The decomposed Y_2O_3 re-precipitate during hot consolidation in the form of nanoscale clusters and near stroichiometric oxides such as $Y_2Ti_2O_7$, Y_2TiO_5, and Y_2O_3 in steels based on Fe-14Cr-1Ti-0.3Mo-0.3Y_2O_3 and $Y_4Al_2O_9$ and $YAlO_3$ in steels based on Fe-16Cr-4Al-2W-0.3Ti-0.3Y_2O_3. Moreover, it is likely that the solutes combine with Fe and Cr and form oxides based on Y-Fe-O, Y-Cr-O, and Fe-Cr-O systems.

In order to understand the phase stability of likely oxides in typical ODS steels, we computed the formation enthalpies of all the probable binary and ternary oxides based on the Fe-Cr-Ti-Al-Y-O system using the Density Functional Theory (DFT) simulation package VASP. Figure1 shows the calculated formation enthalpies plotted as a function of oxygen fraction in the compounds. It is evident that Y_2O_3, $Y_4Al_2O_9$, Y_2TiO_5, $Y_2Ti_2O_7$ and $YAlO_3$ oxides have relatively low formation enthalpies. These are indeed the oxides which are often observed in the microstructure of typical ODS steels. This shows that our DFT calculated formation enthalpies give correct representation of relative stability of likely oxides in ODS steels. Further, formation enthalpies are valuable data for the CALPHAD modeling of phase equilibrium.

Next, we examined the formation mechanism of the oxides via reaction energies. Reaction energy is the energy of a compound relative to the energy from combination of other phases. The convex-hull of reaction energies, a graph of reaction energies as a function of composition, effectively evaluates the stability of a given compound against any linear combination of compounds that have the same average composition. Therefore, we computed reaction energies of 122 likely oxidation or reduction reactions in typical ODS steels. From the pseudo-convex-hull of formation enthalpies, shown in Figure 1, it is evident that oxides of Fe-O, Cr-O, Fe-Cr-O, Y-Fe-O, Y-Cr-O and Fe-Ti-O systems have relatively higher formation enthalpies, appear away from the convex-hull and therefore can be assumed to be unstable compared to those based on Y-Al-O and Y-Ti-O systems which are found at the bottom of the hull. Therefore, to determine the phase stability, we consider only reactions in the Y-Al-Ti-O system. In typical ODS steels with a significant concentration of Al, Ti is not seen to have an appreciable effect on the formation of oxides of the Y-Al-O system. Hence, we first consider

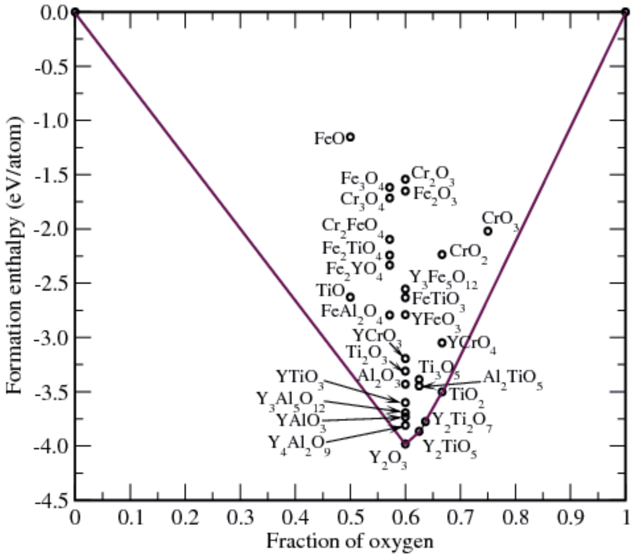

Fig. 1 *DFT computed formation enthalpies of likely oxides of ODS steels plotted as a function of oxygen fraction*

reactions in the Y-Al-O system. Figure 2 shows the projection of the convex-hull of the Y-Al-O system. It shows that Y_2O_3, Al_2O_3 and $Y_3Al_5O_{12}$ are the ground-states, besides the elemental phases. $YAlO_3$ and $Y_4Al_2O_9$, shown by open circles, are placed slightly away from the convex-hull. Table 1 shows the relevant reactions, 1 to 9, for the formation of Y-Al-O ternary oxides. Energies of these reactions show a preference for the formation of $Y_3Al_5O_{12}$. This indicates that, initially the O atoms in the steel matrix combine with solute Y and Al atoms (facilitated by redox interaction) leading to nucleation of Y-O and Al-O complexes, each perhaps in a 2:3 ratio. However, the chemical driving force makes $Y_3Al_5O_{12}$ to nucleate at the expense of Y_2O_3 and Al_2O_3. Moreover, all of above nine reaction energies are of the same order of magnitude. This shows that $YAlO_3$, $Y_4Al_2O_9$ and $Y_3Al_5O_{12}$ can be formed simultaneously by slight changes in the production process. For the Y-Ti-O system, it is evident from Figure 1 that the ground-states are Y_2O_3, TiO_2, Y_2TiO_5 and $Y_2Ti_2O_7$, all of them placed on the pseudo-convex-hull. The relevant reactions for Y-Ti-O oxides are 10 to 13 in Table 1. These reactions show that Y_2TiO_5 and $Y_2Ti_2O_7$ are favored with reference to Y_2O_3 and TiO_2, and hence their presence in the microstructure of ODS steels.

Table 1: Selected reaction energies of oxides of typical ODS steel

Sl.No.	Reaction	ΔH(eV/atom)
1	$Y_2O_3+Al_2O_3 \rightarrow 2YAlO_3$	-0.022
2	$Y_4Al_2O_9+Al_2O_3 \rightarrow 4YAlO_3$	-0.010
3	$2Y_2O_3+Al_2O_3 \rightarrow Y_4Al_2O_9$	-0.016
4	$3Y_2O_3+5Al_2O_3 \rightarrow 2Y_3Al_5O_{12}$	-0.051
5	$Al_2O_3+3YAlO_3 \rightarrow Y_3Al_5O_{12}$	-0.034
6	$Y_2O_3+Y_3Al_5O_{12} \rightarrow 5YAlO_3$	+0.018
7	$7Al_2O_3+3Y_4Al_2O_9 \rightarrow 4Y_3Al_5O_{12}$	-0.042
8	$7Y_2O_3+2Y_3Al_5O_{12} \rightarrow 5Y_4Al_2O_9$	+0.011
9	$2YAlO_3+Y_2O_3 \rightarrow Y_4Al_2O_9$	-0.001
10	$Y_2O_3+TiO_2 \rightarrow Y_2TiO_5$	-0.065
11	$Y_2O_3+2TiO_2 \rightarrow Y_2Ti_2O_7$	-0.038
12	$Y_2Ti_2O_7+Y_2O_3 \rightarrow 2Y_2TiO_5$	-0.040
13	$TiO_2+Y_2TiO_5 \rightarrow Y_2Ti_2O_7$	+0.010

For the formation of oxide nanoparticles in MA/ODS steels, recent experimental studies have proposed a mechanism in which (i) fragmentation of starting Y_2O_3 particles forming finely dispersed fragments occur during early stages of milling, (ii) agglomeration of fragments mixed with matrix constituents form amorphous agglomerates during later stages of milling and (iii) crystallization of the amorphous agglomerates larger than a critical size (20Å) occurs to form oxide nanoparticles during consolidation at 1150°C. It is thus plausible that ball milling mechanically dissolves Cr, Al, Ti and Y_2O_3 in the iron matrix and produces a supersaturated solid solution. The supersaturated ferrite matrix lowers its energy through re-precipitation of the decomposed solutes during the hot consolidation in the form of nanometric clusters and complex stoichiometric oxides such as $Y_2Ti_2O_7$, Y_2TiO_5, and $Y_4Al_2O_9$. The prevailing chemical driving force determines the kind of oxide phase being formed. Our calculated formation and reaction enthalpies show that the chemical driving forces favor the formation of Y_2O_3, $Y_4Al_2O_9$, $YAlO_3$, $Y_3Al_5O_{12}$, $Y_2Ti_2O_7$ and Y_2TiO_5, corroborating their experimental observation.

It is pertinent to note here that the extraordinary mechanical properties of ODS steels is ascribed to the large number of uniformly dispersed highly stable oxide nano-particles smaller than 50 Å. For the structure of these nano-clusters, several structural models are proposed in the literature. A recent experimental study shows that the oxide nanoclusters embedded in the BCC-Fe matrix have a defective NaCl-type TiO structure with a chemical composition of $Ti_{43.9}Y_{6.9}Fe_{3.4}Cr_{1.1}O_{44.7}$.

Formation energies calculated using supercells based on this model are found to be higher than that of TiO, suggesting that the model is unstable. Calculation of coherency strain energy between the oxide nano-particles and the ferrite matrix is planned. We aim to explain the ultra-high stability of the oxide nano-particles against coarsening by combining the bulk formation enthalpies and coherency strain energies.

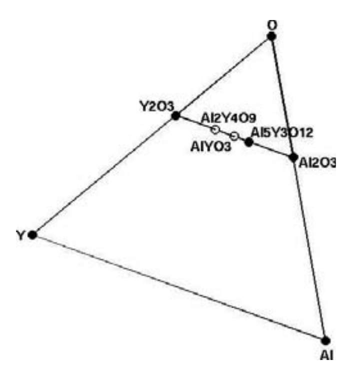

Fig. 2 *Projection of the convex hull of 0 K formation enthalpies of Y-Al-O system. Stable phases are indicated by solid circles. Unstable phases are indicated by open circles*

V.15 Structural, Magnetic and Dielectric Studies on $Gd_{0.7}Y_{0.3}MnO_3$

Materials exhibiting more than one ferroic property with a coupling between them are called multiferroic. Such materials would widen the horizon of applications as one ferroic property could control/modify another. Though coupling between piezo and electric properties is well known, coupling between magnetic and electric is atypical as they are antagonistic to each other. However, manganites with Perovskite structure do exhibit such a coupling. Though the coupling is robust, the critical temperatures are much below ambient temperature, typically 30 K. However, the coupling leading to multiferroic property is of great scientific importance. It is being realized that these materials also exhibit strong magneto-elastic coupling which bring out ferroelectric transition.

Here we report studies on inducing ferroelectric property in an otherwise paraelectric and antiferromagnetic $GdMnO_3$ by 30 at.% substitution of Gd^{3+} with Y^{3+}. Substitution results in requisite structural modification to observe ferroelectric property. The magnetic, dielectric and structural studies in the temperature interval 5 to 70 K were carried out employing thermomagnetization, specific heat, broadband impedance spectroscopy and synchrotron based powder X-ray diffraction (XRD) respectively.

The XRD pattern of $Gd_{0.7}Y_{0.3}MnO_3$ system could be indexed to orthorhombic symmetry belonging to P*bnm* space group. Upon substitution of yttrium, the lattice parameters contract anisotropically. However, the relation $c/\sqrt{2} < a < b$ corresponding to O'distortion of the orthoPerovskite is obeyed. Observed decrease in the lattice parameters is in accordance with the smaller ionic radius of Y^{3+} (1.075 Å) compared to that Gd^{3+} (1.107 Å). Also, estimated average *Mn-O-Mn* bond angle is reduced from 146.1° (for $GdMnO_3$) to ~144.8° and fall in the window range that is amenable for observation of multiferroic property.

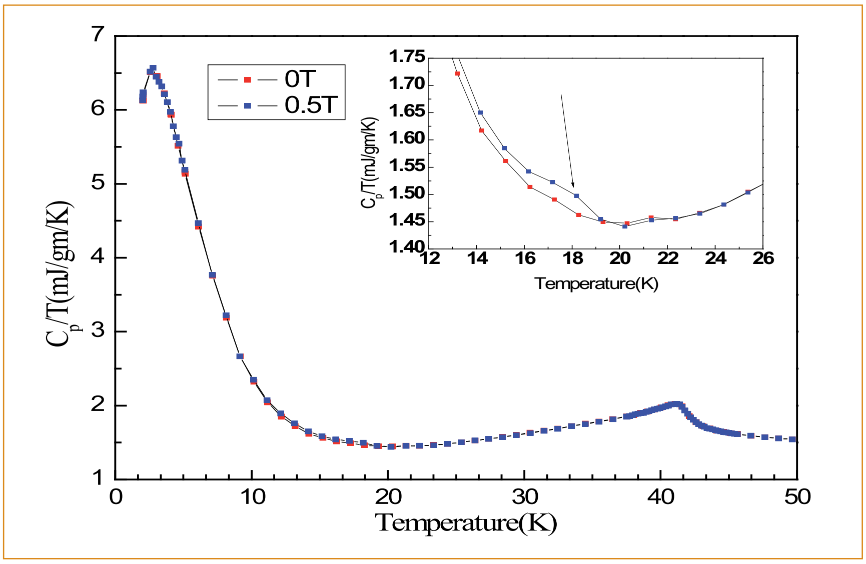

Fig. 1 *Cp/T versus T plot for* $Gd_{0.7}Y_{0.3}MnO_3$ *under an applied magnetic field of 0 and 0.5 T. Inset shows expanded view of the same plot in the temperature interval 12 to 26 K*

From thermomagnetization studies, the susceptibility is seen to increase monotonically (not shown) with lowering of temperature. Absence of signature for magnetic transitions is attributed to the substantial paramagnetic contribution of Gd^{3+} sublattice close to the expected para to antiferromagnetic (AFM) transition temperature (~40 K) of the Mn^{3+} sublattice. Nonetheless, from the Curie-Weiss analysis of the thermomagnetization data, antiferromagnetic interaction between the moments is clearly established. In order to determine the magnetic transition temperatures associated with Gd^{3+} and Mn^{3+} sublattices, specific heat measurements were carried out. A Cp/T versus T plot is shown in Figure 1. A λ-like anomaly, characteristic of antiferromagnetic transition could be observed about 41 K. It is attributed to antiferromagnetic transition of Mn^{3+} sublattice having an incommensurate sinusoidal magnetic structure. This is about 2 K lower compared to that of $GdMnO_3$, On the other hand, anti-ferromagnetic transition temperature of Gd^{3+} sublattice, seen as a prominent anomaly of about 7 K is not affected by Y^{3+} substitution. This clearly indicates that structural effects are predominant compared to dilution effects in weakening the magnetic transition interaction. In addition to these a weak but definite anomaly is observed about 18 K. Strength of this anomaly marginally increases upon application of magnetic field. This indicates the origin of this anomaly lays at a subtle change in the magnetic structure of Mn^{3+} sublattice.

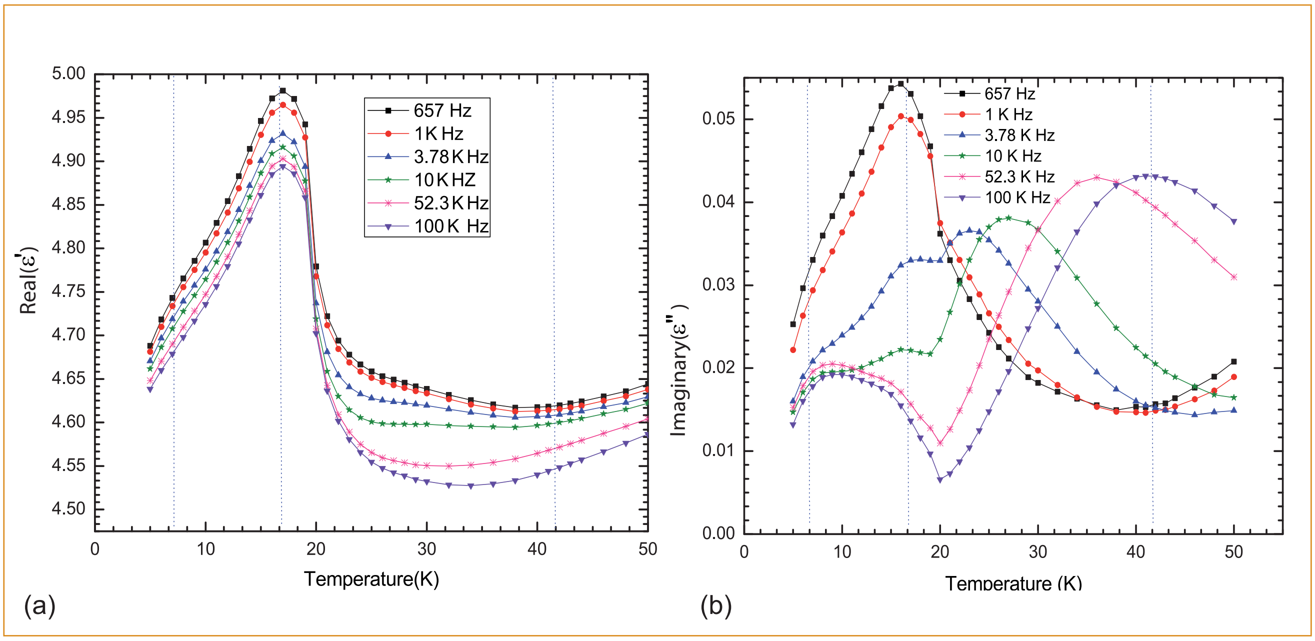

Fig. 2 *Temperature dependence of (a) real (ε') and (b) imaginary (ε”) part of dielectric constant of $Gd_{0.7}Y_{0.3}MnO_3$ measured under different frequencies*

Temperature dependence of the real $\varepsilon'(T)$ and imaginary $\varepsilon''(T)$ parts of permittivity of $Gd_{0.7}Y_{0.3}MnO_3$ measured at different frequencies are shown in Figure 2. Both $\varepsilon'(T)$ and $\varepsilon''(T)$ exhibit for all frequencies, an anomaly in the form of a peak centered about 17 K with a weak shoulder about 7 K. The weak shoulder corresponds to antiferromagnetic transition of Gd^{3+} sublattice. It is interesting to note that magnetic transition of the Gd^{3+} subalttice contributes to dielectric properties of the system. For the parent compound $GdMnO_3$ a step like anomaly has been reported and is ascribed a metamagnetic transition at which the modulation propagation wave vector of Mn^{3+} sublattice abruptly drops from a finite value to zero. Such a transition is shown to leave the ground state of $GdMnO_3$ to be paraelectric. However, the ground state modifies to ferroelectric in the presence of external magnetic field and step like feature in the dielectric response modifies to a peak with concurrent appearance of induced ferroelectric phase transition. Thus, a peak in the dielectric response, instead of step like feature in the present compound indicates induced ferroelectric phase transition. Thus it is inferred that Y substitution is able to induce spontaneous ferroelectric order in $GdMnO_3$, which otherwise has to be induced by external magnetic field. Interestingly, no anomaly associated antiferromagnetic transition of Mn^{3+} sublattice is observed.

It is clearly seen that while the position of anomaly is associated with ferromagnetic and antiferromagnetic of Gd^{3+} sublattice are almost independent of frequency, strength found to dramatically decrease with frequency about the temperature region covering these transitions. In addition to these anomalies, additional broader anomaly evolves with frequency; position of which shifts to higher temperature and increased strength with frequency. The anticorrelation of strength of the anomalies of these processes with frequency clearly indicates that process associated with broad anomaly is different from that associated with ferroelectric. As mentioned above featureless behavior of (T) along with frequency-dispersive (T) indicates a conductive behavior associated with thermally-activated relaxation and is called as para-process.

Variations of the lattice parameters *a*, *b*, c and unit cell volume *v* in the temperature interval 0 to 50 K was studied using angle dispersive X-ray difraction beam line (BL-12) at Indus-2 synchrotron. The lattice parameters exhibit anomalous variations in their temperature dependence about the magnetic transitions antiferromagnetic and induced ferroelectric transition temperatures. It is seen that *a*-axis exhibits negative thermal expansion with a dip about 41 K and steep increase about 20 K. Though *b*-axis also registers a steep increase about 20 K, it exhibits positive thermal expansion between the magnetic transition antiferromagnetic and ferroelectric temperature. On the other hand, *c*-axis in the same temperature range is almost temperature independent, followed by a steep raise about 20 K. It is pertinent to note that all the lattice parameters steeply rise across the ferroelectric transition temperature. This feature may be associated with large magnetocaloric effect in this compound.

V.16 Pressure Induced Phase Transformations in $NaZr_2(PO_4)_3$ Studied by X-Ray Diffraction and Raman Spectroscopy

$NaZr_2(PO_4)_3$ (NZP) belongs to the broad NASICON family with corner sharing PO_4 tetrahedra, ZrO_6 octahedra and Na in large interstitial cavities defined by Zr-P network. It crystallizes in a rhombohedral structure with space group *R-3c* and exhibits anisotropic thermal expansion. The compounds of this family with various ionic substitutions have interesting physical properties such as anisotropic low thermal expansion, ionic conductivity, and host for nuclear waste immobilization. On heating, the *c*-parameter of NZP increases with simultaneous decrease in the *a*-parameter due to coupled rotation of ZrO_6 and PO_4 polyhedra leading to an average low thermal expansion coefficient ($\alpha = 4.5 \times 10^{-6}$/K). Study of structural stability as a function of pressure and temperature in these open framework compounds is of great interest to establish the phase diagram of NZP. Prototype NZP is stable up to 1100 K without any phase transformation but only limited studies are available on its stability with pressure. These studies may also have a bearing on the consequences in case a large pressure pulse gets generated by accidental chemical events etc., at a place where this material is employed for nuclear waste management.

This is a report on our recent investigations of the detailed nature of the structural phase transformation and stability under pressure using a combination of X-ray diffraction in a synchrotron and Raman spectroscopy.

NZP was synthesized by a sol-gel technique. In situ high pressure Raman spectra were recorded up to 20 GPa from a symmetric diamond anvil cell with diamonds of culet diameter 500 μm, using a micro Raman spectrometer with 514 nm laser excitation. Angle dispersive X-ray diffraction experiments at high pressure were carried out at the angle dispersive adaptation of beamline -11 at the INDUS-2 synchrotron source (RRCAT, Indore) with monochromatic X-rays of wavelength 0.46575 Å and beam dimensions of 200 × 200 μm. NZP was loaded in a 250 μm diameter hole in a tungsten gasket in the symmetric diamond anvil cell. Diffraction patterns were recorded using a mar345 imaging plate detector kept at a distance of ~235 mm from the sample which was calibrated using CeO_2 specimen. We carried out X-ray diffraction measurements in a synchrotron to study this transition.

Bulk modulus of the compound for the low pressure phase (up to 5 GPa) is calculated to be 53.2(3) GPa with B′ = 4 by fitting the P-V data to third order Birch-Murnaghan equation of state (Figure 1). It is noteworthy that the bulk modulus of low pressure phase of $RbTi_2(PO_4)_3$ (up to 1.7 GPa) was reported to be 104 GPa. On comparison, it is seen that compressibility increases or lattice softens with substitution of a smaller cation (Na). The increase in compressibility in NZP compounds can be explained as due to the cooperative interaction of bond compression and bond angle bending mechanism.

On further compression of NZP from 5 GPa, five new weak peaks appear, and their intensities increase at higher pressures. This suggests the appearance of a new phase (phase II) that coexists with the original phase at 5 GPa. The new diffraction peaks could be indexed to R3 structure similar to isostructural $RbTi_2(PO_4)_3$. The corresponding variation of lattice parameters with pressure is

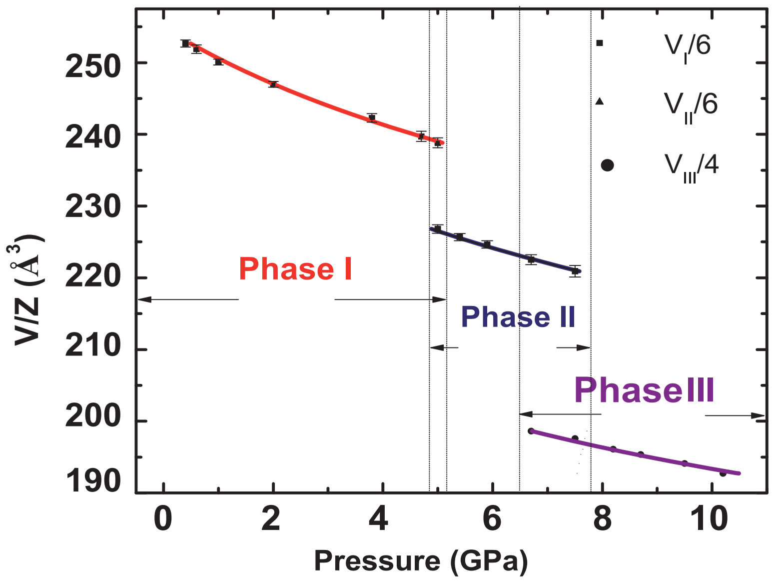

Fig. 1 *Bulk modulus of the compound for the low pressure phase (up to 5 GPa)*

shown in Figure 2. Above 5 GPa the intensities of reflections corresponding to (0 0 9) and (3 0 15) increase significantly, which is responsible for violation of *c*-glide symmetry indicating a transition from *R-3c* to *R3* structure. This transition might be due to a reduction of Zr-O-P angles and the consequent collapse of Na sites similar to the case of $RbTi_2(PO_4)_3$. In this phase, the reduction in the *a*-lattice parameter is more than that of the *c*-parameter that could be due to the rotation of ZrO_6 octahedra along the *c*-axis. The bulk modulus of this phase II (5 - 7.5 GPa) of NZP is found to be 36(1) GPa with B′= 4 whereas the high pressure phase of $RbTi_2(PO_4)_3$ (1.7 - 6 GPa) was found to be 60 GPa with B′ =4. While most solids become less compressible at high pressure NZP shows a different behavior. NZP becomes more compressible with increasing pressure over a limited range of pressures, 5 - 7.5 GPa. Increased compressibility at high pressure has been observed in other flexible framework compounds indicating a commencement of a reversible tilt transition to a structure of lower symmetry.

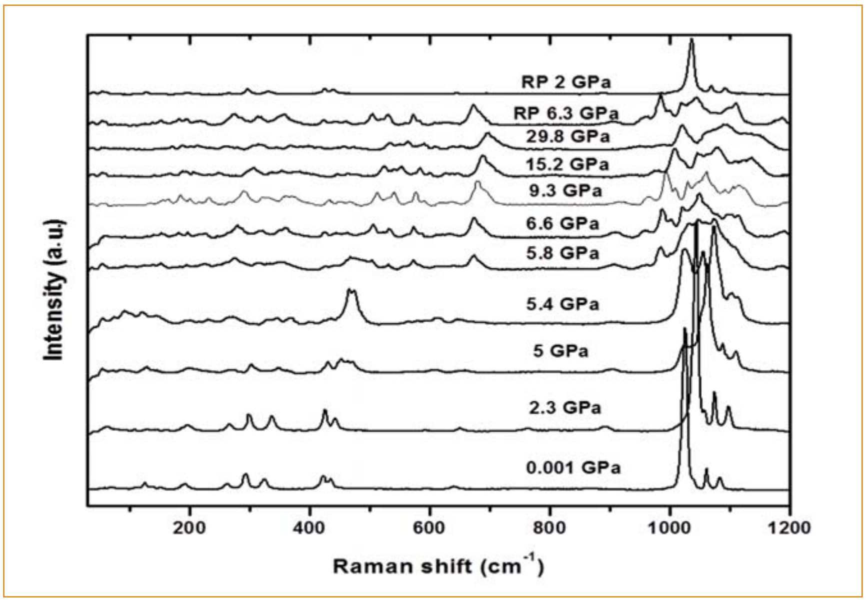

Fig. 2 *The variation of lattice parameters with pressure*

On further compression, several new broad peaks arise around 6.7 GPa with increase in X-ray scattering background indicating the formation of a new phase (phase III) that could be disordered. Coexistence of phases II and III was observed between 6.7 and 7.5 GPa. At 8.2 GPa, the pattern could be indexed to a single, orthorhombic structure with space group Pbcn using POWD software. The bulk modulus B = 65 GPa with B′=4 for this phase III was estimated by fitting the P-V data to the third order Birch Murnaghan equation. The increase in bulk modulus indicates stiffening of the lattice on compression, and this phase is stable up to 10 GPa. $NaZr_2(PO_4)_3$ crystallizes in a rhombohedral structure with space group R-3c (D_{3d}^6) with six formula units in the crystallographic unit cell. Theoretical analysis predicts 25 Raman active and 27 IR active modes from NZP. Raman spectrum of NZP at ambient conditions exhibits 17 distinct Raman bands, similar to that reported earlier.

As the pressure is increased to above 5 GPa, intensities of the bands at 127, 303 and 433 cm^{-1} decrease and new broad bands appear below 500 cm^{-1} with splitting of internal modes around 1000 cm^{-1} indicating a phase transition to a structure of a lower symmetry that was indexed above as phase II with R3 (C_3^4) space group. With two formula units per primitive cell, group theoretical analysis of this phase II using correlation method results in 70 Raman active modes distributed as $\Gamma_{Optical}$ = 35A+35E. Total irreducible representation including acoustic modes is given by Γ_{Total} = 36A+36E. This comprises of internal modes of phosphate unit Γ_{Int}=18A+18E, $\Gamma(PO_4)^{Trans,Lib}$ = 12A +12E and lattice modes Γ_{ext}=6 A +6 E. Two soft modes (72 and 112 cm^{-1}) which show Zr displacements and PO_4 librations respectively suggest phase transition by a polyhedral Zr-O-P tilt mechanism. Thus these modes can be directly related to the structural instability and phase transformation. The frequencies of all modes above phase transtion increase with pressure, indicating a normal positive thermal expansion behavior. Phase III remains stable up to 30 GPa, the highest pressure up to which Raman measurements were carried out.

To conclude, we have investigated high pressure stability of NZP against structural phase transition. High pressure X-ray diffraction confirms two phase transitions around 5 and 6.7 GPa which are indexed to a rhombohedral (R3) and an orthorhombic phase respectively. The bulk modulus for high pressure phases is calculated. Raman spectroscopy confirms these two phase transformations. The behaviour and nature of phonon modes of the high pressure phases are discussed. Two soft E_g modes in the ambient phase are found to be responsible for polyhedral tilt transition at 5 GPa.

V.17 Studies on Superconducting Properties of Magnetron Sputtered Niobium Nitride Thin Films

Niobium nitride (NbN) is a superconductor with a cubic B1 structure which transforms to the superconducting state at a maximum superconducting transition temperature (T_c) of 17 K. NbN has a potential for several applications like Josephson junctions, superconducting single photon detectors, superconducting hot electron bolometers etc. NbN has also a potential for utilization in high magnetic field applications. The important properties of NbN thin films, which make it a preferred material for several applications, include its chemically inert nature and its weak dependence of T_c on radiation damage. Some of these applications require deposition and characterization of NbN thin films at ambient temperature. Thin films deposited at ambient temperature generally become superconducting below 16 K. Deposition of NbN at room temperature is required for fabrication of sensors like SQUIDs etc. NbN thin films deposited on oxidized silicon substrates show reduced T_c due to disorder and interface strain. The residual resistivity ratio is a measure of the disorder in NbN thin films. In general, the superconducting transition width (ΔT_c) increases for thin films deposited under sub-optimum conditions which could be attributed to both disorder and inhomogeneities. Optical measurements on superconducting thin films can be employed as a tool to characterize the superconducting phase; this can be done non-invasively and could also be used during the deposition of the thin film. Measurement of magnetoresistance could also be used as a tool to identify the upper critical field ($Bc_2(0)$) in superconducting thin films. Enhancement of $Bc_2(0)$ by introducing disorder has been demonstrated in many superconductors. Deposition of NbN thin films on non-crystalline substrates and at room temperature introduces disorder and has a potential to increase $Bc_2(0)$. Aluminum nitride (AlN) is an insulator but has good thermal conductivity. Hence AlN can be used as a buffer layer between glass/Si substrates and NbN. In addition, AlN can be used as the insulator in NbN based Josephson junctions. In order to make multilayers of NbN and AlN for applications based on Josephson junctions, it is important to characterize the superconducting properties of NbN thin films deposited on aluminum nitride underlayers.

The NbN thin films were deposited by reactive sputtering in a load locked deposition chamber with a base pressure reaching 8×10^{-8} mbar. The sputtering was carried out using a 100 mm diameter niobium target of 99.999% purity using a mixture of Argon and Nitrogen at different pressures. The NbN thin films were deposited on glass and oxidized silicon substrates. The substrates were sputter cleaned in the load lock chamber and transported to deposition chamber using a magnetic manipulator. The substrates were rotated about a central axis to ensure uniformity in the thickness of the deposited film. The substrate holder is cooled by flowing water to avoid undesirable rise in temperature. The rate of deposition as well as the total thickness of NbN thin films was measured by the in-situ quartz crystal thickness monitor and subsequently measured directly using a surface profiler. NbN thin films with a nominal thickness of 140 nm were deposited on these substrates at a deposition rate of approximately 0.2 nm/s. AlN was deposited by reactive sputtering in the load locked chamber. In films, where AlN is used as a buffer layer, deposition of AlN with a nominal thickness of 35 nm preceded NbN deposition. The thin films have been patterned into standard four probe geometry for electrical resistivity measurements using lift-off photolithography.

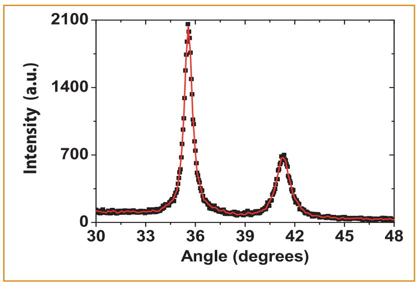

Fig. 1 *GIXRD pattern of niobium nitride thin film*

The thin films were characterized by electrical resistivity measurements down to 4.2 K using a dipstick cryostat. Various parameters like room temperature resistivity (ρ_n), superconducting transition temperature (T_c) and transition width (ΔT_c) were obtained from these measurements. Figure 1 shows glancing incidence x-ray diffraction (GIXRD) measurement indicating the formation of cubic fcc B1 structure but with a lower lattice parameter of 0.4381 nm. The grain size of thin film inferred by using scherrer formula is 35 nm indicating formation of nano-sized grains. The reactively sputtered NbN thin films were found to be superconducting at a maximum temperature of 13.0 K, with more disordered thin films exhibiting superconductivity at lower temperatures. All NbN thin films show a negative temperature dependence of resistance indicating the presence of disorder. The width of the superconducting transition is less than 0.2 K for less disordered films while it increases upto 0.52 K for more disordered film. Superconducting state is characterized by the existence of a gap in the electronic density of states and this energy gap is expected to vanish at T_c. In some materials, this gap structure extends above T_c, not as a full gap but as a depression in electronic density of states and is termed as pseudogap. Pseudogap state in conventional superconductors like NbN has been shown to exist for highly disordered thin films at temperatures T* higher than T_c, but T* merges with T_c for thin films with lower disorder. The pseudo gap temperature T* has also been identified using resistivity measurements. The upturn in the first derivative plot with a nearly constant second derivative is a clear indication of pseudogap and is observed at around 20 K in the NbN thin films while superconductivity sets in at a lower temperature of 13 K implying T* greater than the maximum T_c in these thin films.

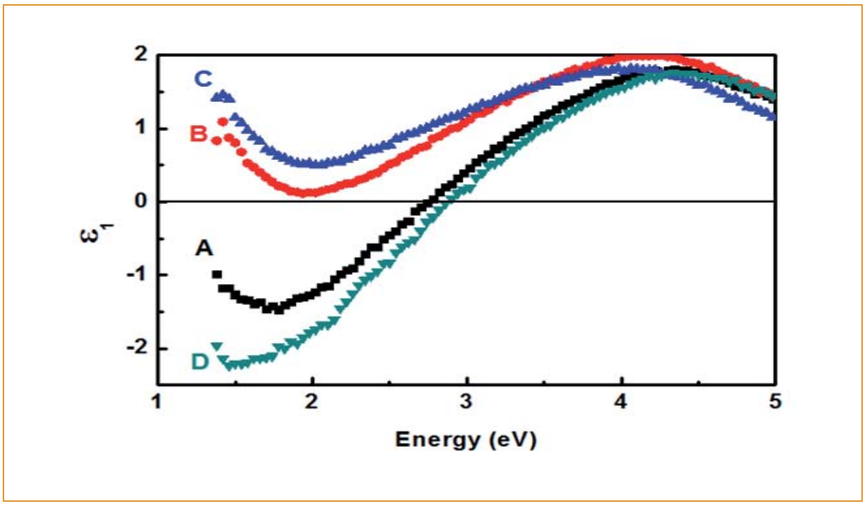

Fig. 2 *Dependence of real part of the dielectric function (ε_1) on incident photon energy*

Four NbN films deposited under different sputtering conditions were taken up for characterization of superconducting and optical properties Superconducting parameters like T_c, T_0 (temperature at which slope of temperature dependence of resistance changes from negative to positive in disordered thin films) and ΔT_c show a non-monotonic behavior with room temperature resistance. The characterization of optical properties of the thin films was carried out using a rotating polarizer type spectroscopic ellipsometer (SOPRA ESVG) in the energy range 1.5 to 5 eV. The metallicity of these samples, as depicted by the variation of ε_1 with energy at low frequencies, also shows a non-monotonic variation with room temperature resistance (Figure 2).

The upper-critical field $B_{c2}(0)$ can be estimated based on Ginzburg-Landau-Abrikosov-Gorkov (GLAG) theory by measuring T_c and the critical field slope $dB_{c2}(T)/dT$ at T_c. Magnetoresistance for two of these films labeled A and B was measured using Quantum Design PPMS system upto a magnetic field of 12 T in steps of 2 T. The other two films labeled C and D were measured using a Cryogenics magnetoresistance setup upto a magnetic field of 15 T in steps of 5 T. The superconducting transition temperature T_c of sample B is progressively decreased from 11.6 K at 0 T to 10.3 K at 12 T while that of sample C is progressively decreased from 13.1 K at 0T to 9.93 K at 15 T. The calculated $B_{c2}(0)$ for sample B is 72 T while that of sample C is 43 T which are considerably higher than the values reported for this system in literature. Deposition of a buffer layer of Aluminum Nitride on glass substrate has resulted in improvement in superconducting properties with the sample exhibiting a sharp superconducting transition of 13.4 K with a transition width of only 0.22 K at 0 T and a $B_{c2}(0)$ of 39 T (Figure 3).

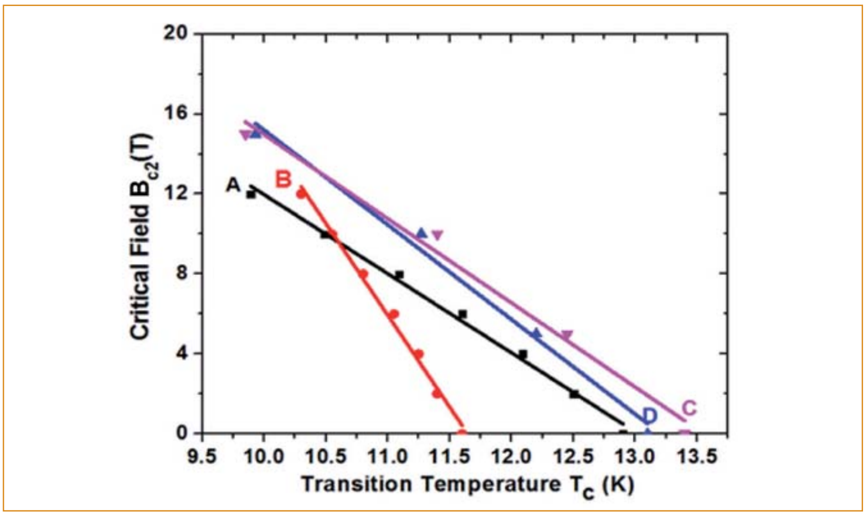

Fig. 3 *Variation of critical field with temperature*

V.18 Electron Energy Loss Spectra of $Y_2Ti_2O_7$ and Y_2TiO_5: A Comparative Study between Experiments and Calculations

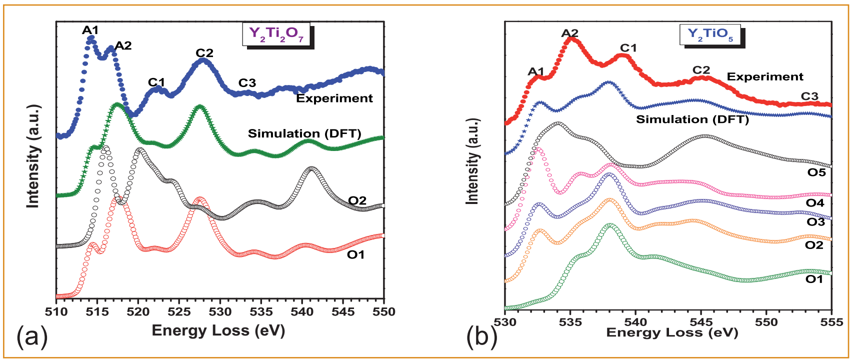

Fig. 1 *The experimental and the (DFT) calculated O K edges of (a) $Y_2Ti_2O_7$ and (b) Y_2TiO_5*

Oxide dispersion strengthened (ODS) steel derives its superior high temperature mechanical strength and radiation resistance from the Y-Ti-O oxide nano particles. In most commercial ODS alloys, these oxide particles are present mainly in the form of either $Y_2Ti_2O_7$ and/or Y_2TiO_5. The stability of the nano particles eventually depends on the strength and the nature of the metal-oxygen (MO) bonds. Hence a comparison of the strength and the nature of the M-O bonds in these two oxide particles can help in deciding the composition of the minor alloying elements Y and Ti. The metal ions in the oxides $Y_2Ti_2O_7$ and Y_2TiO_5 have different coordination numbers and bond lengths. Such complex crystal systems can be effectively characterized with electron energy-loss spectroscopy (EELS).

The powder samples of $Y_2Ti_2O_7$ and Y_2TiO_5 are synthesized by the conventional solid state reaction route from the precursor materials Y_2O_3 and TiO_2. The stoichiometric mixture of the precursor materials for $Y_2Ti_2O_7$ was calcined at 1250°C in air for 48 hours and the mixture for Y_2TiO_5 was calcined at 1500°C in air for 24 hours. The phase formation is confirmed by the powder X-ray diffraction (XRD) measurements.

EELS spectra of $Y_2Ti_2O_7$ and Y_2TiO_5 powder samples are acquired using LIBRA 200FE, a High Resolution Transmission Electron Microscope (HRTEM) operated at 200 kV, equipped with Schottky Field Emission Gun (FEG) source and an in-column omega energy filter.

The Oxygen K edge and Ti L_{23} edge were simulated with CASTEP, a DFT code included in Materials Studio package. CASTEP uses plane wave basis set. PAW (Projector Augmented Wave) pseudopotentials are generated using on-the-fly formalism. PBE version of generalized gradient approximation (GGA) is used in the calculations to describe the exchange and the correlation effects. Convergence tests are carried out for Brillouin zone sampling and plane wave energy cutoff, until the energy converged is better than 0.001 eV/atom.

The Ti L_{23} edge is analysed using the freely available program CTM4XAS (Charge Transfer Multiplet program for X-ray Absorption Spectroscopy). For this simulation, one has to tune the parameters related to configuration, symmetry, Slater integral reduction parameters (F_{dd}, F_{pd}, G_{pd}), spin orbit coupling values, crystal field parameters (which includes symmetry of the crystal system and the energy split *10Dq*), charge transfer parameters (*T(eg)*, *Udd*, *Upd*, etc.) and Lorentzian and/or Gaussian broadening values.

The O K ionization edge in the EELS spectra of both the oxide particles are shown in Figure 1. In the case of any 3d transition metal oxide, the pre edge features in the O K edge arise from the covalent mixing of the metal and the oxygen orbitals, *i.e.*, the pre-edge features A1 and A2 in the O K edges in Figure 1 is a manifestation of the mixing of the 3*d* orbital of Ti and 2*p* orbital of O. The intensity of the peaks A1 and A2 is a measure of the overlap of the above orbitals. The peaks C1, C2 and C3 are typical near edge features of oxygen K-edge. From Figure 1, it

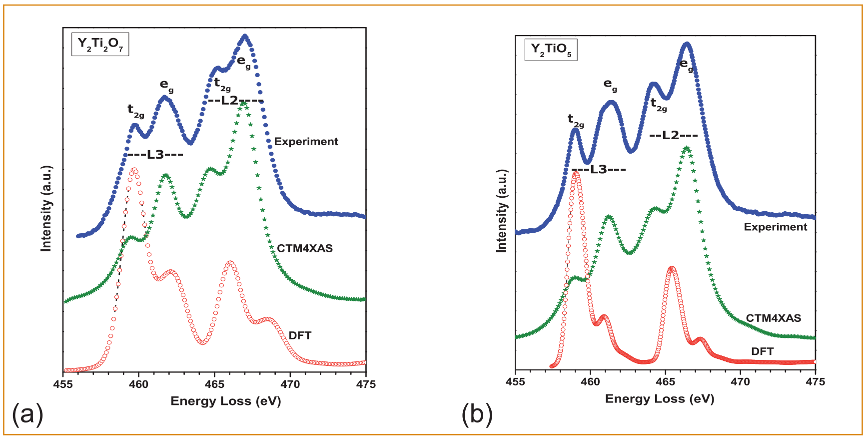

Fig. 2 *The Ti L_{23} edges from experiment, DFT simulation and CTM4XAS for (a) $Y_2Ti_2O_7$ and (b) Y_2TiO_5*

may be observed that the overlap is strong in the case of $Y_2Ti_2O_7$, which means that the bonds are more covalent in $Y_2Ti_2O_7$.

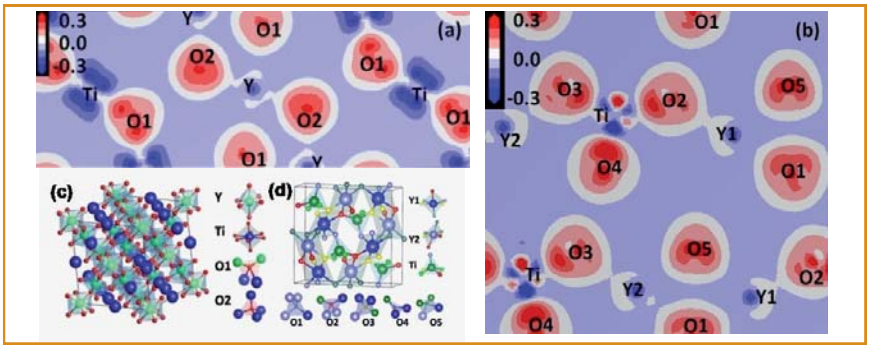

Fig. 3 *Differential charge density, showing the degree of covalency of the (Ti-O) and (Y-O) bonds in (a) $Y_2Ti_2O_7$ and (b) Y_2TiO_5. The unit cell of (c) $Y_2Ti_2O_7$ and (d) Y_2TiO_5*

Figures 2a and 2b show the measured and DFT calculated EELS for Ti L_{23} edge of $Y_2Ti_2O_7$ and Y_2TiO_5 respectively. In both $Y_2Ti_2O_7$ and Y_2TiO_5, the peak positions broadly match but the intensity ratio (L_2:L_3) deviates from experiment. The L_2 peak is stronger than L_3 peak in experiments, further e_g peaks are stronger compared to t_{2g} peaks. However, the DFT calculations show opposite trend in the intensity ratio (L_2:L_3) and intensity of t_{2g} and e_g. This deviation is observed in both the samples. As the DFT codes are not able to account for the multibody interactions fully they cannot calculate the L edges reliably.

Figures 2a and 2b show also the measured and CTM4XAS calculated EELS for Ti L_{23} edge of $Y_2Ti_2O_7$ and Y_2TiO_5 respectively. In $Y_2Ti_2O_7$, Ti atom is octahedrally surrounded by oxygen atoms, and hence in CTM4XAS, O_h (octahedral) symmetry is used in the case of $Y_2Ti_2O_7$.

In order to get chemical insight, we have plotted the electron density difference in both the oxides $Y_2Ti_2O_7$ and Y_2TiO_5. Figure 3a shows the 2D plot of differential charge density in $Y_2Ti_2O_7$ along the plane ($\bar{1}01$) passing through origin and Figure 3b shows similar plot in Y_2TiO_5 along the plane (010) situated at b/4 along the *y*-axis. The plots show that in both the systems, the Ti-O bonds are more covalent than Y-O bonds since there is more accumulation of electron density along the Ti-O bonds as compared to the Y-O bonds. The unit cell of $Y_2Ti_2O_7$ is as shown in Figure 3c a pyrochlore with two different chemical environments for oxygen atoms. O1 is inside the tetrahedron formed by (2Ti, 2Y), and O2 atom inside the tetrahedron formed by (4Y). The blue, green and red balls represent Ti, Y and O atoms respectively. As shown in Figure 3d the unit cell of Y_2TiO_5 is an orthorhombic structure with two inequivalent positions for Y and five inequivalent positions for O atoms. The (light and dark) blue balls represent Y atoms, green balls represent Ti atoms and O atoms are represented by small balls with five different colours. Chemical environments for all the atoms are also shown along with the crystal structures.

Tables 1 and 2 show the formal charge and the calculated Mulliken charge of individual ions in $Y_2Ti_2O_7$ and Y_2TiO_5. The effective ionic charge in the O atoms bonded to Ti in Y_2TiO_5 (O2, O3, O4 and two O5 atoms) shows more covalent nature compared to O1 which is bonded to Y. The TiO bonds in $Y_2Ti_2O_7$ are more covalent compared to those in Y_2TiO_5, which means stronger hybridization of oxygen *2p* orbital with titanium *3d* orbital. These observations comply with our experimental results.

This work demonstrates that the influence of the crystal field splitting is less dominant in Y_2TiO_5, *i.e.*, the peaks A1 and A2 in O K edge of Y_2TiO_5 are weaker than $Y_2Ti_2O_7$. The weaker ionicity of the TiO bond in $Y_2Ti_2O_7$ as compared to that in Y_2TiO_5 is clearly seen.

Table 1: The crystal structure of $Y_2Ti_2O_7$ sample is found to be fcc with space group (227, setting 2).
The lattice parameter value (in Å) is 10.09 (expt.) and 10.15 (calc.)

Atoms	Wyckoff position	Fractional coordinates (DFT relaxed)			Formal charge	Mulliken charge
		x	y	z		
Y	16c	0.50	0.50	0.50	4	1.15
Ti	16b	0.00	0.00	0.00	3	1.43
O1	48f	0.329	0.125	0.125	-2	-0.72
O2	8b	0.375	0.375	0.375	-2	-0.83

Table 2: The crystal structure of Y_2TiO_5 sample is orthorhombic with space group *Pnma* (62). The values of the lattice parameters (*a, b, c*) (in **Å**) are (10.33, 3.699, 11.18) (expt.) and 10.40, 3.701, 11.31) (calc.) respectively

Atoms	Wyckoff position	Fractional coordinates (DFT relaxed)			Formal charge	Mulliken charge
		x	y	z		
Y1	4c	0.1157	0.25	0.2243	3	1.37
Y2	4c	0.1361	0.25	0.5565	3	1.35
Ti	4c	0.1739	0.25	0.8811	4	1.09
O1	4c	0.4941	0.25	0.1047	-2	-0.81
O2	4c	0.2240	0.25	0.0436	-2	-0.77
O3	4c	0.2569	0.25	0.7303	-2	-0.76
O4	4c	0.5075	0.25	0.6556	-2	-0.72
O5	4c	0.2636	0.25	0.3842	-2	-0.73

V.19 Role of Selenium Vacancies and Disorder of Lattice on the Observance of Shubnikov de Hass Oscillations in Topological Insulating Bi_2Se_3

Topological insulators (TI) are a new class of materials that have an insulating bulk and a metallic surface state (Figure 1). This metallic surface state, has a linear dispersion, termed as Dirac dispersion, and has in addition the spin locked to its momentum. This unusual state occurs as a consequence of spin-orbit coupling, of which band inversion and surface metallicity result. The peculiar band structure of the surface electrons render them robust to back scattering, giving rise to dissipationless transport, that could have very useful applications. The charcterisation of the electronic structure of topological insulators has been accomplished using Angle Resolved Photo-Emission Spectroscopy and Scanning Tunneling Microscopy. However, to validate the material property, transport measurements are essential. Here we present investigation of transport properties in topological insulators, Bi_2Se_3, which was erstwhile intensely investigated for its high thermoelectric figure of merit.

It was soon realised in literature that the unusual transport from surface electron could be harnessed if and only if the bulk electronic structure was truly gapped. However in low band gap materials such as Bi_2Se_3, even a nominal concentration of defects invariably leads to electron/hole doping of the semiconductor and the Fermi energy shifts from the centre of the band gap to the bulk conduction or valence band. The Fermi energy saddles both the bulk bands and the surface bands and is detrimental to the realisation of dissipationless transport. Thus a control of defects or disorder is one of the important goals of research in the study of topological insulators. In this investigation we focus on characterising the Se vacancy type defects using positron lifetime measurements. The magneto-transport measurements that provide unique signature of the presence of surface states are understood juxtaposed with the positron results.

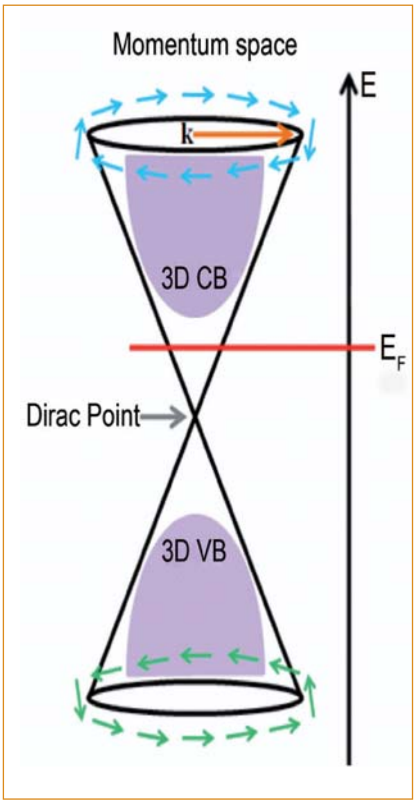

Fig. 1 *Schematic band structure of topological insulators showing the 3-dimensional bulk bands in mauve and linearly dispersed surface bands, spins are locked perpendicular to their momentum in the surface band*

Single crystals of Bi_2Se_3 with nominal compositions Bi_2Se_3, $Bi_2Se_{3.1}$, $Bi_{2.1}Se_3$, that correspond to stoichiometric, Se-rich and Bi-rich samples, were synthesized by melting the required quantities of high purity elements in evacuated quartz tubes at 850ºC (for 24 hours) followed by slow cooling at the rate of 1ºC/hour until 550ºC, keeping at this temperature for 24 hours followed by rapid cooling. The obtained crystals could be easily cleaved along the basal plane leaving a silvery shiny mirror like surface. Laue diffraction measurements were carried out on the cleaved crystals using a Molybdenum x-ray source, and the patterns were recorded in transmission mode using a HD-CR-35 non-destructive testing image plate system. Powder x-ray diffraction (XRD) was carried out on powdered single crystals in an APD 2000 PRO (GNR Analytical Instruments Group, Italy). diffractometer in the Bragg-Brentano geometry. Temperature dependent resistivity measurements, were carried out in a dipper cryostat in the Van der Pauw geometry, with contacts made on the (001) face of the crystals. Magneto-transport measurements were carried out in both, the Van der Pauw geometry and linear geometry in a commercial, 15 T Cryogen-free system from Cryogenic Ltd., UK. The Hall measurements were obtained in the Hall bar geometry in the same setup. Both the resistivity and Hall Effect measurements were carried out simultaneously on each of the single crystals. The contacts to the samples, placed in a puck holder, were done with 25 micron Au wires, with Ag paste, that cures at room temperature.

The resistivity measured in all the three single crystals are shown in Figure 2. The positive temperature co-efficient of resistivity indicates metallic behaviour in all samples, with a tendency to saturate below

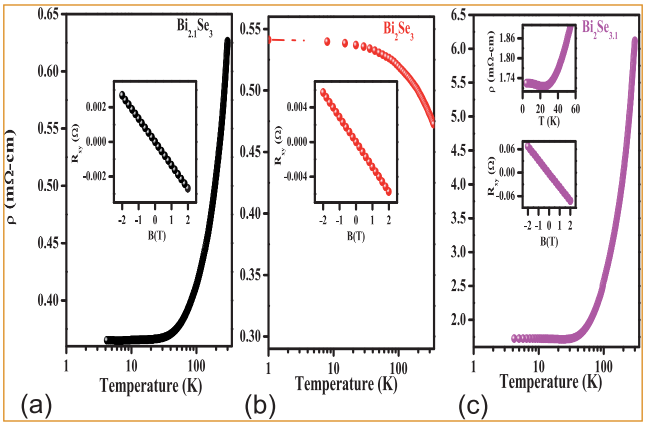

Fig. 2 *Resistivity measurement on (a) $Bi_{2.1}Se_3$, (b) Bi_2Se_3 and (c) $Bi_2Se_{3.1}$ single crystals. The inset shows the Hall resistance versus magnetic field at 4.2 K. In the case of $Bi_2Se_{3.1}$ sample, there is a small upturn at low temperature as shown in the inset*

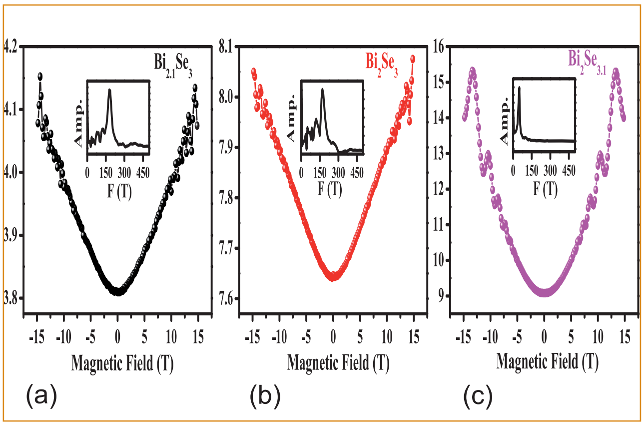

Fig. 3 *Magneto-resistance at 4.2 K in (a) $Bi_{2.1}Se_3$, (b) Bi_2Se_3 and (c) $Bi_2Se_{3.1}$. Quantum oscillations in the magneto-resistance with a single frequency are clearly seen only for the Se rich $Bi_2Se_{3.1}$ sample; insets - the Fourier transform of the SdH oscillations*

30 K. The Hall resistance versus magnetic field is shown in the respective insets, from which it is inferred that electron mobility is highest in the Se excess sample. The magneto-resistance of the corresponding samples measured at 4.2 K in magnetic fields upto 15 T is shown in Figure 3. It is evident from the figure that the resistivity shows periodic oscillations as a function of magnetic field, also in the Se excess sample.

To understand what is special about the Se excess sample, positron lifetime measurements and computations were carried out. The results of the positron density calculations are shown in Figure 4. The positron density distribution for vacancies has been carried out for 441 super-cell, with vacancies in each layer. In defect free Bi_2Se_3, the positron density is confined to the Van der Waals gap, and in the presence of Bi and Se(1) vacancy, it gets localized at the vacancy site. For the Se(2) vacancy within the quintuplet layer, the positron samples both the vacancy and the Van der Waal gap. The overlap of this positron density distribution with the atomic superposition of electron density is used to calculate the corresponding positron lifetimes. This clearly indicates that the positron samples the Van der Waals gap in the pristine Bi_2Se_3 crystal (Figure 4). Further, the calculations indicate that positrons are trapped at the Se(2) vacancy. The positron lifetime experiments carried out in the three samples on which magneto-resistance was done, show that the sample that has distinct oscillations has the lowest positron lifetime. Thus the oscillatory component of resistivity obtained from measured longitudinal resistance, is correlated with lower defect density. It is well known that in the case of the 3D topological insulators, the transport has contributions both from the 2D and 3D electronic states and is determined by the position of the Fermi surface indicated in Figure 1. In order to decipher, the contributions of the transport whether it arises from 2D and 3D electrons, an analysis of the magneto-resistance oscillations was carried out. This analysis seems to point out that the contribution to the transport mainly arises from 2D electrons.

Thus in summary, Se vacancies act as electron donors in Bi_2Se_3, and give rise to transport from both 2D and 3D electrons. To ensure that transport occurs from the Dirac dispersed electrons alone, requires that the Se vacancy be kept to a minimum concentration. Here we have shown that positron annihilation can be used to characterize the number density of Se vacancies and can therefore help in tuning the position of the Fermi level in the system.

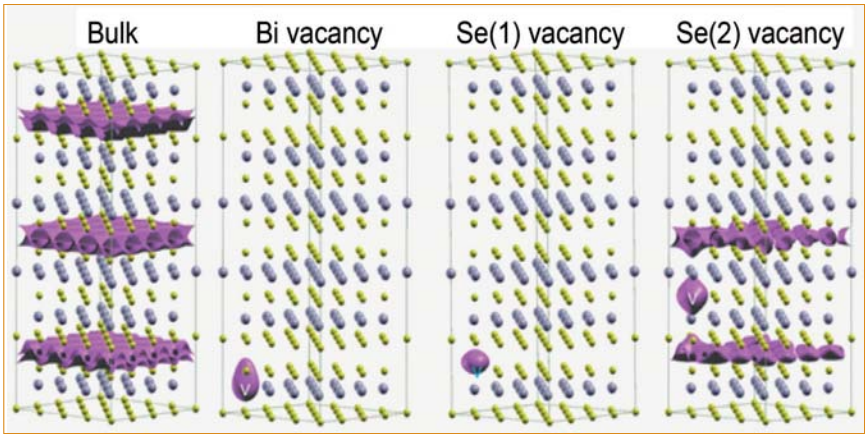

Fig. 4 *Positron density distribution in crystalline Bi_2Se_3 and in the presence of vacancy at Bi, Se(1) and Se(2) sites (purple atoms are Bi and yellow atoms are Se)*

V.20 Anisotropic Friction Behavior in Boronated Graphite

Carbon based materials exhibit unique tribological properties due to the various hybridization states. Three dimensional sp^3 C-C bonding in diamond make it one of the hardest known material due to its strong covalent tetrahedral configuration. In contrast, pseudo-two-dimensional sp^2 C=C bonding in graphite is softer and the most effective solid lubricant. Graphite has excellent mechanical, thermo-physical and chemical stabilities due to its crystal and electronic structures and therefore, it is often used to moderate the neutrons in the high temperature and high temperature gas-cooled reactors. The superior neutron moderation capacity stems from several factors such as thermal stability, low atomic mass, high scattering cross section and negligible absorption cross section. Nuclear graphite consists of a complex poly-granular system with high chemical purity and high graphitization density. The crystal structure consists of series of layers of carbon atoms, which form the 2D hexagonal network of graphene layers. These layers are stacked either in the ABAB….. sequence leading to the hexagonal 2H structure or in the ABCABC….. arrangement conforming to rhombohedral 3R structure. It is yet unclear whether the frictional anisotropy in boronated graphite (nuclear graphite) originates from crystallographic configuration or from unsaturated surface dangling bonds. Anisotropic friction behavior in boronated graphite lattice exists in the disordered phase. To observe anisotropic friction behavior, the tribology tests were carried out in basal and prismatic directions of graphite specimen.

Friction coefficient of boronated graphite distinctly varies when sliding against basal and prismatic planes and these results are shown in Figure 1 and Figure 2. In the direction of basal plane, this value ranges from 0.2 to 0.35, depending upon the sliding speed (Figure 1a). However, in similar test conditions, this value becomes significantly high in prismatic face, ranges from 0.65 to 0.8. This fact can be explained by analyzing the wear depth which is less in the direction of basal face (Figure 1b). However, wear depth is high in prismatic face. Thus, wear depth is directly proportional to the friction coefficient. But no significant change in wear depth with sliding speed is observed in basal and prismatic faces. This can be described by friction coefficient which also does not change with sliding speed. Therefore, wear depth is well corroborated to the frictional energy which is source of energy for loss of material during the sliding. For the tribological evaluation of materials, normal load is one of the important factor on which the friction behavior largely depends. Therefore, load dependent friction behavior of graphite is measured in both the directions (Figure 2a). This value is less in basal plane and increased in prismatic direction and this behavior is similar to the sliding speed mentioned above. However, with increasing load, the friction coefficient is found to increase but this value was insensitive to the sliding speed (Figure 1a). Increase in friction coefficient, results in more wear loss as shown in Figure 2b. The increase in friction coefficient with load is well substantiated from the increasing wear depth.

Graphite surface and wear tracks belonging to both the faces were analyzed to explain distinctive difference in friction behavior. On the graphite surface, (002)

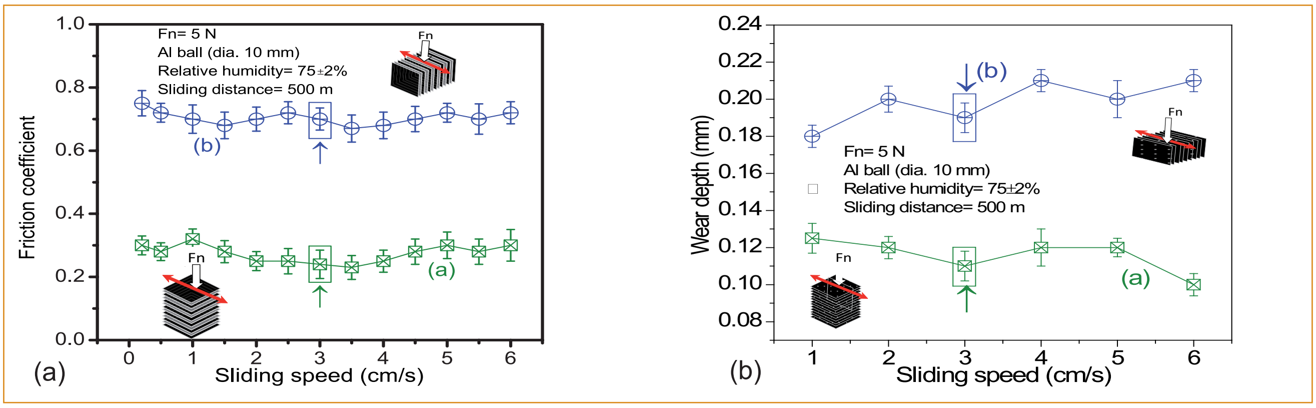

Fig. 1 *Sliding speed dependent (a) friction coefficient and (b) wear depth in the direction of (a) basal and (b) prismatic plane of BG*

plane is prominent in both basal and prismatic directions as evident from hexagonal lattice. This peak becomes weak inside the wear track of basal plane and disappears in the prismatic direction. A new diffraction peak belonging to (110) plane of C8 graphite lattice appears in these wear tracks and this transformation is caused by frictional energy. In both the directions, 3D phase of graphite is observed on the surface which transforms into 2D disordered structure in the wear tracks. Structural disorder in the wear tracks is similar in both the directions as evident from Raman analysis. These facts do not explain such distinctive difference in friction coefficients with respect to directions and therefore, the insensitivity to the structure is observed. Thus, there is a compelling need to consider chemical reactivity of graphite surface and wear tracks to explain this anomaly. Therefore, XPS and FTIR analyses were carried out to establish surface chemistry of wear surface.

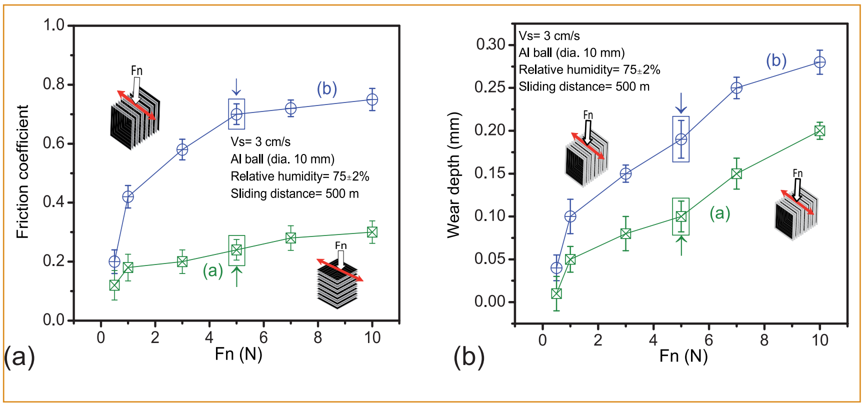

Fig. 2 *Load dependent (a) friction coefficient and (b) wear depth in the direction of (a) basal and (b) prismatic plane of BG*

Surface roughness measured on the basal plane was ~0.15 µm which increases to ~0.28 µm in the prismatic direction of BG sample. However, roughness measured in the wear track after the 20 m sliding distances reduces to ~0.08 and ~0.1 µm in basal and prismatic directions, respectively. Further, after 500 m sliding of distance, these values drop in magnitude to ~0.07 and ~0.09 µm, in basal and prismatic directions, respectively. This fact indicates that influence of roughness on friction behavior of graphite measured in both the directions is negligible. In view of this, the effect of surface roughness on the friction behavior measured in both the directions is ruled out. Strong peak of (111) orientation at 26.4° 2θ on the BG surface of basal and prismatic planes becomes weak inside the wear track formed in the direction of basal plane where friction coefficient is ~0.24. Interestingly, this peak disappears inside the wear track formed in the direction of prismatic plane where friction coefficient is significantly high ~0.7. This clearly indicates disappearance of stacking order of graphite in *c*-axis. Such behavior points to structural transformation which is related to frictional energy dissipation during sliding. High frictional energy in the direction of prismatic plane causes breakdown of (002) hexagonal symmetry and formation of (110) plane of C8 graphite. This is not an abrupt transformation and such a large difference in friction coefficient cannot be explained only on the basis of this fact. It is observed that along the basal plane of graphite surface, the adsorbed oxygen complexes are low due to less unsaturated bonds. However, in the corresponding wear track, more unsaturated bonds are present at the interface of the fractured plane. Such interface generates dangling bonds which is chemically reactive forming oxygen complexes including functionalized C-OH hydroxyl groups resulting in average value of friction coefficient 0.24. Along the prismatic plane of graphite surface, the amount of oxygen complexes is high as compared to basal plane. Consequently, in this wear track, oxygen complexes, oxidized carbonate structure, hydroxylic and carboxylic groups are high indicating large amount of dangling bonds resulting in a high value of friction coefficient of 0.7. Moreover, on the ball scar, large amount of disordered graphitic layers are present when Al ball slid against the prismatic plane. However, less graphite layer on the Al ball scar was observed when sliding against basal plane. Role of formation of tribolayer drives the friction and wear in the sliding system which also acts as a protective layer in some cases.

Friction coefficient decreases if tribolayer is chemically passivated. In contrast, chemically active tribolayer having dangling bonds may join each other and restrict the sliding motion. In the present condition, sliding occurs between the disordered carbon layers where the concentration of dangling bonds is considered to be high at the end of sliding in the direction of prismatic plane. Chemically active carbon atoms combine and form C-C bond between the sliding interfaces. As a result, the upper and lower graphite surfaces chemically join together by a C-C bond which leads to high adhesion resulting in high value of friction coefficient.

V.21 High Pressure Structural Behaviour of YGa_2

Yttrium is a 4d transition metal and it is considered as one belonging to the lanthanide series as it exhibits similar behaviour. In the lanthanide series, the structure sequence: hcp → Sm-type → dhcp → fcc → dist. fcc is observed as a function of decreasing atomic number at ambient conditions. The same structural sequence has been observed in lanthanide elements as function of increasing pressure. This sequence is seen most completely for the heavier lanthanides, while the lighter elements start already at ambient pressure with the high pressure structures of the heavier elements. However, this pressure induced structural sequence has not been attributed to the effect of 4*f* electron states, because similar pressure induced sequence has been seen in La which does not have any 4*f* occupancy. Later, energy band calculations show that the *d*-band contribution to the total energy is what actually drives the lattice through the observed crystal structure sequence. Pressure has the effect of increasing the energy of electrons in the *s*-band relative to the *d*-band, which initiates the *s*→*d* transfer and the number of *d* electrons per atom in the conduction band tends toward 3.

A similar sequence has been observed in the non 4*f* element Y due to the increased 4*d* band occupancy under high pressure. Similar structural behaviour can be expected in their intermetallic compounds also. Since both La and Y exhibit similar high pressure structural behaviour, it will be interesting to investigate their gallides to see whether they exhibit similar structural behavior under high pressure. With this motivation, YGa_2 was investigated under high pressure. YGa_2 system stabilizes in AlB_2 type hexagonal structure (Sp. Group: P6/mmm) at NTP.

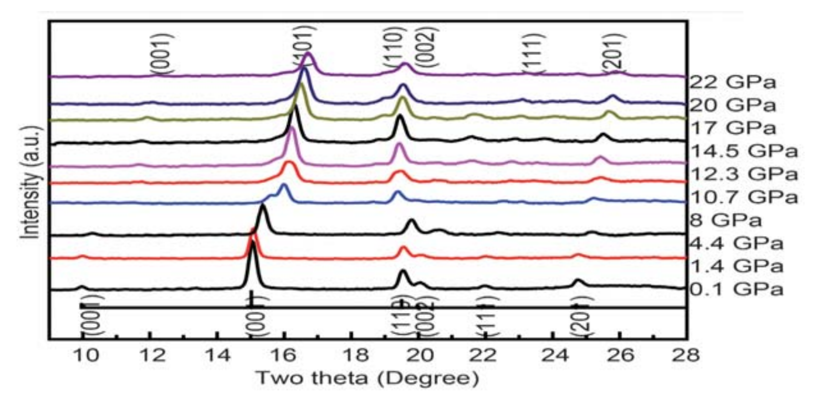

Fig. 1 *HPXRD patterns of YGa_2 up to ~22 GPa obtained with a RAXRG*

This system is isostructural to $LaGa_2$. YGa_2 was prepared by arc-melting stoichiometric quantities of Y (99.99%) and Ga (99.9%) in helium atmosphere.

High Pressure X-Ray Diffraction (HPXRD) studies on YGa_2 were performed in a Mao-Bell type DAC in conjunction with an image plate based MAR 345 dtb using angle dispersive X-ray diffraction up to a pressure of ~22 GPa.

The HPXRD patterns for YGa_2 at various pressures are depicted in Figure 1 up to a pressure of ~22 GPa using laboratory based Rotating Anode X- Ray Generator (RAXRG).

On pressurization, all the Bragg peaks remained intact up to pressure of ~8 GPa except for small changes in their intensities. This indicates that the parent structure remains stable up to this pressure. Above this pressure, several new peaks started appearing, the predominant ones being next to the 100% intensity (101) peak at 2θ=16° and another one before the (110) peak at 2θ=19° (as seen in 8 GPa pattern Figure 1).

The intensities of the diffraction peaks (001),(101),(110),(111) and (112) decreased with pressure and eventually disappeared at ~ 20 GPa.

The structural analysis of the high pressure data on YGa_2 was done on trial and error method and various structures were tried.

The new phase could be indexed to another AlB_2 type hexagonal crystal structure with lattice parameters: *a*=4.1767 Å, *c*=3.4223 Å and *c/a*=0.82. Thus, contrary to the expected similar structural behaviour with $LaGa_2$,(which transforms from hexagonal to orthorhombic structure at high pressure) YGa_2 behaved differently and transformed to another AlB_2 variant hexagonal structure with lower *c/a* ratio. This result is similar to our earlier investigation on $CeGa_2$.

Figure 2 shows the variation of lattice parameters *a* and *c* of the parent hexagonal phase up to ~8 GPa. It is seen, that the lattice parameter *c* decreases more rapidly with pressure compared to *a*.

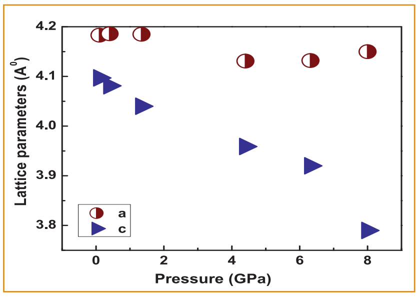

Fig. 2 *Variation of lattice parameters a and c of the parent hexagonal phase of YGa_2 with respect to pressure up to ~8 GPa*

V.22 Asymmetry in Deformation Behaviour of Fe Nanowires: A Molecular Dynamics Study

The rapid progress in computational capability and the availability of reliable inter-atomic potentials makes molecular dynamics (MD) simulations a major tool to probe the mechanical behaviour of materials at atomic scale. In this work, molecular dynamics simulations have been utilized to understand the deformation behaviour of <110>/{111} single crystal bcc Fe nanowires under tensile and compressive loading at a constant strain rate of 1×10^8 s^{-1}. Molecular dynamics simulations were performed in LAMMPS package employing embedded atom method (EAM) potential for bcc Fe given by Mendelev and co-workers. Atom-Eye package has been used for visualization of atomic snapshots. The nanowire had a width of 8.5 nm with 2:1 aspect ratio and contained about 110000 atoms. The stable structure thus obtained is thermally equilibrated to a temperature of 10 K in canonical ensemble.

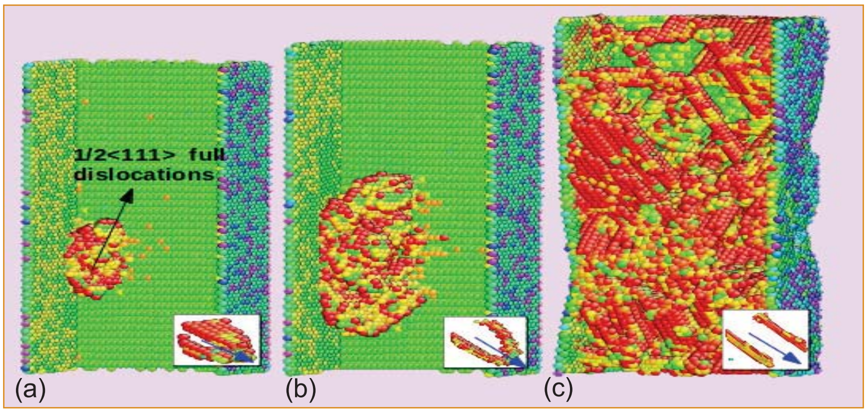

Fig. 1 *The deformation behaviour under tensile loading (a) strain = 14.2%, (b) strain = 14.6% and (c) strain = 17%*

The simulation results show a significant difference in the deformation mechanism in terms of deformation through full dislocation slip during tensile mode (Figure 1) and twinning under compressive loading (Figure 2). Under tensile loading, the nanowire yields by nucleation of collective 1/2<111> full dislocation loops from a single source at the corner of the nanowire (Figure 1a). With increasing strain, these dislocations loops grow in multiple directions as shown in Figure 1b. Since edge dislocations have higher mobility than the screw dislocations, the edge components escape to the surface and as a result straight screw dislocations piles-up in the nanowire (Figure 1c) The observed pile-up of screw dislocations is in agreement with the kinetic pile-up model proposed in bcc systems.

Under compressive loading, the yielding occurs by nucleation of a twin embryo from the corners of the nanowire (Figure 2a). With increasing strain, the twin embryo grows as a full twin on {112} planes as shown in Figure 2b and the further deformation is dominated entirely by twin growth/twin boundary motion along the nanowire axis (Figures 2b and 2c). The twin growth or twin boundary motion proceeds by repeated initiation and glide of 1/6<111> twinning partial dislocations on adjacent {112} planes as typically shown in Figure 2c.

In general, the tension-compression asymmetry in bcc metals can be attributed to non-planar nature of screw dislocation cores. The core of 1/2<111> screw dislocations in bcc metals spreads into several non-parallel planes of <111> zone. As a result, the change in the core structure depends on the direction of the shear stress, which leads to tension-compression asymmetry in bcc Fe. In the present investigation, the observed tension-compression asymmetry is attributed to twinning-antitwinning asymmetry of 1/6<111> partial dislocations on {112} planes.

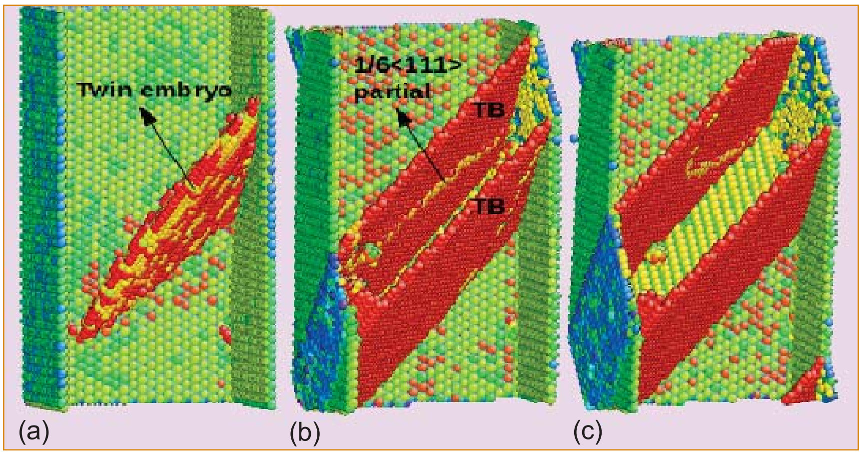

Fig. 2 *The deformation behaviour under compressive loading (a) strain = -9%, (b) strain = -11% and (c) strain = -15%*

V.23 Atomic Scale Study on the Stability and Magnetic Interactions between Magnetite Nanoparticles Dispersed in Zeolite Matrix

Nanoparticles of maghemite and magnetite find a number of applications including drug delivery, high density magnetic recording. For the above applications these nanoparticles should be stable both physically and chemically. These criteria can be met by means of dispersing these particles in any template which is suitable with respect to the application concerned. Stability and magnetic interactions between magnetite nanoparticles as dispersed in Zeolite matrix have been addressed in this study using Mossbauer spectroscopy

Zeolite 13X , chosen as a template for the present study, belongs to a group of crystalline alumino silicate with the basic tetrahedral structural units of SiO_4 and AlO_4 with Si or Al in the center of the tetrahedron (Figure 1). These groups are joined to form a larger unit called sodalite unit (SU) with [Si]/[Al] ratio lying close to 1.2 and the cavity inside SU is known as β cage. In the aluminosilicate structure each tetrahedral group of AlO_4 has an uncompensated charge -1 and hence attractive to positive ions such as Ca^+, Na^+ nearby AlO_4 groups. This work is motivated at studying the binding of magnetite (Fe_3O_4) nanoparticles by Zeolite.

This is done by exploiting the power of the Mossbauer spectroscopy to distinguish between isolated superparamagnetic nanoparticles of Fe_3O_4 as bound in templates and the onset of coarsening subsequent to detrapping and migration from the bound sites in templated structure due to controlled annealing treatments.

These results are compared with that of the coarsening behavior of the bare nanoparticles of superparamagnetic particles of Fe_3O_4 subjected to similar heat treatments in order to elucidate the binding of the nanoparticles by zeolite. Superparamagnetic magnetite particles were prepared by conventional coprecipitation method using appropriate precursor solutions of Fe^{2+} and Fe^{3+} introduced in Zeolite matrix.

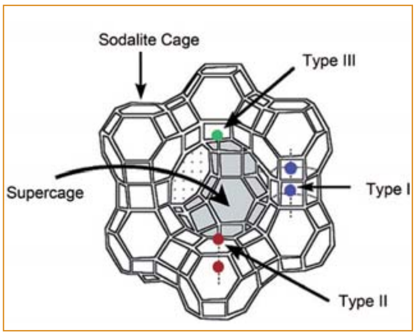

Fig. 1 *Schematic of the frame work of zeolite-13X*

Mossbauer spectrometer was operated in constant acceleration mode and in transmission geometry. ^{57}Co dispersed in Rh matrix with a specific activity of 50 mC has been used as a source. The spectra were calibrated with 10 micron thick α-Fe foil at 300 K and isomer shift values are provided with respect to that of α-Fe. Spectra were fitted to Lorentzian line shapes of line width Γ using a non-linear least squares program to obtain hyperfine parameters such as isomer shift (δ_i), quadrupole splitting (Δ_i) and magnetic hyperfine fields (B_{hf}^i) experienced by relative fractions f_i of distinct ^{57}Fe absorber atoms.

Mossbauer measurements have been carried out at room temperature on the sample subsequent to each annealing treatment at different temperatures. XRD spectrum shows the peaks corresponding to Fe_3O_4 with the mean size around 4 nm (Figure 2). Mossbauer

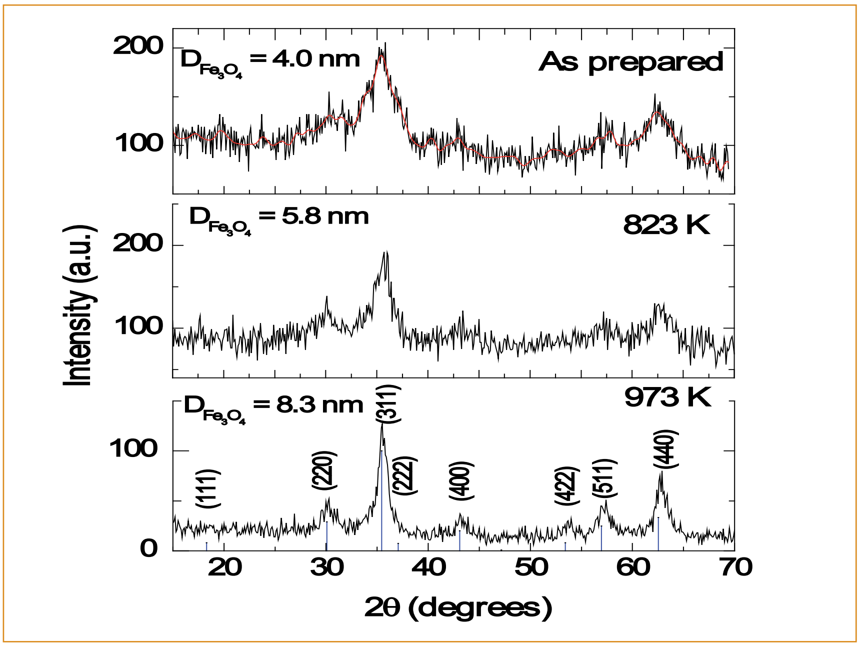

Fig. 2 *XRD spectra of magnetite nanoparticles prepared in zeolite-13X and subsequent to annealing treatments at 823 and 973 K*

spectrum corresponding to the starting sample (Figure 3) exhibits a doublet implying that the spins of the Fe atoms associated with cubic iron oxide nanoparticles fluctuate at a rate close to or higher than 1/τ where τ ≈ 10 ns is the mean lifetime of I=3/2 state of ^{57}Fe resulting in superparamagnetic fluctuation of spins.

Results of the Mossbauer measurements in terms of the variation of quadrupole parameters such as linewidth (Γ_l) , quadrupole splitting (Δ_l) and the relative fraction (f_i) of Fe atoms associated with bare and zeolite dispersed iron oxide nanoparticles with annealing temperature are shown in Figure 4. In the case of bare nanoparticles it is seen that there is a steady increase in (Γ_l) and (Δ_l) in association with a decrease in f_1 corresponding to superparamagnetic particles for Ta>500 K. Occurrence of a damped sextet in the MS implies the onset of coarsening of nanoparticles which must be preceded by two processes viz., detrapping of bound nanoparticles and migration of less bound nanoparticles to a site that could bind these nanoparticles strongly. Occurrence of a broad sextet along with a doublet is seen in the Mossbauer spectrum obtained in bare nanoparticles subsequent to annealing at 523 K. In the case of zeolite dispersed nanoparticles the particles remain superparamagnetic even after annealing at 823 K indicating a strong binding of Fe_3O_4 nanoparticles in zeolite.

Dipole-dipole interactions between nanoparticles would be predominant which varies directly as the product of magnetic moments and inversely as the cube of the distance between them. Annealing at 893 K leads to detrapping of bound nanoparticles thus leading to a decrease in the mean distance of separation between nanoparticles.

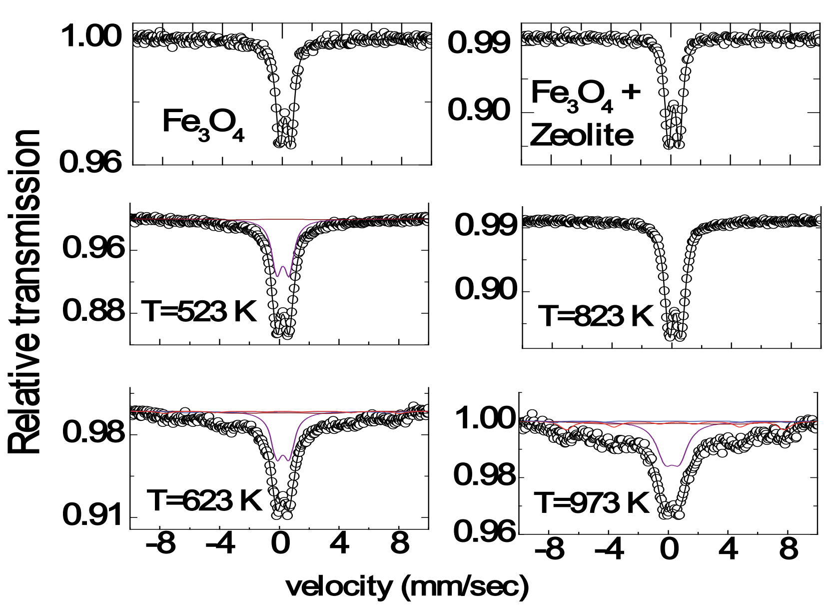

Fig. 3 Mossbauer spectra obtained in bare and Zeolite dispersed magnetite nanoparticles in as prepared condition and subsequent to annealing treatments at temperatures mentioned

This results in an appearance of a damped sextet with close to 40% of Fe atoms experiencing a mean value of Hyperfine field close to 28 Tesla. Thus the present study elucidates a strong binding of magnetite nanoparticles in Zeolite using Mossbauer spectroscopy which might result in a number of new applications.

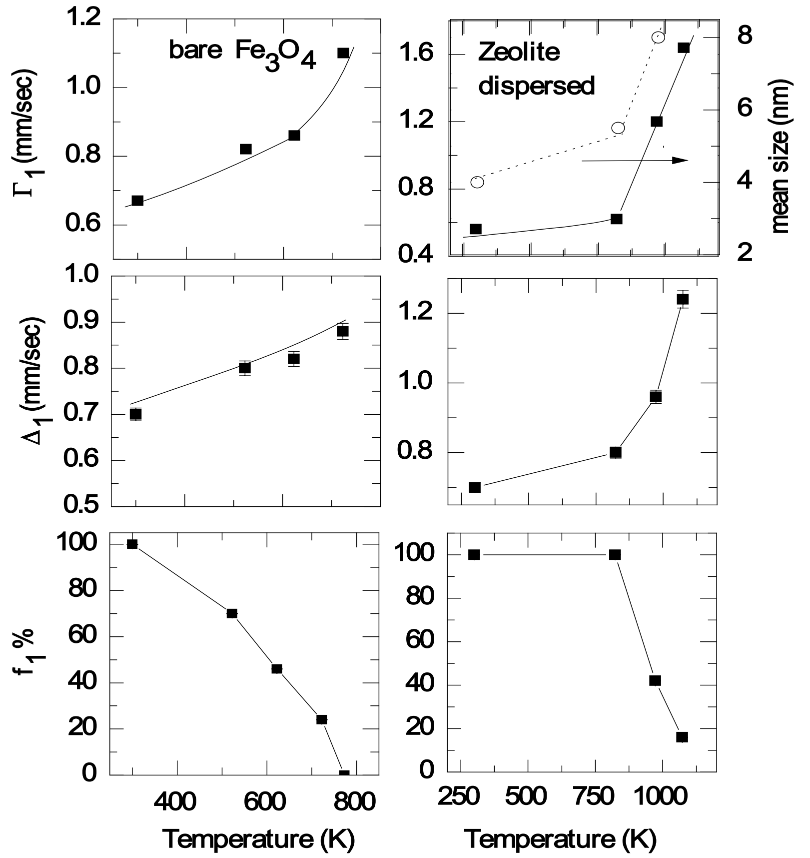

Fig. 4 Variation of hyperfine parameters with temperature in the case of bare and zeolite dispersed magnetite nanoparticles. Variation of the average size of zeolite dispersed Fe_3O_4 particles as deduced using XRD with annealing temperature is shown at the right top of the figure

V.24 Effects of High-energy Si Ion-irradiations on Optical Responses of Ag Nanoparticles in a SiO_2 Matrix: Surface Plasmon Resonance in Quantum Regime

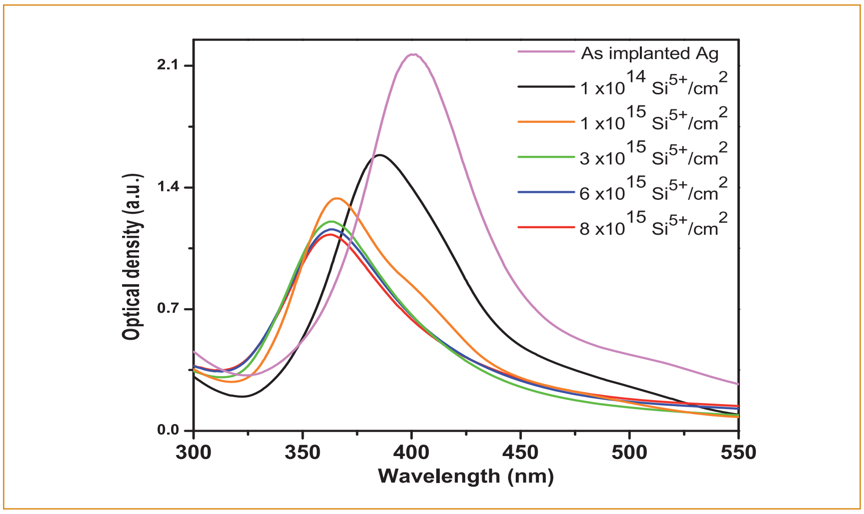

Fig. 1 *Optical absorption spectra of Ag nanoparticles embedded in SiO_2 followed by 9.4 MeV Si^{5+} ion irradiations*

Research studies on optical properties of metal nanoparticles embedded in silicate glasses and other dielectric matrices have received widespread attention due to their high potential for applications in various fields like transparent display, data storage, optical switching and solar energy harvesting, because of their localized surface plasmon resonance (SPR) in presence of external light. The SPR arises from light induced collective excitation of free electrons leading to strong absorption, scattering and local field enhancement in metallic nano structures. SPR of metal nanoparticles crucially depend on sizes and shapes of metal nanoparticles as well as on dielectric constants of media. In particular, plasmon resonances of quantum-sized metal nanoparticles (<5 nm) may offer unique opportunities in medicine, sensor and quantum optics. However, sensing metal particles of sizes <5 nm through the optical absorption spectroscopy is challenging because of the resonance absorption intensity reduces proportionally with the particle volume and collision-broadening . However, experimental difficulties can be partially overcome provided a large number of isolated metal particles of very fine sizes are prepared to scale up for the overall volume fraction. Controlled preparation of such a collection of pure and isolated quantum-sized metal particles is rather challenging by chemical means due to enhanced surface interactions. A unique combinative approach of bottom-up followed by the top-down ion-beam technique has been adopted for the processing of Ag nanoparticles embedded in a SiO_2 matrix. Implantations of 1 MeV Ag^+ ions have been followed for the synthesis of Ag nanoparticles in a SiO_2 matrix in the present study. Subsequently, high energy 9.4 MeV Si^{5+} ion-irradiations have been carried out on embedded Ag nanoparticles to modify the sizes of Ag nanoparticles. As revealed here, Si^{5+} ions "slice" the Ag nanoparticles gradually into fine Ag particles of fairly uniform sizes. UV-visible optical absorption spectra of Ag^+ ion implanted (ion dose: $3{\times}10^{16}$ ions/cm^2) SiO_2 sample before and after the Si^{5+} ion-irradiation has been displayed in Figure 1. High energy Si^{5+} ion irradiations have been carried out with different ion doses (in the range of $1{\times}10^{14}$ to $8{\times}10^{15}$ ions/cm^2) on pristine Ag metallic nanoparticles embedded in the SiO_2 matrix. Systematic shift of the optical absorption resonance peak towards lower wavelengths and concomitant reduction in absorption intensities is apparent with the increase of Si^{5+} ion doses (Figure 1). Decrease in the absorption intensity in this case may be understood (from Mie theory) as a result of size reduction of the Ag nanoparticles due to the Si^{5+} ion-irradiations. Reduction in sizes and decrease in volume fractions of Ag nanoparticles has been confirmed by transmission electron microscopy (TEM) and low frequency Raman scattering (LFRS) measurements. Previous studies have shown that for dipolar optical absorption resonances, spectral shifts are generally quenched with respect to changes in sizes of Ag nanoparticles (within the quasi-static size limits, $\lambda > 2R$) embedded in various matrices. Hence, the classical Mie theory cannot explain the observed blue shift of the optical resonance peaks in finely sized Ag metal particles. As metal particles are reduced to quantum sizes, optical properties differ significantly compared to the Ag nanoparticles of sizes >5 nm. In quantum-sized metal particles, energy bands of

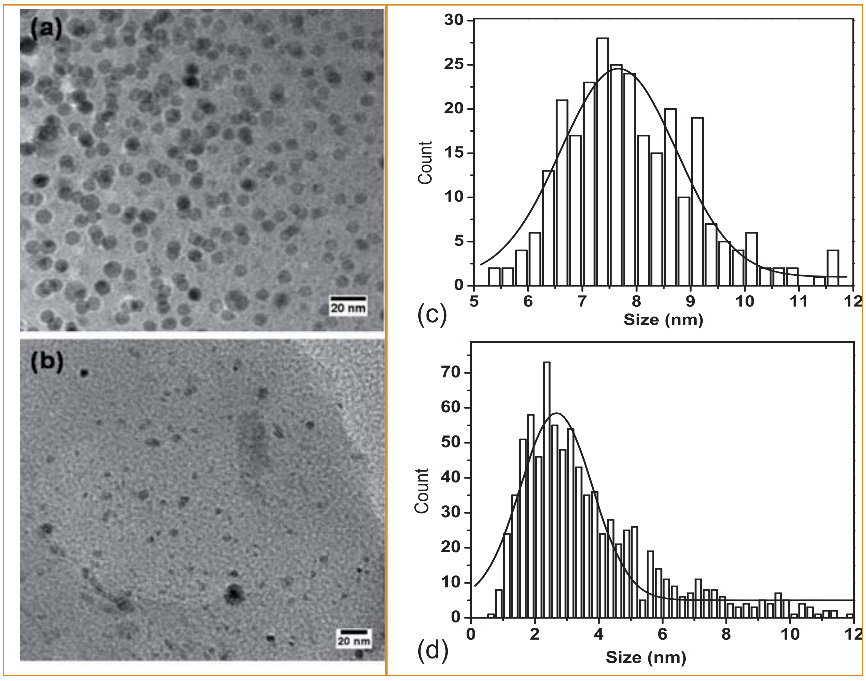

Fig. 2 *TEM images show sizes of Ag nanoparticles SiO$_2$ sample (image (a)) and size histogram is shown in (b). Image (c) shows the Ag nanoparticles after Si^{5+} ion-irradiation and corresponding size histogram is shown in (d)*

conduction electrons may evolve as discrete levels due to strong quantum confinements. As a result, certain electronic or plasmonic transitions may only be possible between the quantized energy levels in fine metal particles. To understand the plasmonic transitions and consequent effects on the optical absorption processes in fine metal particles, quantum mechanical treatments have been prescribed to compute dielectric constants of metal particles. Blueshifts of plasmon peak have been observed upon decrease in nanoparticle sizes. Interestingly, observed blueshifts of plasmon resonance peaks and associated decrease of the optical absorption intensities with gradual decrease in size of Ag particles Figure 1 agree very well with the theoretical calculations carried out by Scholl *et al*. The TEM images of embedded Ag nanoparticles in silica (synthesized by implantation of Ag ions in silica to dose of 5×10^{16} ions/cm^2) before and after high energy Si^{5+} ion irradiation to ion dose of 5×10^{15} ions/cm^2 is shown in Figure 2 along with corresponding size histograms. It can be seen that the average sizes of Ag nanoparticles have reduced from 7.7 to 2.7 nm after Si^{5+} ion irradiation up to dose of 5×10^{15} ions/cm^2. Thermal spike model has been adopted to the temperature dynamics around Ag nanoparticles being irradiated by high energy Si^{5+} ions. Variation of temperature with time at the center of embedded Ag nanoparticles of different sizes is shown in Figure 3a. Figure 3a shows the rise of temperature above 750 K for about ~2 picoseconds. As a result, Ag nanoparticles are likely to melt for a short time. Secondly, temperature increases ($\geq$3000 K) in the surrounding SiO$_2$ matrix along the ion track (Figure 3b). Thus, both Ag nanoparticles and the SiO$_2$ matrix may remain in molten state for short time (~1 ps) allowing transport of atoms through the interface resulting in the reduction in particle size.

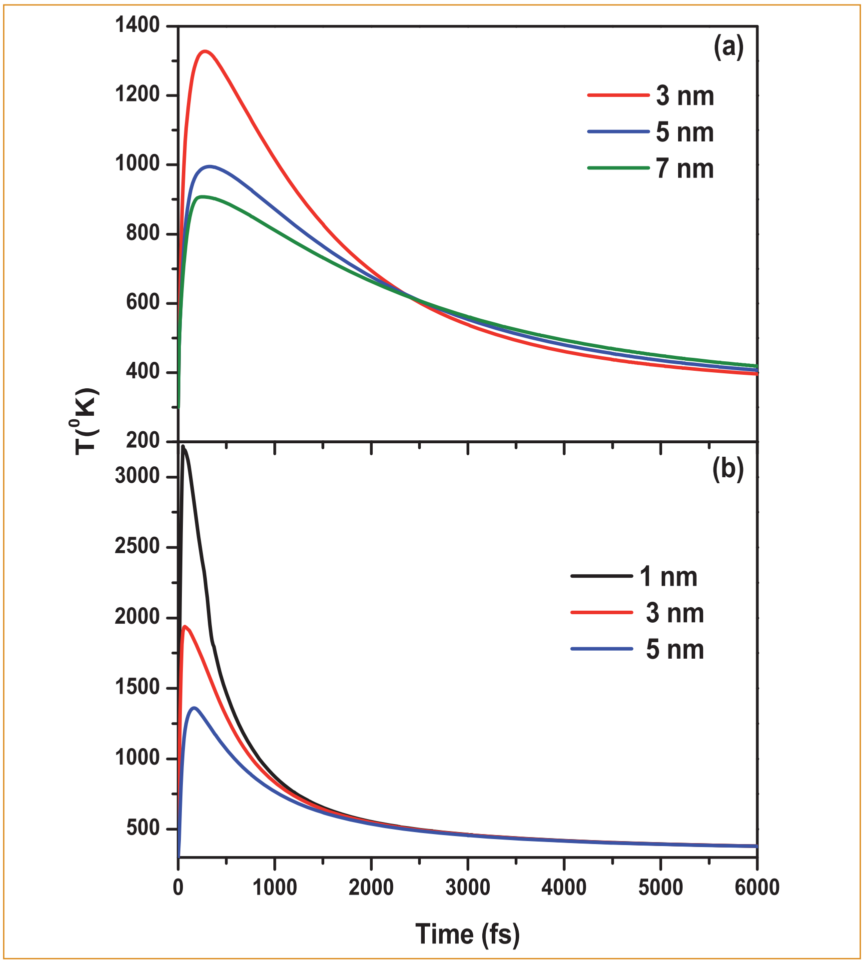

Fig. 3 *Evolutions of temperature of (a) SiO$_2$ matrix at various distances from the ion track and (b) Ag nanoparticles of different diameters embedded in a SiO$_2$ matrix*

V.25 Nanoporous Metallic Materials for Possible Applications in Nuclear Technology

Nano-porous metallic solids (NPMS) are mostly monolithic in architecture with ligament and pore sizes occurring in the range of 1-100 nm. The microstructure of NPMS is bi-continuous in nature, consisting of nanometer sized interconnected ligament networks interspersed with three-dimensional pores. These materials have been made in various shapes and sizes such as thin or thick films, cylinders, rods and cuboids by means of an electrochemical dealloying process.

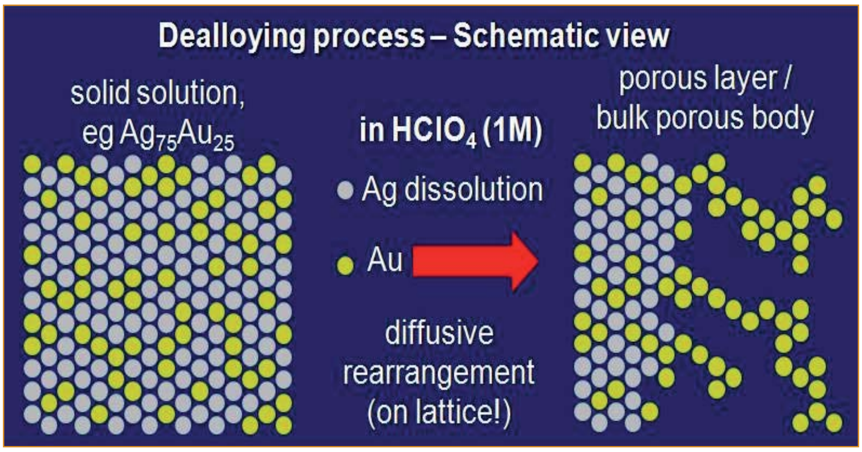

Fig. 1 *Schematic showing dealloying process. Yellow circle denotes Au atoms and grey circle denotes Ag atoms. Left side in the figure illustrates the Ag-Au alloy configuration and right side illustrates formation of porous structure with Au ligaments after the dissolution of Ag atoms*

Figure 1 shows a schematic which illustrates dealloying process. In a binary $Ag_{75}Au_{25}$ alloy Au constitutes superior electrochemical inertness as compared to Ag. Therefore, Ag atoms are electrochemically susceptible towards preferential leaching. On polarization of an $Ag_{75}Au_{25}$ alloy configured as a working electrode in an electrochemical cell, application of a potential just above the critical threshold dealloying potential causes detachment of Ag atoms from the alloy phase which eventually gets dissolved in the solution. Subsequently these accumulate near the counter electrode. This process results in the formation of metallic Au sponge with uniform nanometer sized ligaments and pores.

Figure 2 illustrates the synthesis results for nano-porous Au. Figure 2a shows the photograph of an electrochemical cell with three electrode configuration, taken before and after applying at a control cell potential of 750 mV versus Ag/AgCl (pseudo) in 1 M $HClO_4$ electrolyte solution. This was done by using a potentiostat. The counter or auxiliary electrode used in the dealloying experiment is an Ag coil. Figure 2b shows a few different shaped nanoporous Au specimens prepared from the alloy composition $Ag_{75}Au_{25}$. Scanning electron microscopy image shown in Figure 2c was collected from one such dealloyed nanoporous Au. This image reveals the characteristic features of bi-continuous microstructure with two interpenetrating ligament and pore networks with size centered around 20 ± 2 nm.

The important parameters which control the microstructure in the nanoporous materials, are alloy chemical composition, electrolyte composition, critical potential applied to the cell for the dealloying, electrolyte bath temperature, chemical passivation and related reaction kinetics that prevails at the corrosion interface. An advantage of this dealloying process points to the fact that spatial extent of NPMS remains same as that of the physical volume pristine alloy even after complete leaching of reactive constituent.

Such nanoporous metallic materials have been studied for more than two decades and a comprehensive knowledge base is now available in the literature. Different scientific aspects viz., transport mechanisms for the evolution of nanoporosity, elastic and plastic deformation behavior at smaller length scales and catalytic response and thermal coarsening have been deliberated quite well. The large surface area with high density of pore space entrained in NPMS matrix enables one to tailor or control their physical, mechanical and catalytic properties. This is achieved by exposure of the active pore surface towards interaction with atoms, ions and molecules in fluidic media.

We have studied recently the fundamental processes that govern the strength and plasticity of nanoporous Au with the variation of ligament size *L*. The studies on nanoporous Au using hardness measurements support that the strength of nanoporous metal(s) is increased when the ligament diameter is decreased. For instance, when the ligament diameter is ~10 nm, the ligament mechanical strength in nanoporous

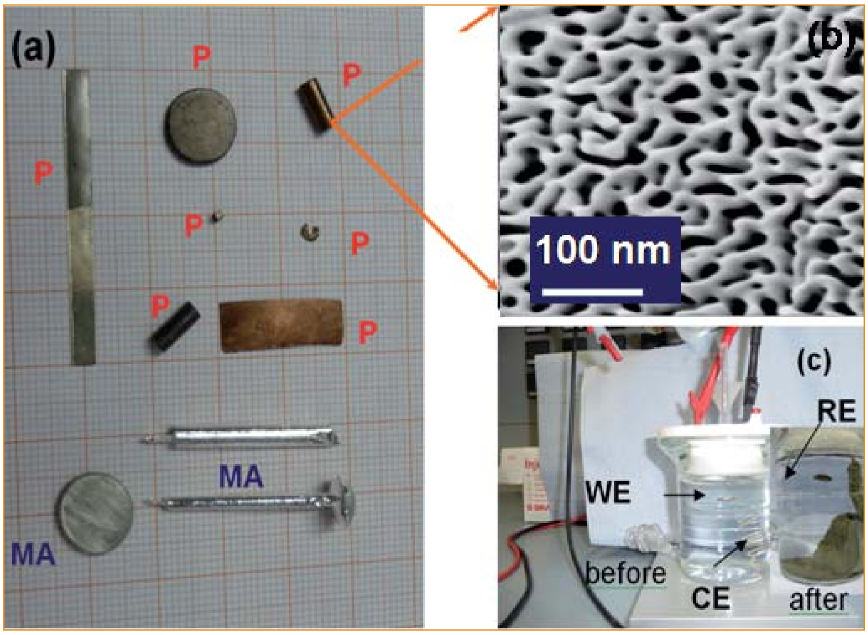

Fig. 2 (a) *Different shapes of nanopoorus samples: 'P' represents porous and 'MA' represents master alloy, (b) typical SEM image of a porous Au showing bi-continuous structure and (c) a model electrochemical cell used for the dealloying experiments. The important developments in the electrochemical cell before and after the completion of the de-alloying process are highlighted. WE- $Ag_{75}Au_{25}$ alloy, CE- Ag coil, RE-Ag/AgCl pseudo electrode*

Au becomes as large as ~ 4.5 GPa, a value close to the theoretical shear strength of the material. In comparison, the same material became softer (ductile) when the ligament diameter exceeds few hundred nanometers. The ligament yield strength in nanoporous Au has been measured from the hardness data, using the known density scaling equation for porous materials that relates the macroscopic yield strength to the microscopic ligament yield strength.

To correlate the strength in NPMS with ligament size, we substitute the ligament yield strength and the ligament size values to the well known Hall-Petch equation, $\sigma = \sigma_0 + k\, d^{\alpha}$, where σ_0 is a frictional stress required to move dislocations, d is the grain size and α is the scaling exponent. It is worth noting that for a three dimensional grain of diameter d, with the dislocation sources at the grain boundary, the power law exponent value in the Hall-Petch equation is -0.5. Figure 3 shows the ligament yield strength as a function of ligament diameter L. It is seen that there is a cross over in the scaling behavior, beyond a ligament diameter ~100 nm. In the size range, 5-100 nm, the variation of ligament yield strength with L yields a scaling exponent of -0.3, which is a distinctly different exponent with a value -0.6 specific to higher ligament sizes.

The reason for the reduced scaling exponent of -0.3 obtained in smaller ligament diameter in nanoporous Au is explained as following. As indicated in the beginning, NPMS comprises of inter connected nm sized ligaments laden with continuous pores. In this geometry, the ligament diameter grows more than the ligament length during coarsening. Moreover, the ligaments in NPMS tend to deform through bending in the presence of external mechanical load. Thus, the observed Hall-Petch exponent of -0.3 arises in nanoporous Au due to constrained directional motion of dislocations in the ligaments. This physical picture is substantiated by the fact that a cross over behavior is seen beyond 100 nm of ligament diameter when the dislocation activity acquires a 3-D character.

With the present knowledge about the performance of NPMS, one can be confident that high surface area nanoporous metallic structures will be an attractive alternative to membrane based hydrogen permeation with enhanced sensitivity, which can find application in H_2 detection in $Na\text{-}H_2O$ system of FBRs.

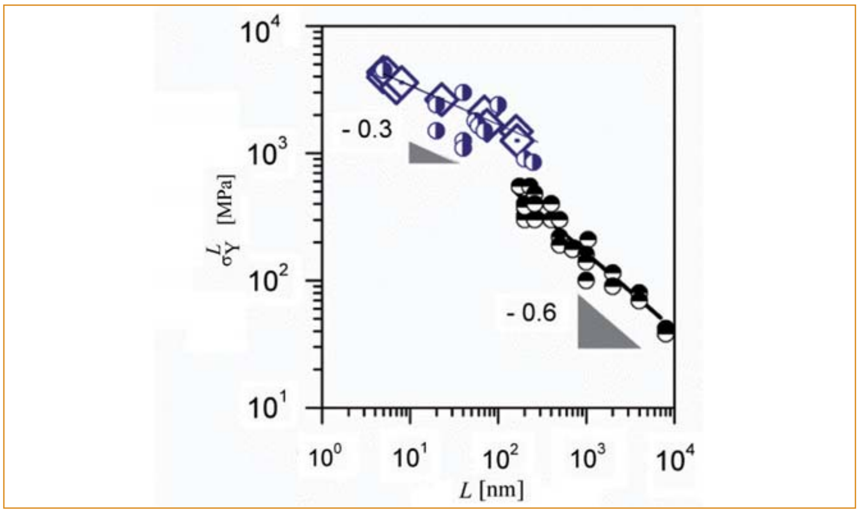

Fig. 3 *Plot of ligament yield strength* σ_Y^L , as a function of ligament diameter L *for nanoporous Au. The thin blue straight line is the best empirical fit of the data with a power law exponent of -0.3. The bold black straight line is the empirical fit of the data with the power law exponent of -0.6. A crossover is seen beyond the ligament diameter 100 nm*

V.26 Nanophosphor: Synthesis, Characterization and Thermoluminescence Studies

Red light emitting Y_2O_3:Eu^{3+} nanophosphor has been synthesized by a low temperature solution combustion method using ethylene diamine tetra acetic acid (EDTA) as fuel at 500 ± 10°C. The studies on the effect of calcination temperature on its structural, photoluminescence (PL), and thermoluminescence (TL), properties are reported here. The crystallinity of the samples increased and the strain is reduced with increasing calcination temperature. The TEM image of as-prepared nanopowder exhibits a crystallite-composed porous frame (Figure 1a). The ultra violet (UV) light induced TL in the material at various calcination temperatures measured by exposing the samples to 254 nm light revealed maximum TL intensity at 1000°C. The increase of TL intensity with calcination temperature is attributed to the decrease of the non-radioactive recombination probability, which occurs through the elimination of quenching defects. Figure 1b shows the variation of TL intensity with UV exposure time for 1000°C calcined Y_2O_3:Eu^{3+} samples. With an increase in the UV exposure time, the growth in the TL intensity of the 116°C peak is more distinct than that of the higher temperature peak. The density of the surface defects responsible for TL increases with an increase in UV exposure, leading to an increase in peak intensity. The fall in TL intensity at higher exposure time is usually a consequence of competition between radiative and non-radiative centers or between different kinds of trapping centers. In the case of UV-exposed samples, the TL response mainly generates from the surface traps. According to track interaction model (TIM), the number of traps generated by the high energy radiation in a track depends upon the cross section and the length of the track inside the matrix. In the case of nanomaterial, the length of the track generated by high energy radiation is of the order of a few tenths of nanomaterial. In nanophosphors, the formation of surface related defects are more as compared to deep defects which can be mapped easily through TL. As the surface to volume ratio is large in nanomaterials, shallow defects (Ea~0.1-0.3eV) are formed unlike for materials in micro-regime, where deep defects are formed.

The PL spectra of the material at various calcination temperatures are studied. Excitation spectra consist of a broadband with a maximum at 240 nm due to the charge transfer (CT) between O^{2-} and Eu^{3+}. The peak position shifts toward the higher wavelength side (Figure 1b) with calcination temperature. The CT energy position depends on the crystal field of ions surrounding O^{2-}, the strength of anion binding, the size of the cation site, and the coordination number. Therefore, in this case, the shift in CTB might be attributed to a change in the environment of O^{2-} with calcination temperature. Figure 2 shows the PL emission spectra of the Y_2O_3:Eu^{3+} nanoparticles as-prepared and calcined at 600-1000°C for 3 hours. The PL measurements show that the intensity of the red emission (611 nm) is highly dependent on the calcination temperature and is about 10 times higher as compared to as-formed samples. The optical band gap (Eg) was found to reduce with an increase of calcination temperature due to the reduction of surface defects. All the samples exhibited sharp and strong emission at 611 nm under excitation of 240 nm with variation in the intensity related to calcination temperature. The spectra show well resolved features, which can be noticed at 582, 588, 593, & 611 nm and assigned to the 5D0 → 7FJ (where J is 1, 2, and 3) transitions. The studies reveal that crystallinity, crystallite size, and the elimination of structural disorder play a major role on the PL intensity and TL properties of these nanophosphors.

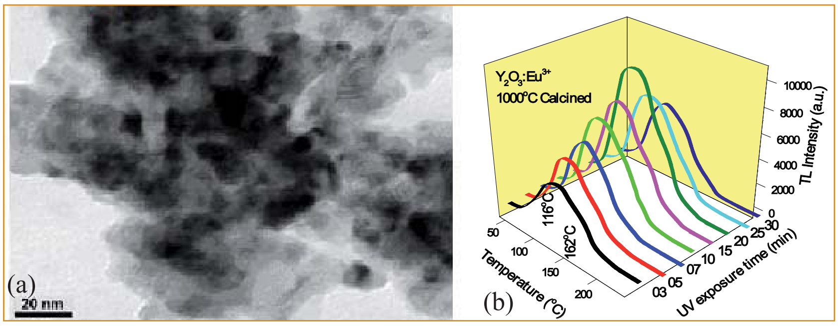

Fig. 1 *(a) TEM images of as-formed Y_2O_3:Eu^{3+} nanophosphor and (b) TL glow curves of Y_2O_3:Eu^{3+} nano-phosphor calcined at 1000°C exposed to UV radiation in the range 3−30 minutes*

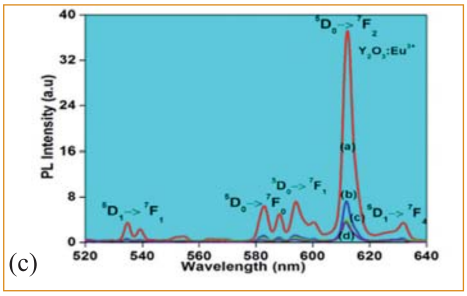

Fig. 2 *PL emission intensities as a function of calcination temperatures for Y_2O_3:Eu^{3+}; (a)1000°C, (b) 800°C, (c) 600°C and (d) 500°C*

V.27

Enhanced Thermal Stability of Phosphate Capped Magnetite Nanoparticles

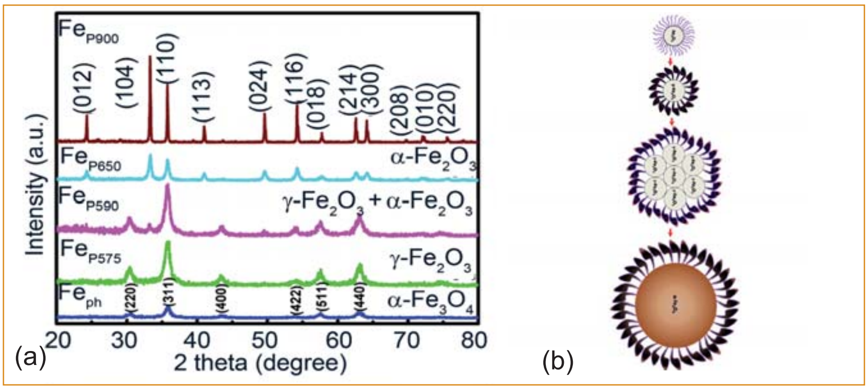

Fig. 1 (a) XRD patterns of Fe_{Ph} nanoparticles annealed in air at 575, 590, 650 and 900°C and (b) schematic representation of Fe_{Ph} nanoparticles during annealing in air at 300 - 900°C

Bare nanoparticles are known for their instability because of oxidation and agglomeration owing to their excess reactivity due to unsaturated surface bonds. Therefore, new strategies are being explored to improve stability of nanoparticles against agglomeration and oxidation. The capping of nanoparticles with suitable molecules or providing protective shell of noble metals are some of the approaches used to overcome these problems. Among the magnetic nanoparticles, magnetite and maghemite are widely used materials because of their interesting magnetic properties. In general, the magnetite nanoparticles are converted to a nonmagnetic phase at ~500°C. Therefore, new strategies are required to produce magnetite nanoparticles with enhanced thermal stability (>500°C), without compromising their magnetic properties.

Our studies show that the phosphate capping on magnetite (Fe_3O_4) nanoparticles can improve their thermal stability dramatically. The phosphate capped Fe_3O_4 nanoparticles are synthesized by a single-step co-precipitation method. The prepared magnetic nanoparticles are characterized using various techniques.

The XRD pattern of air annealed Fe_{Ph} nanoparticles are shown in Figure 1a. For samples annealed upto 575°C , the diffraction patterns show peaks corresponding to the (220), (311), (400), (422), (511) and (440) planes of magnetite. Magnetite has an inverse spinel structure where the Fe^{2+} ions in octahedral sites are sensitive to oxidation. During the process of oxidation of Fe^{2+} into Fe^{3+} (maghemite formation), vacancies are formed, which can be randomly distributed or partially or totally ordered. Maghemite displays superstructure due to cationic and vacancy ordering. Upon oxidation of magnetite, the bulk is subjected to an increasing compressive stress leading to a stoichiometric magnetite core surrounded by an oxidized shell layer of Fe_2O_3. Both magnetite and maghemite are suitable for technological applications and exhibit superparamagnetism below ~15 nm.

When annealed in air, the phosphate capped nanoparticle undergoes a magnetic to non-magnetic phase transition at a temperature of 689°C, as compared to 580°C in the uncoated nanoparticle of similar size. During heating, phosphates at the surface of the particles dehydrate and react with the surface carbonates to form an ester through polyphosphoric acid intermediate. These esters dehydrate to form phosphocarbonaceous char. This reactive nature increases the phosphocarbonaceous char yield, which further crosslink and structurally order as a solid condensed phase by interacting with Fe_3O_4. The shell prevents the intrusion of heat, oxygen, volatiles and mass to and from the core and hinders the oxidation of Fe_3O_4 to γ or α-Fe_2O_3. The small angle X-ray scattering measurements show that the char thickness is ~1.5 nm at ~550°C. At higher temperatures, the coalescence of nanoparticles occurs along with the restructuring of the phosphocarbonaceous shell into a vitreous semisolid layer on nanoparticles, which was confirmed from the small angle X-ray scattering, Fourier transform infra red spectroscopy and transmission electron microscopy measurements.

Based on the above results, a mechanism responsible for the enhanced thermal stability of Fe_{Ph} nanoparticles is proposed. Figure 1b shows the schematic representation of Fe_{Ph} nanoparticles air annealed in the temperature range of 300-900°C. The phosphates on Fe_3O_4 (shown by furry like structure) are converted to phosphocarbonaceous char shell (shown by petals) during annealing.

V.28 Growth of Vertically Aligned Graphene Nanosheets by Plasma Enhanced Chemical Vapor Deposition

After the discovery of carbon 60 (C_{60}) or Buckminsterfullerene in 1985, a new era has started in the field of carbon nanostructures (CNSs). The subsequent work led to the discovery of carbon nanohorns, diamond-like carbon, nano-diamonds, carbon nanotubes and graphene. The graphene, an another breakthrough in carbon wonderland, has created tremendous interest to both physicists and chemists due to its various fascinating properties with potential applications in optoelectronics, supercapacitors, and sensors. Also, the research on graphene helped to invent more new two dimensional layered materials e.g. MoS_2, WS_2, h-BN, silicene and germanene.

The vertical graphene nanosheets (VGNs) is one of the remarkable nanostructures in carbon family. It is a porous 3D network of aligned vertical sheets, freely standing perpendicular to the substrates. Each sheet is composed of a few graphene layers with length and width varying from a few nm to µm. This unique geometry with high surface area, high conductivity, open edges, and easy functionalization capablity make the VGNs the most suitable candidate as electrode material for supercapacitors, fuell cells, chemical & bio sensors, and optoelectronic applications.

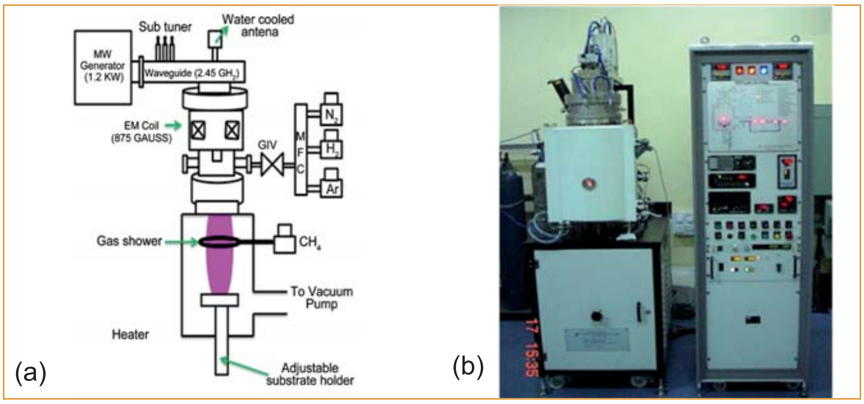

Fig. 1 *(a) Schematic and (b) photograph of ECRCVD set up*

Plasma enhanced chemical vapor deposition (PECVD) techniques have already shown its potential in growing various carbon nanostructures. The main advantages of PECVD are that it is catalyst free, grows at relatively low temperatures, shorter time and is amenable to doping. In addition, the technique is ideal for uniform large area and conformal coatings. In view of proven capability, we consider microwave electron cyclotron resonance PECVD (ECR-PECVD) as a promising technique to fabricate VGNs. The schematic and photograph of the ECR-PECVD is given in Figure 1a and 1b, respectively. The system consists of a microwave plasma source operating at 2.45 GHz with maximum power of 1.2 kW, guided through a rectangular waveguide and introduced into a plasma chamber through a quartz window. An adjustable substrate holder with heater allows manipulation of the gap between the quartz window and the substrate.

For growth of VGNs, CH_4 is used as a source gas and Ar or H_2 or mixed Ar-H_2 is used as diluants. Growth is carried out at substrate temperature of 800°C at microwave power of 400 W. Prior to growth, the substrates are pre-cleaned by Ar plasma under 20 sccm Ar flow

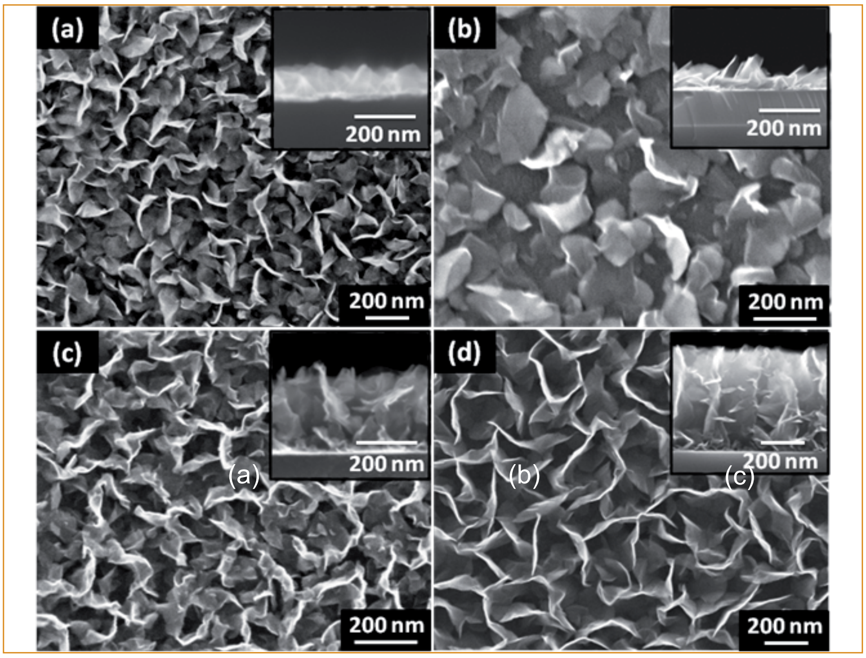

Fig. 2 *SEM micrograph of VGNs with density variation*

for 10 min at 200 W microwave power. Subsequently, CH_4 is fed into the chamber with appropriate amount of dilution gases. The VGNs are synthesized on wide range of substrates including metals (Pt, Ni, Au/Si, Cu, SS304, and SS316), semi-conductors (AlN, Si(111), Si(100), GaN) and insulating materials (Al_2O_3, SiO_x/Si and quartz).

Figure 2a-2d shows the FESEM micrographs of VGNs grown on SiO_2 /Si substrates. The petal-like and maze-like structures with different areal density can be seen in this figure. The cross sectional SEM micrographs, showing the height of these VGNs are given as inset in respective images. The process parameters such as feedstock gases & their composition, microwave power, substrate temperature and pressure have strong influence on the morphology, growth rate and structural properties of the CNSs. By appropriately choosing process parameters and optimizing them, we could achieve complete tunability in morphology, height, areal density, structural quality and electrical properties of CNSs. The vertical height varied from a few nm to microns and the areal density is up to 10^3 μ m^{-2}.

The PECVD synthesized materials suffer from large amount of defects due to ion bombardment from the high density plasma. Hence, it is very important to minimize the defects and gain knowledge over the growth mechanism with respect to the process parameters. Detailed Raman spectroscopic studies are carried out in order to analyze defects and disorder, such as nature of defects, quantification of defect concentration and their correlation with growth mechanism. For the first time, we have identified the type of defects and the transformation of defects in VGNs grown by plasma based systems. The VGNs grown on SiO_2/Si substrates contain predominantly a vacancy-like and hopping defects combination.

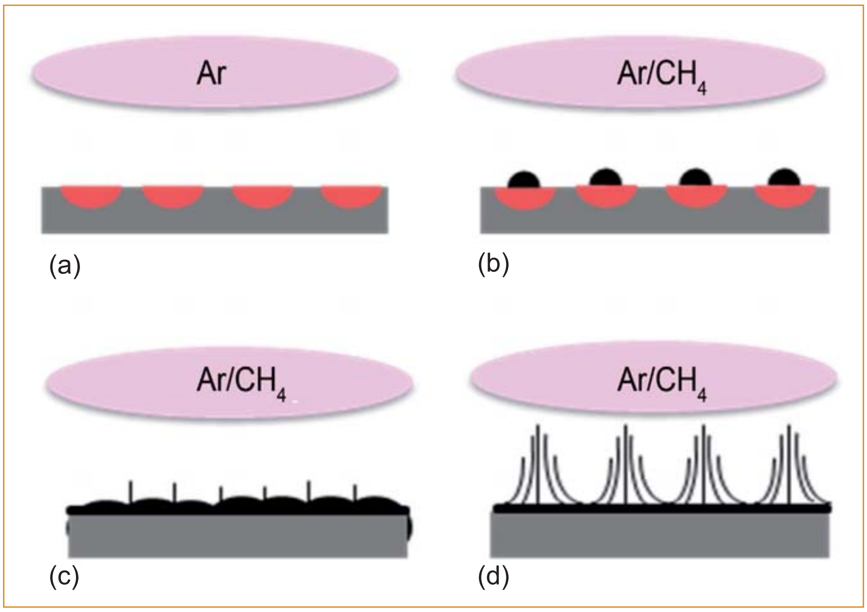

Fig. 3 *Schematic presentation of growth mechanism of VGNs under Ar/CH_4-plasma (a) hot spot formation, (b) nanoisland formation, (c) coalescence of nanoisland and (d) vertical growth*

From SEM analysis, it is found that the dilution of CH_4 with Ar and H_2 results in vertical and planar CNSs, respectively and also the intermediate areal density CNSs structures are obtained when CH_4 is diluted with a mixed Ar-H_2 composition. The growth mechanism of nanographite films having different morphologies are due to the competing growth and etching processes.

Based on our experimental evidences and available literature, the growth mechanism of CNSs having different morphology features on SiO_2 substrates as shown in Figure 3, can be summarized as follows. During pre-cleaning procedure, the Ar plasma removes surface contaminations and partial lattice oxygen from SiO_2 surface thus creating dangling bonds/active sites due to the formation of localized hot spot on the surface of substrates, as shown in Figure 3a. These localized hot spots are, energetically more favorable to adsorb hydrocarbon species. The early stage of nucleation is based on direct adsorption and surface diffusion of carbon species on these defective SiO_2 surface. This initiates the formation of rapid nucleation of carbon nanoislands and heterogeneous amorphous carbon (a-c) buffer layer since the growth rate is extremely high in PECVD. As the coalescence progresses, the stress at nanographitic grain boundaries get released and favors nucleation of carbon in the vertical direction as shown in Figures 3c and 3d. Then, the feedstock gas composition decides whether the growth of vertical structures to be continued or etched out. If the plasma consists of relatively higher concentration of Ar, it would favor the continued growth of vertical layers. On the other hand if the erosion is high due to excess nascent hydrogen, the growth pattern is found to result in a few layer planar nanographite structures. Hence, it is possible to tune morphological features of CNSs with optimal dilution of CH_4 with mixed proportion of Ar and H_2.

V.29 Irreversible Densification of Cesium Loaded Iron Phosphate Glasses under High Pressure

Iron phosphate glasses containing 40 mol% Fe_2O_3 and 60 mol% P_2O_5 (IPG) are found to be very effective in vitrifying high level wastes rich in radioactive cesium sludges. Studying the structural stability of these waste loaded glasses under hostile conditions becomes essential for a comprehensive assessment of the viability of these glasses in nuclear waste disposal. In this context we have carried out, for the first time in situ high pressure Raman spectroscopic studies upto 40 GPa on IPG and Cs loaded IPG-Cesium loading ranging between 5 mol% (IPGC5) to 35 mol%-(IPGC35) in order to investigate the structural stability of these glasses under such harsh conditions.

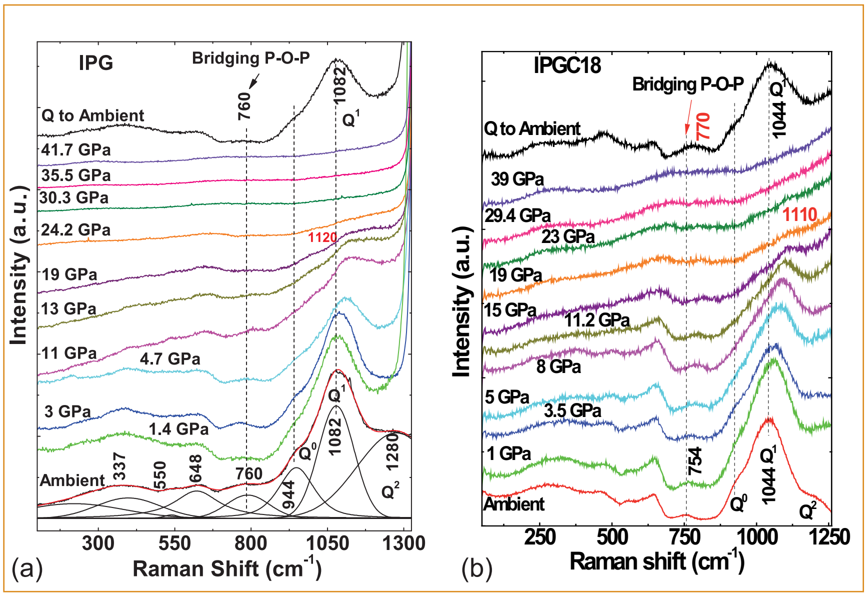

Fig. 1 In-situ high pressure Raman spectra of (a) IPG and (b) IPGC18 along with the decompressed spectra. Resolved peaks are shown for ambient spectrum of IPG sample

XRD studies on IPG and cesium loaded IPG were carried out to check for any evidence of vitrification. A maximum of 35 mol% cesium has been loaded in the IPG matrix without any evident signature of either phase separation or devitrification. In situ high pressure Raman measurements were carried out on micron sized chips of IPG and Cs loaded IPG using a mini diamond anvil cell.

Figures 1a and 1b show the Raman spectral evolution with pressure for both IPG and IPGC18 (18 mol% Cs loaded IPG) respectively. The plotted spectra reveal pressure induced changes in both the spectral position of the bands and the Raman intensities. Positive pressure induced shifts are evident in the initial stages of pressurizing (~40 cm^{-1} shift for an initial increase of pressure upto 20 GPa). These positive shifts imply a compression of bonds leading to densification of the glass matrix. The progressive broadening of the Raman modes arises due to an extensive distribution of bond lengths and bond angles on account of increasing external pressure. The total collapse of Raman intensities at very high pressures (pressures greater than 20 GPa) points to severe disorder/distortion of the phosphate tetrahedral units in the glassy matrix. It is indeed very interesting to note that upon quenching the pressure from ~40 GPa to ambient pressure the bands regain their intensities and width, reverting back to their original positions. This elastic response of IPG is in sharp contrast to the behavior of other tetrahedral glasses like the silicate glasses, wherein permanent densification and structural transformations occur at much lower pressures.

It was also of interest to investigate the structural stability of IPG with higher concentrations of Cs under pressure. Hence high pressure Raman measurements were carried out on heavily doped glasses-26 mol% cesium loaded IPG (IPGC26) and 35 mol% cesium loaded IPG (IPGC35) samples (Figures 2a and 2b) respectively. We observe similar positive pressure induced shifts of the Raman phonons but the extent of hardening is significantly lower as compared to either IPG or IPGC18. With increase in pressure, modes become broad with a systematic fall in intensity, ultimately leading to a featureless spectrum above 20 GPa which once again points to severe disorder/distortions in response to the high external pressures. Quenching these heavily doped samples from their respective peak pressures results in significantly altered spectra, both with respect to spectral intensity, width and position, clearly revealing an irreversible pressure induced transformation (Figures 2a and 2b).

In order to understand the changes associated with pressurizing the glass matrix, detailed peakfit analysis of the Raman modes

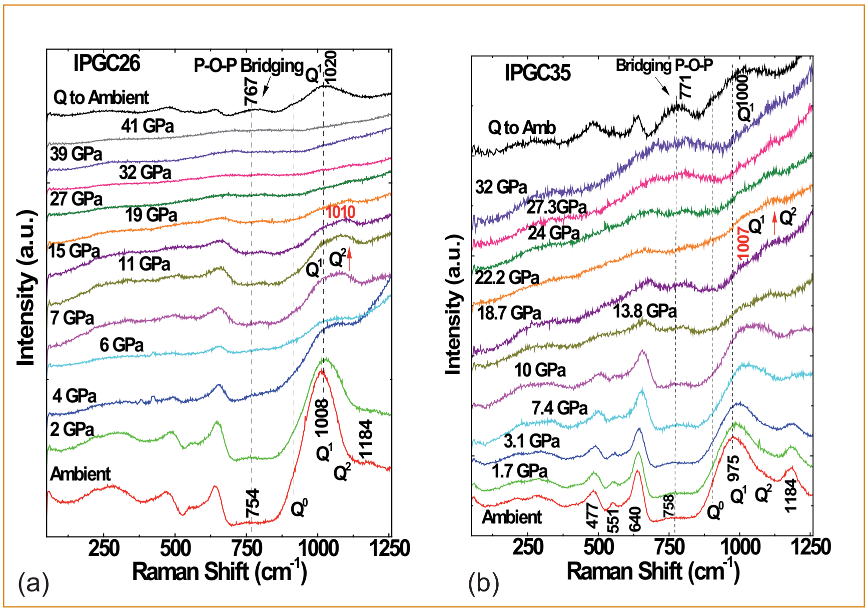

Fig. 2 *In-situ high pressure Raman spectra of (a) IPGC26 and (b) IPGC35 along with the decompressed spectra*

were carried out as a function of pressure. A plot of the variation of normalized area of the modes corresponding to the various constituent units (extended Q^2 meta phosphate units, dimeric Q^1 pyro phosphate units and the isolated Q^0 orthophosphate units) in IPGC35 with pressure, provided excellent proof of the progressive linking of the phosphate tetrahedra with increasing pressure (Figure 3).

Note that in the initial stages of pressurizing a significant drop in Q^0 is observed whilst the Q^1 units are seen to pick up. Beyond 6 GPa the Q^1 units are seen to decrease with a correlated increase in Q^2 units. This is an excellent evidence of a progressive linking of the phosphate tetrahedra.

It was of interest to understand the changes in the Raman modes induced by pressure quenching the samples in more detail. Hence the area normalized spectrum of the sample under ambient condition along with its pressure quenched counterpart has been plotted (Figure 4) for each composition. The position of the major feature corresponding to the P-O stretch frequency of the pyrophosphate Q^1 units that make up the majority of the building blocks in these glasses is seen to systematically get quenched at higher energies for cesium loaded samples beyond 18 mol%. This clearly indicates a reorganization of the glass matrix towards a more denser tetrahedral network. An evident pick up of the intensity of the stretching mode of the bridging P-O-P linkages at 768 cm^{-1} beyond IPGC18 (Figure 4) is observed to excellently scale with cesium content. This provides additional proof of the role of cesium in inducing irreversible cross links in the pressure quenched samples. The above spectral signatures are coherent with an irreversible transformation from a low density amorphous form of the cesium loaded glass to its high density form on exposure to very high external pressures. A systematic increase in the area under the 760 cm^{-1} mode in the pressure quenched samples with increased cesium loading has also been noted.

It is well known that the presence of high field strength modifying cations (beyond ~20 mol% alkali loading levels), in the matrix tends to disproportionate the dimeric pyrophosphate Q^1 linkages that make up the majority of the units of the base glass into extended chains of meta Q^2 and isolated ortho Q^0 units. It is also interesting to note that the observed irreversible changes are evident only for samples loaded beyond IPGC18. Disproportionation of the glass network, for cesium doping beyond 18 mol%, results in the loss of the stable pyrophosphate units which increases interactions within the network. This could be the underlying reason that has facilitated the irreversible changes.

The above study clearly demonstrates for the first time that iron phosphate glasses are indeed structurally very stable matrices and can withstand very high pressures without any major structural modifications as long as the pyrophosphate units remain the major building blocks.

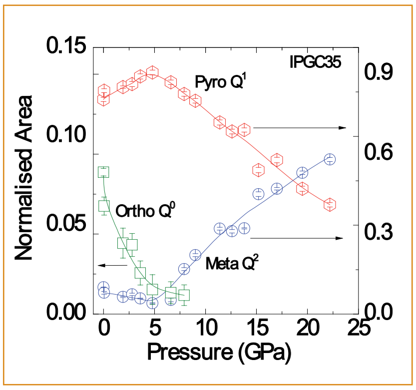

Fig. 3 *Variation of normalized area of Q^0, Q^1 and Q^2 units in IPGC35 with increase in pressure. Lines are guide to the eye*

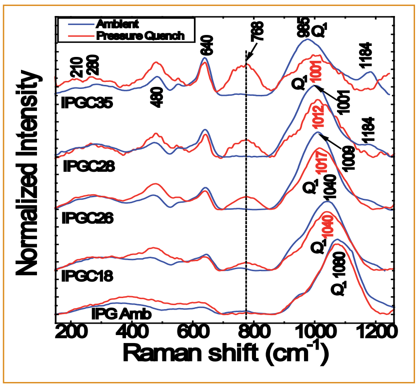

Fig. 4 *Set of area normalized ambient spectra along with its pressure quenched counterpart for all the samples*

V.30

Measurement of Young's Modulus of Polymers Films by Millimeter Sized Cantilever

Cantilevers are the simplest mechanical structures and can be visualized as miniature diving boards anchored at one end. Cantilever based resonators have been used as highly sensitive devices for studying surface-bound materials and detecting chemical vapors, explosives and biological analyses of interest. There are two basic modes of operation of cantilever based sensors, namely static, where the physical deflection of the cantilever is studied and dynamic where the change in resonance frequency/phase is studied. Further, in the dynamic mode, cantilevers can be classified as gravimetric or elastometric. Gravimetric sensing schemes detect the presence of the added mass of the target analyte through a decrease in cantilever resonance frequency, which offers one of the most sensitive mass sensing techniques, approaching single molecule detection. On the other hand, elastometric sensing schemes detect the changes in mechanical properties of the added material through an increase in resonance frequency.

In the present work, a millimeter sized cantilever is used to estimate the Young's modulus of a polymer film. Cantilever used in the present study is a piece of single crystal n-type silicon wafer with dimensions of 5.6 mm (L) x 1 mm (W) x 0.35 mm (T).

Table 1: Measured resonance frequency of cantilevers used in the present work and estimated Young's modulus from the frequency shift

S. No	Millimeter sized cantilever	Resonance frequency (Hz)	Young's modulus of the polymer film (GPa)
1.	Without polymer	13653	---
2.	With polymer	13714	3.96
3.	After gamma exposure	13792	10.1

A precisely cut Bo-PET (Mylar) film (1.5 mmx1 mmx 46 μm) was glued at the fixed end of the cantilever, which is known to be insensitive to mass change. Natural frequency of the cantilever (with and without polymer film) was measured using a laser interferometric vibrometer. The block diagram of the experimental setup and cantilever used in the present work are shown in Figure 1a and 1b respectively. Cantilever was excited using a piezo actuator which was swept by a function generator. By varying the function generator frequency, amplitude of vibration was recorded using the interferometer which in turn was interfaced to a PC. Now, resonance frequency was estimated from the peak of the plot of frequency versus amplitude. Experiment was also repeated after irradiating the cantilever with ^{60}Co gamma source (~1 Mrad). Figure 1c shows the resonance spectrum of the uncoated, polymer coated and after gamma irradiated cantilever. The estimated resonance frequencies from these spectrums are shown in Table 1.

It is evident from the table that resonance frequency increases with polymer film and it further increases after gamma irradiation. In the present work, since the polymer is glued to the fixed end of the cantilever, the frequency shift is entirely attributed to the change in effective Young's modulus. In order to estimate the Young's modulus of the polymer film, the differential Euler-Bernoulli beam equation modified to accommodate the partial polymer coating was employed. The integrals were evaluated, the quadratic equation was numerically solved using a MATLAB program to obtain the Young's modulus of the polymer film. Table 1 shows the estimated Young's modulus using the present method which is around 4 GPa. This value is higher than the typical value of a Mylar film at room temperature (~1 GPa) and may be attributed to the variations in the polymer film thickness. The increase in Young's modulus of the polymer film after gamma irradiation is attributed to the polymer cross linking.

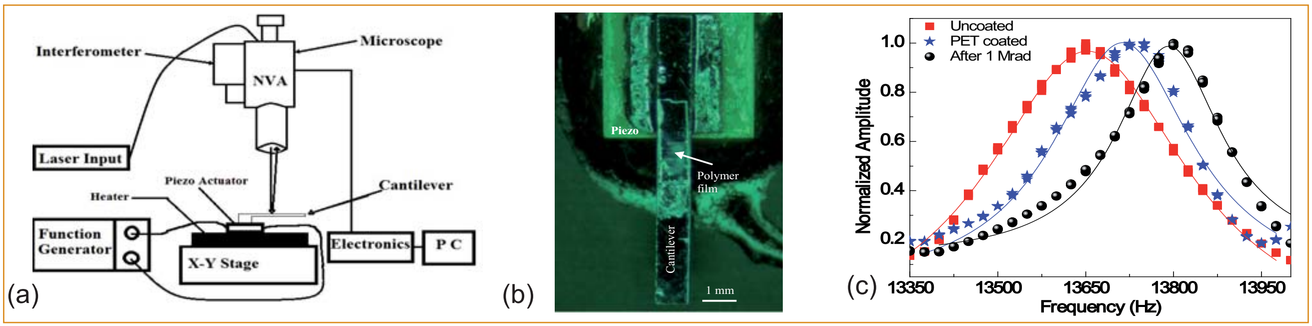

Fig. 1 (a) Block diagram of experimental setup used in the present study using nano vibration analyzer for estimating the natural frequency of the millimeter sized cantilever shown in (b). (c) Resonance spectrum of the cantilever without and with a polymer film and after gamma irradiation. It is clear from this figure resonance frequency increases with polymer film and after gamma irradiation

V.31 Role of SnO_2 Quantum Dots for Sensing Methane at Low Temperature

Methane (CH_4) is the second largest contributor to global warming after CO_2. It has global warming potential (GWP) value of 23 against 1.0 for CO_2. Methane, emitted from a variety of both human-related (anthropogenic) and natural sources, participates in total greenhouse gas emissions by 19%. There is serious apprehension on its emission from coal mine, farmland ventilation or natural gas-fuelled (NGV) vehicles as it can form an explosive mixture in air. Identification of CH_4 at a temperature below 350°C is a challenging task considering its high thermodynamic stability. Hence detection of low concentration of CH_4 at temperatures well below 300°C is of considerable interest. Catalytic materials were used for CH_4 detection in the concentration range of a few hundreds of ppm while flame ionization, and infrared detectors were suitably utilized for instrumental analysis of sub ppm and ppb level hydrocarbons including CH_4. Present state of the art for methane sensing is mainly dominated by the use of catalytic beads containing expensive noble metals like Pd and Pt in metal oxides, acting for CH_4 decomposition at relatively low temperature of 300^{o}C. Stable metal oxides, mainly SnO_2 sensors are widely used for CH_4 detection in the temperature range of 500-600°C. Catalytic metals in a dispersed phase or as electrodes with the SnO_2 semiconductors drive the reaction by lowering the activation energy of the system.However, loading of noble metals affects cost effectiveness and introduces additional process steps. SnO_2 is an important *n*-type semiconductor with a band gap of 3.6 eV at 300 K and has a Debye length of 3 nm. Nanostructured materials offer new horizon for low temperature detection as the size of active sensing materials approaches to the Debye length with the formation of a large depletion region of electronic charge forms after O_2 adsorption. In subsequent interactions with the target gas, chemisorbed oxygen species exchange charge carriers causing a substantial change in the electrical resistance involving the whole grain, not just surface alone. In addition, surface defects as well as enhanced surface to volume ratio with extra surface energy favour detection of a trace toxic gas. Thus, there is a large interest in controlled ultra small nanoparticles (NPs) closely matching to Debye length of 3 nm of SnO_2. Detection of potent CH_4 below 100 ppm at low temperature is still considered to be a challenge with pure SnO_2. In effect, control over the process steps for the preparation of NPs, for gaining large sensor response remained to be explored for CH_4.

A single step SnO_2 QDs preparation following a soft chemical route with no additional processes is reported here. Figure 1 shows HRTEM image of the as-prepared sample with average particle size of ~2.4 nm. Furthermore, HRTEM image displays two distinct '*d*' spacing of 0.345 and 0.278 nm with a measured angle of 68^o between them. This confirms presence of crystalline (110) and (101) planes of rutile SnO_2. However, the *d* (0.345 nm) spacing is higher by ~3.5 % than the reported value (JCPDS # 41-1445) indicating a tensile strength in the as-prepared sample. This particle size is less than the Bohr radius of the SnO_2 (2.7 nm) conforming to QD structure.

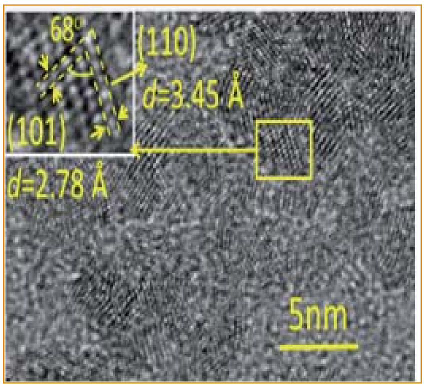

Fig. 1 *TEM image of the ultra-small SnO_2. The inset shows planes of SnO_2 and corresponding angle*

Figure 2 displays optical band gap obtained from absorption spectra using tauc's plot. SnO_2 QDs of 2.4 nm shows a characteristic strong quantum confinement with a band gap of 4.4 eV in comparison to bulk value of 3.62 for the 25 nm of SnO_2 NPs which is obtained by annealing the as-prepared QDs at 800°C in atmospheric conditions.

Raman modes for the annealed

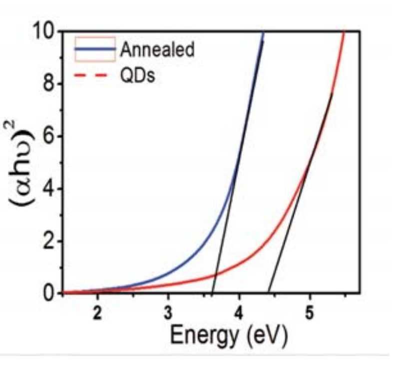

Fig. 2 *Band gap estimations from absorption spectra for SnO_2 NPs*

sample (Figure 3) show peaks at 474, 633 and 775 cm^{-1} corresponding to E_g,A_{1g} and B_{2g} modes, respectively.

In contrast, a strong broad peak at 575 cm^{-1} is observed for the as-prepared QD. This feature is attributed to the off-stoichiometric surface of SnO_2 QDs, mainly due to the in-plane 'O' vacancies. Since surface to volume ratio is high in QDs, the related surface defect peak becomes dominant in the Raman spectra.

Figure 4 depicts sensor response for the as-prepared sample towards CH_4 exposures at a typical temperature of 150°C. Responses are shown as relative variation in resistance (R/R_0) where R_0 is the base line resistance (~56 kΩ at 150°C) before the gas exposure. The ON and OFF signify exposure gas introduction and withdrawal time, respectively followed by a recovery. For *n*-type semiconductor SnO_2, a decrease in resistance results due to the release of bound electrons attached to the chemisorbed oxygen. There is a progressively increasing response with increasing concentrations of CH_4 (Figure 4). Experimentally, a detection of 50 ppm CH_4 with a significant response was recorded. However, a low detection limit is evaluated after considering only sensor signal which is three times above the noise level. The predicted value of around 30 ppm is lowest detectable CH_4 for the pristine SnO_2 system. For a comparative study, sensor response is defined as $S = (R_a\text{-}R_g)/R_a$, where R_a and R_g are the electrical resistances in air and in the presence of the gas, respectively. Responses to various CH_4 concentrations are shown in Figure 5 in the temperature range of 150-250°C for QDs. A monotonous increase in the '*S*' value was observed up to 225°C. Due to desorption effect a moderate decrease in value of *S*, however was noticed above 225°C. The annealed sample at 800°C also responded progressively with increasing concentrations of CH_4 even at a temperature of 150°C. Nevertheless, the sensor signal is comparatively weak and corresponding *S* value is low (S<1%, typically for 400 ppm at 200°C) Chemisorbed oxygen species present at different operating temperatures and their interactions with various oxygen defects namely in-plane and bridging oxygen vacancies are found to be critical for sensing output at low temperature. Activation energy (AE) is therefore a strong function of the possible surface reaction kinetics. Arrhenius plot of ln(S) with 1/T for 400 ppm of CH_4 is shown in Figure 6. Incidentally, AE for QDs (170 meV) is found to be half of the AE of the annealed sample at high temperature regime. Low temperature regime provides similar AE as given by the QDs.

Photoluminescence (PL) study reveals existence of a considerable amount of the in-plane oxygen related vacancies in the ultra small SnO_2 over the annealed one. In addition, temperature dependent PL measurements confirmed in-plane vacancies as swallow donors being close to the conduction band minimum. Dominance of the in-plane vacancies therefore indicate its strong contributions towards improved sensing at low temperature. The QDs which allow making compact and portable sensors have potential uses in monitoring CH_4 detection at affordable low power.

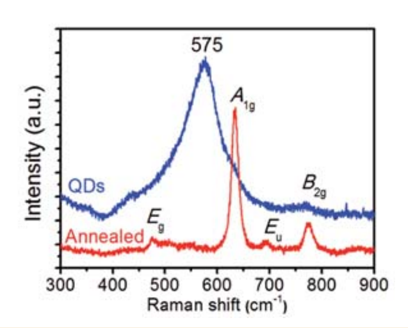

Fig. 3 *Raman spectra for the as-prepared QDs and the annealed samples*

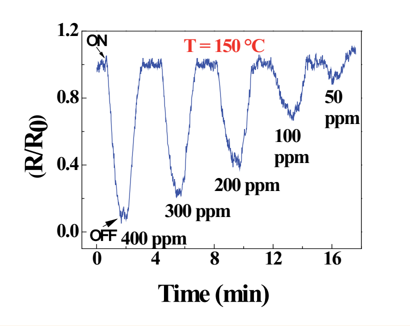

Fig. 4 *Sensor response of the as-prepared sample at 150°C*

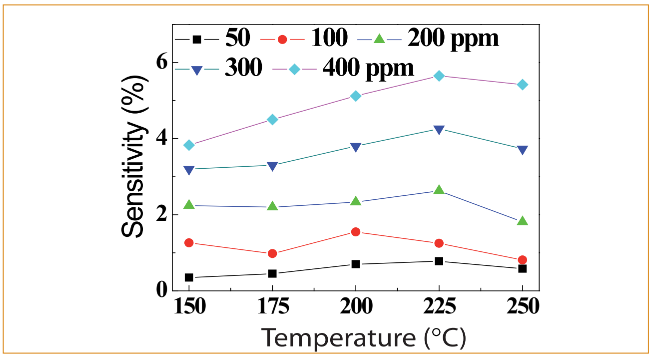

Fig. 5 *CH_4 sensitivity of the QDs*

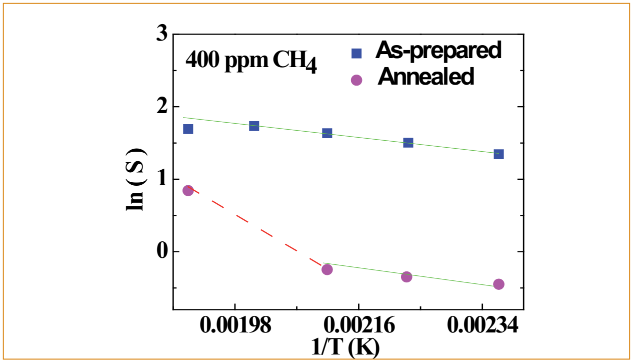

Fig. 6 *Arrhenius plot to deduce AE from temperature dependent sensitivity study*

V.32 Time-frequency Analysis for Understanding Ultrasonic Scattering and Enhancing Signal to Noise Ratio

Ultrasonic wave propagating in high scattering medium such as coarse grain austenitic stainless steel suffers spectral distortion due to high rate of attenuation of its high frequency components. This results in a change in the centre frequency of its power spectrum. Fourier transform based methods are not suitable for analysis of ultrasonic signals obtained from such materials due to poor signal to noise ratio (SNR). In an effort towards adaptive detection of defects in coarse grain type 316 austenitic stainless steel material, time-frequency based short time Fourier transform (STFT) method has been adopted to understand the frequency dependent attenuation and ensemble empirical mode decomposition (EEMD) method in conjunction with signal minimization algorithm has been implemented to improve the SNR.

The plane parallel specimens of 10 and 50 mm thickness were prepared from austenitic stainless steel blanks of coarse (200 μm) grain size. The 10 mm thick specimen was used to understand the frequency dependent attenuation. Flat bottom holes (FBHs) of different sizes were introduced in the 50 mm thick specimen at different depths for adaptive detection of defects. Ultrasonic signals were acquired in immersion mode using 16 and 10 MHz transducers for 10 and 50 mm specimens, respectively.

A novel methodology has been developed to optimize the window size for STFT spectrogram. A continuously moving window of 1.024 μs (512 discrete data points) was found to have optimum resolution in both frequency and time domains. Figure 1 shows the ultrasonic signal obtained from the coarse grain specimen of 10 mm thickness (Figure 1a), its spectrogram (Figure 1b) and the frequency information (Figure 1c) obtained at the first back-wall echo location. It can be clearly seen in Figure 1a that the back-wall echo is submerged in the back-scatter noise due to high scattering in the large grain size specimen. The back-wall echo can neither be distinguished in the time domain nor in the frequency spectrum (Figure 1c). However, the back-wall echo with even such a poor SNR stands out clearly in the spectrogram (Figure 1b). Using the spectrogram, it can be clearly understood that the lower frequency peak is from the back-wall echo while the higher frequency peaks are from the back-scatter noise. This demonstrates the advantage of the STFT method over conventional frequency spectrum based approach for high attenuation materials. Further, the high frequency content in the backscatter signal at depths even more than the back-wall clearly indicates lower frequency dependency for absorption phenomenon as compared to the scattering.

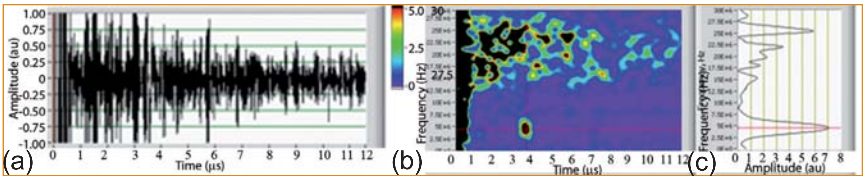

Fig. 1 (a) A-scan signal, (b) its spectrogram and (c) frequency content at the first back-wall location

The STFT method requires the optimization of window for processing the signals. In view of this, EEMD based methodology in conjunction with signal minimization has been developed for adaptive detection of defects in thick coarse grain specimens. The proposed methodology works adaptively for a large range of grain sizes (30-210 μm) and defects at different depths in the 50 mm thick specimen for the probe frequency and sampling rate used in the study. The three intrinsic mode functions (IMFs 3-5) were optimized for detection of defects by analyzing various data sets. Figure 2a shows ultrasonic B-scan acquired covering three FBHs as (A) 3 mm dia., 15 mm deep; (B) 6 mm dia., 25 mm deep; and (C) 6 mm dia., 35 mm deep in the 50 mm thick specimen. It can be clearly seen that all these defect echoes are submerged in noise.

Figure 2b shows the image after implementation of the EEMD methodology. The defects could be successfully detected and imaged with an enhancement of SNR of > 8 dB, demonstrating the effectiveness of the methodology for improving the SNR.

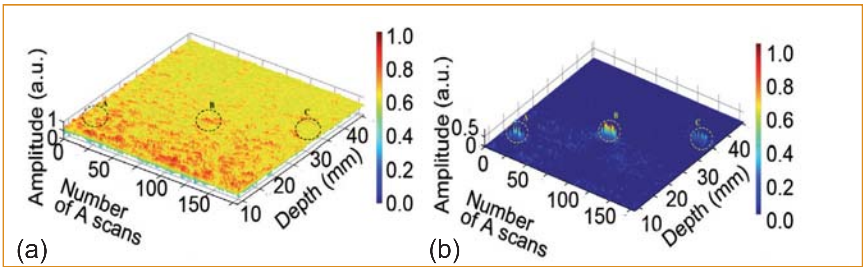

Fig. 2 (a) The time domain unprocessed ultrasonic B-scan image and (b) the B-scan reconstructed by employing minimisation algorithm to the IMFs (3-5) obtained by EEMD processing

V.33 Genetic Algorithm Application in Fuel Bundle Burn-up Optimization for PHWR

The fuel burn-up optimization of nuclear reactors helps in the maximum utilization of fissile materials without violating various safety aspects of the reactor. The fuel bundle burn-up optimization problem selected for the study aims at arriving at appropriate reference discharge burn-up values for the two burn-up zones of 220 MWe Pressurized Heavy Water Reactor (PHWR) core. The zones' reference discharge burn-ups obtained from the optimization can be used as the reference in selecting channels for refuelling. The problem of fuel bundle optimization of PHWR core has a large search space and involves a multimodal domain where multiple solutions are possible. For locating the globally optimal solutions in such cases, meta-heuristic approaches are suited and hence, we employ a genetic algorithm for the study.

Problem formulation

The reactor core of 220 MWe PHWR contains 306 coolant channels; each channel has 12 cylindrical fuel bundles with natural uranium as the fuel. In order to get radial flux flattening, the reactor core is divided into two burn-up zones as shown in Figure 1. The inner zone contains 78 fuel channels and the outer zone contains 228 fuel channels. The present study considers the discharge burn-up of inner zone in the range between 8500 and 11000 MWD/t and that of outer zone in the range between 4000 and 6500 MWD/t.

The aim of the optimization carried out is to find optimum reference discharge burn-up values for the inner and outer zones, in order to obtain maximum average discharge burn-up for the total core (BU_{ave}). The other objectives are the minimization of maximum bundle power (MBP), the minimization of maximum channel power (MCP), and the maximization of effective reactivity multiplication factor (K_{eff}). The units of MBP, MCP, and BUave are kW, MW and MWd/t respectively. The constraints considered are given as: MBP should be less than 430 kW,

MCP should be less than 3.2 MW,

K_{eff} should be greater than 1.0005 and

BU_{ave} should be greater than 6700 MWd/t.

Application of genetic algorithm

As part of representation of the algorithm, a candidate solution (in the present study, burn-up values of inner and outer zones) is encoded as a digital chromosome which has enough information to reproduce the original solution. While being executed, genetic algorithm generate a collection of trial solutions i.e. a population of chromosomes. The fitness value for each such chromosome is calculated by running the neutronics simulation code named TAQUIL. For the study, the genetic algorithm is implemented in C programming language. The genetic algorithm methods, parameters, and values used in the study are given in the Table 1.

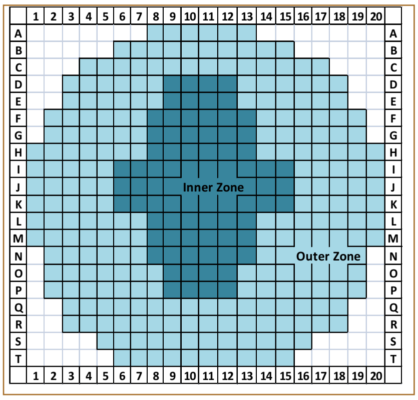

Fig. 1 *The two burn-up zones of the reactor core used for the study*

The results generated by four trial runs of the algorithm, are presented in Table 2. Among the feasible solutions at the final generation, two solutions are extracted, one with a maximum value for BU_{ave} and another with a minimum value for BU_{ave}, and presented in the table. The results show that the algorithm is able to produce feasible solutions towards the final generation. The results also demonstrate the capability of the genetic algorithm in producing a wide range of feasible solutions; that helps the reactor operator in getting more choices when deciding the appropriate discharge burn-ups of the zones of the reactor core.

Table 1: Genetic algorithm related parameters and methods or values used

S.No	Parameter	Methods/ values
1	Encoding	Floating point
2	Population size	50
3	Crossover method	Arithmetical
4	Crossover probability	0.6
5	Mutation method	Non-uniform
6	Mutation probability	0.05
7	Maximum number of generations	100

Table 2: Solutions representing maximum and minimum values obtained for BU_{ave} in the final generation

Tr. No	Max/ Min	Inner zone burn-up	Outer zone burn-up	MBP	MCP	K_{eff}	BU_{ave}
1	Max	10278.69	6037.28	429.70	3.1403	1.000514	6903.36
	Min	10254.69	5828.04	424.89	3.1046	1.001432	6700.70
2	Max	10269.54	6034.63	429.91	3.1418	1.000550	6899.97
	Min	10286.74	5824.56	423.80	3.0970	1.001363	6700.00
3	Max	10281.35	6034.42	429.55	3.1368	1.000520	6900.87
	Min	10266.12	5827.52	424.53	3.1021	1.001404	6701.15
4	Max	10273.44	6039.73	429.93	3.1419	1.000518	6905.17
	Min	10175.80	5834.69	427.51	3.1231	1.001607	6700.59

V.34 Monitoring Damage Evolution of Plain and FlyAsh Concrete Prisms under Cyclic Incremental Loading by Acoustic Emission

The occurrence of cyclic loading, chemical attack and reinforcing steel corrosion causes degradation or damage leading to formation of cracks or defects. Once initiated, cracks can grow at a faster rate and lead to catastrophic failure of the concrete. Therefore, it is important to detect damage in concretes at a very early stage. Acoustic emission technique (AET) is an online NDT method that has potential to detect damage and initiation as well as growth of cracks in concrete. Recently, fly ash concrete is being used for many constructions especially bridges. Fly ash replaced concrete improves the engineering properties and performance of concrete. AET has been used to monitor damage growth in plain and fly ash concrete prisms with different curing periods, subjected to incremental cyclic loading.

Two types of concrete (plain and with 30% fly ash) were used to produce concrete prisms (700 x 150 x 150 mm^3). These prisms were cured for 7 and 28 days. The AE signals generated during four point bending tests of the prisms were recorded using AE DiSP system. A piezoelectric sensor having resonant frequency at 150 kHz was used. Figure 1 shows the photograph of the experimental set up.

Variation of cumulative AE strength and load with time during the cyclic incremental loading of 28 days cured plain and fly ash concrete prisms are shown in Figures 2a to 2b. In plain concrete prism, dominant AE activity is observed only after crossing previous maximum load in the first two cycles. From the third cycle onwards AE activity is generated before previous maximum load at 16 kN. In the fly ash replaced concrete prisms, dominant AE activity is observed only after crossing previous maximum load in first three cycles. From the fourth cycle onwards, AE activity is generated before previous maximum load at 20 kN (shown by arrow). This shows that in 28 days cured fly ash replaced concrete prisms, damage accumulation occurs at higher load as compared to plain concrete prisms.

In order to assess the damage level during cyclic loading of concrete prisms, load ratio as per the recommended practice by NDIS 2421 (Japanese Society for Non Destructive Inspection) has been used. The load ratio is the ratio of load at the onset of AE activity to previous maximum load.

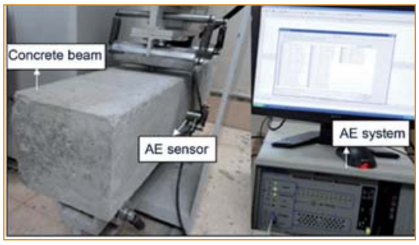

Fig. 1 *Photograph of the experimental setup*

Figures 3a and 3b show the variation of load ratio with loading cycle of plain and fly ash concrete prisms cured for 7 and 28 days respectively. Load ratio for both types of concrete decreases with loading cycle for 7 and 28 days cured prisms. Higher values of load ratio can be observed for 28 days cured fly ash concrete prism in each cycle as compared to 7 days cured prisms. Decrease in the value of load ratio is an indication of damage growth. This result shows that addition of fly ash with proper curing i) increases the strength of concrete and ii) delays damage growth with cyclic loading. This study shows that AET can be successfully used for damage evolution in concrete.

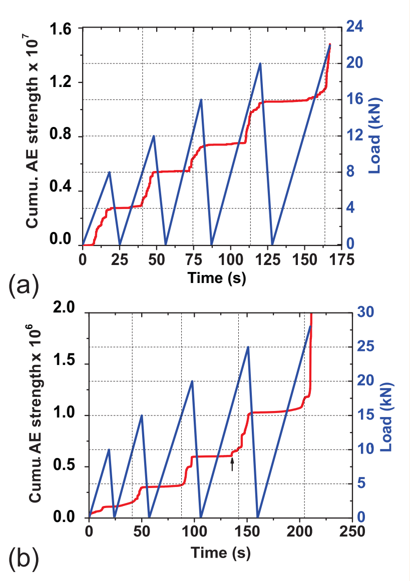

Fig. 2 *Variation of cumulative AE strength and applied load with time during cyclic incremental loading of (a) plain and (b) fly ash concrete prisms at 28 days curing*

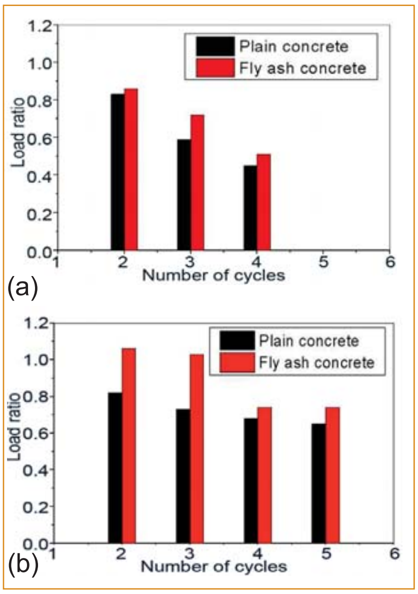

Fig. 3 *Variation of load ratio with loading cycle of plain and fly ash concrete prisms cured for (a) 7 and (b) 28 days*

V.35 Effect of Heat Treatment on Radiation Attenuation Characteristics in High Density Concrete

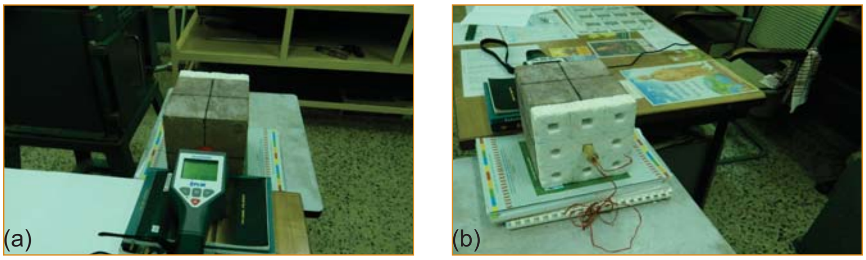

Fig. 1 *Gamma (a) spectrometer and (b) its positioned source*

A study on long-term effect on high density concrete exposed to a sustained temperature in FBR top shield is being carried out at QC laboratory of CEG, IGCAR. In FBR, the high density top shield concrete is subjected to elevated temperatures ranging from 25-180°C during the entire operation life of the reactor. One of the physical properties of significance is the density which is related to the radiation shielding effectiveness. An experimental study was undertaken at RSD to evaluate the effect of sustained exposure to elevated temperature on the radiation attenuation capabilities. Concrete blocks with densities 2.5, 3.65, 4.02 and 4.29 g/cc, 5 blocks in each density were made provided by CEG. Each block was of dimension 15 x 15 x 15cm. The higher density was achieved by adding more proportion of steel balls having diameter 2 cm and lesser. These concrete blocks were subjected to gamma attenuation and neutron attenuation studies before and after the heat treatment. As a first step, the concrete blocks were subjected to heat treatment at 120°C for 14 days and evaluated for radiation attenuation characteristics. Since, the density variation is expected during heat treatment due to the loss of water content in the concrete, the weight of the concrete blocks was also recorded before and after the treatment.

The gammatography technique developed was used for gamma attenuation studies. In this technique, only the transmitted virgin gammas are measured by selected photopeak energy window. A handheld gamma spectrometer (FLIR make identifinder) and a ^{60}Co gamma source of strength 0.046 mCi is used to study the gamma attenuation. The source is positioned along with a detector (Figures 1a and 1b) and typical gamma spectrum recorded. The counts in the energy region between 1080 and 1430 keV covering photopeak areas of 1173 and 1332 keV gammas are recorded for each measurement. The gamma attenuation factor is arrived by comparing the gamma counts with and without concrete blocks. Thus arrived gamma attenuation factors of each block before and after the heat treatment, is compared to evaluate the impact of heat exposure on the radiation shielding properties. The gamma attenuation results are depicted in Figure 2a which clearly indicates a measurable change in gamma attenuation factor after the heat treatment. It is observed that first level heat treatment of 120°C for the duration of fourteen days has resulted in variation of 0.5% in 4.38 g/cc block to 2.5% in 2.45 g/cc block. These variations in the gamma attenuation correlates well with the weight loss observed in each concrete blocks. Since, weight loss is due to the water content, variation in the gamma attenuation factor is lesser in magnitude.

To further confirm that the weight loss is primarily due to the reduction in moisture content, neutron attenuation studies using a 5 Ci Am-Be neutron source with neutron emission rate 1.1 x 10^7 n/s, was undertaken. Figure 2b indicates that there is a considerable reduction (about 22-25%) in the neutron attenuation due to water loss after heat treatment. The decreased magnitude of neutron attenuation factor after heat treatment clearly confirms that the loss is mainly the water content. The gamma and neutron attenuation studies on high density concrete blocks clearly reveal that the first heat exposure of 120°C for fourteen days produces measurable attenuation changes in the concrete.

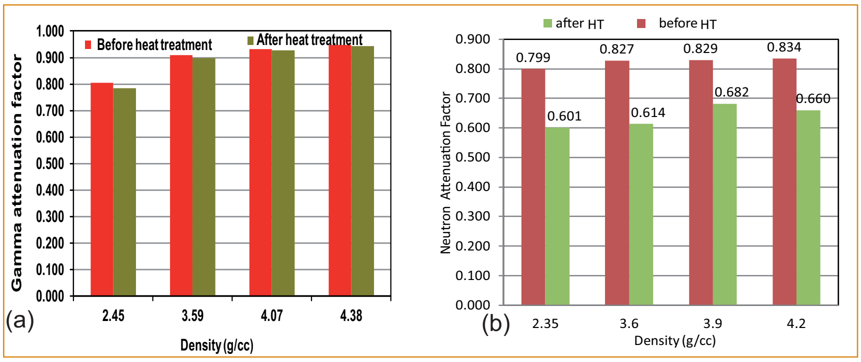

Fig. 2 *(a) Gamma attenuation in high density concrete blocks and (b) neutron attenuation in high density concrete samples*

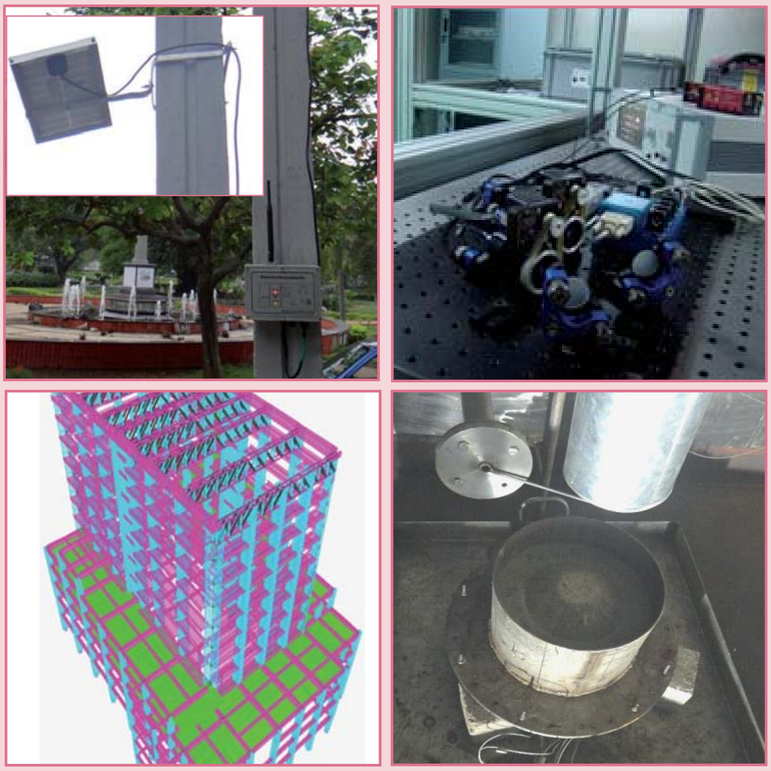

CHAPTER
VI

Infrastructure Facilities

VI.1 Design and Development of Solar based Wireless Sensor Networking Nodes and In-house Development of Wireless Network Analyzer Tools

Wireless sensor networks (WSN) is an emerging technology with a potential to revolutionize the way we sense and transmit the information.

Wireless Sensor Network comprises of multiple sensor nodes to sense the parameter to be monitored, router nodes to forward the data and base station node to get connected to a computer for live display and further processing. These nodes have been developed in-house for deploying them in applications related to nuclear facilities. WSN has been established in IGCAR at FBTR, RCL, INSOT, SADHANA Facility and Computer Centre. These networks are for monitoring/measuring process parameters and established as indoor deployment.

For applications such as radiation monitoring inside the DAE complex, the wireless network has to be deployed outdoors. In such scenario, the nodes cannot be powered from AC mains. Since the lifetime of battery is limited, solar energy has been opted for powering outdoor deployed WSN nodes (Figure 1).

Based on the experiments conducted to analyze the current requirements of WSN sensor and router nodes, the size of solar cells and rechargeable battery has been designed. The nodes were designed with IP68 rated metallic enclosures and industrial grade components to enable them suitable for rugged outdoor conditions. The router nodes were subjected to immersion tests under one metre thick water column and passed. During dark hours or cloudy days, the WSN nodes get powered by the Li ion rechargeable battery. An efficient fast switching circuit has been designed for this purpose and tested successfully. These nodes are being deployed at multiple locations inside DAE complex for radiation monitoring.

From the field experience in the early WSN deployments, the need to have sniffer/handheld network analyzer tool (Figures 2 and 3) that supports IEEE802.15.4 protocol was felt. Since such ready-made devices are not available in the market, the sniffing tools were developed in-house to analyze the network operation during different phases of development and deployment.

Zigbee sniffer has been developed in-house, which when connected to host machine, can be used in promiscuous mode to capture on-air traffic and to measure the signal strength in any channel. Based on functioning, it can be viewed either as packet or spectrum analyzer. As packet analyzer, it can intercept the traffic passing over the wireless network. In WSN, it is very much useful during the deployment phase, to analyze different network scenarios and wireless traffic monitoring. It is also used in the development phase for protocol debugging. As spectrum analyzer, the presence of interference and other cohabitating networks of the area of interest are determined. To analyze multiple channels simultaneously, multi channel sniffer has been designed and developed.

To get better flexibility, portable solutions were designed. Two different platforms-OpenMoko and Android have been chosen to develop these solutions. Applications have been developed for packet analyzer and spectrum analyzer on these platforms. In future, these devices will be used as trusted devices so that it can be used to distribute security keys, to view and control on-the-fly network health parameters and for calibration, configuration, maintenance and upgradation.

Fig. 1 *Solar based WSN router*

Fig. 2 *Zigbee sniffer*

Fig. 3 *Handheld wireless network analyzer*

VI.2 Design and Development of Customized RFID cum Biometric Based Access Control System

Presently, hand geometry based radio frequency identification (RFID) cum biometric based access control systems are installed at nuclear plants/facilities such as FBTR, RML, RCL and RDL. A new customized access control system meeting the requirements laid down by regulators' has been designed.

Access control system, as designed, comprises of access controller unit, RFID readers, hand geometry readers, EM locks, associated power supply units and a server application. The access controller unit has been designed and developed using ARM 7 based microcontroller. It consists of LPC 2478 microcontroller module, ethernet controller module, input module to receive the inputs from RFID and hand geometry readers and memory module to store the configuration, transaction and user details. This controller has been designed to control either two (RFID cum hand geometry readers for entry and RFID reader for exit) or four doors simultaneously (RFID readers for entry and push buttons for exit). The controller card can interface with four RFID readers, two hand geometry units, and four electromechanical locks. This controller has the capability to communicate with the server application through LAN. The firmware is entirely written in Embedded C.

Whenever an employee shows the RFID based identity card at RFID readers, information from the card is sent to the access controller via Wiegand protocol. The controller checks for the employee code in the local database (flash memory). If the corresponding employee code exists in the database, then the controller prompts to verify the biometric of the employee through the hand geometry unit. Once the biometric matches, the controller authorizes for entry or exit by de-energising the EM lock. The transactions (both authorised or rejected) are transmitted over LAN to the server application. If LAN connectivity is down, transactions are stored locally in a micro SD card waiting to be sent to the server when LAN connectivity resumes. By this means, no transactions are lost. Dynamic hand template updating is performed. Local antipassback verification prevents a card-holder from passing the card back. Report generation is made from the transaction table.

Presently the Server Application is designed to interface with 6 access controllers through TCP/IP with each of the controller operating either in two or four door configurations. In two door configuration, both entry and exit can be accessed through RFID card and hand geometry. In four door configuration, entry should be made through RFID and exit using a push-button switch.

The server application was developed using Visual C#. Relational database architecture was designed and developed using Microsoft SQL. The server application periodically updates the local RTC Clock of each controller connected to it. When a controller connected to the server sends a transaction to the server, the server stores the transaction in the database. The server software monitors the health of all the controllers periodically and the various units connected to them, and raise a visual alarm if any of the unit is disconnected. Man machine interface (MMI) is developed for creating new doors, new door profiles, user groups, time profiles, and configurations. The server application communicates with each controller individually to update the user database, configurations and receive log files.

The customized access control system is installed (Figure 1) at one of the laboratories and functioning satisfactorily since September 2014.

Fig. 1 *Controller at SES Lab*

VI.3 Design and Development of Holographic Optical Tweezers

Optical tweezers use tightly focused laser beams to hold and move microscopic particles using a high numerical aperture objective. Tight focussing of a laser beam produce strong gradients in the optical fields in the region surrounding the focal spot, and an associated dipole force on the particle in that region, called the gradient force, which dominates over the scattering force due to radiation pressure causing the object to get confined in the focal spot.

However, many applications require simultaneous control over multitude of particles, positioning them in 3D space at desired locations with desired symmetry. Holographic optical tweezers (HOTs) elegantly extend the basic principle of optical tweezers by incorporating the technique of beam shaping and holography to hold and independently manipulate multitude of particles in real time.

Designed and developed a HOTs setup with an aim to produce about 200 traps at the focal plane. Figure 1 shows the designed optical lay out of HOTs. 1064 nm Nd-YAG fiber coupled laser was chosen as the source for trapping with an aim to carry out studies not only on suspensions of dielectric particles but also on biological samples. HOTs can be used for manipulating particles in real time and design colloidal arrays in three dimensions with desired symmetry and lattice constants. Multiple beams (multiple traps) or patterns of light from a single laser beam are generated by phase modulation technique using a spatial light modulator (SLM).

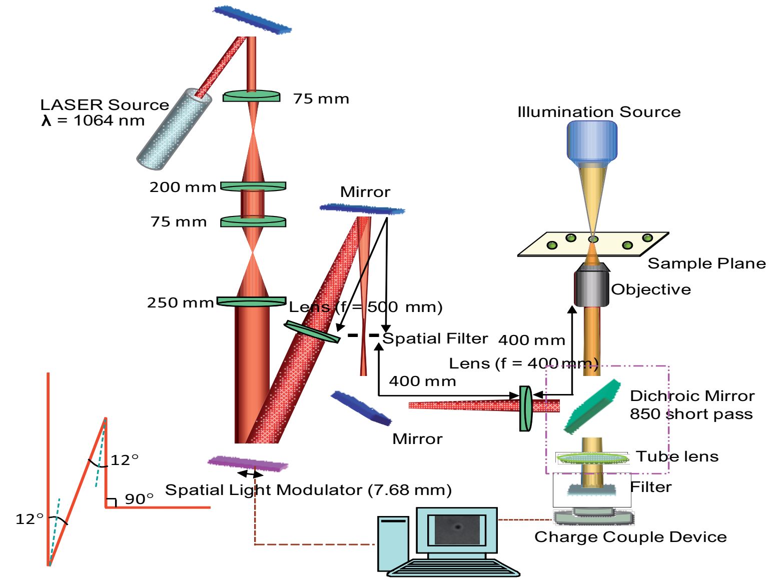

Fig. 1 *The designed optical lay out of holographic optical tweezers*

We have employed a reflective type spatial light modulator consisting of parallel aligned nematic liquid crystal molecules for beam shaping. The elongated nematic liquid crystal molecules do not possess positional order but do exhibit orientational order. The nematic phase possesses dielectric anisotropy. With an applied electric field, they show effective birefringence and thereby retard the phase of the extraordinary component of the incident light. The spatial light modulator is pixelated in nature with liquid crystal molecules. The voltage across each of the pixel can be controlled individually and hence the phase of the incident beam. The phase can also be varied independently at each pixel over the pixelated area of the spatial light modulator.

The optical layout for HOTs is designed for entering the laser beam through the right port of the microscope, where a 850 nm short pass dichroic is placed at an angle 45°meant for reflecting the light from of the sample to the detector. The use of 850 nm short pass dichroic in the path helps simultaneous reflection of the IR laser entering the right port towards the microscope objective and transmission of illumination light containing the sample information towards the camera attached to the trinocular port.

The spatial light modulator is implemented in the HOTs optical layout as follows: The trapping infrared laser beam has been expanded by a series of lenses to fill the active area of the spatial light modulator. The polarization of the beam was aligned parallel to the director axis of the liquid crystal molecules of spatial light modulator for effective phase modulation. The angle of incidence for the laser beam on spatial light modulator was fixed at 6° to avoid cross talk between the pixels of spatial light modulator. Two lenses placed in 4f configuration allow demagnification as well as conversion of angular displacement of the beam to lateral displacement. Demagnification of the beam reflected by the spatial light modulator is adjusted to ensure that it slightly overfills the back aperture of microscope objective. This design of optical layout also keeps Fourier transform relationship between trapping plane and hologram plane.

Figure 2 shows the picture of HOTs setup. As a first step HOTs was tested for its trapping ability by creating a single trap and trapping polystyrene colloidal particles of different sizes. Shallow to deep trap were created by varying the laser power. The traps thus created were characterized for trap stiffness by recording the motion of a trapped particle, and analyzing position fluctuations of the particle. The linear relationship between trap stiffness and laser power is also established by performing single trap experiments with different laser powers.

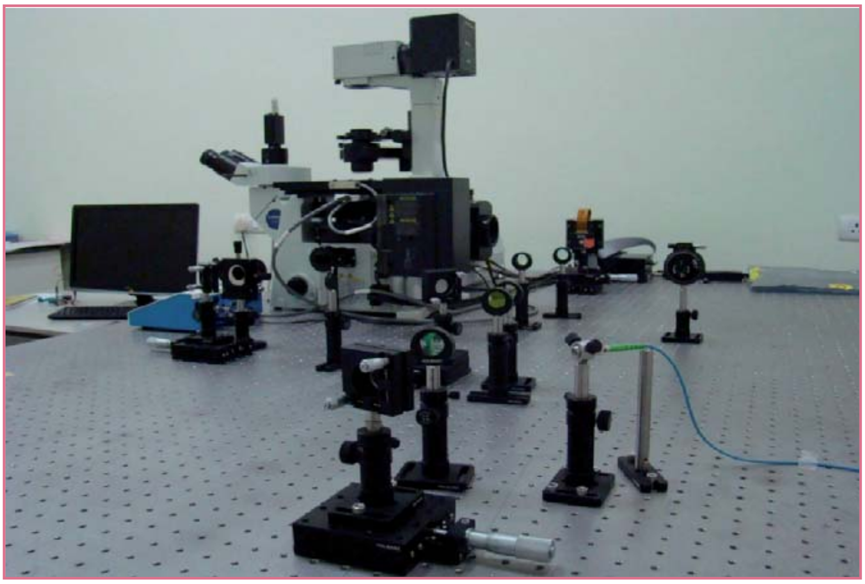

Fig. 2 *Holographic optical tweezer setup*

The spatial light modulator needs to be programmed with designed phase profiles for creating multiple traps and also for positioning them at desired locations. The codes for generating a 4×4 square array of trap spots in two dimensions and moving the trap pattern in a predefined manner at the trapping plane have been generated using random superposition and weighted Gerchberg Saxton (WGS) algorithms.

The spatial light modulator was programmed using phase profiles generated by these algorithms. Further, we have used two methods of calculation for getting the desired pattern in the trapping plane. The first one is based on direct calculation of the field at the desired spots and the second one is based on Fourier transform method used for calculating a continuous pattern of light in the trapping plane. The intensity uniformity correction has been carried out by considering the diffraction effects due to pixelated nature of spatial light modulator, which modulates the field of coherent point light sources centered at each pixel of spatial light modulator at its fourier plane.

Figure 3 shows the hologram for generating an array of 4×4 square array of traps in the trapping plane, and 4×4 square array of traps generated using the spatial light modulator programmed with the hologram. The success of HOTs in organizing polystyrene spheres with 1.2 micron diameters suspended in aqueous medium into 4×4 array with square symmetry is also shown in Figure 3c.

The manipulating capability of HOTs is demonstrated in Figure 3d by arranging eight traps in a circle of radius 17 µm, and then reconfiguring them in real time into a circle of radius 8.5 µm as shown in Figure 3e. The HOTs thus designed and developed by us is capable of creating organized particle assembly in designed patterns. The manipulative capability of HOTs in reconfiguring the organized patterns of traps from one type to other is demonstrated.

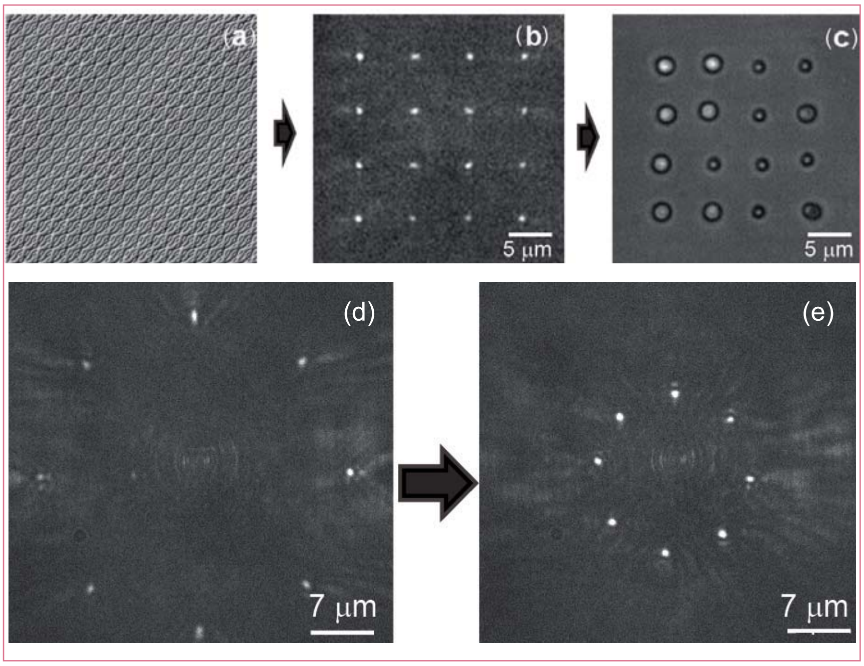

Fig. 3 *(a) A hologram for generating an array of 4×4 focal spots at the trapping plane, (b) A 4×4 array of trap spots generated at the trapping plane by impressing the hologram (shown in (a))on the spatial light modulator, (c)polystyrene spheres(dia.1.2 µm) trapped in a square pattern of focal spots generated shown in (b). An array of eight spots arranged in a circle of radius (d)17 µm and (e) 8.5 µm*

VI.4 System Verilog based Test Bench Development for VLSI Verification as per UVM Methodology

Hardware description language programmed devices (HPD) like complex programmable logic device (CPLD) and field programmable gate arrays (FPGA) lies at the heart of all modern Instrumentation and Control system platforms and poses unique verification challenges both to verification engineers and regulatory authorities. Traditionally, when faced with the task of verifying the correctness of a design, directed tests were the most likely choice. Using this approach, a verification plan with a list of tests, each of which concentrated on a set of related features from the specification document can be created. Given ample time and staffing, directed testing is sufficient to verify many designs.

However, there are two major pitfalls with above mentioned approach

- Creation of directed tests does not scale with increased complexity of design and the number of tests is directly linked to number of engineers writing tests
- With directed tests only expected faults/bugs can be uncovered.

With the advent of hardware verification languages (HVL) like SystemVerilog, OpenVera and e, constrained random stimulus generation and coverage driven verification became the de-facto norm for the verification of reasonably complex designs. To standardize the architecture of test enches using HVLs verification methodologies like verification methodology manual (VMM), open verification methodology (OVM) and universal verification methodology (UVM) came into the fore. A System Verilog based UVM compliant testbench architecture was used for the verification of compact PCI (cPCI) bus target controller and associated glue logic for target specific I/O cards because of the following reasons (Figure 1).

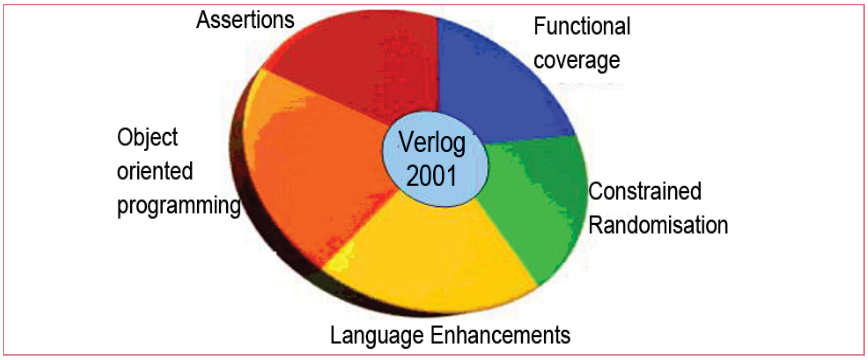

Fig. 1 *System verilog language features*

- Coverage driven verification environment enabling the verification team with tangible metrics for verification signoff
- Constraint random stimulus generation for uncovering unanticipated faults
- High re-usability factor as the modification of the local agent would enable the verification team to functionally verify the integrated IP and custom glue logic for each I/O card on the common verification platform
- Separability of test and the testbench environment
- Independent of tool and based on open source language and methodology.

A virtual sequencer creates the sequence schemes for Transaction Level Packets and passes it to the Sequencer. Two agents (cPCI Master & Local Slave) are the primary structural component of this architecture. Each agent contains a Driver, Monitor and Sequencer. Monitor collects all the functional coverage data. The cPCI and local bus protocol checker has been implemented in the monitor itself using System Verilog Assertions. A scoreboard collects the transmitted data from both the monitors using transaction level modeling Ports. (TLM).The bus monitor collects information from the cPCI bus and checks for protocol violations and informs the verification engineer in case of a violation using assertions (Figure 2).

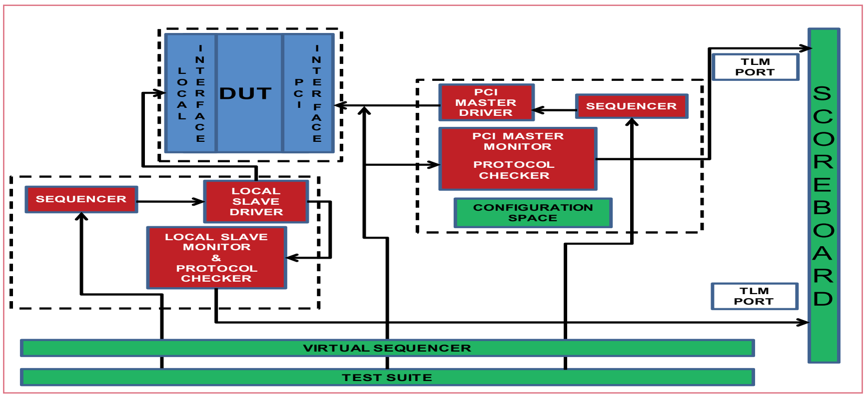

Fig. 2 *Universal verification methodology compliant testbench architecture*

VI.5 Effect of Limited Overpressure on Low Range Differential Pressure Transmitter

In the plants for the reprocessing of nuclear spent fuels, air purge method is used for the measurement of level and density of liquids in process tanks. The purge method uses differential pressure (DP) transmitters for measurement. A common problem experienced in purge based measurements is the formation of choke in the purge probes (as shown in Figure 1).

Whenever there is a choke in the purge probe in the tank, the back pressure at the DP transmitter will increase. This back pressure can be as high as the supply pressure for air purge (generally 2 kg/cm^2). This high pressure can have an adverse effect on the sensing diaphragm of the transmitter, especially on low range DP transmitters which are more sensitive. This high back pressure can also lead to calibration shift in the transmitter.

Though the manufacturer's specification provides information on the effect on accuracy for over pressure (i.e. +/- 0.25% of upper range limit (URL)) at the overpressure limit (136 kg/cm^2) of the transmitter, there is no information available on the effect of overpressure encountered in the purge measurement (i.e. 2 kg/cm^2). The effect on accuracy specified by the manufacturer for limiting overpressure is unacceptable for process measurements. Hence, the effect of limited overpressure on a low range DP transmitter was analysed.

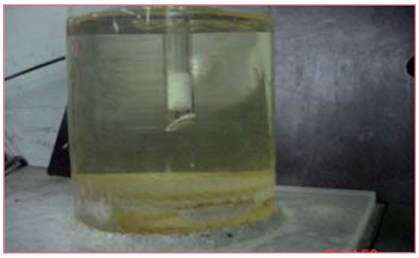

Fig. 1 *Choke in purge probe*

Fig. 2 *Experimental setup*

Using the setup shown in Figure 2, experiments were conducted on two different makes of DP transmitters: DP transmitter type A (with minimum span of 0.5 inch of water column (WC) and maximum span of 25" WC) and DP transmitter type B (with minimum span of 1.08" WC and maximum span of 64" WC). The DP transmitters were zero trimmed initially and were calibrated to a span identical to that of a typical density measurement. Transmitter types A and B were calibrated for 0 to 1" WC and 0 to 1.08" WC, respectively. The current output were 4 mA for 0" WC and 20 mA for full range.

Effect of 2 kg/cm^2 overpressure for one minute

In stage one, overpressure of 2 kg/cm^2 was applied on the low pressure (LP) port of the DP transmitter for one minute. This pressure was chosen because it is the set pressure of the pressure regulating valve in actual purge measurement. The high pressure (HP) port was open to atmosphere. After applying overpressure, calibration of the DP transmitter was checked for any drift in zero or span. The results of stage 1 experiment for both the transmitters indicated that the zero shift was 0.005" WC (which is 0.02% of URL and 0.5% of calibrated span) and shift in the range was insignificant.

Effect of repeated overpressure for 2 kg/cm^2 pressure

In stage two, overpressure of 2 kg/cm^2 was applied on the LP port of the DP transmitter for 10 minutes and the same was repeated for 5 times on a random time interval. Each time on releasing the pressure after 10 minutes, the DP transmitter was checked for zero and range. This exercise was carried out to simulate plant conditions, as choke can recur several times based on the type and concentration of the solution. The results revealed that the effect was significant only at the very first instance of overpressure which was the same as for the previous stage (i.e. zero shift was 0.005" WC and no significant change in range).

Effect of prolonged overpressure for 2 kg/cm^2 pressure

In stage three, overpressure of 2 kg/cm^2 was applied on the LP of the DP transmitters for a period of 24 hours. This was carried out because a choke in the instrumentation probe may take up to one day to get cleared. Till that time the DP transmitter will experience high pressure. The same testing procedure mentioned in previous stages was followed. Similar to previous stages, zero shift observed was 0.005" WC and shift in range was insignificant. However, owing to prolonged overpressure, the transmitters took some time to recover. The recovery time for Type A and type B transmitters were different (type A transmitter took less time compared to type B which took few hours to settle).

The error due to overpressure was 0.5% of calibrated span, where is more than the specified accuracy of the DP transmitter (0.15% of calibrated span). However, the accuracy of 0.5% of calibrated span is acceptable for process requirements.

VI.6 Reliability Enhancement of Criticality Alarm System

Criticality alarm system (CAS) is required for prompt detection of criticality accidents and to raise an audio-visual alarm for immediate evacuation of personnel from the affected areas. The detector of CAS is ionization chamber which senses gamma radiation. Each CAS consists of three independent detection channels which generate channel alarm based on gamma dose rate of 4 R/h or dose alarm of 3 mR in 500 millisecond. The alarm channel of CAS generates CAS alarm based on the 2 out of 3 voting logic to minimize false alarms. The system is designed to be fail-safe, but this makes it prone to false alarms. Five criticality alarm systems are operating 24x7 in CORAL plant. The CAS being used is compact, rugged and simple, but has some limitations.

For ensuring reliable power supply to CAS, each of the three CAS channels, are provided with an independent Class I power supply by sealed maintenance-free (SMF) batteries. The Class I power supply is backed up with Class II power supply.

To improve the reliability of the CAS and to minimize false alarms, certain modifications in hardware as well as software have to be implemented.

Hardware

The gamma dose rate signal for each CAS channel was brought out for connection to an external radiation data acquisition system (RDAS). Alarm test and reset for each channel were carried out for connection to operator switches in the Control Room. Class II power failure signal was generated and brought out for connection to alarm annunciator in the control room.

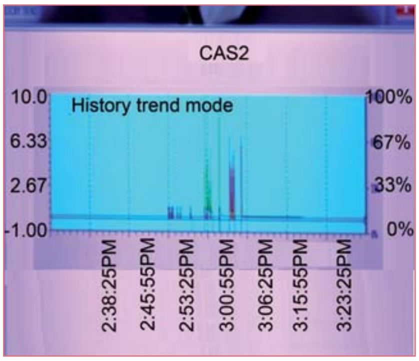

Fig. 1 *Trend of RDAS for CAS*

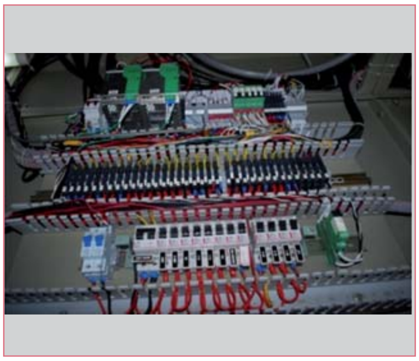

Fig. 2 *CAS hooter power supply system*

Software

Individual CAS channel dose rate signal is connected to RDAS and soft alarm is generated based on dose rate signal with latching. Resetting of the latched channel alarm can be done by the operator.

Current and History trend graphs (Figure 1) for individual CAS channel signals are provided in RDAS.

CAS hooter system

CAS hooter system is provided in CORAL to generate alarm in the plant area.

The alarm from any of the five CAS units will trigger the hooters. Two independent power supply systems are provided for improved reliability of hooters in redundant manner (Figure 2).

Surveillance

The capacity of the batteries (Class I power supply) is tested periodically.

The alarm system testing and RDAS history checking are carried out every week. Calibration of detectors with radioactive source and electronic calibration of transient response of the channels are carried out on annual basis.

Single channel alarm

To minimize false alarms, each CAS channel has been augmented with an additional relay (Figure 3) for channel alarm. The channel alarm contacts are combined as a group alarm for annunciation in the Control Room.

Detailed channel diagnostics

Besides single CAS channel alarm, annunciation of the failure of EHT to the detector is desirable in Control Room. A circuit for this has been designed and prototype PCBs (Figure 4) have been installed in a criticality alarm system unit in the field for testing.

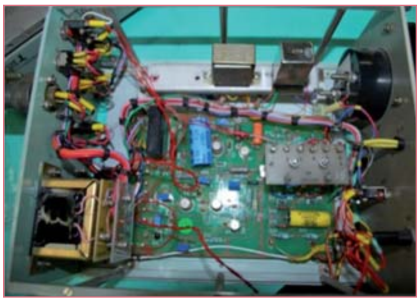

Fig. 3 *CAS single channel with group alarm*

Fig. 4 *Prototype PCB for channel diagnostics*

VI.7 A Comprehensive Monitoring Tool for High Performance Computing Cluster Systems

The four high performance computing (HPC) clusters at IGCAR use parallel file system and high speed low latency infiniband interconnect to achieve the performance in teraFLOPS.

The monitoring of individual nodes in the cluster is achieved using the open source tool, Ganglia. This tool monitors central processing unit utilization. We have developed a HPC monitoring tool that monitors the parallel file system, infiniband interconnect, user logins, processes, jobs, log files and storage utilization. Used together with Ganglia, this tool will provide a complete overview of all HPC systems to administrators. Screenshot of HPC monitoring tool is shown in the Figure 1.

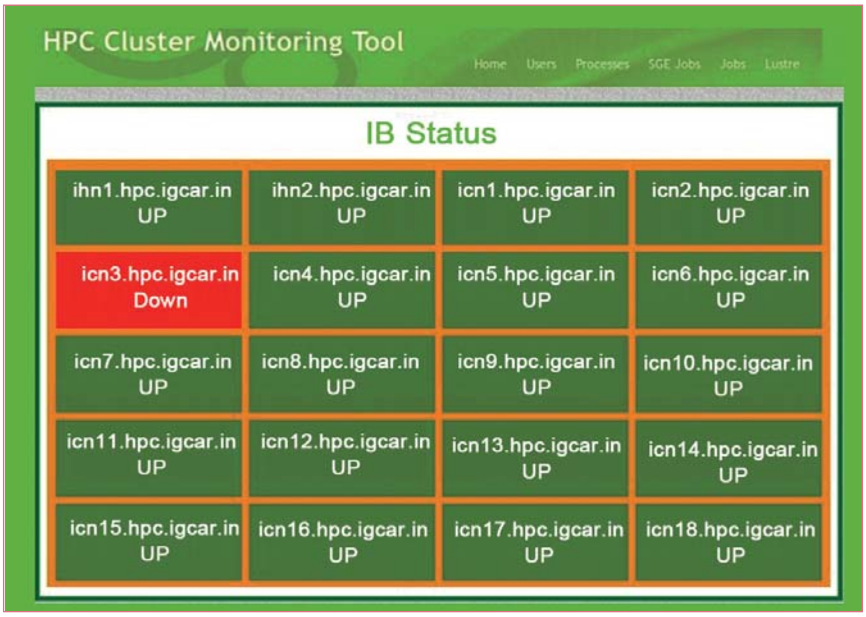

IB Status

ihn1.hpc.igcar.in UP	ihn2.hpc.igcar.in UP	icn1.hpc.igcar.in UP	icn2.hpc.igcar.in UP
icn3.hpc.igcar.in Down	icn4.hpc.igcar.in UP	icn5.hpc.igcar.in UP	icn6.hpc.igcar.in UP
icn7.hpc.igcar.in UP	icn8.hpc.igcar.in UP	icn9.hpc.igcar.in UP	icn10.hpc.igcar.in UP
icn11.hpc.igcar.in UP	icn12.hpc.igcar.in UP	icn13.hpc.igcar.in UP	icn14.hpc.igcar.in UP
icn15.hpc.igcar.in UP	icn16.hpc.igcar.in UP	icn17.hpc.igcar.in UP	icn18.hpc.igcar.in UP

Fig. 1 *Screenshot of high performance computing monitoring tool*

Salient features

Salient features of the HPC monitoring tool are the following:

1. Monitor health and performance statistics of parallel file system (Lustre)
2. Monitor jobs submitted to the job scheduler, sun grid engine (SGE)
3. Save consolidated data on finished SGE jobs
4. Monitor logged in users and their activities in the nodes
5. Monitor processes running on the nodes
6. Monitor infiniband network in the cluster
7. Consolidation, display and analysis of logs from all nodes
8. Monitor used percentage of storage servers.

A web based graphical user interface (GUI) will display the data collected by monitoring cluster nodes. The GUI provides graphs for displaying performance statistics. Users can search log messages based on time, host and message type. Details of individual nodes, processes and SGE jobs in the entire cluster are available from the GUI.

Architecture

Client scripts run on all nodes of the cluster and collect monitoring data through system commands and log files. A PERL daemon script will run continuously on the client nodes, collect data periodically and send data to Lustre monitoring server using sockets.

The HPC monitoring server listens for data from the client nodes. Once data is received, it will parse the data and store it in Postgre SQL database and round Robin database (RRD). The web application will query these databases and display the data (Figure 2). Web programming was done with PHP and Apache used as web server.

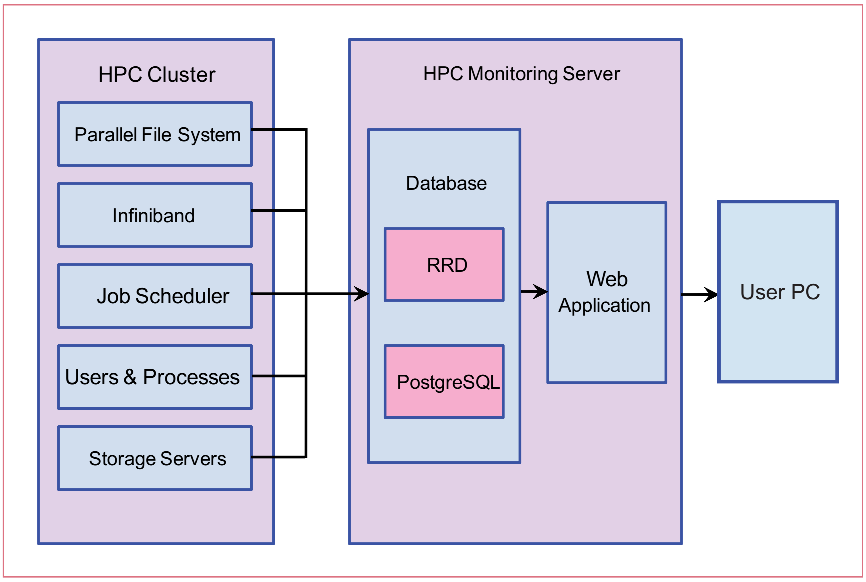

Fig. 2 *Software architecture of HPC monitoring tool*

VI.8 Wi-Fi Communication of On-Line Process Information with Security

The advantages of wireless communication include low setup time, low installation cost, no need of cables, low down time, easy maintenance etc., The major concern for the use of this technology lies in the reliability of data transmission and data security. Till now, this technology has found restricted use in nuclear industry and is mainly used for data monitoring of non-critical application and for redundant communication.

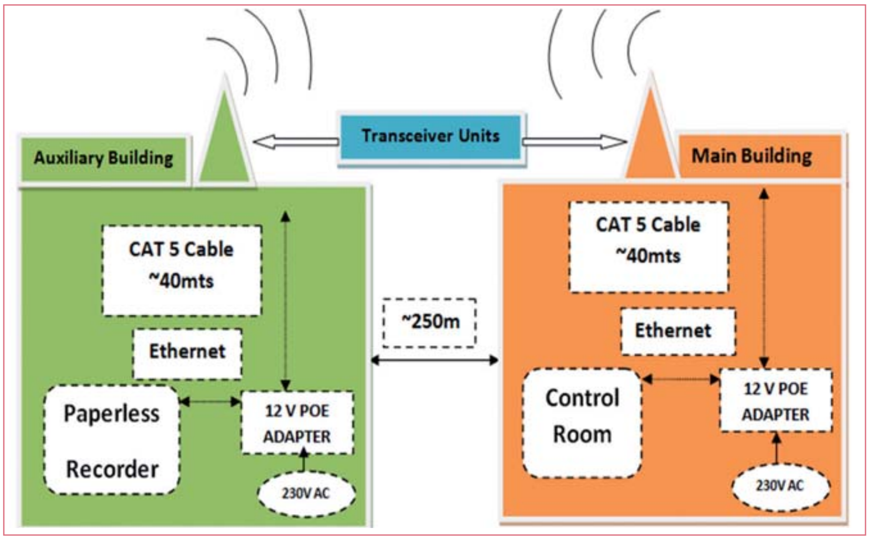

***Fig. 1** Schematic of wireless communication in CORAL*

Configuration in CORAL

There was a requirement of real time monitoring of the parameters of process instruments in CORAL auxiliary building from Main control room. Laying cables between the two buildings was practically difficult. Wireless communication was used to address this issue. The instruments in the auxiliary building are connected to a paperless recorder. Transmission control protocol (TCP) over ethernet output from the recorder is connected to IEEE 802.11 n/a based wireless device. The real time data are wirelessly sent by a transceiver unit mounted on the auxiliary building to the transceiver unit mounted atop of main building. The data transmitted were also found to be reliable. The wireless device uses unlicensed ISM frequency band of 2.4-2.48 GHz and is powered by POE. The baud rate is set at the minimum configurable value of 1 Mbps. The schematic of the setup is shown in Figure 1.

Security Features

The key security features of wireless communication addressed here are use of encrypted transmission, transmitted signal power, directionality of antenna, physical address binding and isolation of networks having wireless communication.

The wireless data transmitted are protected with wi-fi protected access 2 (WPA2) and pre shared key (PSK). WPA2 mandates use AES (advanced encryption standard) algorithm. This makes WPA2 more secure than WPA. The pre shared key is manually changed periodically.

The power of the signal transmitted should be as low as possible without affecting the sensitivity of the receiver. At low power, signal strength is significantly weak over areas outside the physical protection boundaries. Illegal sniffing devices outside the premises cannot hack into the network as the weak signal will be virtually undetectable.

Antennas used in transceiver units for point to point communication should be directional. When the antennas are directional, the transmitted signal is channeled in a particular path. So, the transceiver in the path only receives the signal.

The wireless transceiver units individually have an unique media access control (MAC address).

Using the device configuration software provided by the supplier and password protected access controls, the MAC addresses of the devices can be physically bound to each other. This implies that device A can be connected to device B only and not to any other device. This greatly enhances the security as any intruder trying to connect to the wireless network cannot do so.

The networks having wireless communication used for process monitoring should be isolated from other communication networks for the sake of security considerations.

VI.9 Energy Efficient Air-Conditioning System for Training School at IGCAR

State of art building for training school & training centre was established on the eastern side of IGCAR. The facility consists of modern class rooms, seminar halls, library, laboratories, office rooms and other facilities.

The Training School requires an efficiently controlled and monitored air-conditioning system to meet the following requirements.

- Maintain comfort conditions of 24±1°C, 55 ± 5% RH
- Provision to maintain different comfort conditions in class rooms based on occupancy, seasonal requirement etc.
- Adequate fresh air as per green building ventilation norms
- Remote monitoring and automatic operation
- Energy efficiency and fire safety

Accordingly a state-of-the-art central air conditioning system consisting of double skinned air handling units, chilled water booster pumps with variable frequency drives (VFD), microprocessor controlled variable air volume control dampers (VAV) etc. with features like energy efficiency, fire safety, indoor air quality management and automation was designed and installed to meet an air conditioning requirement of about 375 TR. The system uses chilled water from Central Water Chilling Plant.

Figure 1 shows the schematic of air conditioned system installed at training school. The system includes a set of volume control dampers, variable frequency drives, two-way valves and sensors such as room thermostat, duct static pressure sensor, differential pressure transmitter, return air temperature and RH sensor, CO_2 sensor etc. A dedicated microprocessor based digital controller receives input process parameters from field sensors and controls the equipments based on the set points using control software as per assigned program. The system was programmed and commissioned in a manner to maintain the comfort conditions precisely and efficiently.

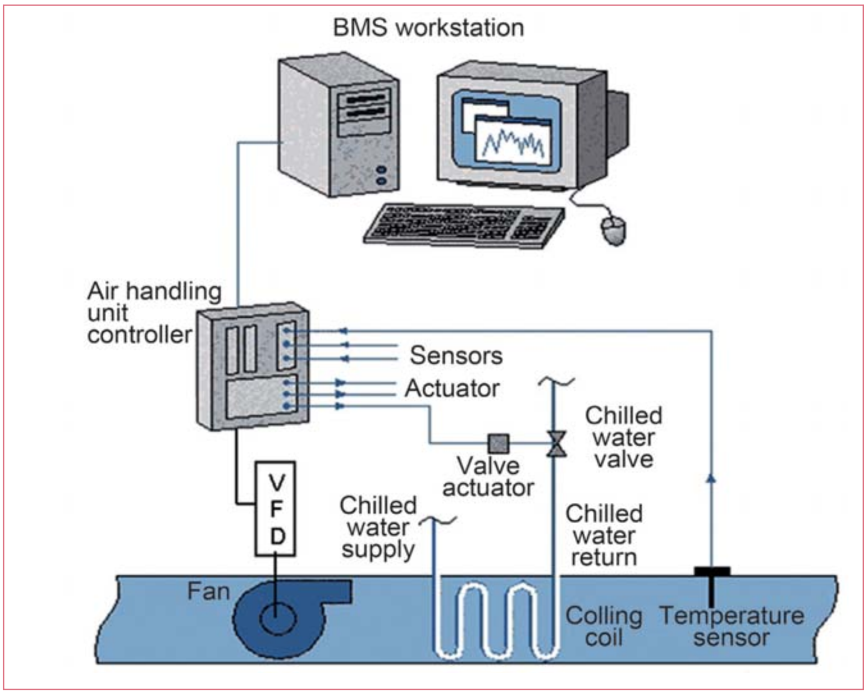

Fig. 1 *Air handling unit with controller and SCADA system*

Figure 2 shows the installation of chilled water pumps along with its control unit and SCADA system. The air-conditioning system was commissioned and functioning satisfactorily in auto mode.

Fig. 2 *Chilled water pump installation*

VI.10 Upgradation of High Voltage System at Central Switching Station with Enhanced Reliability and Improved Safety

Central switching station is the nerve centre for IGCAR electrical power distribution system. The present load demand is about 24 MVA and is expected to grow up to 38 MVA by the end of 12th plan period. It is necessary that adequate capacity of central switching station be maintained to meet the growing power demand of DAE units at Kalpakkam including townships. It is also important that the reliability of the power system is continuously improved. Some of the equipment are more than thirty years old and is highly essential to retrofit the equipment to meet the future load demand.

To mitigate the situation, it was decided to initiate various actions that have improved the system capacity as well as reliability.

Improved reliability and capacity

The 11 kV indoor switch board at central switching station consists of two bus sections and are operating in one out of two configuration. Considering the requirement of increased reliability and load growth, it was required to add one more 11 kV bus section. With this the operating philosophy will be two out of three configuration.

The obsolete 11 kV bus section # A was replaced by state of art panels with enhanced protection system. The panel consists of breakers with much more rugged vacuum circuit breakers (VCB) that have very less maintenance requirement. These panels are equipped with arc flash protection and are designed to withstand higher short circuit capability.

Another constraint in full capacity utilisation was the reduced in-panel rating of incoming breaker and the limited capacity of the old PILC incomer cable to switch gear. The PILC incomer cable to the 11 kV switchgear was replaced by a phase segregated bus duct. The new incoming vacuum circuit breakers circuit is designed for adequate in-panel rating to receive 20 MVA power. The newly installed bus section along with the bus duct is shown in Figure 1.

Review of protection scheme

Introduction of one more layer of 33 kV sub-station (NCCS2) and the third feeder from BHAVINI made it imperative to review the protection scheme so far followed. On detailed analysis, it was observed that with the conventional electromagnetic relays and following conventional graded protection scheme, the system will undergo severe stress during faults.

Fig. 1 Bus section along with the bus duct

This necessitated the introduction of state of the art numerical relays. This state of the art switch gear is having the additional protection towards the safety of operating personnel and having better short circuit withstand capability. The fault recording facility in the numerical relay provides added advantage of fault analysis and improved diagnosis. The installation of new panels and the bus ducts were completed with minimum disturbance to the end users. Enhanced protection scheme was also implemented by proper coordination of the relays and implementation of precise setting in the numerical relays. The new panel was commissioned and energised successfully.

VI.11 Pulsed Eddy Current Testing for Sub-surface Defect Detection: FEM and Experimental Investigation

Non-destructive detection of sub-surface and deep-seated defects by eddy current technique is possible with the use of efficient instrument and probes. For detection of sub-surface defects located beyond 4 mm below the surface in stainless steel plates, finite element model based optimisation of pulsed eddy current probe design has been carried out. The optimisation involves configuration and

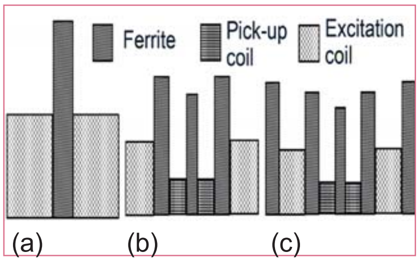

Fig. 1 Different probe configurations considered for optimization (a) probe-A, (b) probe-B and (c) probe-C

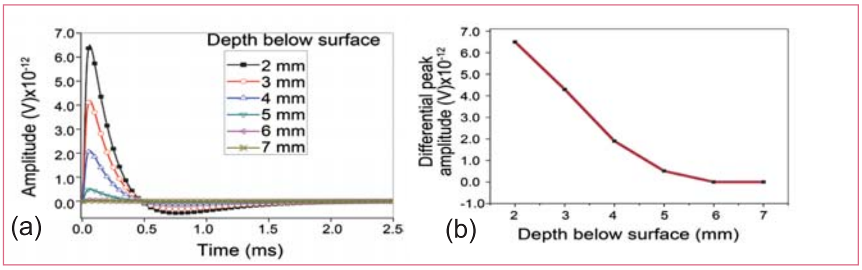

Fig. 2 FEM prediction for probe-B (a) differential induced voltage and (b) differential peak amplitude

dimension of pulsed eddy current probe using the predicted differential induced voltage (difference between induced voltage of receiver coil at defect and defect free region) and induced current density (J_e).

Three most widely used probe configurations viz., absolute ferrite core probe (probe-A), send-receive probe with ferrite core for exciter and pick-up coils without shielding (probe-B) and send-receive probe with ferrite core for exciter and pick-up coils with outer shielding (probe-C) are considered Figure 1 for design optimisation. An AISI type 316 stainless steel plate of 8 mm thickness having flat bottomed holes (FBH) of 5 mm diameter and located at various depths (d) of 2, 3, 4, 5, 6 and 7 mm below surface is considered as test specimen for simulation.

The optimal probe configuration is selected by comparing the induced current density (J_e) at different depths of defect location d and differential induced voltage for different probe configurations. From the model predictions, it is observed that ferrite cored send-receive type probe (probe-B) shows higher sensitivity for detection of sub-surface defects as compared to unshielded absolute (probe-A) and send-receive shielded probes (probe-C). This is attributed to the presence of ferrite core in probe-B, which reduces coupling of primary magnetic field with the receiver coil, thus enhancing detection sensitivity.

The differential induced voltage and its respective differential peak amplitudes of probe-B for sub-surface defects are shown in Figure 2a and 2b respectively. Reduction in differential peak amplitude is observed for defects at farther depths.

Pulsed eddy current instrument shown in Figure 3 has been developed in-house. It comprises of pulse generator that produces 1 to 100 pulses per second voltage pulses and variable pulse width (PW) ranging from 10 to 8000 μsec and a power amplifier. Defects modelled are simulated by machining flat bottomed holes in stainless steel plate. Figure 4a shows the differential peak amplitude and time-to-peak for all flat bottomed holes. With increase in d, decrease in differential peak amplitude and increase in the time-to-peak is observed and these observations are in line with model predictions.

Detection sensitivity of pulsed eddy current probe is evaluated for electrical discharge machining (EDM) notches in a 8 mm thick AISI type 316 stainless steel plate and are shown in Figure 4b. The probe could detect sub-surface defects located up to 6 mm below surface in a 8 mm thick stainless steel plate.

The studies reveal that model based probe optimisation is useful for improving the performance of the pulsed eddy current technique for sub-surface Non-destructive evaluation. The probe and instrument have also been successfully used for generating images of sub-surface defects in stainless steel plates.

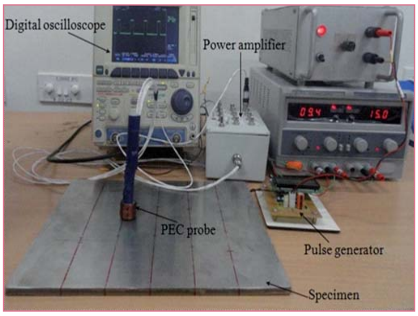

Fig. 3 Pulsed eddy current experiment developed

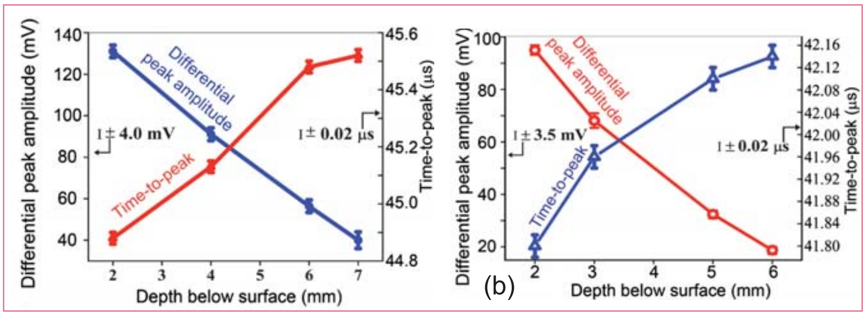

Fig. 4 Experimental result of differential peak amplitude and time-to-peak for (a) FBH and (b) notches located at various depths

VI.12 Infrared Thermography based Defect Detection in Ferromagnetic Specimens using Low Frequency Alternating Magnetic Field Induced Heating

Carbon steel is used for roof slab of PFBR and it is also a potential candidate for construction of safety vessels for future sodium cooled fast breeder reactors. Low carbon ferromagnetic non-alloy steels, like mild steel, are extensively used in various industries like oil and gas pipelines, construction etc. Non-destructive evaluation (NDE) is essential to detect defects early, thus avoiding sudden catastrophic failures in the fabricated components. Infrared thermography (IRT) is one of the NDE methods used for defect detection. We have developed a novel active infrared thermography technique, using low frequency alternating magnetic field induced heating, for defect detection in mild steel components. The proposed technique offers several advantages over conventional active thermography techniques, like fast direct heating, no frequency optimization, no dependence of surface absorption coefficient and penetration depth.

Experiments were performed on four mild steel specimens with artificially fabricated rectangular slots of depths 8.0, 5.0, 3.3 and 3.0 mm. The specimen surfaces were black painted to enhance emissivity. A low frequency magnetizing yoke was used for applying alternating magnetic field on the specimen which was placed in between the two arms of the magnetizing yoke in such a way that the applied flux lines cut across the rectangular slots. The surface temperature distribution during magnetization induced heating and natural cooling was monitored in a non-contact way using an infrared camera. The specimens were initially heated up to 100 seconds using low frequency (50 Hz) alternating magnetic field and the increase in the specimen temperature was monitored from the defect as well as blind sides of the specimens.

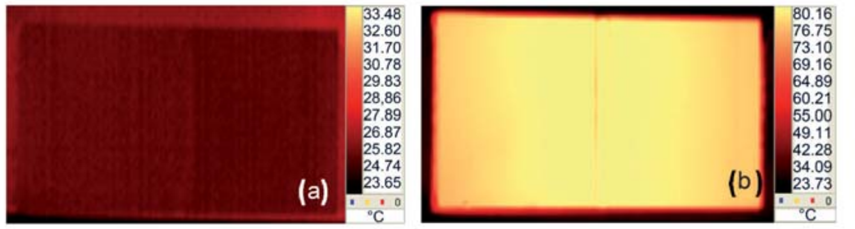

Fig. 1 *Infrared images of the specimen with 8.0 mm depth defect at (a) t = 0 s and (b) t = 100 s during heating (the defect region can be clearly seen in the image)*

The defect regions were observed to be at a higher temperature due to bending of magnetic flux lines at the vicinity of the defects. The defect regions were not seen before AC heating (t=0 seconds) and was clearly visible from the infrared images of the specimens at t=100 seconds (Figures 1a and 1b). The widths of the defects were estimated from the infrared images within an error margin of ±6.7%. The thermal contrast, i.e. the temperature difference between the defect and the defect-free regions increased with time during magnetization induced heating and it was observed that the thermal contrast is lower for deeper defects (Figure 2). The peak thermal contrast, at the end of the heating phase, was found to decay exponentially with increasing defect depth. This was attributed to the reduction in the induction heating due to magnetic flux leakage in the vicinity of the defects. The higher magnetic flux leakage from the deeper defect leads to a lower residual internal magnetic field that ultimately causes a reduced eddy current induced heating. Though the thermal signatures of the defects were not visually discernible from the blind sides of the specimens, the normalized temperature decay rate, determined from the blind sides of the specimens, was found to linearly decrease with logarithm of defect depth. A calibration curve, plotted with the rate of temperature decay versus logarithm of slot depths, enables the detection of unknown defects from the blind sides of the specimens.

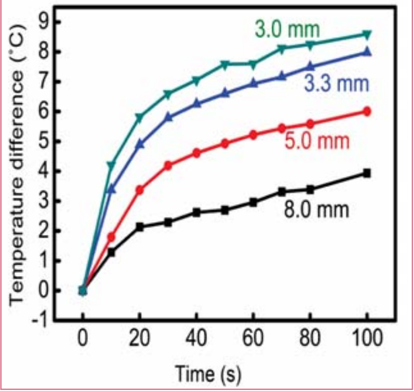

Fig. 2 *Temperature difference between the defect and defect-free regions as a function of time during magnetization induced heating for the blind sides of the specimens*

VI.13 Modelling of Aquatic Circulation in Coastal Ocean Water and Validation for Dispersion Characterization

The problem of marine pollution generally occurs in coastal waters due to developmental and industrial activities and concentration of population along the coastal zones. Under normal operating conditions of nuclear facilities, no discharges are permitted directly into the ocean as per regulatory norms and the liquid effluents are diluted sufficiently before discharge. The dispersion of waste effluents in coastal waters depends on the currents and the wave induced surface water turbulence. The transport of the waste and its dilution in the ocean occurs by physical processes such as advection and diffusion. For environmental safety analysis, it is required to study the marine dispersion and develop suitable numerical models to describe the oceanic dispersion of radionuclides as influenced by the coastal currents.

A three dimensional, primitive equation, sigma coordinate ocean model called 'Princeton ocean model' (POM) is used to simulate coastal circulations for study of the coastal dispersion of hazardous pollutants near Kalpakkam. The model is customized with a curvilinear high resolution (3 km) grid near the coast with high resolution (1 arc-minute) digital bathymetric-topographic information. The model is spin-up for a period of 3-years with the input fields of sea water temperature, salinity, surface winds and surface fluxes obtained from climatological wind temperature, Advanced Scatterometer (ASCAT) satellite surface winds and objectively analyzed fluxes data sets. The stability of the model is checked from depth averaged kinetic energy to obtain flow equilibrium with the ocean environment.

A number of simulations have been conducted in warm start mode using the 3 years' spin-up as the initial conditions and using weather research and forecasting (WRF) atmospheric model wind and fluxes for defining surface boundary conditions at every 24 hours. The study area is bounded by land on the west and opens in the other directions. It is necessary to define certain open boundary conditions (OBCs) in order to prevent any reflection of outgoing waves generated at the open boundary. A number of simulations are performed with open boundary conditions (current and sea surface height (SSH) values) taken from global models like global ocean data assimilation system (GODAS) and NRL-navy layered ocean model (NLOM) for different seasons and results are compared with observations from different sources OSCAR, HF radar, TMI and Argo. The HF radar data near Kalpakkam coast were obtained from INCOIS, Hyderabad for the study domain.

It has been found that after the spin up, a large amount of noise is reduced, and comparatively rest condition is achieved with more reliable to make the impact of wind stress and fluxes on the formation of the surface currents. A significant improvement in the surface circulation is observed in the experiments with open boundary conditions and atmospheric forcing such as wind and fluxes. It is found that when the model is forced with daily wind and fluxes, the surface circulation pattern is more comparable with HF-Radar current observations at the coast (Figure 1). Also, it is found that a very small change in the circulation velocity on the boundaries makes a large change in interior circulation and the vertical mixing of the ocean water. The change in mixing is well depicted in temperature and salinity profiles for the month of December. The simulations show complexity in currents near the coast due to bottom topography and seasonally varying ocean surface wind. A very good agreement has been observed between the simulated currents and the HF-Radar observed currents in various seasons.

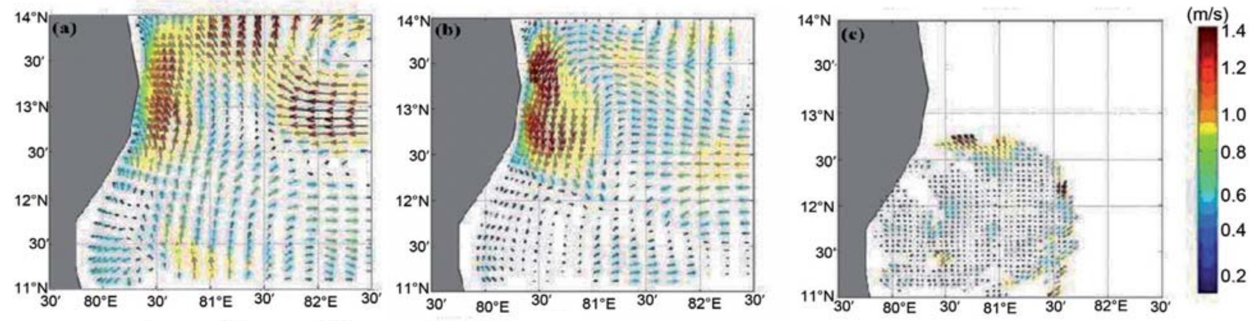

Fig. 1 The surface circulation pattern for 0000UTC 15 December 2012 without using open boundary conditions (a) surface forcings such as surface winds from ASCAT and surface fluxes from objectively analyzed fluxes, (b) surface forcings from WRF simulation and (c) HF radar observation

VI.14 Source Term Modeling for Decision Support System using Environmental Radiation Monitoring

In the event of a nuclear accident leading to dispersion of radioactive material into the environment, an effective counter measure implementation for the protection of public depends on the source term, environmental monitoring programs, use of accurate atmospheric dispersion modelling tools and spatial decision support systems. The Kalpakkam site has been equipped with a decision support system (DSS) called 'online nuclear emergency response system (ONERS)', implemented operationally for preparedness and management of nuclear emergencies. The DSS employs real-time meteorological data, the weather and dispersion model predictions to assess the spatio-temporal evolution of the radioactive plume of accidental releases. Source term is an important input in DSS for predicting the consequences of accidents.

A source-term estimation module has been developed and incorporated in the DSS. The method is based on an inverse dispersion calculation which uses measured dose rates from gamma dose rate monitors distributed in the site and real-time meteorological data. The dose due to a released substance at a ground receptor can be expressed as the sum of the products of all source emission rates and the dispersion factors between the source and that receptor. In the case of a single source and 'n' receptors, the calculated emission rate is given by

$$Q = \frac{1}{n}\sum_{i=1}^{n}(C_i D_i^{-1})$$

Where D_i is the computed dose for unit release at receptor 'i', and C_i is the measured dose at the receptor 'i'. The Gaussian Plume model and a 3D random-walk model (SPEEDI) are used to estimate the plume gamma dose D_i from a given emission source as a function atmospheric processes (winds, mixing/stability) at various receptor locations around the release facility using unit release rate (1 Bq/s). The computed doses are inverted with measured doses at receptor points. While the global precipitation measurement (GPM) with a cloud integration scheme provides conservative dose estimates, the SPEEDI with a point-kernel method for cloud dose is designed to reduce the uncertainties in dose near the source. The inputs for both the models are distance of the detectors from the source of release, height of release point, linear attenuation coefficient in air, energy of the released activity and real-time meteorology (wind speed, direction, stability condition). The source term module uses the online data from various environmental gamma monitors distributed around the site. These comprise the LAN based environmental gamma dose loggers (EGDL) and RF based area gamma dose loggers (AGDL) distributed at various distances within the Kalpakkam DAE site (Figure 1a). Area gamma dose logging system is shown in Figure 1b. The source-term program scans the detectors which fall in a sector of ±45° of the actual plume direction (wind direction) and computes the source term as the average value for the detectors in that scan sector. The program accesses the 10 minutes average real-time meteorological and gamma dose measurements and computes the source term at intervals of every 10 minutes. The module is operationally integrated with DSS and is live, providing the source term at every 10 minutes duration so that the temporal variation in the source term during the accidental conditions can be assessed. Figure 1c shows the snapshot of computed source terms using the inversion algorithm using real-time observations.

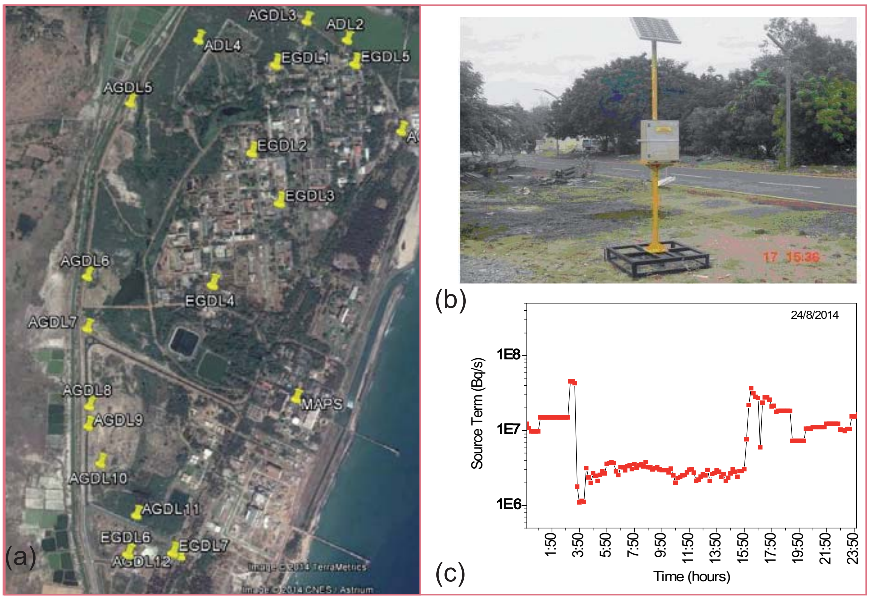

Fig. 1 *(a) Locations of environmental radiation monitoring detectors, (b) area gamma dose logging system and (c) estimated source term using real-time observations*

VI.15 Numerical Simulation of the Transport of a Radionuclide Chain in a Rock Medium

In an unlikely event of failure of the engineered barriers of a high-level waste repository, the active elements would get exposed to the surrounding rock which is a porous medium. In such a situation, the contaminants may come in contact with the underground water and start migrating by advection and diffusion phenomena. Simultaneously, the parent active elements present in the waste would decay into daughters which decay further until the formation of a stable isotope. The migration of the total activity would lead to serious radiological consequences related to public safety and so requires radiological assessment. The experimental determination of contaminant migration is difficult because of the slow advective flow of underground water. It may take several years for the active element to reach a detectable limit even at a spatial location which is only a few meters away from the repository. So numerical simulation is a preferred alternative method to address this problem.

A rock is basically a combination of an interconnected network of tiny fractures and porous blocks of arbitrary sizes. For numerical modeling, a simple geometry of rock structure consisting of an infinite array of identical parallel fractures separated by porous matrices of equal width can be considered (Figure 1a). Considering this geometry, one can represent the migration process by two coupled one dimensional partial differential equations for the i-th member of a radioactive chain. The concerned equations are given below.

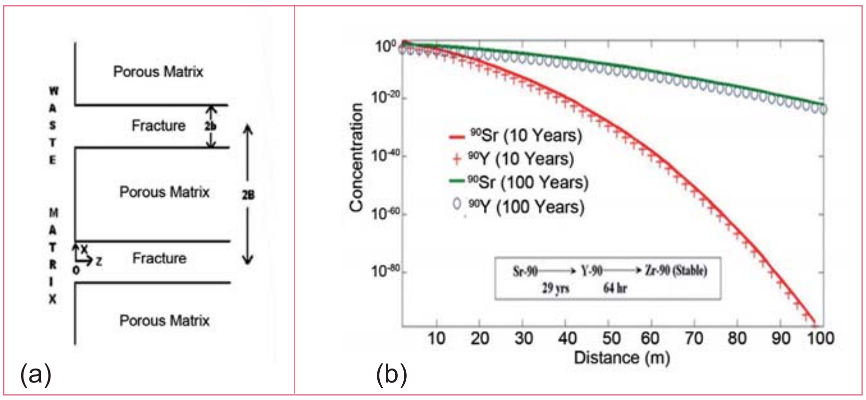

Fig. 1 *(a) The simplified rock geometry and (b) concentration profile of the members of ^{90}Sr chain*

Equation 1 describes the transport along the fracture while Equation 2 (Table 1) indicates the same perpendicular to it. In first equation, C^i represents the concentration of the *i-th* member, D^i is the dispersion coefficient, R^i is the retardation coefficient, v is the flow velocity of water and λ^i is the decay constant of the species. These terms represent the quantities within a fracture. The corresponding quantities for the porous matrix are indicated by a suffix 'p'. The term θ represents the porosity of the matrix. At t=0, the concentration of radioactivity is zero everywhere and this serves as the initial condition. An important point is that for a chain transport, one must consider the Bateman function for the source term. It can be noted that the geometry has a symmetry across the centre-line of the porous matrix (at x=B). Considering these points along with the conservation of mass across the waste matrix-fracture interface and continuity of molecular flux across the fracture-porous matrix interface, Equations 1 and 2 of Table 1 are solved numerically. The results have been validated using open source data/method available in the literature.

The validated numerical code is then applied to model the transport of a chain (^{90}Sr chain) with two members (the third member is non-radioactive and thus it has not been considered for simulation). The reason behind choosing this chain is that ^{90}Sr is an element with reasonable half life (~29 years) present in a large quantity within the initial vitrified waste. Figure 1b represents the concentration profile of the members of this chain. It can be seen that the concentration comes down by a factor of 10^{-20} within a distance of 100 m from the source point (along the fracture) for a period of 100 years. The result of the present study demonstrates the assessment of the migration of a radioactive chain through a rock medium. Further, the study can be extended further to study the migration in other porous medium like soil surrounding waste repositories.

Table 1: Equations

$$\frac{\partial C^i}{\partial t}+\frac{v}{R^i}\frac{\partial C^i}{\partial z}-\frac{D^i}{R^i}\frac{\partial^2 C^i}{\partial z^2}+\lambda^i C^i-\left[\frac{R^{i-1}}{R^i}\right]\lambda^{i-1}C^{i-1}-\frac{\theta D^i{}_p}{R^i b}\left[\frac{\partial C_p{}^i}{\partial x}\right]_{x=b}=0,\ z\geq 0\ ,\ t>0 \qquad -(1)$$

$$\frac{\partial C_p{}^i}{\partial t}-\frac{D_p{}^i}{R_p{}^i}\frac{\partial^2 C_p{}^i}{\partial x^2}+\lambda^i C_p{}^i-\left[\frac{R_p{}^{i-1}}{R_p{}^i}\right]\lambda^{i-1}C_p{}^{i-1}=0\ \ b\leq x\leq B\ ,\ t>0 \qquad -(2)$$

VI.16 Inter-laboratory Comparison Study on Dicentric Chromosomal Assay

The first inter-laboratory comparison study on dicentric chromosomal assay (DCA) for both routine and triage biodosimetry applications has been undertaken between biodosimetry labs located in and around Kalpakkam for capacity building. Four sets of human peripheral blood samples exposed to ten different doses (0 to 5 Gy) of X-rays (3 Gy/min) were shared between the labs and calibration curves constructed. The calibration curve is shown is Figure 1. It is evident that no significant difference was observed between labs regarding their dicentrics data (except at 2 Gy, p<0.05) and calibration curve parameters (t-test with Bonferroni correction, p<0.008).

Validation of calibration curves was done by blind test method where dose blinded samples exposed to X-ray (1 and 2 Gy, at 3 Gy/min dose rate) or gamma radiation (1.71 and 2.14 Gy, at 0.63 Gy/min dose rate; ^{60}Co) were used. The estimated doses were observed to be not significantly different from actual doses (p<0.006, with Bonferroni correction). Usefulness and reliability of the DCA data for triage application was evaluated by scoring 20, 50 and 100 metaphases in the dose range of 0.5-3.0 Gy. The results indicated that scoring 20 metaphases is adequate to detect radiation exposure of 2 Gy and above whereas 50 metaphases is sufficient to determine radiation exposures of 0.5 Gy. This inter-laboratory comparison study also reveals the reliability of DCA as a routine and triage biodosimetry tool in the biodosimetry labs indicated above.

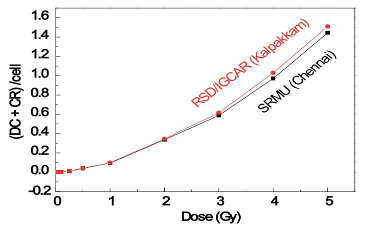

Fig. 1 *Comparison of dicentrics scores from both*

VI.17 Determination of Dose to Public due to ^{90}Sr from Ingestion of Dietary Samples

It is well known that nuclear fission of uranium and plutonium produces many radionuclides. Among them, ^{90}Sr is one of the nuclides released to the environment during nuclear fall-out. Once it is released, this nuclide will be transformed to one of its stable forms such as oxides, carbonates or halides. The transfer of this nuclide to the human being through dietary intake can be estimated by measuring its content in the food items. ^{90}Sr, a pure beta emitter (β max.545.96 keV) has long physical (28.8 years) and biological half-life. It also exhibits biochemical behavior similar to calcium. The most possible pathway is via ingestion of food and water. It enters into the human system via components of food chain such as milk, rice, wheat products and vegetables.

Presence of this nuclide in the body internals cannot be identified by in-vivo methods. A low background gas flow proportional counter available at environmental survey laboratory (ESL) was used for the detection of beta radiation emitted by ^{90}Sr. The efficiency of the counter was calculated using 40K standards and was observed to be 42.20%. The relatively low background of these counters offers a detection limit of 17 mBq.

Since rice is our staple food, samples of Ponni rice received from shops adjacent to Kalpakkam (Kadambadi village) were collected and dried in an oven at 110°C for 2 hours. The dried samples were cooled to room temperature and weighed. The loss in weight reflects the moisture content of the sample. The average loss in weight of all samples after moisture removal was found to be 400 grams. Then the samples were loaded into a muffle furnace maintained at 450°C for 24 hours. The weight of ash in sample was found to be 17 grams.

A portion of the ash was taken, spiked with appropriate concentration of carriers such as Cs, Fe, Ba, Sr. Estimation of strontium present in the sample was carried out by acid leaching the ash followed by separation of interfering elements using standard protocol as followed in ESL, Kalpakkam. Finally the strontium present was precipitated as strontium carbonate, dried and weighed. From the recovery factor (~77%) obtained, the amount of strontium present in the samples was normalized. The activity present in the samples was found to be 17 mBq which is below detection limit. The age dependent dose limits for different age groups have been determined and the values are presented in Table 1. The study shows that the dose to the public resulting from the consumption of rice and consequently this radionuclide is not a concern in this region .

Table 1: Dose for ^{90}Sr due to ingestion

Dose to the public (Sv) x E-10		
<1 year	7-12 years	>17 years
<3.91	<10.02	4.76

VI.18 Thermal Imaging for Early Detection of Breast Cancer

Breast cancer is one the most common cancer among women, other than cervix or lung cancer and is the second leading cause of cancer death in women.

Early detection leads to increased survival rate and cure. A well-researched imaging tool that has found applications for early detection of breast cancer is breast thermography (BT). It is well established that temperature is the best precursor for monitoring the health of a component in the plant or the organ of a human being. Thermography is a temperature based technique that utilises the differences in thermal patterns to qualitatively and quantitatively detect abnormalities. It has found wide applications in predictive condition management in industries.

IGCAR in collaboration with DAE Hospital Kalpakkam has pioneered the application of thermal imaging as a screening tool for early detection of breast cancer. Research studies in collaboration with Sree Ramachandra Medical University and Madras Medical College, Chennai (after appropriate permissions from the respective ethical committees)on over 600 cases in which thermography, mammography, ultrasound and FNAC were undertaken helped in developing a good understanding of breast thermographic images. Appropriate protocols taking into account the physics of heat radiation, the physiology of thermoregulation of the body and based on the guidelines formulated by the various international thermology associations suitably modified for the Indian conditions was then established and validated. As part of a collaborative project, “artificial intelligence based computer aided detection for medical application” between IGCAR and National Engineering College, Kovilpatti a series of camps on breast screening was conducted at Saradha governament higher secondary school, Nallatinputhur, Kovilpatti, Assembly Hall, National Engineering College, Kovilpatti, Mookootumalai, 25 kms from Kovilpatti, K. Pudur, Madurai, MSRIT, Bangalore and Thanjanvur. Over 248 cases were screened and about 49 significant cases confirmed through infrared thermography, USG and mammogram. This represents the first successful attempt in the country for the application of thermal imaging for early detection of breast cancer as part of DAE effort on application of newer technologies for societal applications. System setup is shown in Figure 1 and camera features are given in Table 1.

Fig. 1 *Imaging system setup*

Table 1: Imaging performance

Field of view	25 x 19°
Thermal sensitivity (NETD)	0.05 @ 30°C
Detector type	Focal plane array (FPA), uncooled microbolometer
IR resolution	320 x 240
Spectral range	7.5 to 13 μm
IFOV (with 25° lens)	1.36 mRad

VI.19 Clinical Studies using Magnetocardiography

Facilities to measure magnetic fields associated with the electrical activity of the heart viz., Magnetocardiography (MCG) and with those of the brain viz., Magnetoencephalography (MEG) using SQUID sensors have been established at IGCAR. Towards taking the program forward to clinical use, an evaluation on the diagnostic performance of MCG was conducted on patients with cardiac anomalies in collaboration with JIPMER, Puducherry. About twenty eight patients with various cardiac dysfunctions including structural heart diseases, conduction abnormalities and patients implanted with cardiac pacemakers etc. were brought to IGCAR on four consecutive days accompanied by a cardiologist. Figure 1 shows the 37 channel MCG system operational at IGCAR. MCG signals were measured by aligning the anatomical landmarks on the subject's chest with respect to the sensor array inside the MCG cryostat. This is analogous to the standard lead configuration used in a clinical ECG or Body Surface Potential Mapping (BSPM) setup, except for the fact that no physical contact is required between the sensor and the patient during the MCG measurements in stark contrast to ECG/BSPM. The data were processed for artifact and noise removal using the algorithms which were already developed in the laboratory. Applying these algorithms on the patient's data was especially challenging for subjects with surgical implants; the implants were inevitably present during the MCG measurement and contributed to the contamination of the signal by the artifacts, with amplitude which was found to vary from case to case. Figure 2 depicts a representative MCG signal recorded on a patient with cardiac pacemaker; the low frequency drift in the base line is related to the breathing artifact, which can be eliminated using a suitable denoising algorithm. Periodic spikes seen in the MCG trace represent magnetic signatures of the pacemaker electrical stimulation which can be identified and isolated.

As a sequel to the successful demonstration of the non-invasive measurement of the magnetic field associated with the electrical activity of the bundle of His (which is very weak, of the order of 100-200 femto-Tesla) using the MCG system operational at IGCAR, one of the main objectives of the clinical evaluation study was the comparison of the time instants of the activation of the His bundle activity measured using the invasive electrophysiological (EP) procedure (which is taken as a gold standard in clinical practice) with those measured using the non-invasive MCG technique.

Fig. 1 *Thirty seven channel magnetocardiography system at IGCAR*

Invasive measurement of the His bundle activation using EP involves advancing a multipolar catheter inside the heart of the patient guided by a fluoroscope, and is conventionally employed in clinical settings. Since His bundle is surrounded by nonconducting tissue, it is however difficult to perform electrical measurements.

Four patients for whom the time instant of the activation of the His bundle (namely, the H-V duration) was known in advance through the invasive EP investigation were deliberately included in the study group of subjects selected for carrying out the MCG measurements at IGCAR. It may be noted that determination of H-V duration is crucially important for clinical decisions involving the implantation of a pacemaker in order to reduce the risk associated with life threatening arrhythmias. The MCG traces revealed conspicuous and clearly defined His bundle magnetic field signatures with a biphasic hump like feature, similar in morphology and timing with those observed with the invasive EP study. Figure 3 depicts the time matched traces of the His bundle activation signal (marked as "H" in the figure) measured non-invasively (using MCG at IGCAR) and invasively (using EP at JIPMER) for a patient with a congenital conduction anomaly. The MCG trace is also filtered with pass band 25 Hz to 175 Hz, similar to the filter setting employed in a typical EP, which is shown for comparison. It is evident that the assessments of H-V duration using non-invasive MCG and invasive EP measurement differed by only 4 milliseconds and the His bundle features measured in both the modalities closely resemble each other indicating a physiological consistency. Similarly, the H-V durations measured for two patients

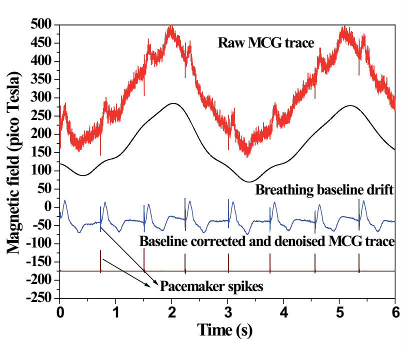

Fig. 2 *Magnetocardiography trace of a pacemaker artifact and its elimination using a suitable denoising algorithm*

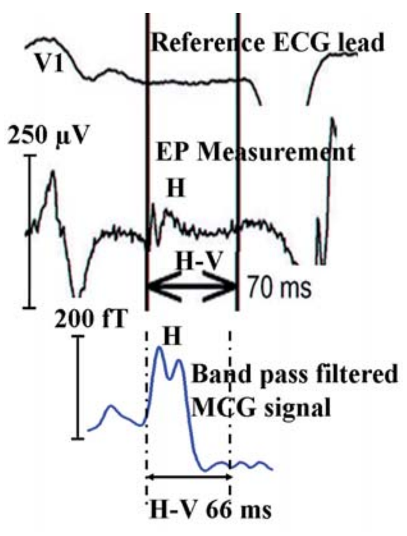

Fig. 3 *H-V interval measured non-invasively using MCG at IGCAR and invasively using electrophysiological procedure at JIPMER*

with congenital pre-excitation abnormality and for a patient with a higher degree conduction block using the two modalities were also compared. The mean difference between the two measurements did not exceed 5 milliseconds, validating the use of MCG for the assessment of His bundle signal. The EP measurement set up in a clinical setting is also equipped with pacing and ablation catheters to extensively evaluate the cardiac activation and to ablate and thereby eliminate any abnormal activation sites inside the heart. However, the non-invasive His bundle measurements using the MCG technique could be used to effectively complement the invasive EP procedures, and provide further corroborative evidence in certain clinically demanding cases for which the catheter ablation or subsequent implantation of pacemaker may not be required and also in some specific applications involving periodic pharmacological interventions on the His Bundle.

It is thus evident from these results that MCG could serve as a completely non-invasive procedure for the clinical assessments on His bundle activation. Besides, successful measurement of the extremely weak magnetic field associated with the electrical activity of the His bundle using the non-invasive MCG technique opens up new opportunities for using the MCG technique for investigation of other weak cardiac signals by harnessing the high sensitivity offered by the SQUID sensors. Scope exists to precisely localize these physiological sources using mathematical approaches which would ultimately aid the clinician for a better interpretation of cardiac anomalies. Indeed, during recent times, MCG has emerged as a promising new technique with greater sensitivity and specificity compared to ECG, which is currently used in clinical practice.

VI.20 Extreme Events Analysis of Tall RC Structure

An Engineering Hall is being designed and constructed to carry out performance evaluation studies and qualification of critical components of future FBRs. High bay of size 40 metres length, 21 metres breadth and 43 metres height is planned for housing a large sodium component testing facility with associated systems. This is a non radioactive sodium facility with no potential for on site radiological contamination. Sodium technology complex includes various facilities like sodium dump pit, material storage area, control room, electrical panel room, sodium cleaning area, office floors, in a total area of 4800 m^2. It has 25 and 10T EOT cranes at 37 metres height of high bay and 5T EOT crane at material storage facility. Inside high bay, isolated reinforced concrete (RC) frame structure is provided to facilitate steel rig columns for supporting the test facility. Foundation is planned at a depth of 8 metres below the existing ground level, where safe bearing capacity of the weathered rock is 50 tons/m^2 Abrasive resistance of the floor is achieved by ironite flooring top, below which lime stone resistant concrete special mix with a suitable plasticizer is proposed for minimizing sodium-concrete interaction in case of sodium leak. Composite roofing system is one of the techno-economical feature planned for both design and construction. Analytical 3-D model of sodium technology complex is shown in Figure 1.

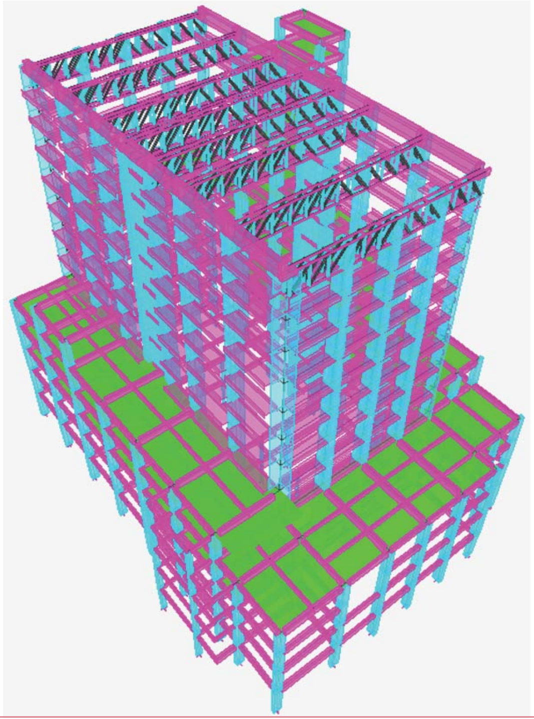

Fig. 1 *Analytical 3-D model of sodium technology complex*

Design basis events

According to the AERB safety code, for site evaluation of nuclear and related facilities, sodium technology complex comes under the category of "general use" boundary and/or offsite chemical hazard. Hence, design basis events due to natural hazards are proposed as per AERB safety code, listed in Table 1. MCE is defined as Maximum Credible Earthquake as per IS 1893, which is twice that of an earthquake event normally considered for a building.

Flood is an important external event to be considered for sodium technology complex design. Hence, floor level of the facility is to be arrived based on the evaluation of design basis flood level (DBFL). Studies were carried out by IIT Madras considering the storm surge, run up; Tsunami generated from a point source and various Tsunamigenic sources (parameters) in Indian Ocean for arriving DBFL. Considering the additional hazard posed to the sodium handling facility by flood, the proposed design basis flood level is based on 1000 year return period which is 7.5 metres above the tidal datum, i.e chart datum (CD). Finally, DBFL for sodium technology complex is fixed as RL+12.9 metres. Based on evaluation of design basis wind speed based on site specific data, 3-sec gust wind speed for 100 year return period is 67 m/sec.

Modeling analysis and design optimization

Physical structure of the sodium technology complex facility is transformed into a mathematical model for structural analysis. Beam and shell elements are used for modeling column, beam, wall, slab, roof truss, etc using the features of commercial software ETABS. Static and dynamic analyses are carried out for fixed, imposed loads and design basis events. Geometric nonlinear analysis is considered for accounting any second order forces generated due to slender behavior of the building. Columns, tie beams and shear walls are arranged such that story drift, the relative displacement at the level of rails and other deformations are within the permissible limits. Individual load case and combinations and the performance of the structure in limit states of stability, serviceability, strength and collapse are checked. Twin beams connecting the critical high bay columns whose unsupported height is equal to the building height reduce column moments and lateral drift as well as torsional behavior of corner columns significantly. Dual systems like shear wall cum moment resisting frame are the important structural features of the building. Optimum member sizes have been arrived after successive iterations of detailed structural analysis and design.

Table 1: Return period for external events

Type of natural hazard	Mean annual frequency of occurrence of event	Return period (years)
Ground acceleration due to earth quake	4×10^{-4}	2500
Flood due to Tsunami or rain	10^{-3}	1000
Wind	10^{-2}	100

VI.21 Effect of Curing Methods and Environment on Properties of Concrete

Curing has a significant influence on the properties of hardened concrete, such as strength and permeability. The concrete specimens lose moisture through evaporation and become dry in the absence of a proper curing. In severe cases, when hydration is eventually stopped, sufficient calcium silicate hydrate (CSH) cannot be developed from the reaction of cement compounds and water. With inadequate calcium silicate hydrate , the development of strength, dense microstructure and refined pore structure is interrupted. A more continuous pore structure will be formed in cover region of concrete, since it is very sensitive to drying. The continuous pore structure formed will allow the ingress of deleterious agents, and thus would cause various durability problems. Moreover, the drying of concrete surfaces results in shrinkage cracks that may aggravate the durability problems.

The movement of water from the concrete soon after placing depends on the temperature and relative humidity of the ambient air and the wind velocity over the surface of the concrete. These are the major factors that decide the method and curing time of concrete. The temperature during curing also controls the rate of progress of the reaction of hydration and subsequently affects the development of strength of concrete; hence it is a function of the time interval and temperature.

Different methods adopted for curing are widely depending on the condition on the site and on the size, shape and position of the member/structure.

When fly ash is one of the ingredients in concrete, it reacts with the primary hydration product (ie. calcium

Table 1: Mix proportion of specimens for curing studies

Grade of mix	M50 (A)	M35 (B)	M35 (C)
Cement(kg)	315	210	320
Fly ash(kg)	210	210	0
Water(kg)	153	147	144
Aggregate coarse & fine(kg)	1083 676	1140 729	1172 855
Admixture (%)	1.6	1.6	0.9

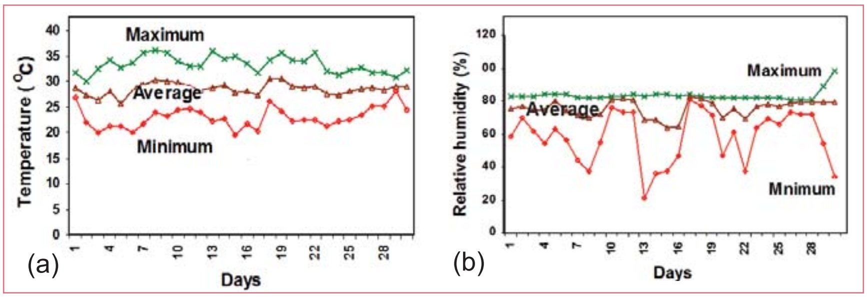

Fig. 1 *(a) Temperature and (b) humidity data of S2 site*

hydroxide) to form calcium silicate hydrate . The rate of hydration is slow, hence curing is essentially required.

This study presents the effect of different curing methods, period of curing and meteorological data on compressive strength and permeability of ordinary concrete and fly ash concrete.

Specimens were cast and tested at three different nuclear power plant sites S1,S2 and S3 in India. Locally available crushed granite stone and crushed and river sand were used as coarse and fine aggregate respectively. Ordinary portland cement and fly ash conforming to the requirements of IS 3812 (Part 1): 2003 has been used in all projects. Normal potable water was used for preparing concrete and also for curing purpose. Sulfonated naphthalene formaldehyde condensate based superplasticizer was used to achieve workability.

Mixes of grade M50 with 40% fly ash (A), grade M35 with 0% (C) and 50% fly ash (B) was used for this study. The details of the mixes are given in Table 1. All the project sites used these proportions keeping the same quantity of cement, fly ash and water. The quantity of plasticizer and aggregate were adjusted for requisite grade of the mix.

Cube specimens of 150 mm size were cast. The exposed surface was covered by plastic sheet and stored in the moulds for 24 hours then de-moulded.

For water curing, specimens were immersed in curing tank and specimens were covered by plastic sheet for sealed curing upto various ages as per the schedule of 7,10, 14, 28 and 56 days. The sealed cured and water cured samples after designated period of curing were stored in an open area.

At all the sites, the metrological data such as humidity and temperature were recorded daily during the period of this study.

Tests were conducted for compressive strength (IS 516) and Rapid Chloride Penetration (ASTM 1202-97) for permeability.

Figures 1a and 1b show the maximum, minimum, day average ambient temperature and relative humidity for one of the sites. Similar details were obtained for all the three sites.

The results showed that,

- The strength of water and sealed cured specimens were comparable. In general, the relative values of rapid chloride penetration test (RCPT) were lowest for water cured samples
- During the curing period at S2, as the temperature variation was high (15°C) there was a strength reduction of around 43% with respect to S1 (Figures 2a and 2b)
- Similarly, when humidity varied too much permeability increased as high as 300%
- Fly ash concrete specimens were more impermeable than ordinary concrete specimens with a curing time of 14 days instead of usual 7 days
- Fly ash concrete specimens attained compressive strength slowly but gain higher strength than ordinary concrete with a curing time of 14 days as shown in Figures 3a to 3c.

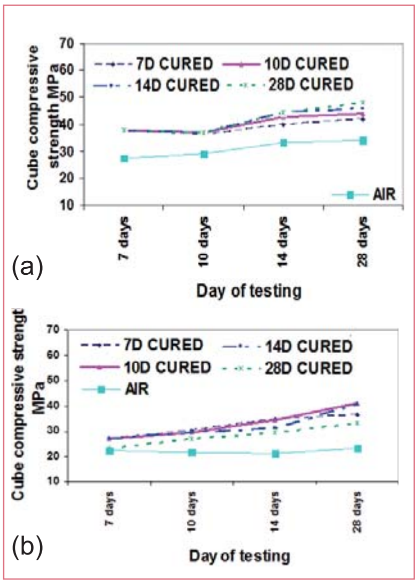

Fig. 2 *Compressive strength of water cured concrete specimens with different curing periods of (a) S1 and (b) S2 sites*

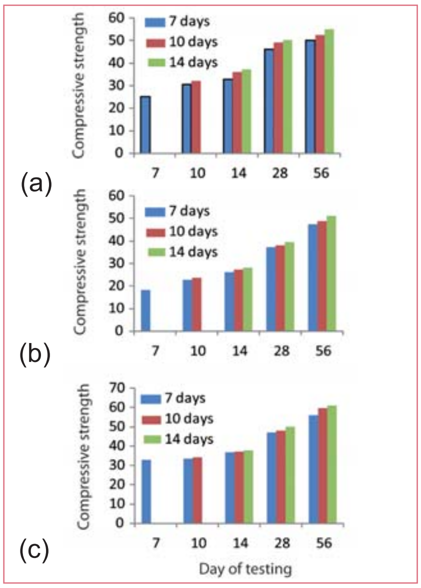

Fig. 3 *Compressive strength of water cured concrete specimens for different periods of S3 results with (a) A, (b) B and (c) C mixes*

VI.22 Intensity Delocalization in High Resolution Phase Contrast Images Due to Local Strain: Effect of Imaging Parameters

Macroscopic and functional manifestation of strain in materials originate from the existence of local strain at the atomic scale, which is essentially the shifts of the atomic/ionic species from their equilibrium positions. Atomic shifts, resulting into localized strain could be due to several reasons e.g. alloying/dealloying, introduction of defects, through deformation, irradiation etc. In non-ferrous alloys, steels, precipitates and interfaces, local strain is very commonly observed. However, understanding the presence of local strain is of immense importance from the view point of understanding properties, service life performance and most importantly understanding the mechanistic role of local strain that directly correlates to properties as it can be further translated for materials design and development.

“Seeing is Believing” being the traditional philosophy among the materials science community, it has been a long-standing question as to how local strain manifests itself in high resolution images and is there a possibility to quantify the strain field. A major break-through in this direction is considered to be the development of geometrical phase analysis (GPA) by several european microscopy groups over last two decades. Geometrical phase analysis is based on Fourier segmentation of the intensity modulation in the image plane along several vectorial directions. Successful implementation of this technique requires a reference region which can be treated as unstrained. The aim of the work is to find out the right defocus under a specific imaging condition to maximize the strain resolution.

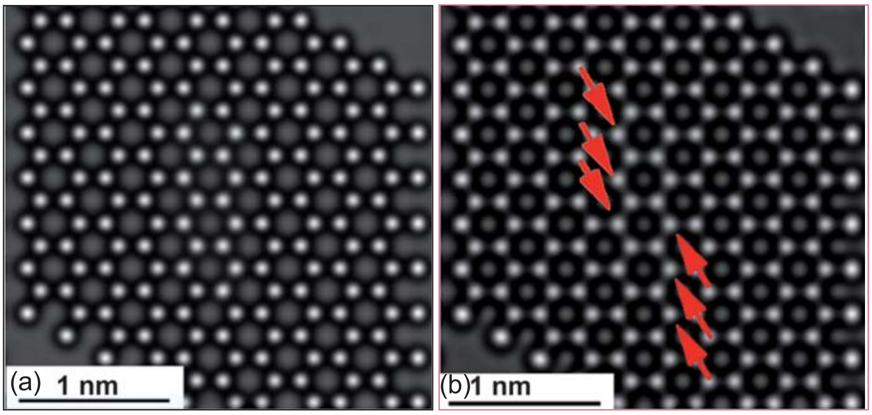

Fig. 1 *Simulated NCS image of (a) unstrained Ti lattice along [0001] and (b) Ti lattice along [0001] direction*

Recently, we have shown that in vanadium-substituted $TiCr_2$ cubic Laves phase, vanadium preferentially occupies the Ti sub-lattice and introduces local strain in the lattice. As an extension to that we have developed a model based on hexagonal Ti and introduced known amount of strain in specific directions. It has been observed that understanding the contrast of the unstrained lattice is the first step to understand the local strain.

In the negative aberration-corrected (NCS) phase contrast image of hexagonal Ti (Figure 1a), bright contrast is originated from the inter-atom column spaces due to the specific nature of electron channeling in this material in combination with other electron-optical parameters. In Figure 1b, intensity delocalization around certain locations of bright contrast is observed due to the presence of strain. The central region of the lattice is ~5% strained. Even though the bright contrast does not represent the position of an atomic column, due to the positional shift in the atomic columns, the electron channeling behavior along inter-atom column spaces also changes.

It is important to note that, with aberration and defocus, the intensity modulation in the image plane may undergo substantial changes.

In addition to aberration, intensity delocalization is a strong function of defocus and the strain present. A systematic study based on experiments and simulation has shown that for negative aberration-corrected images, the correct defocus is the modulus of the Scherzer defocus (focus setting of objective lens that maximises image resolution) with similar value of positive aberration. This condition gives the best possible strain resolution. For positive aberration-corrected images, Scherzer defocus is the correct choice. However, the high resolution image being a 2D projection of 3D object, vectorial segmentation of strain in 3D is not so straight forward. It is worth noting that the intensity delocalization in such images reflects the presence of static displacement fields only. We have established by experiments and simulation on Ti-alloys and Laves phases that strain induced delocalization can be detected and interpreted.

VI.23 Heat Power Estimation from Thermal Images during Tensile Deformation

Mapping evolutions of strain localization using temperature fields has been a challenging task for researchers over the years due to the associated thermal diffusion. The present work deals with the analysis of heat powers (rather temperature) to quantitatively study the kinematics of localized deformations in IS2062 grade E250B mild steel during tensile testing. The experimental procedure involves recording the thermal images during tensile deformation of the specimen using focal plane array based infrared camera. Heat powers associated with the experimentally determined temperature fields are then estimated using two dimensional heat diffusion equation given by:

$$\rho C\left(\frac{\partial\theta}{\partial t}+\frac{\theta}{\tau}\right)-k\left(\frac{\partial^2\theta}{\partial x^2}+\frac{\partial^2\theta}{\partial y^2}\right)=W'_{hs}$$

which takes into account the heat losses due to conduction, convection and radiation.

Figure 1 depicts the spatiotemporal evolutions of temperature and heat power accompanying Lüders instability with the load-time plot superimposed on them. Y axis of the plots represents the complete gauge length, the temperature and heat power evolutions over which are averaged along the gauge width at any particular instant and X axis represents time. Temperature evolutions shown in Figure 1a reveal the strain localizations accompanying Lüders band nucleation (a strain localization phenomenon commonly observed in mild steel) in the upper end of gauge length at about 230 s, its growth followed by nucleation and growth of second band from the lower end the gauge length. However, at any particular instant in the load plateau (254 s-405 s) thermal profiles are highly diffusive with temperature distributed over the entire gauge length thereby blurring the actual zone of strain localization. On the other hand, the estimated heat power evolutions shown in Figure 1b has been found to provide more quantitative information on the nucleation and growth of Lüders bands without the effects of thermal diffusion associated with prior plastic localization. The localization associated with a first band is, in fact, revealed by heat power evolutions much ahead the thermal evolutions at about 210 s itself overcoming the influence of thermoelasticity. The occurrence of delayed yielding during the initial stage of uniform strain hardening (which is not revealed by temperature fields) has been successively studied using heat power evolutions.

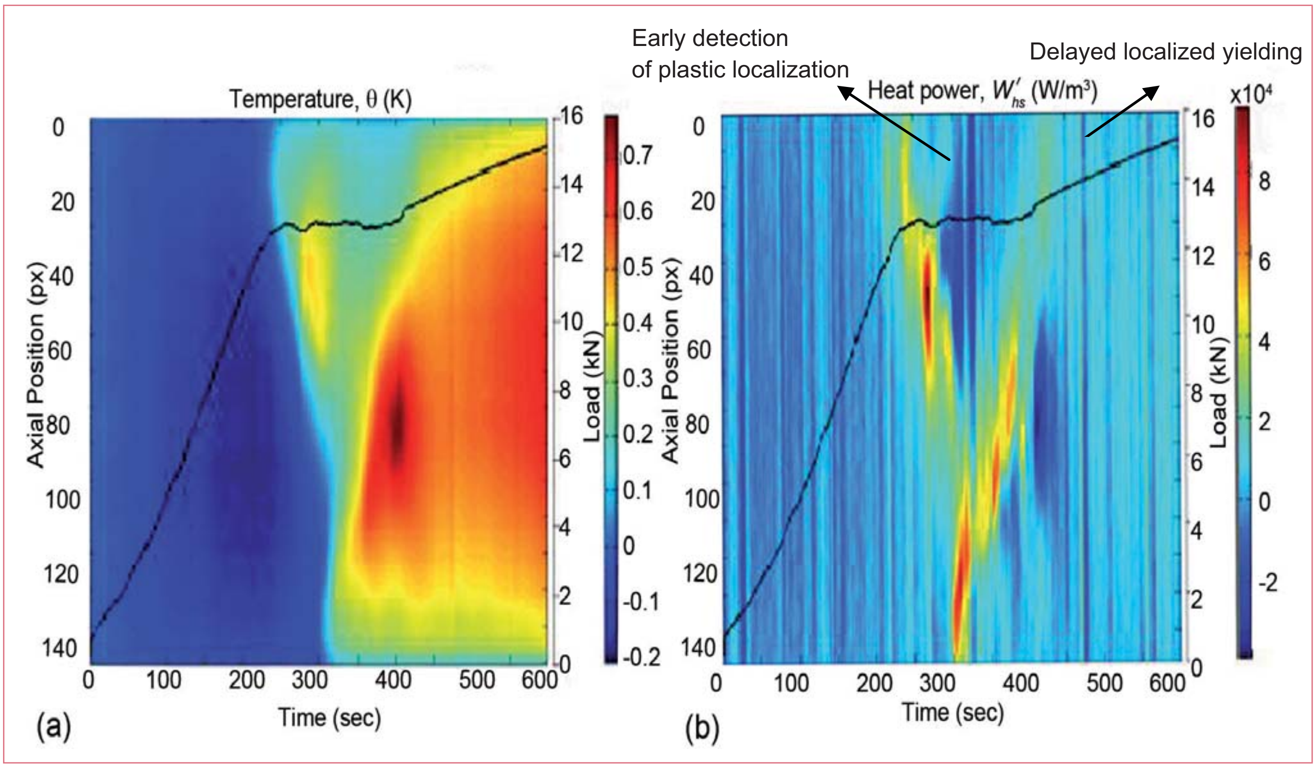
Early detection of plastic localization

Delayed localized yielding

Fig. 1 *Spatio-temporal evolution of (a) temperature and (b) heat power*

VI.24 Application of Six Sigma Concepts in Quality Assurance of Piping Welds

Six Sigma is an advanced quality management concept to improve the quality of process outputs by identifying and removing the causes of defects (errors) and minimizing variability in manufacturing and business processes by using statistical techniques and tools. Processes that operate with “six sigma quality” are assumed to produce long-term defect levels below 3.4 defects per million opportunities (DPMO). For the first time six sigma concept was applied in a Research Centre and in a nuclear plant (Demonstration Fast Reactor Fuel Reprocessing Plant).

Austenitic stainless steel 304L grade is used as a candidate material for fabrication of entire piping work with Gas Tungsten Arc Welding (GTAW) as a welding process. The study is envisaged on the application of six sigma concepts in quality assurance (QA) during the fabrication of complex and high density piping in phased manner using proven DMAIC approach with the broad objective of identifying the redundant and time consuming steps, optimize the project duration and evolve a “Lean management system”.

The entire piping fabrication process is studied using a high level process map as shown in Figure 1 in order to identify the process for improvement. Welding of pipe joints with 100% radiography is observed as a vital link in the entire process flow chart. A sample data around 12000 numbers of butt welded pipe joints out of 70000 joints spanning across all areas of DFRP and all sizes of pipes from DN 8 to DN 25 are selected to assess the base line sigma level and most frequently occurring weld defects through collection of data on weld defects from the weld inspection and radiographic reports using Pareto chart (Figure 2). The base line sigma level is observed as 4.1 sigma (DPMO). Lack of fusion & penetration, tungsten inclusion, oxidation and porosity are the defects which account for most frequent occurrence (Vital few). Subsequently statistical quality control tools such as brainstorming session, cause and effect diagram, histograms, bar charts and Chi-square test for assessing the association between causes are used to identify the “vital few” root causes for the frequent occurrence of welding defects based on the sample data selected earlier.

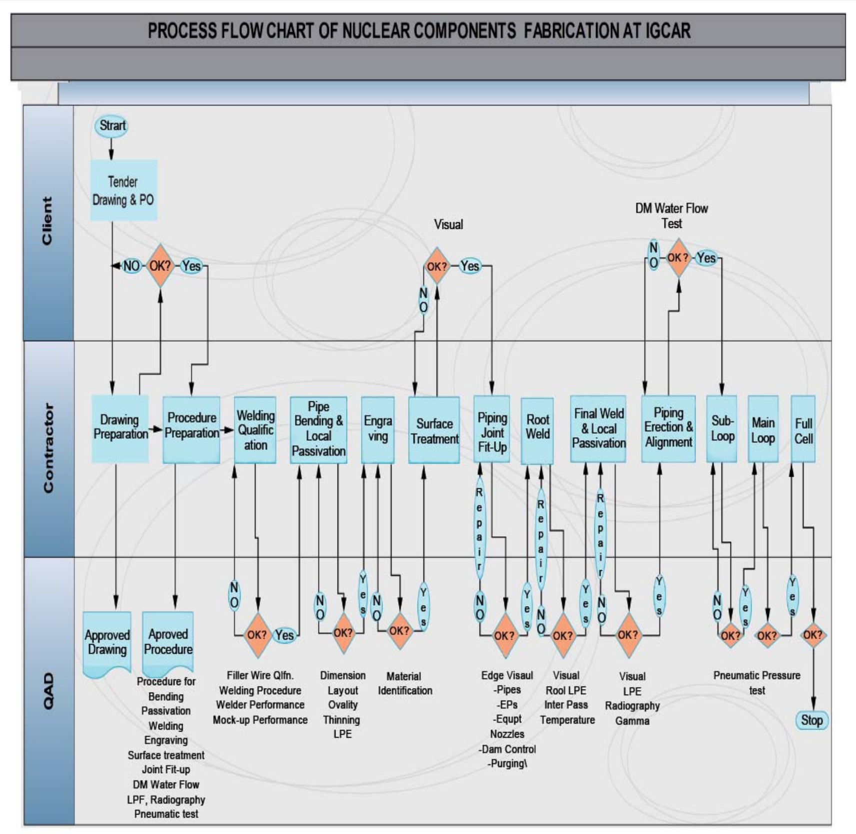

Fig. 1 High level process chart of nuclear components

Welder’s experience in using GTAW, fear of heights (entire piping facility is spanned from -2.5 to +12.5 m elevation), ability to make sound weld deposit in a highly congested area, welder’s basic relevant technical educational qualification and the factor of migration from SMAW to GTAW are found to be main causes for this particular defect. Oxidation is the next major defect and is attributed due to either inadequate argon purging gas at the root or joints are not amenable to purging at all. Further, as stipulated by regulatory body only GTAW can be used for welding. GTAW filler wires with special flux coating has now been successfully standardised which illustrates the need for back purging during root pass welding of pipe joints.

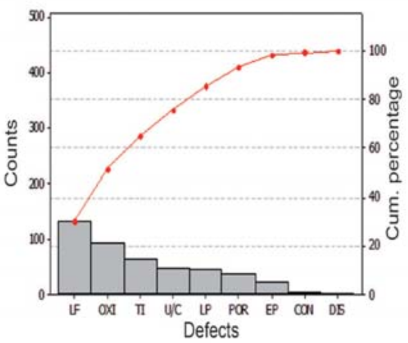

Fig. 2 Pareto chart of weld defects

VI.25 Enhancement of e-services under 'ATOMS'

As a part of e-governance, an online-Automated Workflow Management System (ATOMS) has been implemented at IGCAR. The portal links the employee enables interaction in the domains of Administration, Accounts, Stores and Purchase. Existing services are continuously being upgraded and enhanced by introducing newer services in an effort to move towards a "paper-less" office in due course of time. During the last one year, two important modules, namely, Provident Fund Management and Payroll Generation have been introduced under ATOMS. These packages have resulted in considerable reduction in the workload of staff in Accounts Department and minimized the processing errors. The facilities provided in the online system for PF management and payroll generation are explained below.

Provident Fund (PF) Management: Presently two types of PF accounts are managed , i.e., Contributory Provident Fund (CPF) and General Provident Fund (GPF). Employees are allowed to increase or decrease the monthly PF subscription and also they can avail advance or withdrawal from PF. Annual interest is calculated and credited to the PF account at the end of financial year. These services now have been included under ATOMS, where employees can request for change in monthly subscription, apply advance or withdrawal online. The modules have been developed to calculate the PF annual interest and final settlement. The online PF management module has the following features:

- Paper-less application and processing of subscription change, advance or withdrawal request
- Facility to view PF account details online
- Quick processing of advance or withdrawal request

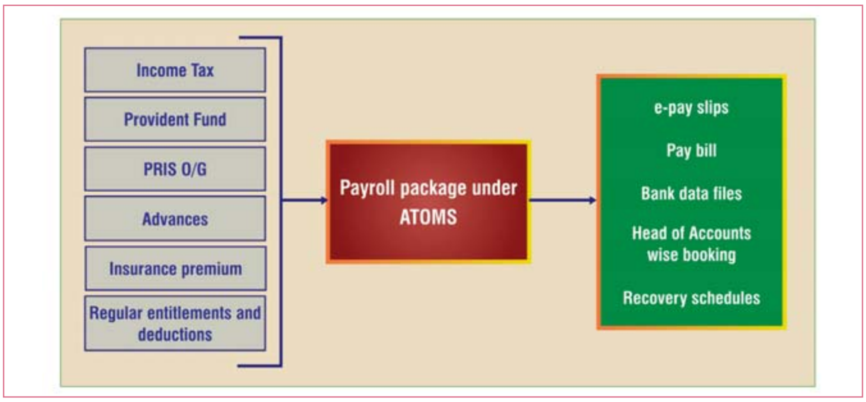

Fig. 1 *Payroll modules under ATOMS*

- Email notification to employees after processing of advance or withdrawal
- Calculation and posting of interest on the last day of financial year
- Automatic transfer of advance data to payroll for recovery of installments

The e-service ensures quick processing and communication thereby avoiding the necessity of the employee to physically go to the Accounts Department to complete the process.

Payroll Generation: Calculation of pay and allowances has been one of the major activities of Accounts. It includes calculation of entitlements and deductions pertaining to each employee on the rolls of organisation. The entitlements and deductions for each employee are different and there are almost about one hundred different categories in each case. To automate these activities and for generation of payroll, a module has been developed and integrated with ATOMS and operationalized. The payroll package under ATOMS encapsulates the following processes:

- Management of pay, entitlements and deductions pertaining to all the employees
- Management of all entitled advances
- Management of premium payments for insurance policies pertaining to LIC and PLI
- Provision to incorporate external recoveries like license fee, electricity charges, damage charges and garage fee from GSO and subscription of thrift and co-operative societies
- Calculation of income tax including the paid as well as projected income for the financial year
- Generation of bank data files and pay bill registers, head of accounts wise booking etc.

Following are the salient features of the payroll package.

- Integration with Administration for employee and pay fixation data
- Providing e-pay slips to the employees
- Providing online calculation sheets for income tax, PRIS-O and PRIS-G

As the business rules are built in the system, the processing becomes person independent

Fig. 2 *PF Management modules under ATOMS*

VI.26 Access to Information Resources: Recent Enhancements

With the increase in the demand for information by the users, the need for better system and efficient retrieval to users is becoming of paramountimportance. All efforts are being made to enhance the methods of accssing the information resources.

Fast Breeder Reactor Portal

A knowledge resource management initiative portal named as 'Bodhi' (Figure1) is put in place with continuous enhancements. This is a centralized repository of knowledge documents. As part of the enhancement, Fast Breeder Reactor(FBR) Portal has been developed, which is the gateway to information pertaining to Fast Breeder Reactors.

A separate research specific resource collections were developed for FBR, FBR Fuels, and Reprocessing etc. These provide a single window access to reports, journal articles, book holdings, IGC publications and internet resources on the topic of relevance(Figure 2). In addition,news clips on nuclear technology are also being made available with regular updates. More photo images from color negative and digital format are put into these systems with necessary metadata. Translated Reports, IGC Journal / conference articles are regularly updated and accessible to the users.

Gatewayof nuclear holdings

All th e holdings relating to nuclearscienceand engineering are organized and made available under nuclear holdings gateway (Figure 3). About 5000 books on the topics relating to nuclear science and engineering have been organized based on the Dublin Core metadata.

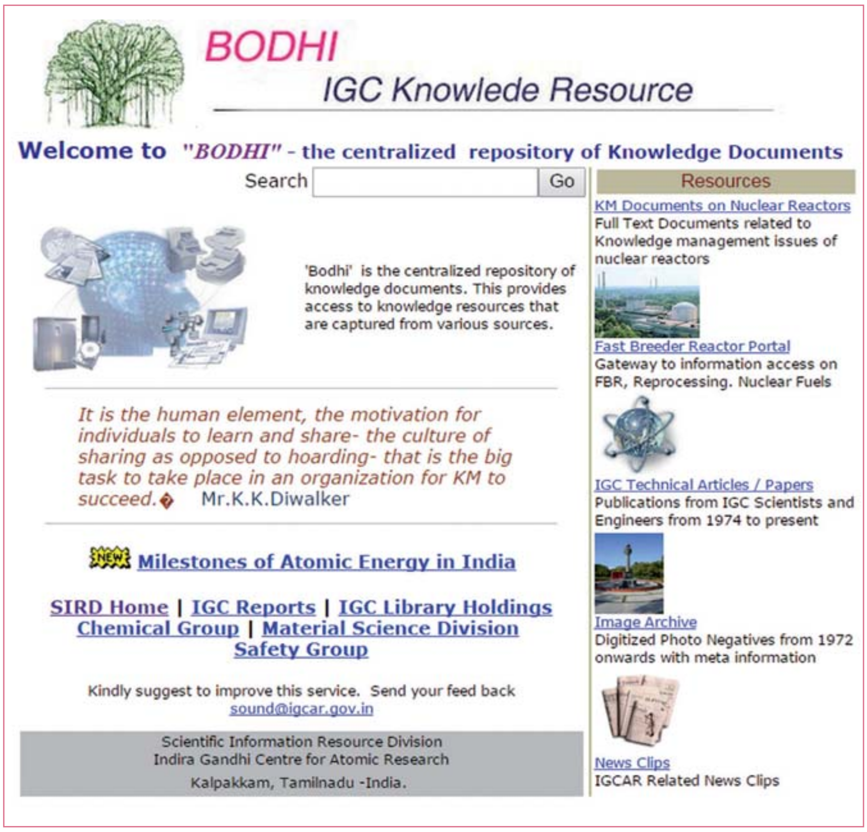

BODHI

IGC Knowlede Resource

Welcome to "BODHI" - the centralized repository of Knowledge Documents

Search ☐ Go

'Bodhi' is the centralized repository of knowledge documents. This provides access to knowledge resources that are captured from various sources.

It is the human element, the motivation for individuals to learn and share- the culture of sharing as opposed to hoarding- that is the big task to take place in an organization for KM to succeed.◆ Mr.K.K.Diwalker

NEW Milestones of Atomic Energy in India

SIRD Home | IGC Reports | IGC Library Holdings
Chemical Group | Material Science Division
Safety Group

Kindly suggest to improve this service. Send your feed back
sound@igcar.gov.in

Scientific Information Resource Division
Indira Gandhi Centre for Atomic Research
Kalpakkam, Tamilnadu -India.

Resources

KM Documents on Nuclear Reactors
Full Text Documents related to Knowledge management issues of nuclear reactors

Fast Breeder Reactor Portal
Gateway to information access on FBR, Reprocessing. Nuclear Fuels

IGC Technical Articles / Papers
Publications from IGC Scientists and Engineers from 1974 to present

Image Archive
Digitized Photo Negatives from 1972 onwards with meta information

News Clips
IGCAR Related News Clips

Fig. 1 *IGC knowledge resource portal (Bodhi)*

For all of these collections,online link to the Table of Content (TOC) were also provided, enabling the users to get more information about the contents of the book being accessed.

Using a web interface, the Table of Contents (TOC) of Journals being subscribed by IGCAR are also made available to the uses. The list of journals being displayed on a weekly bases are being enriched by the links to TOCs with a suitable search interface. TOCs are being

Fast Breeder Reactor Gateway

Where you can get all information on FBR

Home Feedback

FBR Core Fuel loading

Reports
1 FBR Reports
2 IAEA Tecdocs on FBR

Conference Proceedings

1 FBR Conference Proceedings
2 SMIRT
3 ICONE

Books on FBR

IGC Publications on FBR

Articles on FBR

External Links on FBR

Fig. 2 *Fast Breeder Reactor portal*

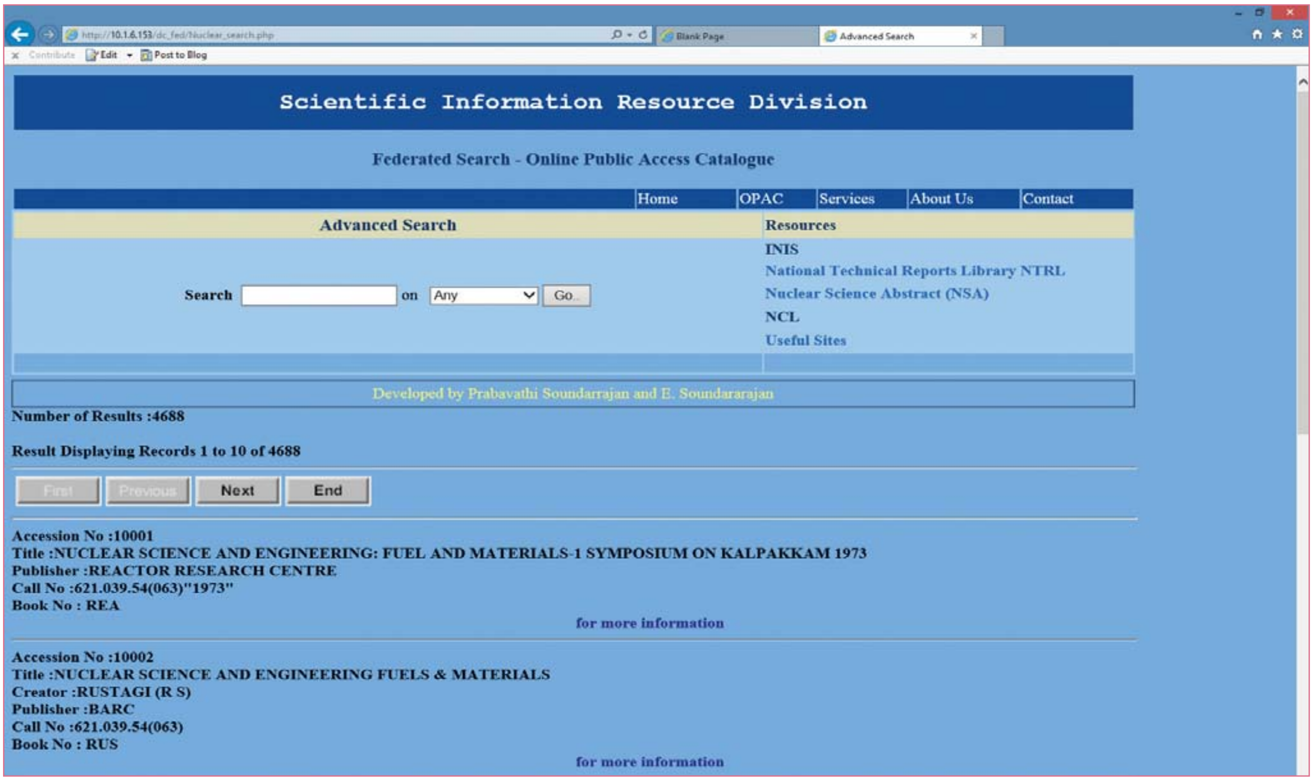

Scientific Information Resource Division

Federated Search - Online Public Access Catalogue

Developed by Prabavathi Soundarrajan and E. Soundararajan

Number of Results :4688

Result Displaying Records 1 to 10 of 4688

Accession No :10001
Title :NUCLEAR SCIENCE AND ENGINEERING: FUEL AND MATERIALS-1 SYMPOSIUM ON KALPAKKAM 1973
Publisher :REACTOR RESEARCH CENTRE
Call No :621.039.54(063)"1973"
Book No : REA

Accession No :10002
Title :NUCLEAR SCIENCE AND ENGINEERING FUELS & MATERIALS
Creator :RUSTAGI (R S)
Publisher :BARC
Call No :621.039.54(063)
Book No : RUS

Fig. 3 *Nuclear holdings gateway*

obtained from several sources such as Internet, digitizing hardcopy, etc.

Information systems on IGC Intranet

Access to the scientific and technical bibliographic and full text resources is being provided across the IGC Intranet on a 24x7 basis, using the 3-tier based high performance server and storage digital infrastructure. Necessary value additions, administration, maintenance, upgrading and updates are being done to the various bibliographic and full text resources such as Library GATEWAY, INIS, Standards, IGC Research Contribution database, Web-OPAC and other e-resources for their continued desktop access over the IGC Network. During this year, a portal for E-books subscribed at SIRD (Figure 4), online user feedback system and MARC-XML to RDBMS tool were developed.

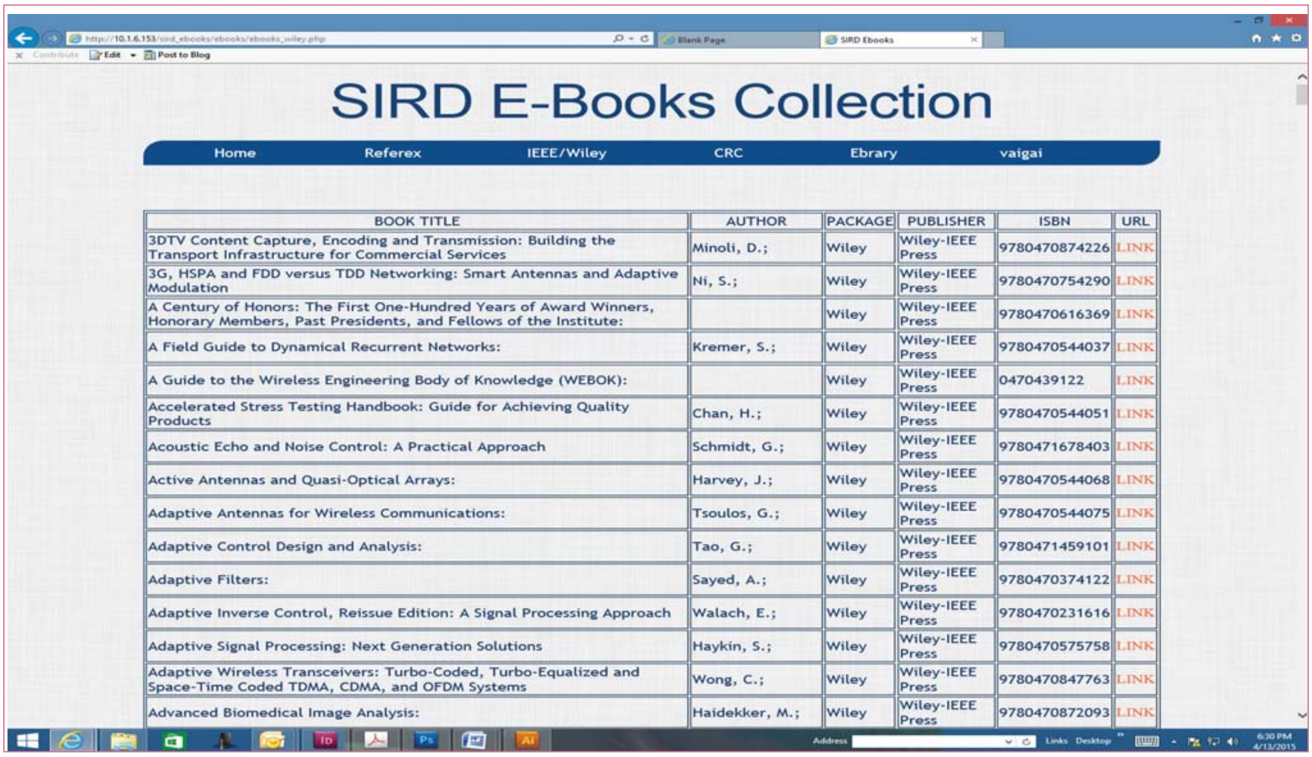

SIRD E-Books Collection

BOOK TITLE	AUTHOR	PACKAGE	PUBLISHER	ISBN	URL
3DTV Content Capture, Encoding and Transmission: Building the Transport Infrastructure for Commercial Services	Minoli, D.;	Wiley	Wiley-IEEE Press	9780470874226	LINK
3G, HSPA and FDD versus TDD Networking: Smart Antennas and Adaptive Modulation	Ni, S.;	Wiley	Wiley-IEEE Press	9780470754290	LINK
A Century of Honors: The First One-Hundred Years of Award Winners, Honorary Members, Past Presidents, and Fellows of the Institute:		Wiley	Wiley-IEEE Press	9780470616369	LINK
A Field Guide to Dynamical Recurrent Networks:	Kremer, S.;	Wiley	Wiley-IEEE Press	9780470544037	LINK
A Guide to the Wireless Engineering Body of Knowledge (WEBOK):		Wiley	Wiley-IEEE Press	0470439122	LINK
Accelerated Stress Testing Handbook: Guide for Achieving Quality Products	Chan, H.;	Wiley	Wiley-IEEE Press	9780470544051	LINK
Acoustic Echo and Noise Control: A Practical Approach	Schmidt, G.;	Wiley	Wiley-IEEE Press	9780471678403	LINK
Active Antennas and Quasi-Optical Arrays:	Harvey, J.;	Wiley	Wiley-IEEE Press	9780470544068	LINK
Adaptive Antennas for Wireless Communications:	Tsoulos, G.;	Wiley	Wiley-IEEE Press	9780470544075	LINK
Adaptive Control Design and Analysis:	Tao, G.;	Wiley	Wiley-IEEE Press	9780471459101	LINK
Adaptive Filters:	Sayed, A.;	Wiley	Wiley-IEEE Press	9780470374122	LINK
Adaptive Inverse Control, Reissue Edition: A Signal Processing Approach	Walach, E.;	Wiley	Wiley-IEEE Press	9780470231616	LINK
Adaptive Signal Processing: Next Generation Solutions	Haykin, S.;	Wiley	Wiley-IEEE Press	9780470575758	LINK
Adaptive Wireless Transceivers: Turbo-Coded, Turbo-Equalized and Space-Time Coded TDMA, CDMA, and OFDM Systems	Wong, C.;	Wiley	Wiley-IEEE Press	9780470847763	LINK
Advanced Biomedical Image Analysis:	Haidekker, M.;	Wiley	Wiley-IEEE Press	9780470872093	LINK

Fig. 4 *E-Books portal at SIRD*

VI.27 Public Awareness Programmes Organized as part of Diamond Jubilee Celebrations of the Department of Atomic Energy at Kalpakkam

Fig. 1 *Colleagues demonstrating the exhibits to students and public during Bharat Nirman Public Information campaign at Puducherry*

The Department of Atomic Energy was established in the year 1954 under the direct charge of the Prime Minister through a Presidential Order. In order to commemorate the sixty years of commendable achievement of the Department, a series of public awareness programmes are conducted across various Units of DAE. As a part of this awareness programme, exhibitions, lecture-cum-demonstration and visits to our Centre are organized targeting students, teachers, professionals and public for dispelling fears and concerns about our organization.

Exhibitions to bring awareness about the Departmental activities

IGCAR is organizing several exhibitions across Tamil Nadu. These exhibitions serve its purpose of demonstrating the benefits of various programmes of our Department and its importance in the day-to-day activities. The exhibition has stalls highlighting the activities of IGCAR and other DAE Units at Kalpakkam. Special posters, exhibits and working models are displayed and demonstrated for educating the public and to make them understand the myths and realities of Nuclear Energy (Figure 1 and Table 1).

Special brochures on the activities of IGCAR, FBTR and other DAE Units at Kalpakkam has been brought out. Some of the brochures are translated to Hindi and Tamil for distribution during various exhibitions.

A calendar has also been brought out by INS Kalpakkam chapter which outlines the beneficial applications of ionising radiations, highlights the developmental works undertaken by DAE and BARC and provides a glimpse of the activities of various constituent units of DAE with career prospects in DAE.

Lecture-cum-Demonstration on handling Radioactivity

Students from secondary and senior secondary (Classes IX and XI) from the KV and AECS schools in the township were given a lecture-cum-demonstration on the activities of DAE and on handling radioactivity. The students were shown around the facilities at IGCAR in December 2014 by a team of members from IANCAS. Kalpakkam chapter of IANCAS is also organizing a number of programmes on this theme at various colleges and schools across the state.

Visit to IGCAR

Visits to facilities at IGCAR for students from various colleges and educational institutions are organized every week. Around 1000 visitors comprising students, faculties and public, visited IGCAR during the last five months. About 100 teachers participating in the in-service programme at AECS were shown various facilities in IGCAR (Table 2).

Table 1: List of exhibitions organised

S. No.	Date	Program	Description
1	September 27- 29, 2014	Bharat Nirman Public Information campaign (PIC) conceptualized by Press Information Bureau	Three days exhibition organized at Tiruvallur town
2	November 17-19, 2014	Bharat Nirman Public Information campaign (PIC) conceptualized by Press Information Bureau	Three days exhibition organized at Puducherry

Table 2: List of visits organised for college students

S. No.	Name of Institution	Date of Visit
1	Department of Nuclear Engineering SRM University, Kattankulathur	20/08/2014
2	Department of Electronic and Communication Engineering, Anna University, Chennai	12/09/2014
3	Smt. Kandukuri Rajalakshmi college for Women, Rajamundri, Andhra Pradesh	07/11/2014
4	Ramakrishna Mission Vivekananda College, Chennai	28/11/2014
5	SRM University	29/12/2014 & 30/12/2014

CHAPTER VII

Awards/ Publication/ News & Events

Awards & Honours

Dr. R. Natarajan, RpG has been conferred with VASVIK Award for the year 2014 for his outstanding contributions in the field of Chemical Sciences & Technology

Dr. K. Nagarajan, CG has been awarded the MRSI Medal for his significant contributions to Materials Science and Engineering by Materials Research Society of India during the annual general body meeting held at Bengaluru during February 12-14, 2014

Dr. S. Venugopal, MMG has been elected as a Fellow of the Academy of Sciences, Chennai

Shri A. Ravishankar, RpG has been elected, Fellow of the Indian National Academy of Engineering

Dr. U. Kamachi Mudali, MMG has been

- elected as Academician (Fellow) of The Asia-Pacific Academy of Materials (APAM)
- conferred with VASVIK Award for the year 2014 for his outstanding contributions in the field of Material & Metallurgical Science & Technology
- awarded the G.D. BIRLA GOLD MEDAL for the year 2014 for his outstanding Research work in the field of Materials Science and Technologies from Indian Institute of Metals, Kolkata

Shri G.V. Prasad Reddy, MMG has been

- received the INAE Young Engineer Award for the year 2013 from the Indian National Academy of Engineering
- awarded the Sudharshan Bhat Memorial Prize for the best Ph.D thesis in Metallurgical and Materials Engineering for the year 2014 from the Department of Metallurgical and Materials Engineering, IIT Madras, Chennai

Ms. Diptimayee Samantaray, MMG has received the Young Metallurgist Award for the year 2014 from the Ministry of steels, Government of India on National Metallurgist Day, for her outstanding contribution in the field of flow behaviour and microstructural evolution of nuclear grade steels

Dr. N. R. Sanjay Kumar, MSG has won the Best Thesis award for the year 2014 for his thesis titled "High Pressure High Temperature Synthesis and Study of novel transition metal carbides" by Indian Physics Association

DAE Awards

Department of Atomic Energy has instituted annual awards for excellence in Science, Engineering and Technology in order to identify best performers in the area of Research, Technology Development and Engineering in the constituent units (other than Public Sector Undertakings and Aided Institutions). The Young Applied Scientist, Young Engineer, Young Technologist, Homi Bhabha Science and Technology Award and Scientific and Technical Excellence Award fall under this category. Group Achievement awards for recognition of major achievements by groups have also been instituted. Life-time Achievement Award is awarded to one who has made a significant impact on the DAE's programmes. They are the icons for young scientists and engineers to emulate. The awards consist of a memento, citation and cash prize.

The recipients of the Awards from IGCAR for the year 2013 are:

Homi Bhabha Science and Technology Award : Dr. B. Purna Chandra Rao, MMG

Scientific and Technical Excellence Award : Shri R. Suresh Kumar, RDG
Dr. N. Subramanian, MSG

Young Applied Scientist/Technologist Award : Shri Sanatana Maharana, RpG
Shri P. Varadharajan, RpG
Shri S.C.S.P. Kumar Krovvidi, FRTG

Young Engineer Award : Ms. Saritha P. Menon, EIRSG
Shri Nimala Sundaram, RDG
Shri Y. V. Nagaraja Bhat, FRTG
Shri Gagan Gupta, RDG

Meritorious Technical Support Award : Shri A. Ananthakumar, CG
Shri K. Arumugam, FRTG
Shri S. Sundaramurthy, RpG
Shri C. Ambujakshan Nair, FRTG
Shri K. Subramanian, ROMG

Meritorious Service Award : Shri R. Ranganathan, Administration
Shri R. Sriram, Accounts

Group Achievement Awards:

Collaborative Research Coordination Under BRNS and Outreach Activities for Human Resource Development

Dr. D.M. Gaitonde, BARC, Group Leader

Dr. M. Sai Baba and Dr. Vidya Sundararajan from RMG and Shri G.Padmakumar from FRTG

The award was shared by colleagues from BARC, IGCAR, NFC, VECC and DAE

Design, Confirmation of Primary Sodium Pump by Analysis Testing and Evaluation

Shri V. Balasubramaniyan, Group Leader

Shri K.V. Sreedharan, Shri S. Athmalingam, Shri Bhagwana Ram Manda, Shri P. Chandrasekaran, Shri S. Chandrasekar, Shri S. Satheesh Kumar, Shri K. Madhusoodhanan, Shri S.L.N. Swamy, Shri M. Sakthivel, Shri Govind Kumar Mishra, Ms. R. Varuna, Dr. K. Velusamy, Shri S. Jalaldeen, Shri K. Natesan, Shri R. Suresh Kumar, Shri Bhuwan Chandra Sati, Shri P. Jayaraj, Shri R. Arulbaskar, Shri Ram Kumar Maity, Shri Juby Abraham, Shri Kulbir Singh and Ms. E. Bagyalakshmi from RDG, Shri V. Prakash, Shri B. K. Sreedhar, Shri Ranga Ramakrishna, Shri P. Anup Kumar, Shri P. Ravi, Shri J. Jaikanth, Shri K. Tamil Selvan, Shri P. Adithan, Shri N. S. Shivakumar, Shri S. Sureshkumar, Shri S. Balakrishnan, Shri A. Gururajan, Shri S. Rajkamal Singh and Shri K. H. Anub from FRTG

Development of In-sodium Sensors for PFBR

Shri B. Babu, Group Leader

Shri B. K. Nashine, Shri C. Asokane, Shri S. Chandramouli, Shri S.K.Dash, Shri G. Vijayakumar, Shri R. Rajendraprasad, Ms. P. Anitha, Ms. M. Mohana, Shri Chandra Sekhar Singh, Shri M. R. Jeyan, Shri M. Kathiravan, Shri V. Gunasekaran, Shri A. Selvakumaran, Shri K.A. Bijoy, Shri A. Ashokkumar, Shri D.K. Saxena, Shri P. Bhavanirajan, Shri Prashant Sharma, Shri Vijay Sharma, Shri Krishnakumar, Shri Gautam Anand, Shri R. Punniyamoorthy, Shri D.Muralidhar, Shri S. Ravishankar, Shri S. Alexander Xavier, Shri Parmanand Kumar, Shri N. Venkatesan, Shri A. Thirunavukkarasu, Shri C. Rajappan, Shri P.C.V. Murugan, Shri R. Shanmugam, Shri C. Adikesavan, Shri M. T. Janakiraman, Shri N. Sreenivas, Shri L. Eagambaram, Shri P.R. Ashokkumar, Shri K. Arumugam, Shri R. Iyappan, Shri N. Mohan, Shri R. Parandaman, Shri S. Kannan, Shri M. Karthikeyan, Shri K. Ramesh, Shri Shaik Rafee, Shri J. Prabhakaran, Shri V. Kumaraswamy, Shri K. Ganesh, Shri Ashish Tiwari, Shri L. Mohanasundaram, Shri L. Muthu, Shri Pothi, Shri P. Lakshmayya, Ms. M. Chandra, Shri B. Veeraraghavan, Shri M.Arjunan, Shri Sudheer Patri, Shri S. Sureshkumar, Shri Tribhuwan Ram, Shri Muhammad Sabih, Ms. S. Narmadha, Shri N. Ravichandran, Shri A. Gururajan, Shri Hadibandhu Singh, Shri C.N. Sridhar, Shri K. Balaji, Shri S. Balakrishnan, Ms. J.I. Sylvia, Shri P. Vijaya Mohana Rao, Shri V.S.Krishnaraj, Shri M. Anbuchelian, Ms. S.Divya, Ms. S. Nagajothi, Shri G. Anandan, Shri P. Bakthavatchalam, Shri C. Ambujakshan Nair, Shri A.Kulanthai, Shri R. Gunasekaran, Shri V. Krishnamoorthy, Shri S.C.S.P. Kumar Krovvidi, Shri J. Jaikanth, Shri T. V. Maran, Shri K. Mohanraj, Shri P. Madankumar, Shri Rakesh Kumar Mourya, Shri Shiv Prakash Ruhela, Shri C. Meikandamurthy, Shri Vijay Tirkey, Shri R. Ramalingam and Shri A. Kolanjiappan from FRTG, Dr. C. Babu Rao, Ms. S. Sosamma, Shri K.A. Gopal, Ms. Romali Biswal and Shri Rajesh Saxena from MMG, Shri M. Krishnamoorthy, Shri K.M. Natarajan, Shri A. Padmanabhan, Shri B. Thiruvengadam, Shri C. Arumugam, Shri G. Ramadoss, Shri J. Abilash and Shri B. Palani from ESG, Shri S.L.N. Swamy, Shri M. Shakthivel, Shri Govind Kumar Mishra, Ms. R. Varuna, Shri B. Madhavan and Ms. R. Vijayashree from RDG, Shri Saju T. Abraham, Shri C. Muniyandi, Shri K. Krishna Chaitanya, Shri P. Narayana Rao, Shri D. Henson Raj and Shri M. V. Kuppusamy from EIRSG

Development, Production and Supply of Enriched Boron Carbide (B_4C) Pellets for PFBR Project as control and Diverse Safety Rods (CSR and DSR)

Dr. S. Anthonysamy, CG and Dr. R.C. Hubli, MG, BARC, Group Leaders

Shri A. Veerapandian, Shri I. Kaliappan, Shri R. Ranganathan, Ms. B. Suhasini, Dr. K. Ananthasivan, Shri G. Rajendra Prasad, Shri R. Krishna Prabhu, Dr. Ashish Jain, Shri M. Stanislas, Shri J.K. Sekar, Shri T. Ramamoorthy, Shri V. Paramasivam, Shri E. Gajendran, Ms. K. Usha Lakshmi, Ms. Umamaheswari Rajendraprasad, Shri V. Suresh Kumar, Shri Y. Ravi, Shri D. Seenivasan, Shri V. Venkatachalam and Ms. Preeti Saroop from CG. Shri G. Mohankrishnan, Dr. C. Anand Babu, Shri D. Sujish, Shri S. Vikraman, Shri S. Suresh, Shri R. Nagaraj, Shri Joby Joseph, Shri V. Nandakumar, Shri R. Kannan, Shri R. R. Sridharan, Shri M. R. Marikumaran, Shri E. Radha, Shri S. Anbarasan and Shri D. Alagar from FRTG, Dr. B. K. Sharma from ROMG, Ms. T. Sridevi and Shri M. Vincent from EIRSG.

The award was also shared by colleagues from BARC, HWB and NFC

Fabrication of Sphere-PAC and Preference Test Fuel Pins and Irradiation in FBTR

Dr. K. Nagarajan, CG, Group Leader

Shri G. Ravisankar, Dr. K. Ananthasivan, Dr. R. Venkata Krishan, Shri Dasarath Maji, Dr. R. Babu, Shri Abhiram Senapati, Shri Gude Jogeswararao, Shri B. Kothandaraman, Shri N. Vinod Kumar, Shri Y. Yuvaraj, Shri D. Kothandan, Shri T.V. Prabhu, Shri R.Padmanabhan, Shri A. Anantha Kumar, Shri R. Lavakumar, Shri Abhishek Kumar Yadav, Shri G. Nantha Kumar, Shri M. Masanam, Shri G. Parthiban, Shri R. Rajaram, Shri K.A. Samuel Kutty, Shri N. Eswaran, Shri P. Arunagiri, Shri V. Dilli Babu, Shri A. Praveen, Shri G. Lakshmanan, Shri R. Kumaran, Shri T. Ramamurthy, Shri E. Nagappan, Shri E. Mohanraj, Shri B. Vijayavelu, Shri Kathiravan, Shri B. Radhakrishnan, Shri M. Saravanan, Shri R. Parthasarathy, Ms. Sai Subbulakshmi, Shri G. Rajendra Prasad, Shri Y. Ravi, Ms. B. Suhasini, Shri J. Prabhakar Rao, Shri Ajay Kumar Keshari, Shri G. Gunasekaran, Shri K. Vijayakumar, Shri D. Vijyakumar, Shri Mohammad Sithick, Shri T. Ravi, Ms. R. Akila, Ms. N. Chitra, Shri Brahmaji Rao and Shri N. Ravi from CG, Shri P. Narayana Rao, Shri Krishna Chaitanya, Shri C. Muniyandi, Shri D. Henson Raj and Shri G. Vijayaraghavan from EIRSG, Shri S.A. Natarajan, Shri P. Karuppasamy, Shri P. Balakrishnan, Shri E. Venkatesh, Shri S. Manimaran, Shri P. Loganathan, Shri K. Narayanan, Shri C. Muthusamy, Shri M. Damodaran from ESG, Shri S. Clement Ravi Chandar, Shri M. Asok Kumar and Shri T. Rajkumar from RDG, Dr. S. Murugan, Shri K.A. Gopal, Shri M. Muthu Ganesh, Shri Rajesh Saxena, Shri R. Ramesh, Shri K. Purushothaman, Dr. Divakar Ramachandran, Shri C.N. Venkiteswaran, Shri A. Vijayaraghavan, Shri V. Anandaraj, Ms. M. Padalakshmi, Shri S. Vinod Kumar and Ms. S. Gomathi from MMG, Shri S.Varatharajan, Shri S. Kanagaraju, Shri K. Kamaludeen, Shri G.N. Chandrasekaran, Shri V. Gunasekaran and Ms. Gowri Lakshmanan from ROMG, Shri N. P. Seshadreesan from FRFCF.

The award was also shared by colleagues from BARC

IGCAR Publications during the Year 2014

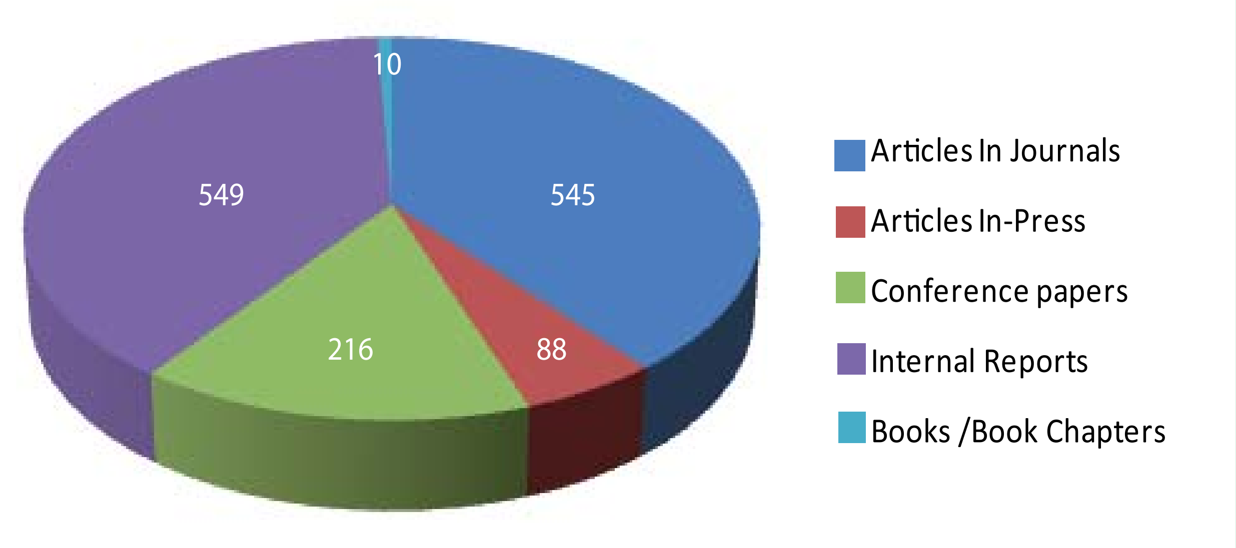

Special Lectures and Colloquia Series

1. "Status of Uranium Resources in the Country" IGC Colloquium by Shri P.S. Parihar, Director, AMD, January 17, 2014
2. "Crystallography, Materials Science and Biology" International Year of Crystallography Lecture series by Dr. R. Chidambaram, Principal Scientific Advisor, Government of India, January 28, 2014
3. "Increasing importance of Chemistry in the Present World" Bhatnagar Memorial Lecture by Prof. K.J. Rao, IISc, Bengaluru, February 12, 2014
4. "Wealth Generation Through University-Industry Partnership" IGC Colloquium by Prof. J.B. Joshi, March 11, 2014
5. "Bio-materials, Bio-device and Story of TTK-Chitra Heart Valve" IGC Colloquium by Prof. M.S. Valiathan, National Research Professor, Government of India, Manipal University, March 21, 2014
6. "A GPS based Tele Disaster Alarm Device" Invited Talk by Shri P. Sudhakar, CMD, ECIL, May 12, 2014
7. "Exploring Nuclear Physics with Lasers" Seaborg Memorial Lecture by Dr. B. Jagatap, Director, Chemistry Group, BARC, Mumbai, June 11, 2014
8. "On Reinventing India as an Innovation Nation" 9th Vikram Sarabhai Memorial Lecture by Dr. R. A. Mashelkar, National Research Professor, August 12, 2014
9. "Innovations in Chemical Industry" Acharya P.C. Ray Memorial Lecture by Prof. M.M. Sharma, Institute of Chemical Technology, Mumbai, August 22, 2014
10. "Art, Craft & Philosophy of Science" IGC Colloquium by Prof. K.R. Rajagopal, Distinguished Professor, Regents Professor, Forsyth Chair in Mechanical Engineering, Senior Research Scientist, Texas Transportation Institute, August 26, 2014

11. "Evolution and Ethos of DAE" First Diamond Jubilee Colloquium by Dr. M.R. Srinivasan, Member, AEC, September 4, 2014
12. "Palliative Care and Assisting Terminally ill Patients" Special Lecture by Shri Satish Kaushik, Rajbala Foundation (A national level health care NGO), September 26, 2014
13. "Innovative Renewable Energy Technologies" INS Colloquium by Dr. Anumakonda Jagadeesh, Director Nayudamma Centre for Development Alternatives, Nellore, October 7, 2014
14. "Nuclear Fuel Fabrication its Challenges & Technological Spin-offs" Know your DAE Lecture series by Shri N. Saibaba, Chief Executive, NFC, Hyderabad, October 10, 2014
15. "100 Years of Diffraction" International Year of Crystallography Lecture series by Prof. Gautam R. Desiraju, IISc, Bangaluru, October 13, 2014
16. "Combating Corruption - Technology as an Enabler" Vigilance Awareness Week Lecture by Shri V. Viswanathan, Company Secretary, BHAVINI, October 27, 2014
17. "Technological and Management Challenges in Technology launch Mega project PFBR" Know your DAE Lecture series by Dr. Prabhat Kumar, CMD, BHAVINI, October 31, 2014
18. "Quasicrystals: The golden Road to Stockholm" International Year of Crystallography Lecture series by Prof. R. Ranganathan, IISc, Bangaluru, November 12, 2014
19. "Destination 120" Madam Curie Memorial Lecture by Prof. Moumita Maiti, Dept. of Physics, IIT Roorkee, December 2, 2014
20. "Electronic Warfare- Role in Information Age" Invited Talk by Ms. J. Manjula, Director DARE, December 19, 2014
21. "Indian Nuclear Power Programme Stage 1 Experiences" Know your DAE Lecture series by Shri G. Nageswara Rao, Director(O), NPCIL, December 26, 2014

Seminars, Workshops and Meetings

1. "International Conference on Structural Integrity (ICONS-2014)" during February 4-7, 2014
2. "Second IGCAR-KAERI Workshop on Sodium Cooled Fast Reactors" during February 18-19, 2014
3. IAEA Technical Meeting on "Development of Advanced Fuels for Fast Reactors" during March 03-06, 2014
4. Seminar on Chemical Engineering in Nuclear Technology (CHEMENT-2014) with theme of "Recent Advances in Fuel Cycle Technologies" during March 06-07, 2014
5. Seminar on "Solid & Liquid Resource Management", June 27, 2014
6. "Electrochemistry & Corrosion Camp 2014 - (ECC 2014)", November 29, 2014
7. "Course on Nuclear Chemical Engineering and Present - day Technologies (CONCEPT-2014)" Workshop for Chemical Engineering Students during December 1-12, 2014
8. "Successful Completion of 20 years of LCTR Operation", December 18, 2014

Nurturing Activities

1. “National Science Day Celebration”, February 28, 2014
2. “National Safety Day Celebration”, March 4, 2014
3. “International Women’s Day Celebration”, March 13 & 30, 2014
4. “Managing Stress at Work Place” National Safety Day Lecture by Dr. Chokkalingam, Professor & Director, Dr. MGR Medical University, Chennai, March 21, 2014
5. “Technology Day Meet 2014”, May 9, 2014
6. “STIPAC Inaugural Function” May 26, 2014 and Valedictory function, July 4, 2014
7. “Meeting of Mentors Committee for Young Officers”, June 23 & July 2, 2014
8. “BITS Pilani Valedictory Function”, July 16, 2014
9. Graduation Function of the OCES 2013, 8th Batch of BARC Training School at IGCAR, July 24, 2014
10. “Quality Circle Annual Meet (QCAM 2014)”, August 25, 2014
11. “Chemistry Outreach Program for the Tamil Medium Schools around Kalpakkam”, September 6, 2014
12. Prof. Brahm Prakash Memorial Materials Quiz 2014 during September 19-20, 2014
13. Interactive Session with Research Scholars by Dr. R.B. Grover, Director, HBNI, November 3, 2014
14. “Physics Popularization Programme for Govt. School Students: A program of DAE@60”, November 22, 2014
15. “All India Science Quiz Competition” during November 25-26, 2014
16. “Yoga for Stress and Diabetes” IGC Colloquium by Dr. H.R. Nagendra, Chancellor, S-VYASA University, Bengaluru, December 17, 2014

Administrative Seminars/Meetings

1. Administrative Colloquia, February 5 & 19, March 21 & 25, April 22, July 24, August 11, 27 & 28 and October 29, 2014.
2. “Hindi Technical Talk”, March 12, 2014
3. “Hindi Workshop”, March 28, June 26, September 15 & December 5, 2014
4. ATI/DAE Intensive Workshop on “Noting and Drafting” during September 8-12, 2014
5. ATI/DAE Programme on “Tamil Essentials”during September 15-19, 2014
6. “Hindi Week - 2014” Celebration during September 22-26, 2014
7. ATI/DAE Workshop on “Reservation in Service” during December 8-10, 2014
8. “Filling of Asset & Liability Return under ATOMS” Interactive Session with IGCAR Employees, December 12, 2014

Conference and Meeting Highlights

First International Conference on Structural Integrity (ICONS-2014)

February 4-7, 2014

Dr. T. Jayakumar, Director, MMG, Dr. P. R. Vasudeva Rao, Director, IGCAR, Shri S.S. Bajaj, Chairman, AERB, Dr. K. Tamilmani, Chief Executive, Center for Military Airworthiness & Certification and Dr. B.P.C. Rao seated on the dais during the inaugural function

The First International Conference on Structural Integrity (ICONS-2014) was successfully organised at Convention Center, Anupuram during February 4-7, 2014. The main objective of ICONS-2014 was to provide a forum for engineers, scientists, academicians, industry experts, plant managers and regulatory personnel to discuss the recent advances and future directions in structural integrity, encompassing design, material selection, stress analysis, manufacturing, materials evaluation, welding, quality assurance, microstructure characterization, corrosion, non-destructive evaluation (NDE), damage mechanics, failure analysis, life extension and related aspects that ensure safe and reliable operation of components in nuclear, defense, aircraft and other industries.

During the inaugural function held on 4th February, Dr. P.R. Vasudeva Rao, Director, IGCAR extended a warm welcome to all the speakers and delegates from abroad and India. He highlighted the need to have a conference series of this kind to bring researchers together to discuss the advances in structural integrity of engineering components and structures. Dr. T. Jayakumar, Chairman, ICONS-2014 gave details about the conference. He stated that more than two hundred and seventy research papers were being presented in fifty four technical sessions and there were sixty two plenary (invited) talks by eminent international experts from thirteen countries including Austria, Australia, Czech Republic, Germany, Hungary, Italy, Japan, Portugal, South Korea, UK and USA. He pointed out that ICONS-2014 had attracted delegates from R&D, academic institutes and industries.

Shri S.S. Bajaj, Chairman, Atomic Energy Regulatory Board (AERB) inaugurated the conference. During the inaugural address, he highlighted the important role of structural integrity in ensuring safe and reliable operation of Pressurized Heavy Water Reactors (PHWRs) as well as Kudankulam Nuclear Power Plant and the significant role played by the regulatory systems. He released the Souvenir of ICONS-2014 and gave the first copy to Dr. K. Tamilmani, Chief Executive, Center for Military Airworthiness & Certification (CEMILAC), Defence Research & Development Organisation (DRDO). Dr. Tamilmani delivered the presidential address and emphasized the importance of materials selection and imparting stringent quality assurance during manufacturing and assembly stages, on the structural integrity, especially in airborne military platforms. He released the CD proceedings of ICONS-2014 consisting of 185 full text of papers presented at the conference. Dr. B.P.C. Rao, Convener, ICONS 2014 proposed a vote of thanks.

Three hundred fifty delegates attended ICONS-2014 and four sessions were conducted in parallel. The closing session of ICONS-2014 was chaired by Dr. T. Jayakumar on February 7, 2014. Dr. David Smith, UK, Dr. Ward Rummel, USA, Dr. Raman Singh, Australia, Dr. G. Raghava, SERC, Chennai, India and Cmdr. Mohamed Salih, Indian Navy, New Delhi spoke and gave feedback. They appreciated the arrangements and congratulated the organisers for successfully conducting the conference and expressed their desire to take part in future conferences. It was decided that the 2nd International Conference on Structural Integrity would be conducted during February 2017.

Second IGCAR-KAERI Workshop on Sodium Cooled Fast Reactors

February 18-19, 2014

Dr. P. R. Vasudeva Rao, Director, IGCAR with delegates of IGCAR-KAERI Workshop

The second IGCAR-KAERI Workshop on sodium cooled fast reactors was held during February 18-19, 2014 at IGCAR, Kalpakkam. KAERI delegation comprising of nine engineers, led by Dr. J.H. Baek, Technical Manager in SFRA/KAERI, visited IGCAR to participate in this workshop. From IGCAR & BHAVINI twenty four delegates attended the workshop. Dr. P.R. Vasudeva Rao, Director, IGCAR, welcomed the KAERI delegation. Dr. P. Chellapandi, Director, Reactor Design Group, summarised the workshop.

IGCAR and KAERI participants presented the progress in research activities in the areas of SFR technology and the future plan of SFR in each country for the items agreed on the workshop agenda. It was especially worthy to note that six parallel sessions were arranged for the detailed face-to-face discussions among the responsible engineers from each country. And after the technical discussions, KAERI delegation was taken for technical visits to the facilities at IGCAR and PFBR simulator at BHAVINI.

The present workshop and interaction was beneficial towards the design of Generation IV Fast Reactors. At the end of the second workshop, future collaborative studies have been proposed in the areas of

- sharing facilities like SADHANA and STELLA-1
- dedicated theme meetings for the presentation of the position papers
- common benchmark studies
- joint development of computer codes for reactor safety
- evolve the criteria associated with clad rupture
- the behaviour of molten debris in the hot pool
- expert support and visit of the engineers/ scientists between KAERI and IGCAR

Delegates of IGCAR-KAERI workshop with Dr. P. R. Vasudeva Rao, Director, IGCAR and senior colleagues of the Centre

IAEA Technical Meeting on Development of Advanced Fuels for Fast Reactors

March 03-06, 2014

Dr. P. R. Vasudeva Rao, Director, IGCAR addressing, Shri U. Basak, Scientific Secretary, IAEA and Dr. K. Nagarajan, Director, CG seated on the dais during the inaugural function

An IAEA Technical Meeting on Development of Advanced Fuels for Fast Reactors was held at IGCAR during March 03-06, 2014. Thirty seven delegates from abroad and other DAE units participated in the meeting. Presentations made during the meeting by eminent scientists included various aspects of advanced fuels, such as fabrication, property measurements, fuels for reactors for transmutation of minor actinides, reactor physics aspects of these reactors and fuel cycle. The presentations were followed by detailed discussions with active participation of all the delegates. After the meeting, there was panel discussion on the possible collaborations between various institutions and IAEA Co-ordinated Research Projects (CRP). Visits to FBTR and PFBR for the outstation delegates were arranged during the meeting.

Participants of the meeting along with senior colleagues of the Centre

Seminar on Chemical Engineering in Nuclear Technology (CHEMENT-2014) with theme of "Recent Advances in Fuel Cycle Technologies"

March 06-07, 2014

A seminar on Chemical Engineering in Nuclear Technology (CHEMENT-2014) with the theme of "Recent Advances in Fuel Cycle Technologies" was jointly organized by Indian Institute of Chemical Engineers (Kalpakkam Regional Center) and IGCAR during March 06-07, 2014. The Seminar was partially sponsored by Board of Research in Nuclear Sciences (BRNS) of the Department of Atomic Energy. This seminar was the second in the series of seminars on Chemical Engineering in Nuclear Technology (CHEMENT). The primary aim of the seminar was to discuss about the advances in fuel cycle technologies with a focus on equipment design, modeling and simulation, plant experience sharing and performance evaluation.

CHEMENT-2014 was attended by leading experts from DAE as well as from reputed academic institutions, several research students and representatives from industry. In the inaugural session, Dr. R. Natarajan, Director, Reprocessing Group and Honorary Chairman, IIChE-KRC welcomed the delegates. The inaugural session was presided over by Shri N. Saibaba, Chief Executive, Nuclear Fuel Complex. Keynote address was delivered by Dr. P.R. Vasudeva Rao, Director, IGCAR. While exploring the challenges and targets for fuel cycle technologies, he stressed the need for new vistas in the reprocessing activities especially for metal fuels and for actinide recycling. He stressed for the creation of new benchmarks and novel challenges and directions. Vote of thanks was proposed by Shri Shekhar Kumar, Honorary Secretary, IIChE-KRC and organizing Secretary, CHEMENT-2014.

There were five technical sessions spanning over two days with intense interactions. A total of fourteen invited talks covering various topics of interest to Nuclear fuel cycle, were delivered by eminent speakers.

In addition to oral technical sessions, forty two contributed papers were presented in poster sessions on both the days. A special interactive session with the students and faculty of chemical engineering departments of various engineering colleges in Tamil Nadu was organized on the second day. Fifteen faculty members and thirty one students from fifteen engineering colleges attended the session. This session consisted of three exclusive talks tailored for students.

At the concluding session, Dr. P.M. Satya Sai, Convener summarized the technical and poster sessions. After presentation of poster awards and feedback from outstation delegates, vote of thanks was proposed by Shri Shekhar Kumar, organizing Secretary, CHEMENT-2014.

The deliberations in CHEMENT-2014 focused on identifying the challenges in areas related to advanced fuel cycle technologies and to evolve an action plan. It provided an opportunity to persons in R&D and in operations to meet and interact with the academia and industries dealing with solvent extraction.

As a concluding event for CHEMENT-2014 on March 12, 2014, IGCAR, IIChE-KRC and BHAVINI felicitated Prof. J.B. Joshi, Homi Bhabha Professor, HBNI on being awarded the Padmabhushan.

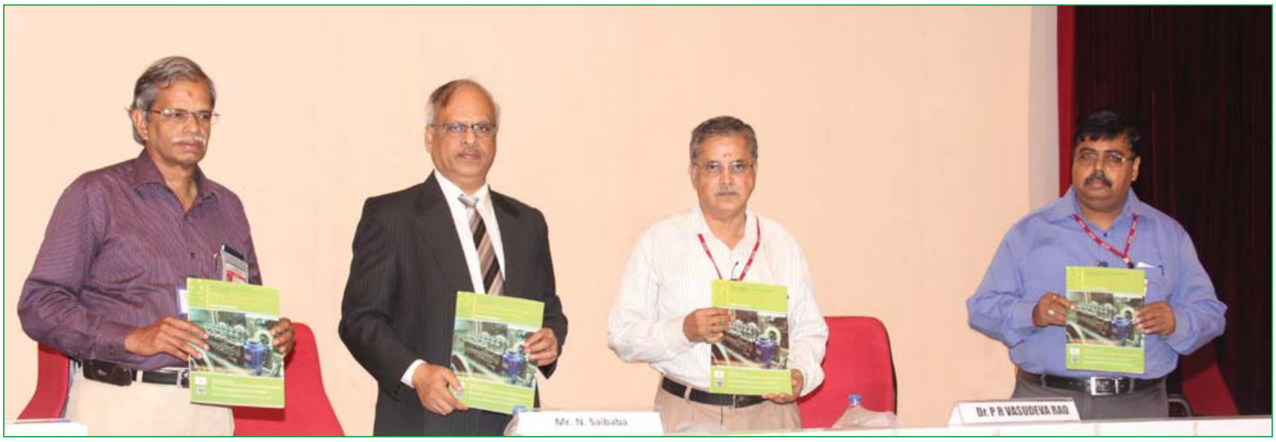

Release of book of abstracts by Chief Guest Shri N. Saibaba, Chief Executive, NFC

BITS Practice School

May 27 July 17, 2014

Dr. P. R. Vasudeva Rao, Director, IGCAR interacting with the students from BITS Practice School during the inaugural function

Twenty five students from BITS Pilani, Hyderabad and Goa campuses underwent BITS Practice School at our Centre during May 27- July 17,2014. This programme aims at exposing the students to industrial and research environments, how the organizations work, to follow and maintain work ethics, study the core subjects and their applications in the organization, participate in some of the assignments given to them in the form of projects.

The students were from various disciplines like, Chemical Engineering, Computer Science & Engineering, Electrical & Electronics Engineering, Electronics & Instrumentation Engineering and Electronics & Communication Engineering, Mechanical Engineering and Master in Information Systems. Dr. R. Natarajan, Director, Reprocessing Group and Project Director, Fast Reactor Fuel Cycle Facility inaugurated the Practice School at IGCAR on May 23, 2014. Dr. P. Srinivasan, Programme Coordinator, BITS Practice School Division participated. Students carried out challenging projects in various Groups of the Centre in line with their discipline. During the period of their stay, they visited various facilities at IGCAR, BHAVINI and MAPS. As a part of the curriculum, Quiz, Project work presentations, group discussions and report writing were done in the Practice School. Dr. P.R. Vasudeva Rao, Director, IGCAR had an interactive session with the students. The valedictory function was held on July 17, 2014. Dr. R. Natarajan, Director, Reprocessing Group & Project Director, Fast Reactor Fuel Cycle Facility delivered the valedictory address and distributed the certificates to the students.

Students from BITS Practice School with Dr. R. Natarajan, Director, RpG and Project Director, FRFCF and senior colleagues of the Centre during the valedictory funcition

Summer Training in Physics and Chemistry (STIPAC - 2014)
May 26 to July 4, 2014

STIPAC students with Dr. P. R. Vasudeva Rao, Director, IGCAR & senior colleagues during the inaugural function

IGCAR has been, for over a decade and a half, successfully running summer training for the pre-final Post Graduate students in Physics & Chemistry. The programme is conducted, generally, from the last week of May to the first week of July of each year. Students from across the country apply for this programme and are selected on the basis of a one page write up on an assigned topic and academic track record. If needed, even a telephonic interview is held. Care is taken to ensure that there is representation from across the states, universities and colleges.

The 16th Summer Training In Physics And Chemistry (STIPAC 2014) programme commenced on 26th May and ended on 4th July 2014. The programme was steered and mentored by Dr. P.R. Vasudeva Rao, Director, IGCAR, Dr. C.S. Sundar, Director, MSG and Dr. K. Nagarajan, Director, CG.

There were twenty students in Physics and twenty in Chemistry, for this year's programme. The write up assigned for screening was "Crystallography and its impact on understanding properties of materials". The courses were run on the theme "Materials: Structure & Properties". The students were assigned to projects/experiments and were encouraged to have hands on experience in various areas of research carried out at the Materials Science and Chemistry Groups. The students also gave a presentation on the projects they carried out.

The inaugural address by Prof. Kamanio Chattopadhyay, IISc, Bangaluru covered various aspects of Quasicrystals.

Apart from the lectures by in house experts, the students were also exposed to experts from other institutions. The students visited BHAVINI, MAPS & FBTR and got an overview of the challenging work being carried in the area of energy production. Dr. Prabhat Kumar, CMD, BHAVINI, elucidated on the Challenges in Large Scale Project Management, and Dr. S. Rathakrishnan, RPS, MAPS opened up their minds to the various issues involved in harnessing Nuclear Energy.

The valedictory address by Prof. U.V. Varadaraju, IIT Madras, Chennai dwelt on Electrochemical Energy Storage Systems.

Prof. U. V. Varadaraju, IIT Madras, Chennai distributing certificate to STIPAC student during the valedictory function

Graduation Function of the Eighth Batch of Trainee Scientific Officers of BARC Training School at IGCAR

July 24, 2014

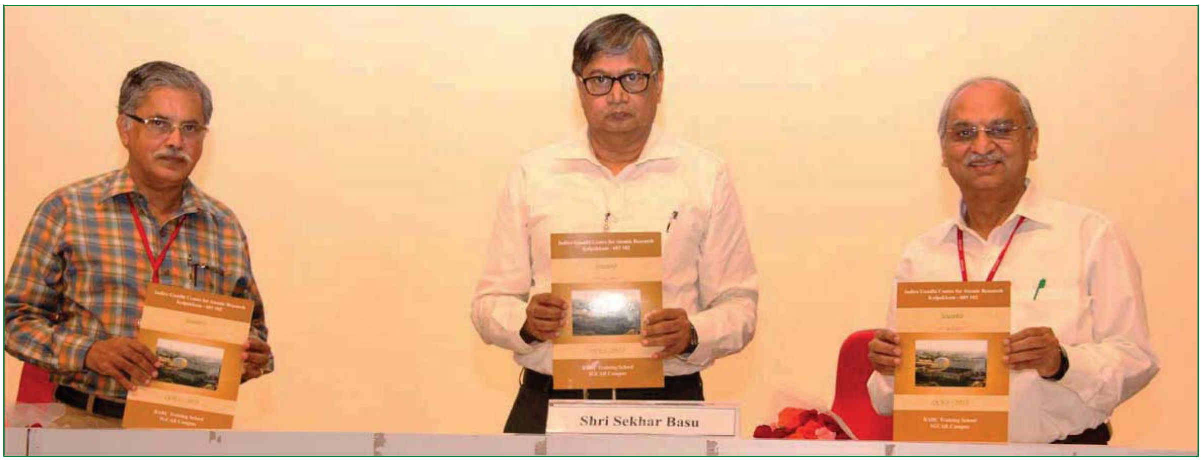

Shri Sekhar Basu, Director, Bhabha Atomic Research Centre, Mumbai, Dr. P. R. Vasudeva Rao, Director, IGCAR, Dr. M. Sai Baba, Associate Director, RMG, during the release of souvenir at the graduation function

The eighth batch of fifty four TSOs from the BARC Training School at IGCAR have successfully completed their training and were graduated in a special ceremony that took place on July 24, 2014 at 11.00 hours in the Sarabhai Auditorium, Homi Bhabha Building, IGCAR. Shri Sekhar Basu, Director, Bhabha Atomic Research Centre, Mumbai, was the Chief Guest. Dr. P. R. Vasudeva Rao, Director, IGCAR welcomed the gathering. Dr. Vidya Sundararajan briefed the audience about the Orientation Course in Engineering and Sciences programme. Shri Sekhar Basu released the souvenir featuring the training school programme in the previous academic year and Dr. P. R. Vasudeva Rao received the first copy. Shri Sekhar Basu gave away the prestigious 'Homi Bhabha Prize' comprising of a medallion and books worth Rs. 5000 to the meritorious toppers from all the disciplines and delivered the presidential address. He also gave away the course completion certificates to all the graduates passing out. A few of the Trainee Scientific Officers passing out shared their experiences, given feedback on the academic programme and their stay at the hostel. Dr. M. Sai Baba, AD, RMG, proposed the vote of thanks.

Eighth Batch of Graduates of BARC Training School at IGCAR with Shri Sekhar Basu, Director, Bhabha Atomic Research Centre, Mumbai, Dr. Prabhat Kumar, Chairman and Managing Director, BHAVINI, Dr. P. R. Vasudeva Rao, Director, IGCAR and senior colleagues of the Centre

Quality Circle Annual Meet (QCAM-2014)

August 25, 2014

Dr. T. Jayakumar, Director, MMG, IGCAR delivering the Presidential address during annual meet of quality circle

Quality circle is a small group of employees doing similar or related work who meet regularly to identify, analyze and solve work related problems usually led by a senior team member. After completing their analysis, they present their solutions to management for implementation and to improve the performance of the organization. Thus, implemented correctly, quality circles can help the organization to reduce costs, increase productivity, and improve employee morale.

In IGCAR, every year the Annual Meet of Quality Circle (QCAM-2014) is conducted and the QC case studies are presented by the QC teams. QCAM-2014 was conducted on August 25, 2014 at Convention Centre and SRI Seminar Hall, Anupuram in parallel sessions. Welcome address was delivered by Shri G.Srinivasan, Director, ROMG, The Presidential address was delivered by Dr. T. Jayakumar, Director, MMG. Dr. R. Raju, Professor, Department of Industrial Engineering, Anna University, Chennai delivered the inaugural address and vote of thanks by Shri G. Kempulraj, Head, Central Workshop Division.

Thirty Quality Circles (about 300 members) from IGCAR, schools from Kalpakkam and neighborhood presented QC case studies in a wide spectrum of topics covering Technical, Research and Development, Services and Education. Professional judges from Quality Circle Forum of India, Chennai chapter, adjudged the QC case study presentations. Under the Mechanical and Manufacturing' stream, the STAR QC Team bagged 'Dr. Placid Rodriguez Memorial Trophy', while PLUTONIUM QC team bagged the 'Shri M.K. Ramamurthy Memorial Trophy' in the Plant Operation and Services category. KURUMBU QC, Government HSS, Vengappakkam won the 'Dr. Sarvepalli Radhakrishnan Memorial Trophy' for School category.

During the valedictory function, the events were summed up by Shri K. G. Subramanian, Convenor, QCAM-2014. The programme concluded with a valedictory address and the prizes were distributed to the participants by Shri G. Srinivasan, Director, ROMG and Shri A. Jyothish Kumar, Associate Director, ESG. Vote of thanks was proposed by Shri T.V Maran, Member Secretary, Organising Committee.

Shri G. Srinivasan, Director, ROMG & senior colleagues of the Centre during the annual meet of quality circle

12th Joint Coordination Committee Meeting of DAE-CEA at IGCAR
November 24-25, 2014

Dr. R.K. Sinha, Chairman AEC, Dr. B. Bigot, Chairman CEA and Dr. P. R. Vasudeva Rao, Director, IGCAR along with delegates during the meeting

The 12th Joint Coordination Committee Meeting of DAE-CEA took place on 24-25th November 2014 at IGCAR, Kalpakkam to review ongoing collaboration between DAE and CEA France. Dr. R.K. Sinha, Chairman, AEC led the Indian delegation and the French delegation was led by Dr. B. Bigot, Chairman, CEA. In their opening remarks both the Chairmen expressed their happiness on the progress of collaboration between the two countries in the field of Nuclear Energy. Dr. P. R. Vasudeva Rao, Director, IGCAR made a presentation on the highlights of the cooperation in the field of basic research and fast reactor safety. He also made a presentation on the strategy for enhancing cooperation in the field of fast reactor safety. Shri P. K. Wattal, BARC made a presentation on summary and highlights of cooperation in the field of waste management. Shri R. C. Sharma, BARC presented the summary and highlights of JHR cooperation. Dr. P. Chellapandi, IGCAR, made a presentation on codes, licences and on possibility of Indian cooperation on PLINIUS-2. Presentation on review of the developments in the field of basic research was made by Dr. B. K. Panigrahi, IGCAR. Dr. A. K. Nayak, BARC made a presentation on possibility of cooperation in the field of In-Vessel retention. During the meeting three implementing agreements were signed between DAE and CEA. All the delegates visited PFBR site, FBTR and RML. Both the Chairmen wished to strengthen the cooperation between the two countries in the nuclear field for mutual benefit.

Dr. R. K. Sinha, Chairman AEC, Dr. B. Bigot, Chairman CEA and Dr. P. R. Vasudeva Rao, Director, IGCAR along with delegates during visit to FBTR

Course on Nuclear Chemical Engineering and Present-day Technologies (CONCEPT-2014)

December 01-12, 2014

Dr. K. Krishnaiah, Professor, Department of Chemical Engineering, IIT Madras, Chennai addressing the participants during inauguration of CONCEPT-2014

To commemorate the diamond jubilee of Department of Atomic Energy, IIChE, Kalpakkam, in collaboration with IGCAR, had organised a winter course, Course on Nuclear Chemical Engineering and Present-day Technologies (CONCEPT-2014) for third year students of BE (Chemical Engineering) during December 01-12, 2014. It was a two-week course in which, in addition to all the aspects of the nuclear fuel cycle, essentiality and environmental impact of nuclear energy were taught. The course was structured in such a way to promote the nuclear technology to the budding chemical engineering graduates, who would not only be inspired to take nuclear technology as their career but also would spread the challenges in the nuclear technology to the general public. CONCEPT-2014 was inaugurated by Prof. K. Krishnaiah on December 01, 2014 and thereafter technical lectures were delivered by senior scientists of IGCAR, BARC and BARCF for the benefit of students. Students were also provided with the preprints of the lecture-contents for further study and perusal. Course content included advanced lectures on solvent extraction, membrane technology and extraction equipment. Visits to Madras Atomic Power Station (MAPS), Fast Breeder Test Reactor (FBTR), Centralised Waste Management Facility (CWMF) and Environmental Survey Laboratory (ESL) were also part of the course. About 44 students from various engineering colleges of Tamil Nadu, including IIT Madras had participated in CONCEPT-2014 and successfully completed the course. A chemical engineering quiz was also organised as a part of the course. In the fond memory of Late Shri N. Srinivasan, former Director, RRC (now IGCAR) and founding member of IIChE-KRC, IIChE-Kalpakkam Regional Centre has instituted an award for the quiz winners. This award will be given annually.

After completion of the course, valedictory function was held at Sarabhai Auditorium, HBB Building, IGCAR on December 12, 2014. The function was inaugurated by Dr. P. R. Vasudeva Rao, Distinguished Scientist and Director, IGCAR. It was presided by Prof. P.S.T. Sai, Head, Chemical Engineering Department of IIT Madras, Chennai. Dr. R. Natarajan welcomed the participants and colleagues. Dr. P. M. Satya Sai briefed the gathering about the course and its contents. For the year 2014, Shri N. Srinivasan memorial Award was awarded to the winners of the chemical engineering quiz by Shri G. R. Balasubramanian, former Advisor to Chairman AEC and erstwhile colleague of late Shri N. Srinivasan at FRD, BARC and IGCAR. Award consisted of a silver medallion and a certificate. All the successful participants were also given certificate of merit. A feedback session was also organised. Honourable Secretary of IIChE-KRC, Shri Shekhar Kumar proposed the vote of thanks.

Eminent Visitors to IGCAR

Dr. Avinash Chander, Scientific Advisor to Defence Minister, with Dr. P. R. Vasudeva Rao, Director, IGCAR and senior colleagues of the Centre

Dr. Avinash Chander, Scientific Advisor to Defence Minister, visited IGCAR on January 02, 2014. After a meeting with Dr. P. R. Vasudeva Rao, Director, IGCAR and senior colleagues of the Centre, Dr. Avinash Chandra visited the Fast Breeder Test Reactor & KAMINI Reactor, Hot Cells and Non-Destructive Evaluation Division and construction site of Prototype Fast Breeder Reactor.

Shri P. S. Parihar, Outstanding Scientist and Director, AMD, Hyderabad, delivered the IGC Colloquium on "Status of Uranium Resources in the Country" during his visit to the Centre on January 17, 2014.

Shri P. S. Parihar, Outstanding Scientist & Director, AMD, Hyderabad, delivering the IGC Colloquium

Dr. R. Chidambaram, Principal Scientific Advisor, Government of India, delivering the lecture, organized as a part of series of lectures to commemorate the International Year of Crystallography

Dr. R. Chidambaram, Principal Scientific Advisor, Government of India, during his visit to the Centre on January 28, 2014, delivered the lecture on "Crystallography, Materials Science and Biology", organized as a part of series of lectures to commemorate the International Year of Crystallography.

Prof. J. B. Joshi, DAE-Homi Bhabha Distinguished Chair Professor and J.C. Bose Fellow, delivered the IGC Colloquium on "Wealth Generation Through University - Industry Partnership" during his visit to our Centre on March 11, 2014.

Prof. J. B. Joshi, DAE-Homi Bhabha Distinguished Chair Professor and J. C. Bose Fellow, delivering the IGC Colloquium

Prof. M. S. Valiathan, Founder-Director, Sree Chitra Tirunal Institute of Medical Sciences and Technology & National Research Professor of Government of India, at Manipal University, delivering the IGC Colloquium

IGC Colloquium on “Biomaterials, Bio-Devices and the Story of the TTK-Chitra Heart Valve” was delivered by Prof. M.S. Valiathan, Founder-Director, Sree Chitra Tirunal Institute of Medical Sciences and Technology & National Research Professor of Government of India, at Manipal University, during his visit to the Centre on March 21, 2014.

Dr. R. K. Sinha, Chairman, AEC during his visit to the Reactor Design Group

Dr. R. K. Sinha, Chairman, AEC and Shri P. Janawadkar, Director, MSG during his visit to the MEG facility, Materials Science Group

Dr. R.K. Sinha, Chairman, Atomic Energy Commission and Secretary, Department of Atomic Energy visited IGCAR during April 12,2014. He met Dr. P.R. Vasudeva Rao, Director, IGCAR, senior colleagues of the Centre and discussed about various programmes in progress. He visited the PFBR preheating mock facility at Reactor Design Group, Magnetocardiography/magnetoencephalography facility at Materials Science Group, Madras Atomic Power Station and construction site of PFBR at BHAVINI.

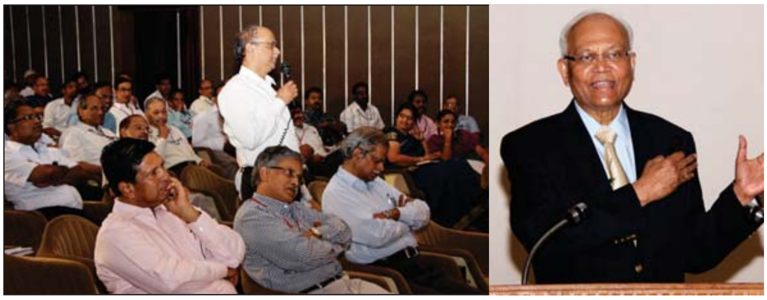

Dr. R. A. Mashelkar, National Research Professor & President of Global Research Alliance delivering the Vikram Sarabhai Memorial Lecture

Dr. R.A. Mashelkar, National Research Professor & President of Global Research Alliance visited IGCAR during August 12,2014. He met Dr. P. R.Vasudeva Rao, Director, IGCAR, senior colleagues of the Centre and discussed about various programmes in progress. During his visit he delivered the Vikram Sarabhai Memorial Lecture on “On Reinventing India as Innovation Nation”. He visited the Madras Atomic Power Station and construction site of PFBR at BHAVINI.

Dr. M.R. Srinivasan, Member, Atomic Energy Commission & Former Chairman, AEC delivering the first Diamond Jubilee Colloquium

Dr. M. R. Srinivasan, Member, Atomic Energy Commission & Former Chairman, AEC, visited the Centre on September 04, 2014. During his meeting with DAC members, he was briefed about the activities of IGCAR by Dr. P.R. Vasudeva Rao, Director, IGCAR, and status of FRFCF by Dr. R. Natarajan, Project Director, FRFCF. After the meeting he delivered the first Diamond Jubilee Colloquium on “Evolution and Ethos of DAE”. He then visited the Interim Fuel Storage Building at Reactor Operation & Maintenance Group and various facilities/laboratories at Metallurgy & Materials, Materials Science, Chemistry and Reactor Design Groups.

Prof. Gautam R. Desiraju, from Indian Institute of Science, delivering the lecture

Prof. Gautam R. Desiraju, Immediate Past President, IUCr, Solid State and Structural Chemistry Unit, Indian Institute of Science, delivered a lecture on “100 Years of Diffraction Celebrating the International Year of Crystallography” organized as a part of series of lectures to commemorate the International Year of Crystallography on October 13, 2014.

Prof. S. Ranganathan, from Indian Institute of Science, Bengaluru delivering the lecture

Prof. S. Ranganathan, NASI Senior Scientist Platinum Jubilee Fellow, Indian Institute of Science and Homi Bhabha Visiting Professor, NIAS, Bengaluru delivered a lecture on “Quasicrystals: The golden Road to Stockholm” organized as a part of series of lectures to commemorate the International Year of Crystallography, during his visit to the Centre.

“Know your DAE” Series

Shri N. Saibaba, Distinguished Scientist and Chief Executive, Nuclear Fuel Complex, delivering the lecture

Shri N. Saibaba, Distinguished Scientist and Chief Executive, Nuclear Fuel Complex, delivered a talk on “Nuclear Fuel Fabrication - Its Challenges and Technological Spin Offs” on October 10, 2014 as a part of “Know your DAE” series being organised to commemorate the Diamond Jubliee of our Department.

Dr. Prabhat Kumar, Chairman & Managing Director, Bharatiya Nabhikiya Vidyut Nigam Ltd (BHAVINI) delivering the lecture

Dr. Prabhat Kumar, Distinguished Scientist, Chairman & Managing Director, Bharatiya Nabhikiya Vidyut Nigam Ltd (BHAVINI), delivered the lecture on “Technological and Management Challenges, in Technology Launch Mega Project-PFBR”, on October 31, 2014, as part of “Know your DAE” series.

Shri G. Nageswara Rao, Director (Operations), Nuclear Power Corporation of India Limited, delivering the lecture

Shri G. Nageswara Rao, Director (Operations), Nuclear Power Corporation of India Limited, delivered a talk on “Indian Nuclear Power Program - Stage 1 Experiences” as a part of “Know your DAE” series being organised to commemorate the Diamond Jubliee of our Department, during his visit to the Centre on December 26, 2014.

IGC COUNCIL

Chairman

Dr. P. R. Vasudeva Rao

Distinguished Scientist & Director, IGCAR

Dr. P.R. Vasudeva Rao, is currently the Director of Indira Gandhi Centre for Atomic Research (IGCAR) and General Services Organization and also Director of Chemistry Group, IGCAR at Kalpakkam. After graduating from Vivekananda College, Chennai, he joined DAE in the 16th batch of BARC training school. He obtained his Ph.D. Degree from Bombay University in 1979. He shifted to IGCAR in 1978 and was instrumental in setting up of the Radiochemistry Laboratory. He is a recipient of the Indian Nuclear Society award (2007) for his contributions in the area of nuclear fuel cycle technologies. He has delivered the MRSI medal lecture in 1998 and has been awarded the MRSI-ICSC Superconductivity and Materials Science Senior Award in 2011. He was also selected for the award of the Silver Medal by the Chemical Research Society of India in 2011. He is a senior professor at the Homi Bhabha National Institute (HBNI) and has nearly 250 publications in peer reviewed international journals. His areas of interest include development of technologies for fast reactors and associated fuel cycles, actinide separations and education in the field of chemical sciences.

Members

Shri Sekhar Basu, a renowned nuclear scientist, is currently the Director of Bhabha Atomic Research Centre (BARC). Earlier he worked as the Project Director of Nuclear Submarine Programme and later as the Chief Executive of the Nuclear Recycle Board in the same institute. Shri Basu is an engineer of exceptional ability who has played a lead role in multiple areas of nuclear science and engineering and is a major contributor in establishing India as a leader in nuclear field.

Shri Basu, born on 20th September 1952, did his schooling from Ballygunge Government School, Kolkata and graduated in Mechanical Engineering from Veermata Jijabai Technological Institute (VJTI), University of Mumbai in 1974. After completion of one year of BARC Training School programme in nuclear science and engineering, he joined the Reactor Engineering Division of BARC in 1975. He started his career by designing fuel for Boiling Water Reactor, which showed excellent reactor performance. Later he took up the responsibility of the development of nuclear submarine propulsion plant and built the land based prototype at Kalpakkam from scratch. He continues to guide the Indian nuclear propulsion programme for the sea going versions. Since 2000, he was also responsible for the design, development, construction and operation of nuclear recycle plants at Tarapur and Kalpakkam, involving reprocessing and nuclear waste management. These plants are performing to international standards. He is pursuing the design of the Integrated Nuclear Recycle Plant, which will take this programme to a higher platform.

As the Chairman of Project Management Board he is responsible for the development of Indian Neutrino Observatory at Tamil Nadu and as Apex Project Co-ordinator, he is pursuing the development of 1 GeV Superconducting Accelerators for the Accelerator Driven System Programme. Shri Basu is also guiding the establishment of nuclear fuel cycle park involving research reactors, fuel fabrication and reprocessing facilities at the Vizag campus of BARC. Work on the design of Indian Pressurised Water Reactor has also been initiated by him.

As Director, BARC, Shri Basu has taken special initiatives for major expansion of the societal programmes of DAE in the field of nuclear agriculture, food preservation and nuclear medicine. While pursuing the basic research in the field of nuclear science and engineering, he is also working towards the expansion of enrichment and strategic programmes. He represented India in concluding ‘Arrangements and Procedures’ with the US Government for reprocessing of US hypothecated fuel and he has chaired the International Committee for the design review of three modules of International Thermonuclear Experimental Reactor (ITER).

He has several publications to his credit in national and international journals. Shri Basu has been conferred several awards and these include: Indian Nuclear Society Award 2002, DAE Awards in 2006 and 2007. He is also a Fellow of the Indian National Academy of Engineers (INAE) and Indian Society for Non Destructive Testing (ISNT). Jadavpur University awarded him with DLit (Honoris Causa) degree in 2013. He was awarded Padma Shri by the Government of India in 2014.

Shri Arun Kumar is a Graduate in Engineering (Metallurgy) and joined Bhabha Atomic Research Centre (BARC), Trombay after completing 16th Batch of Orientation Programme of BARC Training School. He is presently the Director of Nuclear Fuels Group and Head, Radiometallurgy Division in BARC. He had worked initially at Radiometallurgy Division for 14 years. In 1987, he was posted to Advanced Fuel Fabrication Facility (AFFF), BARC, Tarapur which is an Industrial Scale Plant for fabrication of $(U\text{-}Pu)O_2$ fuels. In 2004, he returned to Radiometallurgy Division, Trombay and was designated as Head, Radiometallurgy Division.

Some of the highlights in his career in which he is deeply involved are development of plutonium bearing fuel for thermal and fast reactors, development / fabrication of advanced fuel for fast reactors like mixed carbide, metallic and cermet fuels. Fabrication of Mixed Oxide fuel pins for PFBR is one of the major activities he is currently engaged in. He is a member of IGCAR council, Nuclear Recycle Board, Nuclear Fuel Complex Board and Trombay Council. Apart from these he is also Chairman/Member of many projects & safety committees of BARC. He is recipient of DAE Special Contribution Award for excellence in Science, Engineering & Technology in 2008 and Group Achievement Award for FBTR fuel fabrication in 2009. He has more than 100 technical publications to his credit.

Shri Pradip R. Baviskar is from the Indian Administrative Service of the 1985 Batch, West Bengal Cadre. He is B.Sc. (Chemistry) with Post Graduate Diploma in Marketing Management. Major postings held by him so far include District Magistrate and Collector, Darjeeling District (West Bengal) (1994-1997). Joint Textile Commissioner, Ministry of Textiles, Government of India (1997-2002). Chief Executive Officer, Kolkata Metropolitan Development Authority (KMDA), Kolkata (2004-2009). Chief Vigilance Officer, Mumbai Port Trust (2010-2012). In January 2013, he joined Department of Atomic Energy as Joint Secretary in-charge of R&D wing which deals with units like BARC, IGCAR, RRCAT, VECC and all Aided Institutions under DAE.

Dr. P. Chellapandi is a Distinguished Scientist and Director, Reactor Design Group, IGCAR, Kalpakkam. He is from 22nd batch of BARC training school with first rank and joined IGCAR in 1979. He is responsible for the design and development of fast reactor power plant systems and components including core, shutdown and energy conversion systems. He is one of the key persons, who has been involved in the design and development activities of 500 MWe PFBR. His current activities focus on the development of innovative design features for the future fast breeder reactors beyond PFBR, planned by the Department. He has established two dedicated and unique laboratories at IGCAR: one for structural mechanics and another for safety engineering studies for the design validations. He has formulated many national collaborations with various reputed institutes and played a key role in establishing MoUs, particularly with IIT Madras, IIT Kanpur, IIT Kharagpur and IISc Bangaluru. He is the member of many important national and international committees including Project Design Safety Committee for PFBR (PDSC- PFBR), Apex Committee on Nuclear Power and Associated Fuel Cycle (AC-NP&AFC), Advisory Committee for Project Safety Review of Light Water Reactors (ACPSR-LWR-2), Nuclear Fuel Complex Board of Management, Convener, Task Force for Conceptual Design of Future FBRs, Advisory Committee for Nuclear Reactors & Fuel Cycle Committee (NRFCC) of Board of Research in Nuclear Sciences (BRNS), Advisory

Committee on Codes, Guides and Associated Manuals for Safety in Design of Nuclear Power Plants (ACCGD)and Safety Research Scientific Committee, DAE, International Atomic Energy Agency (IAEA) Technical Working Group on Fast Reactors (TWG-FR), during the period 2006-2011, Chairman for the IAEA Technical Co-Operation Expert Mission for Codes and Standards for Sodium Cooled Fast Reactors. (NSR-1), coordinator from India in executing the implementing agreement under CEA-IGCAR Liquid Metal Fast Reactor Safety projects and an expert consultant for the conceptual design of an in-core sodium loop for high temperature multi sample, high dpa material experiments high flux reactor (JHR), CEA Cadrache. He has an outstanding academic record in Mechanical Engineering and a Gold Medal with perfect grade point average of 10 in his Master's Degree in the field of applied mechanics, from IIT Madras. He has guided more than ~15 PhDs, ~120 M.Tech projects and more than ~300 B.E Projects, all relevant to fast reactor design. He has a very impressive record of publications ~680 to his credit out of which 130 are in journals. He is a Fellow of Indian National Academy of Engineering. He has received the Homi Bhabha Science and Technology Award for the year 1997, Indian Nuclear Society Award and National Design Award in Mechanical Engineering in 2006, Agni Award for Excellence in Self-reliance - DRDO-2007, DAE Group Achievement Awards in 2006, 2007, 2008, 2009, 2010 and 2011 for design, manufacture and erection of PFBR reactor assembly components and Vasvik award 2009. He has been bestowed upon Distinguished Alumnus Award of the IIT Madras in 2010.

Shri S. G. Ghadge is a Mechanical Engineering Graduate from Visvesvaraya National Institute of Technology, Nagpur, and Post Graduate in Nuclear Technology in BARC now known as Homi Bhabha National Institute. He has a distinguished career in the Department of Atomic Energy, Nuclear Power Corporation of India spanning 36 years, which covered multiple fields of Nuclear Reactor Process Design, Commissioning, Operational Improvements, Safety, Thermo Hydraulic Analysis with complex code development. He spearheaded the internal reviews for post Fukushima safety assessment taking into account international thinking and worked out safety enhancement measures arising out of these reviews apart from reviews by AERB. He was member of the Indian delegation to IAEA in the Convention of Nuclear Safety and contributed in generation of design and safety codes and guides for IAEA and AERB. He has several international and national publications to his credit. He is a Distinguished Scientist of the Department of Atomic Energy. Presently his responsibilities encompass design, health, safety, licensing analysis, procurement for 700 MWe PHWR and building up of R&D facility at Tarapur. He is a full time Director on the Board of NPCIL from 1st July 2013.

Dr. P. D. Gupta, Distinguished Scientist is the Director, Raja Ramanna Centre for Advanced Technology, Indore. Dr. Gupta is an internationally known laser-plasma physicist who has made pioneering research contributions in this area. He passed M.Sc. Hons (Physics) from Punjab University in 1972 and joined Bhabha Atomic Research Centre. He is a recipient of four gold medals for securing first rank in various university examinations. He joined BARC in August 1973 after passing out from 16th batch (1972-73) of Training School and was awarded Homi Bhabha Medal and Prize. He received his Ph.D. from Bombay University in 1984 and did his Post-doctoral work at the Department of Electrical Engineering, University of Alberta, Canada during 1984-86. He is recipient of Young Scientist Award of Indian National Science Academy (1984) and Young Associateship of Indian Academy of Sciences (1986-91) and became Fellow of the National Academy of Sciences, India, in 2004. As Director, Dr. Gupta is steering many R&D programmes in frontline areas of accelerators and lasers at RRCAT. These include synchrotron radiation sources and their utilization, development of superconducting radio-frequency cavities for high energy accelerators, proton linac spallation neutron source, cryogenics, magnet technology, ultra-intense laser-plasma interaction, and lasers in research and industry. Dr. Gupta is a Senior Professor of Homi Bhabha National Institute (HBNI), Mumbai, and a member of the Academic Council. He has guided many young researchers for the award of Ph.D. / M.Tech / M.Sc. degrees. He has made ~350 research contributions of which 185 are published in international journals.

Shri M.P. Janawadkar joined Indira Gandhi Centre for Atomic Research, Kalpakkam in 1977 after graduating from the 20th batch of BARC training school and has been working in the area of superconductivity for more than three decades. His research work involved studies on properties of superconductors such as NbTi alloys, Chevrel phase compounds and the High Temperature Superconductors. He was instrumental in setting up the superconducting device fabrication laboratory in Materials Science Group of IGCAR which houses state of the art facilities for thin film deposition, photolithography and reactive ion etching in a Class 1000 Clean Room and has led the program for development of SQUID devices at IGCAR. His group has successfully fabricated Superconducting Quantum Interference Devices (SQUIDs), which are the world's most sensitive detectors of magnetic flux with a sensitivity of 10 femto-Tesla. A wide range of applications of these devices in areas such as SQUID magnetometers, SQUID based Non-Destructive Evaluation etc. have been indigenously developed. During the last few years, he has been involved in setting up facilities for the SQUID based measurement of extremely weak biomagnetic fields such as those associated with physiological activities of human heart and human brain. Shri M.P. Janawadkar was a visiting scholar at Instituto di Cibenetica, Italy in 1986 and at University of California at Berkeley in 1994. He is the recipient of the DAE Technical Excellence Award in 1999, and the Group Achievement Award in 2010. He was awarded MRSI-ICSC Superconductivity and Materials Science Annual Prize in 2013.

Dr. T. Jayakumar, B.Tech. (Metallurgy, REC Warangal), M.S (Metallurgy, IIT Madras), Ph.D (Engineering, University of Saarland, Germany) is currently a Distinguished Scientist and the Director, Metallurgy and Materials Group at IGCAR. Since 1978, he has been engaged in the field of Non-Destructive Evaluation. Over the years he has carried out and steered innovative research and development programmes in the areas of Non-Destructive Evaluation, Failure Analysis and structural integrity of nuclear components specifically for the Fast Breeder Reactor. In the last few years, he is actively coordinating and guiding research activities related to development of materials and manufacturing technologies for sodium cooled fast reactors, associated fuel cycle and Indian fusion programme. He is a Fellow of the Indian National Academy of Engineering. He has been a recipient of several awards such as National NDT Award from ISNT, Metallurgist of the Year award from IIM, Homi Bhabha Science and Technology Award from DAE, Outstanding Services Award from INS. He has co-authored three books, co-edited four books and has published over 270 papers in international journals. He also has six patents to his credit.

Dr. R. Natarajan, Chemical Engineer, is from the 19th batch of BARC training school and joined the Department of Atomic Energy in 1975. He is presently the Director of Reprocessing Group and Project Director, FRFCF in IGCAR. Under his leadership, the CORAL facility, for establishing the process technology for the reprocessing of fast reactor fuels was designed, erected and commissioned. He led the team which has successfully completed the reprocessing of fast reactor spent fuel, with a burn-up of as high as 155 GWd/t of a plutonium rich fuel, which is an international benchmark. He is also responsible for the R&D activities of fast reactor fuel reprocessing and setting up of demonstration as well as the commercial PFBR fuel reprocessing plants. The commissioning of Demonstration Plant (DFRP) for the reprocessing of mixed carbide as well as oxide spent fuels on a demonstration scale, which incorporates design features based on the operating experience of CORAL, has just commenced. The construction activities of various facilities of the fuel cycle facility (FRFCF) for PFBR have started. His specialization is in the design, development of process flow sheets and radiochemical plant design. He also has experience in the design and operation of equipment for thorium-uranium cycles. He has participated in the irradiated thorium fuel reprocessing campaigns at the Reprocessing Development Laboratory and the uranium recovered is used as fuel for the reactor, KAMINI. He has interest in solvent extraction process modeling, extraction equipment design, design of feed clarification systems of high active solutions, acid recovery systems, system designs of radioactive off-gas circuits and ventilation design of radioactive plants. He has over hundred technical presentations and publications to his credit. He has won the prestigious NOCIL Award for Excellence in Design and Development of Process Plant and Equipment for the year 2005 for his contribution in the development of fast reactor fuel reprocessing. He is also the recipient of the INS award for the year 2006 for his contributions to Nuclear Fuel Cycle technologies. He is a Fellow of the Indian National Academy of Engineering and a honorary fellow of Indian Institute of Chemical Engineers.

Shri S. Paramasivam graduated as a Mechanical Engineer from Madras Institute of Technology in the year 1981 and joined BARC in the 25th batch of Training School. After successful completion of training, he was posted at Heavy Water Board Head Office, Mumbai and was associated in mechanical project activities for Heavy Water Plant (Manuguru). In the year 1986, he was transferred to HWP (Manuguru), where he was involved in erection and commissioning activities pertaining to exchange units. He was promoted as Deputy Maintenance Manager (Mechanical) in the year 1998 and as head of Mechanical Maintenance Section in the year 2003. He was posted to HWP (Tuticorin) as Maintenance Manager in the year 2005 and promoted as Officer On Special Duty in the year 2008, subsequently as General Manager of Heavy Water Plant, Tuticorin. In July, 2013, he was appointed as Regional Director, MRPU, DPS, Chennai.

Shri C.K. Pithawa is Distinguished Scientist and Director, Electronics & Instrumentation Group, Bhabha Atomic Research Centre, Trombay, Mumbai. He holds additional charge of Director, Design, Manufacturing and Automation Group, BARC. He did his Degree in Electrical Engineering from Government Engineering College, Rewa in 1973 and joined Reactor Control Division in August 1974 after completing one year training from 17th batch of BARC training school. He did his M.E. in Automation from IISc, Bengaluru in 1981 and M.S. in Electronics from University of Southampton, U.K. in 1986. He is a Fellow of National Academy of Engineering. Shri Pithawa has made significant contributions to the computer based control and monitoring systems for Pressurized Heavy Water Reactors, Light Water Reactors, Research Reactors and for particle accelerators. He is spearheading the development of radiation detectors, reactor instrumentation, semiconductor detectors, ASICs, RF instrumentation, ultrasonic instrumentation, PLC for safety systems, HPC and information security. He was deputed for about two years to Raja Ramanna Centre for Advanced Technology, Indore as Incharge, Indus Accelerator Complex to improve operational performance of Indus-2 accelerator. He has been associated with many important and strategic programmes of DAE. He has received four DAE Group Achievement Awards in 2006, 2008 and 2012 and Special Contribution Award in 2007.

Dr. Prabhat Kumar, Adviser, BHAVINI & Former Chairman and Managing Director, BHAVINI is responsible for construction and commissioning of India's first Prototype Fast Breeder Reactor which has been designed indigenously and launched as a precursor to commercial exploitation of FBRs on a large scale. In his career, he has worked on nuclear system and component design, indigenisation of critical nuclear equipment, participated in erection of the equipment and their commissioning. He has headed Quality Assurance Group of Kudankulam project during its formative years, later he worked for coolant channel life management, remote tooling for reactor inspection, maintenance and started the R&D centre for NPCIL. He has steered many programmes of vital importance for Indian nuclear power plants. He has lead a multi disciplinary team from NPCIL and IGCAR directed towards ensuring a robust construction of PFBR. Dr. Prabhat Kumar is the recipient of Indian Nuclear Society Award for Excellence in Nuclear Technology. In addition, he has been conferred with "Prof. D.R.G. Achar Memorial Medal Award", "Life Time Achievement Award", "Best Philanthropist Award", "CEO with HR orientation Award", "Vignan Sankethika Puraskar", "IIW Sharp Tools Award", "For the sake of Honour Award" and many more awards & honors by various organizations/societies/university for his outstanding contributions in versatile fields. Dr. Prabhat Kumar has held positions of Chairman and expert member for various technical and management committees throughout the country. He is the alternate Chairman for the Site Selection Committee for construction of Nuclear Power Plants in India. Dr. Prabhat Kumar is the National Vice President of Indian Society of Non Destructive Testing (ISNT). He is also the Chairman of Authorized National Board for Company Certification (ANBCC) of Indian Institute of Welding. Dr. Prabhat Kumar has been conferred as the fellow of ISNT and fellow of "Indian National Academy of Engineering".

Shri K.K. Rajan is currently an Outstanding Scientist and Director of both Fast Reactor Technology Group and Engineering Services Group. He is from 24th batch of BARC Training School and joined IGCAR in 1981. He graduated in Electrical Engineering from NIT, Calicut. His initial contributions include purification, transportation and charging of sodium required for FBTR, calibration of FBTR sodium flowmeters and other sodium experiments in support of FBTR. He has been steering a multidisciplinary programme in the area of Sodium Technology. He is primarily responsible for design, construction, commissioning, safe operation and maintenance of high temperature experimental sodium facilities and conducting sodium experiments in support of FBR. He has made substantial contributions towards testing of PBFR model steam generator in SGTF and PFBR fuel handling machines at reactor operating conditions in LCTR. He was also involved in the development of permanent magnet flowmeters and special type of heaters required for FBR sodium systems. He has played a key role in the receipt and safe transfer of 1750 tonnes of nuclear grade liquid sodium to PFBR storage tanks. He has published more than 140 papers in reputed national and international journals. He is a member of Indian Nuclear Society, Instrument Society of India and a fellow of Institution of Engineers (India).

Shri Rajnish Prakash, Distinguished Scientist and Chairman & Chief Executive is steering Heavy Water Board - an organization responsible for production of key input materials (like heavy water, ^{10}B enriched boron, organo-phosphorus solvents) for Indian Nuclear Power Programme. Shri Prakash is a Chemical Engineer from IIT, Roorkee and did his Post-graduation in Chemical Reaction Engineering from IIT Delhi. Shri Prakash is accredited with many credentials like development of speciality catalyst for ammonia based Heavy Water Plants, pilot plant study for development of NH_3-H_2O Exchange process, initiating export of Heavy Water to countries of N. America, Europe and Asia. He is instrumental in promoting non-nuclear applications of deuterium, process development for indigenous production of ^{18}O enriched water and generating awareness in medical fraternity regarding possible use of Deuterium Depleted Water (DDW) in adjuvant treatment of cancer. In recognition of excellent contribution by Shri Prakash for steering the technology for large scale production of strategic materials required for the success of Indian Nuclear Power Programme, “Technology Excellence Award-Strategic Materials” was bestowed on him during Indian Technology Congress-2013 at Bangalore. He was conferred with ‘Outstanding Engineer Award’ at 28th Indian Engineering Congress, Annual Convention of The Institution of Engineers (India) in December, 2013 for his exemplary leadership and steering Heavy Water Board to newer heights in performance and diversification. Shri Prakash is a recipient of DAE’s Group Achievement Award for the year 2009 and 2010.

Shri M. Raju is from Indian Administrative Service of the 2005 Batch, Jammu & Kashmir Cadre. He has done M.Sc. (Microbiology) and M.A. (History). Major postings held by him so far include District Magistrate and Collector, Kargil District (2010-2012), Vice-Chairman, Kargil Renewable Energy Development Agency, Chairman, DSSRB, Additional Secretary, Department of Rural Development, Government of Jammu & Kashmir. In October 2013, he joined Department of Atomic Energy as Internal Financial Adviser, Indira Gandhi Centre for Atomic Research.

Shri N. Saibaba is a Gold medalist from Andhra University. He joined the 19th batch of Training School, Mumbai and is the recipient of Bhabha Award for topping the batch. He developed expertise in the manufacture of seamless tubes in a variety of strategic and exotic materials employing hot and cold deformation processes for meeting critical requirements of Atomic Energy, Space and Defence. He has made several pioneering contributions in the manufacture of critical core components of Power Reactors, some of which were developed for the first time in the country. He was responsible, for developing a new manufacturing route for extremely thin walled "Seamless Calandria Tubes" for the first time in the world. Shri Saibaba, as a team leader, developed a test loop with components made of high temperature alloy Nb-1Zr-0.1C. It is to his credit that the seamless tubes in 304H (Cu) and Inconel-617 for use in the Advanced Ultra Supercritical Boilers were developed to enhance the thermal efficiency of the Thermal Power Plants from 28 to 47%. He is presently engaged as Director on the Boards of UCIL & IREL and IGCAR Council. Presently, he is the Chairman of Indian Institute of Metals (IIM), Hyderabad Chapter and Chairman for Indian Society for Non-Destructive Testing (ISNT), Hyderabad Chapter He is appointed as Chairman for Center of Plant Engineering Services (CoPES). He received Bharat Ratna Sir M. Visvesvaraya Award from the Institution of Engineers (India), DAE Award for Group contribution as Group Leader - 2006, 2009, 2010, 2011 & 2012,INS Award for contributions in the field of Nuclear Fuel Cycle Technologies - 2008, Annual NFC Award for Meritorious contribution - 2005, 2006 & 2007, Outstanding contribution from NFC Management - 1993 & 1998. He is a Fellow of Andhra Pradesh Academy of Sciences, Life Member of IIM, ISNT and INS.

Dr. S.A.V. Satya Murty did his B.Tech. from Jawaharlal Nehru Technological University in 1977. He was a University Gold Medalist in his B.Tech. Later, he joined one year orientation course in Nuclear Science & Engineering (21st Batch) at BARC. He was awarded Homi Bhabha prize for securing 1st rank. In the initial years, he was working in the Central Data Processing System Section of FBTR. In 1981, he joined Computer Division and played a key role in the establishment of Mainframe Computer System for IGCAR. He is instrumental in establishing internet and E-Mail facilities, Network Security Systems, IGCAR Campus network etc. He also played an important role in the installation and development of High Performance Computing Facility, Intra DAE VSAT Network (Anunet), Grid Computing facility, PFBR Simulator, Advanced Visualization Centre, Wireless Sensor Networks lab etc.. He has more than 110 Journal Publications / Conference Papers and edited two International Conference Proceedings. Currently, he is the Director of EIRSG and is responsible for the development of robust I&C systems for PFBR.

Dr. D.N. Sharma, Director, Health Safety and Environment Group, BARC is from 14th OCES of BARC training school and has since then pursued R&D in the area of Fission Process modeling, Radiation Physics, Radiation Protection and allied fields. He was also involved in the development of systems procedure and protocols for radiation safety, Emergency Preparedness & Response both at DAE and at National level. Some of the systems like Aerial Gamma Spectrometer developed by him had got International recognition when it was used for around two years by IAEA team at Georgia (Russia) to search orphan sources. Currently, he is the National Emergency Response Director and member of the Crisis Management Group (CMG) of DAE and BARC. He is a member of a number of National committees constituted by MHA (Ministry of Home affairs) and NDMA (National Disaster Management Authority). He was also a member of RASSC (Radiation Safety Standards committee) of IAEA for nearly 12 years and is currently a member of advisory committee of IAEA for GNSSN (Global Nuclear Safety and Security Network). He played a pivotal and leading role in development of radiation surveillance systems and their mass production. He has untiringly pursued and is successfully implementing deployment of these State-of-the-Art systems at all Seaports, Airports and border crossings of the country for detection and eventual prevention of illicit trafficking of the radioactive materials. He is instrumental in building the capacity of defence forces, paramilitary including police and NDRF at the national level for prompt and effective response against radiological emergencies in the public domain. Towards this endeavor he took pioneering step in design of course contents and field exercises for training these personnel.

Shri G. Srinivasan is a mechanical engineer from the 18th batch of BARC Training School. He joined FBTR project as a designer in 1975, and participated in the design, fabrication and installation of Reactor Assembly Components. He moved over to O&M in 1983. After holding the positions of Senior Engineer (Planning) & Senior Engineer (Technical), he took over as Technical Services Superintendent and later as AD (O&M). He is Director, ROMG since September 2008.

Dr. P.K. Vijayan is a chemical engineer from the 1975 batch of the University of Calicut and obtained his PhD from the Department of Energy Systems Engineering, IIT Bombay in 1989. A Distinguished Scientist, Dr Vijayan is currently working as Director, Reactor Design and Development Group at the Bhabha Atomic Research Centre (BARC). His field of expertise is experimental and theoretical thermal hydraulics of nuclear reactors and has more than three and a half decades of experience in this field. He played a key role in the thermal hydraulic design of Advanced Heavy Water Reactor (AHWR). Dr Vijayan is presently involved in the thermal hydraulic design validation for AHWR and Pressurised Heavy Water Reactor (PHWR-700). He is also leading the Indian High Temperature Reactor and molten salt reactor program. Dr Vijayan and his group established several major research facilities for the Indian PHWR and the AHWR. Besides he is leading the group developing the solar thermal power plant based on the beam down concept. He participated in several International Atomic Energy Agency (IAEA) coordinated research projects and bilateral research projects like Indo-Italian, Indo-German, Indo-UK, Indo-Korea and AERB-US NRC. He also worked as a guest scientist at Gesselschaft for Reaktor Sicherheit (GRS), Garching, Munich, Germany and IAEA, Vienna, Austria. He was invited by IAEA to formulate a training course on ‘Natural circulation phenomena and passive safety systems for advanced water cooled reactors and is a lecturer for this IAEA training course since 2004. He has delivered invited talks at several international conferences and served as an examiner for PhD thesis of several reputed national and foreign universities. He is professor and convener, Board of Studies, Homi Bhabha National Institute (HBNI). He has guided six doctoral thesis students of HBNI and Indian Institute of Technology (IIT), Bombay. He has more than two hundred publications to his credit. He is a recipient of the DAE Technical Excellence and Homi Bhabha Science and Technology awards. He is a life member of several professional bodies like the Indian Nuclear Society, Indian Institute of Chemical Engineers and Indian Society for Heat and Mass Transfer. He was also the vice president of the Indian Society for Heat and Mass Transfer during the period 2009-13.

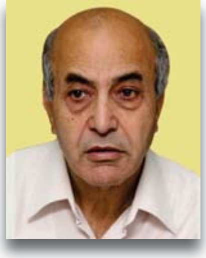

Shri P.K. Wattal is a Graduate in Chemical Engineering and joined Bhabha Atomic Research Centre (BARC), Trombay after completing 18th Batch of Orientation Programme of BARC Training School. Since then, he has been involved with the R&D activities in the area of backend of nuclear fuel cycle. Presently, as Director, Nuclear Recycle Group, BARC, he is heading the Reprocessing & Waste Management Programmes at the back-end of Nuclear Fuel Cycle at Trombay and holding the responsibility of setting up and operation of Reprocessing and Waste Management Plants. Among the international assignments, Shri Wattal is Chairing a Working Group on Rad-waste of Test Blanket Module for ITER Organization, Cadarache, France. He is also leading Indo-French Bilateral Programme on waste management. He is also a Member of Technical Working Group on Nuclear Fuel Cycle Options and Spent Fuel Management (TWGNFCO) of International Atomic Energy Agency (IAEA), Vienna.

Organisation and Activities of Various Groups

Dr. P.R. Vasudeva Rao
Director, IGCAR

Chemistry Group

Dr. P. R. Vasudeva Rao
Director, CG

Dr. M. Joseph
Head, FChD

Dr. R. Sridharan
Head, MCD

Shri R. R. Ramanarayanan
Head, CFD

The Chemistry Group (CG) is responsible for carrying out R&D to provide inputs with respect to all the chemistry aspects of the fast reactor and its fuel cycle. Besides the R&D activities, the Chemistry Group also provides extensive analytical support using a wide range of analytical techniques to all the programmes at Kalpakkam. The areas of R&D in Chemistry Group include sodium chemistry, chemistry of un-irradiated as well as irradiated fuel materials, development of fuel cycle, high temperature chemistry, analytical chemistry, spectroscopy and boron chemistry. Chemistry Group also has been developing instrumentation and facilities in support of the R&D programme. Development of sensors for PFBR and sensors for environmental applications, development of radionuclide traps for PFBR, development of cleaning and decontamination techniques for fast reactor components, development of technology for production of plutonium rich fuels and minor actinide containing fuels through sol-gel route, development of sodium bonding for metallic fuels and pyroprocessing are some of the R&D programmes on the anvil. Recent achievements include the fabrication of test fuel pins containing microspheres of $(U,Pu)O_2$ for irradiation in FBTR, demonstration of uranium recovery from U-Zr slugs by electrorefining, determination of burn-up of MOX(PFBR) test fuel by HPLC and development of unsymmetrical diglyoclamides as candidate extractants for minor actinide partitioning.

Electronics, Instrumentation and Radiological Safety Group

Dr. S.A.V. Satya Murty
Director, EIRSG

Shri N. Murali
AD, ICG & Head, RTSD

Dr. B. Venkatraman
AD, RSEG & Head, RSD

Shri B. Ananthapadmanaban
Head, QAD

Dr. K.K. Satpathy
Head, EnSD

Dr. D. Thirugnanamurthy
Head, EID

The Electronics, Instrumentation and Radiological Safety Group (EIRSG) is actively involved in the development of Instrumentation & Control for the 500 MWe Prototype Fast Breeder Reactor. Towards this the I&C systems are designed with safety and availability of the reactor as the guiding requirements through redundant systems and also keeping in mind the simplicity of design and maintainability. A judicious combination of hardwired and computer based I&C systems, state-of-the-art design, manufacturing processes and testing were employed in the design of I&C systems. The systems developed include safety critical, safety related and non safety I&C systems. The prototype systems were qualified after rigorous environmental, EMI/EMC and seismic testing. The application software developed was subjected to thorough Verification & Validation procedures. The group is also developing a full scope replica type Operator Training Simulator for PFBR. An advanced visualization centre was established and various PFBR systems are modeled for visualization in 3D and walkthrough. R&D activities in the areas of innovative instrumentation using pulsating sensors, Wireless Sensor Networks for use in future reactors, computational intelligence, knowledge management etc. are in progress. State-of-the-art computational facilities with a total processing power of about 30 teraFLOPS and data communication facilities are being provided. To take care of the security challenges the security electronics systems are constantly deployed and upgraded. The group is also responsible for providing quality assurance/quality control services for all the major projects being undertaken by IGCAR through the ISO 9001-2008 certified Quality Assurance Division. The Radiological Safety Division of the Group is responsible for R&D activities in the areas of radioactivity transport and improving the radiation detection and measurements through advanced techniques. This Division provides health physics and radiation safety services for the radioactive facilities in IGCAR. Environmental and Industrial Safety Division provides industrial safety services to all the facilities at IGCAR. This Division also carries out R&D in the domain of aquatic and terrestrial biodiversity and sediment characterization. The Group organizes public awareness programmes on radiation safety and nuclear energy in addition to training and awareness programmes on industrial, radiation and fire safety to occupational workers.

Engineering Services Group

Shri K.K. Rajan
Director, ESG

Shri A. Jyothish Kumar
AD, ESG & Head, ESD

Shri C. Sivathanu Pillai
AD, CEG

Shri C. Chandran
Head, AC&VSD

Shri B. Harikrishnan
Head, CMWD

Shri G. Kempulraj
Head, CWD

Shri C. Sundaramurthy
Head, ASED

The Engineering Services Group (ESG) is responsible for providing quality services and activities pertaining to Civil engineering, Electrical Engineering, Voice Communication Systems, Air-conditioning and Ventilation Systems, Material Handling Equipments and Central Workshop activities. The group also coordinates the BSNL requirements of the Centre. The group has a mandate to establish additional infrastructure requirements so as to meet Design, R&D and operational objectives of IGCAR. The group has expert teams with capability to design, engineer and execute systems under their jurisdiction. Electricity, water, quality-air and other services including services from Central Workshop are being extended to other units of DAE located at Kalpakkam. The nature of work involves interaction with several State Government and Central Government Organisations. AC&VSD is responsible for providing reliable air-conditioning and ventilation services to various radioactive laboratories and R&D facilities of the Centre.

Fast Reactor Technology Group


Shri K.K. Rajan
Director, FRTG


Shri B. Babu
Head, IDSD


Shri B. K. Nashine
Head, DDRSD


Shri G. Padmakumar
Head, SEHD & CTD


Shri V. Prakash
Head, VDD

Fast Reactor Technology Group (FRTG) has the mandate of development and testing of reactor components of FBRs. The group is responsible for the engineering development and testing of many components of PFBR in air, water and sodium. Design validation of critical components of FBRs are achieved through experiments in sodium and water using full scale/scaled down models. FRTG has acquired expertise in the development of sensors and devices for sodium application, such as- EM flow meters, level probes, leak detectors, cold traps and electromagnetic pumps. The group is entrusted with the responsibility of engineering development towards scaling up of pyro processing techniques from laboratory to engineering scale and setting up of engineering scale facilities which is in progress. Expertise has been developed in sodium handling in the design, construction, commissioning and operation of high temperature sodium systems. The major sodium test facilities of FRTG include 5.5 MWt Steam Generator Test Facility (SGTF) for testing the model steam generators of FBRs, SADHANA loop for experimentally demonstrating natural convection based safety grade decay heat removal system of FBRs, Large Component Test Rig (LCTR) for testing critical full scale FBR components, In Sodium Test facility (INSOT) for creep and fatigue testing of advanced materials and Sodium Water Reaction Test (SOWART) facility to study self wastage and impingement wastage of SG tubes. Recent achievements of FRTG towards PFBR include qualification and testing of reactor components like Inclined Fuel Transfer Machine (IFTM), Transfer Arm(TA), under sodium ultrasonic scanner, design, fabrication and qualification of extended spark plug type leak detector, in-sodium calibration of permanent magnet flowmeters and sodium testing of RADAR level probes. FRTG is also involved in the developmental efforts towards improving the economics and enhancing the safety of future FBRs. The fabrication of integrated cold trap for in-vessel purification, integrated testing of Stroke Limiting Device with CSRDM, development of in-sodium pressure measurement device and ex-vessel level probe for sodium applications are some of the activities that was pursued for future FBRs. Major activities currently being pursued in FRTG include development of SONAR device for subassembly vibration measurement, conduct of high temperature tribology and thermal striping experiments for evaluating FBR component materials and design, fabrication and erection of various test facilities namely Sodium Facility for Component Testing, Sodium Technology Complex and Engineering Hall-IV.

Materials Science Group

Shri M.P. Janawadkar
Director, MSG

Dr. G. Amarendra
Head, MPD

Dr. A. Bharathi
Head, CMPD

Dr. A.K. Tyagi
Head, SND

The Materials Science Group (MSG) has the mandate of pursuing high quality basic research on topical problems in Materials Science and comprises of three divisions. The Condensed Matter Physics Division focuses on the investigation of structure and physical properties of materials under extreme conditions such as high pressures, low temperatures, high temperatures and high magnetic fields. Active research programs related to the use of Raman Spectroscopy for studies of vibrational properties of materials, use of Dynamic Light Scattering and Confocal Microscopy for studies on soft condensed matter, use of laser heated diamond anvil cell facility for synthesis of materials under high pressures and high temperatures and investigations on physical properties of novel materials at low temperatures, high magnetic fields and high pressures are being pursued. Several SQUID based measuring systems such as high field SQUID magnetometer, SQUID VSM, SQUID based set-up for Non-Destructive Evaluation (NDE), and multichannel SQUID based systems for Magneto-cardiography (MCG) and Magneto-encephalography (MEG) have been successfully designed and assembled. The Materials Physics Division focuses on studies on Ion beam simulation of radiation damage using a 1.7 MV tandem accelerator, studies on defects using Positron Annihilation Spectroscopy and Computer simulation of material properties. Several nuclear techniques such as Time Differential Perturbed Angular Correlation (TDPAC), Auger Electron Spectroscopy, Mossbauer Spectroscopy etc. have been used for the study of condensed matter, while positron beam set-up is used for depth resolved studies of defects. The Surface and Nanoscience Division focuses on studies on thin films, multilayers and hard coatings using a variety of techniques such as Secondary Ion Mass Spectrometry, nanomechanical testing and Scanning Probe Microscopy. Research activities relating to sensors based on nanomaterials, micromachined cantilevers and MEMS are being pursued.

Metallurgy and Materials Group


Dr. T. Jayakumar
Director, MMG


Dr. A. K. Bhaduri
AD, MDTG


Dr. U. Kamachi Mudali
AD, CSTG


Dr. S. Venugopal
AD, GRIP & Head, RIRD


Dr. M. Vijayalakshmi
AD, PMG


Shri Jojo Joseph
Head, PIED


Dr. K. Laha
Head, MMD


Shri E. Mohandas
Head, MSSCD


Dr. B. Purna Chandra Rao
Head, NDED


Dr. Saroja Saibaba
Head, MTPD


Dr. Shaju K. Albert
Head, MTD

The Metallurgy and Materials Group (MMG) of IGCAR has been nurturing a vibrant research and development programme which is targeted to provide a comprehensive knowledge-base and active support to a variety of materials related issues of India's sodium cooled fast reactors (SFR) and associated closed fuel cycle activities. In the recent past, MMG has made major strides towards the successful development of three generations of nuclear structural materials aimed at withstanding demanding operating and environmental conditions. A few notable among them include: swell-resistant austenitic and high Cr-based ferritic steels, especially the oxide dispersion strengthened (ODS) variety for SFR core components. Besides, MMG is also involved in the development of an array of novel application specific or functional materials such as ferroseals for sodium pumps, ferroboron for meeting the requirement of cheap and alternate neutron shield material, iron based soft magnetic alloy for control rod applications and corrosion resistant materials, coatings for aqueous and pyrochemical reprocessing applications. In addition, MMG has also pioneered the design, fabrication and in-pile testing of irradiation capsules. Extensive post irradiation examination facilities established have been effectively utilized for obtaining extremely valuable data on the in-pile performance of various fuels, structural and shielding materials. In an allied perspective, MMG has immensely contributed towards developing a spectrum of nuclear application specific non destructive evaluation (NDE) techniques for inspecting and qualifying large sized and intricate reactor components. The human resource expertise of MMG is one of a balanced and unique blend of experienced and energetic talents, whose specialty touches almost all branches of theoretical and experimental aspects of materials science, component manufacturing & inspection-qualification technology. Mention must be made of MMG's contribution on the development of advanced welding techniques for joining special materials with tight control over process parameters and ensuring component integrity, automated and robotic systems for remote inspection of critical nuclear engineering components as well as for post irradiation examination facilities. On the theoretical front, robust modelling protocols for predicting high temperature phase stability, thermophysical properties, deformation behavior and mechanical properties of materials under various loading conditions etc. are also being pursued by MMG. It is not an exaggeration to say that MMG houses a truly sprawling and state of the art materials characterization and testing facilities that have been put into use for catering to the materials developmental issues of not only fission and fusion nuclear reactors; but also for the advanced ultra super critical (AUSC) power plant programme. Besides, availability of top quality technical expertise has made it possible to attract many a young brain to pursue their research programmes at MMG under the banner of Homi Bhabha National Institute (HBNI).

Reactor Design Group


Dr. P. Chellapandi
Director, RDG


Shri K. Madhusoodanan
AD, PPG & Head, I&CD


Shri P. Puthiyavinayagam
AD, CDG


Shri P. Selvaraj
AD, RAG


Shri V. Balasubramaniyan
Head, RCD


Dr. K. Devan
Head, RND


Shri A. John Arul
Head, RSDD


Shri B. K. Nashine
Head, SED


Shri S. Raghupathy
Head, CHMD


Shri N. Theivarajan
Head, PPCD


Dr. K. Velusamy
Head, MHD

The Reactor Design Group (RDG) is responsible for analysis of FBR power plant systems, design and development of components including core, shutdown, handling mechanisms and balance of plant. The group is responsible for getting safety clearance from Atomic Energy Regulatory Board (AERB). The group comprises of Core Design Group (CDG), Reactor Analysis Group (RAG), Power Plant Group (PPG), Reactor Components Division (RCD) and Component Handling & Mechanism Division (CHMD). The group also executes R&D in the domain of structural mechanics, thermal hydraulics and safety engineering, involving national and international institutions. It provides design support to the construction and commissioning of 500 MWe Prototype Fast Breeder Reactor (PFBR), which is under construction at Kalpakkam. It also provides analytical support to other groups in the Centre including Fast Breeder Test Reactor (FBTR) as well as for other strategic and high end technologies in the country. The responsibility of the group includes developing high quality human resource for the design and analysis of SFRs in the country. It is currently engaged in conceptualizing as well as detailing the innovative reactor components for the reactor assembly of future SFRs. The group has about 145 scientists and engineers. These apart, it has a modern design office with many advanced modeling and analysis softwares, Structural Mechanics Laboratory (SML) having state-of-the-art facilities for carrying out tests on large components, high temperature structural integrity and seismic tests with large sized shake tables and safety research laboratory (SRL) for carrying out tests in the domain of severe accidents and to study the science & technology of sodium fires and fire extinguishers. This group has expertise in the domain of design of mechanisms operating in sodium, mechanical design and analysis of components as per the American (ASME) and French (RCC-MR) design codes, thermal hydraulics of liquid metal, plant dynamics etc. The group is periodically providing design supports to other national mission projects, especially in space and other energy sectors.

Reprocessing Group

Dr. R. Natarajan
Director, RpG

Shri A. Ravishankar
AD, RPOG

Shri V. Sundararaman
AD, PDCG & Head, FRPD

Shri B. M. Anandarao
Head, RPDD

Dr. U. Kamachi Mudali
Head, RRDD

Shri V. Vijayakumar
Head, RPOD

The success of Indian Fast Breeder Reactor (FBR) programme depends on closing the fuel cycle within a short period so that the inventory of fissile material outside the reactor can be as small as possible. The Reprocessing Group (RpG) of IGCAR is responsible for achieving this objective. Various activities with regard to the fast reactor fuel reprocessing technology such as the design, construction and operation of the reprocessing plants are being undertaken by this group. There are facilities to carry on extensive engineering scale testing of equipment and systems before installation in radioactive hot cells. Chopper, dissolver, feed clarification equipment, centrifugal extractors and different types of pulse columns are few important equipments that are being developed for deployment in fast reactor fuel reprocessing plants. Apart from equipment development, research is towards understanding and solving various process, chemistry and analytical problems of fast reactor fuel reprocessing such as, process flow sheet studies to improve the plant performance for higher recoveries and reduced waste generation, mathematical modeling of solvent extraction of the complex U-Pu system, solvent management, development of alternate solvent-diluent systems, development of online monitoring of Pu for process control, liquid flow metering in high radioactive fields, development of material handling equipment inside the hot cells etc. In one of the hot cell facilities, uranium was recovered from irradiated thorium rods using THOREX process which is used as fuel in KAMINI reactor and in FBTR (as PFBR test fuel). The other hot cell facility, called CORAL (Compact facility for Reprocessing Advanced fuels in Lead cells) commissioned in 2003, is being deployed as a versatile test bed for validating the process flow sheet and scaling up of equipment designs for fast reactor fuel reprocessing, by processing the FBTR spent fuel. This experimental facility has been used for reprocessing several batches of mixed carbide fuels irradiated in FBTR with 25, 50, 100 and 155 GWd/t burn-ups. This has provided valuable experience to the design of Demonstration Fast Reactor Fuel Reprocessing Plant in which all the types of fuels, such as the mixed carbide and oxide of different compositions, will be reprocessed on a regular basis. DFRP is also designed to reprocess PFBR fuel sub-assemblies for demonstrating the reprocessing of irradiated PFBR oxide fuels.In addition to these activities, RpG is also carrying out the design of the reprocessing plant, for reprocessing spent fuels of PFBR on commercial basis.

Reactor Operations and Maintenance Group


Shri G. Srinivasan
Director, ROMG


Shri K.V. Suresh Kumar
AD, OMG


Ms. S. Usha
AD, TTG


Dr. S. Anthonysamy
Project Manager, DFMF


Shri A. Babu
Head, RMD


Shri N. Kasinathan
Head, RAD


Shri G. Shanmugam
Head, ROD


Dr. B.S. Panigrahi
Head, RC


Shri S. Varatharajan
Head, TSD

The Reactor Operation and Maintenance Group (ROMG) is responsible for safe operation of Fast Breeder Test Reactor (FBTR) and KAMINI Reactor within the limits given in technical specification documents. The group also takes part in the operational safety review of PFBR Project documents. The Training section of the group is responsible for training the O&M staff of PFBR and future FBRs besides training O&M staff of FBTR and KAMINI. Progressive modifications in FBTR to increase its availability and for gaining newer experience in operation, utilizing the reactor for irradiation of advanced fuels and materials for fast reactors and conducting safety related experiments form a major part of ROMG's activities.

Resources Management Group


Dr. M. Sai Baba
AD, RMG & Head,
SIRD/SPHRDD

Resources Management Group (RMG) has the mandate of planning and management of financial (budget), human and scientific information resources of the Centre. The group comprises of the Scientific Information Resource Division, Strategic Planning and Human Resources Development Division and OCES- Training Section.

Scientific Information Resource Division has the mandate of providing information resources both in the print form and digital form. The information resources are being provided on the desktop by digital networking with special emphasis to cater to the needs of students and young scholars. The Division, is involved in publishing of important documents of the Centre like IGC Newsletter, IGC Report, Annual Report, Benchmark, which showcase the activities of the Centre and offers photography, bindery and auditorium services to all the Groups in the Centre.

Strategic Planning and Human Resources Development Division has the mandate of providing strategic perspectives to decision making in the Centre. Important activities of this Division are Budget Planning and monitoring, which involves preparation of proposals, generation of periodic reports and review to meet the targets projected and implementing Workflow Management System to integrate the flow of information between employee, administration, accounts and purchase. This Division also interacts and coordinates with National and International delegates towards facilitating collaborative projects with various academic and industrial institutions. Technical Coordination, Liaisoning and conducting Public Awareness Programmes for dispelling fears and concerns about our organization to public and media is also the mandate of the Strategic Planning and Human Resources Development Division.

OCES- Training Section is responsible for conducting the Academic Programmes of BARC Training School at IGCAR

Fast Reactor Fuel Cycle Facility

Dr. R. Natarajan
Project Director

Fast Reactor Fuel Cycle Facility is entrusted with the work of planning, designing and constructing the Fast Reactor Fuel Cycle Facility to close the fuel cycle of PFBR. FRFCF is a multi unit project involving BARC, IGCAR and NFC. IGCAR is piloting the work on this project. The Group interacts with the participating groups from different units of DAE. Coordination of activities related to design of the facility, obtaining regulatory and statutory approvals for the project, preparation of the detailed project report, processing for obtaining financial sanction and development of infrastructure at the project site, is the mandate of this group.

Madras Regional Purchase Unit

Shri S. Paramasivam
RD, MRPU

Material Management activities for IGCAR, GSO, BARCF & HWP(T) are taken care of by Madras Regional Purchase Unit (MRPU) which comes under Directorate of Purchase & Stores of Department of Atomic Energy. Procurement and payment to suppliers are carried out at Chennai and inventory and accounting are carried out by Central Stores at Kalpakkam. MRPU was the first DAE unit to introduce e-tendering and more than 70% of files were processed by e-tendering mode in the e-tender portal www.tenderwizard.com/DAE. During the year 2014, MRPU processed about 4300 indents with an estimated cost of 770 Crores and released about 3700 purchase orders worth 372 Crores.

Technical Co-ordination & Quality Control Division

Shri N. Vijayan Varier
Head, TC&QCD

Technical Co-ordination & Quality Control Division is primarily responsible for quality control of several critical equipments for IGCAR and provides technical co-ordination services in the Western Region. TC&QCD also participates in a number of R&D activities which are being carried out at BARC towards meeting the mandate of IGCAR and PFBR. TC&QCD participates in the R&D activities for development of high temperature fission chambers, other neutron detectors for PFBR along with various divisions of BARC and ECIL, under sodium ultrasonic scanner, PIED scanner for pressure tube, sweep arm scanner, ISI vehicle development and manufacture at Pune and sputter ion pump development at BARC and inspection. TC&QCD participated in the inspection activities for the major components of welded grid plate technology development, inner vessel section model technology development for welding of tri-junction forging, safety grade decay heat exchanger and air heat exchanger models, sodium to air heat exchanger, ECR Heaters and PFBR Neutron Detector Assembly components for development.

Administration & Accounts

Shri M. Raju
Internal Financial Adviser

Shri N. G. Krishnan
Chief Administrative Officer

Shri K. R. Sethuraman
AO(R&SR) & Secretary, IGCSC

LIST OF IMPORTANT ABBREVIATIONS

AC&VSD	Air Conditioning and Ventilation System Division
AERB	Atomic Energy Regulatory Board
ASED	Architecture & Structural Engineering Division
BARC	Bhabha Atomic Research Centre
BARCF	Bhabha Atomic Research Centre Facilities
BHAVINI	Bharatiya Nabhikiya Vidyut Nigam Limited
CD	Computer Division
CDG	Core Design Group
CED	Civil Engineering Division
CEG	Civil Engineering Group
CFD	Chemical Facilities Division
CG	Chemistry Group
CTD	Chemical Technology Division
CHMD	Components Handling & Mechanism Division
CMPD	Condensed Matter Physics Division
CMWD	Contracts & Major Works Division
CORAL	Compact facility for Reprocessing Advanced fuels in Lead cell
CSTG	Corrosion Science & Technology Group
CWD	Central Workshop Division
DDRSD	Device Development and Rig Services Division
DFMFF	Demonstration Facility for Metallic Fuel Fabrication
EID	Electronics and Instrumentation Division
EIRSG	Electronics and Instrumentation and Radiological Safety Group
EnSD	Environmental & Safety Division
ESD	Electrical Services Division
ESG	Engineering Services Group
FBR	Fast Breeder Reactor
FBTR	Fast Breeder Test Reactor
FChD	Fuel Chemistry Division
FRFCF	Fast Reactor Fuel Cycle Facility
FRPD	Fuel Reprocessing Process Division
FRTG	Fast Reactor Technology Group
GRIP	Group for Remote Handling, Robotics, Irradiation Experiments and PIE
GSO	General Services Organisation
IAEA	International Atomic Energy Agency
IIT	Indian Institute of Technology
IDSD	Instrumentation Development & Services Division
IMSc	Institute of Mathematical Sciences
ICD	Instrumentation & Control Division
ICG	Instrumentation & Control Group
LMFBR	Liquid Metal Cooled Fast Breeder Reactor
MAPS	Madras Atomic Power Station
MCD	Materials Chemistry Division
MDTG	Materials Development and Technology Group
MHD	Mechanics & Hydraulics Division
MMD	Mechanical and Metallurgy Division
MMG	Metallurgy and Materials Group
MPD	Materials Physics Division
MRPU	Madras Regional Purchase Unit
MSG	Materials Science Group
MSSCD	Materials Synthesis & Structural Characterization Division
MTD	Materials Technology Division
MTPD	Microscopy & Thermo-Physical Property Division
NDED	Non-Destructive Evaluation Division
NFC	Nuclear Fuel Complex
NICB	Nuclear Island Connected Building
NPCIL	Nuclear Power Corporation of India Ltd.
PDCG	Process Design & Commissioning Group
PFBR	Prototype Fast Breeder Reactor
PHWR	Pressurized Heavy Water Reactor
PIED	Post Irradiation Examination Division
PMG	Physical Metallurgy Group
PPCD	Power Plant Control Division
PPG	Power Plant Group
PDCG	Process Design & Commissioning Group
QAD	Quality Assurance Division
RAD	Reactor Analysis Division
RAG	Reactor Analysis Group
RCD	Reactor Components Division
RDG	Reactor Design Group
RIRD	Remote Handling, Irradiation Experiments and Robotics Division
RMD	Reactor Maintenance Division
RMG	Resources Management Group
RND	Reactor Neutronics Division
ROD	Reactor Operation Division
ROMG	Reactor Operation and Maintenance Group
RPDD	Reprocessing Plant Design Division
RpG	Reprocessing Group
RPOD	Reprocessing Plant Operations Division
RPOG	Reprocessing Projects & Operation Group
RRDD	Reprocessing Research and Development Division
RSD	Radiological Safety Division
RSDD	Reactor Shielding and Data Division
RSEG	Radiological Safety & Environmental Group
RTSD	Real Time Systems Division
SED	Safety Engineering Division
SE&HD	Sodium Experiments & Hydraulics Division
SGTF	Steam Generator Test Facility
SIRD	Scientific Information Resource Division
SND	Surface and Nanoscience Division
SOWART	Sodium Water Reaction Test facility
SPHRDD	Strategic Planning & Human Resource Development Division
TC&QCD	Technical Coordination & Quality Control Division
TSD	Technical Services Division
TTG	Technical & Traning Group
VDD	Vibration Diagnostics Division

INDIRA GANDHI CENTRE FOR ATOMIC RESEARCH

Dr. P. R. VASUDEVA RAO
DIRECTOR, IGCAR

IGC COUNCIL

IGC SCIENTIFIC COMMITTEE [IGCSC]

DIRECTOR'S ADVISORY COMMITTEE [DAC]

Dr. P. R. VASUDEVA RAO
DIRECTOR
CHEMISTRY GROUP

Shri M.P. JANAWADKAR
DIRECTOR
MATERIALS SCIENCE GROUP

Dr. S.A.V. SATYA MURTY
DIRECTOR
ELECTRONICS, INSTRUMENTATION AND RADIOLOGICAL SAFETY GROUP

Dr. T. JAYAKUMAR
DIRECTOR
METALLURGY & MATERIALS GROUP

Shri K.K. RAJAN
DIRECTOR
ENGINEERING SERVICES GROUP

Dr. P. CHELLAPANDI
DIRECTOR
REACTOR DESIGN GROUP

Shri K.K. RAJAN
DIRECTOR
FAST REACTOR TECHNOLOGY GROUP

Shri G. SRINIVASAN
DIRECTOR
REACTOR OPERATIONS & MAINTENANCE GROUP

Dr. R. NATARAJAN
PROJECT DIRECTOR
FAST REACTOR FUEL CYCLE FACILITY

Dr. R. NATARAJAN
DIRECTOR
REPROCESSING GROUP

Dr. M. SAI BABA
ASSOCIATE DIRECTOR
RESOURCES MANAGEMENT GROUP

Shri N. VIJAYAN VARIER
HEAD
TECHNICAL CO-ORDINATION & QUALITY CONTROL DIVISION*

Shri M. RAJU
INTERNAL FINANCIAL ADVISER
ACCOUNTS

Shri N.G. KRISHNAN
CHIEF ADMINISTRATIVE OFFICER
ADMINISTRATION

as on 31-12-2014

*Stationed at BARC, Mumbai

Groups / Divisions / Heads

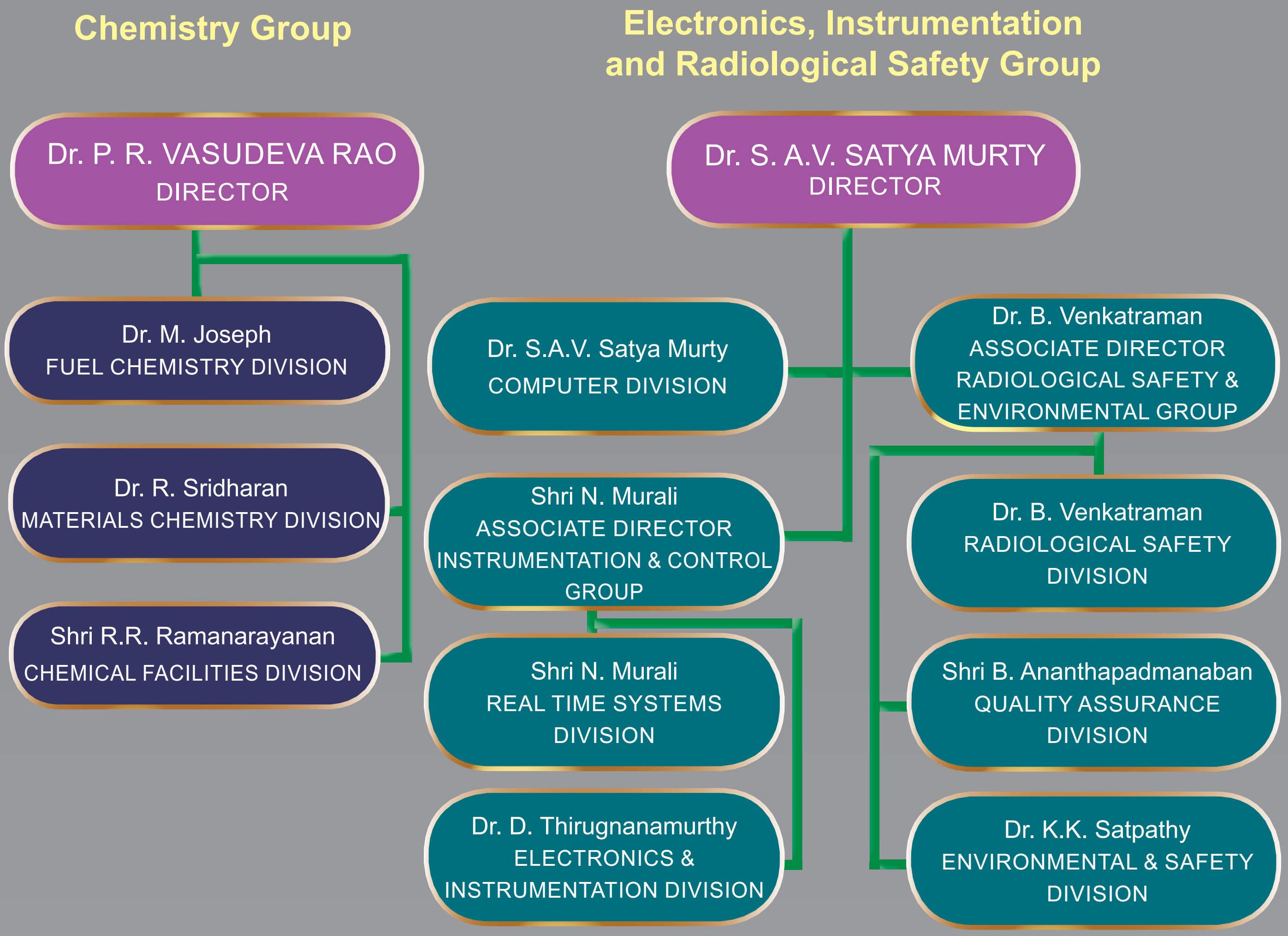

Chemistry Group

Dr. P. R. VASUDEVA RAO
DIRECTOR

- Dr. M. Joseph
  FUEL CHEMISTRY DIVISION
- Dr. R. Sridharan
  MATERIALS CHEMISTRY DIVISION
- Shri R.R. Ramanarayanan
  CHEMICAL FACILITIES DIVISION

Electronics, Instrumentation and Radiological Safety Group

Dr. S. A.V. SATYA MURTY
DIRECTOR

- Dr. S.A.V. Satya Murty
  COMPUTER DIVISION
- Dr. B. Venkatraman
  ASSOCIATE DIRECTOR
  RADIOLOGICAL SAFETY & ENVIRONMENTAL GROUP
  - Dr. B. Venkatraman
    RADIOLOGICAL SAFETY DIVISION
  - Shri B. Ananthapadmanaban
    QUALITY ASSURANCE DIVISION
  - Dr. K.K. Satpathy
    ENVIRONMENTAL & SAFETY DIVISION
- Shri N. Murali
  ASSOCIATE DIRECTOR
  INSTRUMENTATION & CONTROL GROUP
  - Shri N. Murali
    REAL TIME SYSTEMS DIVISION
  - Dr. D. Thirugnanamurthy
    ELECTRONICS & INSTRUMENTATION DIVISION

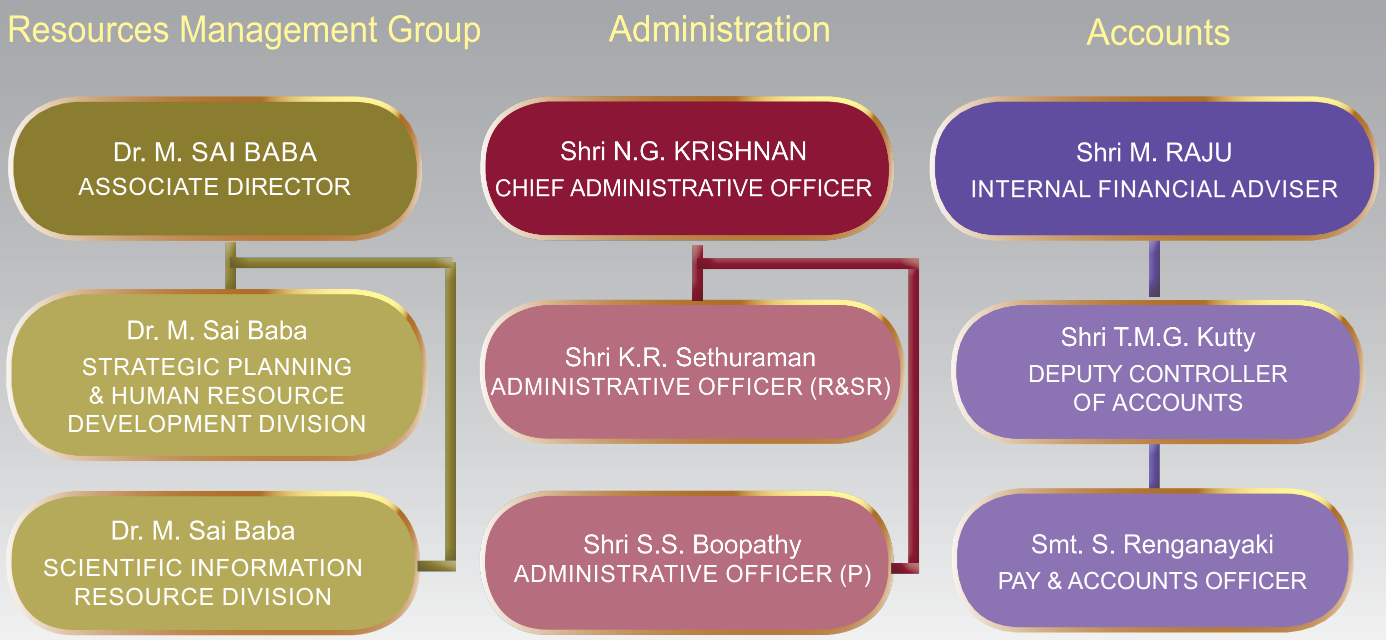

Resources Management Group

Dr. M. SAI BABA
ASSOCIATE DIRECTOR

- Dr. M. Sai Baba
  STRATEGIC PLANNING & HUMAN RESOURCE DEVELOPMENT DIVISION
- Dr. M. Sai Baba
  SCIENTIFIC INFORMATION RESOURCE DIVISION

Administration

Shri N.G. KRISHNAN
CHIEF ADMINISTRATIVE OFFICER

- Shri K.R. Sethuraman
  ADMINISTRATIVE OFFICER (R&SR)
- Shri S.S. Boopathy
  ADMINISTRATIVE OFFICER (P)

Accounts

Shri M. RAJU
INTERNAL FINANCIAL ADVISER

- Shri T.M.G. Kutty
  DEPUTY CONTROLLER OF ACCOUNTS
  - Smt. S. Renganayaki
    PAY & ACCOUNTS OFFICER

Groups / Divisions / Heads

Engineering Services Group

- **Shri K.K. RAJAN**
  DIRECTOR
  - Shri A. Jyothiskumar
    ASSOCIATE DIRECTOR ENGINEERING SERVICES GROUP
    - Shri A. Jyothiskumar
      ELECTRICAL SERVICES DIVISION
    - Shri G. Kempulraj
      CENTRAL WORKSHOP DIVISION
  - Shri C. Chandran
    AIR-CONDITIONING & VENTILATION SYSTEM DIVISION
  - Shri C. Sivathanu Pillai
    ASSOCIATE DIRECTOR CIVIL ENGINEERING GROUP
    - Shri C. Sivathanu Pillai
      CIVIL ENGINEERING DIVISION
    - Shri C. Sundaramurthy
      ARCHITECTURE & STRUCTURAL ENGINEERING DIVISION
    - Shri B. Harikrishnan
      CONTRACTS & MAJOR WORKS DIVISION

Fast Reactor Technology Group

- **Shri K.K. RAJAN**
  DIRECTOR
  - Shri V. Prakash
    VIBRATION DIAGNOSTICS DIVISION
  - Shri G. Padmakumar
    CHEMICAL TECHNOLOGY DIVISION
  - Shri B.K. Nashine
    DEVICE DEVELOPMENT & RIG SERVICES DIVISION
  - Shri G. Padmakumar
    SODIUM EXPERIMENTS & HYDRAULICS DIVISION
  - Shri B. Babu
    INSTRUMENTATION DEVELOPMENT & SERVICES DIVISION

Materials Science Group

- **Shri M.P. JANAWADKAR**
  DIRECTOR
  - Dr. A. Bharathi
    CONDENSED MATTER PHYSICS DIVISION
  - Dr. G. Amarendra
    MATERIALS PHYSICS DIVISION
  - Dr. A.K. Tyagi
    SURFACE & NANOSCIENCE DIVISION

Metallurgy & Materials Group

- **Dr. T. JAYAKUMAR**
  DIRECTOR
  - Dr. S. Venugopal
    ASSOCIATE DIRECTOR GROUP FOR REMOTE HANDLING, ROBOTICS, IRRADIATION EXPERIMENTS AND PIE (GRIP)
    - Shri Jojo Joseph
      POST IRRADIATION EXAMINATION DIVISION
    - Dr. S. Venugopal
      REMOTE HANDLING, IRRADIATION EXPERIMENTS AND ROBOTICS DIVISION
  - Dr. U. Kamachi Mudali
    ASSOCIATE DIRECTOR CORROSION SCIENCE & TECHNOLOGY GROUP
  - Dr. B. Purna Chandra Rao
    NON-DESTRUCTIVE EVALUATION DIVISION
  - Dr. A.K. Bhaduri
    ASSOCIATE DIRECTOR MATERIALS DEVELOPMENT AND TECHNOLOGY GROUP (MDTG)
    - Dr. K. Laha
      MECHANICAL METALLURGY DIVISION
    - Dr. Shaju K. Albert
      MATERIALS TECHNOLOGY DIVISION
  - Dr. M. Vijayalakshmi
    ASSOCIATE DIRECTOR PHYSICAL METALLURGY GROUP
    - Shri E. Mohandas
      MATERIALS SYNTHESIS & STRUCTURAL CHARACTERIZATION DIVISION
    - Dr. Saroja Saibaba
      MICROSCOPY & THERMO-PHYSICAL PROPERTY DIVISION

Groups / Divisions / Heads

Reactor Design Group

Dr. P. CHELLAPANDI
DIRECTOR

- **Shri P. Puthiyavinayagam**
  ASSOCIATE DIRECTOR
  CORE DESIGN GROUP
  - **Dr. K. Devan**
    REACTOR NEUTRONICS DIVISION
  - **Shri A. John Arul**
    REACTOR SHIELDING AND DATA DIVISION
- **Shri K. Madhusoodanan**
  ASSOCIATE DIRECTOR
  POWER PLANT GROUP
  - **Shri K. Madhusoodanan**
    INSTRUMENTATION & CONTROL DIVISION
  - **Shri N. Theivarajan**
    POWER PLANT CONTROL DIVISION
- **Shri V. Balasubramaniyan**
  REACTOR COMPONENTS DIVISION
- **Shri P. Selvaraj**
  ASSOCIATE DIRECTOR
  REACTOR ANALYSIS GROUP
  - **Dr. K. Velusamy**
    MECHANICS & HYDRAULICS DIVISION
  - **Shri B. K. Nashine**
    SAFETY ENGINEERING DIVISION
- **Shri S. Raghupathy**
  COMPONENTS HANDLING & MECHANISM DIVISION

Reactor Operations & Maintenance Group

Shri G. SRINIVASAN
DIRECTOR

- **Shri K.V. Suresh Kumar**
  ASSOCIATE DIRECTOR
  OPERATION & MAINTENANCE GROUP
  - **Shri B. Babu**
    REACTOR MAINTENANCE DIVISION
  - **Shri G. Shanmugam**
    REACTOR OPERATION DIVISION
  - **Dr. B.S. Panigrahi**
    REACTOR CHEMIST
- **Ms. S. Usha**
  ASSOCIATE DIRECTOR
  TECHNICAL & TRAINING GROUP
  - **Shri S. Varatharajan**
    TECHNICAL SERVICES DIVISION
- **Dr. S. Anthonysamy**
  PROJECT MANAGER
  DEMONSTRATION FACILITY FOR METALLIC FUEL FABRICATION
- **Shri N. Kasinathan**
  REACTOR ANALYSIS DIVISION

Reprocessing Group

Dr. R. NATARAJAN
DIRECTOR

- **Shri V. Sundararaman**
  ASSOCIATE DIRECTOR
  PROCESS DESIGN & COMMISSIONING GROUP
  - **Shri V. Sundararaman**
    FUEL REPROCESSING PROCESS DIVISION
- **Shri A. Ravishankar**
  ASSOCIATE DIRECTOR
  REPROCESSING PROJECTS & OPERATION GROUP
  - **Shri V. Vijayakumar**
    REPROCESSING PLANT OPERATIONS DIVISION
  - **Shri B.M. Anandarao**
    REPROCESSING PLANT DESIGN DIVISION
- **Dr. U. Kamachi Mudali**
  REPROCESSING RESEARCH & DEVELOPMENT DIVISION

Published by Scientific Information Resource Division, IGCAR, Kalpakkam - 603 102